MASARYK UNIVERSITY
FACULTY OF MEDICINE
DEPARTMENT OF PATHOLOGICAL PHYSIOLOGY

CELL DEATH AND CELLULAR SECRETION: KEY FACTORS IN CARCINOGENESIS

Habilitation thesis

Brno 2025

RNDr. Jan Balvan, Ph.D.

© Jan Balvan, Masaryk University, 2025

Acknowledgement

I would like to express my deepest gratitude to my former supervisor and current mentor, Professor Michal Masařík, for giving me the opportunity and freedom to delve into scientific areas that I find both enriching and fulfilling.

I am truly grateful to my colleagues, especially Martina Raudenská, Klára Hánělová, Jaromír Gumulec, Tomáš Vičar and Jiří Navrátil, for their collaborative spirit and for fostering a dynamic and engaging working environment.

I would also like to thank Professor Kateřina Kaňková for her unwavering support and for creating a welcoming atmosphere at her institute. Similar thanks go to Professor Petr Babula.

I would like to acknowledge the invaluable guidance and assistance of our colleagues at the Czech Society for Extracellular Vesicles, who contributed greatly to our experimental efforts.

Finally, I am deeply grateful to my wife and children for the inspiration, joy and purpose they bring to my life, and to my parents and sister for their unwavering support, love and trust throughout my journey.

Table of contents

Table of contents 4
Preface 5
1 Introduction 6
2 Overal hypotheses and objectives of the research 10
3 Methodology: overview of experimental approaches and athor's contribution to the field 12
3.1 Quantitative Phase Imaging 12
3.2 Isolation and purification of phosphatidylserine-positive extracellular vesicles 13
4 Results 14
4.1 Cell death in cancer pathogenesis 14
4.2 A novel method for the determination of cell death and the distinction of specific subtypes 34
4.2.1 Microscopic methods for the study of the dynamics of cells 34
4.3 Detection and distinction of a specific type of cell death by quantitative phase imaging 60
4.4 Mechanisms of cell death resistance in metastatic cancer cells 121
4.4.1 Autophagy as a mechanism of resistance 121
4.5 Crosstalk between cell death and extracellular vesicle secretion 156
4.5.1 Crosstalk between autophagy and extracellular vesicle secretion 156
4.6 Phosphatidylserine-positive extracellular vesicles in intercellular communication in the tumor microenvironment 205
5 Discussion 243
6 Conclusion 247
7 References 248

Preface

This habilitation thesis comprises a selection of publications from 2014 to 2024 to which I have contributed as first author, corresponding author, or co-author during my scientific career. These publications are all unified by a common theme concerning cancer cell death, resistance mechanisms, and their relation to cellular secretion. The research presented here focuses on various aspects of cell death in the context of cancer, including resistance mechanisms to oxidative stress and the autophagy process. Particular emphasis is placed on methodological approaches for detecting and distinguishing between different types of cell death in various cancer cell lines.

Subsequent sections explore the relationship between autophagy, cell death mechanisms, and repair processes, as well as extracellular vesicle secretion in cancer cells. Particular attention is given to phosphatidylserine-positive extracellular vesicles and their role in intercellular communication. The accompanying commentary highlights my contributions to the field of cancer cell death and provides a brief overview of the topics discussed. Further detailed information on each subject can be found in the attached original publications.

The enclosed scientific publications received financial support from projects funded by the Ministry of Health of the Czech Republic (3 projects) and the Grant Agency of the Czech Republic (2 projects).

1 Introduction

The ability to maintain homeostasis, the stability of the internal environment in the face of a changing external environment, is one of the main reasons for the evolutionary success of mammals and other multicellular organisms. The stability of the internal environment is a state of equilibrium, a balance between cell division and cell death, the disturbance of which leads to pathophysiological changes in the organism. While cell division creates the "mass of the organism", cell death shapes it into the desired form. Cell death is a fundamental biological process that is essential for the development, growth and survival of the organism. It is involved in tissue remodelling and eliminates excess cells during development, as well as damaged, transformed and pathogen-infected cells [1].

Cell death has long been at the centre of attention in cancer research. It was first noticed in the context of necrosis, which was observed in hypoxic areas of growing tumors. It was also associated with therapy, as both radiation and chemotherapy were designed to induce the death of malignant cells, but at the cost of being toxic to normal tissue. In 1972, John Kerr and colleagues introduced the term "apoptosis" to describe the process by which cells die through a physiological self-destruction mechanism, distinguishing it from necrosis, which occurs due to catastrophic events like freezing or burning. They examined both apoptosis and necrosis in relation to cancer, highlighting that cell death as a feature of malignant tumors. They noted, "Both apoptotic bodies and mitotic figures are often abundant in rapidly growing tumors; it is the balance between the two that dictates the growth rate." They predicted that inducing apoptosis could be a potential cancer treatment, as they observed that radiation therapy increased apoptosis rates in squamous cell carcinomas, and that oophorectomy led to higher apoptosis rates in mammary tumors in rats [2]. Initially, their findings received little attention, but interest surged in the late 1980s. Furthermore, the failure of cells to undergo apoptosis has been directly associated with the development of cancer in humans and may contribute to its resistance to treatment [3].

Research on cell death has made significant progress over the past three decades, uncovering the mechanisms behind this essential biological process and paving the way for new therapies for cancer and possibly other conditions, including certain autoimmune disorders and

infectious diseases. These diseases could potentially benefit from treatments that target pathogenic cells, such as autoantibody-producing plasma cells or infected cells, using BH3-mimetic drugs. Deciphering the mechanisms of cell death has enabled their classification. Currently, we distinguish programmed, regulated, and accidental cell death. Programmed cell death refers to the types that participate in the physiological development of multicellular organisms. Regulated cell death (apoptosis, necroptosis, pyroptosis, etc.; **Fig. 1**) is defined as cell death that is carried out by genetically encoded mechanisms, in contrast to accidental cell death, which is triggered by drastic changes in the external environment (such as dramatic fluctuations in temperature or pH). Another important classification is the distinction between apoptosis and lytic cell death, in terms of their effect on surrounding tissues and the immune system. Whereas apoptosis is generally discrete from the immune system and does not cause inflammation, lytic cell death, such as necroptosis, pyroptosis or ferroptosis, is accompanied by rupture of the cell membrane, damage to neighbouring cells, activation of the immune system and the induction of varying degrees of inflammation [4].

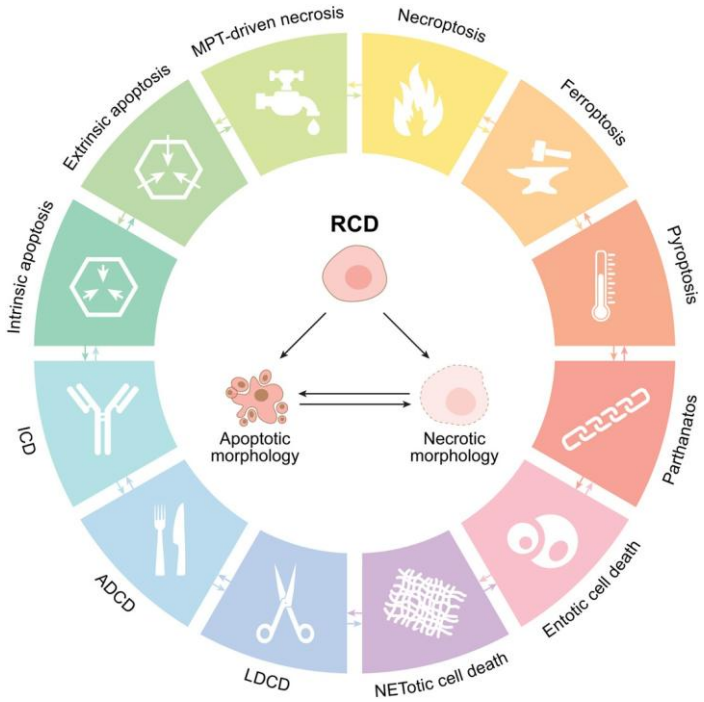

Figure 1. **Major cell death subroutines**. Each of regulated cell death (RCD) modes is initiated and propagated by molecular mechanisms that exhibit a considerable degree of interconnectivity. Moreover, each type of RCD can manifest an entire spectrum of morphological features ranging from fully necrotic to fully apoptotic, as well as an immunomodulatory profile ranging from anti-inflammatory and tolerogenic to pro-inflammatory and immunogenic. *ADCD*: autophagy-dependent cell death, *ICD*: immunogenic cell death, *LDCD*: lysosome-dependent cell death, *MPT*: mitochondrial permeability transition. Image adopted from [4].

Cell death is not just a final event in the life of a cell. It has significant consequences for surrounding tissues and the entire organism. Regardless of the specific type of cell death, it is always associated with the release of various molecules or extracellular vesicles. Many of these cellular components can transmit signals directly or carry bioactive molecules for indirect signalling. After binding to membrane receptors on nearby cells or being taken up by recipient cells, these molecules affect downstream functions through intercellular communication and signal transduction. In general, interactions between dead cells and their healthy neighbours are mediated by extracellular vesicles and soluble factors that are either actively or passively released [5].

Extracellular vesicles (EVs) are a diverse collection of lipid bilayer-enclosed particles that are actively produced and released into the extracellular environment by nearly all cell types; **Fig. 2**. This secretion is a widespread process observed in all life forms, including both prokaryotes and eukaryotes, and occurs under conditions ranging from normal physiological states to pathological ones. Once regarded as insignificant cellular debris, modern research has revealed their crucial function as bioactive carriers. EVs act as vehicles for the transport of a variety of cellular components, enabling complex intercellular communication and playing a key role in numerous biological processes [6]. EVs carry a wide range of cargo, including proteins such as cell surface receptors, signalling molecules, transcription factors, enzymes and components of the extracellular matrix. They also include lipids and nucleic acids (such as miRNA, mRNA and DNA) that can be transferred from donor to recipient cells, facilitating intercellular communication and molecular exchange [7]. EVs have been implicated in several pathological conditions, including heart disease, neurodegenerative disorders and cancer. Different subtypes of EVs are categorised based on their mechanisms of synthesis and release, including exosomes and apoptotic bodies. They can also be classified according to the cell type from which they originate, such as those derived from platelets or endothelial cells, or the physiological state of the cells. The primary types of EVs include microvesicles, exosomes and apoptotic bodies, but recent findings have identified additional categories, including large oncosomes, migrasomes, ectosomes, exomeres, supermeres and membrane particles [8].

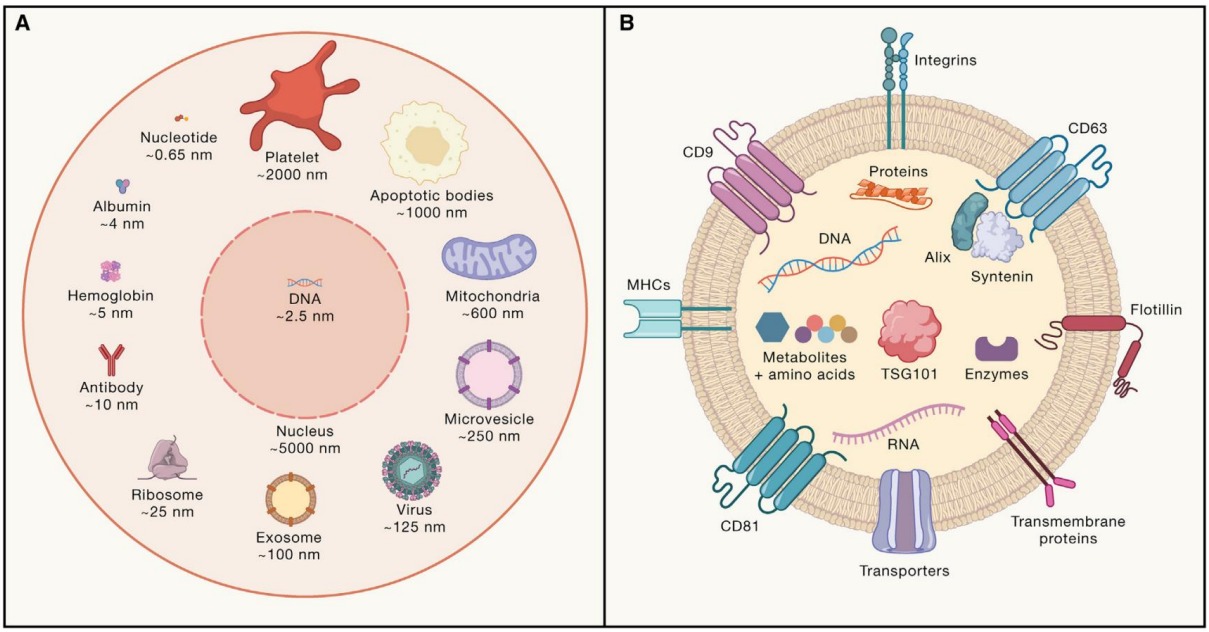

Figure 2. **Relative size and cargo of EVs**

(A) Average size of exosomes and microvesicles with respect to cellular components, including abundant proteins (albumin, hemoglobin, antibodies), organelles (ribosomes, mitochondria), nucleotides and DNA, and virus, as well as cellular byproducts: apoptotic bodies and platelets (B) Composite cargo of exosomes, including surface receptors (proteins, ns, glycans, ion channel receptors, G-protein coupled receptors, enzyme-linked receptors, integrins, etc.), transmembrane proteins (FasL, PD-L1, etc.), intracellular proteins, metabolites, lipids, and nucleic acids. Image taken from [7].

2 Overall hypotheses and objectives

- Over the past two decades, the field of cell death has seen some truly groundbreaking discoveries. Regulated, genetically encoded processes of lytic cell death (necroptosis, pyroptosis, ferroptosis, etc.) have been described, refuting the widely perpetuated dogma of necrosis as an unprogrammed type of cell death. The great importance of these regulated types of cell death in the development of chronic inflammatory and autoimmune diseases, as well as cancer, motivated us to write a book, especially for medical and science students, in an attempt to fill the gap in the Czech study materials (Buněčná smrt, její význam ve fyziologii a patologické fyziologii, 2021; Grada Publishing.). Despite extensive knowledge of apoptosis, alternative cell death pathways are often overlooked. This is particularly relevant in head and neck squamous cell carcinomas (HNSCC), where molecular heterogeneity contributes to unpredictable clinical responses and complicates treatment strategies. Understanding the specific mechanisms of cell death is crucial, as they can significantly influence therapeutic outcomes. Given this situation, we aimed to summarize the available information on the issue of cell death in the context of cancer and its therapy.

- The development of light microscopy methods in recent years has been fundamental to the significant growth in cell biology research. Quantitative phase imaging (QPI) is a cutting-edge light microscopy technique that allows for the precise measurement of cell mass. As all forms of cell death are accompanied by changes in cell mass (e.g. disintegration into apoptotic bodies, changes in the cell membrane during lytic cell death), we hypothesized that these cell death processes could be detected and distinguished using cell mass measurements provided by QPI. We also aimed to validate this concept in different models, so we used QPI and coupled image analysis methods to analyse the dynamic behaviour of the cell population over time when testing different agents, including antivirals, nanomaterials and cytotoxic agents.

- Resistance to cell death is one of the classic hallmarks of cancer. Although the role of autophagy in tumor biology is often described as a double-edged sword, our preliminary results suggest that it plays a greater role in adaptation and resistance than in cell death. We hypothesized that autophagy, cell-in-cell structures, and polyploidisation may contribute significantly to cell survival due to remodelling and dedifferentiation into a pluripotent state. These processes are often associated with tumor cell self-renewal and the development of treatment resistance. Furthermore, we hypothesized that long-term stress caused by reactive oxygen species and starvation could influence cell metabolism and the autophagic flux. Subsequently, we also tried to elucidate the involvement of autophagic processes in the dedifferentiation of cancer cells and self-renewal of their population.

- The important role of autophagy in enabling cancer cells to resist chemotherapy has led to the investigation of autophagy inhibitors as potential adjuncts to therapy. Furthermore, the use of these inhibitors has been considered not only in cancer treatment, but also in the treatment of other diseases (e.g. hydroxychloroquine for treating COVID-19). Recognising the interconnected nature of the endosomal pathway, autophagy, lysosomal degradation, and extracellular vesicle secretion, we hypothesized that modulating autophagy would significantly alter the proteomic composition of extracellular vesicles and influence cytokine production.

3 Methodology: overview of experimental approaches and author's contribution to the field

While the majority of commonly used methodologies have been extensively documented in the existing literature and in our published articles, this chapter will primarily emphasize the techniques we have newly developed or refined. These methods, in my view, represent a particularly valuable contribution to the field due to their novelty, effectiveness, and potential for broader application.

3.1 Quantitative Phase Imaging

Quantitative Phase Imaging (QPI) techniques were employed to facilitate time-lapse observation of subtle, previously invisible changes in the quantitative phase dynamics of cells, including alterations in cell mass distribution, which are discernible in micrographs. We propose that the dynamic changes measured by QPI, such as cell motility, mass distribution, cell density, membrane microblebbing, nuclear morphology, content homogeneity, and other relevant parameters, are characteristic of specific cell death pathways. Importantly, these observations can be conducted without fixation, labeling, or harvesting of cells, which can significantly impact cellular characteristics.

In recent developments, deep learning has emerged as a leading approach for various image analysis tasks, including cell segmentation and classification. A robust training dataset is essential for the successful application of these techniques. For cell segmentation tasks, labels were generated using a custom semi-automatic tool. To facilitate the detection and classification of cell death, we utilized simultaneously acquired fluorescence microscopy channels, which incorporated cell death-specific fluorescent stains to serve as the ground truth for training. This fluorescent labeling provides real-time insights into the presence and type of cell death; however, long-term experiments may be compromised by phototoxicity affecting cell behavior.
To mitigate these challenges, a trained deep learning network was used to extract information directly from label-free images. New morphological features, such as the cell dynamic score and the degree of cell boundary indentation, were developed and utilized to provide biological insights into cellular processes.

3.2 Isolation and purification of phosphatidylserine-positive extracellular vesicles

Extracellular vesicles (EVs) are enveloped by a double lipid membrane that incorporates proteins and lipids sourced from the secreting cells. Among these molecular constituents, phosphatidylserine (PS) is typically located on the intracellular side of the membrane in viable cells, facilitated by the enzymatic action of lipid flippase. Notably, PS is also present on the exterior surface of EVs membranes. Furthermore, T-cell immunoglobulin domain and mucin domain-containing protein 4 (Tim4), a receptor that plays a significant role in the phagocytosis of apoptotic cells by macrophages, binds PS through its IgV domain in a calcium-dependent manner. Building upon these insights, we used a protocol for the purification of EVs utilizing Tim4-conjugated magnetic beads (MagCapture™ Exosome Isolation Kit PS, **Fig.3**). These magnetic beads are designed to capture EVs from biological samples, including culture supernatants and serum, in the presence of calcium ions. The captured EVs can be released by elution with a buffer containing a chelating agent. This method allows for the straightforward purification of intact EVs and achieves a higher purity than traditional EV isolation techniques.

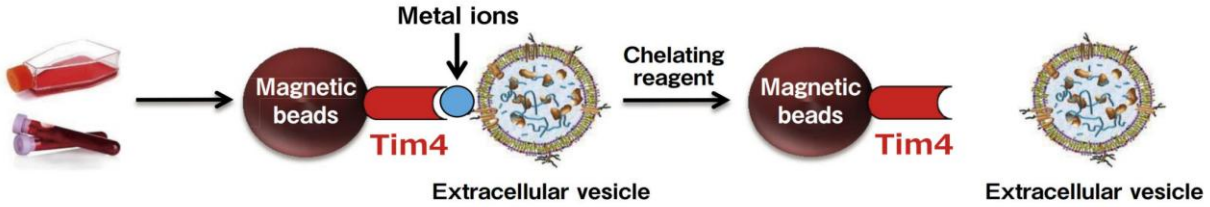

Figure 3. **Principle of a method for the isolation of phosphatidylserine-positive extracellular vesicles using magnetic beads with the Tim4 receptor. Image adopted from https://labchem-wako.fujifilm.com/us/category/03239.html.**

3.3 Use of artificial intelligence tools

In this work, tools using artificial intelligence algorithms DeepL Translate, DeepL Write and Chat GPT-4o were used to check the grammatical and stylistic quality of the work.

4 Results

4.1 Cell death in cancer pathogenesis

Cell death is a complex process that can be categorized based on morphological features, cellular context, and triggering stimuli. A pivotal development in this field occurred in 2018 with a publication in *Cell Death & Differentiation*, which introduced key distinctions between regulated cell death (RCD) and accidental cell death (ACD). While ACD results from overwhelming injury stimuli that lead to uncontrolled cell death, RCD is characterized as an orderly process governed by genetic regulation to maintain cellular stability. Often referred to as programmed cell death (PCD), RCD includes various types such as apoptosis, autophagy-dependent death, necroptosis, and others.

Mammalian cells can activate different signaling pathways in response to irreparable disturbances, resulting in diverse cell death outcomes. Each RCD type exhibits unique initiation mechanisms and can affect cellular morphology and immune responses. In cancer therapy, the goal is frequently to induce apoptosis; however, oncogenic alterations and aberrant tumor microenvironments can limit the effectiveness of this strategy. There is a consensus that cancer cells may not be able to evade all forms of cell death, underscoring the need for personalized treatment approaches.

This review article (1) and our book (2) explore various forms of programmed cell death (PCD), their connections to different pathologies, including cancer, and potential therapeutic opportunities arising from the unique sensitivities of specific HNSCC subgroups to different PCD pathways.

Author's publications relevant to this chapter

1. Raudenská, M., Balvan, J. & Masařík, M. Cell death in head and neck cancer pathogenesis and treatment. *Cell Death and Disease* 12, 192 (2021).

   IF (2021) 9.696; 59 citations

2. Balvan J, Raudenská M, Masařík M. *Buněčná smrt a její význam ve fyziologii a patologické fyziologii*. Grada Publishing, a.s.: Praha, 2021.

Raudenská et al. *Cell Death and Disease* (2021)12:192
https://doi.org/10.1038/s41419-021-03474-5

Cell Death & Disease

REVIEW ARTICLE Open Access

Cell death in head and neck cancer pathogenesis and treatment

Martina Raudenská[1,2], Jan Balvan[3] and Michal Masařík[1,2,3,4]

Abstract

Many cancer therapies aim to trigger apoptosis in cancer cells. Nevertheless, the presence of oncogenic alterations in these cells and distorted composition of tumour microenvironment largely limit the clinical efficacy of this type of therapy. Luckily, scientific consensus describes about 10 different cell death subroutines with different regulatory pathways and cancer cells are probably not able to avoid all of cell death types at once. Therefore, a focused and individualised therapy is needed to address the specific advantages and disadvantages of individual tumours. Although much is known about apoptosis, therapeutic opportunities of other cell death pathways are often neglected. Molecular heterogeneity of head and neck squamous cell carcinomas (HNSCC) causing unpredictability of the clinical response represents a grave challenge for oncologists and seems to be a critical component of treatment response. The large proportion of this clinical heterogeneity probably lies in alterations of cell death pathways. How exactly cells die is very important because the predominant type of cell death can have multiple impacts on the therapeutic response as cell death itself acts as a second messenger. In this review, we discuss the different types of programmed cell death (PCD), their connection with HNSCC pathogenesis and possible therapeutic windows that result from specific sensitivity to some form of PCD in some clinically relevant subgroups of HNSCC.

FACTS

- How cancer cells die is very important because the specific type of cell death has different immunomodulatory impact crucial for the therapeutic response.
- Scientific consensus describes many different cell death subroutines with different regulatory pathways and cancer cells are not able to avoid all of cell death types at once.
- Resistance to one type of cell death can confer sensitivity to another type.
- Specific sensitivity of cancer cells to some form of programmed cell death provides an interesting therapeutic window.
- Human papillomavirus (HPV) can interfere with some cell death regulatory pathways.

OPEN QUESTIONS

- How do different cell death regulatory pathways interact with each other and with secretory and/or endocytic pathways?
- Is a certain genetic background in cancer cells tightly related to specific resistance and sensitivity to different kinds of cell death?
- Can be different types of programmed cell death modulated and switched?

Introduction

Head and neck squamous cell carcinomas (HNSCC) are the fifth most common cancer globally. They emerge in the upper aero-digestive tract (including the oral cavity, pharynx and larynx). HNSCC exhibit high levels of heterogeneity and deep differences in therapeutic response[1].

Correspondence: Michal Masařík (masarik@med.muni.cz)
[1]Department of Physiology, Faculty of Medicine, Masaryk University / Kamenice 5, CZ-625 00 Brno, Czech Republic
[2]Department of Chemistry and Biochemistry, Mendel University in Brno, Zemedelska 1, CZ-613 00 Brno, Czech Republic
Full list of author information is available at the end of the article
Edited by F. Pentimalli

© The Author(s) 2021
Open Access This article is licensed under a Creative Commons Attribution 4.0 International License, which permits use, sharing, adaptation, distribution and reproduction in any medium or format, as long as you give appropriate credit to the original author(s) and the source, provide a link to the Creative Commons license, and indicate if changes were made. The images or other third party material in this article are included in the article's Creative Commons license, unless indicated otherwise in a credit line to the material. If material is not included in the article's Creative Commons license and your intended use is not permitted by statutory regulation or exceeds the permitted use, you will need to obtain permission directly from the copyright holder. To view a copy of this license, visit http://creativecommons.org/licenses/by/4.0/.

Official journal of the Cell Death Differentiation Association

SPRINGER NATURE CDDpress

Conventional HNSCC classification and clinical management are mainly based on clinical staging and grading, and anatomic location. However, for most of the advanced HNSCC, clinical staging does not correlate with treatment responses or prognosis and pre-operative clinical assessment of tumour and nodal involvement is often in disagreement with pathological T and N stage[2]. Variability in prognosis and molecular profiles of different head and neck tumours have attracted much attention in recent years as tumour heterogeneity represents a grave challenge for oncologists and seems to be a critical component of therapeutic response, cancer recurrence and patient survival. HPV infection probably covers most of the HNSCC heterogeneity. Beyond the role of HPV, current molecular classification categorises HNSCC into classical (CL), basal (BA) and mesenchymal (MS) subtype. HPV + tumours are not gathered into one group but fall into the MS and CL subgroup[3]. Genomic and proteomic data obtained from many HNSCC patients have demonstrated that HPV-positive (HPV +) and HPV-negative (HPV−) HNSCC are different clinical entities[4]; (Box 1). Although the role of HPV in dysregulation of DNA damage response (DDR) is well established[5], the influence of HPV on triggering of different kinds of cell death in HNSCC is discussed in a lesser extent, which is unfortunate because many viruses, including HPV, have developed numerous strategies to modulate host cell death to persist in the host for a long time without being eliminated. Accordingly, a growing spectrum of evidence suggests that the HPV-derived oncoproteins, such as E6 and E7 or E5, can inhibit death receptor signalling[6]. Nevertheless, the effect of HPV infection on other cell death types is not often discussed.

Box 1 HPV: the resource of heterogeneity in HNSCC

HPV positivity is detected in about 25% of HNSCCs[207]. HPV-positive (HPV +) and HPV-negative (HPV-) HNSCCs are derived from different anatomical locations (HPV-negative cases are particularly located within the oral cavity, hypopharynx and larynx) and also have different mutation profiles, molecular characteristics, immune landscapes and clinical prognosis[208,209]. The immunologic profile of HPV + HNSCC was associated with a better outcome[24]. Accordingly, many studies demonstrated better response to therapy in HPV + HNSCC patients[4]. HPV infection also influences the genetic landscape of HNSCCs tumours and their predisposition to cell death. Despite the p53 tumour suppressor is the best-known target of HPV protein E6, some active p53 may still occur in HPV + HNSCC because these tumours usually harbour the wild-type form of the *TP53* gene. On the other hand, HPV-unrelated HNSCCs often have p53 mutations[14,15]. In HPV-negative HNSCC, deletion of 9p21 22 occurs early in cancerogenesis and the function of the tumour suppressor p16 is lost. On the contrary, when HPV protein E7 inactivates the Rb protein, p16 is overexpressed[210]. Proteins p16 and p53 are deeply involved in senescence and apoptosis.

Deep understanding of the sensitivity or resistance to a specific cell death type given by certain genetic background and/or microenvironment that occur during the HNSCC pathogenesis may reveal targets for novel therapeutic approaches. We suggest that different approaches should be employed for therapy of different subgroups of HNSCC patients as the predominant type of cell death can have multiple impacts on the therapeutic response as cell death acts as a second messenger that guides both immune system and tissue microenvironment to ensure tissue repair and homoeostasis[7]. In this review, we discuss the different types of cell death, their connection with HNSCC pathogenesis and possible therapeutic windows that result from specific cell death sensitivity in some subgroups of HNSCC.

Intrinsic apoptosis

Apoptosis is a form of regulated cell death demarcated by the mitochondrial outer membrane permeabilization (MOMP) and accelerated by executioner caspases, mainly caspase-3. Once activated, caspase-3 cleaves target substrates such as poly(ADP-ribose) polymerase (PARP) and Lamin B which leads to the demise of the cell. While MOMP is essential for intrinsic cell death, the same is not true for caspases[8]. Nevertheless, the activity or inactivity of caspases provides a mechanism, which determines whether mitochondria initiate an immunologically silent or a pro-inflammatory type of cell death. If caspase activity is blocked following MOMP, cell death is accompanied by a type I interferon (IFN) response that alerts the immune system[9,10]. This response can be managed by mitochondria-dependent activation of the cGAS/STING pathway. Engagement of caspase-independent cell death displays potent anti-tumourigenic effects, often leading to complete tumour regression in the organism with intact immunity[9]. However, HPV + HNSCC cells respond poorly to activators of the cGAS-STING pathway. The attenuation of IFN responses results from the direct blockade of STING by viral protein E7[11]. Despite this fact, HPV + cancer cells can be still more easily recognisable by the immune system as HPV antigens could be presented together with common danger signals from dying cancer cells[12].

HPV replication occurs in terminally differentiating epithelium and requires the activation of cellular DNA replication proteins. However, unplanned DNA replication can result in apoptosis and therefore the viral E6 protein induces the degradation of tumour suppressor p53 and the pore-forming protein BAK to prevent apoptosis[13]. Nevertheless, active p53 may still occur in HPV + HNSCC because these tumours usually harbour the wild-type form of the *TP53* gene. On the other hand, in HPV- HNSCC, p53 is mostly mutated[14,15]. Despite the wild-type form of the *TP53* gene, persistent infection with high-risk HPV

Conventional HNSCC classification and clinical management are mainly based on clinical staging and grading, and anatomic location. However, for most of the advanced HNSCC, clinical staging does not correlate with treatment responses or prognosis and pre-operative clinical assessment of tumour and nodal involvement is often in disagreement with pathological T and N stage[2]. Variability in prognosis and molecular profiles of different head and neck tumours have attracted much attention in recent years as tumour heterogeneity represents a grave challenge for oncologists and seems to be a critical component of therapeutic response, cancer recurrence and patient survival. HPV infection probably covers most of the HNSCC heterogeneity. Beyond the role of HPV, current molecular classification categorises HNSCC into classical (CL), basal (BA) and mesenchymal (MS) subtype. HPV + tumours are not gathered into one group but fall into the MS and CL subgroup[3]. Genomic and proteomic data obtained from many HNSCC patients have demonstrated that HPV-positive (HPV +) and HPV-negative (HPV−) HNSCC are different clinical entities[4]; (Box 1). Although the role of HPV in dysregulation of DNA damage response (DDR) is well established[5], the influence of HPV on triggering of different kinds of cell death in HNSCC is discussed in a lesser extent, which is unfortunate because many viruses, including HPV, have developed numerous strategies to modulate host cell death to persist in the host for a long time without being eliminated. Accordingly, a growing spectrum of evidence suggests that the HPV-derived oncoproteins, such as E6 and E7 or E5, can inhibit death receptor signalling[6]. Nevertheless, the effect of HPV infection on other cell death types is not often discussed.

Box 1 HPV: the resource of heterogeneity in HNSCC

HPV positivity is detected in about 25% of HNSCCs[207]. HPV-positive (HPV +) and HPV-negative (HPV-) HNSCCs are derived from different anatomical locations (HPV-negative cases are particularly located within the oral cavity, hypopharynx and larynx) and also have different mutation profiles, molecular characteristics, immune landscapes and clinical prognosis[208,209]. The immunologic profile of HPV + HNSCC was associated with a better outcome[24]. Accordingly, many studies demonstrated better response to therapy in HPV + HNSCC patients[4]. HPV infection also influences the genetic landscape of HNSCCs tumours and their predisposition to cell death. Despite the p53 tumour suppressor is the best-known target of HPV protein E6, some active p53 may still occur in HPV + HNSCC because these tumours usually harbour the wild-type form of the *TP53* gene. On the other hand, HPV-unrelated HNSCCs often have p53 mutations[14,15]. In HPV-negative HNSCC, deletion of 9p21 22 occurs early in cancerogenesis and the function of the tumour suppressor p16 is lost. On the contrary, when HPV protein E7 inactivates the Rb protein, p16 is overexpressed[210]. Proteins p16 and p53 are deeply involved in senescence and apoptosis.

Deep understanding of the sensitivity or resistance to a specific cell death type given by certain genetic background and/or microenvironment that occur during the HNSCC pathogenesis may reveal targets for novel therapeutic approaches. We suggest that different approaches should be employed for therapy of different subgroups of HNSCC patients as the predominant type of cell death can have multiple impacts on the therapeutic response as cell death acts as a second messenger that guides both immune system and tissue microenvironment to ensure tissue repair and homoeostasis[7]. In this review, we discuss the different types of cell death, their connection with HNSCC pathogenesis and possible therapeutic windows that result from specific cell death sensitivity in some subgroups of HNSCC.

Intrinsic apoptosis

Apoptosis is a form of regulated cell death demarcated by the mitochondrial outer membrane permeabilization (MOMP) and accelerated by executioner caspases, mainly caspase-3. Once activated, caspase-3 cleaves target substrates such as poly(ADP-ribose) polymerase (PARP) and Lamin B which leads to the demise of the cell. While MOMP is essential for intrinsic cell death, the same is not true for caspases[8]. Nevertheless, the activity or inactivity of caspases provides a mechanism, which determines whether mitochondria initiate an immunologically silent or a pro-inflammatory type of cell death. If caspase activity is blocked following MOMP, cell death is accompanied by a type I interferon (IFN) response that alerts the immune system[9,10]. This response can be managed by mitochondria-dependent activation of the cGAS/STING pathway. Engagement of caspase-independent cell death displays potent anti-tumourigenic effects, often leading to complete tumour regression in the organism with intact immunity[9]. However, HPV + HNSCC cells respond poorly to activators of the cGAS-STING pathway. The attenuation of IFN responses results from the direct blockade of STING by viral protein E7[11]. Despite this fact, HPV + cancer cells can be still more easily recognisable by the immune system as HPV antigens could be presented together with common danger signals from dying cancer cells[12].

HPV replication occurs in terminally differentiating epithelium and requires the activation of cellular DNA replication proteins. However, unplanned DNA replication can result in apoptosis and therefore the viral E6 protein induces the degradation of tumour suppressor p53 and the pore-forming protein BAK to prevent apoptosis[13]. Nevertheless, active p53 may still occur in HPV + HNSCC because these tumours usually harbour the wild-type form of the *TP53* gene. On the other hand, in HPV- HNSCC, p53 is mostly mutated[14,15]. Despite the wild-type form of the *TP53* gene, persistent infection with high-risk HPV

presents a major risk factor in HPV-associated cancers. It was shown that NF-κB activity is involved in the establishment of persistent HPV infection as activation of NF-κB by HPV proteins limits viral replication through degradation of protein E1[16]. Unfortunately, NF-κB signalling can contribute to cisplatin resistance and cancer cells survival. Chemoresistant HNSCC cells with active NF-κB signalling respond to chemotherapy by promoting histone deacetylation and generation of heterochromatin. Therefore, targeted inhibition of histone deacetylases may be used as a possible therapeutic strategy for disrupting tumour resistance caused by NFκB[17]. NF-κB-mediated stabilisation of SNAI2 (Slug) can also underlie the inflammation-induced epithelial–mesenchymal transition (EMT) and metastasis in HNSCC[18]. On the other hand, NF-κB activation leads to reduced levels of nuclear BRCA1, impaired and prolonged DNA damage repair, prolonged accumulation of γH2AX foci and increased genomic instability[17]. As NF-κB induces the expression of various pro-inflammatory genes and participates in inflammasome activation[19,20] and activation of the DDR has been linked to the increased presentation of major histocompatibility complex I (MHC I) molecules on the cell surface, this can result in increased recognition of cancer cells by cytotoxic T-lymphocytes[21]. Accordingly, HPV-positivity was correlated with increased T-cell infiltration, increased immune cytolytic activity, T-cell-inflamed immune microenvironment, the higher diversity of T-cell receptors, immune effector cell activation and improved response to anti-PD-1 therapy[22]. Infiltration of tumours with CD8 + cytotoxic T-lymphocytes has been associated with a favourable prognosis in several tumour types and may represent a predictive biomarker for cancer immunotherapy[23]. Consequently, the immunologic profile of HPV-positive HNSCC was associated with a significantly better outcome[24]. The HPV-specific immune response is also suggested to play a role in the significantly better response of HPV-positive patients to radiotherapy[25]. This higher sensitivity does not probably result from increased apoptosis or permanent G1-arrest but is rather associated with high levels of residual double-strand breaks and extensive G2-arrest[26] and can be connected with a radiation-induced loss of cell surface CD47 enhancing the immune-mediated clearance of HPV + cancer cells[27]. Further evidence of the easier immune recognition is the fact that DNA damage generally induces higher expression of multiple ligands activating receptors of NK cells, such as NKG2D or DNAM1[21,28,29]. The DDR-mediated activation of NK cells may importantly contribute to the recognition and removal of pre-malignant and malignant cells[30].

E1∧E4 is a viral protein profusely expressed in HPV-infected epithelia. It binds to the cytokeratin networks and in some cases induces their collapse. When cytokeratin is not present in the cell, E1∧E4 associates with mitochondria soon after its synthesis and induces the detachment of mitochondria from microtubules. This is followed by a severe reduction in the mitochondrial membrane potential and an induction of MOMP[31]. Interestingly, multiple studies have shown that HPV-positive oropharyngeal carcinomas are more likely to present reduced keratinization[32] and more favourable outcome[33]. This can be connected to fast induction of MOMP in cells with low keratinization[31]. MOMP sensitivity can be especially supposed in HPV + mesenchymal subtypes (MS) of HNSCC as MS-signature contains downregulation of markers for epithelial differentiation and keratinization[3]. On the other hand, BA HNSCC subgroup exhibits high levels of epithelial keratinization and differentiation[34,35]. It is also possible that high cellular keratin content can confer some protection against MOMP triggered by mitochondria-binding chemotherapeutics as it was shown that high levels of keratin 6 cause chemoresistance to platinum drugs[36].

Furthermore, it has been demonstrated that HPV-positive HNSCC cells use mitochondrial respiration and produce high levels of cytochrome c oxidase (COX), the key enzyme in the mitochondrial respiratory pathway. E6 oncoproteins also increased mitochondrial mass, protein levels of mitochondrial complexes (I to IV), ATP synthase and the voltage-dependent anion channel (VDAC). On the other hand, in HPV-negative HNSCC the mitochondrial OXPHOS is decreased and glycolysis is preferred due to non-functional p53[37–40]. Consequently, HPV-positive HNSCC may be more sensitive to mitochondria-targeted treatments, such as mitocans. Accordingly, HPV oncoprotein E7 enhances ceramide-mediated mitochondrial fission and lethal mitophagy in response to chemotherapy-induced mitochondria damage[41].

The higher expression of VDAC, high mitochondria mass, and sensitivity to MOMP can also facilitate the therapeutic effect of cisplatin in HNSCC as cisplatin preferentially binds mitochondrial DNA and VDAC in the mitochondrial membrane[42]. TP53 mutations in HPV-negative HNSCC cells correlates with a metabolic shift toward glycolysis suggesting some beneficial effects of glycolytic inhibition during anticancer treatment. In contrast, wtTP53 expressing HPV-positive cells probably require inhibition of both, the mitochondrial respiration and glycolysis, to become sensitised to treatment[40].

Extrinsic apoptosis

Typically, extrinsic apoptosis is induced by the binding of the death ligands to death receptors, which then recruit adaptor molecules and initiator caspases to form the death-inducing signalling complex (DISC). Initiator caspases are then activated by proximity-induced cleavage at the DISC and in turn activate executioner caspases, which

leads to the demise of the cell. In cancer cells, DISC formation is often weak and amplification of the death signal via the mitochondrial pathway is necessary for apoptosis.

From the view of death ligands and receptors, *TNFSF10* (encoding TRAIL) is the only gene found to be significantly altered in HNSCC. The most common alterations in components of the DISC found in HNSCC are amplifications of *FADD* gene (25% of HNSCC) and mutations of gene *CASP8* encoding procaspase-8 (10% of HNSCC). Interestingly, except HNSCC, there are no other tumour types with >10% incidence of *CASP8* mutations. The alterations in *CASP8* and *FADD* genes are significantly mutually exclusive, suggesting that they can be synthetically lethal[43] as FADD and caspase-8 are needed for TRAIL-induced activation of NF-κB[44].

In HPV-positive HNSCC, HPV proteins modulate apoptosis to prevent cell demise at early stages of viral infection. HPV16 E5 protein inhibits TRAIL signalling by interfering with the formation of DISC and subsequent cleavage of procaspases-8 and -3, as well as PARP. E5 also decreases the cell surface expression of the FAS receptor[45]. Similarly, it has been reported that E6 can inhibit apoptosis induced by TNF, FAS and TRAIL through the accelerated degradation of pro-apoptotic proteins such as FADD and/or procaspase-8 or through interactions with proteins that form DISC. Although E6 suppresses activation of both caspase-3 and caspase-8, it does not affect apoptotic signalling through the mitochondrial pathway fundamentally[46–49]. HPV-16 E6 and E7 oncoproteins upregulate *BIRC3* (*C-IAP2*) expression conferring the resistance to apoptosis[50]. In primary human keratinocytes, the HPV16 E7 protein alone increased both spontaneous and TNF-α-induced apoptosis but co-expression of E7 and E6 has cancelled the E7-mediated apoptosis[51]. The HPV E2 protein represses the expression of the viral oncogenes and activates viral DNA replication. An intact E2 gene is common in HPV16 positive oropharyngeal carcinomas but rare in HPV18-associated carcinomas. Cells expressing HPV18 E2 had perinuclear clustering of the mitochondria, higher ROS production, and loss of the cristae structure[52]. The presence of an intact E2 gene is associated with higher HPV viral load and improved clinical outcome[53]. The E2 protein induces apoptosis in both normal and HPV-transformed cells through activation of caspase-8[54,55].

The finding that HPV16 E6 protein stimulates the degradation of the c-Myc oncoprotein seems rather surprising[56]. Nevertheless, c-Myc promotes oncogene-induced senescence (OIS) which is a critical tumour-suppressor mechanism preventing the transformation of cells. c-Myc promotes OIS through the transcriptional activation of p14/Arf/INK4B followed by p53 activation[57]. p14/Arf/INK4B is encoded by *CDKN2A*. HPV-positive HNSCCs rarely have *TP53* and *CDKN2A* mutations[58] and overexpression of c-Myc can activate OIS in these cells. HPV16 can remain infectious for 2 weeks on senescent cells but require cell cycle re-activation for successful HPV infection[59]. Consequently, downregulation of c-Myc may be beneficial for HPV infection because of reduction of the senescent phenotype. On the contrary, most of the smoking-related HNSCCs demonstrate TP53 and CDKN2A inactivation[34] and therefore do not force HPV to c-Myc downregulation. These tumours can exploit the oncogenic force of c-Myc without OIS induction. Accordingly, it was demonstrated that HPV + oral SCC patients with a history of tobacco use have a significantly poorer prognosis even compared to HPV − patients[60]. Nevertheless, *CDKN2A* copy number loss predicted poor survival independently of other clinical and treatment factors[61].

Crosstalk between apoptosis and autophagy

Caspases play a critical role in the crosstalk between autophagy and apoptosis as many autophagy-related proteins are recognised and cleaved by caspases (for example ATG3, ATG5, ATG16L1 or Beclin-1). In most cases, ATG proteins are degraded by caspases and the autophagic response is shut off[62]. In some special cases, the pro-autophagic proteins can be cleaved by caspases and converted into pro-apoptotic ones. For example, caspase-mediated cleavage of Beclin-1 inactivates autophagy and enhances apoptosis by promoting the release of pro-apoptotic factors from mitochondria[63] and enhancing caspase-9 activity[64].

The inhibition of essential apoptotic proteins during cancerogenesis can switch a cellular stress response from the default apoptotic pathway to autophagy. Accordingly, the role of autophagy regarding cell death should be rather protective. Nevertheless, the autophagy machinery can also interact with apoptosis in another way. As mentioned above, caspase-8 is activated by DISC. Another way of caspase-8 activation is managed by autophagosomes. This is executed by binding to the autophagic cargo receptor p62[65]. In the case that procaspase-8 is not activated in DISC, for example under high levels of c-FLIP$_L$[66], which is a frequent event in HNSCC[67], this mechanism can rescue caspase-8 activity and enables cell death. This mechanism involves autophagosomes but not necessarily autophagic flux and degradation of cargo in autolysosomes. Consequently, late-stage autophagy inhibitors such as chloroquine or hydroxychloroquine can preserve this pro-apoptotic effect but can weaken some protective effects of autophagy. Thus, autophagic proteins either directly or through their caspase-cleaved fragments can effectively influence apoptosis. In addition to the above mentioned, ATG12 interacts with Bcl-2 and Mcl-1 and promotes apoptosis by acting upstream of

mitochondria[68]. ATG12 also forms a complex with ATG3 regulating mitochondrial integrity during mitophagy[69]. Furthermore, cells undergoing BAX/BAK-mediated apoptosis show signs of activation of unc-51 like autophagy activating kinase 1 (ULK1) and marks of autophagy. This autophagic flux is triggered early in the apoptotic signalling and therefore an activation of the apoptosome or caspases are not necessary. This BAX/BAK-mediated autophagy inhibits the secretion of the pro-inflammatory IFN-β produced in response to mitochondrial damage which may be important for keeping immunological silence during apoptosis[70].

Necroptosis

Necroptosis is an alternative mode of regulated cell death displaying features of apoptosis and necrosis. Necroptosis is characterised by the formation of a complex called the necrosome that consists of the proteins RIPK1, RIPK3 (receptor-interacting serine/threonine–protein kinases 1 and 3) and mixed lineage kinase domain-like pseudokinase (MLKL). MLKL translocating towards the plasma membrane results in the formation of pores, causing an inflammatory response. Loss of RIPK1 and RIPK3 function by promoter hypermethylation strongly correlated with metastatic disease and poor prognosis in HNSCC patients[71,72].

In normal circumstances, caspase-8 blocks necroptosis by cleaving RIPK1 and CYLD[73]. Inactivation of caspase-8 activity was not shown in HPV + HNSCC[74]. On the contrary, the stimulation of caspase-8 activity and concomitant re-localisation to the nucleus due to the interaction between viral E6 protein and caspase-8 was shown in both high and low-risk HPV types. E6 appears able to stimulate caspase-8 activity without apoptosis triggering[75,76]. This nuclear accumulation of caspase-8 was reported also in HPV-positive tumour cell lines and cervical cancer[77]. Protein E6 most likely recruits caspase-8 to the nucleus to perform functions that are beneficial either for the viral life cycle or in the maintenance of cell proliferation in E6 transformed cells. For example, active caspase-8 suppresses necroptotic cell death mediated by RIPK3 and MLKL and cleavage of RIPK1 by caspase-8 is a mechanism for dismounting death-inducing complexes, which is essential for limiting cell death in response to tumour necrosis factor α (TNFα)[78]. Moreover, HPV oncoproteins downregulate the expression of IFITM1 and RIPK3 to escape from IFNγ- and TNFα-mediated antiproliferative effects and necroptosis[79].

The gene *CASP8* encoding caspase-8 is mutated in 10% of HNSCC tumours analysed by The Cancer Genome Atlas[34]. Caspase-8 plays an important role in the apoptotic response of HNSCC to cisplatin and knockdown of caspase-8 substantially decreased apoptosis and cisplatin sensitivity[80]. But it is possible that HNSCC subtypes with caspase-8 mutations can be more sensitive to necroptosis triggering (e.g. by TNF-α) (see Fig. 1). Accordingly, a subgroup of oral cavity tumours with good clinical outcomes displayed inactivating mutations of caspase-8[34]. Consequently, targeting the necroptotic pathway seems to be a relevant therapeutic approach with compromised caspase-8 activity. However, the triggering of necroptosis should be done with caution. Necroptotic cells were shown to promote the migration and invasion of HNSCC cells in vitro through releasing DAMPs and RIPK1 can activate the NF-κB pathway in tumour cells which can lead to increased migration, invasion and proliferation[81,82]. Accordingly, TNF-α inhibits the growth of non-malignant cervical keratinocytes but stimulates proliferation of HPV-immortalised and cervical carcinoma-derived cell lines when mitogens such as epidermal growth factor (EGF) or serum are depleted[83]. Therefore, the triggering of necroptosis should be accompanied with suitable synergic treatment securing inactivation of the NF-κB pathway (see Fig. 1). It was shown that loss of caspase-8 function in combination with SMAC mimetic treatment sensitises HNSCC to radiation through induction of necroptosis, in case that RIPK3 function is maintained[84]. SMAC mimetics stimulate degradation of cIAP1 and cIAP2 and disrupt the activation of NF-κB[85,86]. Furthermore, the linear ubiquitin chain assembly complex (LUBAC) can also mediate NF-κB signalling and induce cell death resistance[87,88]. Inhibition of NF-κB activation by LUBAC inhibitors sensitised lung squamous cell carcinoma to cisplatin, suggesting a possible utilisation of these inhibitors and other NF-κB pathway inhibitors (e.g. curcumin) also in HNSCC patients[89–92].

The important role in necroptosis induction may also play autophagy as autophagy inhibition or specifically ULK1 inhibition can enhance necroptosis by tumour necrosis factor (TNF) and toll-like receptor (TLR) ligands[93–95]. This pro-survival function of ULK1 is mediated via the phosphorylation of RIPK1 at Ser357[96]. The pro-survival function of autophagy is also supported by COP9 (Constitutive Photomorphogenesis 9) signalosome function. COP9 signalosome suppresses RIPK1-RIPK3–mediated necroptosis by regulating autophagosome maturation. Impaired autophagosome maturation causes necroptosis[97,98]. Proteins of COP9 signalosome are often overexpressed in cancer[99]. However, the crosstalk between autophagy and cell death can be more complex as the death-triggering function of ULK1 by the enhancement of PARP1 activity[100], the scaffolding role of the autophagy proteins in balancing necroptosis and apoptosis (via the SQSTM1/p62-dependent recruitment of RIPK1)[101], or the anti-autophagic function of RIPK1 (via the control of transcription factor EB[102]) were also described.

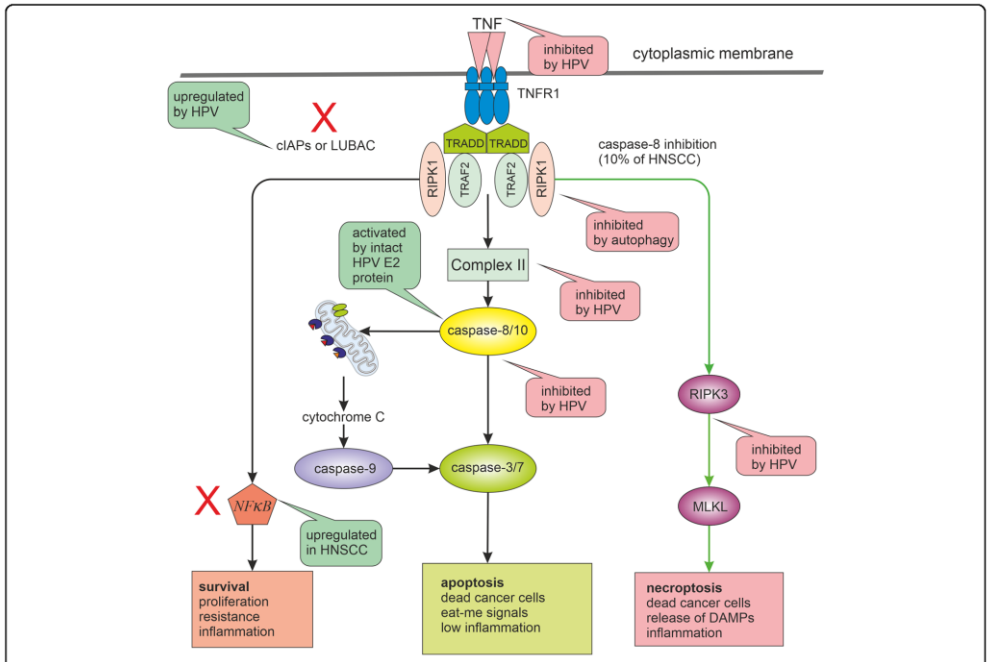

Fig. 1 Alternative pathways of TNF signalling and their alterations in HNSCC. TNF signalling can lead to different results. It depends on the post-translational modification and activation of key molecules such as caspase-8, RIPK1 and NF-κB. While active caspase-8 triggers apoptosis and suppresses necroptosis, its inactivity (e.g. by mutations) leads to necroptosis through RIPK3 activation. If the RIPK1 signal is modified by the addition of ubiquitin, cell death can be attenuated, and the cell receives a signal for survival and proliferation by the transcription factor NF-κB. NF-κB pathway inhibitors such as LUBAC inhibitors or SMAC mimetics can sensitise HNSCC cells to necroptosis or apoptosis. For successful anticancer treatment response, the pathway marked by red exes should be inhibited (inhibition of autophagy should be also beneficial for necroptosis triggering). The TNF signalling pathways are also significantly influenced by HPV infection and by the genetic background of HNSCC. Green bubbles indicate activation and pink inhibition of the process. LUBAC linear ubiquitin chain assembly complex, c-IAPs inhibitors of apoptosis, RIPK receptor-interacting serine/threonine–protein kinases, MLKL mixed lineage kinase domain-like pseudokinase.

Necroptosis has dual effects as promoter or reducer of tumour growth in different types of cancer. As a backup form of cell death in cells with apoptosis failure, necroptosis can prevent tumorigenesis. Nevertheless, it can also trigger metastasis and immunosuppression. This can be caused by the release of IL-33 during necroptosis[103]. IL-33 seems to be involved in the shaping of the immunosuppressive environment during cancerogenesis[104,105] and high expression of IL-33 in cancer-associated fibroblasts (CAFs) and tumour cells was associated with poor prognosis[106,107]. While these data suggest that IL-33 blockade may be beneficial for HNSCC patients, further investigations are needed to define all downstream signalling targets dependent on IL-33. Furthermore, the necrosome can promote oncogenesis via CXCL1 and Mincle-induced immune suppression[108]. On the other hand, necroptotic cells can provide both antigens and inflammatory cytokines to dendritic cells for antigen cross-priming which activates cytotoxic CD8 + T-lymphocytes demonstrating cytolytic effects and defence against tumorigenesis. RIPK1 expression and NF-κB activation are essential for this tumour suppressive mechanism[109]. Induction of necroptosis was also shown to induce anti-tumour immunity in an HMGB1-, nucleotide- and T-cell-dependent manner[110].

Pyroptosis

Pyroptosis is initiated by inflammatory caspases (1, 4 and 5) upon activation of the canonical or non-canonical inflammasome pathways. In the canonical inflammasome pathway, caspase-1 mediates the cleavage of gasdermin D (GSDMD) and the maturation of pro-inflammatory interleukins (IL-1β and IL-18). GSDMD pores then induce cell lysis, cell death and the leakage of intracellular

components into the extracellular space. The non-canonical inflammasome pathway can be initiated by the direct binding of caspase-4 and -5 to lipopolysaccharide from Gram-negative bacteria[8]. Another way to activate pyroptosis is caspase-3/Gasdermin E (GSDME) pathway. Caspase-3 can be activated by mitochondrial intrinsic and death receptor pathway. The activated caspase-3 then cleaves GSDME. Cleaved GSDME N-fragments form pores in the plasma membrane, causing pyroptosis[111] (see Fig. 2). This activation of GSDME may divert TNF-induced apoptosis to pyroptosis. Because GSDME expression is often silenced in tumour cells, which is not the case of healthy cells, this caspase-3 activity may be responsible for serious side effects of many chemotherapeutic regimens[112]. Pyroptosis can also be activated by caspase-8 and subsequent cleavage of GSDMD[113]. In the absence of GSDMD, caspase-1 can activate caspase-8, caspase-3, and caspase-7 and induce apoptosis, making apoptosis a backup programme for dysfunctional pyroptosis. Accordingly, tissue samples of HNSCC without the presence of lymph node metastasis showed high expression of caspase-1[114]. During apoptosis, caspase-3 and -7 specifically block cleavage of GSDMD[115]. In contrast, expression of inactive caspase-8 or pan-caspase inhibition induces the formation and subsequent activation of caspase-1. This mechanism triggers pyroptosis in cells with dysfunctional apoptosis[116]. Caspase-1 is also involved in the facilitation of cytoprotective autophagy during hypoxia-induced mitochondrial stress by activating LC3 and Beclin-1 and favouring clearance of damaged mitochondria[117]. In the feedback loop, autophagy downregulates inflammasomes as activation of autophagy by inflammatory signals limits IL-1β production by targeting inflammasomes for destruction. Both the AIM2 and NLRP3 inflammasomes can be recruited to p62 and engulfed by autophagosomes[118]. On the other hand, inhibition of autophagy enhances inflammasome activity[118]. Many studies have suggested that mitochondrial defects may promote inflammasome activation through excessive ROS production, mitochondrial cardiolipin exposure or release of mitochondrial DNA[119].

Inflammation belongs among major causes of HNSCC cancerogenesis. Accordingly, inflammasome NLRP3 expression was enhanced in human HNSCC tissues and the IL-1β concentration was increased in the peripheral blood of these patients[120]. The increased expression of NLRP3 was also associated with tumour growth, invasiveness, metastasis, development of cancer stem cells (CSCs) and their self-renewal in HNSCC[121–123]. Furthermore, it has been reported that high NLRP3 expression is associated with poor clinical outcome in 5-FU-treated oral squamous cell carcinoma (OSCC) patients and NLRP3 knockdown increased 5-FU-induced apoptosis in OSCC cells[124]. Blockage of the NLRP3 inflammasome/IL-1β pathway by MCC950 improved anti-tumour immune responses in an HNSCC mouse model[120] and blockade of the IL-1β pathway by biopharmaceutical drug anakinra has overcome erlotinib resistance in HNSCC xenografts[125]. On the other hand, alcohol has been shown to promote both the release of IL-1β and pyroptosis[126]. Infection of human keratinocytes with HPV16 also induced the secretion of IL-1β. Yet, upon expression of the viral early genes, IL-1β transcription is blocked, because HPV16 derived E6 protein can antagonise IL-1β production by inhibiting IRF6 transcription and upregulation of sirtuin 1 (SIRT1)[127,128]. Knockdown of SIRT1 upregulates AIM2 expression and triggers pyroptosis[128]. SIRT1 expression was associated with good prognosis in HNSCC patients[129]. Nevertheless, cigarette smoke impairs SIRT1 activity and promotes pro-inflammatory responses in epithelial cells[130]. HPV E7 may also inhibit pyroptosis by promoting TRIM21-mediated degradation and ubiquitination of the IFI16 inflammasome[131].

Although pyroptosis seems to have rather tumour-promoting effects in HNSCC, the exogenous activation of pyroptosis has recently been shown to trigger powerful anti-tumour effect[112]. As many tumour cells have an innate resistance to apoptosis, the induction of pyroptosis may provide an efficient cancer therapy strategy. Indeed, interventions with some chemotherapeutic agents cause a switch from caspase 3-dependent apoptosis to pyroptosis by activation of GSDME[112,132] and unleashing of inflammasome activation augments the efficacy of some immune checkpoint inhibitors[133]. GSDME also enhances the number and activity of tumour-infiltrating natural-killer (NK) and CD8 + T-lymphocytes, as well as phagocytosis of tumour cells by tumour-associated macrophages. Moreover, granzyme B produced by NK cells also activates pyroptosis in target cells by cleaving GSDME at the same site as caspase-3, thereby establishing a positive feedback loop. However, this mechanism of tumour suppression is abrogated in perforin-deficient mice or mice without killer lymphocytes[134]. Caspase-3 activation and cytochrome c release in response to apoptotic stimuli are significantly reduced in GSDME-deficient cells[135]. Uncleavable or pore-defective GSDME proteins are also not tumour suppressive and many cancer-associated GSDME mutations reduce GSDME function, suggesting that GSDME inactivation is a strategy developed by cancer cells to reach the immune evasion[134]. A decrease in GSDME expression and function was shown in radioresistant HNSCC[136].

Ferroptosis

Ferroptosis is independent of caspase activity. Instead, ferroptotic cells die following iron-dependent membrane lipid peroxidation. Importantly, tumour cells capable of

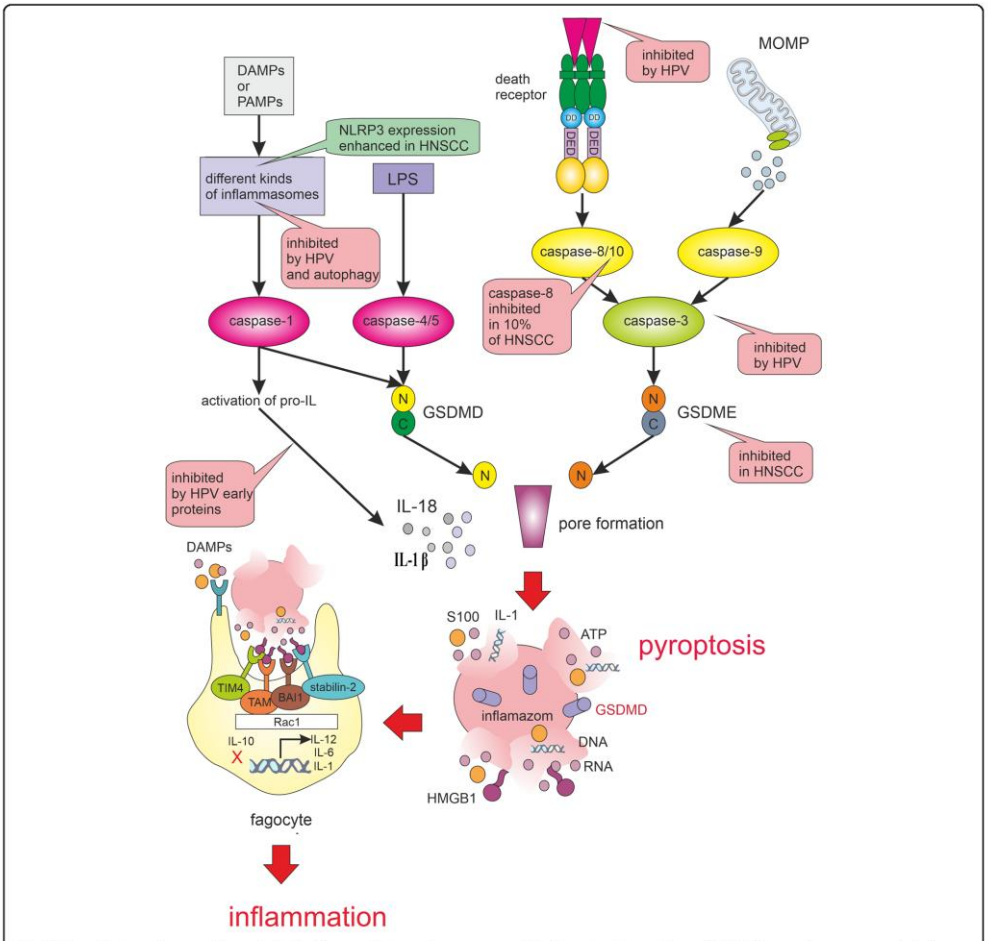

Fig. 2 Pyroptosis pathways. Pyroptosis is triggered when damage-associated molecular patterns (DAMPs) or pathogen-associated molecular patterns (PAMPs) activate the inflammasomes. Active inflammasomes lead to the cleavage and activation of caspase-1. The activated caspase-1 cleaves Gasdermin D (GSDMD). The N-fragment of GSDMD form cell membrane pores resulting in pyroptosis. Activated caspase-1 also promotes the maturation and secretion of interleukins IL-1β and IL-18. When pathogen-derived lipopolysaccharide (LPS) binds to the precursor of caspase-4/5, it can also cause GSDMD cleavage and induction of pyroptosis. Another way to activate pyroptosis is caspase-3/Gasdermin E (GSDME) pathway. Caspase-3 can also be activated by mitochondrial outer membrane permeabilization (MOMP) and death receptor pathways. The activated caspase-3 then cleaves GSDME and produces GSDME N-fragments, The N-fragment of GSDME form cell membrane pores resulting in pyroptosis. Pyroptosis results in membrane rupture and the release of DAMPs that are detected by phagocyte receptors, such as TIM 4 (T cell immunoglobulin mucin receptor 4), BAI 1 (brain-specific angiogenesis inhibitor 1), stabilin-2 and TAM (Tryo3-Axl-Mer receptor). DAMPs recognition leads to the production of pro-inflammatory interleukins (e.g. IL-1, IL-6) and IL-12, which activates NK cells and induces the differentiation of naive CD4 T cells. The pyroptotic signalling pathways are significantly influenced by HPV infection and by the genetic background of HNSCC. Green bubbles indicate activation and pink inhibition of the process.

evading other types of cell death probably maintain or acquire a sensitivity to ferroptosis. Given that HNSCC cells often manifest an increased intracellular iron concentration due to a high level of TFRC1 (transferrin receptor 1 responsible for cellular iron uptake)[137] and a low abundance of ferroportin (responsible for iron

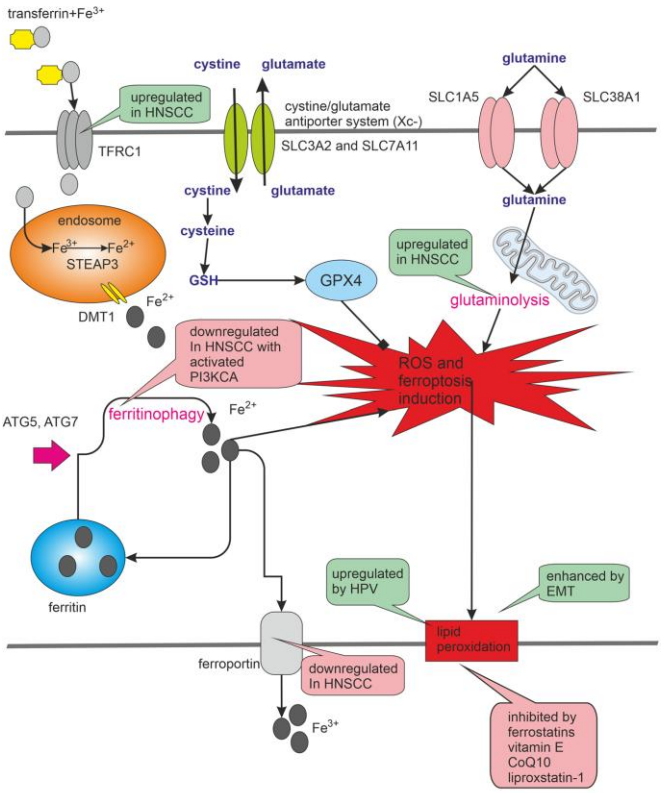

Fig. 3 Ferroptosis. Ferroptosis is characterised by iron-induced lipid peroxidation. The intracellular concentration of iron can be affected by the activity of transferrin, transferrin receptor and ferroportin, or by the release of iron from ferritin, which is often managed by ferritinophagy. HNSCC cells often manifest an increased intracellular iron concentration due to a high level of TFRC1 (transferrin receptor 1 responsible for cellular iron uptake) and a low abundance of ferroportin (responsible for iron efflux). The non-physiological degree of lipid peroxidation and the initiation of ferroptosis is prevented by glutathione and glutathione peroxidase 4 (GPX4) activity. Ferroptosis could be also prevented with chelating agents or vitamin E, which casts a bad light on the benefits of antioxidants in the treatment of some ferroptosis-prone cancers. Glutamine and glutaminolysis also play a crucial role in the activation of ferroptosis. PI3KCA is among the most frequently mutated and activated genes in HNSCC. PIK3CA activation can lead to increased mTOR activity and decreased autophagy. Consequently, the presence of PI3KCA activation may predispose these cancer cells to avoid autophagy, ferritinophagy and ferroptosis. The ferroptotic signalling pathways are significantly influenced by HPV infection and by the genetic background of HNSCC. Green bubbles indicate activation and pink inhibition of the process.

efflux)[138], ferroptosis-inducing therapy can be expected to effectively induce cell death in HNSCC cells without affecting normal tissue; see Fig. 3. Interestingly, the *TFRC* gene is located in the genomic region frequently amplified in HNSCC (3q29)[139].

The induction of ferroptosis can be reversed by glutathione peroxidase 4 (GPX4) and ferroptosis suppressor protein 1 (FSP1). The blockade of cystine-glutamate antiporter (Xc–) system and cystine import is important for the induction of ferroptosis as inhibitors of (Xc–) system including sulfasalazine and erastin have been shown to induce ferroptosis[140]. The system (Xc–) consists of two subunits, SLC3A2 and SLC7A11. The expression of the SLC7A11 subunit is suppressed by protein p53 that inhibits cystine uptake and sensitises cells to ferroptosis. Even some mutated forms of p53, which are no longer able to induce apoptosis or senescence, do not lose their effect on the induction of ferroptosis[141].

Tumour cells having mesenchymal features (tumour cell lines of mesenchymal origin, epithelial tumour cell

lines that have undergone EMT and tumour cells exhibiting mesenchymal state-mediated resistance to antitumour therapy) appear to be particularly sensitive to ferroptosis. These cells usually have a higher activity of enzymes that promote the synthesis and storage of long-chain polyunsaturated fatty acids (PUFAs), which are a source of lipid peroxidation during oxidative stress. As a result, such cells are highly sensitive to GPX4 inhibition and ferroptosis. The interrelationship of mesenchymal phenotype and sensitivity to lipid peroxidation appears to be a result of the high expression of the protein ZEB1 (Zinc finger E-box-binding homeobox 1), which functions in both EMT and lipogenic processes. Deletion of ZEB1 was able to remove sensitivity to GPX4 inhibition in these cells[142]. ZEB1 was identified as a key player in the inflammation-induced promotion of EMT in HNSCC[143]. Accordingly, the MS subgroup of HNSCC characterised as having an elevated expression of EMT-associated genes could be the most sensitive to ferroptosis. In epithelial cells, interactions mediated by E-cadherin suppress ferroptosis by activating the intracellular NF2 and Hippo signalling pathway[144]. Furthermore, HPV16-derived E6 and E7 oncoproteins induce expression of the EMT-activating transcriptional factors Slug, Twist, ZEB1 and ZEB2[145].

Another mechanism underlying ferroptosis was observed after erastin treatment. Erastin can bind with VDAC2 on the mitochondrial outer membrane, where it alters membrane permeability and the ion selectivity of the channels (allows only cations to move into mitochondria), causing mitochondrial dysfunction and ROS release that ultimately leads to glutathione (GSH) depletion and ferroptosis[146]. Recently, it was also found that activation of ferroptosis by erastin increases the level of lysosomal-associated membrane protein 2a (LAMP2), thereby promoting chaperone-mediated autophagy, which in turn promotes the degradation of GPX4[147]. Ferroptosis seems to be also tightly associated with ferritinophagy as inhibition of ferritinophagy by blockage of autophagy or knockdown of NCOA4, which mediates the selective autophagic degradation of ferritin, abrogated the accumulation of ROS and cellular labile iron[148]. HPV16 oncoproteins mute the host autophagic response at different levels of the autophagic pathway. E5 interferes with the phagophore assembly, while E6 and E7 inhibit autophagosome/lysosome fusion[149,150]. This autophagy inhibition may provide some resistance against ferroptosis in HPV-positive HNSCC, but the exact influence of HPV on ferritinophagy is currently not clear because it was also shown that HPV16 E6/E7 oncoproteins can activate autophagy via accelerating autophagosome formation and degradation[151].

PI3KCA is among the most frequently mutated and activated genes in HNSCC in both HPV-positive and negative diseases (56 and 34%, respectively)[34]. Interestingly, PIK3CA activation in HPV-positive HNSCC can lead to increased mTOR activity and decreased autophagy[152]. Consequently, the presence of PI3KCA activation may predispose these cancer cells to avoid autophagy, ferritinophagy and ferroptosis. It was shown that aspirin or its active metabolite salicylate induce autophagy by inhibiting the acetyltransferase activity of EP300[153,154]. This effect of aspirin may be especially beneficial for HNSCC patients with PI3KCA over-activation. Accordingly, the use of nonsteroidal anti-inflammatory drugs (NSAID), such as aspirin, caused improved survival among HNSCC patients with PIK3CA mutations. Among subjects with PIK3CA mutations or amplification, regular NSAID use (≥6 months) conferred markedly prolonged disease-specific survival and overall survival compared to non-regular NSAID users[155]. In our opinion, this could be partly a consequence of autophagy and ferroptosis reactivation. Autophagy induction by rapamycin also showed the synergistic effects with irradiation in oral squamous cell carcinoma cells[156].

In the absence of glutamine or inhibition of glutaminolysis, blocked cystine import cannot induce ferroptosis. Since many types of tumours, including HNSCC, are dependent on glutaminolysis[157] and glutaminolysis is necessary to induce ferroptosis, can these tumour cells be more sensitive to induction of ferroptosis? Glutamine is synthesized by the enzyme glutamine synthetase (GS) from glutamate and ammonia. Glutamate is generated from glutamine during glutaminolysis, which is a series of biochemical reactions degrading the amino acid glutamine to glutamate, aspartate, CO_2, pyruvate, lactate, alanine and citrate[157]. Both glutaminase-1 (GLS1) and glutaminase-2 (GLS2) are involved in glutaminolysis, but only GLS2 mediates ferroptosis and is a transcriptional target of the p53 protein. Accordingly, GLS2 has been recognised as a tumour suppressor and GLS1 more as an oncoprotein[158]. GLS1 expression was correlated with a poor survival rate in HNSCC patients[159]. It was also demonstrated that high expression of system (Xc−) components and glutamine transporter ASCT2 is correlated with undifferentiated status in HNSCC[160] and ASCT2-dependent glutamine uptake is involved in the progression of HNSCC[161]. Sulfasalazine is a specific inhibitor of (Xc−)-mediated cystine transport and inhibits the growth of HNSCC cells[162]. It was shown that the cytotoxicity of sulfasalazine relies on ASCT2-dependent glutamine uptake and glutamate dehydrogenase (GLUD)-mediated α-ketoglutarate production. Therefore, the activity of glutaminolysis-related proteins, such as ASCT2 and GLUD, can be probably used as a biomarker to predict the efficacy of sulfasalazine therapy in HNSCC[160]. On the other hand, sulfasalazine resistant HNSCC cells were found to highly express aldehyde dehydrogenase

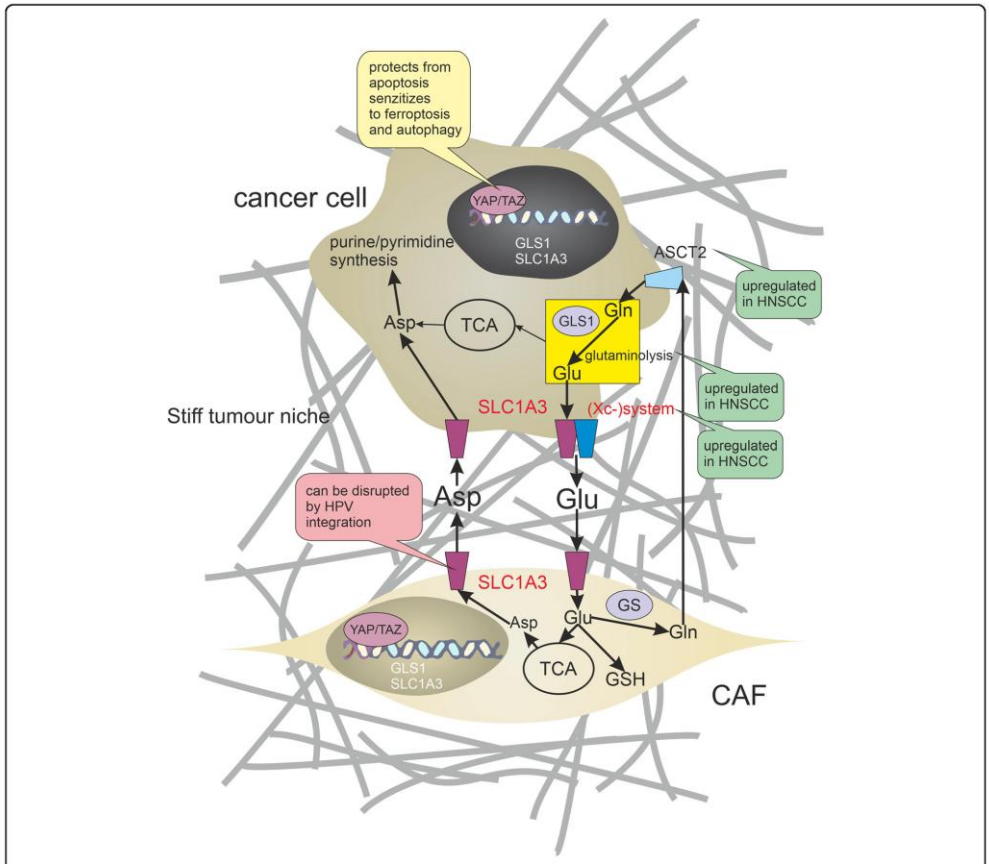

Fig. 4 Metabolic symbiosis between cancer-associated fibroblasts and HNSCC cells. HNSCC cells undergo numerous metabolic changes including increased glutaminolysis. Glutaminolysis produces large pools of intracellular glutamate. Upregulation of the cystine/glutamate antiporter ((Xc–) system) and excitatory amino acid transporter (SLC1A3) promotes aberrant glutamate (Glu) release from cancer cells. Increased stiffness of extracellular matrix during tumour progression induces cancer-associated fibroblasts (CAFs) to import glutamate (through SLC1A3) and release aspartate (Asp) and glutamine (Gln) supporting cancer cell purine/pyrimidine synthesis. Glutamine synthetase (GS) is often overexpressed in these CAFs. CAFs can also promote chemoresistance through the production of glutathione (GSH). Establishing of this metabolic symbiosis is coordinated by a YAP/TAZ-dependent mechanotransduction pathway. Green bubbles indicate activation and pink inhibition of the process.

ALDH3A1 which plays a key role in the protection of cells from lipid peroxidation. This resistance was reversed by knockdown of ALDH3A1 or by ALDH inhibitor dyclonine[163]. Several studies have also revealed that transporters ASCT2 and (Xc–) mediate resistance in HNSCC cells after cetuximab, cisplatin and AG1478 treatment[164–166].

High concentrations of extracellular glutamate can block cystine uptake by the (Xc–) system and induce ferroptosis[167,168]. As cancer cells secrete high concentrations of glutamate through the activity of the cystine/glutamate antiporter (Xc–) system, they can be sensitive to ferroptosis when they have no support of other cells in the tumour microenvironment (TME). Nevertheless, increased stiffness of extracellular matrix during tumour progression induces CAFs to import glutamate (through SLC1A3) and release aspartate and glutamine supporting cancer cell proliferation; see Fig. 4. Glutamine synthetase (GS/GLUL) is often overexpressed in these CAFs[169]. In some cases, *SLC1A3* gene can be interrupted by HPV integration[170,171]. The metabolic symbiosis enables cancer

cells to get rid of ferroptosis-promoting glutamate and to gain glutamine. This metabolic exchange can take place also between cancer cells and M2-macrophages[172]. Consequently, blocking the transport of glutamate into the CAFs or M2-macrophages may lead to enhanced sensitivity of glutamine-addicted cancer cells to ferroptosis. Nevertheless, this approach should be used with caution because increased levels of extracellular glutamate have been associated with the progression of cancer-induced pain[173].

Establishing of glutamate metabolic symbiosis by metabolic reprogramming is coordinated by a YAP/TAZ-dependent mechanotransduction pathway[174]; see Fig. 4. Accordingly, levels of nuclear YAP/TAZ in fibroblasts associated with perineural invasion of HNSCC were higher than those in the stroma of normal mucosa[175]. YAP expression was elevated at the invasive front of HNSCC tumours[176] and also as a consequence of PIK3CA overexpression[177]. Although YAP activation in tumour stroma can lead to avoiding ferroptosis caused by a high concentration of glutamate in TME, YAP itself can promote ferroptosis under some circumstances by upregulating ferroptosis modulators ACSL4 and transferrin receptor TFRC[144]. It seems possible that YAP/TAZ activity balances the tendency of cancer cells to undergo a distinct form of cell death as nuclear accumulation and activation of YAP/TAZ protect cells from apoptosis but sensitise cells to ferroptosis and autophagy[144,178].

Some cells in TME, such as CD8 + T-cells, can induce ferroptosis in tumour cells and the insensitivity to PD-L1 inhibitors is often accompanied by resistance to ferroptosis[179]. One of the key factors causing the immunogenicity of ferroptotic cancer cells may be HMGB1[180]. Cancer cells undergoing ferroptosis release HMGB1 in an autophagy-mediated manner, when autophagy promotes HMGB1 acetylation, resulting in HMGB1 release[181]. Although HMGB1 serum and tissue levels were found to be elevated in HNSCC, they are associated rather with chemoattraction of regulatory T cells (Treg) and promoting of their immunosuppressive functions[182]. Ferroptosis was also associated with an increased expression of cyclooxygenase-2 and the release of prostaglandin E2 (PGE2) which facilitates immune evasion of tumour cells[183].

Targeted therapy of non-apoptotic programmed cell deaths in cancer

The development of new antineoplastic drugs targeting programmed cell death suitable for clinical use is a demanding and time-consuming process. Therefore, the effects of previously approved drugs on any type of programmed cell death should be intensively studied. The potential for such type of clinical use has been attributed to some cholesterol-lowering drugs, muscle relaxants, antimalarials or anti-rheumatic drugs such as sulfasalazine, lanperisone, statins, artesunate or aspirin.

Sulfasalazine (Azulfidine) has been repurposed to induce ferroptosis via inhibition of (Xc−) system. Cytotoxicity of sulfasalazine relies on glutamine uptake and α-ketoglutarate production[162]. However, HNSCC cancer cells are capable of developing resistance. Resistance to ferroptosis induced by sulfasalazine may be overcome by ALDH inhibitor dyclonine or inhibition of CISD2[163,184]. Both pharmacological and genetic inhibition of SLC7A11 induce ferroptotic cell death and increase the cytotoxicity of cisplatin in HNSCC cells, which were resistant to cisplatin before this inhibition[185]. Activation of ferroptosis also appears to contribute to the efficacy of radiotherapy[186] or some novel anticancer drugs with potential in HNSCC treatment, such as dihydroartemisinin[187]. (Xc−)-targeted therapy may also kill undifferentiated HNSCC cells expressing variant isoforms of CD44 (CD44v) and concurrently may sensitise the remaining HNSCC cells to available treatments including EGFR-targeted therapy[165].

Lanperisone is a modified form of muscle relaxant tolperisone and selectively kills K-Ras-mutant cells through the induction of ROS, which is mediated through iron and ferroptosis pathways[188]. Ferroptosis may also be induced by statins as statins target the mevalonate pathway, which is crucial for GPX4 maturation[189]. This fact opens novel prospects of statins as therapeutic agents in cancer[190]. Another inductor of ferroptosis is probably artesunate and its derivatives. Artesunate is a medication used to treat malaria and can also produce ROS and cause oxidative stress in cancer cells. In pancreatic ductal adenocarcinoma, HNSCC and ovarian cancer cells, the antitumour effect of artesunate was mediated by induction of ferroptosis[185].

Many proven anticancer drugs show a profound effect on programmed cell death. Dabrafenib, a B-RAF inhibitor approved for the treatment of melanoma, has also been shown to be a potent, high-affinity RIPK3 inhibitor that blocks TNF-α-induced necroptosis[191]. Other clinically approved drugs that may inhibit necroptosis include vemurafenib, sorafenib, pazopanib and ponatinib[192]. In contrast, induction of necroptosis has been identified as an important effector mechanism of oxaliplatin, mitoxantrone or 5-fluorouracil in anti-tumour activity[193,194]. In some tumour cells, inhibition of caspases is essential for the induction of necroptosis. Inhibitors of caspase activity can block caspase-8-mediated cleavage of RIPK1 and stabilise RIPK1-containing protein complexes. Inhibitors of caspase activity (e.g. IDN-7314, Z-VAD) are being tested as a novel approach in adjuvant chemotherapy of colorectal cancer showing resistance to 5-fluorouracil[194]. Induction of necroptosis also appears to be beneficial in the treatment of leukaemias and neuroblastomas[195,196].

Some results indicate that cisplatin and Val-boroPro (Talabostat) induce pyroptosis in cancer cells suggesting that they may provide additional advantages in the treatment of cancers with high levels of GSDME expression[197,198]. Ferroptosis can be induced by altretamine and sorafenib. Altretamine is an orally administered alkylating agent which is currently used as a secondary therapy for advanced ovarian carcinoma. It directly binds and inactivates GPX4[199]. Sorafenib is a kinase inhibitor approved for the treatment of renal cell carcinoma, hepatocellular carcinoma and thyroid carcinoma. Sorafenib induces ferroptosis independent from the oncogenic status of Ras, RAF, PIK3CA and p53 in cancer cell lines originating from different solid tumours[200]. Sorafenib increased the antiproliferative effect of cisplatin without affecting apoptosis in HNSCC cells, also enhanced HNSCC radiosensitivity[201]. Cisplatin alone was found to be a potent inducer of ferroptosis[202].

The only clinically approved autophagy inhibitors nowadays are chloroquine (CQ) and hydroxychloroquine (HCQ)[203]. HCQ is currently in various stages of clinical trials as monotherapy or as part of combination therapy for solid tumours, however, pharmacodynamic studies suggest that the maximum permitted dose of HCQ (1200 mg/day) shows only slight inhibition of autophagy in vivo. This may be due to the reduced absorption of the drug into cells in an acidic environment (pH around 6.5), which is unfortunately typical of the tumour microenvironment[204]. Many CQ analogues with promising metabolic and antineoplastic effects are also in clinical trials[205]. Furthermore, some otherwise used compounds may have a profound effect on autophagy. For example, pro-apoptotic BH3-mimetic compounds such as ABT737, competitively disrupt the interaction between Beclin-1 and BCL2 or BCL-XL liberating Beclin-1 from an inhibitory complex and thus induce autophagy[206]. Aspirin induces autophagy via inhibition of the acetyltransferase EP300 and recapitulates features of caloric restriction[153,154].

Conclusion

Many HNSCC cancer therapies aim to induce apoptosis to suspend tumour growth. However, avoiding apoptosis is one of the key hallmarks of cancer and the presence of genetic heterogeneity and supporting TME severely limits the clinical efficacy of these approaches. Nevertheless, scientific consensus describes many different cell death subroutines with different regulatory pathways and cancer cells are probably not able to avoid all of cell death types at once. Therefore, a more focused and individualised therapeutic approach is needed to address the specific advantages and disadvantages of individual tumours. A full understanding of the sensitivity or resistance to specific cell death type given by certain genetic background and/or microenvironment that occurs during the HNSCC pathogenesis may reveal specific and effective targets for novel tailored therapeutic approaches. The genetic fingerprint of individual tumours can direct the development of novel agents to selectively hit the tumour cells while sparing the healthy ones. For example, HPV-positive HNSCC may be more sensitive to mitochondria-targeted treatments, such as mitocans, and the MS subgroup of HNSCC, having an elevated expression of EMT-associated genes, could be the most sensitive to ferroptosis. Consequently, the future development of agents that directly target cell death pathways could lead to disease regression even in patients with poor prognosis.

Author details
[1]Department of Physiology, Faculty of Medicine, Masaryk University / Kamenice 5, CZ-625 00 Brno, Czech Republic. [2]Department of Chemistry and Biochemistry, Mendel University in Brno, Zemedelska 1, CZ-613 00 Brno, Czech Republic. [3]Department of Pathological Physiology, Faculty of Medicine, Masaryk University / Kamenice 5, CZ-625 00 Brno, Czech Republic. [4]BIOCEV, First Faculty of Medicine, Charles University, Prumyslova 595, CZ-252 50, Vestec, Czech Republic

Author contributions
M.R. and J.B. developed the rationale of the review. M.R., J.B. and M.M. wrote the paper.

Ethics statement
No ethics approvals were required for this paper.

Funding statement
This work was supported by funds from the Faculty of Medicine, Masaryk University to Junior researcher (Jan Balvan), by Grant Agency of the Czech Republic (GACR - 18-03978S), by the Ministry of Health of the Czech Republic (NU20J-08-00018), by funds from Specific University Research Grant, as provided by the Ministry of Education, Youth and Sports of the Czech Republic in the year 2021 (MUNI/A/1698/2020 and MUNI/A/1246/2020), and by the "Center for Tumour Ecology—Research of the Cancer Microenvironment Supporting Cancer Growth and Spread" (reg. no. CZ.02.1.01/0.0/0.0/16_019/0000785) supported by the Operational Programme Research, Development and Education.

Conflict of interest
The authors declare that they have no conflict of interest.

Publisher's note
Springer Nature remains neutral with regard to jurisdictional claims in published maps and institutional affiliations.

Received: 3 September 2020 Revised: 26 January 2021 Accepted: 27 January 2021
Published online: 18 February 2021

References

1. Lemaire, F. et al. Differential expression profiling of head and neck squamous cell carcinoma (HNSCC). *Br. J. Cancer* **89**, 1940–1949 (2003).
2. Koch, W. M., Ridge, J. A., Forastiere, A. & Manola, J. Comparison of clinical and pathological staging in head and neck squamous cell carcinoma: results from Intergroup Study ECOG 4393/RTOG 9614. *Arch. Otolaryngol. Head. Neck Surg.* **135**, 851–858 (2009).
3. Keck, M. K. et al. Integrative analysis of head and neck cancer identifies two biologically distinct HPV and three non-HPV subtypes. *Clin. Cancer Res.* **21**, 870–881 (2015).

4. Leemans, C. R., Snijders, P. J. F. & Brakenhoff, R. H. The molecular landscape of head and neck cancer. *Nat. Rev. Cancer* **18**, 269–282 (2018).
5. Wallace, N. A. & Galloway, D. A. Manipulation of cellular DNA damage repair machinery facilitates propagation of human papillomaviruses. *Semin. cancer Biol.* **26**, 30–42 (2014).
6. Garnett, T. O. & Duerksen-Hughes, P. J. Modulation of apoptosis by human papillomavirus (HPV) oncoproteins. *Arch. Virol.* **151**, 2321–2335 (2006).
7. Legrand, A. J., Konstantinou, M., Goode, E. F. & Meier, P. The diversification of cell death and immunity: memento mori. *Mol. Cell* **76**, 232–242 (2019).
8. Galluzzi, L. et al. Molecular mechanisms of cell death: recommendations of the Nomenclature Committee on cell death 2018. *Cell Death Differ.* **25**, 486–541 (2018).
9. Giampazolias, E. et al. Mitochondrial permeabilization engages NF-kappaB-dependent anti-tumour activity under caspase deficiency. *Nat. Cell Biol.* **19**, 1116–1129 (2017).
10. Rongvaux, A. et al. Apoptotic caspases prevent the induction of type I interferons by mitochondrial DNA. *Cell* **159**, 1563–1577 (2014).
11. Shaikh, M. H., Bortnik, V., McMillan, N. A. J. & Idris, A. cGAS-STING responses are dampened in high-risk HPV type 16 positive head and neck squamous cell carcinoma cells. *Microb. Pathog.* **132**, 162–165 (2019).
12. Andersen, A. S., Koldjaer Sølling, A. S., Ovesen, T. & Rusan, M. The interplay between HPV and host immunity in head and neck squamous cell carcinoma. *Int. J. Cancer* **134**, 2755–2763 (2014).
13. Thomas, M. & Banks, L. Human papillomavirus (HPV) E6 interactions with Bak are conserved amongst E6 proteins from high and low risk HPV types. *J. Gen. Virol.* **80**, 1513–1517 (1999).
14. Kimple, R. J. et al. Enhanced radiation sensitivity in HPV-positive head and neck cancer. *Cancer Res.* **73**, 4791–4800 (2013).
15. Maruyama, H. et al. Human papillomavirus and p53 mutations in head and neck squamous cell carcinoma among Japanese population. *Cancer Sci.* **105**, 409–417 (2014).
16. Nakahara, T. et al. Activation of NF-κB by human papillomavirus 16 E1 limits E1-dependent viral replication through degradation of E1. *J. Virol.* **89**, 5040–5059 (2015).
17. Almeida L., et al. NF kappa B mediates cisplatin resistance through histone modifications in head and neck squamous cell carcinoma (HNSCC). *FEBS Open Bio.* **4**, (2013)
18. Liu, S. et al. Stabilization of slug by NF-kappaB is essential for TNF-alpha -induced migration and epithelial-mesenchymal transition in head and neck squamous cell carcinoma cells. *Cell Physiol. Biochem.* **47**, 567–578 (2018).
19. Boaru S. et al. NLRP3 inflammasome expression is driven by NF-κB in cultured hepatocytes. *Biochem. Biophys. Res. Commun.* **458**, 700–706 (2015).
20. Bauernfeind, F. G. et al. Cutting edge: NF-kappaB activating pattern recognition and cytokine receptors license NLRP3 inflammasome activation by regulating NLRP3 expression. *J. Immunol.* **183**, 787–791 (2009).
21. Galluzzi, L., Yamazaki, T. & Kroemer, G. Linking cellular stress responses to systemic homeostasis. *Nat. Rev. Mol. Cell Biol.* **19**, 731–745 (2018).
22. Wang, J. et al. HPV-positive status associated with inflamed immune microenvironment and improved response to anti-PD-1 therapy in head and neck squamous cell carcinoma. *Sci. Rep.* **9**, 13404 (2019).
23. Fridman, W. H., Pagès, F., Sautès-Fridman, C. & Galon, J. The immune contexture in human tumours: impact on clinical outcome. *Nat. Rev. Cancer* **12**, 298–306 (2012).
24. Badoual, C. et al. PD-1-expressing tumor-infiltrating T cells are a favorable prognostic biomarker in HPV-associated head and neck cancer. *Cancer Res.* **73**, 128–138 (2013).
25. Park, J. W. et al. Human papillomavirus type 16 E7 oncoprotein causes a delay in repair of DNA damage. *Radiother. Oncol.* **113**, 337–344 (2014).
26. Rieckmann, T. et al. HNSCC cell lines positive for HPV and p16 possess higher cellular radiosensitivity due to an impaired DSB repair capacity. *Radiother. Oncol.* **107**, 242–246 (2013).
27. Vermeer, D. W. et al. Radiation-induced loss of cell surface CD47 enhances immune-mediated clearance of human papillomavirus-positive cancer. *Int. J. Cancer* **133**, 120–129 (2013).
28. Gasser, S., Orsulic, S., Brown, E. J. & Raulet, D. H. The DNA damage pathway regulates innate immune system ligands of the NKG2D receptor. *Nature* **436**, 1186–1190 (2005).
29. Sayitoglu E. C. et al. Boosting natural killer cell-mediated targeting of sarcoma through DNAM-1 and NKG2D. *Front. Immunol.* **11**, 40 (2020).
30. Lopez-Soto, A., Gonzalez, S., Smyth, M. J. & Galluzzi, L. Control of metastasis by NK cells. *Cancer Cell* **32**, 135–154 (2017).
31. Raj, K., Berguerand, S., Southern, S., Doorbar, J. & Beard, P. E1 empty set E4 protein of human papillomavirus type 16 associates with mitochondria. *J. Virol.* **78**, 7199–7207 (2004).
32. Buckley, L., Jackett, L., Clark, J. & Gupta, R. HPV-related oropharyngeal carcinoma: a review of clinical and pathologic features with emphasis on updates in clinical and pathologic staging. *Adv. Anat. Pathol.* **25**, 180–188 (2018).
33. Elrefaey, S., Massaro, M. A., Chiocca, S., Chiesa, F. & Ansarin, M. HPV in oropharyngeal cancer: the basics to know in clinical practice. *Acta Otorhinolaryngol. Ital.* **34**, 299–309 (2014).
34. Lawrence, M. S. et al. Comprehensive genomic characterization of head and neck squamous cell carcinomas. *Nature* **517**, 576–582 (2015).
35. Walter, V. et al. Molecular subtypes in head and neck cancer exhibit distinct patterns of chromosomal gain and loss of canonical cancer genes. *PloS ONE* **8**, e56823 (2013).
36. Lim, S. C., Parajuli, K. R. & Han, S. I. Keratin 6, induced by chronic cisplatin exposure, confers chemoresistance in human gastric carcinoma cells. *Oncol. Rep.* **42**, 797–804 (2019).
37. Jung, Y. S. et al. HPV-associated differential regulation of tumor metabolism in oropharyngeal head and neck cancer. *Oncotarget* **8**, 51530–51541 (2017).
38. Puzio-Kuter, A. M. The role of p53 in metabolic regulation. *Genes Cancer* **2**, 385–391 (2011).
39. Cruz-Gregorio, A. et al. E6 oncoproteins from high-risk human papillomavirus induce mitochondrial metabolism in a head and neck squamous cell carcinoma model. *Biomolecules* **9**, 351 (2019).
40. Sandulache, V. C. et al. Individualizing antimetabolic treatment strategies for head and neck squamous cell carcinoma based on TP53 mutational status. *Cancer* **118**, 711–721 (2012).
41. Thomas, R. J. et al. HPV/E7 induces chemotherapy-mediated tumor suppression by ceramide-dependent mitophagy. *EMBO Mol. Med.* **9**, 1030–1051 (2017).
42. Yang, Z. et al. Cisplatin preferentially binds mitochondrial DNA and voltage-dependent anion channel protein in the mitochondrial membrane of head and neck squamous cell carcinoma: possible role in apoptosis. *Clin. Cancer Res.* **12**, 5817–5825 (2006).
43. Leonard, B. C. & Johnson, D. E. Signaling by cell surface death receptors: alterations in head and neck cancer. *Adv. Biol. Regul.* **67**, 170–178 (2018).
44. Grunert, M. et al. The adaptor protein FADD and the initiator caspase-8 mediate activation of NF-κB by TRAIL. *Cell Death Dis.* **3**, e414–e414 (2012).
45. Kabsch, K. & Alonso, A. The human papillomavirus type 16 E5 protein impairs TRAIL- and FasL-mediated apoptosis in HaCaT cells by different mechanisms. *J. Virol.* **76**, 12162–12172 (2002).
46. Filippova, M., Parkhurst, L. & Duerksen-Hughes, P. J. The human papillomavirus 16 E6 protein binds to Fas-associated death domain and protects cells from Fas-triggered apoptosis. *J. Biol. Chem.* **279**, 25729–25744 (2004).
47. Duerksen-Hughes, P. J., Yang, J. & Schwartz, S. B. HPV 16 E6 blocks TNF-mediated apoptosis in mouse fibroblast LM cells. *Virology* **264**, 55–65 (1999).
48. Lagunas-Martínez, A., Madrid-Marina, V. & Gariglio, P. Modulation of apoptosis by early human papillomavirus proteins in cervical cancer. *Biochimica et Biophysica Acta Cancer* **1805**, 6–16 (2010).
49. Garnett, T. O., Filippova, M. & Duerksen-Hughes, P. J. Accelerated degradation of FADD and procaspase 8 in cells expressing human papilloma virus 16 E6 impairs TRAIL-mediated apoptosis. *Cell Death Differ.* **13**, 1915–1926 (2006).
50. Yuan, H. et al. Human papillomavirus type 16 E6 and E7 oncoproteins upregulate c-IAP2 gene expression and confer resistance to apoptosis. *Oncogene* **24**, 5069–5078 (2005).
51. Stöppler, H. et al. The E7 protein of human papillomavirus type 16 sensitizes primary human keratinocytes to apoptosis. *Oncogene* **17**, 1207–1214 (1998).
52. Lai, D. et al. Localization of HPV-18 E2 at mitochondrial membranes induces ROS release and modulates host cell metabolism. *PloS ONE* **8**, e75625 (2013).
53. Anayannis, N. V. et al. Association of an intact E2 gene with higher HPV viral load, higher viral oncogene expression, and improved clinical outcome in HPV16 positive head and neck squamous cell carcinoma. *PloS ONE* **13**, e0191581–e0191581 (2018).
54. Demeret, C., Garcia-Carranca, A. & Thierry, F. Transcription-independent triggering of the extrinsic pathway of apoptosis by human papillomavirus 18 E2 protein. *Oncogene* **22**, 168–175 (2003).
55. Webster, K. et al. The human papillomavirus (HPV) 16 E2 protein induces apoptosis in the absence of other HPV proteins and via a p53-dependent pathway. *J. Biol. Chem.* **275**, 87–94 (2000).
56. Gross-Mesilaty, S. et al. Basal and human papillomavirus E6 oncoprotein-induced degradation of Myc proteins by the ubiquitin pathway. *Proc. Natl Acad. Sci. USA* **95**, 8058–8063 (1998).

57. Ko, A. et al. Oncogene-induced senescence mediated by c-Myc requires USP10 dependent deubiquitination and stabilization of p14ARF. *Cell Death Differ.* **25**, 1050–1062 (2018).
58. Stransky, N. et al. The mutational landscape of head and neck squamous cell carcinoma. *Science* **333**, 1157–1160 (2011).
59. Broniarczyk, J., Ring, N., Massimi, P., Giacca, M. & Banks, L. HPV-16 virions can remain infectious for 2 weeks on senescent cells but require cell cycle re-activation to allow virus entry. *Sci. Rep.* **8**, 811 (2018).
60. Duray, A. et al. Human papillomavirus DNA strongly correlates with a poorer prognosis in oral cavity carcinoma. *Laryngoscope* **122**, 1558–1565 (2012).
61. Chen, W. S. et al. CDKN2A copy number loss is an independent prognostic factor in HPV-negative head and neck squamous cell carcinoma. *Front. Oncol.* **8**, 95 (2018).
62. Tsapras, P. & Nezis, I. P. Caspase involvement in autophagy. *Cell Death Differ.* **24**, 1369–1379 (2017).
63. Wirawan, E. et al. Caspase-mediated cleavage of Beclin-1 inactivates Beclin-1-induced autophagy and enhances apoptosis by promoting the release of proapoptotic factors from mitochondria. *Cell Death Dis.* **1**, e18 (2010).
64. Furuya, D., Tsuji, N., Yagihashi, A. & Watanabe, N. Beclin 1 augmented cis-diamminedichloroplatinum induced apoptosis via enhancing caspase-9 activity. *Exp. Cell Res.* **307**, 26–40 (2005).
65. Young, M. M. et al. Autophagosomal membrane serves as platform for intracellular death-inducing signaling complex (iDISC)-mediated caspase-8 activation and apoptosis. *J. Biol. Chem.* **287**, 12455–12468 (2012).
66. Hughes, M. A. et al. Co-operative and hierarchical binding of c-FLIP and caspase-8: a unified model defines how c-FLIP isoforms differentially control cell fate. *Mol. Cell* **61**, 834–849 (2016).
67. Li, X. et al. Overexpression of cFLIP in head and neck squamous cell carcinoma and its clinicopathologic correlations. *J. Cancer Res. Clin. Oncol.* **134**, 609–615 (2008).
68. Rubinstein, A. D., Eisenstein, M., Ber, Y., Bialik, S. & Kimchi, A. The autophagy protein Atg12 associates with antiapoptotic Bcl-2 family members to promote mitochondrial apoptosis. *Mol. Cell* **44**, 698–709 (2011).
69. Radoshevich, L. et al. ATG12 conjugation to ATG3 regulates mitochondrial homeostasis and cell death. *Cell* **142**, 590–600 (2010).
70. Lindqvist, L. M. et al. Autophagy induced during apoptosis degrades mitochondria and inhibits type I interferon secretion. *Cell Death Differ.* **25**, 784–796 (2018).
71. McCormick, K. D. et al. Innate immune signaling through differential RIPK1 expression promote tumor progression in head and neck squamous cell carcinoma. *Carcinogenesis* **37**, 522–529 (2016).
72. Shi, F. et al. EBV(LMP1)-induced metabolic reprogramming inhibits necroptosis through the hypermethylation of the RIP3 promoter. *Theranostics* **9**, 2424–2438 (2019).
73. O'Donnell, M. A. et al. Caspase 8 inhibits programmed necrosis by processing CYLD. *Nat. Cell Biol.* **13**, 1437–1442 (2011).
74. Beck T. N. & Golemis E. A. Genomic insights into head and neck cancer. *Cancers Head Neck.* **1**, 1 (2016).
75. Moody, C. A., Fradet-Turcotte, A., Archambault, J. & Laimins, L. A. Human papillomaviruses activate caspases upon epithelial differentiation to induce viral genome amplification. *Proc. Natl Acad. Sci. USA* **104**, 19541–19546 (2007).
76. Manzo-Merino, J., Massimi, P., Lizano, M. & Banks, L. The human papillomavirus (HPV) E6 oncoproteins promotes nuclear localization of active caspase 8. *Virology* **450–451**, 146–152 (2014).
77. Aréchaga-Ocampo, E. et al. HPV+ cervical carcinomas and cell lines display altered expression of caspases. *Gynecologic Oncol.* **108**, 10–18 (2008).
78. Newton, K. et al. Cleavage of RIPK1 by caspase-8 is crucial for limiting apoptosis and necroptosis. *Nature* **574**, 428–431 (2019).
79. Ma, W. et al. Human papillomavirus downregulates the expression of IFITM1 and RIPK3 to escape from IFNγ- and TNFα-mediated antiproliferative effects and necroptosis. *Front. Immunol.* **7**, 496 (2016).
80. Hammon, R. J., Michaud, W. A. & Rocco, J. W. Status of the intrinsic and extrinsic apoptotic pathways in HNSCC and impact on sensitivity to etoposide-, TRAIL-, and Cisplatin-induced cell death: molecular biology and therapeutics. *Int. J. Radiat. Oncol., Biol., Phys.* **88**, 515 (2014).
81. Jackson-Bernitsas, D. G. et al. Evidence that TNF-TNFR1-TRADD-TRAF2-RIP-TAK1-IKK pathway mediates constitutive NF-kappaB activation and proliferation in human head and neck squamous cell carcinoma. *Oncogene* **26**, 1385–1397 (2007).
82. Li, J. et al. Necroptosis in head and neck squamous cell carcinoma: characterization of clinicopathological relevance and in vitro cell model. *Cell Death Dis.* **11**, 391 (2020).
83. Gaiotti, D. et al. Tumor necrosis factor-alpha promotes human papillomavirus (HPV) E6/E7 RNA expression and cyclin-dependent kinase activity in HPV-immortalized keratinocytes by a ras-dependent pathway. *Mol. Carcinog.* **27**, 97–109 (2000).
84. Uzunparmak, B. et al. Caspase-8 loss radiosensitizes head and neck squamous cell carcinoma to SMAC mimetic-induced necroptosis. *JCI Insight.* **5**, e139837 (2020).
85. Safferthal, C., Rohde, K. & Fulda, S. Therapeutic targeting of necroptosis by Smac mimetic bypasses apoptosis resistance in acute myeloid leukemia cells. *Oncogene* **36**, 1487–1502 (2017).
86. Mahoney, D. J. et al. Both cIAP1 and cIAP2 regulate TNFalpha-mediated NF-kappaB activation. *Proc. Natl Acad. Sci. USA* **105**, 11778–11783 (2008).
87. Taraborrelli, L. et al. LUBAC prevents lethal dermatitis by inhibiting cell death induced by TNF, TRAIL and CD95L. *Nat. Commun.* **9**, 3910 (2018).
88. Amin, P. et al. Regulation of a distinct activated RIPK1 intermediate bridging complex I and complex II in TNFα-mediated apoptosis. *Proc. Natl Acad. Sci. USA* **115**, E5944–E5953 (2018).
89. Ruiz, E. J. et al. LUBAC determines chemotherapy resistance in squamous cell lung cancer. *J. Exp. Med.* **216**, 450–465 (2019).
90. Lun, M. et al. Nuclear factor-kappaB pathway as a therapeutic target in head and neck squamous cell carcinoma: pharmaceutical and molecular validation in human cell lines using Velcade and siRNA/NF-kappaB. *Ann. Clin. Lab Sci.* **35**, 251–258 (2005).
91. Duarte, V. M. et al. Curcumin enhances the effect of cisplatin in suppression of head and neck squamous cell carcinoma via inhibition of IKKβ protein of the NFκB pathway. *Mol. Cancer Ther.* **9**, 2665–2675 (2010).
92. Duffey, D. C. et al. Inhibition of transcription factor nuclear factor-kappaB by a mutant inhibitor-kappaBalpha attenuates resistance of human head and neck squamous cell carcinoma to TNF-alpha caspase-mediated cell death. *Br. J. Cancer* **83**, 1367–1374 (2000).
93. Lim J. et al. Autophagy regulates inflammatory programmed cell death via turnover of RHIM-domain proteins. *Elife.* **8**, e44452 (2019).
94. Wu, W. & Stork, B. Regulating RIPK1: another way in which ULK1 contributes to survival. *Autophagy* **16**, 1544–1546 (2020).
95. Bray, K. et al. Autophagy suppresses RIP kinase-dependent necrosis enabling survival to mTOR inhibition. *PloS ONE* **7**, e41831–e41831 (2012).
96. Wu, W. et al. The autophagy-initiating kinase ULK1 controls RIPK1-mediated cell death. *Cell Rep.* **31**, 107547 (2020).
97. Su, H., Li, F., Ranek, M. J., Wei, N. & Wang, X. COP9 signalosome regulates autophagosome maturation. *Circulation* **124**, 2117–2128 (2011).
98. Xiao, P. et al. COP9 signalosome suppresses RIPK1-RIPK3–mediated cardiomyocyte necroptosis in mice. *Circ. Heart Fail.* **13**, e006996 (2020).
99. Lee, M.-H., Zhao, R., Phan, L. & Yeung, S.-C. J. Roles of COP9 signalosome in cancer. *Cell Cycle* **10**, 3057–3066 (2011).
100. Joshi, A. et al. Nuclear ULK1 promotes cell death in response to oxidative stress through PARP1. *Cell Death Differ.* **23**, 216–230 (2016).
101. Goodall, M. L. et al. The autophagy machinery controls cell death switching between apoptosis and necroptosis. *Dev. Cell* **37**, 337–349 (2016).
102. Yonekawa T. et al. RIP1 negatively regulates basal autophagic flux through TFEB to control sensitivity to apoptosis. *EMBO Rep.* **16**, 700–708 (2015).
103. Shlomovitz, I. et al. Necroptosis directly induces the release of full-length biologically active IL-33 in vitro and in an inflammatory disease model. *FEBS J.* **286**, 507–522 (2019).
104. Pastille, E. et al. The IL-33/ST2 pathway shapes the regulatory T cell phenotype to promote intestinal cancer. *Mucosal Immunol.* **12**, 990–1003 (2019).
105. Schiering, C. et al. The alarmin IL-33 promotes regulatory T-cell function in the intestine. *Nature* **513**, 564–568 (2014).
106. Chen, S. F. et al. The paracrine effect of cancer-associated fibroblast-induced interleukin-33 regulates the invasiveness of head and neck squamous cell carcinoma. *J. Pathol.* **231**, 180–189 (2013).
107. Ishikawa, K. et al. Expression of interleukin-33 is correlated with poor prognosis of patients with squamous cell carcinoma of the tongue. *Auris Nasus Larynx* **41**, 552–557 (2014).
108. Seifert, L. et al. The necrosome promotes pancreatic oncogenesis via CXCL1 and Mincle-induced immune suppression. *Nature* **532**, 245–249 (2016).
109. Yatim, N. et al. RIPK1 and NF-κB signaling in dying cells determines cross-priming of $CD8^+$ T cells. *Science* **350**, 328–334 (2015).

110. Werthmöller, N., Frey, B., Wunderlich, R., Fietkau, R. & Gaipl, U. S. Modulation of radiochemoimmunotherapy-induced B16 melanoma cell death by the pan-caspase inhibitor zVAD-fmk induces anti-tumor immunity in a HMGB1-, nucleotide- and T-cell-dependent manner. *Cell Death Dis.* **6**, e1761 (2015).
111. Lu, H. et al. Molecular targeted therapies elicit concurrent apoptotic and GSDME-dependent pyroptotic tumor cell death. *Clin. Cancer Res.* **24**, 6066–6077 (2018).
112. Wang, Y. et al. Chemotherapy drugs induce pyroptosis through caspase-3 cleavage of a gasdermin. *Nature* **547**, 99–103 (2017).
113. Sarhan, J. et al. Caspase-8 induces cleavage of gasdermin D to elicit pyroptosis during Yersinia infection. *Proc. Natl Acad. Sci. USA* **115**, E10888–E10897 (2018).
114. Chung, C. H. et al. Molecular classification of head and neck squamous cell carcinomas using patterns of gene expression. *Cancer Cell* **5**, 489–500 (2004).
115. Taabazuing, C. Y., Okondo, M. C. & Bachovchin, D. A. Pyroptosis and apoptosis pathways engage in bidirectional crosstalk in monocytes and macrophages. *Cell Chem. Biol.* **24**, 507–14.e4 (2017).
116. Willson, J. A matter of life and death for caspase 8. *Nat. Rev. Mol. Cell Biol.* **21**, 63 (2020).
117. Sun, Q. et al. Caspase 1 activation is protective against hepatocyte cell death by up-regulating beclin 1 protein and mitochondrial autophagy in the setting of redox stress. *J. Biol. Chem.* **288**, 15947–15958 (2013).
118. Shi, C.-S. et al. Activation of autophagy by inflammatory signals limits IL-1β production by targeting ubiquitinated inflammasomes for destruction. *Nat. Immunol.* **13**, 255–263 (2012).
119. Yuk, J.-M., Silwal, P. & Jo, E.-K. Inflammasome and mitophagy connection in health and disease. *Int. J. Mol. Sci.* **21**, 4714 (2020).
120. Chen, L. et al. Blockage of the NLRP3 inflammasome by MCC950 improves anti-tumor immune responses in head and neck squamous cell carcinoma. *Cell Mol. Life Sci.* **75**, 2045–2058 (2018).
121. Wang, H. et al. NLRP3 promotes tumor growth and metastasis in human oral squamous cell carcinoma. *BMC Cancer* **18**, 500 (2018).
122. Bae, J. Y. et al. P2X7 receptor and NLRP3 inflammasome activation in head and neck cancer. *Oncotarget* **8**, 48972–48982 (2017).
123. Huang, C. F. et al. NLRP3 inflammasome activation promotes inflammation-induced carcinogenesis in head and neck squamous cell carcinoma. *J. Exp. Clin. Cancer Res.* **36**, 116 (2017).
124. Feng, X. et al. The role of NLRP3 inflammasome in 5-fluorouracil resistance of oral squamous cell carcinoma. *J. Exp. Clin. Cancer Res.* **36**, 81 (2017).
125. Stanam, A., Gibson-Corley, K. N., Love-Homan, L., Ihejirika, N. & Simons, A. L. Interleukin-1 blockade overcomes erlotinib resistance in head and neck squamous cell carcinoma. *Oncotarget* **7**, 76087–76100 (2016).
126. Wang, F. et al. Alcohol accumulation promotes esophagitis via pyroptosis activation. *Int. J. Biol. Sci.* **14**, 1245–1255 (2018).
127. Ainouze, M. et al. Human papillomavirus type 16 antagonizes IRF6 regulation of IL-1β. *PLoS Pathog.* **14**, e1007158 (2018).
128. So, D. et al. Cervical cancer is addicted to SIRT1 disarming the AIM2 antiviral defense. *Oncogene* **37**, 5191–5204 (2018).
129. Noguchi, A. et al. SIRT1 expression is associated with good prognosis for head and neck squamous cell carcinoma patients. *Oral. Surg. Oral. Med. Oral. Pathol. Oral. Radiol.* **115**, 385–392 (2013).
130. Di Vincenzo, S. et al. Cigarette smoke impairs Sirt1 activity and promotes pro-inflammatory responses in bronchial epithelial cells. *Eur. Respir. J.* **46**, PA5105 (2015).
131. Song, Y. et al. HPV E7 inhibits cell pyroptosis by promoting TRIM21-mediated degradation and ubiquitination of the IFI16 inflammasome. *Int. J. Biol. Sci.* **16**, 2924–2937 (2020).
132. Rogers, C. et al. Cleavage of DFNA5 by caspase-3 during apoptosis mediates progression to secondary necrotic/pyroptotic cell death. *Nat. Commun.* **8**, 14128 (2017).
133. Segovia M. et al. Targeting TMEM176B enhances antitumor immunity and augments the efficacy of immune checkpoint blockers by unleashing inflammasome activation. *Cancer Cell.* **35**, 767–781.e6 (2019).
134. Zhang, Z. et al. Gasdermin E suppresses tumour growth by activating anti-tumour immunity. *Nature* **579**, 415–420 (2020).
135. Rogers, C. et al. Gasdermin pores permeabilize mitochondria to augment caspase-3 activation during apoptosis and inflammasome activation. *Nat. Commun.* **10**, 1689 (2019).
136. Huang W. et al. DFNA5 attenuated in head and neck squamous cell carcinoma acquired with radio-resistance and associated with PD-L2 (2020).
137. Shan, L. et al. Visualizing head and neck tumors in vivo using near-infrared fluorescent transferrin conjugate. *Mol. Imaging* **7**, 42–49 (2008).
138. Lenarduzzi, M. et al. Hemochromatosis enhances tumor progression via upregulation of intracellular iron in head and neck cancer. *PloS ONE* **8**, e74075 (2013).
139. Järvinen, A. K. et al. Identification of target genes in laryngeal squamous cell carcinoma by high-resolution copy number and gene expression microarray analyses. *Oncogene* **25**, 6997–7008 (2006).
140. Dixon, S. J. et al. Ferroptosis: an iron-dependent form of nonapoptotic cell death. *Cell* **149**, 1060–1072 (2012).
141. Jiang, L. et al. Ferroptosis as a p53-mediated activity during tumour suppression. *Nature* **520**, 57–62 (2015).
142. Viswanathan, V. S. et al. Dependency of a therapy-resistant state of cancer cells on a lipid peroxidase pathway. *Nature* **547**, 453–457 (2017).
143. Dohadwala, M. et al. The role of ZEB1 in the inflammation-induced promotion of EMT in HNSCC. *Otolaryngol. Head Neck Surg.* **142**, 753–759 (2010).
144. Wu, J. et al. Intercellular interaction dictates cancer cell ferroptosis via NF2–YAP signalling. *Nature* **572**, 402–406 (2019).
145. Jung, Y. S., Kato, I. & Kim, H. R. A novel function of HPV16-E6/E7 in epithelial-mesenchymal transition. *Biochem. Biophys. Res. Commun.* **435**, 339–344 (2013).
146. Yagoda, N. et al. RAS-RAF-MEK-dependent oxidative cell death involving voltage-dependent anion channels. *Nature* **447**, 864–868 (2007).
147. Wu, Z. et al. Chaperone-mediated autophagy is involved in the execution of ferroptosis. *Proc. Natl Acad. Sci. USA* **116**, 2996–3005 (2019).
148. Gao, M. et al. Ferroptosis is an autophagic cell death process. *Cell Res.* **26**, 1021–1032 (2016).
149. Belleudi, F., Nanni, M., Raffa, S. & Torrisi, M. R. HPV16 E5 deregulates the autophagic process in human keratinocytes. *Oncotarget* **6**, 9370–9386 (2015).
150. Mattoscio D., Medda A. & Chiocca S. Human papilloma virus and autophagy. *Int. J. Mol. Sci.* **19**, 1775 (2018).
151. Tingting, C. et al. Human papillomavirus 16E6/E7 activates autophagy via Atg9B and LAMP1 in cervical cancer cells. *Cancer Med.* **8**, 4404–4416 (2019).
152. Sewell, A. et al. Reverse-phase protein array profiling of oropharyngeal cancer and significance of PIK3CA mutations in HPV-associated head and neck cancer. *Clin. Cancer Res.* **20**, 2300–2311 (2014).
153. Pietrocola, F. et al. Aspirin recapitulates features of caloric restriction. *Cell Rep.* **22**, 2395–2407 (2018).
154. Castoldi, F., Pietrocola, F., Maiuri, M. C. & Kroemer, G. Aspirin induces autophagy via inhibition of the acetyltransferase EP300. *Oncotarget* **9**, 24574–24575 (2018).
155. Hedberg, M. L. et al. Use of nonsteroidal anti-inflammatory drugs predicts improved patient survival for PIK3CA-altered head and neck cancer. *J. Exp. Med.* **216**, 419–427 (2019).
156. Wu, S. Y. et al. Ionizing radiation induces autophagy in human oral squamous cell carcinoma. *J. BUON* **19**, 137–144 (2014).
157. Kamarajan, P. et al. Head and neck squamous cell carcinoma metabolism draws on glutaminolysis, and stemness is specifically regulated by glutaminolysis via aldehyde dehydrogenase. *J. Proteome Res.* **16**, 1315–1326 (2017).
158. Gao, M. & Jiang, X. To eat or not to eat—the metabolic flavor of ferroptosis. *Curr. Opin. Cell Biol.* **51**, 58–64 (2018).
159. Yang, J. et al. Targeting cellular metabolism to reduce head and neck cancer growth. *Sci. Rep.* **9**, 4995 (2019).
160. Okazaki, S. et al. Glutaminolysis-related genes determine sensitivity to xCT-targeted therapy in head and neck squamous cell carcinoma. *Cancer Sci.* **110**, 3453–3463 (2019).
161. Zhang, Z. et al. ASCT2 (SLC1A5)-dependent glutamine uptake is involved in the progression of head and neck squamous cell carcinoma. *Br. J. Cancer* **122**, 82–93 (2020).
162. Zimmermann, P., Bette, M., Giel, G., Stuck, B. A. & Mandic, R. Influence of the xc-cystine/glutamate antiporter inhibitor sulfasalazine on the growth of head and neck squamous cell carcinoma cell lines. *Laryngo Rhino Otol.* **97**, 10050 (2018).
163. Okazaki, S. et al. Synthetic lethality of the ALDH3A1 inhibitor dyclonine and xCT inhibitors in glutathione deficiency-resistant cancer cells. *Oncotarget* **9**, 33832–33843 (2018).
164. Tao, X. et al. AP1G1 is involved in cetuximab-mediated downregulation of ASCT2-EGFR complex and sensitization of human head and neck squamous cell carcinoma cells to ROS-induced apoptosis. *Cancer Lett.* **408**, 33–42 (2017).

165. Yoshikawa, M. et al. xCT inhibition depletes CD44v-expressing tumor cells that are resistant to EGFR-targeted therapy in head and neck squamous cell carcinoma. *Cancer Res.* **73**, 1855–1866 (2013).
166. Zhang, P. et al. xCT expression modulates cisplatin resistance in Tca8113 tongue carcinoma cells. *Oncol. Lett.* **12**, 307–314 (2016).
167. Gao, M., Monian, P., Quadri, N., Ramasamy, R. & Jiang, X. Glutaminolysis and transferrin regulate ferroptosis. *Mol. Cell* **59**, 298–308 (2015).
168. Murphy, T. H., Miyamoto, M., Sastre, A., Schnaar, R. L. & Coyle, J. T. Glutamate toxicity in a neuronal cell line involves inhibition of cystine transport leading to oxidative stress. *Neuron* **2**, 1547–1558 (1989).
169. Yang, L. et al. Targeting stromal glutamine synthetase in tumors disrupts tumor microenvironment-regulated cancer cell growth. *Cell Metab.* **24**, 685–700 (2016).
170. Ferber, M. J. et al. Preferential integration of human papillomavirus type 18 near the c-myc locus in cervical carcinoma. *Oncogene* **22**, 7233–7242 (2003).
171. Liu, L. et al. Identification of reliable biomarkers of human papillomavirus 16 methylation in cervical lesions based on integration status using high-resolution melting analysis. *Clin. Epigenetics* **10**, 10 (2018).
172. Palmieri, E. M. et al. Pharmacologic or genetic targeting of glutamine synthetase skews macrophages toward an M1-like phenotype and inhibits tumor metastasis. *Cell Rep.* **20**, 1654–1666 (2017).
173. Fazzari, J., Linher-Melville, K. & Singh, G. Tumour-derived glutamate: linking aberrant cancer cell metabolism to peripheral sensory pain pathways. *Curr. Neuropharmacol.* **15**, 620–636 (2017).
174. Bertero, T. et al. Tumor-stroma mechanics coordinate amino acid availability to sustain tumor growth and malignancy. *Cell Metab.* **29**, 124–40.e10 (2019).
175. Wang, Y. et al. Fibroblasts in head and neck squamous cell carcinoma associated with perineural invasion have high-level nuclear yes-associated protein (YAP) expression. *Acad. Pathol.* **2**, 2374289515616972 (2015).
176. Ge, L. et al. Yes-associated protein expression in head and neck squamous cell carcinoma nodal metastasis. *PloS ONE* **6**, e27529 (2011).
177. García-Escudero, R. et al. Overexpression of PIK3CA in head and neck squamous cell carcinoma is associated with poor outcome and activation of the YAP pathway. *Oral. Oncol.* **79**, 55–63 (2018).
178. LeBlanc L. et al. Yap1 safeguards mouse embryonic stem cells from excessive apoptosis during differentiation. *Elife.* **7**, e40167 (2018)
179. Wang, W. et al. CD8(+) T cells regulate tumour ferroptosis during cancer immunotherapy. *Nature* **569**, 270–274 (2019).
180. Yamazaki, T. et al. Defective immunogenic cell death of HMGB1-deficient tumors: compensatory therapy with TLR4 agonists. *Cell Death Differ.* **21**, 69–78 (2014).
181. Wen, Q., Liu, J., Kang, R., Zhou, B. & Tang, D. The release and activity of HMGB1 in ferroptosis. *Biochem. Biophys. Res. Commun.* **510**, 278–283 (2019).
182. Wild, C. A. et al. HMGB1 is overexpressed in tumor cells and promotes activity of regulatory T cells in patients with head and neck cancer. *Oral. Oncol.* **48**, 409–416 (2012).
183. Yang, W. S. et al. Regulation of ferroptotic cancer cell death by GPX4. *Cell* **156**, 317–331 (2014).
184. Kim, E. H., Shin, D., Lee, J., Jung, A. R. & Roh, J.-L. CISD2 inhibition overcomes resistance to sulfasalazine-induced ferroptotic cell death in head and neck cancer. *Cancer Lett.* **432**, 180–190 (2018).
185. Roh, J. L., Kim, E. H., Jang, H. J., Park, J. Y. & Shin, D. Induction of ferroptotic cell death for overcoming cisplatin resistance of head and neck cancer. *Cancer Lett.* **381**, 96–103 (2016).
186. Lang, X. et al. Radiotherapy and immunotherapy promote tumoral lipid oxidation and ferroptosis via synergistic repression of SLC7A11. *Cancer Disco.* **9**, 1673–1685 (2019).
187. Lin, R. et al. Dihydroartemisinin (DHA) induces ferroptosis and causes cell cycle arrest in head and neck carcinoma cells. *Cancer Lett.* **381**, 165–175 (2016).
188. Shaw, A. T. et al. Selective killing of K-ras mutant cancer cells by small molecule inducers of oxidative stress. *Proc. Natl Acad. Sci. USA* **108**, 8773–8778 (2011).
189. Chen, J. J. & Galluzzi, L. Fighting resilient cancers with iron. *Trends Cell Biol.* **28**, 77–78 (2018).
190. Pisanti, S., Picardi, P., Ciaglia, E., D'Alessandro, A. & Bifulco, M. Novel prospects of statins as therapeutic agents in cancer. *Pharm. Res.* **88**, 84–98 (2014).
191. Cruz, S. A., Qin, Z., Stewart, A. F. R. & Chen, H. H. Dabrafenib, an inhibitor of RIP3 kinase-dependent necroptosis, reduces ischemic brain injury. *Neural Regen. Res.* **13**, 252–256 (2018).
192. Fulda, S. Repurposing anticancer drugs for targeting necroptosis. *Cell Cycle* **17**, 829–832 (2018).
193. Yang, H. et al. Contribution of RIP3 and MLKL to immunogenic cell death signaling in cancer chemotherapy. *Oncoimmunology* **5**, e1149673–e1149673 (2016).
194. Oliver Metzig, M. et al. Inhibition of caspases primes colon cancer cells for 5-fluorouracil-induced TNF-α-dependent necroptosis driven by RIP1 kinase and NF-κB. *Oncogene* **35**, 3399–3409 (2016).
195. Huang, X. et al. Bypassing drug resistance by triggering necroptosis: recent advances in mechanisms and its therapeutic exploitation in leukemia. *J. Exp. Clin. Cancer Res.* **37**, 310 (2018).
196. Valter, K., Zhivotovsky, B. & Gogvadze, V. Cell death-based treatment of neuroblastoma. *Cell Death Dis.* **9**, 113 (2018).
197. Zhang, C. C. et al. Chemotherapeutic paclitaxel and cisplatin differentially induce pyroptosis in A549 lung cancer cells via caspase-3/GSDME activation. *Apoptosis* **24**, 312–325 (2019).
198. Johnson, D. C. et al. DPP8/DPP9 inhibitor-induced pyroptosis for treatment of acute myeloid leukemia. *Nat. Med.* **24**, 1151–1156 (2018).
199. Woo, J. H. et al. Elucidating compound mechanism of action by network perturbation analysis. *Cell* **162**, 441–451 (2015).
200. Lachaier, E. et al. Sorafenib induces ferroptosis in human cancer cell lines originating from different solid tumors. *Anticancer Res.* **34**, 6417–6422 (2014).
201. Möckelmann, N. et al. Effect of sorafenib on cisplatin-based chemoradiation in head and neck cancer cells. *Oncotarget* **7**, 23542–23551 (2016).
202. Guo, J. et al. Ferroptosis: a novel anti-tumor action for Cisplatin. *Cancer Res. Treat.* **50**, 445–460 (2018).
203. Liu T., Zhang J., Li K., Deng L. & Wang H. Combination of an autophagy inducer and an autophagy inhibitor: a smarter strategy emerging in cancer therapy. *Front. Pharmacol.* **11**, 408 (2020).
204. Chude C. I. & Amaravadi R. K. Targeting autophagy in cancer: update on clinical trials and novel inhibitors. *Int. J. Mol. Sci.* **18**, 1279 (2017).
205. Al-Bari, M. A. Chloroquine analogues in drug discovery: new directions of uses, mechanisms of actions and toxic manifestations from malaria to multifarious diseases. *J. Antimicrob. Chemother.* **70**, 1608–1621 (2015).
206. Maiuri, M. C. et al. BH3-only proteins and BH3 mimetics induce autophagy by competitively disrupting the interaction between Beclin 1 and Bcl-2/Bcl-X(L). *Autophagy* **3**, 374–376 (2007).
207. Kreimer, A. R., Clifford, G. M., Boyle, P. & Franceschi, S. Human papillomavirus types in head and neck squamous cell carcinomas worldwide: a systematic review. *Cancer Epidemiol. Biomark. Prev.* **14**, 467–475 (2005).
208. Descamps, G., Wattiez, R. & Saussez, S. Proteomic study of HPV-positive head and neck cancers: preliminary results. *BioMed. Res. Int.* **2014**, 430906 (2014).
209. Canning, M. et al. Heterogeneity of the head and neck squamous cell carcinoma immune landscape and its impact on immunotherapy. *Front. Cell Dev. Biol.* **7**, 52 (2019).
210. Kobayashi, K. et al. A review of HPV-related head and neck cancer. *J. Clin. Med.* **7**, 241 (2018).

17. Vistejnova L, Dvorakova J, Hasova M, *et al*: The comparison of impedance-based method of cell proliferation monitoring with commonly used metabolic-based techniques. Neuroendocrinol Lett 30: 121-127, 2009.
18. Carroll AG, Voeller HJ, Sugars L and Gelmann EP: p53 oncogene mutations in 3 human prostate-cancer cell-lines. Prostate 23: 123-134, 1993.
19. Rubin SJ, Hallahan DE, Ashman CR, *et al*: 2 prostate carcinoma cell-lines demonstrate abnormalities in tumor suppressor genes. J Surg Oncol 46: 31-36, 1991.
20. Sztalmachova M, Hlavna M, Gumulec J, *et al*: Effect of zinc(II) ions on the expression of pro- and anti-apoptotic factors in high-grade prostate carcinoma cells. Oncol Rep 28: 806-814, 2012.
21. Schmieg FI and Simmons DT: Characterization of the in vitro interaction between SV40 T-antigen and p53: mapping the p53 binding-site. Virology 164: 132-140, 1988.
22. Gonin S, Diaz-Latoud C, Richard MJ, *et al*: p53/T-antigen complex disruption in T-antigen transformed NIH3T3 fibroblasts exposed to oxidative stress: correlation with the appearance of a Fas/APO-1/CD95 dependent, caspase independent, necrotic pathway. Oncogene 18: 8011-8023, 1999.
23. Barr MP, Gray SG, Hoffmann AC, *et al*: Generation and characterisation of cisplatin-resistant non-small cell lung cancer cell lines displaying a stem-like signature. Plos One 8: 1-19, 2013.
24. Liu J, Liu YP, Habeebu SSM and Klaassen CD: Metallothionein (MT)-null mice are sensitive to cisplatin-induced hepatotoxicity. Toxicol Appl Pharmacol 149: 24-31, 1998.
25. Siddik ZH: Cisplatin: mode of cytotoxic action and molecular basis of resistance. Oncogene 22: 7265-7279, 2003.
26. Wang D and Lippard SJ: Cellular processing of platinum anticancer drugs. Nat Rev Drug Discov 4: 307-320, 2005.
27. Gravina GL, Marampon F, Di Staso M, *et al*: 5-Azacitidine restores and amplifies the bicalutamide response on preclinical models of androgen receptor expressing or deficient prostate tumors. Prostate 70: 1166-1178, 2010.
28. Aitken RJ, Whiting S, De Iuliis GN, McClymont S, Mitchell LA and Baker MA: Electrophilic aldehydes generated by sperm metabolism activate mitochondrial reactive oxygen species generation and apoptosis by targeting succinate dehydrogenase. J Biol Chem 287: 33048-33060, 2012.
29. Komatsu M, Waguri S, Ueno T, *et al*: Impairment of starvation-induced and constitutive autophagy in Atg7-deficient mice. J Cell Biol 169: 425-434, 2005.
30. Cao C, Subhawong T, Albert JM, *et al*: Inhibition of mammalian target of rapamycin or apoptotic pathway induces autophagy and radiosensitizes PTEN null prostate cancer cells. Cancer Res 66: 10040-10047, 2006.
31. Masarik M, Gumulec J, Hlavna M, *et al*: Monitoring of the prostate tumour cells redox state and real-time proliferation by novel biophysical techniques and fluorescent staining. Integr Biol 4: 672-684, 2012.
32. Kuwana T and Newmeyer DD: Bcl-2-family proteins and the role of mitochondria in apoptosis. Curr Opin Cell Biol 15: 691-699, 2003.
33. Kharaziha P, Rodriguez P, Li Q, *et al*: Targeting of distinct signaling cascades and cancer-associated fibroblasts define the efficacy of Sorafenib against prostate cancer cells. Cell Death Dis 3: 1-10, 2012.
34. Li GQ, Chen XG, Wu XP, *et al*: Effect of dicycloplatin, a novel platinum chemotherapeutical drug, on inhibiting cell growth and inducing cell apoptosis. Plos One 7: 1-13, 2012.
35. Kondo Y, Kuo SM, Watkins SC and Lazo JS: Metallothionein localization and cisplatin resistance in human hormone-independent prostatic tumor-cell lines. Cancer Res 55: 474-477, 1995.
36. Suzuki Y, Kondo Y, Himeno S, Nemoto K, Akimoto M and Imura N: Role of antioxidant systems in human androgen-independent prostate cancer cells. Prostate 43: 144-149, 2000.
37. Yamasaki M, Nomura T, Sato F and Mimata H: Metallothionein is up-regulated under hypoxia and promotes the survival of human prostate cancer cells. Oncol Rep 18: 1145-1153, 2007.
38. Costello LC, Fenselau CC and Franklin RB: Evidence for operation of the direct zinc ligand exchange mechanism for trafficking, transport, and reactivity of zinc in mammalian cells. J Inorg Biochem 105: 589-599, 2011.
39. Bell SG and Vallee BL: The metallothionein/thionein system: an oxidoreductive metabolic zinc link. Chembiochem 10: 55-62, 2009.
40. Pratibha R, Sameer R, Rataboli PV, Bhiwgade DA and Dhume CY: Enzymatic studies of cisplatin induced oxidative stress in hepatic tissue of rats. Eur J Pharmacol 532: 290-293, 2006.

4.2 A novel methodological approach for the direct determination of cell death and the distinction of specific subtypes

4.2.1 Microscopic methods for the study of the dynamics of cells

Because of its non-invasive nature, label-free imaging is a valuable approach for studying biological processes, including cell death. However, conventional microscopic methods such as phase contrast (PC) and differential interference contrast (DIC) often produce shadow artifacts that complicate automatic segmentation. This research aimed to assess the effectiveness of various published segmentation workflow steps – including image reconstruction, foreground segmentation, cell detection (seed-point extraction), and instance segmentation - using a dataset comprising the same cell types captured through different contrast microscopy techniques.

We developed a series of routines designed for the segmentation of viable adherent cells cultured in dishes, utilizing images obtained from phase contrast, differential interference contrast, Hoffman modulation contrast, and quantitative phase imaging. Our study conducted an extensive evaluation of existing segmentation techniques suitable for label-free images. We highlighted the importance of the image reconstruction phase, which allows for the application of segmentation methods that were previously ineffective on label-free data. Additionally, we analyzed various foreground segmentation approaches (including thresholding, feature extraction, level-set techniques, graph cuts, and machine learning-based methods), seed-point extraction techniques (such as Laplacian of Gaussians, radial symmetry and distance transforms, iterative radial voting, maximally stable extremal regions, and learning-based methods), as well as methods for segmenting individual cells. We validated an appropriate selection of techniques for each type of microscopy and made our findings publicly available online [9, 10].

Author's publications relevant to this chapter

1. Vicar, T., Balvan, J., *et al*. Cell segmentation methods for label-free contrast microscopy: review and comprehensive comparison. *BMC bioinformatics* **20**, 360, (2019).

IF (2019) 3.242; 129 citations (WOS)

Vicar *et al. BMC Bioinformatics* (2019) 20:360
https://doi.org/10.1186/s12859-019-2880-8

BMC Bioinformatics

METHODOLOGY ARTICLE Open Access

Cell segmentation methods for label-free contrast microscopy: review and comprehensive comparison

Tomas Vicar[1,2], Jan Balvan[3,4], Josef Jaros[6,7], Florian Jug[5], Radim Kolar[1], Michal Masarik[3,4] and Jaromir Gumulec[2,3,4*]

Abstract

Background: Because of its non-destructive nature, label-free imaging is an important strategy for studying biological processes. However, routine microscopic techniques like phase contrast or DIC suffer from shadow-cast artifacts making automatic segmentation challenging. The aim of this study was to compare the segmentation efficacy of published steps of segmentation work-flow (image reconstruction, foreground segmentation, cell detection (seed-point extraction) and cell (instance) segmentation) on a dataset of the same cells from multiple contrast microscopic modalities.

Results: We built a collection of routines aimed at image segmentation of viable adherent cells grown on the culture dish acquired by phase contrast, differential interference contrast, Hoffman modulation contrast and quantitative phase imaging, and we performed a comprehensive comparison of available segmentation methods applicable for label-free data. We demonstrated that it is crucial to perform the image reconstruction step, enabling the use of segmentation methods originally not applicable on label-free images. Further we compared foreground segmentation methods (thresholding, feature-extraction, level-set, graph-cut, learning-based), seed-point extraction methods (Laplacian of Gaussians, radial symmetry and distance transform, iterative radial voting, maximally stable extremal region and learning-based) and single cell segmentation methods. We validated suitable set of methods for each microscopy modality and published them online.

Conclusions: We demonstrate that image reconstruction step allows the use of segmentation methods not originally intended for label-free imaging. In addition to the comprehensive comparison of methods, raw and reconstructed annotated data and Matlab codes are provided.

Keywords: Microscopy, Cell segmentation, Image reconstruction, Methods comparison, Differential contrast image, Quantitative phase imaging, Laplacian of Gaussians

Background

Microscopy has been an important technique for studying biology for decades. Accordingly, fluorescence microscopy has an irreplaceable role in analyzing cellular processes because of the possibility to study the functional processes and morphological aspects of living cells. However, fluorescence labeling also brings a number of disadvantages. These include photo-bleaching, difficult signal reproducibility, and inevitable photo-toxicity (which results not only from staining techniques but also from transfection) [1]. Label-free microscopy techniques are the most common techniques for live cell imaging thanks to its non-destructive nature, however, due to the transparent nature of cells, methods of contrast enhancement based on phase information are required.

The downside of contrast enhancement is an introduction of artifacts; Phase contrast (PC) images contain halo and shade-off, differential image contrast (DIC) and Hoffman Modulation Contrast (HMC) introduce non-uniform

*Correspondence: j.gumulec@med.muni.cz
[2]Department of Physiology, Faculty of Medicine, Masaryk University, Kamenice 5, CZ-62500 Brno, Czech Republic
[3]Department of Pathological Physiology, Faculty of Medicine, Masaryk University, Kamenice 5, CZ-62500 Brno, Czech Republic
Full list of author information is available at the end of the article

© The Author(s). 2019 **Open Access** This article is distributed under the terms of the Creative Commons Attribution 4.0 International License (http://creativecommons.org/licenses/by/4.0/), which permits unrestricted use, distribution, and reproduction in any medium, provided you give appropriate credit to the original author(s) and the source, provide a link to the Creative Commons license, and indicate if changes were made. The Creative Commons Public Domain Dedication waiver (http://creativecommons.org/publicdomain/zero/1.0/) applies to the data made available in this article, unless otherwise stated.

shadow-cast artifacts (3D-like topographical appearance). Although various segmentation procedures have been developed to suppress these artifacts, a segmentation is still challenging.

On the other hand, quantitative phase imaging (QPI), provides artifact-free images of sufficient contrast. Although there are no standardized methods for the segmentation of QPI-based images, fundamental methods for segmentation of artifact-free images (e.g. from fluorescence microscopy) will be utilized.

In this review, we describe and compare relevant methods of the image processing pipeline in order to find the most appropriate combination of particular methods for most common label-free microscopic techniques (PC, DIC, HMC and QPI). Our aim is to evaluate and discuss the influence of the commonly used methods for microscopic image reconstruction, foreground-background segmentation, seed-point extraction and cell segmentation. We used real samples - viable, non-stained adherent prostatic cell lines and captured identical fields of view and cells manually segmented by a biologist. Compared to microscopic organisms like yeast or bacteria, adherent cells are morphologically distinctly heterogeneous and in label-free microscopy, the segmentation is therefore still a challenge. We will use the most common imaging modalities used by biologist and we will provide a recommendation of image processing pipeline steps for particular microscopic technique.

The segmentation strategies tested herein are selected to provide the most heterogeneous overview of recent state of the art excluding the simplest and outdated methods (e.g. simple connected component detection, ultimate erosion, distance transform without h-maxima etc.). Deep-learning strategies are intentionally not included due to their distinct differences, high demands on training data and the range of possible settings (training hyperparameters, network architecture, etc.).

Results

In the paragraphs below we provide a detailed summary of each image processing step from the pipeline (see Fig. 1), followed by short description of achieved results. We start with description of "all-in-one" tools and continue with image reconstruction, foreground-background segmentation, cell detection and final single cell segmentation (i.e. instance segmentation).

Due to the large number of tested methods and approaches, we have decided to introduce a specific designation of the methods. We used prefix in order to refer to image reconstruction ('r'), foreground-background segmentation ('s') and cell detection ('d') and finally to all-in-one tools ('aio'). The list of these designations, number of parameters to be adjusted in these methods and computational demands are provided in Table 1.

"All-in-one" tools

First, we performed an analysis with the available commercial and freeware "all-in-one" tools including FARSIGHT [2], CellX [3], Fogbank [4], FastER [5], CellTracer [6], SuperSegger [7], CellSerpent [8], CellStar [9], CellProfiler [10] and Q-PHASE' Dry mass guided watershed (DMGW) [11]. As shown in Table 2 the only algorithm providing usable segmentation results for raw images is Fogbank, which is designed to be an universal and easy to set segmentation tool. Very similar results were provided by CellProfiler, which is easy to use tool allowing to crate complete cell analysis pipelines, however, it works sufficiently only for reconstructed images. The QPI' dedicated DMGW provided exceptional results, but for this microscopic technique only. The remaining methods did not provide satisfactory results on label free data; FastER, although user-friendly, failed because of the nature of its maximally stable extremal region (MSER) detector. FARSIGHT failed with the automatic threshold during foreground segmentation. CellX failed in both the cell detection with gradient-based Hough transform and in the membrane pattern detection because of indistinct cell borders. The remaining segmentation algorithms - CellStar, SuperSegger, CellSerpent - were completely unsuitable for label-free non-round adherent cells with Dice coefficient < 0.1 and thus are not listed in Table 2 and Fig. 4.

Because of the low segmentation performance of the examined "all-in-one" methods, we decided to divide the segmentation procedure into four steps - (1) image reconstruction (2) background segmentation, (3) cell detection (seed expansion) and (4) segmentation tailored to the specific properties of individual microscopic techniques (see Fig. 1).

Image reconstruction

As shown, the performance of most "all-in-one" methods is limited for label-free data, in particular due to the presence of contrast-enhancing artifacts in microscopic images. Image reconstruction was therefore employed to reduce such artifacts. Methods by Koos [12] and Yin [13] (further abbreviated rDIC-Koos and rDIC-Yin, respectively) were used for DIC and HMC images. Images of PC microscopy were reconstructed by Top-Hat filter involving algorithm by the Dewan [16] (rPC-TopHat), or Yin method (rPC-Yin) [14].

Generally, following conclusions apply for image reconstructions:

- No distinctive differences in image reconstruction efficacy were observed between the microscopic methods apart from QPI, as shown in Fig. 2 (described by area under curve, AUC, see Methods for details).
- The AUC of QPI was distinctly higher with values near 0.99

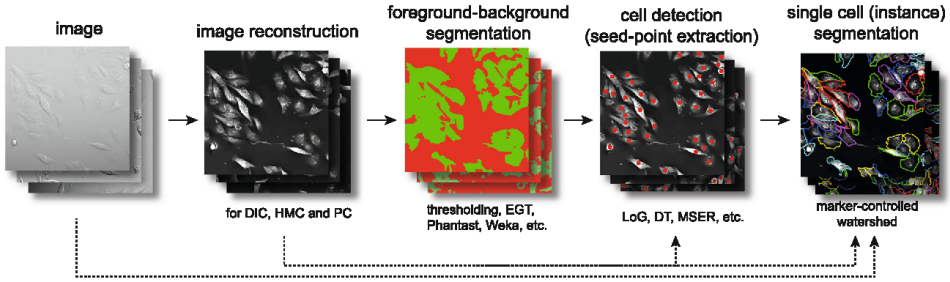

Fig. 1 Block diagram showing segmentation approach. For details of individual steps, see Results and Materials and Methods.EGT, empirical gradient treshold; LoG, Laplacian of Gaussians, DT, distance transform, MSER maximally stable extremal region

- Computationally more-demanding methods (rDIC-Koos and rPC-Yin) perform better except for relatively simple rPC-Top-Hat, which provides similar results
- Probability maps generated by sWeka or sIllastik can be used like reconstructions in later segmentation steps. The advantage of this approach is the absence of the need to optimize parameters.

DIC and HMC reconstructions

With regard to the morphology of reconstructed images, rDIC-Koos provides a detailed structure of the cells with distinctive borders from the background. For rDIC-Yin [13], details of the reconstructed cells are more blurred and uneven background with the dark halos around the cells (see Fig. 2) complicating the following segmentation. As a result, AUC of rDIC-Yin was distinctly lower as compared with the others.

Both rDIC-Koos [12] and rDIC-Yin [13] methods work on the principle of minimizing their defined energy function. The main difference is that better-performing Koos [12] uses l1-norm (instead of l2) for sparse regularization term. Yin's l2-norm, on the other hand, enables derivation of closed form solution, which is much simpler and thus faster to compute. Time needed for the reconstruction is dramatically different - 2.1 s, 36.6 min, 13.1 min and 0.17 s for rDIC-Koos, rDIC-Yin, rPC-Koos and rPC-TopHat, respectively. rDIC-Koos also introduces a parameter for the number of iterations, which is however insensitive within the tested range.

Although these methods were not designed for use on HMC images, the same conclusions also apply for the reconstruction of those images, which showed only slightly worse results. The results of reconstruction accuracy can be seen in Fig. 2. Combinations of the best-performing parameters are listed in the Additional file 1.

Phase contrast reconstruction

From the perspective of cellular morphology of reconstructed images, rPC-TopHat creates artifacts between closely located cells with the borders precisely distinguishable. Reconstruction based on rPC-Yin [14] causes an even background without observable artifacts around the cells, however cell borders are missing and mitotic cells are not properly reconstructed (see Fig. 2).

The optimization of the PSF parameters of rPC-Yin reconstruction is problematic. The PSF parameters of a particular microscope are not always listed or known. Searching for these parameters with optimization proved to be complicated. Because the optimizing function is not smooth and contains many local local extrema, the result changes significantly and chaotically even with a small change of parameters or, at the same time, combinations of parameter settings give very similar (near optimal) results.

Regarding the computational times, the rPC-Yin reconstruction works very similarly as the rDIC-Koos approach for DIC, with similar computational difficulties. The result of a simple top-hat filter unexpectedly turned out to be comparable to the complex and computationally difficult rPC-Yin method. For the reconstruction performance see Fig. 2, for optimal parameter setting see the Additional file 1.

Foreground-background segmentation

In the next step of the workflow, the image foreground (cells) was segmented from the image background. Both unprocessed and reconstructed images were used. Following strategies were used for the foreground-background segmentation: (a) Thresholding-based methods: simple threshold (sST), automatic threshold based on Otsu et al. [17] (sOtsu), and Poisson distribution-based treshold (sPT) [2], (b) feature-extracting strategies: empirical gradient threshold (sEGT) [18] and approaches specific for PC microscopy by Juneau et al. (sPC-Juneau) [19], Jaccard et al. (sPC-Phantast) [21], and Topman (sPC-Topman) [20]), (c) Level-Set-based methods: Castelles et al. [22] (sLSCaselles), and Chan-Vese et al. [23] (sLS-

Table 1 List of tested segmentation methods and all-in-one segmentation tools and definition of abbreviations

Segmentation step	Abbreviation	Description	Setable parameters	Computational time	Ref.
All in one tools					
	aioFasright	Nucleus editor of Farsight toolkit	N/A	4.96 s	[2]
	aioCellX	segmentation, fluorescence quantification, and tracking tool CellX	N/A	10.30 s	[3]
	aioFogbank	single cell segmentation tool FogBank according Chalfoun	N/A	12.00 s	[4]
	aioFastER	fastER - user-friendly tool for ultrafast and robust cell segmentation	N/A	0.42 s	[5]
	aioCellProfiler	tool for cell analysis pipelines including single cell segmentation	N/A	11.8 s	[10]
	aioDMGW	Dry mass-guided watershed method, (Q-PHASE, Tescan)		1.00 s	
Reconstruction					
	rDIC-Koos	DIC/HMC image reconstruction according Koos	2	36.60 min	[12]
	rDIC-Yin	DIC/HMC image reconstruction according Yin	2	2.10 s	[13]
	rPC-Yin	PC image reconstruction according Yin	4	13.10 min	[14]
	rPC-Tophat	PC image reconstruction according Thirusittampalam and Dewan	1	0.17 s	[15, 16]
Foreground-background segmentation					
	sST	simple thresholding	1	< 0.01 s	
	sOtsu	thresholding using Gaussian distribution	0	<0.01 s	[17]
	sPT	thresholding using Poisson distribution	0	<0.01 s	[2]
	sEGT	empirical gradient threshold	3	0.24 s	[18]
	sPC-Juneau	Feature extraction approach according Juneau	3	0.26 s	[19]
	sPC-Topman	Feature extraction approach according Topman	4	0.35 s	[20]
	sPC-Phantast	Phantast toolbox developed by Jaccard	5	0.35 s	[21]
	sLS-Caselles	Level-set with edge-based method	2	31.40 s	[22]
	sLS-ChanVese	Level-set with region-based method	2	11.10 s	[23]
	sGraphCut	Graph-Cut applied on recosntructed and raw data	2	15.80 s	[24]
	sWekaGraphCut	Graph-Cut applied on probability maps generated by Weka	2	31.80 min**	[24]
	sIlastikGraphCut	Graph-Cut applied on probability maps generated by Ilastik	2	31.52 min**	[24]
	sIlastik	machine learning tool by Sommer	N/A	31.20 min+21 s*	[25].
	sWeka	machine learning tool by Arganda-Carreras	N/A	27.60 min+2.20 min*	[26]
Cell detection (seed-point extraction)					
	dLoGm-Peng	multiscale LoG by Peng	4	3.60 s	[27]
	dLoGm-Kong	multiscale LoG by Kong	5	4.20 s	[28]
	dLoGg-Kong	generalized LoG filter by Kong	2	46.40 s	[28]
	dLoGg-Xu	generalized LoG filter by Xu	3	5.10 s	[29]

Table 1 List of tested segmentation methods and all-in-one segmentation tools and definition of abbreviations (*Continued*)

Segmentation step	Abbreviation	Description	Setable parameters	Computational time	Ref.
	dLoGh-Zhang	Hessian analysis of LoG images by Zhang	1	8.90 s	[30]
	dFRST	fast radial-symmetry transform	5	153.10 s	[31]
	dGRST	generalized radial-symmetry transform	5	572.30 s	[32]
	dRV-Qi	radial voting methods by Qi et al.	5	95.00 s	[33]
	dDT-Threshold	distance transform by Thirusittampalam, threshold-generated foreground	4	0.11 s	[15]
	dDT-Weka	distance transform by Thirusittampalam, sWeka-generated foreground	3	0.11 s‡	[15]
	dMSER	maximally stable extremal region method (MSER)	3	2.10 s	[34]
	dCellDetect	machine learning method based on MSER	1	141.70 s/60.20 s*	[35]
Single cell (instance) segmentation					
	MCWS†	Marker-conttrolled watershed	0	1.40 s	
	MCWS-dDT†	Marker-conttrolled watershed on DT image	0	1.41 s	

For detailed list of optimized parameters see Additional file 1. * computational time for learning based approaches indicated as two values for learning and classification. ** computational time for Weka+Graph cut combination shown as sum time of these methods. ‡ not includes time for Weka probability map creation, † indicate final segmentation step following foreground-background segmentation and seed-point extraction. Number of parameters in "all-in-one" approaches not shown because of the GUI-based nature, similarly, not shown for learning-based approaches, see Methods section for details. Computational time shown for one 1360×1024 DIC field of view

ChanVese), (d) Graph-cut [24], and (e) Learning-based Ilastik [25], and Trainable Weka Segmentation [26].

Based on the obtained results, this step can be considered the least problematic in segmentation, with the following general findings:

- Well-performing methods (e.g. sWeka, sIllastik, sLS-Caselles,sEGT, sPC-Juneau) are robust enough to work even on unreconstructed data.
- Image reconstruction improves foreground-background segmentation efficacy and once reconstructed, there are no distinct differences in segmentation efficacy between microscopic techniques
- QPI performs dramatically better even unreconstructed
- Learning-based methods (sWeka and sIlastik) perform better by a few units of percents. Its performance can further be improved with GraphCut.
- More time-consuming methods (sLS-Caselles, sLS-ChanVese, sGraphCut, sWeka, sIlastik) does not necesarily provide better results. For detailed results, see chapters below and Fig. 3.

Threshold-based approaches

The Simple threshold (sST) provides better results than automatic thresholding techniques assuming Poisson distribution (sPT) or Otsu method (sOtsu). The potential of these automatic techniques lies in the segmentation of images, where optimal threshold value varies between the images. However, this is not necessary for QPI images (constant background value increases success of sST) and for reconstructed images with background removal (background values are close to zero, so the histogram cannot be properly fitted with Gaussian or Poison distribution, see Table 2). There are not any parameters to optimize for sOtsu and sPT methods, which is the main advantage. The results of thresholding could be potentially improved by morphological adjustments. Regarding the computational times, these are the simplest and thus the fastest possible methods, which are listed mainly to provide basic idea about the segmentability of our data.

Feature-extraction-based approaches

The feature-based approaches - sEGT, sPC-Topman, sPC-Phantast and sPC-Juneau are all mainly based on the extraction of some feature image, which is then thresholded and morphologically modified. Because of feature thresholding strategies, the segmentation is possible without the image reconstruction. Thus these methods are among the most straightforward approaches to extract and threshold some local features (e.g. absolute value of gradient or local standard deviation).

All these methods can be easily adjusted, have the same number of parameters and the segmentation performance is very similar (see Table 1) with slightly better-performing sEGT. Compared to the other feature-extraction-based methods, sEGT includes elimination of small holes.

Table 2 The segmentation efficacy (shown as Dice coefficient) of individual segmentation steps on raw and reconstructed image data

Method	Segmentation efficacy (Dice coefficient)									
	QPI	DIC			HMC			PC		
	raw	raw	rDIC Koos [12]	rDIC Yin [13]	raw	rDIC Koos [12]	rDIC Yin [13]	raw	rPC Yin [14]	rPC TopHat [15]
Foreground-background segmentation										
sWekaGraphCut	0.96	0.86	0.89	0.84	0.86	0.84	0.84	0.86	0.80	0.84
sIllastikGraphCut	0.94	0.87	0.89	0.84	0.87	0.84	0.84	0.80	0.80	0.84
sWeka	0.94	0.85	0.87	0.80	0.85	0.82	0.79	0.81	0.72	0.81
sIlastik	0.94	0.85	0.86	0.80	0.82	0.82	0.79	0.84	0.72	0.82
sLS-Caselles	0.88	0.83	0.82	0.79	0.84	0.79	0.79	0.77	0.75	0.79
sEGT	0.89	0.88	0.85	0.64	0.86	0.79	0.70	0.74	0.68	0.79
sPC-Phantast	N/A	N/A	N/A	N/A	N/A	N/A	N/A	0.77	N/A	N/A
sPC-Juneau	0.85	0.85	0.84	0.59	0.82	0.77	0.69	0.73	0.72	0.76
sPC-Topman	N/A	N/A	N/A	N/A	N/A	N/A	N/A	0.72	N/A	N/A
sLS-ChanVese	0.61	0.48	0.74	0.55	0.68	0.67	0.36	0.64	0.65	0.76
sGraphCut	0.92	0.38	0.78	0.64	0.32	0.59	0.58	0.40	0.70	0.74
sST	0.92	0.339	0.76	0.61	0.31	0.72	0.53	0.40	0.69	0.73
sPT	0.83	0.34	0.60	0.34	0.30	0.46	0.08	0.29	0.67	0.73
sOtsu	0.62	0.34	0.36	0.31	0.28	0.16	0.18	0.24	0.51	0.66
Cell detection (seed point extraction)										
dGRST	0.94	0.65	0.79	0.85	0.75	0.81	0.85	0.81	0.77	0.88
dLoGm-Kong	0.90	0.83	0.90	0.86	0.72	0.84	0.85	0.52	0.69	0.78
dFRST	0.94	0.58	0.78	0.82	0.70	0.78	0.82	0.82	0.74	0.88
dLoGm-Peng	0.89	0.71	0.86	0.78	0.69	0.83	0.86	0.51	0.73	0.84
dLoGg-Kong	0.85	0.83	0.80	0.84	0.74	0.82	0.83	0.43	0.72	0.79
dDT-Weka	0.81	0.68	0.81	0.74	0.73	0.72	0.75	0.80	0.76	0.78
dLoGg-Xu	0.84	0.77	0.80	0.80	0.65	0.81	0.78	0.52	0.71	0.78
dDT-Threshold	0.94	0.26	0.91	0.86	0.54	0.86	0.84	0.49	0.76	0.81
dRV-Qi	0.77	0.61	0.57	0.58	0.70	0.48	0.48	0.82	0.59	0.65
dMSER	0.93	0.06	0.55	0.58	0.29	0.82	0.69	0.65	0.79	0.68
dCellDetect	0.92	0.00	0.88	0.89	0.00	0.83	0.84	0.00	0.71	0.81
dLoGh-Zhang	0.82	0.13	0.52	0.64	0.25	0.63	0.65	0.49	0.70	0.61
Single cell (instance) segmentation										
MCWS-dDT†	0.77	0.58	0.66	0.61	0.47	0.54	0.55	0.52	0.37	0.62
MCWS†	0.82	0.55	0.69	0.63	0.26	0.54	0.53	0.41	0.39	0.60
aioFogbank	0.71	0.54	0.55	0.42	0.44	0.38	0.39	0.46	0.34	0.19
aioCellProfiler	0.69	0.37	0.55	0.38	0.19	0.45	0.27	0.09	0.41	0.54
aioDMGW	0.82	0.08	0.62	0.38	0.00	0.48	0.29	0.10	0.39	0.65
aioFasright	0.21	0.15	0.43	0.00	0.00	0.26	0.14	0.03	0.37	0.57
aioCellX	0.34	0.03	0.08	0.21	0.02	0.18	0.05	0.07	0.03	0.16
aioFastER	0.09	0.03	0.07	0.00	0.02	0.17	0.01	0.25	0.08	0.06

Sorted by Dice coefficient (high to low). N/A, not applicable, for foreground background segmentation, methods designated for PC image were not deployed on other microscopic modalities

The performance of feature-extraction methods is technique-dependent with the highest scores for DIC and QPI and the lowest (but still high) for PC. This is mostly due to halos in PC; although sPC-Topman and sPC-Phantast are extended by the elimination of PC artifact regions, sPC-Topman have even worse results

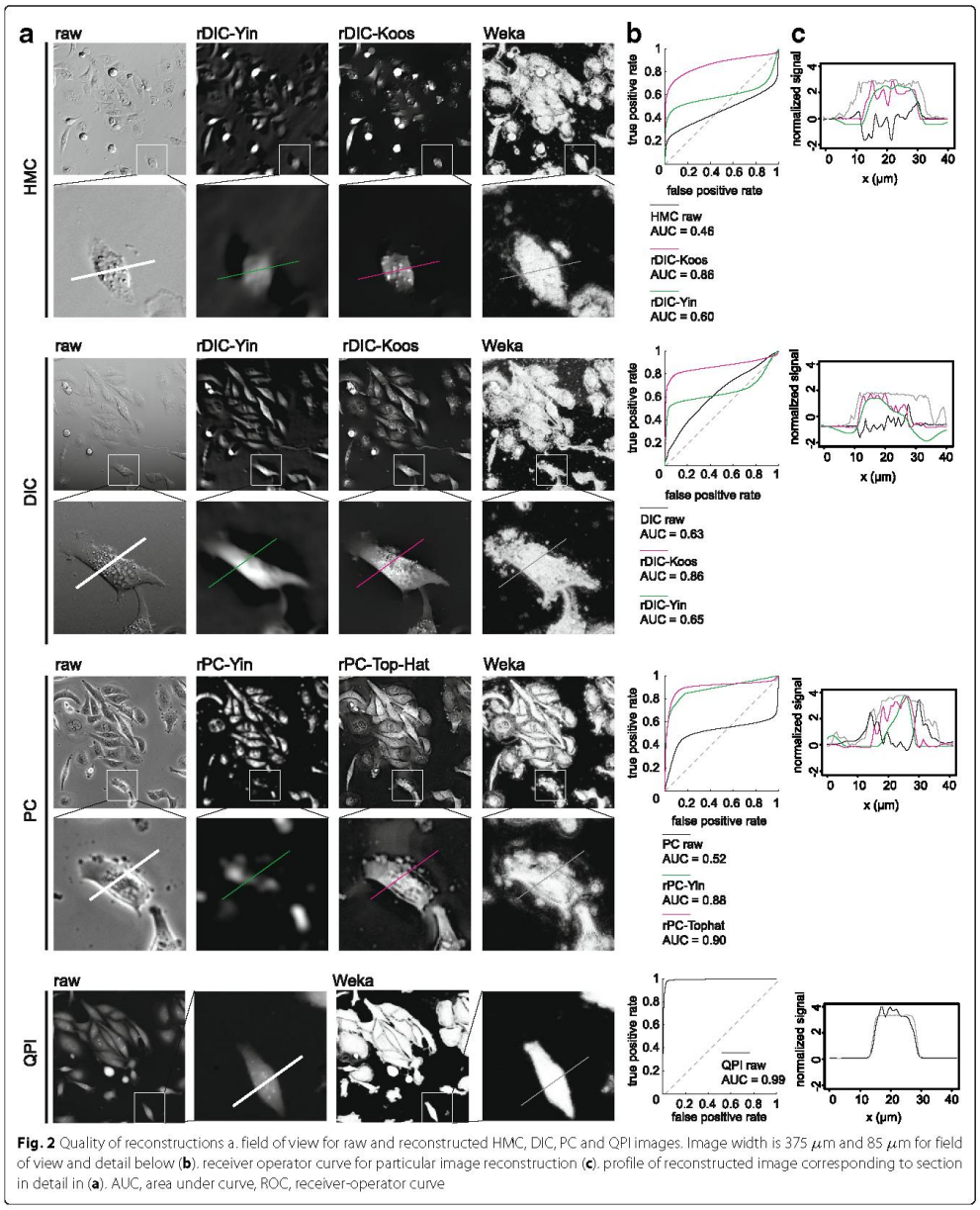

Fig. 2 Quality of reconstructions a. field of view for raw and reconstructed HMC, DIC, PC and QPI images. Image width is 375 μm and 85 μm for field of view and detail below (**b**). receiver operator curve for particular image reconstruction (**c**). profile of reconstructed image corresponding to section in detail in (**a**). AUC, area under curve, ROC, receiver-operator curve

than sEGT or sPC-Juneau and sPC-Phantast leads to a slight improvement only for a cost of more parameters to be set.

From feature thresholding methods, sEGT was shown to be the best with only a small number of parameters and great versatility. Because of its percentile based threshold,

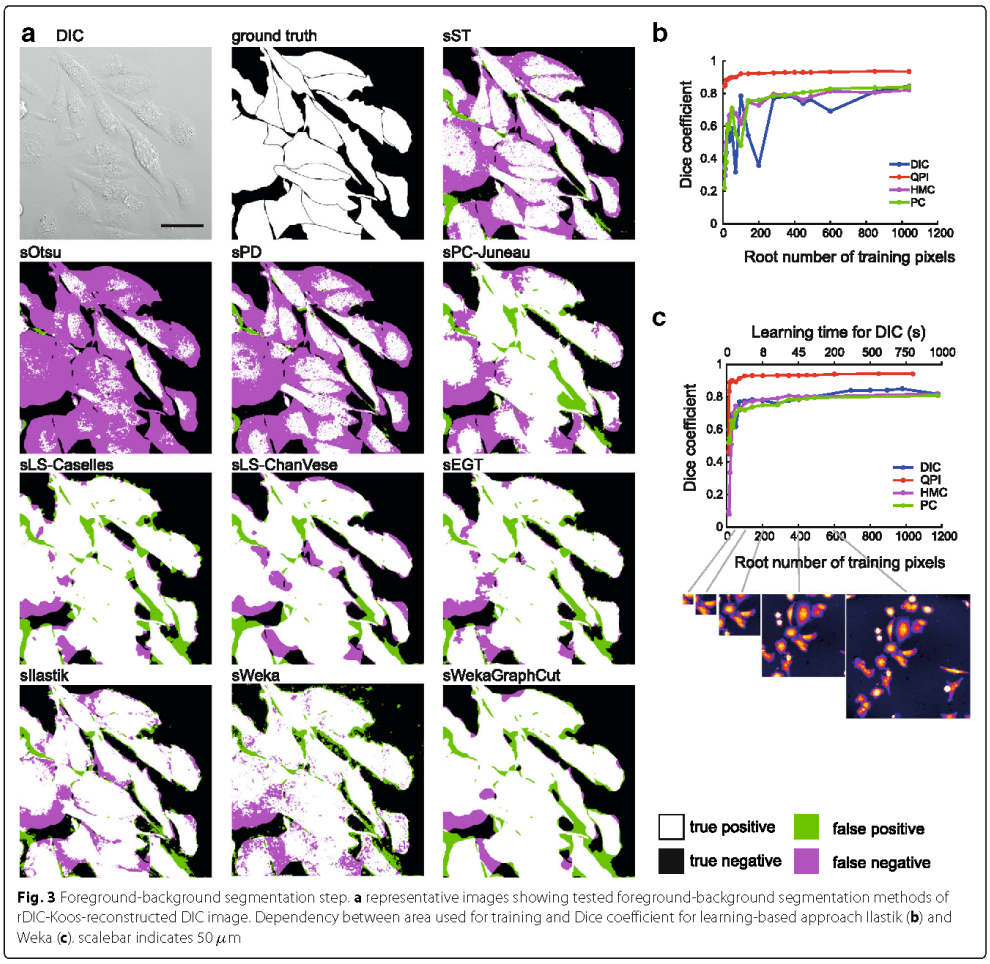

Fig. 3 Foreground-background segmentation step. **a** representative images showing tested foreground-background segmentation methods of rDIC-Koos-reconstructed DIC image. Dependency between area used for training and Dice coefficient for learning-based approach Ilastik (**b**) and Weka (**c**). scalebar indicates 50 μm

it can be used even with a default setting, which achieves e.g. 0.84 Dice coefficient value for QPI. Compared to threshold-based methods, feature-extraction strategies perform approximately 10% better. Considering the computational demands, these methods are very simple and fast - comparable to simple thresholding.

Level-set-based approaches

Both sLS-Caselles [22] and sLS-ChanVese [23] active contours tended to shrink too much, which was compensated by setting additional force to negative sign, which leads to a tendency of the contour to grow. The increase of the additional force leads to a better Dice coefficient value until a breaking point, after which it leads to the total divergence of the contour. Still, the value of additional force had a much greater influence than the smoothness parameter.

Compared to the above-mentioned foreground-background segmentation strategies, the level-set based methods are relatively complicated and computationally difficult (tens of seconds vs. less than 1 s per FOV, Table 1). In their basic forms, two parameters are needed to be set. Another great disadvantage is that proper initialization is required, mainly the sLS-Caselles method

is very sensitive to initialization. Based on segmentation results, sLS-ChanVese is applicable on reconstructed images only, and does not even reach the segmentation efficacy of simple threshold results. On the other hand, sLS-Caselles is applicable on raw images, but only for PC images it surpasses the otherwise much faster sEGT.

Graph-cut

There is a large number of methods and modifications based on Graph-Cut. Herein, we tested the basic model only. When Graph-cut was employed on the reconstructed images (sGraphCut), the highest Dice coefficient was obtained among non-trainable approaches except for rPC-Tophat, being surpassed by sLS-ChanVese. Nevertheless, Graph-Cut does not outperform simple threshold dramatically, providing roughly 2% increase in Dice coefficient and is only suitable for reconstructed data.

Regarding differences between microscopic methods, the Graph-cut approach was most suitable for reconstructed DIC images, followed by PC and HMC. Regarding the computational times, this method performs similarly as the level-set-based strategies (tens of seconds per FOV - Tables 1 and 2). Optimized values are shown in Additional file 1.

Trainable approaches

Trainable Weka segmentation (sWeka) and Ilastik (sIlastik) were employed in this step. Similarly to the feature-extracting approaches, these are applicable on raw, unreconstructed data. Both sIlastik and sWeka outperformed all tested foreground-background segmentation methods with Dice coefficient up to 0.94 for QPI and up to 0.85 for DIC, HMC and PC.

Regardless of the imaging modality used, there was an identifiable "breakpoint" in the dependency between the area size used for learning and the segmentation efficacy after which no dramatic increase in Dice coefficient was observed, see Fig. 3. For DIC, PC, and HMC it was approx. at the size 70×70 px., for QPI, distinctly smaller area was necessary, approx. 25×25 px. These areas roughly correspond to the cell size. However, to demonstrate the theoretical maximum of this method and to compare it with Ilastik, learning from one whole FOV for DIC, HMC, and PC and from 3 FOVs for QPI was deployed (see Table 2.

Next, an effect of learning from one continuous area in one FOV, or smaller patches of same sizes from multiple FOVs was tested. On DIC data it was demonstrated that learning from multiple areas causes significant, but slight 2% increase increase in Dice coefficients.

No increase of Dice coefficient was observed when different filters were enabled apart from the set of default ones ("default" vs "all") as well as changing of minimum/maximum sigma. This was tested with a random search approach and with the Dice coefficient varying ± 0.01. Both Weka and Ilastik provide almost the same segmentation results and are identically time-demanding.

There are two parameters to be optimized: terminal weights and edge weight. Edge weight (designated as "smoothness" in the GUI, range 0-10) reflects a penalty for label changes in the segmentation (higher values cause smoother result).

Furthermore, probability maps generated by sWeka and Ilastik under optimal settings were exported and these maps were further segmented by Graph-Cut (sWekaGraphCut/sIlastikGraphCut) and optimized in a same manner as sGraphCut on reconstructed data. A slight increase of the segmentation efficacy caused the sWekaCraphCut/sIlastikCraphCut combination to be the most efficient foreground-background segmentation method for QPI, HMC, and PC, only being surpassed by EGT on raw DIC image data. More importantly, this was achieved without the need of the image reconstruction.

Cell detection (seed-point extraction)

Once the foreground (cells) is separated from the background, the next step is to identify individual cells (seed points). The following strategies were used: (a) Cell shape-based, Laplacian of Gaussian (LoG) variants Peng et al. [27] (dLoGm-Peng), Kong et al.[28] (dLoGm-Kong), Hessian Zhang et al.[30] (dLoGh-Zhang), generalized Kong et al. [28] (dLoGg-Kong), generalized Xu et al. [29] (dLoGg-Xu), (b) Cell shape-based, generalized radial symmetry transform [32] (dGRST), fast radial symmetry transform [31] (dFRST), (c) Qi et al.[33] radial voting (dRV-Qi), (d) distance transform [15] (dDT-Threshold, dDT-Weka), (e) Maximally Stable Extremal Region [34] (dMSER), and (f) dCellDetect [35]. Following general conclusions are applicable for this segmentation step:

- Seed-point extraction is crucial step of cell segmentation
- The requirement of reconstructed images is a significant bottleneck of the seed-point extraction
- multiscale and generalized LoG are among the most robust and to some extent work also on unreconstructed data
- Radial symmetry transform-based strategies perform well
- Seed-point extraction is exceptional on QPI data
- Learning-based approach dCellDetect provide exceptional results on reconstructed data.

Laplacian of Gaussian-based strategies

Multiscale LoG filters (dLoGm-Peng and dLoGm-Kong) perform similarly as generalized versions (dLoGg-Kong

and dLoGg-Xu), but Hessian-based LoG (dLoGh-Zhang) were significantly worse in some cases. As for the traditional microscopic methods, LoG approaches enables the highest achievable segmentation efficacy. It was found out that particular combinations of reconstruction-LoG filter perform better than others; an optimal reconstruction-seed-point extraction combination is rDIC-Koos followed by dLoGm-Peng for DIC, rDIC-Koos plus dLoGm-Kong for HMC, and rPC-Tophat plus dLoGm-Peng for PC. Moreover, there were dramatic differences in cell detection between QPI and the remaining contrast-enhancing microscopic methods. On the other hand, there were no differences with Dice coefficient 0.9 for both QPI and DIC with dLOGm-Kong (Fig. 4).

Hessian variant dLoGh-Zhang achieved low segmentation efficacy on our samples of adherent cells (of various sizes) due to the use of one estimated optimal kernel size only (see Table 2). dLoGg-Kong originally completely fails for some modalities due to the wrong cell size estimation caused by sub-cellular structures, which produce higher signal then cells. This was eliminated by introducing a new σ_{min} parameter, limiting the lower scale.

Regarding the computational times, LoG-based are among faster techniques, being surpassed only by the distance transform.

Radial symmetry transform-based strategies

Compared to the computationally-simple LoG-based techniques, the dFRST [31] and generalized dGRST [32] provide better results for unreconstructed QPI images and, notably, for unreconstructed HMC and PC images. On reconstructed data, a possible application is for PC data with results very close to QPI segmentation. Nevertheless, computational times in the orders of hundreds of seconds need to be taken into account.

Radial voting

Radial voting (dRV-Qi) approach [33] does not achieve the results of fast LoG-based strategies for all microscopic modalities, either raw or reconstructed, while being computationally comparable to radial symmetry transform-based approaches. Thus, it is considered not suitable for such data.

Distance transform

The strong advantage of the distance transform [15] is its speed, which is the highest among other seed-point extraction strategies. Segmentation efficacy of the tested version with optimal thresholding (dDT-Threshold) is the highest among all microscopies except for PC, but image reconstruction is needed. An alternative approach is to use WEKA for binary image generation (dDT-Weka), where cells are less separated than in a case of optimal threshold.

Maximally stable extremal region

Compared to the relatively consistent performance of LoG between microscopic techniques, the dMSER approach [34] is distinctly more suitable for HMC reconstructed by rDIC-Koos and PC reconstructed by rPC-Yin, where the segmentation performance as well as computational requirements are identical or similar to LoG.

CellDetect

The CellDetect approach uses [35] maximally stable extremal region for segmentation. Adherent cells in unreconstructed DIC/HMC/PC images are, however, dramatically heterogeneous structures. Thus, there are no elements registered for learning and thus the performance of CellDetect was similar to aioFastER methods. On the reconstructed data, it performs similarly as LoG- or distance transform-based methods. Nevertheless, because the trainable nature of this technique, enormous computational time demands must be taken into account (up to 100-fold higher than DT). Segmentation of microscopic elements of low shape heterogeneity (e.g. yeast) would profit from CellDetect significantly.

Single cell (instance) segmentation

The data which underwent reconstruction, foreground segmentation and seed-point extraction were finally segmented by Marker-controlled watershed (MCWS) applied on distance transform or on images directly. Compared to previous steps, errors generated by this step have only minimal impact on overall segmentation quality, providing few-pixel-shifts to one or other adjacent cells. The distance transform approach is more universal but, in case the cells are well-separated, MCWS-only approach can provide better results. When compared to "all-in-one" segmentation strategies, the approach proposed by us provides dramatically better results except of proprietary software for quantitative phase imaging (see Table 2). With this in regard, the development of a new method which is strictly based on the nature of mass-distribution-QPI images could provide even better results.

Finally, it was assessed how the segmentation accuracy's individual steps are affected by morphological aspects of cells. Following aspects were studied (Fig. 5): cellular circularity and level of contact of cells with other cells (isolated cells vs cells growing together in densely populated areas, expressed as a percentage of cellular perimeter in contact with other cells). The circularity ranged 38.2 to 63.5%, median 51.2%, (percentage of cells with a circularity 100%: 2.1%), the percentage of perimeter ranged 4.1–41.9%, median 22.0% (percentage of cells with no contact with others 21.7%). Cells with circularity ranges 0–40% and 70–100% were considered low- and high-circularity cells. Regarding the

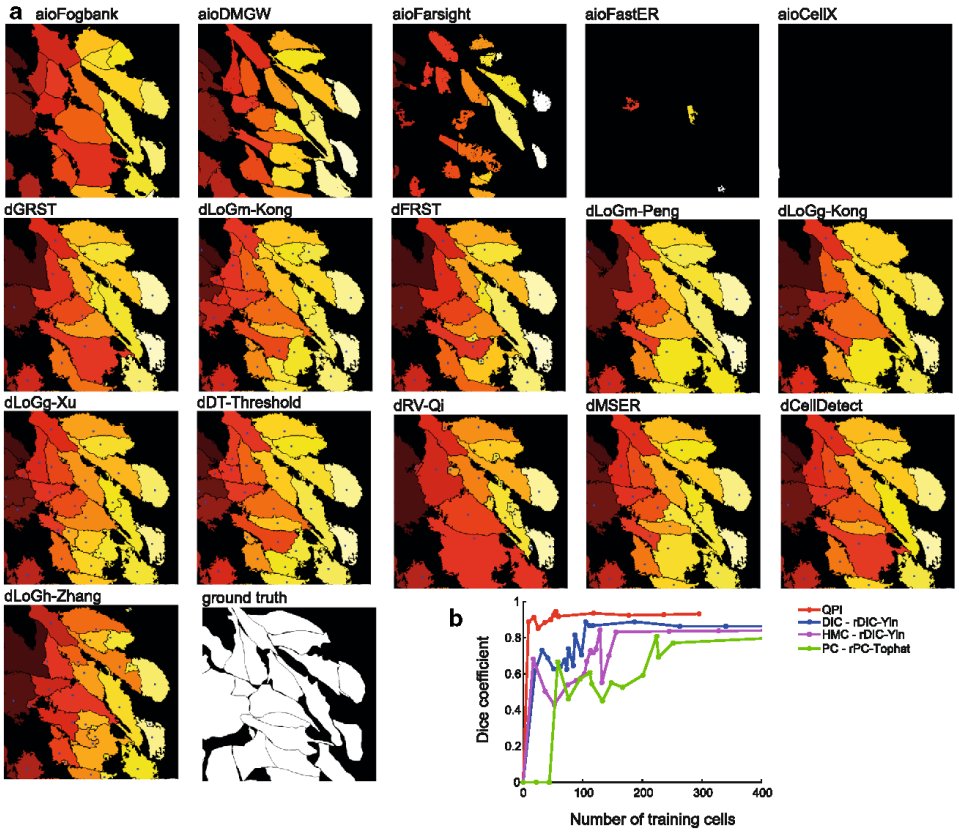

Fig. 4 Seed-point extraction segmentation step and all-in-one segmentation approaches. **a** Results of segmentation, representative image of rDIC-Koos-reconstructed DIC image followed by foreground-background segmentation with Traniable Weka Segmentation. Blue points indicate seeds based on which cells are segmented using marker-controlled watershed. Note absence of seed-points for "all-in-one" segmentation approaches. **b** Dependency between number of cells used for training and Dice coefficient for Celldetect

degree of contact with other cells, cells whose 0–15% and 50–100% of perimeter was in contact with other cells were designated "isolated" and "growing together", respectively.

It was found out that the reconstruction method does not affect a difference in segmentation accuracy between highly- and low-circular cells (the segmentation accuracy in highly circular cells is in average 15% better for all reconstruction methods) without significant variations for individual methods. Seed-point extraction, however, is much more cell-shape-dependent (Fig. 5c). Because these methods are blob detectors by nature, the result is better for more circular cells with most methods. However, the dDT-Treshold and dCellDetect are not affected by circularity and are among the most efficient segmenting tools at the same time.

Regarding the effect of a degree of contact with other cells, method of image reconstruction does not affect a difference in segmentation between densely and sparsely populated areas (20% better segmentation results for isolated cells). Seed-point extraction accuracy is however even more profoundly affected by a level of contacts with other cells (in average 25% better segmentation for isolated cells).

Discussion

During the last two decades, the amount of approaches to segment microscopic images increased dramatically. The

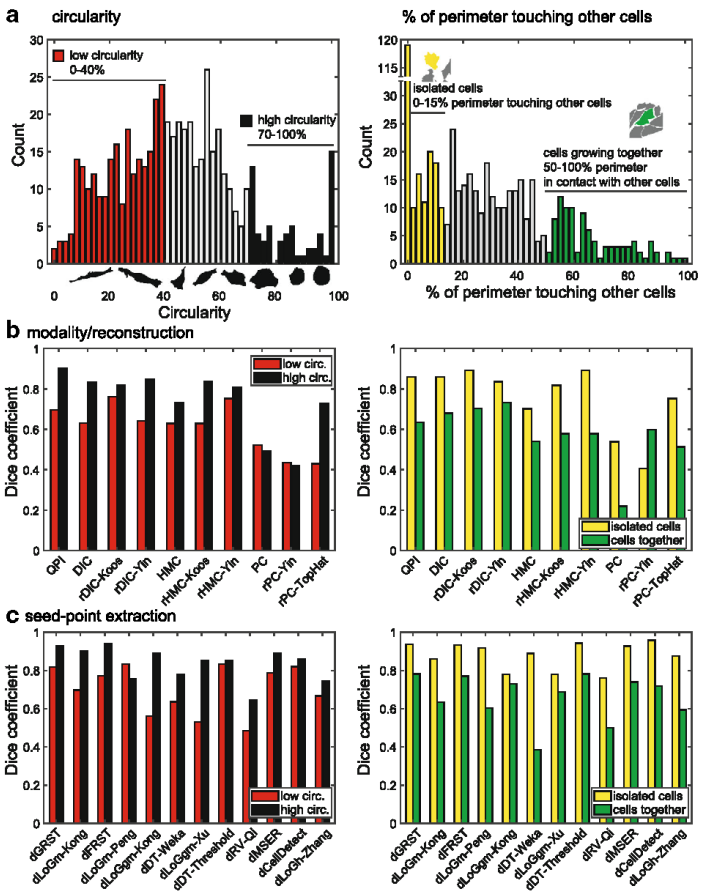

Fig. 5 Cell segmentation efficacy and cell morphology. **a** histograms showing distribution of circularity and level of contact with other cells (shown as percentage of cell perimeter touching with other cells. Based on histograms, low/high circularity and isolated/growing together groups were created. **b** effect of cell reconstruction, on segmentation accuracy, subset of low/high circularity and low/high contact with other cells (for this step, dLoGm-Kong was used in next segmentation step for all methods). **c** effect of various Seed-point extraction methods, effect of low/high circularity and low/high contact on segmentation efficacy. Last step is shown for QPI data only

precise segmentation of label-free live-cell microscopic images remains challenging and not completely solved task. Furthermore, different microscopic techniques make this task more difficult due to different image properties provided.

Accordingly, the aim of this study was to compare the most heterogeneous spectrum of segmentation methods to real data of the same cells from multiple contrast microscopic modalities. The properties of each processing step has been evaluated and segmentation accuracy has been compared.

We used human adherent cells, which are much more heterogeneous in shape and thus much bigger challenge for segmentation than the segmentation of spherical bacteria or yeast. Based on the described results, we can now summarize, discuss and suggest several findings directed to both biologists and bioinformaticians from different points of view.

Segmentability of microscopic techniques

When considering a microscopy technique for label-free segmentation, there were no dramatic differences in the segmentation efficacy between DIC, HMC or PC. However, the highest segmentation efficacy was obtained when QPI microscopy was used due to the higher image quality (without significant artefacts and high image contrast). In principle, approaches originally intended for fluorescence segmentation are applicable for these images. QPI technique should be also the choice, when a fast, high throughput segmentation is desirable, because no image reconstruction is needed and simple thresholding with MSER - Seeded watershed provides satisfactory results.

Performance of segmentation steps

Regarding individual processing steps, the most crucial are image reconstruction and seed-point extraction methods. Foreground-background segmentation, on the other hand, can be considered the least problematic part, where no dramatic differences between methods were observed, except that learning-based approaches scored better. Regarding the seed-point extraction, however, a reconstructed image is needed for almost all approaches (except dDT-Weka), making seed-point extraction dependent on precise reconstruction. Not all foreground-background segmentation methods need reconstructed images, because some are compatible with raw DIC or PC images (e.g. sWeka, sLS-Caselles, sEGT) and generally perform well. Omitting the reconstruction step will need the seed point extraction methods applicable to raw data (eg. dDT-Weka or DT with different foreground-background segmentation), which can slightly reduce the quality of cell segmentation. It was also evident, that not all reconstruction algorithms are suitable for the seed-point extraction (high Dice coefficient in the foreground segmentation step does not guarantee suitability for the seed-point extraction). It also cannot be stated that the time-consuming methods are dramatically better-performing in the seed-point extraction. Here, the learning-based approach provided better results, too. Below we provide short workflow summary for each microscopic technique:

- QPI – this technique usually provides images with the best image properties with respect to automated image processing. We observed that Weka probability map segmented with Graph-cut, followed by seed-point extraction with dGRST and finally segmented by Marker-controlled watershed gives superior results. In general, any segmentation approach used, QPI gained the highest segmentation efficacy.
- PC – for this modality we suggest simple and fast reconstruction with Top-Hat filter, and dGRST or dFRST for seed-point extraction. Graph-cut applied to probability Weka probability maps produce best foreground-background segmentation. Final segmentation is slightly improved if Marker-controlled watershed is applied to distance transform image (instead of intensity image).
- DIC/HMC – the images from these modalities are similar, which leads us to suggestion that the same pipeline can be applied to both. We suggest to use rDIC-Koos method for reconstruction and Graph-cut applied to probability Weka probability maps for foreground-background segmentation. Thresholding with distance transform (dDT-Threshold) is best for seed-point extraction, finally segmented by Marker-controlled watershed. Although DIC and HMC have a lot of similar features, DIC produce generally better results.

All-in-one packages are extremely popular in biologist community and more or less provide the complex solution for single cell segmentation task. However, these packages implement common image processing methods (some of them described here) and together with graphical user interface and interactions, provide rich possibilities for segmenting the images. We can conclude that FogBank and CellProfiler tools achieve the highest segmentation efficacy among these approaches (without need of programming skills) and it is also universal for various imaging modalities. Both FogBank and CellProfiler use a similar generalizable approach based on the combination of watershed and distance transform, however, CellProfiler also includes a possibility to build complete cell analysis pipelines and as such should be default choice without programming.

Deep-learning remarks

Intentionally, our focus was set on a spectrum of traditional strategies while the rapidly-developing spectrum of deep-learning-based segmentation was omitted. The main practical limitation of application of deployment of pre-trained U-net or other deep learning method (transfer learning) is the need for sufficiently large training dataset (covering different modalities and cell types/shapes). However, the image databases for segmentation tasks are not as large and complex as ImageNet [36], which became a standard for pre-training of classification-based networks. For this reason, available models use only pre-trained encoder [37], which is pre-trained for classification on ImageNet. As such, we leave this investigation for future work, where deeper-comparison is highly needed, especially for different amounts of training data and from view of computational requirements.

Despite the tremendous success of deep learning approaches applied in many computer vision tasks

including live cell imaging, there is no straightforward way how to use these methods for cell segmentation of touching dense populated cells. One of the approaches to achieve separated mask for each cell is to predict simple binary foreground mask, but giving higher weight to correct prediction on the boundary as in [38]. Another simple solution is to predict three pixel classes – background, foreground and cell boundary as in [39], which provides better separation of cells. On the other hand, deep learning can be also used for cell detection by regression of 2D Gaussians on the position of centroids as in [40]. In [41], authors combined detection and segmentation into simultaneous prediction with one U-Net network, where one prediction map predicts distance to cell boundary (after thresholding we obtain foreground-background segmentation) and second map predicts distance to cell centroid (detections are obtained with local maxima detection). These techniques are very promising, however, their testing is out of scope of this paper because our dataset is not sufficiently large for training of these algorithms and there is no standard way how to use deep learning for cell segmentation, leading to enormous number of possible setups to test in order to achieve fair comparison to classical methods.

Remarks and limitations

Because of Matlab platform was used, the information regarding computational time is approximate with a large software-dependent space for its reduction. All segmentation steps were performed in a sequential way. Thus parallel processing may provide a distinct improvement for most of the methods, but this was beyond the scope of this study. Based on a distinctive difference in a segmentation accuracy between "all-in-one" methods and individual methods reviewed herein, well-performing methods usually have more than three parameters to be set (usually not even corresponding with morphological features of the cells). Thus it is still difficult, if not impossible, to automatize the whole segmentation process. In a spite of this, deep-learning approaches provide some alternative – instead of setting optimized parameters, user needs just to provide a training dataset.

Although there are several excellent reviews on such segmentation, a study practically comparing the to-date best-performing approaches on real data from various microscopic techniques is still missing. In [42] the authors review a broad spectrum of segmentation methods to segment histological images. In [43] the authors focus on available tools with GUI. The author of [44] summarizes historical progress of cell segmentation methods. There are also works on comparing QPI, DIC and PC, but in [45], the authors compare modalities without segmentation and in [46] authors test algorithms only on QPI data, without considering image reconstructions. In Ulman et al. [47] the authors compared segmentation and tracking on various microscopic methods, including 2D fluorescent, DIC and PC. Many detection errors can be eliminated with tracking. Thus the comparisons with our review might be rather relative. Similarly to our results, one of the best-performing algorithms "KTH-SE" used a relatively simple thresholding together with a precise seed-point extraction (tracking in their case). This underlines the fact that a precise seed-point extraction is the most crucial segmentation aspect. Also a segmentation performance was significantly lower in the "Fluo-C2DL-MSC" dataset characteristic by low circularity of cells.

Our study has several limitations. These include the focus on the segmentation of adherent cells, not those cultivated in the 3D matrix or suspension-cultured counterparts. Also the ground truth manual segmentation was performed by a human, although experienced biologist. The problem of overlapping cells was present, although relatively rare. Using the learning-based approaches it was demonstrated that those surpass the transitional strategies. This predicts a future success for deep-learning methods and probably also their future superiority. Also, in accordance with cell time-lapse trend in microscopy, cell segmentation is just the first part of the story with cell tracking being another one.

Conclusion

In this study, we performed a comprehensive testing of image processing steps for single cell segmentation applicable for label-free images. We searched for published methods, which are used by biologists and bioinformaticians, we assessed the suitability of used data and we carefully tested particular segmentation steps (image reconstruction, foreground-background segmentation, seed-point extraction and cell segmentation) and compared them with available "all-in-one" approaches. As expected, learning-based methods score among the best-performing methods, but well-optimized traditional methods can even surpass these approaches in a fraction of the time. We demonstrated that the image reconstruction step makes it possible to use segmentation methods not directly applicable on the raw microscopic image.

Herein we collected a unique set of similar field-of-view image of the same cells acquired by multiple microscopic techniques and annotated by experienced biologist. The raw and reconstructed data is provided, together with the annotated ground truth and Matlab codes of all approaches.

Methods

Dataset

Cell culture and culture condition

PNT1A human cell line was used in the experiment. This cell line was derived from normal adult prostatic epithelial

cells immortalized by transfection with a plasmid containing SV40 genome with defective replication origin. The cell line was purchased from HPA Culture Collections (Salisbury, UK). PNT1A cells were cultured in RPMI-1640 medium supplemented with antibiotics (penicillin 100 U/ml and streptomycin 0.1 mg/ml) with 10% fetal bovine serum (FBS). Prior microscopy acquisition, cells were maintained at 37°C in a humidified (60%) incubator with 5% CO_2 (Sanyo, Japan). Intentionally, high passage number of cells was used ($>$ 30) in order to describe distinct morphological heterogeneity of cells (rounded and spindle-shaped, relatively small to large polyploid cells). For acquisition purposes, cells were cultivated in Flow chambers μ-Slide I Luer Family (Ibidi, Martinsried, Germany).

Microscopic image acquisition and dataset characteristics

QPI microscopy was performed on Tescan Q-PHASE (Tescan, Brno, Czech Republic), with objective Nikon CFI Plan Fluor 10 $\times$ /0.30 captured by Ximea MR4021MC (Ximea, Münster, Germany). Imaging is based on the original concept of coherence-controlled holographic microscope [48, 49], images are shown as a 32bit file with values corresponding to pg/μm^2 recalculated from radians according to Barer and Davies [50, 51].

DIC microscopy was performed on Nikon A1R microscope (Nikon, Tokyo, Japan) with a Nikon CFI Plan Apo VC 20 $\times$ /0.75 objective captured by a Jenoptik ProgRes MF CCD camera (Jenoptik, Jena, Germany).

HMC microscopy was performed on Olympus IX71 microscope (Olympus, Tokyo, Japan) with Olympus CplanFL N 10 $\times$ /0.3 RC1 objective captured by Hamamatsu Photonics ORCA-R2 CCD camera (Hamamatsu Photonics K.K., Hamamatsu, Japan).

PC microscopy was performed on a Nikon Eclipse TS100-F microscope, with a Nikon CFI Achro ADL 10 $\times$ /0.25 objective captured by Jenoptik ProgRes MF CCD camera.

The captured dataset characteristics are summarized in Table 3. All data were manually segmented by an expert in cell biology as ground truth for segmentation and detection. Same areas of sample were captured using these microscopes, but due to the cell movement and different FOV size the overlap is not absolute.

All-in-one segmentation tools

Here are described "all-in-one" approaches (designated with "aio" prefix).

aioFARSIGHT

FARSIGHT toolkit 0.4.5 module Nucleus editor [2] consists of an automatic Poisson threshold binarization refined with graph-cut (applied on a binary foreground image) and produces initial segmentation containing cell clusters. Next, Multiscale Laplacian-of-Gaussian is used to produce feature map (image where blobs are enhanced - see "LoG filters" section for more details), which is segmented by local clustering algorithm. This clustering algorithm then produces rough cell cluster separation. Finally α-Expansions (multilabel graph cut) is used to refine segmentation, with novel method of Graph colouring for more efficient computation (see [2] for more details).

The first set of parameters was cell-shape-derived: "min scale" and "max scale" (the minimum and maximum scale of the multiscale Laplacian of Gaussian filter) were set based on a measured radius of equivalent circle of cells, "xy clustering res" (resolution of the local maximum clustering) was set similarly as "min scale", and "min object size" was set as the area of the smallest cell. The second set of parameters was optimized: "high sensitivity" (enable/disable high sensitivity binarization), "finalize segmentation" (enable/disable the segmentation refinement step), "use distance map" (enable/disable the use of the distance constraint to select the LoG scales), and "refinement range" (parameter sets the maximum distance that an initial contour can be shifted).

aioCellX

Dimopoulos et al. [3] approach consists of seed generation with gradient-based Hough transform, construction of membrane patterns images for each seeed (cross-correlation with estimated membrane profile) and segmentation of each such image with graph-cut. After that, statistical morphological outliers are removed and individual regions are combined (almost identical regions are merged and overlaps are resolved).

CellX includes a GUI, where user can interactively set cell size range, maximal cell length and estimated membrane profiles.

aioFogbank

In Chalfoun et al. [4] Fogbank, foreground is segmented with EGT. Seeds are detected as connected regions after percentile thresholding (with some distance and size constraints). Pixels above a defined percentile level are then connected to the nearest seed-point. Either intensity or gradient image and either Euclidean or geodesic distance are used for computation.

Table 3 Data-set summary

Modality	FOV size	Image size	Num. of FOVs	Num. of cells
QPI	376×376 μm	600×600 px	18	637
PC	1253×944 μm	1360×1024 px	10	2387
DIC	627×472 μm	1360×1024 px	11	862
HMC	867×660 μm	1344×1024 px	11	1297

aioFastER

Hilsenbeck et al. [5] FastER applies MSER to construct component tree and SVM for classification of regions into groups of cells or false detections. Finally non-overlapping regions with the highest score are selected. It shares CellDetect similarities (see "CellDetect" section), but this algorithm uses 9 features for SVM classification only and does not compute globally optimal solution, thus being computationally faster. To achieve complete segmentation (not only detection as CellDetect), authors modified their approach on the algorithmic level. Size constraints of cells (measured min/max cell size) were set and "de-noise" parameter setting were optimized (off/on/strong). Larger number of FOVs used for training were tested without improvement.

Dry mass-guided watershed

The dry mass-guided watershed method (designated as aioDMGW) is a thresholding-based approach, implemented as a part of Analyzer module of Q-PHASE software 6.803 (Tescan, Brno, Czech Republic). First the phase image is slightly smoothed and foreground is separated from background using thresholding. Then watershed starting from the local maxima is performed. The decision of merging of touching segments, or leaving them separated, is based upon the sums of pixel values (i.e. dry mass) in each touching segment. The optimized parameters are: threshold; min segment sum (the minimum accepted sum of pixel values in each segment used to filter out noise and cell debris); max merge sum (the threshold of sum of pixel values of touching segments used to decide if the segments should be merged or left separated).

aioCellProfiler

The CellProfiler [10] is a strong segmentation tool, however, we perceive it more as a platform where a substantial part of the segmentation strategies used here can be reproduced. Nevertheless, we evaluated output of "IndetifyPrimaryObject" module, which combines thresholding and watershed. Watershed is used twice, for seed-point extraction and final single cell segmentation, and it is applied to either intensity or DT image. Additionally, module uses some smoothing and it remove seed-points bellow some allowed distance. Measured range of cell radiuses and optimal threshold (see Additional file 1) were used and we optimized betwen application to intensity or DT image for both steps.

Other all-in-one tools

Following algorithms were reviewed but not used in comparison with reasons stated below:

CellTracer [6] consists of 3 steps – foreground segmentation, border segmentation and cell segmentation by model fitting. This approach is more suitable for yeast- or bacteria-shaped objects (coccus- or bacillus-shaped with distinctive borders). Similar issues were observed in SuperSegger [7], CellSerpent [8] or CellStar [9].

Image reconstruction techniques

DIC, HMC and PC image formation process can be described as convolution between the original image of the scene and 2D PSF. For PC images *PSF* is [13]

$$PSF_{PC}(x,y) = \delta(x,y) - airy\left(\sqrt{x^2+y^2}\right) \tag{1}$$

where $\delta(\cdot)$ is Dirac delta function and $airy(\cdot)$ is Airy pattern. This leads to halo and shade-off artifacts (see Fig. 2). For DIC image *PSF* is difference of two Gaussians [52]:

$$PSF_{DIC}(x,y) = -xu\exp\left(-\frac{x^2+y2}{\sigma}\right) - yv\exp\left(-\frac{x^2+y2}{\sigma}\right) \tag{2}$$

where σ is Gaussian standard deviation and $\mathbf{u} = [u\ v]^T$ is unit vector specifying shear direction. It means that DIC image is derivation under shear direction visible as 3D-like topographical appearance (see Fig. 2). The inverse PSF then can be used for image reconstruction. The goal of these reconstruction algorithms is to produce image of blob-like cells qualitatively corresponding to cell mass (similar to QPI). The methods described bellow are designated with prefix "r" (reconstruction), original modality and author, where possible.

DIC reconstruction methods were well reviewed in [12]. Based on the results of this study, two methods were chosen: (a) fast, computationally-efficient Yin et al. approach [13] (in following parts designated as "rDIC-Yin") and (b) more computationally-demanding Koos et al. [12] (designated as "rDIC-Koos"). HMC images have the similar properties as DIC and therefore the same reconstruction algorithms were tested.

For PC reconstruction [14], two methods were chosen (a) more complex computationally-demanding method based on PSF model (designed as "rPC-Yin") (b) simple Top-hat filtering (designated as "rPC-Tophat").

rDIC-Koos

Method proposed by Koos [12] (rDIC-Koos) uses an energy minimization with data term and total variation regularization term

$$E = \frac{1}{2}\iint_{\Omega}(\mathbf{u}\cdot\nabla(K*\hat{f}) - \mathbf{g})^2 + w_s|\nabla\hat{f}|d\Omega \tag{3}$$

where $\cdot$ denotes dot product, ∇ denotes gradient, $\mathbf{u} = [u\,v]^T$ is unit vector specifying shear direction, Ω is image domain and K is kernel which approximate PSF without derivative (Gaussian function), where $\nabla K = PSF_{DIC}(x,y)$.

Euler-Lagrange equation of data term for symmetric kernel K leads to

$$u\partial_x g + v\partial_y g - \iint_W K\left(u^2\partial_x^2\hat{f} + 2uv\partial_x\partial_y + v^2\partial_y^2\hat{f}\right) = 0 \tag{4}$$

where ∂_x and ∂_y denotes partial derivatives and W is a local window (with size of kernel). Finally, this can be solved with gradient descent iterative method as

$$\hat{f}^{(t+1)} = \hat{f}^{(t)} - w_a\left(u^2\partial_x^2\hat{f}^{(t)} + 2uv\partial_x\partial_y\hat{f}^{(t)} + v^2\partial_y^2\hat{f}^{(t)}\right) * K + u\partial_x G + v\partial_y G - div\left(\frac{\nabla\hat{f}^{(t)}}{||\nabla\hat{f}^{(t)}||}\right) \tag{5}$$

where $\hat{f}^{(t+1)}$ is reconstructed image in next iteration, *div* denotes divergence. Last term is proposed by total variation regularization.

Besides of shear angle, which is assumed to be known (or recognizable from image - typically multiple of 45), rDIC-Koos method has three parameters - weight of smoothness (total variation) regularization w_s, step size of gradient descent w_a and number of iteration *it*. Smooth regularization sets compromise between noise elimination and details preservation. Too large step size leads to method divergence and too small step size leads to slow convergence. Number of iterations has a small influence on the result; default value 20000 was used. For setting of other parameters see Additional file 1.

rDIC-Yin

Yin et al. [13] presented a reconstruction method for DIC images (rDIC-Yin) working with multiple shear directions, but with some simplification in equations it also works on images with one shear angle direction. Authors assumed that distortion of the microscope can be modeled by convolution with PSF

$$\mathbf{g} = \mathbf{d} * \mathbf{f} \tag{6}$$

where $\mathbf{d}$ is PSF (in general a directional first-derivative-of-Gaussian kernel, but simple difference without Gaussian is used for simplification), $\mathbf{g}$ is acquired image and $\mathbf{f}$ is original image. Simple inverse filtering leads to highly noisy images, which can be reduced by regularization. This can be achieved with optimization of energy function which must be minimized over whole image domain

$$\mathbf{E}(\hat{\mathbf{f}}) = (\mathbf{d} * \hat{\mathbf{f}} - \mathbf{g})^2 + w_s(\mathbf{a} * \hat{\mathbf{f}})^2 + w_r\hat{\mathbf{f}}^2 \tag{7}$$

This equation is composed of data term, smooth term and sparse term (all with l_2 penalization, where w_s and w_r are weights for the smooth and sparse regularizations, respectively). $\hat{\mathbf{f}}$ is reconstructed image (approximation of $\mathbf{f}$). Smoothness is achieved by setting a restored pixel value to be close to the average of its neighbors (where $\mathbf{a} = [1, 1, 1; 1, -8, 1; 1, 1, 1]/8$). Sparse regularization causes the value of background pixels to be close to zero. Optimization of function has close-form solution in Fourier space ($\hat{\mathbf{F}} = \mathcal{F}\{\hat{\mathbf{f}}\}$ etc.)

$$\hat{\mathbf{F}} = -(\mathbf{D} \odot \mathbf{G}) \oslash (w_s\mathbf{A} \odot \mathbf{A} + w_r - \mathbf{D} \odot \mathbf{D}) \tag{8}$$

where "$\oslash$" and "$\odot$" denotes element-wise division and multiplication, respectively.

Besides shear angle, rDIC-Yin has two parameters only, w_s and w_r, which set smoothness and sparse regularizations, respectively.

rPC-Yin

In [14] Yin et al. used a deconvolution with sparse constraint regularization to reconstruct PC images. This method was further expanded with dictionary of diffraction patterns [53], which deals with problematic mitotic cells. This method is in fact a segmentation method as presented in the Su at al. paper [53] and it therefore cannot be used as preprocessing (i.e. reconstruction) step. rPC-Yin [14] is very similar to rDIC-Yin [13] with modified equation 7 to linear equation system with l_1 penalization for the sparse term.

$$\mathbf{E}(\bar{\hat{\mathbf{f}}}) = (\mathbf{H}\bar{\hat{\mathbf{f}}} - \bar{\mathbf{g}})^2 + w_s\bar{\hat{\mathbf{f}}}^T\mathbf{L}\bar{\hat{\mathbf{f}}} + w_r|\Lambda\bar{\hat{\mathbf{f}}}| \tag{9}$$

where $\bar{\hat{\mathbf{f}}}$ and $\bar{\mathbf{g}}$ are vectorized restored and acquired images, $\mathbf{H}$ is the transfer matrix of the image formation model and $\mathbf{L}$ is Laplacian matrix (corresponding to different expression of operators $\mathbf{d}$ and $\mathbf{a}$ in the equation 7). Λ is positive diagonal matrix defining sparseness, w_s and w_r are weights for the smooth and sparse regularizations. Because of l_1 penalization of sparseness (known to be better than l_2) there in no closed-form solution. It can be solved with an iterative algorithm which is based on non-negative multiplicative updating (for more implementation details see [14]). PSF (which leads to $\mathbf{H}$) is then modeled by the equation 1, where airy pattern is

$$airy(r) = R\frac{J_1(2\pi Rr)}{r} - (R - W)\frac{J_1(2\pi(R - W)r)}{r} \tag{10}$$

where R and W are PSF-dependent parameters - outer radius (R) and ring width (W) of phase ring and $J_1(\cdot)$ is the first order Bessel function of the first kind. rPC-Yin has also optimization parameters w_s and w_r which define weights of components of optimized energy function. Other parameters not discussed in [14] were set to default value ($radius = 2, epsilon = 100, gamma = 3, scale = 1, maxiter = 100, tol = 10^{-16}$). Because of large computational time, optimization of PSF and optimization parameters was done separately - first proper PSF was found (other parameters set to default value $w_s = 1$ and $w_r = 0.5$) and then optimal W and R values were used in optimization of w_s and w_r.

rPC-Tophat

Top-hat filtering (referred here as rPC-Tophat) was used by Thirusittampalam et al. [15] and Dewan et al. [16] for halo artifacts elimination. This simple heuristic approach shows very promising results and it is considered as the next PC reconstruction technique in this paper.

Reconstruction based on top-hat filtering with disk-shaped structuring element has only one adjustable parameter - radius of structuring element, which is roughly equal to the radius of the cell, with optimal value $r = 16$.

Foreground-background segmentation

Thirteen methods has been tested and to make it more clear, the methods are designated with prefix "s" (segmentation), original modality and the author, where possible.

Thresholding

Three threshold-based techniques were used for the foreground-background segmentation. Simple threshold (named as sST) and two automatic threshold algorithms, Otsu [17] (sOtsu) and Poisson distribution [2] (sPT).

Automatically determined thresholds varies between FOVs, so a better result can be expected. sOtsu assumes that gray-scale values are mixture of two Gaussian distributions. Nevertheless, for the adherent cell images the mixture of two Poisson distributions is sometimes more suitable [2], thus sPT was tested. For ST, threshold value was optimized with 100 steps between minimal and maximal value.

Empirical gradient threshold

Chalfoun et al. [18] described an empirical gradient threshold method (referred here as sEGT), which uses empirically derived model for threshold estimation. sEGT was described to work with different microscopic modalities (PC, DIC, brightfield and fluorescence) and is applicable also on the others, including raw (unreconstructed) images. sEGT utilizes a Sobel operator to compute absolute value of gradient, then the percentile-based threshold is found, followed by the binary morphological operations. Three parameters must be set beforehand: minimal cell size (removing small objects), minimal hole (removing small holes) and manual fine-tune (decreasing or increasing the estimated threshold). For all these methods minimal object size was determined from a ground true mask of the training images.

sPC-Juneau

Juneau et al. [19] described simple segmentation method (referred here as sPC-Juneau) designed for PC images. It computes a range map (difference between minimum and maximum in local window), which is then thresholded. Consequently, all holes and small objects in the binary image are removed. Thus these parameters are optimized: window size, threshold and minimal object size. Although originally designed for PC images, it is applicable for other modalities as well.

sPC-Phantast

Jaccard et al. [21] developed a software toolbox PHANTAST consisting of foreground segmentation techniques specialized for PC microscopy images. It computes local contrast

$$C = \frac{\sqrt{G * I^2 - (G * I)^2}}{G * I} \tag{11}$$

where G is a Gaussian kernel with standard deviation σ. The resulting local-contrast image is then globally thresholded and halos are corrected. For halos correction, the gradient direction is computed by eight Kirsch filters (8 directions). Halo pixels are initialized with boundary pixels of binary image, then iteratively each halo pixel points to its gradient direction and two adjacent directions, where each of these three pixels is marked as halo if it is considered foreground (for bright halos gradient points in and for dark cells gradient points out). Maximum cell area fraction removed as halo is restricted and after elimination of halos, small objects and holes are removed. This leads to 5 parameters - Gaussian σ, threshold, halo area fraction, minimal hole size and minimal object size.

sPC-Topman

Topman et al. [20] described another method for foreground segmentation originally intended for PC images. This approach applies two filters, one with a small and one with a large local window computing the standard deviation, where both are thresholded. The result is an intersection of these two binary images, where binary image from large window is morphologically eroded (with morphological element of half the size of the large window) and final image is morphologically opened and closed. This leads to 4 parameters - two window sizes, threshold, and morphological element size.

LevelSets

Matlab implementation of level-set method with function *activecontour* was used. This implementation includes an edge-based method [22] (referred as sLS-Caselles) and region-based method [23] (referred as sLS-ChanVese). Both methods use a Sparse-Field implementation [54] for contour evolution and both have two adjustable parameters - smoothness of the result contour and additional force, which leads to a tendency of the contour to grow or shrink. While sLS-ChanVese segments the image into

two regions based on the mean region intensities, sLSCaselles segments the image based on the edges. The level-set methods were initialized with morphologically-dilated binary results of Weka segmentation, because it provides similar initial contours for all modalities. Number of iterations of the evolution was set to 1000, which was shown to be enough for all types of images and all parameter settings.

Trainable Weka Segmentation

Next, a machine learning tool for microscopy pixel classification Trainable Weka Segmentation v.3.2.13 was used [26] (designated as sWeka). Compared to previous foreground-background segmentation strategies, this approach was primarily used directly on the raw data. Weka was trained using the following default training features (Gaussian blur, Sobel filter, Hessian eigenvalues, difference of Gaussians filter, membrane projections) as well all remaining available filters (variance filter, minimum filter, maximum filter, median filter, anisotropic diffusion, bilateral filter, lipschitz filter, kuwahara filter, gabor filters, Sobel filter, laplacian filter, structure, entropy filter). For these filters it is also possible to set a σ range, which specifies the filter size. Other parameters were set to default values, random forest classifier was set to 200 trees (WEKA FastRandomForest). Because of learning nature of this approach, the effect of following factors on segmentation efficacy was optimized: (a) number of fields of view used for learning (b) training features used for learning ("all" and "default" training features), (c) effect of various fields of view used for training (one continuous area in one FOV, or smaller patches of same sizes from multiple FOVs), (d) size of FOV used for learning (increasing the area from 6×6 px to 1360×1024 px). Moreover, probability maps were exported and used for further analyses.

Ilastik

Another tested machine learning tool for pixel classification was Ilastik v.1.3.0 [25]. Ilastik uses a random forest classifier [55] with 100 trees and is very similar to WEKA. Ilastik was launched using the following settings: enabled all training features: raw intensity, gradient magnitude, difference of Gaussians, Laplacian of Gaussian, structure tensor eigenvalues and the Hessian matrix eigenvalues - all with 7 Gaussian smoothings with $\sigma = 0.3 - 10px$.

Ilastik was optimized accordingly as Weka. It allows a computationally expensive automatic selection of suitable features. Based on a first optimization step, there was no significant difference between "optimal" and "all" features. Thus, in a spite of this and a fact that Ilastik has less available features then WEKA, "all" features were used in further steps.

Graph-cut approach

An ImageJ plugin for Graph-Cut (v. 1.0.2) based on the reimplementation of Kolmogorov's maxflow v3.01 library [24] was used. The following data were used as an input for Graph-Cut: (a) Probability maps generated by Weka (referred as sWekaGraphCut), (b) images reconstructed with approaches described in "Image reconstruction approaches" and (c) raw image data (both referred as sGraphCut). There are two parameters to be optimized: terminal weight and edge weight. Edge weight (designated as "smoothness" in the GUI, range 0-10) reflects a penalty for label changes in the segmentation (higher values cause smoother result). Terminal weights (designated as "foreground bias", range 0-1) correspond to a cost of assigning background pixels to the foreground.

Terminal weights (foreground bias in GUI) affect the segmentation efficacy distinctly, thus its optimization is crucial. On the other hand, edge weight (smoothness) corresponds to the size of individual cells and has been roughly estimated from 0.4 to 0.8 for used cell sizes (between 1000 and 4000 pixels, respectively).

Cell detection (seed-point extraction)

The cell detection (seed-point extraction) plays a key role in the segmentation of the overlapping objects. For densely clustered and touching cells a precise cell detection has the most significant influence to the final segmentation accuracy. The primary goal in the cell detection is to recognize the presence of the individual objects in the image. Finally, combination of successful foreground-background separation followed by identification of individual cells enable to segment individual cells. There is a considerable amount of methods for cell detection and the mostly used and cited methods are described and evaluated in this paper. Because most of the described methods require blob-like cells, image reconstruction is necessary in most cases (except LoG and generalized LoG filters by Kong et al. [28]).

The tested seed-point extraction methods usually include parameters related to the cell radius (minimal and maximal). For this reason we estimated these values from the ground truth masks. Background segmentation from the previous step was used to eliminate falsely detected seeds in the background. Some of the tested methods already include this step (e.g. dLoGg-Xu [29]). The binary background masks produced by trainable Weka segmentation were used for this purpose. For clarity, the methods described bellow are designated with prefix "d" (detection), image processing approach and author, where possible.

LoG filters

Because of distinctive popularity of the LoG filter for the blob object detection, many modifications of this detector

exist, e.g. multi-scale LoG, Hessian LoG, generalized LoG. LoG filter at a scale σ is defined by equation

$$LoG(\mathbf{x},\sigma) = \nabla^2 G(\mathbf{x},\sigma) = \frac{\sigma^2 - ||\mathbf{x}||^2}{2\pi\sigma^6} e^{\frac{-||\mathbf{x}||^2}{2\sigma^2}}, \quad (12)$$

where G is 2D Gaussian function, $\mathbf{x} = (x, y)$ and $||\cdot||$ is Euclidean norm [27]. In principle, this filter works as a matched filter for blobs.

Multi-scale LoG filtering uses a bag of LoG filters with m different sigma values, which leads to $m - D$ feature space. As proved by Lindeberg [56], LoG responses must be normalized $LoG(\mathbf{x},\sigma)_{norm} = \sigma^\gamma LoG(\mathbf{x},\sigma)$ for scale invariance, where $\gamma = 2$ for scale invariance, but it can be refined for a preference of larger or smaller objects.

Peng et al. [27] used Maximum Intensity Projection (MIP) of the series of LoG-filtered images $MIP(\mathbf{x}) = \max_\sigma(LoG_{norm}(\mathbf{x},\sigma))$, with threshold applied to resulting 2D image, where binary objects correspond to the detected cells. This method (further designated as dLoGm-Peng) has the following parameters: minimal sigma σ_{min}, maximal sigma σ_{max}, sigma step $\Delta\sigma$, γ and threshold.

Kong et al. [28] searched for local maxima higher than defined threshold in whole $m - D$ LoG scale space with elimination of overlapping regions by a pruning process. In the pruning process, the overlapping blobs are eliminated, where only blob with larger value in $m - D$ scale space is preserved. This method has these parameters: σ_{max}, sigma step $\Delta\sigma$, γ, threshold and maximal overlap ratio. Here for σ the logarithmic step is used. This method is referred as dLoGm-Kong.

Hessian analysis of LoG (referred as dLoGh-Zhang) described by Zhang et al. [30] uses the same bag of LoG-filtered images, but optimal scale identification and cell center detection is different. It is known, that local Hessian matrix is positive definite for blob-like structures. The Hessian H (computed from LoG-filtered image) at position (x,y) can be approximated with differences in 2×2 neighborhood. Each connected region with a positive definite Hessian is considered as cell, where H is a positive definite matrix when H_{11} is positive and $det(H)$ is positive.

$$H(x,y,\sigma) = \begin{pmatrix} \frac{\partial LoG(x,y;\sigma)}{\partial x^2} & \frac{\partial LoG(x,y;\sigma)}{\partial x \partial y} \\ \frac{\partial LoG(x,y;\sigma)}{\partial y \partial x} & \frac{\partial LoG(x,y;\sigma)}{\partial y^2} \end{pmatrix}. \quad (13)$$

Optimal is considered a such scale where the mean intensity of the LoG-filtered image is maximal on the positive definite locations, and these positive definite regions are the detected cells. Method is insensitive to choice of range and steps of σ, which leaves only γ parameter to be optimized. Zhang [30] also uses unsupervised classification to identified true cells only, but in our case this leads to deterioration of the results only and thus was not included in the testing.

Intuitively rotationally-symmetric LoG kernels are very sensitive to irregular cell shape. For this reason Kong et al. [28] proposed a generalized LoG filter (referred as dLoGg-Kong) for the detection of the elliptical shapes. They derived an equation for elliptical kernel with two standard deviations σ_x, σ_y and orientation Θ. Method also includes a specific scale normalization with a parameter α and automatic choice of sigma range based on the initial analysis with circular LoG filters. For every pixel position, a feature image is created as a sum of all filter responses and detected cells are local maxima in this image (see [28] for more details). Thanks to the automatic σ estimation, there is one parameter only - α. Method uses integer kernel sizes smaller than estimated σ_{max}. Small kernels produce false peaks on a sub-cellular structures in our data. These artefacts are eliminated by adding a σ_{min} parameter, which corresponds to a minimal cell radius.

Xu et al. (referred as dLoGg-Xu) [29] sped up this technique by summation of the filters with the same kernel orientation Θ, which is possible thanks to the distributive property of convolution. Instead of automatic estimation of σ range, they estimate it from cell radii. Moreover this technique includes a different normalization (without parameter) and mean-shift clustering for elimination of multiple-time detected seeds. Parameters of this method are: σ range and mean shift window size.

A similar approach was described also in Peng et al. [27] method. Parameter range of σ is estimated based on cell radius as $\sigma = r/\sqrt{2}$. For dLoGm-Peng we used estimated σ_{max} and σ_{min}. Step of σ ($\Delta\sigma$) is insensitive parameter, therefore we set it to 1. For setting of other parameters see Additional file 1. Authors [27] used $\gamma = 2$, which is proven to lead to the theoretical scale invariance. When $\gamma < 2$ the smaller objects are preferred, for $\gamma > 2$ the larger objects are preferred. Appropriate setting of γ leads to mean Dice coefficient improvement +0.089 for dLoGm-Peng method and for this reason we add γ to optimized parameters for both dLoGm-Peng and dLoGm-Kong methods. Similarly for dLoGm-Kong we used estimated σ_{max} and σ_{min} with 13 logarithmic steps like the authors[28] (for other parameter settings see Additional file 1). Extension by γ parameter leads to 3 parameters (besides of cell radii), which are sensitive and must be properly set. Both generalized LoG methods try to avoid parameters setting, where dLoGg-Xu has cell size-related parameters only (we set it based on estimated radius) and dLoGg-Kong has one adjustable parameter - scale normalization factor, but cell size estimation is automatic. Both generalized LoG methods are computationally expensive (see Table 1), but dLoGg-Xu reduces the computational time by a reduction of number of convolutions.

Distance transform

Distance transform (DT) of foreground image is defined as a distance to the nearest background pixel (Euclidean distance is chosen as metric). Local maxima of the generated distance map are considered as cells. This method often detects many false cells. For this purpose h-maxima transform is used [15], which uses a grayscale morphology for elimination of small local maxima, where parameter h sets the depth of local maxima to be eliminated. We used two modifications of this method; dDT-Threshold, where binary foreground is computed with optimized threshold and dDT-Weka, where foreground from Weka segmentation is used. Other parameter of this method is maximal size of objects and holes, which are eliminated before applying of the DT.

Fast radial-symmetry transform

Fast radial-symmetry transform [31] (referred as dFRST) is a general method for the detection of circular points of interest applicable to approximately circular objects. Pixels with absolute value of gradient greater than threshold β vote in its gradient direction at the distance of radius $r \in R$, where R is set of radii, determined based on object/cell size. If bright blobs are only considered detection, positions of affected pixel is given by an equation

$$P(\mathbf{x}) = \mathbf{x} + round\left(\frac{g(\mathbf{x})}{\|g(\mathbf{x})\|} r\right) \tag{14}$$

where $g(\mathbf{x})$ represents the gradient and *round* operator rounds each vector element to its nearest integer. On position $P(x)$, an orientation projection image O_r is increased by 1 and magnitude projection image M_r by $\|g(\mathbf{x})\|$. Transformation is defined as mean over all radii

$$S = \frac{1}{N} \sum_{r \in R} F_r * G_r \tag{15}$$

where

$$F_r(\mathbf{x}) = \frac{M_r(\mathbf{x})}{k} \left(\frac{|\hat{O}_r(\mathbf{x})|}{k}\right)^{\alpha} \tag{16}$$

$$\hat{O}_r(\mathbf{x}) = \begin{cases} O_r(\mathbf{x}) & \text{if } |O_r(\mathbf{x})| < k \\ k & otherwise \end{cases} \tag{17}$$

where G_r is a Gaussian kernel, α is the radial strictness parameter and k is a scaling factor normalizing different radii (where typically $k \approx 10$). Inspired by Ram et al. [57], we use a gray-scale dilatation to small local maxima suppression in S. Local maxima are then considered as cells. As R we use all integer values between estimated minimal and maximal cell radius. The parameters for this method include: radial strictness α, scaling factor k, size of morphology structuring element δ, and gradient threshold β.

Generalized Radial-symmetry transform

The generalized radial-symmetry transform as described by Bahlman et al. [32] (referred as dGRST) is able to deal with elliptical shapes because affine transform is employed.. Similarly to generalized LoG filters, we can compute response for different axis scalings and rotations. The dGRST principle is similar to dFRST method, but the gradient $g(x)$ is transformed to

$$\hat{g}(\mathbf{x}) = GMG^{-1}M^{-1}g(\mathbf{x}) \tag{18}$$

where

$$M = \begin{bmatrix} 0 & 1 \\ -1 & 0 \end{bmatrix} \tag{19}$$

and G is affine transformation matrix - for ellipse it is rotation and scaling with parameters θ, a and b. We can set $r = 1$ and used a and b to adjust the size of the desired ellipse axis. All integer values between estimated minimal and maximal cell radius with $a > b$ and 6 steps for θ were used for a and b. Bahlmann at al. [32] mentioned also a Gaussian kernel specified by affine transformation parameters θ, a and b. For consistency with dFRST, we use Gaussian kernel with $\sigma = 0.5$ distorted with G transformation. Remaining parameters are identical to dFRST.

Radial voting

Qi et al. [33] presented a modification of radial voting for cells in histopathology specimens (reffered here as dRV-Qi). It is based on an iterative radial voting described previously [58], but works as a single-path voting followed by a mean-shift clustering. Every pixel with position $\mathbf{x} = [x, y]$ vote in Gaussian smoothed gradient direction $\alpha(\mathbf{x})$, with cone shaped-kernel function (voting area).

$$A(x, y, r_{min}, r_{max}, \Delta) = \{x + rcos\phi, y + rsin\phi | r_{min} < r < r_{max}, \theta - \Delta < \phi < \theta + \Delta\} \tag{20}$$

where θ is an angle of vector $\alpha(\mathbf{x})$, $\{r_{min}, r_{max}\}$ is kernel radial range and Δ is the kernel angular range. In addition, voting sector is weighted by Gaussian function with center located at kernel center. Every pixel (with gradient above certain threshold) update voting image V by adding voting pixel gradient magnitude $|g(\mathbf{x})|$ to all pixels under kernel. Voting image is then thresholded with several thresholds and results are summed and clustered with mean-shift algorithm. For more details see [33]. We used estimated r_{min} and r_{max} from the ground truth images, thresholds were set to 0.2, 0.3,...0.9-times the maximum of image, and we optimized sigma of gradient Gaussian smoothing, sigma of Gaussian for kernel and mean shift bandwidth. We also vote with all pixels, not only with pixels with high gradient magnitude, because computational time of our implementation is not dependent on number of voting pixels. Besides [33] we also tested original [58]

and newer [59] methods, but both were less suitable for adherent cells.

Maximally stable extremal region

Extremal regions of gray-value image are defined as connected components of thresholded image $I_t = I > t$ for some t in this method (designated as dMSER). As described in [34], dMSER produces stable extremal regions of image which are stable in sense of area variation w.r.t. changing threshold t. Minimal stability of extracted region can be set with two parameters - threshold step δ defining the percentage of intensity range and maximal relative area change with this step. This method generates many regions which can overlap. Finally, the smallest regions generated with the highest threshold are picked. This is achieved by finding of the local maxima in the sum of binary images of all regions. Another option is the usage of most stable region from the overlapped ones, but this was shown to be noneffective in our case.

CellDetect

Arteta et al. [35] implementation of CellDetect uses MSER to identify the candidate regions, followed by a classification of true regions. Method extracts 92-dimensional feature vector with object histograms and shape descriptors. Training proceeds in two phases. In the first phase, training of binary SVM and its evaluation is done, which produces score for each region. Region with one seed-point and highest score (one for each seed-point) is used as ground truth for the next phase. In the second phase, structured SVM is used for classification of the regions within each tree created from the overlapping regions, but non-overlap constrains are included. For more details see [35]. Method requires few training images with simple dot annotation and proper setting of MSER detector to achieve high recall.

Single cell (instance) segmentation

After image reconstruction, foreground-background segmentation and seed-point extraction, individual cells were segmented using Marker-controlled (or seeded) watershed [60]. This step showed to be less crucial, because inaccuracy in placing border between cells has a small influence to segmentation efficacy only. Thus, for combining of foreground and seeds into the final segmentation, we test only this simple but very robust technique. Note that more advanced methods exist - e.g. graph-cut [61], or level-set [62] based.

Maker-controlled watershed is similar to classic watershed approach, with restriction of local minima positions into detected seeds location, which can be simply done with mathematical morphology operations. Besides of straightforward application on our images, we proposed a second approach applied on DT image, which does not require an intensity valley between separated cells. For DT image we use geodesic distance transform [63] with distances from seeds (the distance within the foreground pixels only, ignoring the background).

General parameter optimization strategy

Grid search with 10 steps was used for the optimization of parameters of all methods, where suitable range was selected experimentally by a few manual tests. Parameters with large searched range (relatively large difference between lower and upper bound) were searched with logarithmic scale. The same parameters ranges were used for all modalities. All parameters were properly set for training images and then these values were used for all testing images. For background segmentation and detection methods Dice coefficient was used as an objective function (used e.g. in [18]). For image reconstruction techniques the area under ROC curve (AUC) generated by thresholding was used (as well as in [14] or [12]). Because of large computational difficulty of some methods, we attempted to eliminate such parameters from optimization, which does not influence the objective function. If threshold is optimized parameter, its value was optimized between a minimal and maximal intensity of image pixels, with 100 steps for simplicity. Before application of each method, images were normalized into interval [0,1], where minimal and maximal values of the first image of each sequence were used as a reference for the normalization.

Evaluation of results

The F_1 score (Dice coefficient) was used as a measure of segmentation accuracy for (1) foreground-background segmentation, (2) seed-point extraction, and (3) single cell segmentation, with following modifications:

Foreground-background segmentation evaluation

For the evaluation of cell segmentation, Dice coefficient was used as follows:

$$Dice = \frac{2|X \cap Y|}{|X| + |Y|} \tag{21}$$

where $|\cdot|$ is number of pixels of region, X and Y are ground truth and result segmentation, respectively. Dice coefficient is equal to F_1-score, but this term is used for pixel-wise evaluation. Another metric used for segmentation evaluation is Jaccard index, which is related to Dice coefficient as:

$$Jaccard = \frac{Dice}{2 - Dice} \tag{22}$$

which is monotonically increasing function on interval $< 0, 1 >$ (the range of Dice values). This means that order

of quality of segmentation algorithms w.r.t. Jaccard is same as w.r.t. Dice coefficient and for this reason we evaluated only Dice coefficient.

Dice coefficient was computed for evaluation of the foreground segmentation results using all pixels in the image.

Seed-point extraction evaluation

Single dot labels (seeds) are considered as cell detection results. If some method produces pre-segmented regions, then centroids are used as labels. Because our ground truth corresponds to the binary segmented cells, we consider as TP (true positive) such cells having one seed only. As FP (false positive) are considered cells with additional seeds in one cell and with seeds outside cells. FN (false negative) are cells without any seed. To evaluate the performance of the cell detection, Dice coefficient (F_1 score) was used

$$Dice = \frac{2TP}{2TP + FP + FN}. \tag{23}$$

In some papers the accuracy of the centroid positions is also evaluated. Nevertheless, these positions are not very significant for cell segmentation. Therefore, we didn't evaluate this accuracy.

Single cell segmentation evaluation

For single cell segmentation evaluation the F_1 score (Dice coefficient) is used in a similar manner as for foreground-background segmentation evaluation with following modifications: We dealt with correspondence of objects. We used same evaluation of correspondence as [64] in their SEG evaluation algorithm – cell are considered as matching if:

$$|X \cap Y| > 0.5|X| \tag{24}$$

which ensures unambiguous pairing. The final measure of Dice was calculated as the mean of the Dice coefficient of all the reference objects. The cells which are on the image boundary were labeled and they are not included in the evaluation.

A computer with following specifications was used to estimate computational times: Intel Core i5-6500 CPU, 8 GB RAM.

Additional file

Additional file 1: Optimal values for parameters of individual reconstruction methods (xlsx table). * highest value not reducing sensitivity, ** not learned because of identification of small number of regions. nan, not a number. (XLSX 17 kb)

Abbreviations

AUC: Area under curve; DIC: Differential image contrast; DMGW: Dry mass-guided watershed; DT: Distance transform; EGT: Empirical gradient treshold; FOV: Field of view; FRST: First radial symmetry transform; GRST: Generalized Radial symmetry transform; HMC: Hoffman modulation contrast LoG: Laplacian of Gaussian; MCWS: Marker-controlled watershed; MIP: Maximum intensity projection MSER: maximally stable extremal region; PC: Phase contrast; PD: Poisson distribution; PSF: Point spread function; PT: Poisson treshold; ROC: Receiver-operator curve; RV: Radial voting; ST: Simple treshold

Acknowledgements

We thank prof. Radim Chmelik from Brno University of Technology for enabling the DIC microscopy in their facility and Tomas Slaby from Tescan a.s., Brno, for their kind help with operating the quantitative phase microscopy and with processing of the data using their software.

Funding

This work was supported by the Czech Science Foundation GACR 18-24089S and by funds from the Faculty of Medicine, Masaryk University to Junior researcher (Jaromir Gumulec). Josef Jaros was supported by project of Masaryk University (MUNI/A/1298/2017). We acknowledge the support of NVIDIA Corporation with the donation of the Titan Xp GPU used for this research. None of the funding bodies had any role in the design of the study and collection, analysis and interpretation of data, and in writing the manuscript.

Availability of data and materials

Annotated image dataset and image reconstructions used in our study are available for download in the Zenodo repository (https://zenodo.org, Digital Object Identifier: https://doi.org/10.5281/zenodo.1250729). Matlab code is available at GitHub https://github.com/tomasvicar/Cell-segmentation-methods-comparison.

Authors' contributions

TV designed the workflow, selected segmentation methods, performed analysis in Matlab and Python and wrote manuscript. JB performed in vitro experiments, designed experiment, JJ performed HMC and helped with in vitro experiments, FJ designed foreground-background segmentation and seed-point extraction structure, helped with trainable approaches and graph cut, RK helped with selection of segmentation strategies and corrected the manuscript, MM provided ideas for segmentation, supported in vitro experiment, JG designed experiment, wrote manuscript and coordinated work. All the authors have read and approved the final manuscript.

Ethics approval and consent to participate

not applicable.

Consent for publication

not applicable.

Competing interests

The authors declare that they have no competing interests.

Publisher's Note

Springer Nature remains neutral with regard to jurisdictional claims in published maps and institutional affiliations.

Author details

[1]Department of Biomedical Engineering, Faculty of Electrical Engineering and Communication, Brno University of Technology, Technicka 3058/10, CZ-61600 Brno, Czech Republic. [2]Department of Physiology, Faculty of Medicine, Masaryk University, Kamenice 5, CZ-62500 Brno, Czech Republic. [3]Department of Pathological Physiology, Faculty of Medicine, Masaryk University, Kamenice 5, CZ-62500 Brno, Czech Republic. [4]Central European Institute of Technology, Brno University of Technology, Purkynova 656/123, CZ-612 00 Brno, Czech Republic. [5]Max Planck Institute of Molecular Cell Biology and Genetics, Pfotenhauerstr. 108, DE-01307 Dresden, Germany. [6]Department of Histology and Embryology, Faculty of Medicine, Masaryk University, Kamenice 5, CZ-62500 Brno, Czech Republic. [7]International Clinical Research Center, St. Anne's University Hospital, Pekarska 664/53, CZ-65691 Brno, Czech Republic.

Received: 8 February 2019 **Accepted:** 7 May 2019
Published online: 28 June 2019

References

1. Wang Z, Millet L, Chan V, Ding H, Gillette MU, Bashir R, Popescu G. Label-free intracellular transport measured by spatial light interference microscopy. J Biomed Opt. 2011;16(2):026019–0260199. https://doi.org/10.1117/1.3549204.

2. Al-Kofahi Y, Lassoued W, Lee W, Roysam B. Improved automatic detection and segmentation of cell nuclei in histopathology images. IEEE Trans Biomed Eng. 2010;57(4):841–52. https://doi.org/10.1109/TBME.2009.2035102.
3. Dimopoulos S, Mayer CE, Rudolf F, Stelling J. Accurate cell segmentation in microscopy images using membrane patterns,. Bioinformatics (Oxford, England). 2014;30(18):2644–51. https://doi.org/10.1093/bioinformatics/btu302.
4. Chalfoun J, Majurski M, Dima A, Stuelten C, Peskin A, Brady M. FogBank: a single cell segmentation across multiple cell lines and image modalities,. BMC Bioinformatics. 2014;15(1):6598. https://doi.org/10.1186/s12859-014-0431-x.
5. Hilsenbeck O, Schwarzfischer M, Loeffler D, Dimopoulos S, Hastreiter S, Marr C, Theis FJ, Schroeder T. Faster: a user-friendly tool for ultrafast and robust cell segmentation in large-scale microscopy. Bioinformatics. 2017;33(13):2020-28. https://doi.org/10.1093/bioinformatics/btx107.
6. Wang Q, You L, West M. Celltracer: Software for automated image segmentation and line-age mapping for single-cell studies. Duke University; 2018. http://www.stat.duke.edu/~mw/MWextrapubs/Wang2008.pdf.
7. Stylianidou S, Brennan C, Nissen SB, Kuwada NJ, Wiggins PA. Supersegger: robust image segmentation, analysis and lineage tracking of bacterial cells. Mol Microbiol. 2016;102(4):690–700.
8. Bredies K, Wolinski H. An active-contour based algorithm for the automated segmentation of dense yeast populations on transmission microscopy images. Comput Vis Sci. 2011;14(7):341–52.
9. Versari C, Stoma S, Batmanov K, Llamosi A, Mroz F, Kaczmarek A, Deyell M, Lhoussaine C, Hersen P, Batt G. Long-term tracking of budding yeast cells in brightfield microscopy: Cellstar and the evaluation platform. J R Soc Interface. 2017;14(127):20160705.
10. Carpenter AE, Jones TR, Lamprecht MR, Clarke C, Kang IH, Friman O, Guertin D. a., Chang JH, Lindquist R. a., Moffat J, Golland P, Sabatini DM. CellProfiler: image analysis software for identifying and quantifying cell phenotypes,. Genome Biol. 2006;7(10):100. https://doi.org/10.1186/gb-2006-7-10-r100. http://arxiv.org/abs/arXiv:1201.3109v1.
11. Tescan AS. Q-PHASE: Quantitative, Label-free Imaging Cytometry. https://www.tescan.com/en-us/technology/light-microscopy/q-phase. Accessed 30 Apr 2018.
12. Koos K, Molnár J, Kelemen L, Tamás G, Horvath P. DIC image reconstruction using an energy minimization framework to visualize optical path length distribution. Sci Rep. 2016;6:30420. https://doi.org/10.1038/srep30420.
13. Yin Z, Ker DFE, Kanade T. Restoring DIC microscopy images from multiple shear directions. In: Lecture Notes in Computer Science (including Subseries Lecture Notes in Artificial Intelligence and Lecture Notes in Bioinformatics). vol. 6801 LNCS; 2011. p. 384–97. https://doi.org/10.1007/978-3-642-22092-0.
14. Yin Z, Kanade T, Chen M. Understanding the phase contrast optics to restore artifact-free microscopy images for segmentation. Med Image Anal. 2012;16(5):1047–62. https://doi.org/10.1016/j.media.2011.12.006. http://arxiv.org/abs/NIHMS150003.
15. Thirusittampalam K, Hossain MJ, Ghita O, Whelan PF. A novel framework for cellular tracking and mitosis detection in dense phase contrast microscopy images. IEEE J Biomed Health Inf. 2013;17(3):642–53. https://doi.org/10.1109/TITB.2012.2228663.
16. Dewan MAA, Ahmad MO, Swamy MNS. A method for automatic segmentation of nuclei in phase-contrast images based on intensity, convexity and texture. IEEE Trans Biomed Circ Syst. 2014;8(5):716–28. https://doi.org/10.1109/TBCAS.2013.2294184.
17. Otsu N. A threshold selection method from gray-level histograms. IEEE Trans Syst Man Cybern. 1979;9(1):62–6. https://doi.org/10.1109/TSMC.1979.4310076.
18. Chalfoun J, Majurski M, Peskin A, Breen C, Bajcsy P, Brady M. Empirical gradient threshold technique for automated segmentation across image modalities and cell lines. J Microsc. 2015;260(1):86–99. https://doi.org/10.1111/jmi.12269.
19. Juneau P-M, Garnier A, Duchesne C. Selection and tuning of a fast and simple phase-contrast microscopy image segmentation algorithm for measuring myoblast growth kinetics in an automated manner. Microsc Microanal. 2013;19(4):855–66.
20. Topman G, Sharabani-Yosef O, Gefen A. A method for quick, low-cost automated confluency measurements. Microsc Microanal. 2011;17(6):915–22.
21. Jaccard N, Griffin LD, Keser A, Macown RJ, Super A, Veraitch FS, Szita N. Automated method for the rapid and precise estimation of adherent cell culture characteristics from phase contrast microscopy images. Biotech Bioeng. 2014;111(3):504–17.
22. Caselles V, Kimmel R, Sapiro G. Geodesic active contours. Int J Comput Vis. 1997;22(1):61–79.
23. Chan TF, Vese LA. Active contours without edges. IEEE Trans Image Process. 2001;10(2):266–77. https://doi.org/10.1109/83.902291.
24. Boykov Y, Kolmogorov V. An experimental comparison of min-cut/max-flow algorithms for energy minimization in vision. IEEE Trans Pattern Anal Mach Intell. 2004;26(9):1124–37. https://doi.org/10.1109/TPAMI.2004.60.
25. Sommer C, Straehle C, Köthe U, Hamprecht FA. Ilastik: Interactive learning and segmentation toolkit. In: 2011 IEEE International Symposium on Biomedical Imaging: From Nano to Macro; 2011. p. 230–3. https://doi.org/10.1109/ISBI.2011.5872394.
26. Arganda-Carreras I, Kaynig V, Rueden C, Eliceiri KW, Schindelin J, Cardona A, Seung HS. Trainable weka segmentation: a machine learning tool for microscopy pixel classification. Bioinformatics. 2017. https://doi.org/10.1093/bioinformatics/btx180.
27. Peng H, Zhou X, Li F, Xia X, Wong STC. Integrating multi-scale blob/curvilinear detector techniques and multi-level sets for automated segmentation of stem cell images. In: 2009 IEEE International Symposium on Biomedical Imaging: From Nano to Macro. IEEE; 2009. p. 1362–5. https://doi.org/10.1109/ISBI.2009.5193318. http://ieeexplore.ieee.org/document/5193318/.
28. Kong H, Akakin HC, Sarma SE. A generalized laplacian of gaussian filter for blob detection and its applications. IEEE Trans Cybern. 2013;43(6):1719–33. https://doi.org/10.1109/TSMCB.2012.2228639.
29. Xu H, Lu C, Berendt R, Jha N, Mandal M. Automatic nuclei detection based on generalized laplacian of gaussian filters. IEEE J Biomed Health Inform. 2017;21(3):826–37.
30. Zhang M, Wu T, Bennett KM. Small blob identification in medical images using regional features from optimum scale. IEEE Transactions on Biomedical Engineering. 2015;62(4):1051–62. https://doi.org/10.1109/TBME.2014.2360154.
31. Loy G, Zelinsky A. Fast radial symmetry for detecting points of interest. IEEE Trans Pattern Anal Mach Intell. 2003;25(8):959–73. https://doi.org/10.1109/TPAMI.2003.1217601.
32. Bahlmann C. Fast radial symmetry detection under affine transformations. In: Proceedings of the 2012 IEEE Conference on Computer Vision and Pattern Recognition (CVPR). CVPR '12. Washington, DC: IEEE Computer Society; 2012. p. 932–9. http://dl.acm.org/citation.cfm?id=2354409.2354741.
33. Qi X, Xing F, Foran DJ, Yang L. Robust segmentation of overlapping cells in histopathology specimens using parallel seed detection and repulsive level set. IEEE Trans Biomed Eng. 2012;59(3):754–65.
34. Matas J, Chum O, Urban M, Pajdla T. Robust wide-baseline stereo from maximally stable extremal regions. Image Vis Comput. 2004;22(10):761–7. https://doi.org/10.1016/j.imavis.2004.02.006.
35. Arteta C, Lempitsky V, Noble JA, Zisserman A. Learning to Detect Cells Using Non-overlapping Extremal Regions. Miccai. 2012;Figure 1:1–8. https://doi.org/10.1007/978-3-642-33415-3.
36. Russakovsky O, Deng J, Su H, Krause J, Satheesh S, Ma S, Huang Z, Karpathy A, Khosla A, Bernstein M, et al. Imagenet large scale visual recognition challenge. Int J Comput Vis. 2015;115(3):211–52.
37. Iglovikov V, Shvets A. Ternausnet: U-net with vgg11 encoder pre-trained on imagenet for image segmentation. 2018. arXiv preprint arXiv:1801.05746.
38. Ronneberger O, Fischer P, Brox T. U-Net: Convolutional Networks for Biomedical Image Segmentation. Medical Image Computing and Computer-Assisted Intervention. 2015. https://doi.org/10.1007/978-3-319-24574-4_28.
39. Sadanandan SK, Ranefall P, Wählby C. Feature Augmented Deep Neural Networks for Segmentation of Cells. Computer Vision – ECCV 2016 Workshops. In: Computer Vision – ECCV 2016 Workshops. Amsterdam: Springer International Publishing; 2016. https://doi.org/10.1007/978-3-319-46604-0_17.
40. Van Valen DA, Kudo T, Lane KM, Macklin DN, Quach NT, DeFelice MM, Maayan I, Tanouchi Y, Ashley EA, Covert MW. Deep learning automates the quantitative analysis of individual cells in live-cell imaging experiments. PLoS Comput Biol. 2016;12(11):1005177.

41. Schmidt U, Weigert M, Broaddus C, Myers G. Cell detection with star-convex polygons. In: Medical Image Computing and Computer Assisted Intervention - MICCAI 2018 - 21st International Conference, Granada, Spain, September 16-20, 2018, Proceedings, Part II; 2018. p. 265–73. https://doi.org/10.1007/978-3-030-00934-2_30.
42. Xing F, Yang L. Robust nucleus/cell detection and segmentation in digital pathology and microscopy images. IEEE Rev Biomed Eng. 2016;9:234–63. https://doi.org/10.1109/RBME.2016.2515127.
43. Wiesmann V, Franz D, Held C, Münzenmayer C, Palmisano R, Wittenberg T. Review of free software tools for image analysis of fluorescence cell micrographs. J Microsc. 2015;257(1):39–53.
44. Meijering E. Cell segmentation: 50 years down the road [life sciences]. IEEE Signal Process Mag. 2012;29(5):140–5.
45. Kasprowicz R, Suman R, O'Toole P. Characterising live cell behaviour: Traditional label-free and quantitative phase imaging approaches. Int J Biochem Cell Biol. 2017;84:89–95.
46. Loewke NO, Pai S, Cordeiro C, Black D, King BL, Contag CH, Chen B, Baer TM, Solgaard O. Automated cell segmentation for quantitative phase microscopy. IEEE Trans Med Imaging. 2017.
47. Ulman V, Maška M, Magnusson KEG, Ronneberger O, Haubold C, Harder N, Matula P, Matula P, Svoboda D, Radojevic M, Smal I, Rohr K, Jaldén J, Blau HM, Dzyubachyk O, Lelieveldt B, Xiao P, Li Y, Cho S-Y, Dufour A, Olivo-Marin JC, Reyes-Aldasoro CC, Solis-Lemus JA, Bensch R, Brox T, Stegmaier J, Mikut R, Wolf S, Hamprecht FA, Esteves T, Quelhas P, Demirel Ö, Malström L, Jug F, Tomančák P, Meijering E, Muñoz-Barrutia A, Kozubek M, Ortiz-de-Solorzano C. An objective comparison of cell tracking algorithms. Nat Methods. 2017. https://doi.org/10.1038/NMETH.447.
48. Kolman P, Chmelík R. Coherence-controlled holographic microscope. Opt Express. 2010;18(21):21990–2004. https://doi.org/10.1364/OE.18.021990.
49. Slabý T, Kolman P, Dostál Z., Antoš M., Lošťák M, Chmelík R. Off-axis setup taking full advantage of incoherent illumination in coherence-controlled holographic microscope. Opt Express. 2013;21(12):14747–62. https://doi.org/10.1364/OE.21.014747.
50. Davies H, Wilkins M. Interference microscopy and mass determination. Nature. 1952;169(4300):541. https://doi.org/10.1038/169541a.
51. Barer R. Refractometry and interferometry of living cells. J Opt Soc Am. 1957;47(6):545–56. https://doi.org/10.1364/JOSA.47.00054.
52. Koos K, Molnar J, Horvath P. DIC Microscopy Image Reconstruction Using a Novel Variational Framework. 2015. International Conference on Digital Image Computing: Techniques and Applications (DICTA). 2015. https://doi.org/10.1109/DICTA.2015.7371252.
53. Su H, Yin Z, Kanade T, Huh S. Phase contrast image restoration via dictionary representation of diffraction patterns. Med Image Comput Comput Assist Interv. 2012;15(3):615–22.
54. Whitaker RT. A level-set approach to 3d reconstruction from range data. Int J Comput Vis. 1998;29(3):203–31.
55. Breiman L. Random forests. Mach Learn. 2001;45(1):5–32. https://doi.org/10.1023/A:1010933404324.
56. Lindeberg T. Feature detection with automatic scale selection. Int J Comput Vis. 1998;30(2):79–116.
57. Ram S, Rodríguez JJ. Symmetry-based detection of nuclei in microscopy images. In: 2013 IEEE International Conference on Acoustics, Speech and Signal Processing; 2013. p. 1128–32. https://doi.org/10.1109/ICASSP.2013.6637826.
58. Parvin B, Yang Q, Han J, Chang H, Rydberg B, Barcellos-Hoff MH. Iterative voting for inference of structural saliency and characterization of subcellular events. IEEE Trans Image Process. 2007;16(3):615–23. https://doi.org/10.1109/TIP.2007.891154.
59. Lu C, Xu H, Xu J, Gilmore H, Mandal M, Madabhushi A. Multi-pass adaptive voting for nuclei detection in histopathological images. Sci Rep. 2016;6:33985. https://doi.org/10.1038/srep33985.
60. Parvati K, Rao P, Mariya Das M. Image segmentation using gray-scale morphology and marker-controlled watershed transformation. Discret Dyn Nat Soc. 2008;2008:384346. https://doi.org/10.1155/2008/384346.
61. Daněk O, Matula P, Ortiz-de-Solórzano C, Muñoz-Barrutia A, Maška M, Kozubek M. Segmentation of touching cell nuclei using a two-stage graph cut model. In: SCIA: 2009. Oslo: Springer. p. 410–19. https://doi.org/10.1007/978-3-642-02230-2_42.
62. Zhou Y, Kuijper A, Heise B, He L. Cell Segmentation Using Level Set Method. Linz: Johannes Kepler University; 2007. https://pdfs.semanticscholar.org/33b2/7d8696026b5f4f7eac7095ff30e9c920621a.pdf.
63. Ikonen L, Toivanen P. Shortest routes on varying height surfaces using gray-level distance transforms. Image Vis Comput. 2005;23(2):133–41.
64. Maška M., Ulman V, Svoboda D, Matula P, Matula P, Ederra C, Urbiola A, España T, Venkatesan S, Balak DMW, Karas P, Bolcková T., Štreitová M, Carthel C, Coraluppi S, Harder N, Rohr K, Magnusson KEG, Jaldén J, Blau HM, Dzyubachyk O, Křížek P, Hagen GM, Pastor-Escuredo D, Jimenez-Carretero D, Ledesma-Carbayo MJ, Muñoz-Barrutia A, Meijering E, Kozubek M, Ortiz-de-Solorzano C. A benchmark for comparison of cell tracking algorithms. Bioinformatics. 2014;30(11):1609–17. https://doi.org/10.1093/bioinformatics/btu080.

Ready to submit your research? Choose BMC and benefit from:

- **fast, convenient online submission**
- **thorough peer review by experienced researchers in your field**
- **rapid publication on acceptance**
- **support for research data, including large and complex data types**
- **gold Open Access which fosters wider collaboration and increased citations**
- **maximum visibility for your research: over 100M website views per year**

At BMC, research is always in progress.

Learn more biomedcentral.com/submissions



4.3 Detection and distinction of a specific type of cell death by quantitative phase imaging

Cell viability and cytotoxicity assays are essential for drug screening and evaluating the effects of therapeutic agents. While biochemical assays provide preliminary insights, they should be confirmed by methods that directly assess cell death. The predominant type of cell death can be analysed by flow cytometry (FCM). However, the lack of cell morphology insights can lead to misclassification, especially in lytic types of cell death. Therefore, we compared FCM analysis using annexin V/propidium iodide assays with multimodal holographic microscopy (MHM), which integrates fluorescence. Our results showed that the Annexin V+/PI- phenotype does not specifically indicate early apoptosis, necessitating the combination of morphological criteria with Annexin V/PI for accurate cell death classification. Our work introduced a rapid, label-free approach using quantitative phase imaging (QPI) to monitor morphological changes during cell death, aiming to distinguish between apoptosis and lytic forms of cell death based on distinct morphological features. We classified lytic and non-lytic cell deaths based on defining features: The "dance of death" for apoptosis, and cellular swelling and membrane rupture indicative of different types of lytic cell death. Our results demonstrated that morphological and dynamic features monitored by QPI can accurately detect cell death, achieving 76% accuracy against manual annotation. Furthermore, using QPI data alongside machine learning, we identified dynamic changes in cell morphology during both caspase-dependent and independent cell death pathways, using cell density and pixel intensity change as key parameters, termed Cell Dynamic Score (CDS). Our results are the first study introducing CDS and cell density as a parameter typical for individual cell death subroutines (prediction accuracy 75.4 % for caspase 3,7-dependent versus caspase 3,7-independent cell death). The following articles include two methodological articles describing the development of a new method for detecting cell death, and publications in which these microscopic methods have been successfully applied.

Author's publications relevant to this chapter

1. Vicar T, Raudenska M, Gumulec J, Balvan J. The quantitative-phase dynamics of apoptosis and lytic cell death. *Scientific Reports*, 10, 1566 (2020)
   IF (2019) 4.380; 58 citations (WOS)
2. Balvan J, Krizova A, Gumulec J, Raudenska M, Sladek Z, Sedlackova M, *et al*. Multimodal holographic microscopy: Distinction between apoptosis and oncosis. *PLoS ONE,* 10, e0121674 (2015)

IF (2015) 3.752; 56 citations (WOS)

3. Fojtů, M., Balvan, J., *et al*. Black Phosphorus Cytotoxicity Assessments Pitfalls: Advantages and Disadvantages of Metabolic and Morphological Assays. *Chemistry – A Europian Journal*, **25**, 349–360 (2019)
   IF (2019) 4.857; 20 citations (WOS)
4. Eyer, L.; Svoboda, P.; Balvan, J.; *et al*. Broad-Spectrum Antiviral Activity of 3′-Deoxy-3′-Fluoroadenosine against Emerging Flaviviruses. *Antimicrobial Agents and Chemotherapy*, 65, e01522-20, (2021)
   IF (2021) 5.938; 10 citations (WOS)
5. Peng X., Urso M., Balvan J., *et al*. Self-propelled magnetic dendrite-shaped microrobots for photodynamic prostate cancer therapy. *Angewande Chemie International Edition Engl*. **61**, e202213505 (2022)
   IF (2019) 16.6; 43 citations (WOS)
6. Ussia M, Urso M, Kratochvilova M, Navratil J, Balvan J, *et al*. Magnetically Driven Self-Degrading Zinc-Containing Cystine Microrobots for Treatment of Prostate Cancer *Small*, 2023, 19: 2208259 (2023)
   IF (2023) 13; 22 citations (WOS)
7. Fojtů, M.; Balvan, J., *et al*. 2D Germanane Derivative as a Vector for Overcoming Doxorubicin Resistance in Cancer Cells. *Applied Materials Today 20*, 100697 **(2020)**
   IF (2019) 10.041; 10 citations (WOS)

www.nature.com/scientificreports

SCIENTIFIC REPORTS
natureresearch

OPEN

The Quantitative-Phase Dynamics of Apoptosis and Lytic Cell Death

Tomas Vicar[2,4], Martina Raudenska[1,3], Jaromir Gumulec[2,3] & Jan Balvan[2*]

Cell viability and cytotoxicity assays are highly important for drug screening and cytotoxicity tests of antineoplastic or other therapeutic drugs. Even though biochemical-based tests are very helpful to obtain preliminary preview, their results should be confirmed by methods based on direct cell death assessment. In this study, time-dependent changes in quantitative phase-based parameters during cell death were determined and methodology useable for rapid and label-free assessment of direct cell death was introduced. The goal of our study was distinction between apoptosis and primary lytic cell death based on morphologic features. We have distinguished the lytic and non-lytic type of cell death according to their end-point features (Dance of Death typical for apoptosis versus swelling and membrane rupture typical for all kinds of necrosis common for necroptosis, pyroptosis, ferroptosis and accidental cell death). Our method utilizes Quantitative Phase Imaging (QPI) which enables the time-lapse observation of subtle changes in cell mass distribution. According to our results, morphological and dynamical features extracted from QPI micrographs are suitable for cell death detection (76% accuracy in comparison with manual annotation). Furthermore, based on QPI data alone and machine learning, we were able to classify typical dynamical changes of cell morphology during both caspase 3,7-dependent and -independent cell death subroutines. The main parameters used for label-free detection of these cell death modalities were cell density (pg/pixel) and average intensity change of cell pixels further designated as Cell Dynamic Score (CDS). To the best of our knowledge, this is the first study introducing CDS and cell density as a parameter typical for individual cell death subroutines with prediction accuracy 75.4% for caspase 3,7-dependent and -independent cell death.

Analysis of cell viability and the distinction of specific cell death subtype represent a key aspect in many areas of cell biology. This kind of information is also highly important for drug screening and cytotoxicity tests of antineoplastic or other therapeutic drugs. Cell death is considered reversible until a first 'point-of-no-return' is overstepped. While no exactly defined biochemical event can be taken as an undisputable proof of this point-of-no-return, cell should be taken as dead when any of these situations occur: (1) the cell has lost the integrity of its plasma membrane; (2) the cell and its nucleus has undergone complete fragmentation into discrete bodies (apoptotic bodies); (3) the cellular corpse has been engulfed and digested by a neighbouring cell[1]. Cells that are arrested in the cell cycle should be counted as viable[2].

Methods for cell death analysis are usually based on various basic cell functions such as enzyme activity, semi-permeability of the mitochondrial or cellular membrane, cell adherence, ATP production, the presence of specific markers, or changes of functionality due to specific inhibitor (genetical or pharmacological)[3]. Methods for cell death detection form two main groups: a) methods that directly measure cell death; and b) methods that analyse biochemical processes or features characteristic for viable cells[4]. Even though indirect tests are very helpful to obtain preliminary preview, their results should be confirmed by methods based on direct cell death assessment[3]. According to NCCD (Nomenclature Committee on Cell Death), the currently accepted definition of cell death and its subroutines is based particularly on genetical, biochemical, pharmacological, and functional parameters, rather than morphological aspects[1]. Specific methods for apoptosis and lytic cell death detection are focused on typical biochemical parameters such as visualization of phosphatidylserine exposure, executioner caspases activation, or DNA fragmentation in the case of apoptotic cell death; and loss of barrier function and subsequent permeabilization of the plasma membrane with the release of specific death associated molecular patterns (DAMP) during lytic cellular demise[1]. Nevertheless, almost all these methods are based on fluorometric or

[1]Department of Physiology, Faculty of Medicine, Masaryk University/Kamenice 5, CZ-625 00, Brno, Czech Republic. [2]Department of Pathological Physiology, Faculty of Medicine, Masaryk University/Kamenice 5, CZ-625 00, Brno, Czech Republic. [3]Department of Chemistry and Biochemistry, Mendel University/Zemedelska 1, CZ-613 00, Brno, Czech Republic. [4]Department of Biomedical Engineering, Faculty of Electrical Engineering and Communication, Brno University of Technology, Technicka 3058/10, Brno, Czech Republic. *email: jan.balvan@med.muni.cz

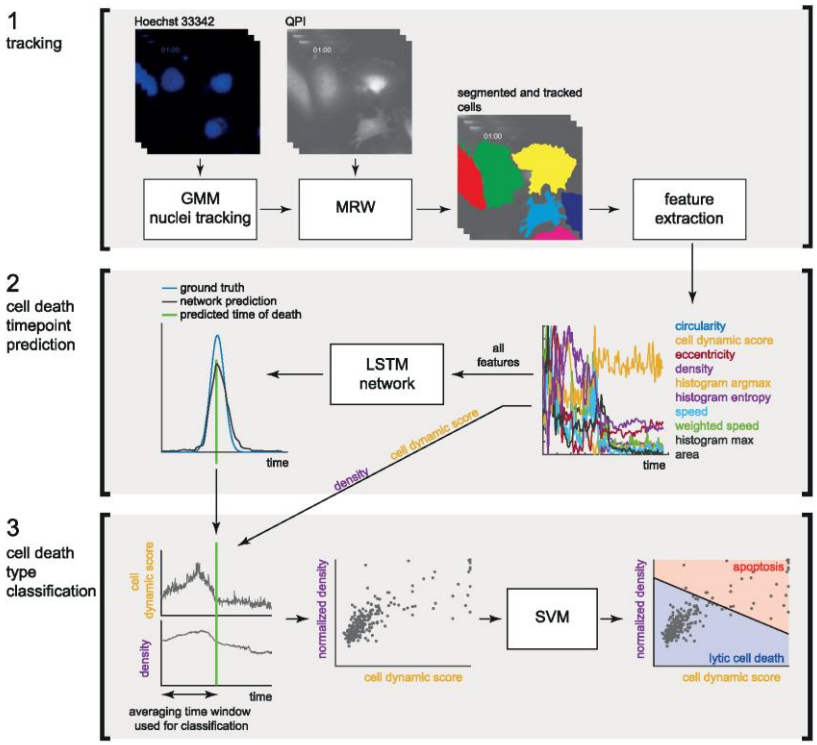

Figure 1. Block diagram of cell death subroutine classification. The process is divided into three steps: cell tracking, prediction of timepoint of death and cell death type classification. (1) cell tracking results from a tracked and segmented cells (for detail regarding tracking see Fig. 2) and set of extracted quanitative-phase-based features listed in the second step, (2) prediction of timepoint of death for each cell. Long-short term memory (LSTM) neuronal network is used for this step and all features mentioned in the step 2 were included for this prediction. (3) Cell death type classification is based on two parameters: density and cell dynamic score (CDS). Based on them, Support Vector Machine classifier (SVM) is used for cell death type classification as "apoptotic" or "lytic". The input parameters for this analysis are: (i) interval minus 10 h to timepoint of death (predicted in the previous step), and (ii) manually annotated death type (apoptosis vs lytic cell death). Figure shows the average cell dynamic score and mass density, LNCaP cells after 0.1 μM doxorubicin treatment (N = 61 apoptosis and 53 lytic cell death). GMM, Gaussian Mixture Model; MRW, Movement Regularized Watershed; QPI, quantitative phase image.

colourimetric endpoint visualization of the analyzed parameter and belong among indirect assays. Such indirect endpoint analyses are prone to the misleading results as we have shown in our previous work[5]. Although morphological aspects of cell death are not generally recommended to determine cell death subroutines[1], it would be a mistake to completely ignore them. Recent progress in Quantitative Phase Imaging techniques (QPI) has enabled the observation of time-dependent subtle changes unrecognizable to the naked eye (such as cell mass distribution) on micrographs. These changes in cell mass distribution, cell density, micro-blebbing of the cell membrane, nuclear shape, homogeneity of cell content, and many other parameters, which can be typical for individual cell death subroutines, can be observed without fixation, labelling or cell harvesting.

In this article, we demonstrate a methodology useable for rapid assessment of direct cell death that is based on NCCD recommendations (Fig. 1). The goals of our study were (a) estimation of time point of cell demise and (b) distinction between apoptosis and primary lytic cell death based on morphologic features. We were able to distinguish the lytic and non-lytic type of cell death according to their end-point features (Dance of Death typical for apoptosis versus swelling and membrane rupture typical for all kinds of necrosis common for necroptosis, pyroptosis, ferroptosis and accidental cell death). Using advanced quantitative label-free phase imaging (QPI), we were also able to observe typical dynamical changes of cell morphology during both caspase 3, 7-dependent and -independent cell death subroutines and to determine the moment of cell death. Dynamical, time-dependent

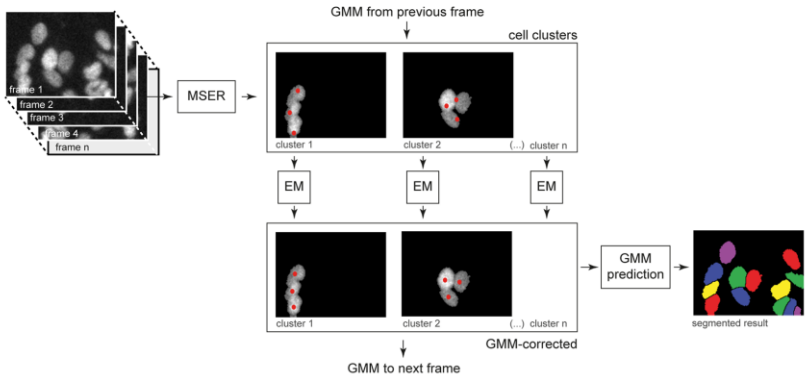

Figure 2. Block diagram of cell tracking algorithm. Cell tracking is used in the first step of the algoritm, see Fig. 1. Nuclear staining with Hoechst 33342 from individual frames is used as an input. Maximally stable extremal region (MSER) is used to segment cell clusters in which the subsequent expectation maximalization (EM) tracking is performed separatelly. Red dots represent individual nuclei (centers of Gaussians of the Gaussian mixture model (GMM)). Finally, GMM is used to split individual nuclei masks.

changes in cell mass distribution maps were used for the label-free distinction between typical morphological patterns appropriate for caspase-dependent and caspase-independent cell death subroutines.

As model cells, prostate cancer cell lines DU145, LNCaP, and benign cell line PNT1A established by immortalization of normal adult prostatic epithelial cells were used. These cell lines were not selected because of the clinical relevance, but rather because of their radically different size and accessibility for the automatic segmentation algorithm. We expected cellular size to be the factor influencing the rate of morphological changes during cell death. Cell death was triggered by doxorubicin and staurosporine, two commonly known inducers of apoptosis with a distinct induction of caspase cleavage and consequently a distinct morphological manifestation[6,7]. Cell death induced by black phosphorus (BP) was detected as an example of difficult detection conditions[8].

Cell tracking is an essential step in cell image analysis. Even though many methods exist[9], there is no universal and sufficiently robust method applicable to QPI, especially for touching cells and if correct tracking through whole image sequence is needed. Simple available tools like TrackMate[10] have shown to be insufficient, thus we have developed a new tracking method tailored for our dataset.

The number of existing methods for the detection of cell death in label-free time-lapse images is very limited. In[11] authors detect cell death event in Phase Contrast Microscopy using features time-series (size, roundness, speed etc.) and classify each time point as alive or death with transductive support vector machine. In comparison, our technique based on quantitative microscopy data uses more features and more advanced Long Short-Term Memory (LSTM) neural network.

There are several techniques for static cell image classification including extraction of features and application of classifier[12,13] or application of convolutional neural network[14]. These techniques can be also possibly applied for a distinction of different types of cell death, however, we decided for using only two features for this distinction in order to make our results easily interpretable, while also incorporating new features describing cell dynamics.

Methods

Chemical and biochemical reagents. RPMI-1640 medium, fetal bovine serum (FBS) (mycoplasma-free), penicillin/streptomycin, and trypsin were purchased from Sigma Aldrich Co. (St. Louis, MO, USA). Phosphate buffered saline PBS was purchased from Invitrogen Corp. (Carlsbad, CA, USA). Ethylenediaminetetraacetic acid (EDTA), staurosporine, doxorubicin and all other chemicals of ACS purity were purchased from Sigma Aldrich Co. (St. Louis, MO, USA) unless noted otherwise. z-VAD-FMK was purchased from Promega (Madison, Wisconsin, USA). Black phosphorus was kindly provided by Dr. Martin Pumera.

Cell culture and cultured cell conditions. LNCaP cell line was established from a lymph node metastase of the hormone-refractory patient and contains a mutation in the androgen receptor (AR) gene. This mutation creates a promiscuous AR that can bind to different types of steroids. LNCaP cells are AR-positive, PSA-positive, PTEN-negative and harbor wild-type p53[15,16]. PNT1A is an immortalized non-tumorigenic epithelial cell line. PNT1A cells harbour wild-type p53. However, SV40 induced T-antigen expression inhibits the activity of p53. This cell line had lost the expression of AR and prostate-specific antigen (PSA)[17]. DU-145 cell line is derived from the metastatic site in the brain and contains P223L and V274F mutations in p53. This cell line is PSA and AR-negative and androgen independent[18]. All cell lines used in this study were purchased from HPA Culture Collections (Salisbury, UK) and were cultured in RPMI-1640 medium with 10% FBS. The medium was supplemented with antibiotics (penicillin 100 U/ml and streptomycin 0.1 mg/ml). Cells were maintained at

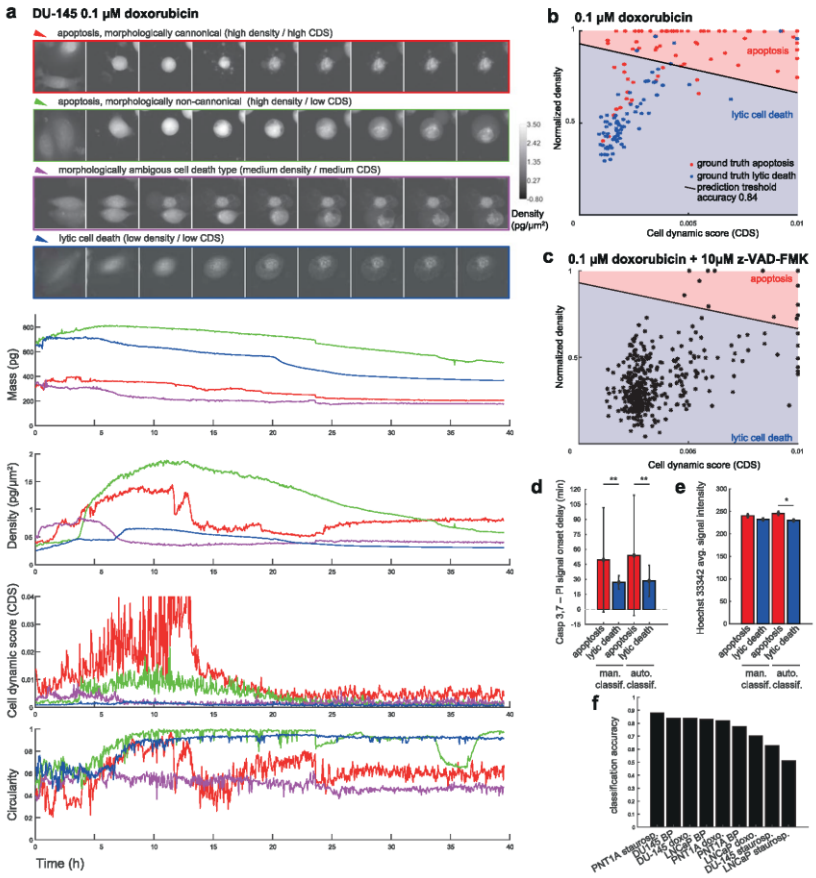

Figure 3. Quantitative phase-related parameters of cells dying by apoptotic and lytic cell death. DU-145 cells exposed to 0.1 µM doxorubicin. (**a**) Real-time QPI signals for canonical apoptosis (red), lytic cell death (blue), morphologically non-canonical apoptosis (green), and ambiguous cell death type (violet) based on a proposed classification algorithm. (**b**) classification of cell death type according to cell dynamic score and normalized density. N = 160 cells. (**c**) Inhibitor of apoptosis z-VAD-FMK (10 µM) decreases proportion of cells classified as "apoptotic" (characteristic by high density/high cell dynamic score (CDS)). N = 381 cells. (**d**) verification of classification accuracy determined in previous step by the measured signal delay of fluorescence onset of Casp 3,7 and PI. Apoptotic cells display a delay in PI signal onset compared to Casp 3,7. This delay was determined both for automatic and manual classification. (**e**) verification of classification accuracy determined in previous step by the nuclear signal intensity measured by Hoechst 33342. Apoptotic cells display an increased Hoechst 33342 intensity because of nuclear shrinkage. *Indicate $p < 0.05$, **indicate $p < 0.001$. Bar charts are shown as mean and standard error. (**f**) prediction accuracy for all other cell types (PNT1A and LNCaP and DU-145 cells) exposed to other treatments (staurosporine and black phosphorus, for results see Supplementary Figs. 2 to 12). See Fig. 7. for quantitative phase and fluorescent images in critical timepoints of particular cells. BP, black phosphorus; PI, propidium iodide; CDS, cell dynamic score.

37 °C in a humidified (60%) incubator with 5% CO_2 (Sanyo, Japan). Cell lines were not tested on mycoplasma contamination.

Cell death was induced using 0.5 µM staurosporine, 0.1 µM doxorubicin, or 400 µg/mL of black phosphorus. Caspase activity was inhibited by 10 µM z-VAD-FMK.

Correlative time-lapse quantitative phase-fluorescence imaging. QPI and fluorescence imaging were performed by using multimodal holographic microscope Q-PHASE (Telight a.s., Brno, Czech Republic).

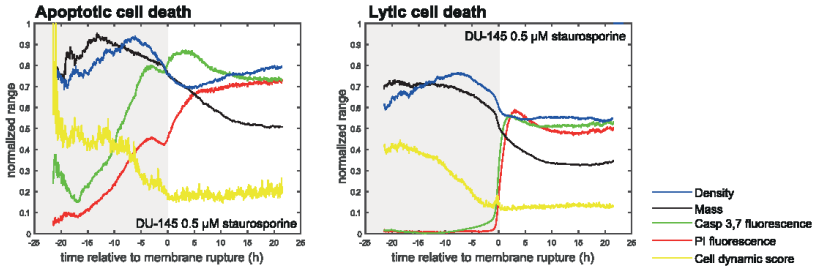

Figure 4. Apoptotic and lytic cell death subroutines and their quantitative phase and caspase 3,7 and propidium iodide signals. Average curves of particular parameters for manually annotated DU-145 cells dying by apoptotic cell death (N = 105) and by lytic cell death (N = 148). Before averaging, signals are aligned to the timepoint of death.

To determine the amount of caspase-3/7 product accumulation, cells were loaded with 2 µM CellEvent™ Caspase-3/7 Green Detection Reagent (Life Technologies, Carlsbad, CA, USA) according to the manufacturer's protocol and visualized using FITC 488 nm filter. To detect the cells with a loss of plasma membrane integrity, cells were stained with 1 ug/ml propidium iodide (Sigma Aldrich Co., St. Louis, MO, USA) and visualized using TRITC 542 nm filter. Nuclear morphology and chromatin condensation were analyzed using Hoechst 33342 nuclear staining (ENZO, Lausen, Switzerland) and visualized using DAPI 461 nm filter. Cells were cultivated in Flow chambers µ-Slide I Lauer Family (Ibidi, Martinsried, Germany). To maintain standard cultivation conditions (37 °C, humidified air (60%) with 5% CO_2) during time-lapse experiments, cells were placed in the gas chamber H201 - for Mad City Labs Z100/Z500 piezo Z-stages (Okolab, Ottaviano NA, Italy). To image enough cells in one field of view, Nikon Plan 10/0.30 was chosen. For each of three cell lines and each of three treatments, seven fields of view were observed with the frame rate 3 mins/frame for 24 or 48 h respectively.

Holograms were captured by CCD camera (XIMEA MR4021 MC-VELETA), fluorescence images were captured using ANDOR Zyla 5.5 sCMOS camera. Complete quantitative phase image reconstruction and image processing were performed in Q-PHASE control software. Cell dry mass values were derived according to[19] and[20] from the phase (Eq. (1)), where m is cell dry mass density (in pg/µm^2), φ is detected phase (in rad), λ is wavelength in µm (0.65 µm in Q-PHASE), and α is specific refraction increment (≈0.18 µm^3/pg). All values in the formula except the φ are constant. The value of φ (Phase) is measured directly by the microscope.

$$m = \frac{\varphi\lambda}{2\pi\alpha} \quad (1)$$

Integrated phase shift through a cell is proportional to its dry mass, which enables studying changes in cell mass distribution[20].

Cell dry mass tracking. The custom method for automatic cell tracking and measuring of selected features was developed and implemented in MATLAB. Although tracking is not the main contribution of this article, it is a necessary step for our analysis and there is no available method suitable for QPI. The proposed tracking method consists of two main steps - nuclei tracking followed by expansion of each nucleus region to the whole cell.

Nuclei tracking is done by Gaussian Mixture Model (GMM) fitting to nuclei image (Hoechst 33342) in each frame by Expectation-Maximization (EM) algorithm (a similar method is used for segmentation in[21]). For each frame, Gaussians are provided from the previous frame and their parameters are updated by several steps of EM. Before the application of GMM, background pixels are eliminated by segmentation using Maximally Stable Extremal Region (MSER)[22]. Gaussians parameters are optimized for each nuclei cluster separately. In the first frame, positions of Gaussians are initialized manually and the covariance matrices are initialized as an identity matrix. The whole algorithm is summarized in Fig. 2 and for more details see[23]. This method does not recognise division of cells. For the next analysis, we use only cells, which occur in the whole image sequence without division or joining with other cell (which appears mainly due to tracking and segmentation errors).

The previous step provides tracked nuclei, but for extraction of most of the cell features, we need cell segmentation. However, nuclei can be used as seeds for segmentation in each frame. We can use simple thresholding for segmentation of foreground in QPI cell image, where the threshold value can be the same in all frames, which provides sufficient results for a distinction between foreground and background, but a separation of single cells is very problematic. We use tracked nuclei as seeds for proper division of the foreground binary mask F_t (obtained by tresholding) to the single cells binary mask S_t. Seeded watershed[24] is used on the negative of the original image O_t with nuclei tracking result as seedpoints. Watershed results (boundary lines) are then used for division of the foreground mask.

However, the simple application of the watershed algorithm leads to a fast mass exchange between cells due to segmentation errors, which is very undesirable for precise feature extraction. For this reason, we introduced a simple modification named Movement Regularized Watershed (MRW), in order not to allow dramatic contour

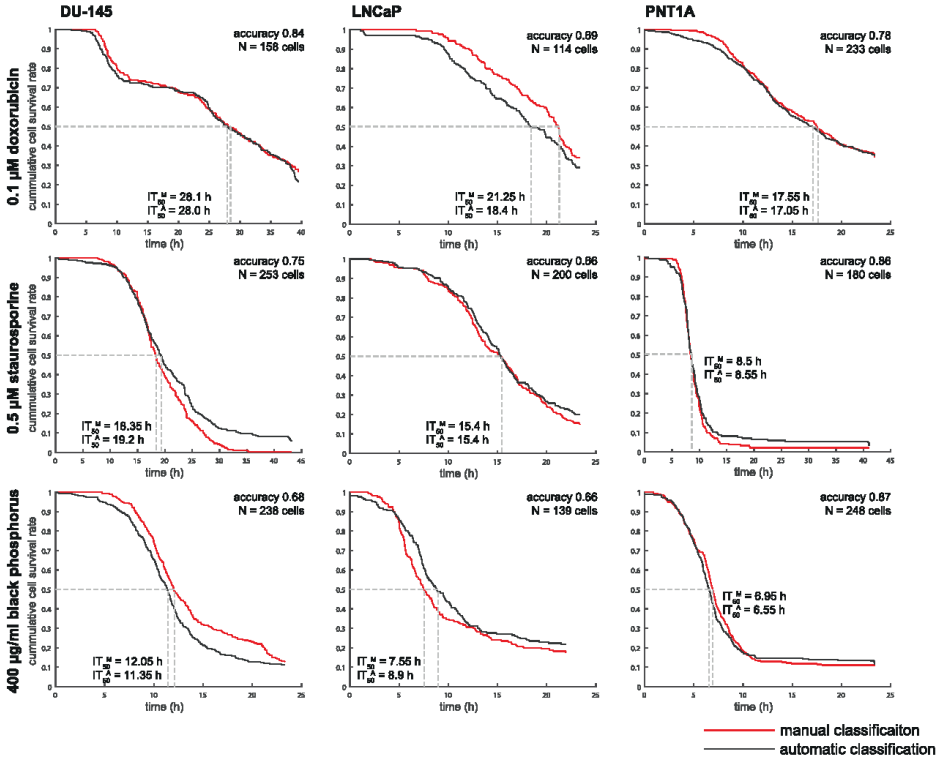

Figure 5. Comparison of manual and automatic cell death timepoint prediction, cumulative survival rate of cells exposed to cell death inducers. $ITA_{50}{}^{M}$, inhibition time for 50% of cell population, manually annotated; $ITA_{50}{}^{A}$, inhibition time for 50% of cell population, automatically annotated. Cross-validation is used for accuracy calculation and construction of automatic cell survival rates.

changes between frames. This can be achieved by incorporating the mask from the previous frame to the actual frame watershed calculation. This can be done by modifying O_t and F_t as

$$O_t^*(x, y) = \begin{cases} O_t(x, y), & \hat{S}_{t-1}(x, y) = 0 \\ -\infty, & otherwise \end{cases}$$

$$F_t^*(x, y) = \begin{cases} F_t(x, y), & \hat{F}_{t-1}(x, y) = 1 \\ 0, & otherwise \end{cases}$$

where $\hat{S}_{t-1}(x, y)$ and $\hat{F}_{t-1}(x, y)$ are an eroded versions of single cell segmentation and dilated version of foreground segmentation from the previous frame, respectively. Modified $O_t^*(x, y)$ and $F_t^*(x, y)$ are used in the seeded watershed algorithm. Modification of $O_t^*(x, y)$ forbid high area exchange between cells in consecutive frames and modification of $F_t^*(x, y)$ forbid high contour movement into the background between frames. Maximal possible contour movement than can be set by the amount of erosion and dilatation.

Manual dataset annotation. For each cell line and each treatment, seven FOVs were processed by the tracking method and only complete tracklets were kept for manual annotation. Overall, 819 PNT1A, 755 DU-145, and 581 LNCaP cells with annotated cell death were analysed. Timepoints of cell death and apoptotic or lytic cell death morphotype were manually annotated by a skilled professional (JB). Following parameters were considered: Casp 3,7 signal, PI signal, nuclear morphology, plasma membrane rupture and blebbing, surface detachment and cell rounding. A total number of 230, 196 and 220 apoptotic morphotypes for DU-145, LNCaP and PNT1A, respectively, was detected. A total number of 421, 237 and 441 lytic cell death morphotypes for DU-145, LNCaP and PNT1A, respectively, was detected. Remaining cells survived the treatment.

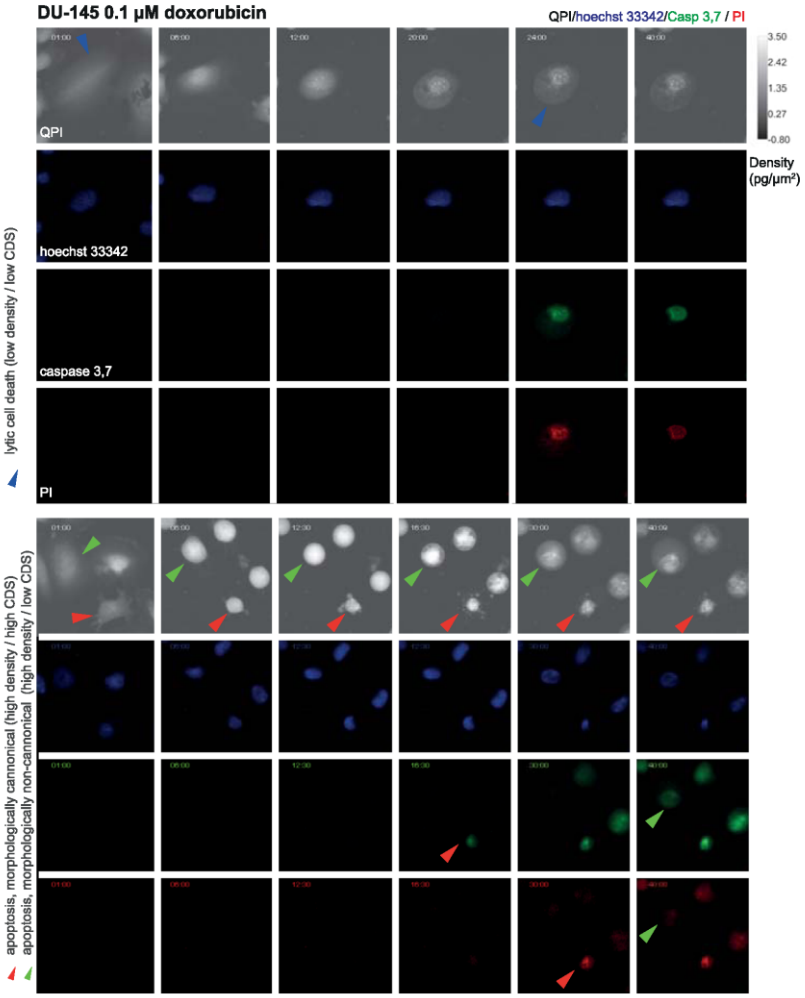

Figure 6. Characteristic quantitative phase and fluorescence images of lytic and apoptotic cell death. Data correspond to time signals shown in Fig. 3. Blue arrows indicate particular cell dying by lytic cell death and membrane rupture, red (canonical apoptosis) and green (noncanonical apoptosis) arrows indicate particular apoptotic cells and their fluorescence onset of Casp 3,7 and PI signal: Apoptotic cells display a delay in PI signal onset compared to casp 3,7. 10x magnification. FOV size approx. 107 µm. CDS, cell dynamic score; QPI, quantitative phase image; PI, propidium iodide.

Feature extraction. For further analysis, we extracted several cell features including cell mass, area, mass density (average pixel brightness), cell speed (centroid movement), circularity, eccentricity and maximum of the histogram, the position of maxima of histogram and entropy of histogram. Besides the classical cell features, we introduce tailored feature Cell Dynamic Score (CDS). CDS is a mean Euclidian distance between cell pixels in the actual and the following frame computed as

$$CDS = \frac{1}{|M_n|}\sqrt{\sum_{\mathbf{x}\in M_n}(I_{n-1}(\mathbf{x}) - I_n(\mathbf{x}))^2}$$

where M_n is a set of poisitons defined by the cell segmentation mask in the n-th frame and I_n is the n-th frame of QPI. CDS provides information about the speed of change of the cell pixel values due to both movement and

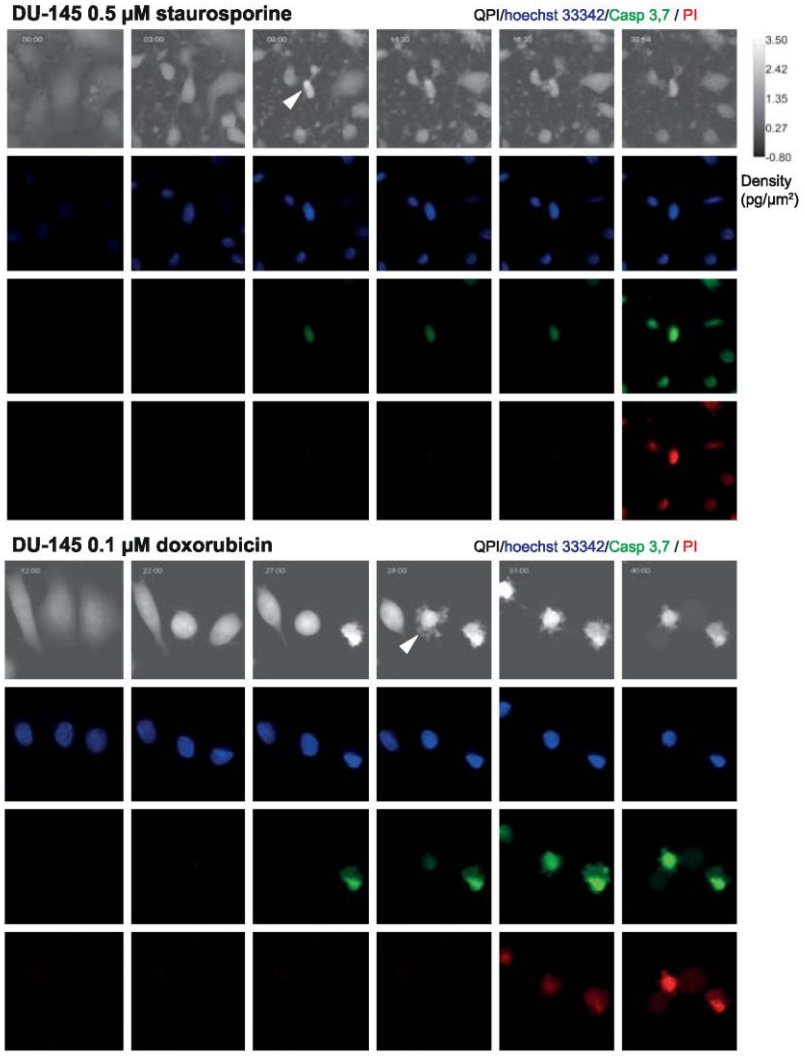

Figure 7. Morphological differences of staurosporine- and doxorubicin-induced apoptosis. White arrows indicate persisting attachment of staurosporine-treated cells and surface detachment of doxorubicin-treated ones in QPI. 10x magnification. FOV size approx. 107 µm. QPI, quantitative phase image; PI, propidium iodide.

morphological changes, but it is not much dependent on the segmentation quality, because the same mask is used in both frames. All these features were evaluated in all frames, where the result is a set of signals describing the cell behaviour in time.

Label-free algorithm for cell death detection. Besides the significant mass decrease of dead cells, various feature evolvement types were observed during detected cell deaths, which complicate the expert specification of the detected phenomenon, thus machine learning approach was chosen for this task. Bidirectional Long Short-term Memory (BiLSTM) networks[25] have shown to be very successful for signal classification and regression tasks, thus it is suitable for the purpose of detection of cell death in analysed cell signals. Manual annotation of cell death timepoint is converted to a signal with a Gaussian curve at a death timepoint. The proposed approach is inspired by the detection of correlation filters[26], where the aim is to regress the Gaussian curve on the desired

position, where Gaussian represents uncertainty in position. Long-short term memory (LSTM) network has been trained for the regression of Gaussian curves created on the time of cell death (with sigma 50), where the whole method is summarized in Fig. 1.

According to[27], the network was set to two BiLSTM layers (with 100 units) and 3 fully connected layers (with 100, 50 and 100 neurons) with ReLu and dropout with probability 0.5. The whole network was optimized using Mean Square Error loss and ADAM optimizer[28] with learning rate 10^{-3}, $\beta_{1=}0.9$, $\beta_{2=}0.999$, gradient clipping to norm 1[29], weight decay 10^{-3}, batch size 256 and 40 epochs. We augment our training dataset with random clipping (shortening each signal by at most 1/3 of length). One network was trained for all 9 cell lines/experiments evaluated by cross-validation, where one FOV from all experiments was used for testing and the rest for training. Cell death time was identified as a maximum in the network response with a value higher than the chosen threshold 0.4. Quality of cell detection is evaluated in terms of accuracy, where detection is considered as correct if it detects a death in a ±5 h (±100 frames) window from ground truth cell death or if death is not detected and the cell is labelled as alive (at the end of the experiment).

Cell death type identification. We observed two distinct dynamical patterns of cell mass manipulation during cellular death, where each cell was manually labelled as one of these types. To quantify these morphological types we extracted average values of extracted features in 200 frames (10 h) before cell death (shorter time window is used if more timepoints are not available). We trained linear Support Vector Machine (SVM) classifier for automatic classification of these cell death types. SVM classifier was trained for each cell line (one for all three treatments) because cell lines are morphologically different. All possible subsets of features were tested and classification accuracy was evaluated. Only density and CDS were finally used because accuracy does not increase significantly with the addition of other features (accuracy 75.4% and 76.2% for two and three features, respectively), where two features can be comprehensibly visualized. These two features have also a distinct biological meaning and its difference in an average aligned signal can be confirmed in Fig. 1.

Furthermore, the correctness of the classification was confirmed by the analysis of nucleus shrinkage and by Casp 3,7–PI signal onset delay in fluorescence data. Nucleus shrinkage was measured as an average Hoechst 33342 brightness in 200 frames (10 h) before cell death (based on nuclei mask produced by GMM tracking). Casp 3,7–PI signal onset delay was measured as a time difference (delay) between the time when Casp 3,7 signals reach 1/3 of its average value after cell death (average in widnow of 200 frames) and the cell death time (which corresponds to a steep PI signal increase). The output of this analysis is shown in Fig. 3d,e.

Results

Automatic cell death detection. After induction of cell death by using 0.5 µM staurosporine, 0.1 µM doxorubicin, or 400 µg/mL of BP, respectively, 11 morphological parameters detectable by QPI (see Fig. 1) and their real-time values were collected. Effector caspase 3/7 activity, nuclear morphology and membrane integrity (propidium iodide signal; PI) were verified using time-lapse fluorescent microscopy to estimate ground truth for cell death detection based on cell mass parameters. The decrease in cell dry mass (pg), cell density (pg/pixel), and the Cell Dynamic Score (CDS; see the methodological part for equation) measured by QPI was in clear relationship with the onset of propidium iodide and caspase signalling. Furthermore, dead cells showed no longer any significant changes in CDS. (see Fig. 4). Based on QPI features, automatic and label-free detection of IT_{50} (time of half-maximal inhibition effect for given treatment concentration) can be performed (see Fig. 5). Its evaluation is based on automatic cell detection of cell death using the LSTM network, where we can easily accumulate the number of dead cells assuming that all cells are alive at the start of the image sequence. This parameter is important because IC_{50} values can be significantly different in different time points (such as 24 h versus 48 h treatment[30]). For IT_{50} of tested compounds and cell lines see Fig. 5. Automatic detection of cell death showed 76% accuracy compared to the manual detection of cell death based on the fluorescent PI signal and morphological criteria visible to the naked eye.

Cell density and cell dynamic score reflect subroutine of cell death. Based on QPI data, we were able to distinguish two different subroutines of cell death: a) cells having high cell density and intensive blebbing of the plasma membrane (high CDS) followed by plasma membrane rupture and b) cells having low cell density and low CDS before plasma membrane rupture (see Fig. 6 and Supplementary Videos 1–2). These variants occupied extreme positions on the CDS versus cell density plot (see Fig. 3b and Supplementary Fig. 1). Time-lapse images and QPI features of these cells are shown in Fig. 3a and Supplementary Figs. 3 and 8. Based on fluorescent data referring caspase 3, 7 activity, nuclear morphology and membrane integrity (PI signal); see Fig. 6 and Supplementary Figs. 2–12, the a) type of cell death with high CDS and high cell density is *bona fide* apoptosis because PI signal was delayed over caspase signals and shrinkage of the nucleus was apparent (Fig. 3e). Moreover, cells with high CDS and high cell density were only rarely presented in z-VAD-FMK treated population, see Fig. 3c; Z-VAD-FMK is a cell-permeable pan-caspase inhibitor that irreversibly binds to the catalytic site of caspase proteases and inhibits apoptosis. On the other hand, the b) type of cell death is *bona fide* lytic cell death as PI and caspase signals were displayed simultaneously and no significant shrinkage of the nucleus was apparent. Cells near the dividing line showed a)-like and b)-like features to varying degrees. Casp 3,7–PI signal onset delay and nucleus shrinkage (described in Methods) were quantified for both automatic and manual labels of cell death types (see Fig. 3d and Supplementary Table 1), which confirmed the existence of these two cell death subroutines. Furthermore, apoptosis and lytic cell death were visually detected by the expert according to the fluorescent signals and eye-visible cell morphology. The automatic label-free distinction of cell death subroutine showed 75.4% accuracy (average of all cells and treatments) compared manual distinction of cell death type based on fluorescent signals and eye-visible morphological criteria; (see Fig. 3f). Interestingly, no cells showed a gradual cell rounding

and loss of surface contact during staurosporine treatment. Other treatments caused such phenomena relatively often. For illustration see Fig. 7.

Discussion

The basic requirement for a good method of cell death detection is the ability to detect a robust parameter in a highly reproducible and if possible inexpensive manner under changing conditions caused by the cell heterogeneity. In this study, we suggest that morphological and dynamical features extracted from the QPI cell image are suitable for cell death detection. QPI enables the time-lapse observation of subtle changes in the cell mass distribution unrecognizable by the naked eye, and therefore provides detailed information on cell morphology and cell mass topography during cell death. Cell dry mass can be calculated directly from phase values detected in each pixel[31–33]. Cell dry mass is the direct result of biosynthetic and degradative processes within a cell and is, therefore, a promising indicator of cell fate including cell death[34,35]. The distribution of cell mass during the processes of cell death is significantly changing in time with a typical steep decrease of the cell mass due to the rupture of the plasma membrane or cell fragmentation. This phenomenon *is bona fide* universal for all cell types and was also observed in target cells after contact with a cytotoxic T-cells[34]. Plasma membrane rupture can be otherwise measured by quantification of the release of intracellular enzymes from the cell into the cell culture medium. Nevertheless, the enzymatic activity of these enzymes can be seriously affected by differences in the pH between intracellular environment and culture medium and by time spent in the extracellular space[3].

Based on QPI data, we were also able to distinguish two specific subroutines of cell death (Fig. 3a–e). While the cell death subroutine a) (*bona fide* apoptosis) showed a high cell density and strong fluctuation in CDS before cell death; during the subroutine b) (*bona fide* lytic cell death) the cell density was low and CDS was relatively stable after the initial decline. These variants occupied extreme positions on the CDS versus cell density plot. Cells near the dividing line (see Fig. 3b) probably succumb to another subroutine of cell death such as pyroptosis or necroptosis, as neither staurosporine nor doxorubicin is a specific apoptosis inductor[36,37]. The a) type of cell death was characteristic by a decrease in the cell area, a gradual cell rounding and a loss of surface contact (this phenomenon was not observed in the case of staurosporine treatment) followed by membrane blebbing (known as "dance of death"); see Fig. 3 and Supplementary Fig. 2 to 12[38]. Since membrane blebbing during apoptosis results from caspase-mediated activation of ROCK I, it can be assumed that apoptosis was involved in these cases[39]. At the final stages of apoptosis, the actin cytoskeleton is degraded[40,41]. Due to the hydrophobic nature of the apoptotic bodies, they undergo the plasma membrane fusion in the culture medium. The membrane of this post-apoptotic body subsequently cracks and culminates in secondary necrosis (in our case depicted by a steep decrease of cell mass) in the absence of phagocytes[42,43]. The b) type of observed cell death presented persisting large cytoplasmic membrane blebs or multiple small blebs and cell swelling leading to the final cell membrane rupture. This type of dying cells was adherent during the whole process. It can be assumed that lytic cell death was involved in these cases[3]. Although several studies based on QPI detection of cell death have been published earlier, they do not include the distinguishing of specific subroutines of cell death and have failed to capture the entire process of cell death, including the early stages due to short intervals of QPI capturing[44–46]. From an image analysis point of view, we introduce a new powerful technique for cell tracking and segmentation, capable of robustly track cell thought the whole image sequence. We also introduced a completely new method for the detection of cell death in time-series of measured cell features using LSTM neural network. To the best of our knowledge, this is also the first study introducing CDS and cell density as a parameter typical for individual cell death subroutines.

Data availability

The Matlab code is available at GitHub (https://github.com/tomasvicar/CellDeathDetect). Annotated quantitative phase image dataset (with cell tracking masks and labels of cell death timepoints and types of death) used in the manuscript is available at Zenodo repository (www.zenodo.org), https://doi.org/10.5281/zenodo.2601562.

Received: 11 October 2019; Accepted: 15 January 2020;
Published online: 31 January 2020

References

1. Galluzzi, L. *et al.* Molecular mechanisms of cell death: recommendations of the Nomenclature Committee on Cell Death 2018. *Cell Death Differ.* **25**, 486–541 (2018).
2. Kroemer, G. *et al.* Classification of cell death: recommendations of the Nomenclature Committee on Cell Death 2009. *Cell Death Differ.* **16**, 3–11 (2009).
3. Galluzzi, L. *et al.* Guidelines for the use and interpretation of assays for monitoring cell death in higher eukaryotes. *Cell Death Differ.* **16**, 1093–1107 (2009).
4. Kepp, O., Galluzzi, L., Lipinski, M., Yuan, J. Y. & Kroemer, G. Cell death assays for drug discovery. *Nat. Rev. Drug. Discovery* **10**, 221–237 (2011).
5. Balvan, J. *et al.* Multimodal holographic microscopy: distinction between apoptosis and oncosis. *PLoS One* **10**, e0121674 (2015).
6. Palchaudhuri, R. *et al.* A Small Molecule that Induces Intrinsic Pathway Apoptosis with Unparalleled Speed. *Cell Rep.* **13**, 2027–2036 (2015).
7. Yang, F., Teves, S. S., Kemp, C. J. & Henikoff, S. Doxorubicin, DNA torsion, and chromatin dynamics. *Biochimica Et. Biophysica Acta-Reviews Cancer* **1845**, 84–89 (2014).
8. Fojtů, M. *et al.* Black Phosphorus Cytotoxicity Assessments Pitfalls: Advantages and Disadvantages of Metabolic and Morphological Assays. *Chem. – A Eur. J.* **25**, 349–360 (2019).
9. Ulman, V. *et al.* An objective comparison of cell-tracking algorithms. *Nat. Methods* **14**, 1141 (2017).
10. Tinevez, J.-Y. *et al.* TrackMate: An open and extensible platform for single-particle tracking. *Methods* **115**, 80–90 (2017).
11. Huh, S. & Kanade, T. Apoptosis detection for non-adherent cells in time-lapse phase contrast microscopy. *Med. Image Comput. Comput Assist. Interv.* **16**, 59–66 (2013).

12. Manivannan S. *et al.* HEp-2 Cell Classification Using Multi-resolution Local Patterns and Ensemble SVMs. In: 2014 1st *Workshop on Pattern Recognition Techniques for Indirect Immunofluorescence Images* (ed^(eds) (2014).
13. Bs, D. & Subramaniam, K. H. R. N. *HEp-2 cell classification using artificial neural network approach* (2016).
14. Li, H. *Deep CNNs for HEp-2 Cells Classification: A Cross-specimen Analysis* (2016).
15. Skjoth, I. H. & Issinger, O. G. Profiling of signaling molecules in four different human prostate carcinoma cell lines before and after induction of apoptosis. *Int. J. Oncol.* **28**, 217–229 (2006).
16. Mitchell, S., Abel, P., Ware, M., Stamp, G. & Lalani, E. Phenotypic and genotypic characterization of commonly used human prostatic cell lines. *BJU Int.* **85**, 932–944 (2000).
17. Raudenska, M. *et al.* Cisplatin enhances cell stiffness and decreases invasiveness rate in prostate cancer cells by actin accumulation. *Sci. Rep.* **9**, 1660 (2019).
18. Chappell, W. H. *et al.* p53 expression controls prostate cancer sensitivity to chemotherapy and the MDM2 inhibitor Nutlin-3. *Cell cycle* **11**, 4579–4588 (2012).
19. Prescher, J. A. & Bertozzi, C. R. Chemistry in living systems. *Nat. Chem. Biol.* **1**, 13–21 (2005).
20. Park, Y., Depeursinge, C. & Popescu, G. Quantitative phase imaging in biomedicine. *Nat. Photonics* **12**, 578–589 (2018).
21. Jung, C., Kim, C., Chae, S. W. & Oh, S. Unsupervised Segmentation of Overlapped Nuclei Using Bayesian Classification. *IEEE Trans. Biomed. Eng.* **57**, 2825–2832 (2010).
22. Nistér D, Stewénius H. *Linear Time Maximally Stable Extremal Regions* (2008).
23. Vicar, T. Robust Cell Nuclei Tracking Using Gaussian Mixture Shape Model. In: *24th Conference STUDENT EEICT 2018* (ed^(eds). Brno University of Technology, Faculty of Electrical Engineering and Communication (2018).
24. Pinidiyaarachchi, A. & Wählby, C. Seeded watersheds for combined segmentation and tracking of cells. In: *International Conference on Image Analysis and Processing* (ed^(eds). Springer (2005).
25. Graves, A., Mohamed, A. & Hinton, G. Speech recognition with deep recurrent neural networks. In: *2013 IEEE International Conference on Acoustics, Speech and Signal Processing* (ed^(eds) (2013).
26. Henriques, J. F., Caseiro, R., Martins, P. & Batista, J. High-Speed Tracking with Kernelized Correlation Filters. *IEEE Trans. Pattern Anal. Mach. Intell.* **37**, 583–596 (2015).
27. Reimers, N. & Gurevych, I. Optimal hyperparameters for deep lstm-networks for sequence labeling tasks. *arXiv preprint arXiv:170706799* (2017).
28. Kingma, D. P. & Ba, J. Adam: A method for stochastic optimization. *arXiv preprint arXiv:14126980* (2014).
29. Pascanu, R., Mikolov, T. & Bengio, Y. On the difficulty of training recurrent neural networks. In: *International conference on machine learning* (ed^(eds) (2013).
30. Gumulec, J. *et al.* Cisplatin-resistant prostate cancer model: Differences in antioxidant system, apoptosis and cell cycle. *Int. J. Oncol.* **44**, 923–933 (2014).
31. Slabý, T. *et al.* Coherence-controlled holographic microscopy for live-cell quantitative phase imaging. (ed^(eds) (2015).
32. Chmelik, R. *et al.* Chapter 5 - The Role of Coherence in Image Formation in Holographic Microscopy. In: Progress in Optics (ed^(eds Emil W). Elsevier (2014).
33. Kolman, P. & Chmelik, R. Coherence-controlled holographic microscope. *Opt. Express* **18**, 21990–22003 (2010).
34. Zangle, T. A., Burnes, D., Mathis, C., Witte, O. N. & Teitell, M. A. Quantifying biomass changes of single CD8+ T cells during antigen specific cytotoxicity. *PLoS One* **8**, e68916 (2013).
35. Popescu, G. *et al.* Optical imaging of cell mass and growth dynamics. *Am. J. Physiol.-Cell Physiology* **295**, C538–C544 (2008).
36. Simenc, J. & Lipnik-Stangelj, M. Staurosporine induces different cell death forms in cultured rat astrocytes. *Radiology Oncol.* **46**, 312–320 (2012).
37. Sugimoto, K., Tamayose, K., Sasaki, M., Hayashi, K. & Oshimi, K. Low-dose doxorubicin-induced necrosis in Jurkat cells and its acceleration and conversion to apoptosis by antioxidants. *Br. J. Haematol.* **118**, 229–238 (2002).
38. Galluzzi, L. *et al.* Molecular definitions of cell death subroutines: recommendations of the Nomenclature Committee on Cell Death 2012. *Cell Death Differ.* **19**, 107–120 (2012).
39. Coleman, M. L. *et al.* Membrane blebbing during apoptosis results from caspase-mediated activation of ROCK I. *Nat. Cell Biol.* **3**, 339–345 (2001).
40. Coleman, M. L. & Olson, M. F. Rho GTPase signalling pathways in the morphological changes associated with apoptosis. *Cell Death Differ.* **9**, 493–504 (2002).
41. Desouza, M., Gunning, P. W. & Stehn, J. R. The actin cytoskeleton as a sensor and mediator of apoptosis. *Bioarchitecture* **2**, 75–87 (2012).
42. Silva, M. T. Secondary necrosis: the natural outcome of the complete apoptotic program. *FEBS Lett.* **584**, 4491–4499 (2010).
43. Hanahan, D. & Weinberg, R. A. Hallmarks of Cancer: The Next Generation. *Cell* **144**, 646–674 (2011).
44. Pavillon N, *et al.* Early Cell Death Detection with Digital Holographic Microscopy. *PLoS One* 7 (2012).
45. Khmaladze, A. *et al.* Cell volume changes during apoptosis monitored in real time using digital holographic microscopy. *J. Struct. Biol.* **178**, 270–278 (2012).
46. Pavillon, N. *et al.* Cell morphology and intracellular ionic homeostasis explored with a multimodal approach combining epifluorescence and digital holographic microscopy. *J. Biophotonics* **3**, 432–436 (2010).

Acknowledgements

This work was supported by funds from the Faculty of Medicine, Masaryk University to Junior researcher (Jan Balvan), and by Grant Agency of the Czech Republic (18–24089 S). Black phosphorus was kindly provided by Dr. Martin Pumera and Dr. Zdenek Sofer from University of Chemistry and Technology Prague, Czech republic. We acknowledge Dr. Michaela Fojtu for her kind assistance with black phosphorus preparation and Telight, a.s. for support to Telight Q-PHASE technology.

Author contributions

Tomas Vicar: image analysis, data interpretation, manuscript preparation; Martina Raudenska: wrote the manuscript, study design; Jaromir Gumulec: interpretation of results, manuscript preparation; Michal Masarik: study design, study concepts; Jan Balvan: study design, microscope operation, interpretation of results, writing the manuscript.

Competing interests

The authors declare no competing interests.

Additional information

Supplementary information is available for this paper at https://doi.org/10.1038/s41598-020-58474-w.

Correspondence and requests for materials should be addressed to J.B.

Reprints and permissions information is available at www.nature.com/reprints.

Publisher's note Springer Nature remains neutral with regard to jurisdictional claims in published maps and institutional affiliations.

Open Access This article is licensed under a Creative Commons Attribution 4.0 International License, which permits use, sharing, adaptation, distribution and reproduction in any medium or format, as long as you give appropriate credit to the original author(s) and the source, provide a link to the Creative Commons license, and indicate if changes were made. The images or other third party material in this article are included in the article's Creative Commons license, unless indicated otherwise in a credit line to the material. If material is not included in the article's Creative Commons license and your intended use is not permitted by statutory regulation or exceeds the permitted use, you will need to obtain permission directly from the copyright holder. To view a copy of this license, visit http://creativecommons.org/licenses/by/4.0/.

© The Author(s) 2020

PLOS ONE

RESEARCH ARTICLE

Multimodal Holographic Microscopy: Distinction between Apoptosis and Oncosis

Jan Balvan[1,2], Aneta Krizova[2,3], Jaromir Gumulec[1,2], Martina Raudenska[1,2], Zbysek Sladek[4], Miroslava Sedlackova[5], Petr Babula[6], Marketa Sztalmachova[1,2], Rene Kizek[2,7], Radim Chmelik[2,8], Michal Masarik[1,2]*

1 Department of Pathological Physiology, Faculty of Medicine, Masaryk University, Brno, Czech Republic, **2** Central European Institute of Technology, Brno University of Technology, Brno, Czech Republic, **3** TESCAN Brno, s.r.o., Brno, Czech Republic, **4** Department of Morphology, Physiology, and Animal Genetics, Mendel University in Brno, Brno, Czech Republic, **5** Department of Histology and Embryology, Faculty of Medicine, Masaryk University, Brno, Czech Republic, **6** Department of Physiology, Faculty of Medicine, Masaryk University, Brno, Czech Republic, **7** Department of Chemistry and Biochemistry, Mendel University in Brno, Brno, Czech Republic, **8** Institute of Physical Engineering, Faculty of Mechanical Engineering, Brno University of Technology, Brno, Czech Republic

* masarik@med.muni.cz

CrossMark
click for updates

OPEN ACCESS

Citation: Balvan J, Krizova A, Gumulec J, Raudenska M, Sladek Z, Sedlackova M, et al. (2015) Multimodal Holographic Microscopy: Distinction between Apoptosis and Oncosis. PLoS ONE 10(3): e0121674. doi:10.1371/journal.pone.0121674

Academic Editor: Robert M. Hoffman, AntiCancer Inc., UNITED STATES

Received: October 3, 2014

Accepted: February 3, 2015

Published: March 24, 2015

Copyright: © 2015 Balvan et al. This is an open access article distributed under the terms of the Creative Commons Attribution License, which permits unrestricted use, distribution, and reproduction in any medium, provided the original author and source are credited.

Data Availability Statement: All relevant data are within the paper.

Funding: The financial support from CEITEC CZ.1.05/1.1.00/02.0068 and project for conceptual development of research organization (Faculty of Medicine, Masaryk university - ROZV/24/LF5/2014) is greatly acknowledged. Part of the work was carried out with the support of core facilities of CEITEC – Central European Institute of Technology under CEITEC-open access project, ID number LM2011020, funded by the Ministry of Education, Youth and Sports of the Czech Republic under the activity "Projects of major infrastructures for research,

Abstract

Identification of specific cell death is of a great value for many scientists. Predominant types of cell death can be detected by flow-cytometry (FCM). Nevertheless, the absence of cellular morphology analysis leads to the misclassification of cell death type due to underestimated oncosis. However, the definition of the oncosis is important because of its potential reversibility. Therefore, FCM analysis of cell death using annexin V/propidium iodide assay was compared with holographic microscopy coupled with fluorescence detection - "Multimodal holographic microscopy (MHM)". The aim was to highlight FCM limitations and to point out MHM advantages. It was shown that the annexin V+/PI– phenotype is not specific of early apoptotic cells, as previously believed, and that morphological criteria have to be necessarily combined with annexin V/PI for the cell death type to be ascertained precisely. MHM makes it possible to distinguish oncosis clearly from apoptosis and to stratify the progression of oncosis.

Introduction

Cell necrobiology is a rapidly developing field of cell biology that defines various modes of cell death pursuant to biochemical, morphological, and molecular changes accompanying distinct types of cell death including the tissue response [1].

Identification of the exact type of cell death following the cell injury is important for diagnostics, dose-response, and toxicological studies. It is extremely important to assess and interpret correctly the cellular response to severe injury including changes that occur before and after the cell death, because cell death changes could be the earliest signal of toxic reactions to a variety of drugs including the anticancer treatment. Cells can die through a number of different mechanisms *inter alia* by apoptosis, autophagy, necrosis, or oncosis. Nevertheless, two major

development and innovations". The funders had no role in study design, data collection and analysis, decision to publish, or preparation of the manuscript.

Competing Interests: The cooperation with commercial company (TESCAN) does not alter the authors' adherence to PLOS ONE policies on sharing data and materials.

types of cell death are accidental cell death and programmed cell death. When assessing the major effect of a particular therapeutic drug, it is essential to know which type of cell death is involved most in the drug response. If the main mechanism involved in the cell death is oncosis followed by necrosis, the cells lose membrane integrity and release their intracellular contents, which are often aggressive, proinflammatory, and cause damage to the surrounding tissue [2]. By contrast, apoptotic cells may not promote inflammation because they are usually ingested by phagocytes before releasing their intracellular contents [3]. An important biochemical event leading to oncosis /necrosis, as opposed to apoptosis, is a rapid decrease of intracellular ATP [4, 5]. The assessment of oncosis is frequently neglected, although it is an important pre-lethal phase that follows a serious cell injury and, unlike in necrosis, some mechanisms possibly exist for reversing the process [5].

Many changes typical for these two main types of cell death (accidental and programmed cell death) are detectable by flow-cytometry. Nevertheless, relying solely on the flow-cytometry could lead to the misclassification of the cell death type since—similarly as apoptotic cells—oncotic cells could exhibit external *phosphatidylserine* residues (PS) while maintaining membrane integrity. As a result, oncotic cells could display the annexin V+/PI− phenotype, formerly supposed to be specific of apoptotic cells [6, 7]. Similarly, the TUNEL assay is also known to be non-specific for apoptosis/oncosis differentiation [8–10]. Consequently, morphological criteria are considered the most reliable evidence of apoptosis [11, 12]. Characteristics of apoptosis, oncosis, and necrosis are summarized in Table 1.

In this paper, we present a methodology that can be used for the rapid assessment of cell viability and distinction of oncosis and apoptosis utilizing multimodal holographic microscope (MHM). MHM combines holographic microscopy with the well-known fluorescence microscopy. The employed holographic microscopy (HM) is based on an off-axis setup with an incoherent source. In contrast with the HM laser source, the incoherent HM source enables high-quality quantitative phase imaging free of speckles and parasitic interferences, comparable with the lateral resolution of conventional wide-field microscopes. Owing to the off-axis setup, only

Table 1. Characteristic features of apoptosis, oncosis, and necrosis.

Feature	Oncosis	Necrosis	Apoptosis
Cell size	increased (swelling)*	increased (swelling)*	reduced (shrinkage)*
Plasma membrane	intact* in the early phase; increased throughput depending on the phase of oncosis	disrupted*	intact*; altered orientation of lipids
Nucleus	Nucleus dilatation* and clumping of chromatine* reticular nucleolus	karyolysis* and caspase independent DNA fragmentation,lysis of nucleolus	nuclear chromatin condensation*; fragmentation of DNA into nucleosome size fragments, irregularity of nucleus*
Specific features	swelling of organelles; membrane blebs*	increasingly translucent cytoplasm*; swelling of ER and loss of ribosomes; swollen mitochondria with amorphous densities; lysosome rupture; plasma membrane rupture*; myelin figures	apoptotic bodies*; pseudopod retraction*; spherical shape of cells*
Energy balance	ATP depletion	ATP depletion	retained ATP production
PI/annexin V assay	annexin V+/ PI−*; annexin V+/PI+*	annexin V+/PI+*	annexin V+/ PI−*
Adjacent inflammation	frequent	frequent	rare

* indicates typical features of distinct cell death, easy observable by using MHM. ER—endoplasmatic reticulum; ATP—adenosine triphosphate; PI—propidium iodide. According to our results and [4, 5, 43].

doi:10.1371/journal.pone.0121674.t001

Table 2. Classification of holographic methods.

Method	Optical setup	Illumination source	Properties
Phase-shifting microscopes	In-line (zero angle between object and reference beam)	Low-coherence (halogen lamp, LED)	+ suppressed coherence noise
			+ coherence-gating effect
			+ lateral resolution of conventional microscopes
			– slow: 3 images for reconstruction
Digital holographic microscopes	off-axis (non-zero angle between object and reference beam)	High-coherence (laser)	– coherence noise
			– lateral resolution 2x worse than in conventional microscopes
			+ fast: 1 image/reconstruction
Coherence-controlled holographic microscopes	off-axis	low-coherence	+ suppressed coherence noise
			+ coherence-gating effect
			+ lateral resolution of conventional microscopes
			+ fast: 1image/reconstruction

doi:10.1371/journal.pone.0121674.t002

one hologram is needed for image reconstruction and very fast processes can be observed [13]. General characteristics of different holographic methods are summarized in Table 2. Holographic microscopy is a method of quantitative phase imaging. Providing intrinsic high contrast, phase images allow an easy segmentation of cells from the image background and monitor morphological and position changes over the time [14]. Fluorescence imaging is combined with holographic microscopy in a way that the focus plane in both methods is at the same position. This allows an easy transition between the two methods, imaging in the same conditions and nearly at the same time points. This unique combination enables a label-free observation of processes such as morphological and position changes preceding the cell death and a follow-up fluorescence verification of cell death types in one field of view using a single instrument.

In this study, PC-3 prostatic cell lines treated with plumbagin in concentrations exceeding IC50 were chosen as a model because our laboratory has a long-term experience in studying this ROS-generating agent and in characterizing this cell line [15–17]. In sum, the aim of this study was to highlight limitations of the flow-cytometry analysis of cell death and to point out advantages of MHM imaging. The hypothesis is that MHM is capable of differentiating between apoptosis and oncosis more accurately than flow-cytometry. Thus, we demonstrate a new possible application of this innovative microscopic technique.

Materials and Methods

Chemical and biochemical reagents

Ham's F12 medium, mycoplasma-free foetal bovine serum (FBS), penicillin/streptomycine and trypsine were purchased from PAA Laboratories GmbH (Pasching, Austria). Phosphate-buffered saline (PBS) was purchased from Invitrogen Corp. (Carlsbad, CA, USA). Ethylenediaminetetraacetic acid (EDTA), plumbagin and other chemicals of ACS purity were purchased from Sigma-Aldrich Co. (St. Louis, MO, USA), unless noted otherwise.

Cell cultures

Human PC-3 prostate cancer cells were used in this study. The PC-3 cell line was established from the prostatic adenocarcinoma (Grade 4) of a 62-year-old Caucasian male and derived

from a metastatic site in the bones. The PC-3 cell line was purchased from HPA Culture Collections (Salisbury, UK).

Cultured cell conditions

The PC-3 cells were cultured in Ham's F12 medium with 7% FBS. The medium was supplemented with penicillin (100 U/ml) and the cells were kept at 37°C in the humidified incubator with 5% CO2.

Plumbagin treatment

The stock solution of plumbagin was prepared in dimethylsulfoxide (DMSO) and diluted with the medium. Controls were added an equal volume of DMSO (final concentration $\leq$ 0.1%). The plumbagin treatment was initialized after the cells reached ~50% confluence. Previously, IC50 for plumbagin was determined as 1.50 μM using MTT. Thus, a treatment with 2 μM of plumbagin was used in this experiment to ensure the initiation of cell death.

Multimodal holographic microscopy

The design of the Multimodal Holographic Microscope (IPE BUT, TESCAN, Brno, Czech Republic) is based on the original concept of the Coherence-Controlled Holographic Microscope [18, 19].

Holographic microscopy was initiated after 2 h of the plumbagin treatment. Time-lapse monitoring was performed for 2 h (in total 4 h of plumbagin treatment) at a frame-rate of 1 frame/min. The cells were observed in flow chambers μ-Slide I Luer Family cat. Num. 80196 (Ibidi, Martinsried, Germany) in Ham's F12 medium. Nikon Plan 10×/0.3 and Nikon Plan Fluor 20×/0.5 objectives were used for both holographic and fluorescence observations. Interferograms for holography were taken using a CCD camera (XIMEA MR4021MC-VELETA). The fluorescence mode used a plasma light source (Sutter Instrument Lambda XL) and a CCD camera (XIMEA MR285MC-BH, 1392×1040px) was used to capture the images.

Holographic and fluorescence images were collected by custom software. In fluorescence image there is no need for other image processing; however, holographic raw data have to be numerically reconstructed. The numerical reconstruction is performed by the custom software where the established methods of the fast Fourier-transform [20] and phase unwrapping [21, 22] are implemented. The output from the software is an unwrapped phase image. This image has intrinsic high contrast and can be processed by an available image processing software.

We used particularly the ImageJ functions of *Thresholding* and *Analysed Particles*. At chosen time points of the time-lapse observation, the cells were segmented from the background, a threshold value for the segmentation being 0.21 rad (0.05 pg/pixel). Each cell was controlled visually, and cells in contact were separated manually. Measurements of cell surface, cell dry mass and mean cell dry mass followed.

TEM visualization of ultrastructure. PC-3 cells were gently harvested by repetitive pipetting and spun down (2000 rpm, 5 min.). Briefly, the cells were fixed with 3% glutaraldehyde in a cacodylate buffer for 2 hours and washed three times for 30 minutes in 0.1 M cacodylate buffer. Then they were fixed with 0.02 M OsO4 dissolved in 0.1 M cacodylate buffer, dehydrated in alcohol, and infiltrated with acetone and No. 1 Durcuptan mixture overnight. On the following day, the cells were infiltrated with No. 2 Durcuptan mixture, embedded and polymerized. Ultrathin sections (90 nm, Ultramicrotome LKB, Bromma, Stockholm, Sweden) were transferred onto grids covered with a Formvar membrane (Marivac Ltd., Halifax, Canada). 2% uranyl acetate and Reynolds solution were used for contrast staining. The sections were viewed in the transmission electron microscope (Morgagni 268, FEI Europe B.V., Eindhoven

Netherlands). Software AnalySIS (Soft Imaging System, GmbH, Münster, Germany) was used for a picture analysis of the cell ultrastructure.

Annexin V/propidium iodide flow-cytometry

Double-staining with fluorescein isothiocyanate (FITC)/propidium iodide (PI) was performed using the annexin V-FLUOS-staining kit (Roche Applied Science) according to the manufacturer's protocol in order to determine percentages of viable, apoptotic, and necrotic cells following the exposure to plumbagin (2 uM). Briefly, the cells were harvested by repetitive pipetting and washed two times with PBS (centrifuged at 2000 rpm for 5 min). Then they were re-suspended in 100 μl of the annexin V-FLUOS labelling solution and incubated for 15 min. in the dark at 15–25°C. Annexin V-FITC binding was detected by flow cytometry (Partec GmbH, Münster, Germany) (Ex = 488 nm, Em = 533 nm, FL1 filter for annexin V-FLUOS and FL3 filter for PI). The data were analyzed using the FloMax software version 2.5 (Partec GmbH, Münster, Germany).

Results

Development of the multimodal holographic microscope

The employed multimodal holographic microscope was developed in cooperation between researchers from the Brno University of Technology and the TESCAN Brno Company. The MHM design (IPE BUT, TESCAN, Brno, Czech Republic) is based on the concept of the Coherence-Controlled Holographic Microscope (CCHM) described in [19]. This novel optical setup of CCHM overcomes drawbacks of the previous concept [18], while preserving all benefits and enabling multimodal imaging.

The holographic mode setup is shown in Fig. 1. It is based on the Mach-Zehnder-type interferometer. The light from the source (S) passes through the collector lens (CL) and is divided by the beam splitter (BS) into two separated optical paths—object and interferometer reference arm. The beams are directed by mirrors (M). Both arms consist of condenser (C), objective (O) and tube lens (TL). In the reference arm, a diffraction grating (DG) is placed. The output lenses (OL) focus the beams onto the output plane. There the object beam and the reference beam recombine and create an interference fringes pattern (hologram), which is captured by the camera (D).

The amplitude and the phase image are reconstructed numerically from the hologram. The process of the numerical reconstruction is based on the fast Fourier transform methods [20]. For time-lapse sequences, the image processing discussed in [23] is applied. The entire image reconstruction and image processing are performed by our own software. The resulting phase image can be used for classic image processing and analysis, e.g. for segmentation that defines what is the background and what is the cell in the image. From the phase image, various other visualization modalities can be easily obtained by simple numerical calculations [24]. Here we used a simulated differential interference contrast (simulated DIC) that was calculated as a 1D gradient of the quantitative phase image.

Flow-cytometry analysis of cell death

First, non-stained cells (control) were analyzed using flow-cytometry to set the annexin V /PI gating regions (Fig. 2A). Consequently, non-treated cells and cells treated with plumbagin for 3 h were analyzed (Fig. 3B and C, resp.). Four different phenotypes were distinguished: (a) annexin V−/PI− (lower left quadrant, Q3); estimated as viable cells; (b) annexin V+/PI− (lower right quadrant, Q4); usually estimated as apoptotic cells, but probably could contain larger

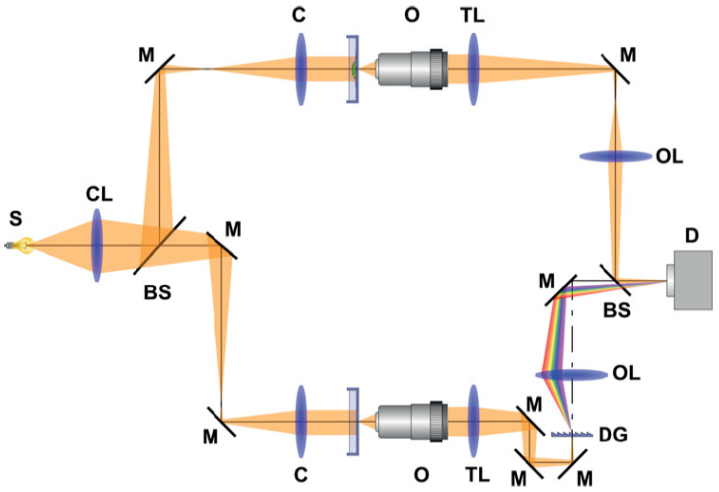

Fig 1. Holographic mode setup in Multimodal holographic microscope is based on the Mach-Zehnder-type interferometer. The light is divided into two separate optical paths—object arm and interferometer reference arm. Both arms consist of condenser (C), objective (O) and tube lens (TL). In the reference arm, a diffraction grating (DG) is placed. The object beam and the reference beam recombine in the output plane and create interference fringes pattern, which is captured by the camera (D). S—source; CL—collector lens; BS—beam splitter; M—mirror; C—condenser; O-objective; TL—tube lens; DG—diffraction grating; OL—output lens; D—detector.

doi:10.1371/journal.pone.0121674.g001

quantities of oncotic cells; (c) annexin V−/PI+ (upper left quadrant, Q1); fragments of damaged cells; (d) annexin V+/ PI+ (upper right quadrant, Q2); late apoptotic and necrotic cells.

Compared to the non-treated cells, the fraction of annexin V+/PI− cells increased distinctly to 30.55% (compared to 4.50% in the non-treated sample), and the fraction of annexin V+/PI + increased up to 7.75% (compared to 1.70% in the non-treated sample). Furthermore, the studied cells were back-gated in the dot plot with the forward scatter/side scatter parameters of these treated cells. As a result of the back-gating, two different annexin V+/PI− populations can be seen (gated in green colour) (Fig. 2C, lower dot plot, arrows R1 and R2). Therefore, additional re-gating was performed. As a result, annexin V+/ PI− and lower FSC (region R1, supposed apoptosis) formed 9.51% of cells, and annexin V+/ PI− and higher FSC (region R2, supposed oncosis) formed 13.22% of cells (gating process not shown).

Time-lapse holographic microscopy

Subsequently, the same plumbagin-treated PC-3 cell line was observed using MHM. Attention was focused on changes in the cellular morphological features including cell shape, cell mass, cell spreading area, and typical structures, which could be seen in the injured cells. Using the time-lapse analysis, we identified 32% of cells which increased their volume and showed increasing blebs in the plasma membrane during the time-lapse analysis (designated as "increase size" in Fig. 2D), 24% of cells, which decreased their volume and showed apoptotic bodies (designated as "decrease size"), and 44% of cells with the unchanged volume during the 2 h of monitoring. From the phase images, we also measured cell surface mass over the time-lapse

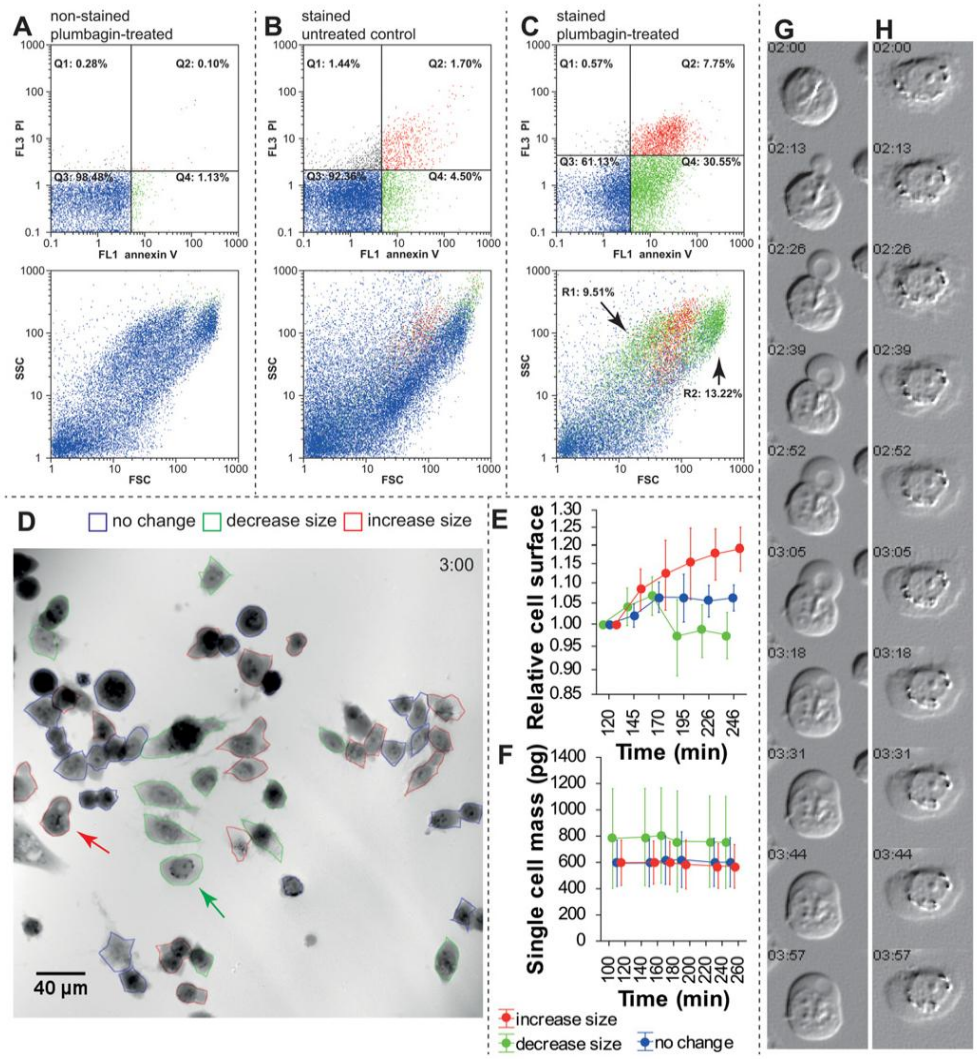

Fig 2. Differences in cell death estimation between flow cytometry and holographic microscopy. A. Plumbagin treatment, no annexin V/PI staining, used for gating set-up. Upper dot plot indicates annexin V/PI fluorescence, lower dot plot indicates FSC/SSC of these cells colour-coded according to gating regions. **B.** Annexin V/PI staining, untreated cells. 92% are double negative for staining. **C.** Annexin V/PI staining after 3 h of the experiment. See increased populations of annexin V-positive (green gating) and double positive (red staining). In FSC/SSC scatter plot, arrows indicate two populations (gating regions) of annexin V+/PI− cells: (R1) smaller cells (lower FSC) and (R2) larger cells (higher FSC). See the Results section for details. **D.** Multimodal holographic microscope, phase image. 10 × magnification 3 h after 2 µM plumbagin treatment. Red-outlined cells show size increase and oncotic phenotype, green-outlined cells show surface area decrease and apoptotic phenotype, blue-outlined cells show no changes during 2 h monitoring. For typical morphological criteria of oncotic/apoptic cells see (Table 1) **E.** Relative change of cell surface in individual cells (relative to initial time point). Colour coding of individual cells is based on (D). **F.** Mass of individual cells in pg. Note a significantly higher mass of the "decrease-size" cell population. **G.** Time-lapse of typical oncotic

"increase size" cell indicated by red arrow in (D), simulated digital interference microscopy **H.** Time-lapse of typical "decrease size" apoptotic cell indicated by green arrow in (D). Simulated digital interference microscopy. FSC—forward scatter, SSC—side scatter, PI—propidium iodide.

doi:10.1371/journal.pone.0121674.g002

observation (Fig. 2E-F). Accordingly, the surface area of the cells differed significantly between these three groups of cells, $F(2, 244) = 31.05$, $p < 0.001$, namely at later time points. With regard to cell mass, the results are in accordance with the assumption that this parameter remains nearly unchanged over this short time in the cell cycle. 90% of the observed cells changed their mass by less than 7%, $F(5, 244) = 0.03$, $p = 0.99$. In contrast, the mass of cells was significantly higher in the "decrease size" group of cells as compared to the "no change" and "increase size" groups, $F(5, 244) = 4.68$, $p = 0.01$; the mass of the "decrease size" cells was on average 1.3-fold higher (Fig. 2F).

By contrast to oncosis or necrosis, which are associated with the cell swelling and increased cell volume, apoptosis is connected with the loss of cell volume during the cell shrinkage (for detailed characterization of morphological changes of each cell death type see the below section of this text). Regarding the fact, 2×3 two way contingency tables were created to compare HM with the flow-cytometry results (no size change in HM vs. double-negative cells in FCM; "increase size" vs. annexin V+/PI+ population, and "decrease size" vs. annexin V+/PI− population). There was a significant difference between the assays; the proportion of the "increase size" cells was significantly higher when determined by holographic microscopy, $\chi^2 = 18.043$, $p = 0.0001$ (Table 3). Because two annexin V+/PI− populations (green) were found on the FSC/SSC dot-plot by back gating, another chi-squared test was performed. Unlike in the previous testing, the "increase size" was compared with the annexin V+/PI+ population (Q2) plus R2 population (see above for details) and the "decrease size" included only the R1 gating region. Although there was still a significant difference, the proportional difference between the assays was not that profound and hence the p-level was higher (Table 3).

Assessment of apoptotic, oncotic, and necrotic cells morphology

Consequently, morphology of the cells after the plumbagin treatment was described using MHM, light microscopy, and verified at ultrastructural level using transmission electron microscopy (TEM). In agreement with the previous chapter, three populations of cells were observed according to size changes. Apart from cellular shrinking or swelling, other characteristics typical of distinct cell deaths were observed in MHM (see Table 1). In the oncotic cells, an intact plasma membrane with cytoplasmic blebs, nuclear chromatin clumping, and nucleus dilatation were detected. The formation of cytoplasmic blebs is well apparent in the time lapse (Fig. 2G).

Some major morphological features connected with necrosis were observed too, including multiple and large cytoplasmic blebs, translucent cytoplasm, cell swelling ended by cell membrane disruption and nucleus dilatation (Fig. 3). In contrast, the shrinking group of cells exhibited characteristics typical of apoptosis: spherical shape of the cells, chromatin condensation, nuclear membrane irregularity and indeed the formation of multiple apoptotic bodies considered as an advanced stage of apoptosis (Fig. 3A, second column). Based on these characteristics, typical morphological criteria visible in MHM are illustrated in scheme (Fig. 3B). By using the fluorescence mode of MHM, we detected annexin V staining in all observed types of cell deaths (oncosis, necrosis, and apoptosis as well; Fig. 3A). In early apoptotic cells, annexin V positivity was detected, namely nearby the cell membrane (Fig. 3A, first column).

All mentioned morphological characteristics were corroborated by light microscopy (data not shown) and at the ultrastructural level by using TEM. Further cell death features observable

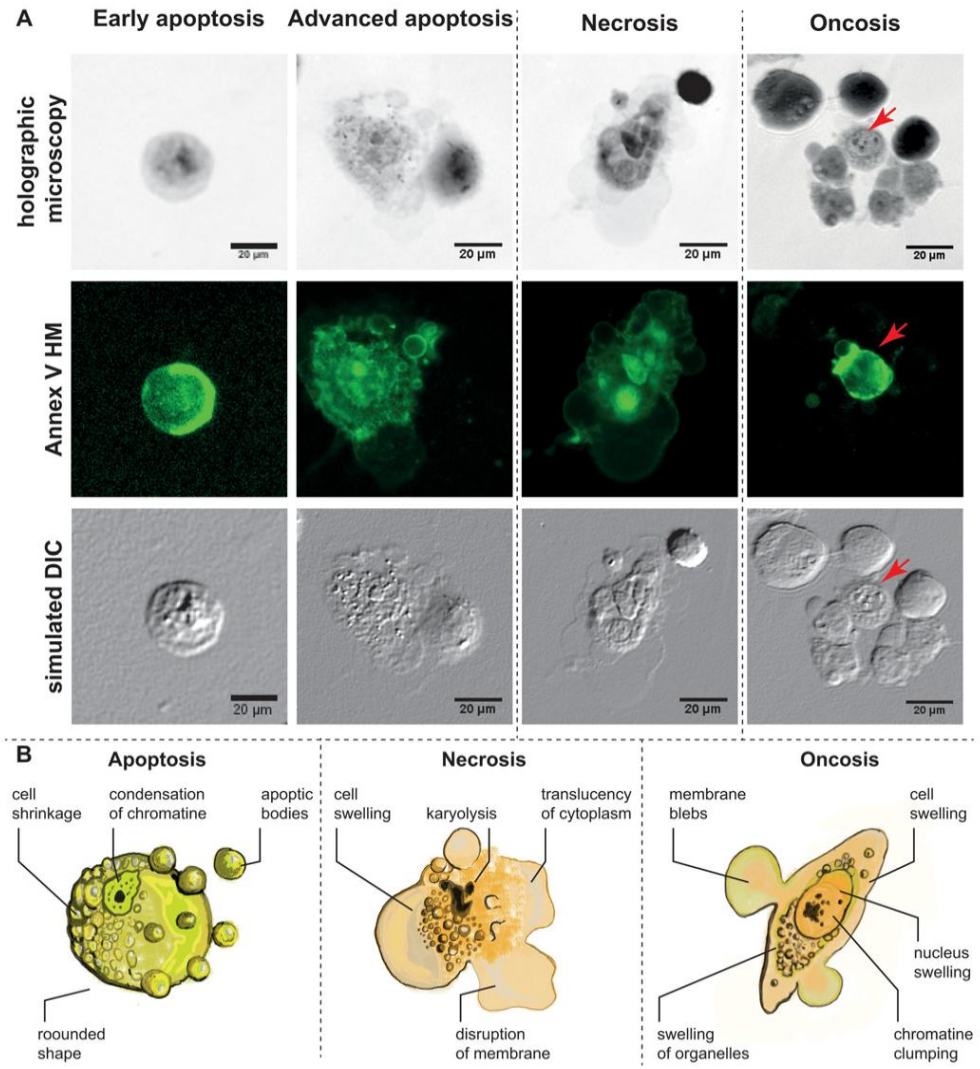

Fig 3. Morphology of Apoptotic, necrotic and oncotic cells. A. Characteristic apoptotic, necrotic and oncotic cells in multimodal holographic microscope, simulated DIC (differential interference contrast). 20 × magnification was used in MHM. Annexin V staining for the verification of cell membrane alteration. Red arrow indicates annexin V-positive "advanced" oncotic cell. Apoptotic cells displayed in initial step (left) with the typically round-shaped cells and in advanced step with the formation of apoptotic bodies. **B.** Scheme of typical apoptotic, necrotic and oncotic cells. Typical characteristics visible by MHM phase image. For a detailed description of the characteristic features of apoptotic, necrotic, and oncotic cells, see Table 1.

doi:10.1371/journal.pone.0121674.g003

Table 3. Two-way contingency table of the observed cell death frequencies based on morphological criteria and flow-cytometry analysis.

Technique	Cell classification			χ2	p level
	normal	increase size	decrease size		
phase images from MHM	44	32	24	-	-
Flow-cytometry†	61	8	31	18.04	0.0001
Flow-cytometry, adjusted for oncosis‡	61	13	21	10.85	0.0044

† For "flow cytometry", annexin V+/ PI+ cells are designated as "increase size", and annexin V+/PI− cells are designated as "decrease size". Compared to phase images from MHM.

‡ for „flow cytometry, adjusted for oncosis", annexin V+/ PI− cells gated by lower FSC (i.e. smaller cells, arrow R1 in Fig. 2C) are designated as "decrease size" (reflect "true apoptosis"), and summed annexin V+/PI+ and annexin V+/PI− cells gated by higher FSC (i.e. larger cells, arrow R2 in Fig. 2C) are designated as "increase size" (reflect necrosis and oncosis, resp.). Compared to phase images from MHM. PI—propidium iodide, FSC—forward scatter.

doi:10.1371/journal.pone.0121674.t003

only with TEM were found. *Inter alia*, dilatation of endoplasmic reticulum (ER) and Golgi apparatus, condensation of mitochondria followed by their swelling and rupture, formation of cytoplasmic vacuoles, swollen and ruptured lysosomes, lysis of nucleolus and karyolysis in oncotic/necrotic cells were apparent (Fig. 4 and unpublished data). In apoptotic cells, significant nuclear fragmentation was observed (Fig. 4).

According to our results, MHM is not able to recognize ultrastructural details of cells (mitochondria, ER, etc.), but is more suitable for detecting membrane blebs and apoptotic bodies. The recognition of membrane blebs and apoptotic bodies in MHM was even better than with TEM.

Assessment of oncosis progression using MHM

Multimodal holographic microscope combines holographic imaging with fluorescent imaging. The unique device makes it possible to combine the assessment of main morphologic features with annexin V/PI staining using a single instrument in one field of view. Thus, this technique was employed for an in-depth analysis of oncotic cells.

Cells with the characteristic morphological criteria of oncosis exhibit various conditions of the PI/annexin V staining. We identified the following variants of oncotic cells: (1) small membrane blebs, higher mass of cells and annexin V−/PI− staining; (2) more frequent/larger plasmatic blebs, gradual loss of spindle cell shape, clumping of chromatin, annexin V+/ PI − staining; (3) more frequent/larger plasmatic blebs, lower mass of cells, significant swelling of nucleus with a still distinguishable nuclear membrane and chromatin condensation, annexin V +/PI+; (4) annexin V+/PI+ combined with the homogenization of nuclear structure, cell membrane disruption with a partial extrusion of cell contents, and other morphological criteria of necrosis (Fig. 5). Based on these apparently gradual morphological and staining characteristics, a staging of oncosis was suggested as follows: normal cells/oncosis transition, early oncosis, late oncosis, oncosis/necrosis transition.

Discussion

Methods of quantitative phase imaging are rapidly developing at present. Although their principles had been known for many years, the methods were not widely used until computer technology recorded a sufficient progress.

Phase-shift ing microscopes [25–27] provide images with the suppressed coherence noise and lateral resolution comparable to that of conventional microscopes. They use low-coherence sources and owing to that, the coherence gating effect can be exploited. Disadvantage is the fact that three images, each with a different induced phase shift, have to be captured for one

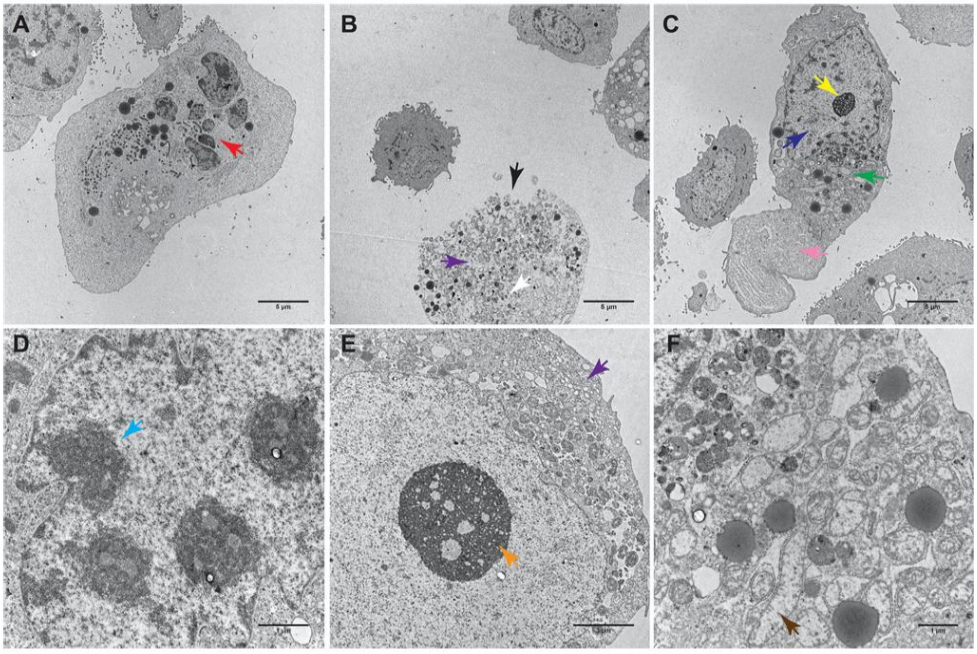

Fig 4. Characteristic apoptotic, necrotic and oncotic cells in transmission electron microscope (TEM). A. Apoptotic cell, overall view, 2800 ×. **B.** necrotic cell, 2800 ×. **C.** oncotic cell, 2800 ×, **D.** Detail of apoptotic cell nucleus, 5600 ×. **E.** Detail of necrotic cell, 14000 ×. **F.** Detail of oncotic cell cytoplasm, 11000 × magnification. Red arrow—nuclear fragmentation. Black arrow—rupture of plasmatic membrane. White arrow—karyolysis. Yellow arrow—reticular nucleolus. Dark blue arrow—dilatation of nucleus. Green arrow—dilatation of ER and Golgi. Pink arrow—cytoplasmic bleb. Light blue arrow—chromatin condensation. Violet arrow—formation of cytoplasmic vacuoles. Orange arrow—initial lysis of nucleolus. Brown arrow—mitochondrial swelling.

doi:10.1371/journal.pone.0121674.g004

numerical reconstruction. Therefore, mechanical displacements have to be used and the acquisition rate is limited.

On the other hand, digital holographic microscopes with the off-axis setup and laser sources [28–30] allow a fast acquisition rate because only a single image is needed for the reconstruction. However, coherence noise is higher, lateral resolution is lower, and the coherence gating effect cannot be used.

The employed MHM is based on the Coherence-Controlled Holographic Microscope (CCHM) [18] and links advantages of the both previously developed methods of holographic microscopy. Moreover, MHM enables to combine holographic microscopy with other techniques [19].

MHM allows quantitative phase contrast imaging combined with other proven methods such as fluorescence microscopy. The method constitutes an overlap of traditional microscopy techniques. Information in the phase image provides values of optical path delay caused by the observed cell. These values are directly proportional to the cell dry mass, originally published in [31, 32], and therefore, an evaluation of cell mass changes is possible [33–36]. Owing to this, holographic microscopy and similar techniques of quantitative phase imaging are useful tools

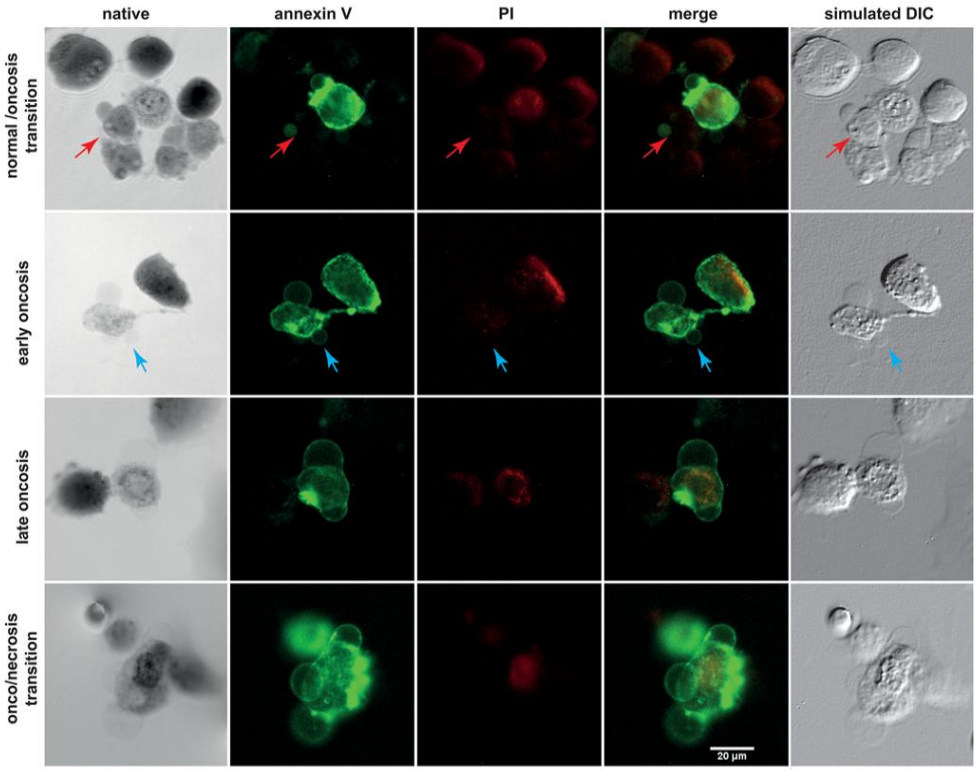

Fig 5. Estimation of oncosis progression by multimodal holographic microscopy. Annexin V (green) and propidium iodide (PI, red) staining. Initial step of oncosis (first row, red arrow) is annexin V−/PI− and thus distinguishable only by native morphology, see typical cytoplasmic bleb in the phase image. This causes false-negativity by flow-cytometry. Second, early oncotic cells feature larger blebs and are annexin V+/PI−. Late oncosis is double positive for staining, with no apparent karyolysis. Advanced oncosis/necrosis transition is typical by double-positive staining and karyolysis.

doi:10.1371/journal.pone.0121674.g005

for research in cell biology, such as cell dynamics studies, cancer research [37], intracellular mass transport [38], membrane fluctuations [39], cell cycle [33], cell growth [34] and others [40]. Digital holographic microscopy is highly suitable for studying dynamic processes, which are important for the analysis of living cells. Its potential for utilization in basic and applied research is promising. Accordingly, the monitoring of green- or red- fluorescent protein-expressing cells appears to be very promising using this instrument. Such a technique allows the visualization of cellular processes such as cell cycle, cell death, nuclear cytoplasma dynamics of viable cells in real time, which is expedient as compared with the use of artificial fluorescent staining techniques [41, 42].

In this study, we focused on distinguishing apoptosis from oncosis as a relevant example of the possible MHM use. Many authors use the annexin V/PI assay for the detection and quantification of apoptosis but often do not validate the type of cell death by assessing morphological features. In healthy cells, phosphatidylserine residues (PS) occur on the inner side of the

cytoplasmic membrane. PS is externalized during apoptosis or, as our results showed, also in early oncosis by flipping from the inner to the outer layer of plasma membrane to enable the binding of annexin V. Propidium iodide (PI) detects cells with a disrupted plasma membrane by nuclear DNA staining. Unfortunately, using the conventional annexin V/PI assay in flow-cytometry, it is not always simple to differentiate apoptosis from oncosis [6], because, as our results showed, oncosis and apoptosis can occur simultaneously in the quadrant Q4 (annexin V +/PI−) of the dot plot. Thus, significant difference between the estimation of cell death using FCM and morphological criteria was observed. Therefore, it was not surprising that the estimation of cell processes using FCM and MHM differed significantly and led to the overestimation of the apoptotic population using FCM.

Interestingly, the back gating of flow-cytometry fluorescence data gave us unique results. Back gating of the annexin V+/PI− population to the forward scatter/side scatter dot plot visualized two sharply demarcated different populations: (1) a population of smaller annexin V + cells (lower FSC parameter, marked as R1 in Fig. 2), and (2) a population of larger annexin V + cells. In addition, back gating of the annexin V+/PI+ population to FSC/SSC dot plot brought us an additional information regarding the cell size: these double-positive cells ranged in size between the two annexin V+ populations. In accordance with the knowledge of the size of apoptotic, necrotic, and oncotic cells, this back gating allowed us to distinguish the populations of small apoptotic cells from the large oncotic cells. This back gating also confirmed that (double-positive) necrotic cells are larger than apoptotic cells and demonstrated that the necrotic cell population is smaller than that of the oncotic cells. These findings were taken into account for a further comparison of FCM and MHM. This time, however, the population of oncotic cells was added to necrotic cells and not to apoptotic cells. This "FCM adjustment for oncosis" resulted in markedly reduced differences between FCM and MHM; the difference was still significant though. Consequently, morphological criteria were shown to be the most reliable evidence of apoptosis. Apart from the cellular shrinking, other characteristics typical of apoptotic cells were apparent in MHM, e.g. nuclear irregularity, spherical cell shape, chromatin condensation, formation of multiple apoptotic bodies, and annexin V positivity, particularly near the cell membrane. Predominant characteristics typical of oncotic cells observable in MHM were cellular swelling, nuclear chromatin clumping, and formation of organelle-free blebs in the cytoplasmic membrane. These typical morphological criteria of distinct cell deaths were in compliance with results obtained from the transmission electron microscope (TEM) and also with the previous studies [4, 5, 43]. Thus, MHM can be considered a sufficient tool to estimate the cell fate.

Because oncosis and apoptosis can occur in response to the same drug, it is very important to distinguish carefully between these different kinds of cell death when testing new therapeutic drugs [44, 45]. Great emphasis is put also on the dynamic assessment of the prevalent effect of a particular therapeutic drug at different concentrations [46], because many dose–response studies have shown that cells exposed to lower concentrations of drugs such as cisplatin, etoposide, arsenic trioxide or doxorubicin, mostly exhibit the morphological characteristic of apoptosis but at higher doses, their morphology is typical for oncosis [4, 44, 47]. Dynamic (real-time) monitoring of treated cells is another important MHM application. The real-time monitoring makes it possible to observe particular cell death phases including the final fate of cells after the treatment, which is a significant advantage as compared with the common light microscopy providing only a kind of the end-point analysis. It was demonstrated that even if the cells are driven to oncosis, there could be some mechanisms to reverse the process [4, 5], which can be easily captured by real-time MHM monitoring. Thus, MHM might provide a new valuable insight into cell biology.

Author Contributions

Conceived and designed the experiments: JB MR JG MM. Performed the experiments: JB AK M. Sedlackova M. Sztalmachova ZS PB. Analyzed the data: JG RK MR MM PB. Contributed reagents/materials/analysis tools: MM RK RC. Wrote the paper: JB AK JG MR ZS MM.

References

1. Wlodkowic D, Skommer J, Darzynkiewicz Z. Cytometry in Cell Necrobiology Revisited. Recent Advances and New Vistas. Cytometry A. 2010; 77A: 591–606.
2. Haanen C, Vermes I. Apoptosis and inflammation. Mediators Inflamm. 1995; 4: 5–15. PMID: 18475609
3. Rock KL, Kono H. The inflammatory response to cell death. Annual Review of Pathology: Mechanisms of Disease. Palo Alto: Annual Reviews; 2008. p. 99–126.
4. Weerasinghe P, Buja LM. Oncosis: An important non-apoptotic mode of cell death. Experimental and Molecular Pathology. 2012; 93: 302–308. doi: 10.1016/j.yexmp.2012.09.018 PMID: 23036471
5. Trump BF, Berezesky IK, Chang SH, Phelps PC. The pathways of cell death: Oncosis, apoptosis, and necrosis. Toxicologic Pathology. 1997; 25: 82–88. PMID: 9061857
6. Lecoeur H, Prevost MC, Gougeon ML. Oncosis is associated with exposure of phosphatidylserine residues on the outside layer of the plasma membrane: A reconsideration of the specificity of the annexin V/Propidium iodide assay. Cytometry. 2001; 44: 65–72. PMID: 11309810
7. Krysko O, de Ridder L, Cornelissen M. Phosphatidylserine exposure during early primary necrosis (oncosis) in JB6 cells as evidenced by immunogold labeling technique. Apoptosis. 2004; 9: 495–500. PMID: 15192332
8. Grasl-kraupp B, Ruttkay-nedecky B, Koudelka H, Bukowska K, Bursch W, Schulte-hermann R. In-situ detection of fragmented DNA (tunel assay) fails to discriminate among apoptosis, necrosis, and autolytic cell-death—A cautionary note. Hepatology. 1995; 21: 1465–1468. PMID: 7737654
9. Buja LM, Entman ML. Modes of myocardial cell injury and cell death in ischemic heart disease. Circulation. 1998; 98: 1355–1357. PMID: 9760287
10. Freude B, Masters TN, Kostin S, Robicsek F, Schaper J. Cardiomyocyte apoptosis in acute and chronic conditions. Basic Res Cardiol. 1998; 93: 85–89. PMID: 9833169
11. Mahdi EJ, Alshahrani AM, Abdulsatar AA, Mahdi JG. Morphological evaluation of apoptosis induced by salicylates in HT-1080 human fibrosarcoma cells. Journal of Microscopy and Ultrastructure. 2014; 2: 20–27.
12. Jolly PD, Smith PR, Heath DA, Hudson NL, Lun S, Still LA, et al. Morphological evidence of apoptosis and the prevalence of apoptotic versus mitotic cells in the membrana granulosa of ovarian follicles during spontaneous and induced atresia in ewes. Biology of Reproduction. 1997; 56: 837–846. PMID: 9096863
13. Chmelik R, Slaba M, Kollarova V, Slaby T, Lostak M, Collakova J, et al. Chapter 5—The Role of Coherence in Image Formation in Holographic Microscopy. In: Wolf E, editor. Progress in Optics. Amsterdam: Elsevier; 2014. p. 267–335.
14. Dunn GA, Zicha D. Phase-shifting interference microscopy applied to the analysis of cell behavior. Symposia of the Society for Experimental Biology. 1993; 47: 91–106. PMID: 8165581
15. Gumulec J, Balvan J, Sztalmachova M, Raudenska M, Dvorakova V, Knopfova L, et al. Cisplatin-resistant prostate cancer model: Differences in antioxidant system, apoptosis and cell cycle. International Journal of Oncology. 2014; 44: 923–933. doi: 10.3892/ijo.2013.2223 PMID: 24366574
16. Holubova M, Axmanova M, Gumulec J, Raudenska M, Sztalmachova M, Babula P, et al. KRAS NF-kappaB is involved in the development of zinc resistance and reduced curability in prostate cancer. Metallomics. 2014; 6: 1240–53. doi: 10.1039/c4mt00065j PMID: 24927480
17. Masarik M, Gumulec J, Hlavna M, Sztalmachova M, Babula P, Raudenska M, et al. Monitoring of the prostate tumour cells redox state and real-time proliferation by novel biophysical techniques and fluorescent staining. Integrative Biology. 2012; 4: 672–684. doi: 10.1039/c2ib00157h PMID: 22592803
18. Kolman P, Chmelik R. Coherence-controlled holographic microscope. Optics Express. 2010; 18: 21990–22003. doi: 10.1364/OE.18.021990 PMID: 20941100
19. Slaby T, Kolman P, Dostal Z, Antos M, Lost'ak M, Chmelik R. Off-axis setup taking full advantage of incoherent illumination in coherence-controlled holographic microscope. Optics Express. 2013; 21: 14747–14762. doi: 10.1364/OE.21.014747 PMID: 23787662
20. Kreis T. Digital holographic interference-phase measurement using the fourier-transform method. J Opt Soc Am A Opt Image Sci Vis. 1986; 3: 847–855.

21. Goldstein RM, Zebker HA, Werner CL. Satellite radar interferometry—two-dimensional phase unwrapping. Radio Sci. 1988; 23: 713–720.
22. Ghiglia DC, Pritt MD. Two-dimensional phase unwrapping: theory, algorithms, and software: Wiley; 1998.
23. Zikmund T, Kvasnica L, Tyc M, Krizova A, Collakova J, Chmelik R. Sequential processing of quantitative phase images for the study of cell behaviour in real-time digital holographic microscopy. J Microsc. 2014: 117–125. doi: 10.1111/jmi.12190 PMID: 25354652
24. Wang Z, Millet L, Chan V, Ding H, Gillette MU, Bashir R, et al. Label-free intracellular transport measured by spatial light interference microscopy. J Biomed Opt. 2011; 16.
25. Dubois F, Joannes L, Legros JC. Improved three-dimensional imaging with a digital holography microscope with a source of partial spatial coherence. Applied Optics. 1999; 38: 7085–7094. PMID: 18324255
26. Zhang T, Yamaguchi I. Three-dimensional microscopy with phase-shifting digital holography. Optics Letters. 1998; 23: 1221–1223. PMID: 18087480
27. Xu L, Miao JM, Asundi A. Properties of digital holography based on in-line configuration. Opt Eng. 2000; 39: 3214–3219.
28. Cuche E, Bevilacqua F, Depeursinge C. Digital holography for quantitative phase-contrast imaging. Optics Letters. 1999; 24: 291–293. PMID: 18071483
29. Carl D, Kemper B, Wernicke G, von Bally G. Parameter-optimized digital holographic microscope for high-resolution living-cell analysis. Applied Optics. 2004; 43: 6536–6544. PMID: 15646774
30. Shin D, Daneshpanah M, Anand A, Javidi B. Optofluidic system for three-dimensional sensing and identification of micro-organisms with digital holographic microscopy. Optics Letters. 2010; 35: 4066–4068. doi: 10.1364/OL.35.004066 PMID: 21124614
31. Davies HG, Wilkins MHF. Interference microscopy and mass determination. Nature. 1952; 169: 541–541. PMID: 14929230
32. Barer R. Refractometry and interferometry of living cells. J Opt Soc Am. 1957; 47: 545–556. PMID: 13429433
33. Girshovitz P, Shaked NT. Generalized cell morphological parameters based on interferometric phase microscopy and their application to cell life cycle characterization. Biomed Opt Express. 2012; 3: 1757–1773. doi: 10.1364/BOE.3.001757 PMID: 22876342
34. Popescu G, Park Y, Lue N, Best-Popescu C, Deflores L, Dasari RR, et al. Optical imaging of cell mass and growth dynamics. Am J Physiol Cell Physiol. 2008; 295: C538–C544. doi: 10.1152/ajpcell.00121.2008 PMID: 18562484
35. Rappaz B, Cano E, Colomb T, Kuehn J, Depeursinge C, Simanis V, et al. Noninvasive characterization of the fission yeast cell cycle by monitoring dry mass with digital holographic microscopy. J Biomed Opt. 2009; 14.
36. Shaked NT, Satterwhite LL, Rinehart MT, Wax A. Quantitative Analysis of Biological Cells Using Digital Holographic Microscopy, Holography, Research and Technologies. Rosen J, editor. Rijeka: InTech; 2011.
37. Janeckova H, Vesely P, Chmelik R. Proving Tumour Cells by Acute Nutritional/Energy Deprivation as a Survival Threat: A Task for Microscopy. Anticancer Research. 2009; 29: 2339–2345. PMID: 19528500
38. Boss D, Kuehn J, Jourdain P, Depeursinge C, Magistretti PJ, Marquet P. Measurement of absolute cell volume, osmotic membrane water permeability, and refractive index of transmembrane water and solute flux by digital holographic microscopy. J Biomed Opt. 2013; 18.
39. Rappaz B, Barbul A, Hoffmann A, Boss D, Korenstein R, Depeursinge C, et al. Spatial analysis of erythrocyte membrane fluctuations by digital holographic microscopy. Blood Cells Mol Dis. 2009; 42: 228–232. doi: 10.1016/j.bcmd.2009.01.018 PMID: 19324576
40. Popescu G. Quantitative phase imaging of cells and tissues. 1st ed. New York: McGraw-Hill Professional; 2011.
41. Hoffman RM, Yang M. Subcellular imaging in the live mouse. Nat Protoc. 2006; 1: 775–782. PMID: 17406307
42. Yamamoto N, Jiang P, Yang M, Xu MX, Yamauchi K, Tsuchiya H, et al. Cellular dynamics visualized in live cells in vitro and in vivo by differential dual-color nuclear-cytoplasmic fluorescent-protein expression. Cancer Res. 2004; 64: 4251–4256. PMID: 15205338
43. Edinger AL, Thompson CB. Death by design: apoptosis, necrosis and autophagy. Current Opinion in Cell Biology. 2004; 16: 663–669. PMID: 15530778
44. Gonzalez VM, Fuertes MA, Alonso C, Perez JM. Is cisplatin-induced cell death always produced by apoptosis? Mol Pharmacol. 2001; 59: 657–63. PMID: 11259608

45. Hinson JA, Roberts DW, James LP. Mechanisms of acetaminophen-induced liver necrosis. Handb Exp Pharmacol. 2010: 369–405. doi: 10.1007/978-3-540-79088-4_17 PMID: 20020374

46. Chanan-Khan A, Srinivasan S, Czuczman MS. Prevention and management of cardiotoxicity from anti-neoplastic therapy. J Support Oncol. 2004; 2: 251–266. PMID: 15328825

47. Zhu JB, Okumura H, Ohtake S, Nakamura S, Nakao S. The molecular mechanism of arsenic trioxide-induced apoptosis and oncosis in leukemia/lymphoma cell lines. Acta Haematol. 2003; 110: 1–10. PMID: 12975549

Check for updates
ChemPubSoc Europe
DOI: 10.1002/chem.201804434
CHEMISTRY A European Journal Full Paper

Nanoparticles | *Hot Paper*

Black Phosphorus Cytotoxicity Assessments Pitfalls: Advantages and Disadvantages of Metabolic and Morphological Assays

Michaela Fojtů,[a, b] Jan Balvan,[b, c] Martina Raudenská,[b, c] Tomáš Vičar,[b] Daniel Bouša,[a] Zdeněk Sofer,[a] Michal Masařík,[b, c] and Martin Pumera*[a, c]

Abstract: Black phosphorus (BP) belongs to a group of 2D nanomaterials and nowadays attracts constantly increasing attention. Parallel to the growing utilization of BP nanomaterial increase also the requirements for the thorough comprehension of its potential impact on human and animal health. The aim of this study was to compare and discuss five assays commonly used for the cytotoxicity assessments of nanomaterials with a special focus on BP nanoparticles. A comprehensive survey of factors and pitfalls is provided that should be accounted for when assessing their toxicity and pointed to their inconsistency. BP might introduce various levels of interference during toxicity assessments depending on its concentration applied. More importantly, the BP toxicity evaluation was found to be influenced by the nature of assay chosen. These are based on different principles and do not have to assess all the cellular events equally. A commercial assay based on the measurement of protease activity was identified to be the most suitable for the BP toxicity assessment. Further, the benefit of time-lapse quantitative phase imaging for nanomaterial toxicity evaluation was highlighted. Unlike the conventional assessments it provides real-time analysis of the processes accompanying BP administration and enables to understand them deeper and in the context.

Introduction

The explosion of research interest in the field of nanotechnology resulted over the last two decades in the evolution of a spectrum of nanoparticles' applications that are still being broadened. Special group of nanoparticles represent 2D nanomaterials extensively investigated for their applicability in the field of catalysis,[1,2] water pollution,[3] optoelectronic,[2] and biosensor development.[3–5] In last years, these proved to have a significant potential also in biomedical applications, especially in the treatment of cancer. They were successfully used as a non-toxic delivery platform for anticancer drugs.[6,7] Further, 2D nanomaterials showed great promises in the photothermal therapy (PTT), since they are capable of light energy conversion to heat while creating hyperthermia. Besides, they may also be used as a non-toxic photosensitizer for the photodynamic therapy (PDT) that is based on a generation of reactive oxygen species (ROS).[8] Further, 2D nanomaterials were repeatedly reported to inhibit the bacterial growth, to be applicable for the in situ disinfection and described as a promising alternative strategy to combat with the antibiotic resistance of bacteria and biofilms.[9,10] Nanomaterials such as graphene, transition-metal dichalcogenides, or black phosphorus are particles with the third dimension reduced to the sub-nanometer length scale, therefore are termed "2D nanomaterials".[11] Growing application potential of 2D nanomaterials and their increasing incorporation in commercial products are simultaneously placing great demands on their safety for human and animal health, as well as for the environment in general.[12] Therefore, thorough and comprehensive toxicity evaluation should represent crucial decisive milestone preceding the material introduction to the industrial applications.

Black phosphorus (BP) is the most stable among the three phosphorus allotropes. Individual BP atoms create a 2D structure. Since they are in sp^3-hybridization state, phosphorus layers are wrinkled, but still vertically stacked and holding together via weak van der Waals forces.[13] Due to this weak bonding between individual phosphorus layers, bulk BP can be exfoliated into a thin material of few- or single-layer structure.[14] BP evinces a high level of anisotropy. Therefore, changes in the BP structure alter its behaviour and electro-

[a] Dr. M. Fojtů, Dr. D. Bouša, Prof. Z. Sofer, Prof. M. Pumera
Department of Inorganic Chemistry
University of Chemistry and Technology Prague
Technická 5, 166 28 Prague 6 (Czech Republic)
E-mail: pumera.research@gmail.com

[b] Dr. M. Fojtů, Dr. J. Balvan, Dr. M. Raudenská, T. Vičar, Dr. M. Masařík
Department of Physiology, Faculty of Medicine
Masaryk University, Kamenice 5
625 00 Brno (Czech Republic)

[c] Dr. J. Balvan, Dr. M. Raudenská, Dr. M. Masařík, Prof. M. Pumera
Central European Institute of Technology
Brno University of Technology
Technická 3058/10, 616 00 Brno (Czech Republic)

Supporting information and the ORCID identification number(s) for the author(s) of this article can be found under: https://doi.org/10.1002/chem.201804434.

© 2019 Wiley-VCH Verlag GmbH & Co. KGaA, Weinheim

ChemPubSoc Europe

CHEMISTRY A European Journal Full Paper

15213765, 2019, 1, Downloaded from https://chemistry-europe.onlinelibrary.wiley.com/doi/10.1002/chem.201804434 by Masaryk University, Wiley Online Library on [17/02/2025]. See the Terms and Conditions (https://onlinelibrary.wiley.com/terms-and-conditions) on Wiley Online Library for rules of use; OA articles are governed by the applicable Creative Commons License

chemical properties.[15] This is favourable for a wide spectrum of diverse applications. Further, after exposure to air or water, it degrades to nontoxic phosphorus intermediates as P_xO_y, thus is considered to be biodegradable.[4,16] Prospective introduction of BP in industrial applications and in the area of biomedicine are holding huge potential. On the other hand, before this happens we should be aware of BP interactions with the environment and with living organisms including human. Therefore, it is absolutely crucial to precisely, quantifiably and reproducibly assess the toxicity of this recently introduced material. Several reports have outlined the difficulties associated with nanoparticle toxicity assessments.[17] In vitro toxicity assessments represent the first key step towards elucidation of the nanomaterial safety profile. These assays are principally based on the evaluation of various molecular events comprising changes in the DNA structure, generation of reactive oxygen species (ROS), disruption of metabolic activity, disruption of cellular membrane, or changes in a cellular morphology. Most of the published studies concerning with the toxicity of nanomaterials use one of the well-established viability assays based on colorimetric and fluorometric detection (Figure 1, Table 1). These assays enable high-throughput toxicity assessment and are considered as a golden standard.[18] Nevertheless, it should be noted that these assays were primarily developed for cytotoxicity assessment of soluble and preferably also colourless compounds. When determining the toxicity of nanomaterials, especially those of 2D shape, their rich surface chemistry should be taken into consideration. Functional groups presented on the particle surface frequently interact with the chemicals used in these conventional assays. Further, since the 2D nanoparticles are usually dark-coloured, the distortion of assessed parameters, for example, absorbance of the solution, may be growing with the increasing concentration of the material. On top of it, peculiarities of each individual toxicity assay should be considered, for example, LDH assay as will be explained below. All these factors may impact the evaluated parameters and consequently, the data may be unintentionally manipulated. This altogether leads either to overestimation, or more dangerously underestimation of the nanomaterial-associated risk. More importantly, it gives rise to some incorrect conclusions regarding the particle biocompatibility, nanotoxicity and safety in general.

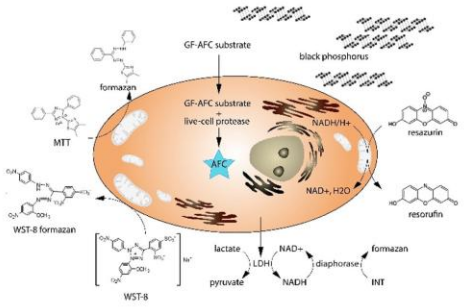

Figure 1. Schematic summary depicting principles of cell viability detection assays used within this study. GF-AFC: glycyl-phenylalanyl-aminofluorocoumarin, LDH: lactate dehydrogenase, INT: 2-*p*-iodophenyl-3-*p*-nitrophenyl-5-phenyl tetrazolium chloride, WST: 8-2-(2-methoxy-4-nitrophenyl)-3-(4-nitrophenyl)-5-(2,4-disulfophenyl)-2*H*-tetrazolium, monosodium salt, MTT: 3-(4,5-dimethyl-2-thiazolyl)-2,5-diphenyl-2*H*-tetrazolium bromide.

Among the most intensively used methods for evaluating cell proliferation and viability belong tetrazolium-salt based assays (MTT, WST, XTT and other) allowing simple, rapid, high-throughput, and inexpensive determination of compound toxicity. MTT, WST-8 and resazurin assay together with non-tetrazolium LDH and Multi-Tox Glo assays are commonly employed for the determination of nanomaterials' toxicity in in vitro toxicological studies.

The assays used in this study were primarily developed for the toxicity assessment of soluble and preferably colourless compounds. Evaluation of nanomaterials' toxicity using these well-established assays should still be possible. However, it

Table 1. Comparison of methods for cellular viability assessment used in this study.

Method	Principle	Advantages	Limitations
MTT	conversion of MTT to water insoluble formazan by enzymes located in cytoplasm and mitochondria	rapid, simple, inexpensive, sensitive, versatile, reliable, appropriate for first rounds of high-throughput studies	can not discriminate between cytotoxic and antiproliferative effects, not working well for assessing compounds altering mitochondrial metabolism
WST-8	enzymatic conversion of WST-8 dye to water-soluble formazan	rapid, simple, sensitive, versatile, reliable, appropriate for the first rounds of high-throughput studies	not working well for assessing compounds altering mitochondrial metabolism
resazurin	reduction of resazurin to resorufin by enzymes located in mitochondria, cytosol and microsomes	rapid, simple, versatile, reliable, appropriate for the first rounds of high-throughput studies	not working well for assessing compounds altering mitochondrial metabolism, sensitive to the presence of proteins in the culture medium
LDH assay	measurement of LDH activity in extracellular medium	rapid, simple evaluation	detects only cell deaths accompanied by LDH leakage, LDH stability and enzymatic activity in supernatants might be affected by several factors
MultiTox	measuring of specific protease activity	rapid, versatile, reliable, allows data normalization	due to the higher cost less appropriate for high-throughput studies

© 2019 Wiley-VCH Verlag GmbH & Co. KGaA, Weinheim

ChemPubSoc Europe

CHEMISTRY A European Journal Full Paper

15213765, 2019, 1, Downloaded from https://chemistry-europe.onlinelibrary.wiley.com/doi/10.1002/chem.201804434 by Masaryk University, Wiley Online Library on [17/02/2025]. See the Terms and Conditions (https://onlinelibrary.wiley.com/terms-and-conditions) on Wiley Online Library for rules of use; OA articles are governed by the applicable Creative Commons License

might be not as trivial as it may seem due to their complex physicochemical properties.[19] The MTT salt is widely utilized for the viability assessment. MTT assay is based on colorimetric assessment of dark purple insoluble formazan produced by metabolically active cells by reduction of yellow 3-(-4,5-dimethylthiazol-2-yl)-2,5-diphenyl tetrazolium bromide. For a long time, it was believed that this reduction is taking place mainly in the mitochondria and is catalysed predominantly by mitochondrial succinate dehydrogenase. However, several reports then confirmed that the main site of MTT reduction is in the cytoplasm with the reduced nicotinamide adenine dinucleotide (NAD) coenzyme being the main source of reducing power, followed by ascorbic acid, dihydrolipoic acid, cysteine, tocopherols, and glutathione.[20,21] The resulting insoluble formazan is then solubilized by an organic solvent (e.g., DMSO, isopropanol) prior spectrophotometric measurement. The extent of the MTT reduction is then proportional to the number of viable cells. Several factors may influence the MTT readout, including changes in activity of oxidoreductases, metabolic and energetical fluctuations, or oxidative stress. Therefore, in fact, the MTT assay does not measure the number of viable cells, but rather a complex set of enzyme activities reflecting the level of cellular metabolic state.[22]

Another assay included in this study uses the WST-8 dye belonging to the second generation of tetrazolium salts. These salts are in general cell-membrane impermeable because of their net negative charge hampering them to enter the cell. The reduction site is apparently cell surface, or the transplasma membrane electron transport.[21] The reaction product is water-soluble formazan. Therefore, one reaction step is eliminated compared with the MTT assay since there is no need for using organic solvents. The WST-8 assay results may be influenced by the similar factors as MTT since they principally resemble.[22] Resazurin assay is a fluorescent viability assay based on detecting the cellular metabolic activity. Blue non-fluorescent resazurin is reduced to pink highly fluorescent resorufin by dehydrogenase enzymes located in mitochondria, cytosol and microsomes of metabolically active cells. Therefore, the amount of resorufin produced is proportional to the number of metabolically active cells.[23] Lactate dehydrogenase (LDH) assay is assessing the activity of extracellular LDH released from cells into the extracellular space after irreversible cell damage accompanied by cell membrane injury. Among the advantages of the LDH assay are speed, simplicity and reliability. Moreover, when evaluating this assay, the cells themselves are not taking part in the reaction. Since the LDH is released outside the cell, its activity is quantified from the supernatant.[24] The MultiTox-Glo Multiplex Cytotoxicity Assay™ (further termed "MultiTox") is a commercial kit for measuring a relative number of live and dead cells. This assay measures two protease activities: one is a marker of cell viability, the other determines the number of dead cells. In this study, we used only live cell detection based on measuring cell-permeant peptide substrate that is cleaved by live-cell protease. This generates a fluorescent signal proportional to the number of living cells.[25]

This study provides a deeper insight into limitations of individual viability assays for the toxicity evaluation of BP nanoparticles. Further, flow-cytometry and quantitative phase time-lapse imaging is employed to clarify the differences among individual toxicity assays that are usually disregarded in studies determining the safety of nanomaterials.

Results and Discussion

Synthesis and characterization of black phosphorus

Black phosphorus (BP) was synthesized by high pressure conversion of red phosphorus. The red phosphorus synthesized was exfoliated by share-force milling in DMF.[26] The morphology of BP nanoparticles was investigated by AFM and TEM (Figure 2). The AFM shows the particles lateral size in the range of 100–300 nm with thickness in the range of 5 to 60 nm. The morphology of particles together with height profile are shown in Figure 2a, b. The small size of the particles was also confirmed by TEM which shows the aggregates of nanoplates with size in the range of tenth to few hundred nanometers. The TEM image with SAED and corresponding HR-TEM image are shown on Figure 2c, d.

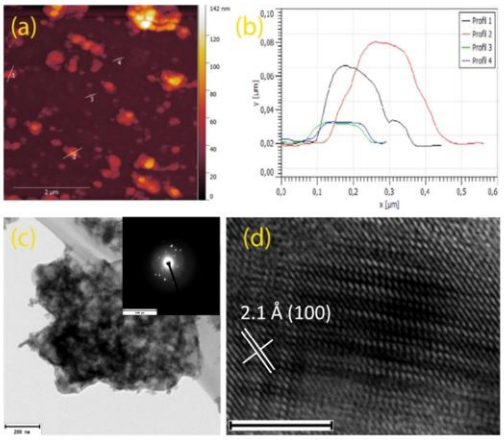

Figure 2. (a) Morphology and (b) height profile of BP nanoparticles, (c) the TEM image and (d) corresponding HR-TEM image (scale bar corresponds to 5 nm).

The X-ray diffraction shows significant broadening of diffraction pattern. The broadening of diffraction pattern corresponds to crystallite size in the range of 10 to 50 nm (Figure 3). The Raman spectroscopy shows the presence of three dominant phonon modes A1g, B2g and A2g characteristic for black phosphorus. The Raman spectra are shown on Figure 3a. The X-ray diffraction shows significant broadening of diffraction pattern (Figure 3b). The crystallite sizes were refined according to the Scherrer formula. The diffraction pattern broadening in (0*k*0) direction correspond to the crystallite size of 33 nm. The broadening originating from in-plane diffraction pattern correspond to the crystallite size in the range of 5–20 nm for indi-

© 2019 Wiley-VCH Verlag GmbH & Co. KGaA, Weinheim

ChemPubSoc Europe

CHEMISTRY A European Journal Full Paper

15213765, 2019, 1, Downloaded from https://chemistry-europe.onlinelibrary.wiley.com/doi/10.1002/chem.201804434 by Masaryk University, Wiley Online Library on [17/02/2025]. See the Terms and Conditions (https://onlinelibrary.wiley.com/terms-and-conditions) on Wiley Online Library for rules of use; OA articles are governed by the applicable Creative Commons License

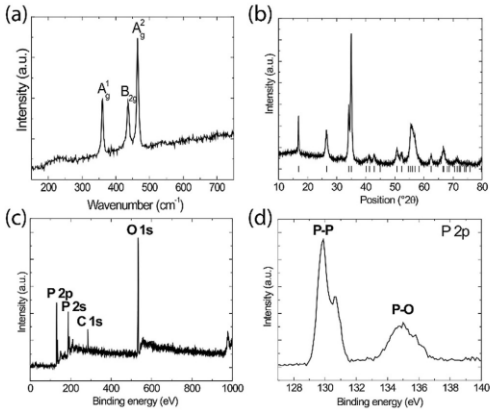

Figure 3. (a) Raman spectra of BP nanoparticles, (b) the X-ray diffractogram, (c) the survey XPS spectra and (d) the high-resolution P 2p spectra.

vidual crystallographic planes. The real particle sizes are bigger since each particle can be composed of several crystallites.[10,27] The chemical composition was verified by X-ray photoelectron spectroscopy. The survey XPS spectra show the presence of phosphorus (P 2p and P 2s characteristic peaks) as well as carbon from surface adsorption and oxygen from surface adsorption and oxygen from surface oxidation (Figure 3c). The oxidation of exfoliated BP in aqueous environment shows two peaks at 130 eV characteristic for P–P bonds in BP and broad P–O bond at 135 eV (see high-resolution XPS spectra of P 2p region on the Figure 3d).

Cell mass calculation

Two cell lines were selected for the BP interference experiments. These were not chosen because of their tissue origin, but due to their different size, since we expect the BP toxicity to be also cell size/mass dependent. A2780 cell line represents the population of cells with smaller size, PC-3 cell culture is a representative of cell line with cells of greater diameter. An interesting phenomenon concerning another 2D nanomaterial, graphene oxide (GO), was formerly observed in a study by Chang et al.[28] They found out that the cytotoxicity of GO particles and reduced graphene oxide (rGO) sheets particle is size-dependent.[28] Similar impact of cellular size/mass on cytotoxicity might be also expected. Therefore, A2780 and PC-3 cells were characterized with respect to their morphology using quantitative phase imaging (Figure 4a, b, respectively).

All analysed parameters (Table 2) were calculated as an average of values acquired by image analysis of 200 cells for each cell line. PC-3 cell mass was more than twice as high than the A2780 cell mass; 574.8 pg and 272.0 pg, respectively. Simultaneously, PC-3 cell area was more than four times bigger than in the case of A2780 cells; 1218.2 μm^2 and 294.8 μm^2, respectively.

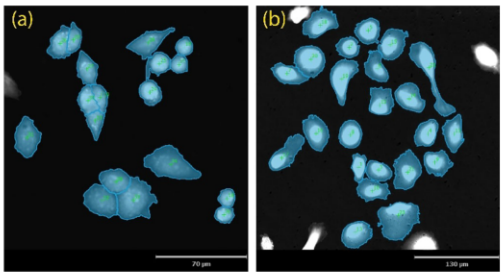

Figure 4. Morphological characterization of (a) A2780 and (b) PC-3 cell line. Example of quantitative phase image segmentation used for further analysis. For each cell line 200 randomly chosen cells were analysed. Average A2780 cell mass was 272.0 ± 144.9, average PC-3 cell mass 574.8 ± 255.1.

Table 2. Morphological characterization of A2780 and PC-3 cell line. Morphological parameters were acquired after quantitative phase image segmentation. For each cell line 200 randomly chosen cells were analyzed.

	Mass [pg]	Area [mm^2]	Perimeter [μm]	Circularity [%]
A2780	272.0 ± 144.9	294.8 ± 242.1	74.1 ± 33.6	67.9 ± 13.0
PC-3	574.8 ± 255.1	1218.2 ± 469.1	161.8 ± 43.2	59.9 ± 14.6

Cytotoxicity assessment of black phosphorus

The cytotoxicity of the BP particles was assessed in two cell lines (Figure 5): human ovarian cancer cell line A2780 and human prostate cancer cell line PC-3. Cell cultures were exposed to BP treatment in a broad concentration range 0–400 $\mu g\,mL^{-1}$ for 24 hours. In this study, we used BP in the form of a colloidal solution in DMF (dimethylformamide). Organic solvents are known for damaging the cellular structures and inducing cytotoxicity.[29] Therefore, to exclude the additional secondary toxicity caused by DMF solvent and misinterpretation of BP toxic effect, DMF was separated from the particles by double centrifugation (14000 rpm, 4 °C, 60 min) followed by washing with sterile water.

First, the toxicity of BP in A2780 cell line was assessed (Figure 5a). In general, the toxicity of BP particles differed significantly depending on the cytotoxicity assay used. The BP half-maximal inhibition concentrations (IC_{50} values) for the ovarian cancer cell line A2780 and BP were 82.5 ± 3.3 $\mu g\,mL^{-1}$ for MTT assay, 61.0 ± 7.8 $\mu g\,mL^{-1}$ for WST-8 assay, 47.7 ± 6.1 $\mu g\,mL^{-1}$ for resazurin assay, 236.9 ± 27.8 $\mu g\,mL^{-1}$ for LDH assay, and 66.7 ± 3.7 for MultiTox-Glo assay (Table 3).

After that, we assessed the toxicity of BP nanomaterial against PC-3 cells (Figure 5b). The toxicity of BP particles again varied according to the assay used. The IC_{50} values assessed by individual assays were determined as follows: ≥ 400 $\mu g\,mL^{-1}$ for MTT assay, 144.1 ± 13.3 $\mu g\,mL^{-1}$ for WST-8 assay, 90.0 ± 1.7 $\mu g\,mL^{-1}$ for resazurin assay, 106.4 ± 12.7 $\mu g\,mL^{-1}$ for LDH assay, and ≥ 400 $\mu g\,mL^{-1}$ for MultiTox assay (Table 3). In general, all methods used confirmed relatively low cytotoxicity of BP

© 2019 Wiley-VCH Verlag GmbH & Co. KGaA, Weinheim

ChemPubSoc Europe

CHEMISTRY A European Journal Full Paper

15213765, 2019, 1, Downloaded from https://chemistry-europe.onlinelibrary.wiley.com/doi/10.1002/chem.201804434 by Masaryk University, Wiley Online Library on [17/02/2025]. See the Terms and Conditions (https://onlinelibrary.wiley.com/terms-and-conditions) on Wiley Online Library for rules of use; OA articles are governed by the applicable Creative Commons License

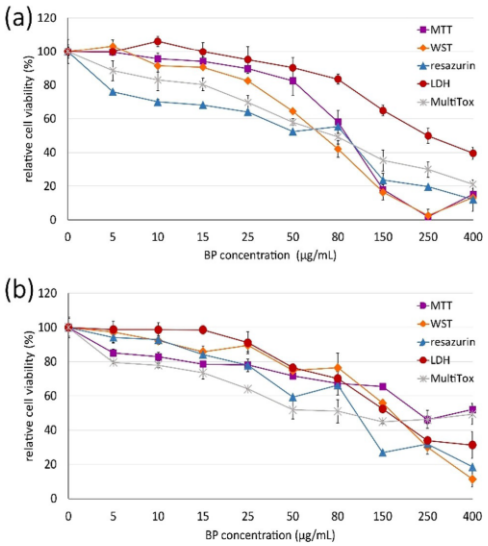

Figure 5. Relative viability of (a) ovarian cancer cell line A2780 and (b) prostate cancer cell line PC-3 after administration of BP assessed by MTT assay (purple), WST-8 assay (orange), resazurin assay (blue), LDH assay (red), and MultiTox-Glo assay (grey). The *x* axis represents BP concentration, range 0–400 μg mL^{-1}, the *y* axis represents relative cell viability. Values are average of three independent measurements, each performed in tetraplicate. Data are displayed as mean ± SD.

Table 3. Comparison of half-maximal inhibition concentration values (IC_{50}) for individual cell lines and assays used for their determination. Data are displayed as mean ± SD.

	IC_{50} A2780 [μg mL^{-1}]	IC_{50} PC-3 [μg mL^{-1}]
MTT	82.5 ± 3.3	≥400
WST-8	61.0 ± 7.8	144.1 ± 13.3
resazurin	47.7 ± 6.1	90.0 ± 1.7
LDH assay	236.9 ± 27.8	106.4 ± 12.7
MultiTox	66.7 ± 3.7	≥400

for both cell lines up to the concentration of around 15 μg mL^{-1}. Similar toxicity of BP was obtained also in our previous study.[6] For this BP concentration the lowest viability was determined by resazurin assay for both cell lines, 68.1% for A2780 and 84.2% for PC-3 cell line, the highest viability was again for both cell lines assessed by LDH assay, 99.9% for A2780 cell line and 98.6% for PC-3 cell line.

The percentages of viable cells differed significantly among the respective type of viability assessment, various BP concentrations applied and cell lines. Among all assays the biggest difference in determined viability values after application of the same BP concentration was of 48.5% in the case of A2780 cell line (applied BP concentration 150 μg mL^{-1}) and the in the case of PC-3 cell line of about 40.7% (applied BP concentration 400 μg mL^{-1}). In general, all assays except the LDH determined PC-3 cell line to be less sensitive towards BP effect, especially in higher BP concentrations.

In overall, the results obtained from all five cytotoxicity assays differed extensively highlighting both, their high degree of mutual inconsistency when assessing the BP cytotoxicity and apparently also considerable differences among A2780 and PC-3 cell lines concerning their sensitivity towards BP nanoparticles. Recently, Song et al. reported concentration- and time-dependent toxicity of layered BP against fibroblasts using WST-8 kit.[30] After 24 h treatment, they did not detect severe signs of toxicity (cell viability around 82%) up to the concentration of 4 μg mL^{-1} BP. In our study, similar viability (82%) was determined using WST-8 after application of 25 μg mL^{-1} of BP to A2780 cells (the PC-3 cells were even less sensitive to the BP presence). However, not all types of cell death are necessarily accompanied with the reduction of mitochondrial enzymes activity, or LDH leakage out of the cell. This again highlights the need to combine several types of techniques for cytotoxicity measurement. In general, we should be fully aware of that even when analysing other types of nanomaterials, similar degree of inconsistency between individual cytotoxicity assessments and cell lines might be expected. To determine which assay reflects the real cell viability most accurately, Annexin V-FITC/PI staining was subsequently performed.

The background signal of BP particles was determined in the concentration range from 0 to 400 μg mL^{-1} for both cell lines and all the assays except LDH assay (Figure 6). In LDH assay the particles are not presented in the reaction, therefore the BP particle background signal was not defined.

As for the BP particles' interference, the MTT, WST-8, and resazurin assays show similar patterns in BP-induced background signal. In these, an increase of background signal grew proportionally with the BP concentration, starting to be significantly increased from the concentration around 50–80 μg mL^{-1}. This trend might be attributed to their similar principle, for example, measurement of the similar set of enzyme activities. In the MTT assay the background signal comprised from 0–94.2% (A2780) and 0–40.9% (PC-3) of the total signal (peaking for A2780 and PC-3 cells in the BP concentration range of 250 and 400 μg mL^{-1}, respectively), in the WST-8 assay from 0–93.1% (A2780) and 89.6% (PC-3) of signal (peaking for A2780 and PC-3 cells in the BP concentration 250 and 400 μg mL^{-1}, respectively), in resazurin assay from 0–86.8% (A2780) and 83.8% (PC-3) of signal (peaking in the BP concentration 400 μg mL^{-1}). The MultiTox assay, based on the measurement of protease activity, showed mildest fluctuations of background signal through the whole concentration range ranging from 0–31.9% (A2780) and 27.9% (PC-3) of signal (peaking in the BP concentration 400 μg mL^{-1}).

In terms of the BP interference, we may consider LDH and MultiTox as the most suitable methods for determination of BP toxicity: The LDH assay because of the lack of background signal rising from the absence of BP particles. The MultiTox assay was then chosen due to the mildest fluctuations in background signal across the whole concentration range.

© 2019 Wiley-VCH Verlag GmbH & Co. KGaA, Weinheim

ChemPubSoc Europe

CHEMISTRY A European Journal Full Paper

15213765, 2019, 1, Downloaded from https://chemistry-europe.onlinelibrary.wiley.com/doi/10.1002/chem.201804434 by Masaryk University, Wiley Online Library on [17/02/2025]. See the Terms and Conditions (https://onlinelibrary.wiley.com/terms-and-conditions) on Wiley Online Library for rules of use; OA articles are governed by the applicable Creative Commons License

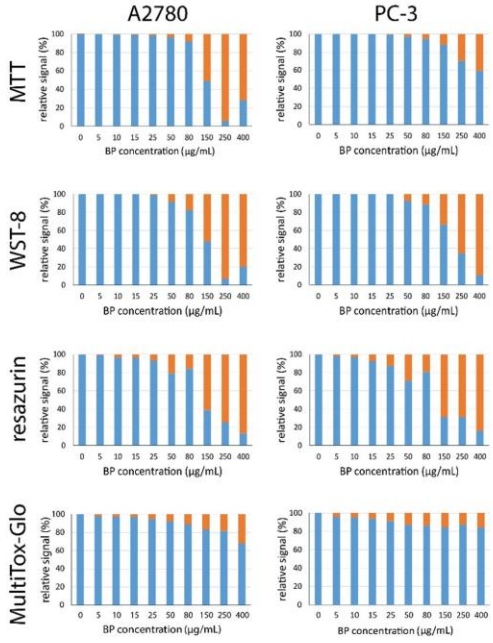

Figure 6. Participation of BP background (orange) on the final signal. BP in the concentration ranging from 0 to 400 $\mu g\,mL^{-1}$. The BP background signal in LDH assay is not stated since the BP particles are not taking part in the cytotoxicity determining reaction. The *x* axis represents BP concentration ($\mu g\,mL^{-1}$), the *y* axis stands for relative signal (%). Values are average of three independent measurements, each performed in tertaplicate.

Annexin V/propidium iodide flow cytometry

The accuracy of toxicity assessments was verified by flow-cytometric analysis using Annexin V-FITC/PI staining. The A2780 and PC-3 cells were treated with 0, 25, 50, 80, and 400 $\mu g\,mL^{-1}$ BP. Individual cell stages were identified by the extent of Annexin V expression on the surface of cells and total propidium iodide (PI) uptake using flow cytometry. In the lower BP concentration range (up to 80 $\mu g\,mL^{-1}$ BP), the A2780 cells maintained a high viability (more than 80%), however, the highest BP concentration led almost directly to cell death associated with the rupture of plasma membrane (primary, or secondary necrosis): Annexin V+/PI+ cells (Figure S1, Table S1). In the PC-3 cells these processes remained rather low (less than 5.5%) up to the concentration of 80 $\mu g\,mL^{-1}$ BP, but unlike the A2780 cells percentage of PI− cells exposing phosphatidylserine (PS) on the outer leaflet of an intact plasma membrane (early apoptotic, or early oncotic): Annexin V+/PI−, was gradually increasing (up to nearly 21% compared to less than 8% in case of A2780 cells). Generally, in the PC-3 cells BP administration primarily induced cell death associated with the exposure of PS in the outer leaflet of the plasma membrane of PI negative cells after administration of lower BP concentrations, the necrotic processes were accompanied to a larger extent of necrotic processes accompanied with the loss of the plasma membrane barrier function occurred only after administration of the highest BP concentration, 400 $\mu g\,mL^{-1}$. Rupture of the cell membrane commonly associated with the necrotic processes was largely occurring after administration of 400 $\mu g\,mL^{-1}$ of BP to the smaller A2780 cells (Figure 7). Only 4.73% of the cells remained viable and cell death without plasma membrane rupture stands just for less than 5% of cell deaths, while the necrotic processes were the cause of cell death in almost 66.23% of cases (Table 4). Different results

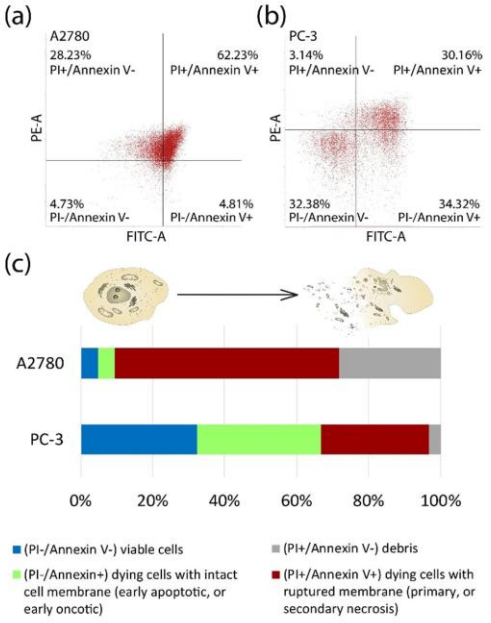

Figure 7. Distribution of viable, early apoptotic, late apoptotic and necrotic (a) A2780 cells and (b) PC-3 cells treated with 400 $\mu g\,mL^{-1}$ BP analysed by the extent of Annexin V expression on the surface of cells and total PI uptake using flow cytometry. (c) Diagram showing percentage representation of A2780 and PC-3 cells treated with 400 $\mu g\,mL^{-1}$ BP in various states determined using flow cytometry; viable cells (blue), early apoptotic (green), late apoptotic and necrotic stages (red) and cellular debris (grey).

Table 4. Representation of viable, early apoptotic, late apoptotic and necrotic A2780 cells and PC-3 cells treated with 400 $\mu g\,mL^{-1}$ BP analysed by the extent of expression of Annexin V on the surface of cells and total PI uptake using flow cytometry expressed in percentages; viable cells (PI−/Annexin V−), early apoptotic (PI−/Annexin V+), late apoptotic and necrotic stages (PI+/Annexin V+) and cellular debris.

	PI−/Annexin−: viable cells	PI−/Annexin+: dying cells with intact membrane	PI+/Annexin+: dying cells with ruptured membrane	PI+/Annexin−: debris
A2780	4.73	4.81	62.23	28.23
PC−3	32.38	34.32	30.16	3.14

© 2019 Wiley-VCH Verlag GmbH & Co. KGaA, Weinheim

ChemPubSoc Europe

CHEMISTRY A European Journal Full Paper

15213765, 2019, 1, Downloaded from https://chemistry-europe.onlinelibrary.wiley.com/doi/10.1002/chem.201804434 by Masaryk University, Wiley Online Library on [17/02/2025]. See the Terms and Conditions (https://onlinelibrary.wiley.com/terms-and-conditions) on Wiley Online Library for rules of use; OA articles are governed by the applicable Creative Commons License

were obtained after application of the same BP concentration to PC-3 cells, where more than 32.38% of PC-3 cells remained viable, which is almost seven times more than in the case of the A2780 cell line. The percentage of early apoptotic PC-3 cells was about 34.32% (7-times more than in the A2780 cell line) and the extent of necrotic processes was just 30.16% (twice less than in A2780 cell line). We have shown that BP might induce various level of cellular damage and employ diverse cell death mechanisms depending on the cell line selected and concentration of BP used.

Interestingly, treating A2780 cell with 400 $\mu g\,mL^{-1}$ BP increased the percentage of cellular debris nearly nine times (3.14% for PC-3 cells and 28.23% for A2780 cells). This can be most likely attributed to the presence of apoptotic bodies and most importantly to the disseminated nuclei, organelles and cellular residues released after the cell membrane rupture as a result of intensive necrotic processes. The extent of cellular debris is therefore most evident in A2780 cells after application of the highest BP concentration.

Among the assays mentioned above, the LDH assay at the first glance might seem as the best choice for the toxicity assessment of nanomaterials. The nanomaterials are not taking part in the reaction and therefore, the contribution of unwanted interactions of nanomaterial with the assay's reagents are prevented. Nevertheless, according to our observations, the LDH assay is not optimal for the toxicity determination of BP particles, and this for three reasons: firstly, since the principle of this assessment resides in measuring of released LDH after cell membrane rupture, it is not possible to detect cells undergoing early apoptosis using this assessment. LDH is only released from apoptotic blebs after secondary necrosis occurs.[31] As our results from follow-up flow-cytometry analysis revealed, the proportion of the BP-induced apoptotic cells may extensively differ among cell lines. Therefore, LDH assay may underestimate the real material toxicity by not detecting early apoptotic processes. Secondly, another problem arises if the percentage of material-induced apoptotic cells differs between cell lines extensively as in this case. If the toxicity would be assessed only by LDH assay the cells undergoing apoptosis would be not detected and the toxicity results would be consequently incomparable and misleading. And finally, the level of *LDHA* gene expression might greatly differ between the cell lines. In fact, A2780 and PC-3 cells are not an exception, PC-3 cells were identified to overexpress *LDHA*.[32] This explains why the LDH kit among all other assays was the only one which identified PC-3 cells to be more sensitive to the BP administration, even though according to the flow-cytometry data and the level of induced primary and secondary necrosis it should be the other way around.

The flow-cytometry data revealed a concentration dependent toxicity of BP correspondingly with the data acquired from viability assessment. More specifically, in the case of A2780 cells the percentage of Annexin V+/PI+ cells increased with increasing BP concentration, with the most rapid growth within the concentration range 80–400 $\mu g\,mL^{-1}$. In the PC-3 cell line, the percentage of Annexin V+/PI+ cells also gradually increased with increasing BP concentration, although even more crucial was the presence of early apoptotic processes. Therefore, the Annexin V-FITC/PI staining study helped us to further identify another phenomenon influencing the toxicity assays outputs. After administration of the same BP concentration, cells of different size may have very distinct fate. A limited capability to detect more types of frequently occurring cell death events is one of the reasons why some of the assays might be not suitable for the nanoparticle toxicity evaluation. For example, the LDH assay measures enzymatic activity of LDH released from cells undergoing necrosis after cell membrane rupture. Nevertheless, no LDH is released during early apoptosis[33] and therefore, LDH assay cannot detect it. This statement is supported also by the toxicity data where all viability assays except the LDH assay identified A2780 cells to be more sensitive to the BP effect than PC-3 cells (Table 3). Flow cytometric data were in general in agreement with the MTT and MultiTox assay. However, since MTT evinces a concentration-dependent interference, the MultiTox assay was among other four assays identified to be the most suitable for assessing the BP nanotoxicity. It should be noted, that each of these assays has its own advantages and limitations. Thus, it is absolutely crucial to be aware of pitfalls each of them may be bringing. Therefore, to avoid false positive and false negative results, the combination of at least two well-established methods is highly recommended.

Time-lapse holographic microscopy

To investigate the interaction of BP with cells in more detail, quantitative phase time-lapse imaging was employed. Time-lapse experiments are especially beneficial when analysing material toxicity since, unlike the other "black box end-point methods", enable understanding the accompanied processes not only in context, but also in real time. Time-lapse holographic microscopy is capable of automatic cell segmentation and real-time data quantification (Figure 8). After treating the cells with 80 $\mu g\,mL^{-1}$ BP, amount of accumulated BP was observed. A2780 and PC-3 cells show a very similar trend of BP accumulation with phosphorus average accumulation speed 1.86 and 2.73 percent of cell area covered per minute, respectively (Figure 8a). The PC-3 cells accumulated the BP more rapidly, especially within the first eight hours. The BP accumulation was gradually increasing within the 24 hours in both cell lines. Another evaluated parameter was cell mass (Figure 8b), which in the case of PC-3 cells slightly increased, while A2780 cells rather shrank in the course of time. This decrease in cellular mass is typical for dying cells.[34] Interestingly, the peaks in graphs for the A2780 BP accumulation curve and A2780 cell mass may be observed at the same time. Therefore, A2780 most likely reached a limiting amount of BP accumulated within the cell and their cell membrane ruptured because of induced necrotic processes. No such a phenomenon was observed within the PC-3 cell line. Accumulated BP caused a significant reduction in the motility in both cell lines (Figure 8c). Interestingly, the motility of PC-3 cells was increasing within the first three hours before it started to decrease. This motility drop was most likely caused by a large amount of BP accumu-

© 2019 Wiley-VCH Verlag GmbH & Co. KGaA, Weinheim

ChemPubSoc Europe

CHEMISTRY A European Journal Full Paper

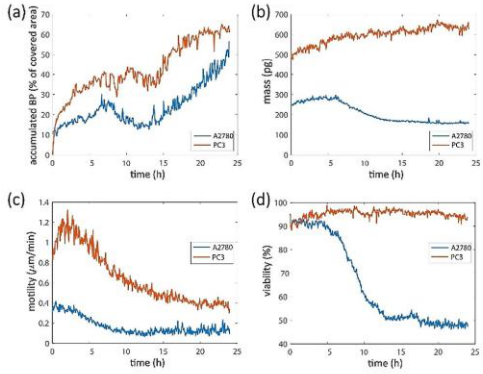

Figure 8. Quantitative phase time-lapse imaging of A2780 and PC-3 cells after administration of 80 $\mu g\,mL^{-1}$ BP. Several parameters were evaluated for both cell lines including (a) BP accumulation in A2780 (blue) and PC-3 cells (orange) expressed as a percentage of BP covered area, (b) changes in cell mass, (c) changes in cellular motility, and (d) cell viability. All the evaluated parameters were monitored for 24 hours for each cell line.

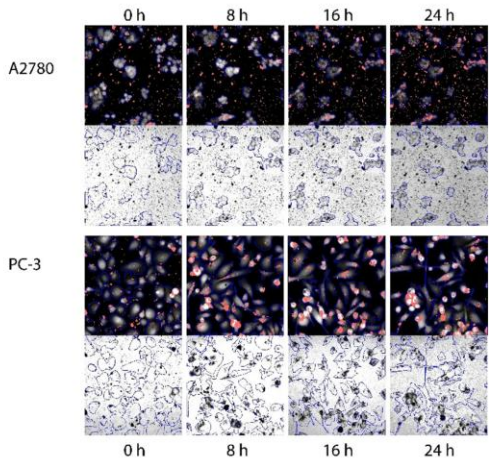

Figure 9. Colocalisation experiment of black phosphorus particles and A2780 and PC-3 cells carried out by merging of phase (upper black images) and amplitude imaging (lower grey images) 0, 8, 16, and 24 hours after BP administration. In phase images (upper black), cells are demarcated by blue line, BP particles are visible as a red dots clustering thru the course of time. In amplitude images (lower grey), cells are demarcated by blue line, BP particles are visible as a black material clustering thru the course of time.

lated within the cell. This oversize cargo then reduced the cell locomotion. On the other hand, the motility of A2780 cells was decreasing right from the first moments after administrating BP and was slowly declining for eight hours. After exceeding initial eight hours after BP administration, the A2780 cell locomotion almost stopped for the rest of the measurement. Since the A2780 cell size is lower than the PC-3 cell size, they are probably also capable only of carrying a lower amount of BP. This may be the cause of their earlier locomotion arrest. Finally, the cell viability was measured within the 24 hours (Figure 8d). According to the data acquired by quantitative phase imaging administration of 80 $\mu g\,mL^{-1}$ BP did not reduce the PC-3 viability significantly while the A2780 viability decreased to 50%. Interestingly, unlike the A2780 cells, the PC-3 cells seem to absorb BP actively. This can be seen from colocalization experiments and the videos (Figure 9, video S1 and video S2, respectively).

Conclusions

In vitro cytotoxicity assays are common tools for the general safety assessment of nanomaterials as they have a fundamental role in the prediction of their safety for humans, animals and the environment. The wide employment of viability assays in the toxicity evaluation of nanoparticles led in some cases to the ignoring of their biochemical principle, possible interferences and limitations. Here we reported the importance of considering the type of cell death BP induces and the variability of its effect among individual cell lines. A comparison of five assays, which are routinely used for the cytotoxicity evaluation, revealed their inconsistency in the BP toxicity assessment. This was attributed to several phenomena: a different level of background signal BP is inducing in individual assays, different response of distinct cell lines to the BP presence and finally to the nature of each assay which are based on different principles and do not have to assess all the cellular events equally. Finally, a commercial assay which is based on measurement of protease activity, was concluded to be the most suitable assay for determining BP particles' toxicity. It shows the lowest background signal and secondly, the data are in the satisfactory level of agreement with flow-cytometric data and quantitative phase imaging by holographic microscope. These time-lapse experiments obtained by holographic microscope were found to be exceptionally beneficial since these provided an understanding of the accompanied processes in context and in real time. In a summary, our data highlighted the importance of combining several cytotoxicity assessments and the indispensability of determining the type of cell death that the cells are undergoing after administration of nanomaterials. We should be aware of the fact, that BP particles might induce distinct processes in different cell lines. It is absolutely crucial to select the most appropriate method, or to combine it with principally different one, as well as to rigorously evaluate the data these might provide.

Experimental Section

Material preparation

Synthesis of black phosphorus was performed by wrapping the red phosphorus (10 g; 99.999%, Sigma–Aldrich, Czech Republic) in graphite foil and loading it in the high pressure/high-temperature uniaxial pressing apparatus of 20 mm size. After that, the sample was exhibited to the pressure of 6 GPa and the temperature of

© 2019 Wiley-VCH Verlag GmbH & Co. KGaA, Weinheim

15213765, 2019, 1, Downloaded from https://chemistry-europe.onlinelibrary.wiley.com/doi/10.1002/chem.201804434 by Masaryk University, Wiley Online Library on [17/02/2025]. See the Terms and Conditions (https://onlinelibrary.wiley.com/terms-and-conditions) on Wiley Online Library for rules of use; OA articles are governed by the applicable Creative Commons License

ChemPubSoc Europe

CHEMISTRY A European Journal Full Paper

15213765, 2019, 1, Downloaded from https://chemistry-europe.onlinelibrary.wiley.com/doi/10.1002/chem.201804434 by Masaryk University, Wiley Online Library on [17/02/2025]. See the Terms and Conditions (https://onlinelibrary.wiley.com/terms-and-conditions) on Wiley Online Library for rules of use; OA articles are governed by the applicable Creative Commons License

600 °C for 30 min, at a rate of 100 °C min^{-1}. Subsequently, the apparatus was cooled down to the room temperature at the same rate. The graphite foil was removed and resulted black phosphorus was grinded in the agate mortar. Powder containing particles of the size below 0.5 mm was obtained by subsequent sieving the material. Then it was dispersed in DMF by ultrasonication (6.25 mg mL^{-1}; 400 W; 15 min) followed by milling under argon atmosphere in the share force milling apparatus at 17000 rpm in a glass jacketed vessel at 15 °C for 1 h.

Material characterization

X-ray powder diffraction data were collected at room temperature on Bruker D8 Discoverer (Bruker, Germany) powder diffractometer with parafocusing Bragg–Brentano geometry using $Cu_{K\alpha}$ radiation ($\lambda = 0.15418$ nm, $U = 40$ kV, $I = 40$ mA). Data were scanned over the angular range 10–80° (2θ) with a step size of 0.016° (2θ). Data evaluation was performed in the software package EVA. The AFM measurements were carried out on the Ntegra Spectra from NT-MDT. The surface scans were performed in a tapping (semi-contact) mode. Cantilevers with a spring constant of 1.5 kN m^{-1} equipped with a standard silicon tip with curvature radius lower than 10 nm were used for all measurements. For the measurement sample suspension (1 mg mL^{-1}) was drop-casted on freshly cleaved mica substrate. The measurement was performed under ambient condition with a scan rate of 1 Hz and scan line of 512. InVia Raman microscope (Renishaw, England) in backscattering geometry with CCD detector was used for Raman spectroscopy. DPSS laser (532 nm, 50 mW) with applied power of 5 mW and 50× magnification objective was used for the measurement. Instrument calibration was achieved with a silicon reference which gives a peak position at 520 cm^{-1} and a resolution of less than 1 cm^{-1}. The samples were suspended in deionized water (1 mg mL^{-1}) and ultrasonicated for 10 min. The suspension was deposited on a small piece of silicon wafer and dried. High resolution X-ray photoelectron spectroscopy (XPS) was performed using an ESCAProbeP spectrometer (Omicron Nanotechnology Ltd, Germany) with a monochromatic aluminum X-ray radiation source (1486.7 eV). Wide-scan surveys of all elements were performed, with subsequent high-resolution scans of the P 2p peak. Relative sensitivity factors were used to evaluate the carbon-to-oxygen (C/O) ratios from the survey spectra. The samples were placed on a conductive carrier made from a high purity silver bar. An electron gun was used to eliminate sample charging during measurement (1–5 V).

Chemical and biochemical reagents

RPMI-1640 medium, Ham's F12 medium, fetal bovine serum (FBS) (mycoplasma-free), penicillin-streptomycin and trypsin were purchased from PAA Laboratories GmbH (Pashing, Austria). Phosphate buffered saline (PBS) was purchased from Invitrogen Corp. (Carlsbad, CA, USA). Annexin-V-FLUOS Staining Kit was purchased from Roche (Mannheim, Germany). Cell Counting Kit-8 (for WST-8 assay) was obtained from Dojindo Laboratories (Kumamoto, Japan), Multi-Tox-Glo Multiplex Cytotoxicity Assay was purchased from Promega Corporation (Madison, WI, USA), Pierce LDH Cytotoxicity Assay Kit was purchased from Thermo Fischer Scientific (Waltham, MA, USA). Thiazolyl blue tetrazolium bromide (for MTT assay), resazurin sodium salt (for resazurin assay), ethylenediaminetetraacetic acid (EDTA), dimethyl sulfoxide (DMSO) and all other chemicals of ACS purity were purchased from Sigma Aldrich Co. (St. Louis, MO, USA), unless noted otherwise.

Cell line and cell culture

Two human cell lines were used in this study. The human ovarian cell line A2780 was established from a tumour tissue of an untreated patient with ovarian cancer. The cell line was cultivated in RPMI-1640 medium with 10% FBS supplemented with antibiotics (penicillin 100 U mL^{-1} and streptomycin 0.1 mg mL^{-1}). The PC-3 human prostate cell line established from a grade 4 prostatic adenocarcinoma and was cultivated in Ham's medium with 10% FBS supplemented with antibiotics (penicillin 100 U mL^{-1} and streptomycin 0.1 mg mL^{-1}). Cell lines chosen for this experiment were not selected because of some kind of clinical relevance, but rather because of their morphology since A2780 and PC-3 cells differ in size. We expect cellular morphology to be the factor influencing the particle intake. While A2780 cells are small, PC-3 cells are rather larger and possess larger surface area. The cells were grown in the incubator at 37 °C in humidified 5% CO_2 mixture with ambient air. Both cell cultures used in this study were purchased from Health Protection Agency Culture Collections (Salisbury, UK).

Cell mass calculation

Measurement of A2780 and PC-3 cellular size was performed by quantitative phase imaging by Tescan multimodal holographic microscope Q-PHASE. Cells were cultivated in Flow chambers μ-Slide I Lauer Family (Ibidi, Martinsried, Germany). To image enough number of cells in one field of view, objectives Nikon Plan 10/0.30 were chosen. Holograms were captured by CCD camera (XIMEA MR4021 MC-VELETA). The entire image reconstruction and image processing were performed in Q-PHASE control software. From each cell line 200 randomly selected cells were subjected image analysis. Cell dry mass values are derived according to Prescher, Bertozzi, and Wayne[35] from phase, according to Equation (1):

$$m = \frac{\varphi\lambda}{2\pi\alpha} \quad (1)$$

where m represents cell dry mass density (in pg μm^{-2}), φ detected phase (in rad), λ wavelength in μm (0.65 μm in Q-PHASE), and α specific refraction increment, which is ≈0.18 μm^3 pg^{-1}. Detected phase values are dependent on two spatially and temporally variable parameters; refractive index and thickness of the sample, according to Equation (2):

$$\varphi = \frac{2\pi(\mathrm{ns} - \mathrm{nm})ts}{\lambda} \quad (2)$$

where n_s and n_m are refractive indexes of sample and medium and t_s is a thickness of the sample (in μm).

Statistical analysis and image processing

Quantitative phase images were analysed with Q-PHASE control software, which includes segmentation based on watershed with region merging, followed by feature extraction (mass, circularity and position) for next analysis.

Preparation of particles for biological analysis

Biological experiments were initiated by sonicating the BP stock solution (6.25 mg mL^{-1} in a DMF) for 15 min in iced bath. The suspension of particles in desired amount was toped up with sterile water up to 500 μL and resulted suspension of particles was centrifuged (14000 rpm, 4 °C, 60 min). After that, the supernatant was removed, and sediment of particles was dispersed again in 1 mL of

© 2019 Wiley-VCH Verlag GmbH & Co. KGaA, Weinheim

ChemPubSoc Europe

CHEMISTRY A European Journal Full Paper

15213765, 2019, 1, Downloaded from https://chemistry-europe.onlinelibrary.wiley.com/doi/10.1002/chem.201804434 by Masaryk University, Wiley Online Library on [17/02/2025]. See the Terms and Conditions (https://onlinelibrary.wiley.com/terms-and-conditions) on Wiley Online Library for rules of use; OA articles are governed by the applicable Creative Commons License

sterile water and centrifuged (14000 rpm, 4 °C, 60 min). Particles were used for the further analysis after removing of supernatant and adding the amount of culture media required for analysis.

Cytotoxicity assessment of black phosphorus

MTT viability test: The A2780 cells were seeded on 96-well plate at density 1×10^4 cells/well in RPMI-1640 medium, containing both 10% FBS and 1% penicillin-streptomycin, incubated at 37 °C in humidified 5% CO_2 mixture. The PC-3 cells were seeded on 96-well plate at density 8×10^3 cells/well in Ham's medium, containing both 10% FBS and 1% penicillin-streptomycin, incubated also at 37 °C in humidified 5% CO_2 mixture. After 48 h, the cell culture medium was removed and replaced with a new media containing BP. The BP concentrations ranged from 0 to 400 $\mu g\,mL^{-1}$. After incubating the cells for 24 h 200 μL of medium containing 1 $mg\,mL^{-1}$ MTT reagent per well was added. Plates were kept in humidified atmosphere at 37 °C for 4 h, wrapped in the aluminium foil. After that, the medium containing MTT was exchanged with 200 μl/well of 99.9% DMSO to dissolve formazan crystals. Then, 25 μL/well of glycine buffer was added to DMSO, gently shaken, and the absorbance was read at a wavelength of 570 nm using Cytation 3 Imaging multimode imaging reader (BioTek Instruments, Winooski, VT, USA). The IC_{50} values were calculated by fitting the data with a logistic function to create sigmoidal dose-response curve. The curve is described by four variables: upper limit, lower limit, skewness of the function, and log IC_{50}. The IC_{50} values define a concentration of compound required to inhibit the cell growth by 50%. All the measurements were performed in tetraplicates.

WST-8 assay: Both the A2780 and the PC-3 cells were seeded at the same density as mentioned above and treated with BP in the same way and for the same time as in the case of MTT viability assay. The WST-8 assay was then performed according the manufacturer's instructions. The absorbance was measured at 450 nm using Cytation 3 Imaging multimode imaging reader (BioTek Instruments, Winooski, VT, USA). The IC_{50} value was defined. All the measurements were performed in tetraplicates.

LDH cytotoxicity assay: Both the A2780 and the PC-3 cells were seeded at the same density as mentioned above and treated with BP in the same way and for the same time as in the case of MTT viability assay. The LDH assay was then performed according the manufacturer's instructions. The absorbance was measured at 490 nm using Cytation 3 Imaging multimode imaging reader (BioTek Instruments, Winooski, VT, USA). The IC_{50} value was defined. All the measurements were performed in tetraplicates.

Resazurin viability assay: Both the A2780 and the PC-3 cells were seeded at the same density as mentioned above and treated with BP in the same way and for the same time as in the case of MTT viability assay. After incubating the cells for 24 h 100 μL of medium containing 0.15 $mg\,mL^{-1}$ resazurin reagent per well was added. Plates were kept in humidified atmosphere at 37 °C for 4 h, wrapped in the aluminium foil. After that, fluorescence was recorded using 560 nm excitation and 590 nm emission filter using Cytation 3 Imaging multimode imaging reader (BioTek Instruments, Winooski, VT, USA). The IC_{50} value was defined. All the measurements were performed in tetraplicates.

MultiTox-Glo multiplex cytotoxicity assay: Both the A2780 and the PC-3 cells were seeded at the same density as mentioned above and treated with BP in the same way and for the same time as in the case of MTT viability assay. After incubating the cells for 24 h, 50 μL of the GF-AFC reagent per well was added. Plates were wrapped in the aluminium foil, orbitally shaken to ensure homogeneity, and incubated in humidified atmosphere at 37 °C for 2 h. After that, fluorescence was recorded using 400 nm excitation and 505 nm emission filter using Cytation 3 Imaging multimode imaging reader (BioTek Instruments, Winooski, VT, USA). The IC_{50} value was defined. All the measurements were performed in tetraplicates.

Measurement of background signal

The background signal of BP particles in the concentration range from 0 to 400 $\mu g\,mL^{-1}$ for particular culture media and individual assays was measured as described in methods above without the presence of cells. The only exception was LDH assay in which the background signal cannot be measured since the BP particles are not taking part in the cytotoxicity determining reaction. In this assay, before the absorbance measurement the cellular supernatant is transferred to a new plate and mixed with a reaction mixture prepared from lyophilized substrate mix and assay buffer supplied by manufacturer.

Annexin V/propidium iodide flow-cytometry

Annexin-V-FLUOS Staining Kit (Roche Applied Science) was used for double-staining the cells with fluorescein isothiocyanate (FITC)/propidium iodide (PI) according to manufacturer's instructions to determine percentages of viable cells, early apoptotic cells, or late apoptotic and necrotic cells following the exposure to assorted concentrations of BP. The cells were seeded on a Petri dish ($d=$ 60 mm) and their number was recalculated in the way the final confluence there corresponds the confluence in a well of 96-well plate in viability assessments. After 48 h, the cells were treated with assorted concentrations of BP (amount of BP corresponding 0, 25, 50, 80, and 400 $\mu g\,mL^{-1}$ concentrations during viability assessments). Since the BP nanomaterial sediments on the bottom of the plates and dishes we concluded that the most relevant recalculation will be based on the surface area exposed to BP than on the concentration. The amount of BP applied was recalculated in this way, so it corresponds the BP amount applied in viability assessments. After 24 h treatment, the cells were harvested using a scraper and washed twice with PBS (centrifuged at 2000 rpm for 5 min). Then, they were resuspended in 100 μL of Annexin-V-FLUOS staining solution and incubated for 15 min at a laboratory temperature and in the dark. Cells were resuspended in 500 μL of incubation buffer and Annexin V-FITC binding was detected by flow cytometry (BD FACSVerse, BD Biosciences) using 488 nm excitation and 515 nm bandpass filter for fluorescein detection and filter >600 nm for PI detection. The data were analysed using the BD FACSuite software.

Time-lapse holographic microscopy

Quantitative phase imaging of living cells was obtained using Q-PHASE, the coherence-controlled holographic microscope, CCHM (Tescan, Brno, Czech Republic). The microscope setup is based on off-axis holography and incorporates a diffraction grating to allow imaging with both spatially and temporally low-coherent illumination. This leads to a high quality of QPI compared to coherent-illumination digital holographic microscopy (DHM) by suppressing coherence noise (speckles), interferences and diffraction artefacts, while the lateral resolution is enhanced closer to a standard light microscope. The off-axis configuration of the system enables a single shot QPI acquisition.[36]

Quantitative phase time-lapse imaging was initiated immediately after treating the cells with 80 $\mu g\,mL^{-1}$ BP. Time-lapse monitoring was performed for 24 h at a frame-rate of 1 frame/3 min. The cells

© 2019 Wiley-VCH Verlag GmbH & Co. KGaA, Weinheim

ChemPubSoc Europe

CHEMISTRY A European Journal Full Paper

15213765, 2019, 1, Downloaded from https://chemistry-europe.onlinelibrary.wiley.com/doi/10.1002/chem.201804434 by Masaryk University, Wiley Online Library on [17/02/2025]. See the Terms and Conditions (https://onlinelibrary.wiley.com/terms-and-conditions) on Wiley Online Library for rules of use; OA articles are governed by the applicable Creative Commons License

were observed in flow chambers μ-Slide I Luer Family Cat. No. 80196 (Ibidi, Martinsried, Germany) in RPMI-1640 (for A2780 cells) and Ham's medium (for PC-3 cells). Nikon Plan 10×/0.3 was used for both holographic observations. Interferograms for holography were taken using a CCD camera (XIMEA MR4021MC). The fluorescence mode used a solid-state light source (Lumencor Aura II) and a sCMOS camera (Andor Zyla 5.5, 2560×2160px) was used to capture the images.

The holographic raw data must be numerically reconstructed. The numerical reconstruction is performed by the custom software where the established methods of the fast Fourier-transform and phase unwrapping are implemented. The output from the software is an unwrapped phase image. This image has intrinsic high contrast and can be processed by an available image processing software.

Dry cell mass tracking and determination of the weight threshold for living cells

Single cell mass measurements were performed using the original Q-PHASE software, which provides dry cell mass and motility (cell centroid movement between frames) data for individual cells. The initial distribution of A2780 cell masses was log-normal, with a range of 130–500 pg. Most of the cells had dry mass $\geq$130 pg and $\leq$400 pg, only small fraction was larger with dry masses higher than 500 pg. At the time 0, all tracked cells in the population were alive (verified visually by coherence-controlled holographic microscopy), with cell dry mass $>$130 pg. Consequently, we determined the cell mass threshold of viable A2780 cells as 130 pg. Similarly, we determined viable PC-3 cells with threshold 250 pg, but no dead cells were observed.

Cell-phosphorus colocalization measurement

For the colocalization of BP particles and cells, the novel method based on the merging of phase and amplitude imaging was used. This method combines quantitative phase imaging of weakly scattering or absorbing objects (cells) with the reconstructed amplitude imaging (similar to the bright field microscopy) of amplitude objects (BP or metal particles) recalculated from the hologram. Phosphorus accumulation was analysed using MATLAB custom script. Cells were segmented by thresholding of quantitative phase image (threshold 0.07 pg μm^{-1}) followed by removing of small objects and holes ($<$100 px). Similarly, BP particles were segmented by thresholding of amplitude image (threshold 3000). Overlay of cells and phosphorus areas was used for computation of the amount of accumulated phosphorus, which was determined as percent of the area of the cells (foreground) covered by the phosphorus. Moreover, phosphorus above/under the cells were also considered, thus percentage of background (outside cells) covered area was subtracted as correction and average of 5 field of views were computed for every sample. The disadvantage of this approach is that we are not able to quantify the amount of phosphorus in volume units or concentration, but we can analyse an increase in its amount in the cells.

Acknowledgements

This work was supported in part by grants from the Czech Science Foundation (18-24089S and 17-11456S). Z.S. and D.B. were supported by specific university research (MSMT No. 20-SVV/2018). M.F. was supported also by Grant Agency of Masaryk University (MUNI/A/1157/2017). This work was supported by the project Advanced Functional Nanorobots (reg. No. CZ.02.1.01/0.0/0.0/15_003/0000444 financed by the EFRR). Further, we would like to acknowledge Dr. Petr Beneš and Tereza Kučírková from the Faculty of Science, Masaryk University for their kind help with the flow cytometry measurement.

Conflict of interest

The authors declare no conflict of interest.

Keywords: 2D nanomaterials · black phosphorus · cytotoxicity · holographic microscopy · interference · nanoparticles · viability

[1] F. Feng, J. C. Wu, C. Z. Wu, Y. Xie, *Small* **2015**, *11*, 654–666; S. Bai, Y. J. Xiong, *Sci. Adv. Mater.* **2015**, *7*, 2168–2181.
[2] H. J. Yin, Z. Y. Tang, *Chem. Soc. Rev.* **2016**, *45*, 4873–4891.
[3] Z. P. Smith, B. D. Freeman, *Angew. Chem. Int. Ed.* **2014**, *53*, 10286–10288; *Angew. Chem.* **2014**, *126*, 10452–10454.
[4] P. Bollella, G. Fusco, C. Tortolini, G. Sanzo, G. Favero, L. Gorton, R. Antiochia, *Biosens. Bioelectron.* **2017**, *89*, 152–166.
[5] G. H. Yang, C. Z. Zhu, D. Du, J. J. Zhu, Y. H. Lin, *Nanoscale* **2015**, *7*, 14217–14231; X. R. Gan, H. M. Zhao, X. Quan, *Biosens. Bioelectron.* **2017**, *89*, 56–71.
[6] M. Fojtu, X. Y. Chia, Z. Sofer, M. Masarik, M. Pumera, *Adv. Funct. Mater.* **2017**, *27*, 7.
[7] a) W. Tao, X. B. Zhu, X. H. Yu, X. W. Zeng, Q. L. Xiao, X. D. Zhang, X. Y. Ji, X. S. Wang, J. J. Shi, H. Zhang, L. Mei, *Adv. Mater.* **2017**, *29*, 10; b) X. B. Zhu, X. Y. Ji, N. Kong, Y. H. Chen, M. Mahmoudi, X. D. Xu, L. Ding, W. Tao, T. Cai, Y. J. Li, T. Gan, A. Barrett, Z. Bharwani, H. B. Chen, O. C. Farokhzad, *ACS Nano* **2018**, *12*, 2922–2938; c) S. G. Wang, Y. Chen, X. Li, W. Gao, L. L. Zhang, J. Liu, Y. Y. Zheng, H. R. Chen, J. L. Shi, *Advanced Materials* **2015**, *27*, 7117–7122; d) X. Y. Yang, X. Y. Zhang, Z. F. Liu, Y. F. Ma, Y. Huang, Y. Chen, *J. Phys. Chem. C* **2008**, *112*, 17554–17558; e) J. Q. Liu, L. Cui, D. Losic, *Acta Biomater.* **2013**, *9*, 9243–9257; f) N. S. Gao, J. P. Nie, H. F. Wang, C. Y. Xing, L. Mei, W. Xiong, X. W. Zeng, Z. C. Peng, *J. Biomed. Nanotechnol.* **2018**, *14*, 1883–1897.
[8] a) L. Cheng, C. Wang, L. Z. Feng, K. Yang, Z. Liu, *Chem. Rev.* **2014**, *114*, 10869–10939; b) C. X. Sun, L. Wen, J. F. Zeng, Y. Wang, Q. Sun, L. J. Deng, C. J. Zhao, Z. Li, *Biomaterials* **2016**, *91*, 81–89; c) Z. B. Sun, H. H. Xie, S. Y. Tang, X. F. Yu, Z. N. Guo, J. D. Shao, H. Zhang, H. Huang, H. Y. Wang, P. K. Chu, *Angew. Chem. Int. Ed.* **2015**, *54*, 11526–11530; *Angew. Chem.* **2015**, *127*, 11688–11692; d) Y. T. Zhao, L. P. Tong, Z. B. Li, N. Yang, H. D. Fu, L. Wu, H. D. Cui, W. H. Zhou, J. H. Wang, H. Y. Wang, P. K. Chu, X. F. Yu, *Chem. Mater.* **2017**, *29*, 7131–7139; e) H. Li, C. Soria, F. Griscelli, P. Opolon, J. Soria, P. Yeh, C. Legrand, J. P. Vannier, D. Belin, M. Perricaudet, H. Lu, *Human Gene Ther.* **2005**, *16*, 1157–1167; f) H. Wang, X. Z. Yang, W. Shao, S. C. Chen, J. F. Xie, X. D. Zhang, J. Wang, Y. Xie, *J. Am. Chem. Soc.* **2015**, *137*, 11376–11382; g) J. D. Shao, H. H. Xie, H. Huang, Z. B. Li, Z. B. Sun, Y. H. Xu, Q. L. Xiao, X. F. Yu, Y. T. Zhao, H. Zhang, H. Y. Wang, P. K. Chu, *Nat. Commun.* **2016**, *7*, 13.
[9] a) Z. Z. Feng, X. M. Liu, L. Tan, Z. D. Cui, X. J. Yang, Z. Y. Li, Y. F. Zheng, K. W. K. Yeung, S. L. Wu, *Small* **2018**, *14*, 16; b) X. Z. Xie, C. Y. Mao, X. M. Liu, Y. Z. Zhang, Z. D. Cui, X. J. Yang, K. W. K. Yeung, H. B. Pan, P. K. Chu, S. L. Wu, *ACS Appl. Mater. Interfaces* **2017**, *9*, 26417–26428; c) X. Z. Xie, C. Y. Mao, X. M. Liu, L. Tan, Z. D. Cui, X. J. Yang, S. L. Zhu, Z. Y. Li, X. B. Yuan, Y. F. Zheng, K. W. K. Yeung, P. K. Chu, S. L. Wu, *ACS Cent. Sci.* **2018**, *4*, 724–738; d) C. Y. Mao, Y. M. Xiang, X. M. Liu, Z. D. Cui, X. J. Yang, Z. Y. Li, S. L. Zhu, Y. F. Zheng, K. W. K. Yeung, S. L. Wu, *ACS Nano* **2018**, *12*, 1747–1759.
[10] L. Tan, J. Li, X. M. Liu, Z. D. Cui, X. J. Yang, K. W. K. Yeung, H. B. Pan, Y. F. Zheng, X. B. Wang, S. L. Wu, *Small* **2018**, *14*, 11.
[11] D. Y. Wang, W. Zhao, *Abstr. Pap. Am. Chem. Soc.* **2015**, *249*, 1.
[12] S. Sajjad, S. A. K. Leghari, A. Iqbal, *ACS Appl. Mater. Interfaces* **2017**, *9*, 43393–43414.

 © 2019 Wiley-VCH Verlag GmbH & Co. KGaA, Weinheim

ChemPubSoc Europe

CHEMISTRY A European Journal Full Paper

[13] a) W. Yang, L. Gan, H. Q. Li, T. Y. Zhai, *Inorg. Chem. Front.* **2016**, *3*, 433 – 451; b) R. Gusmão, Z. Sofer, M. Pumera, *Angew. Chem. Int. Ed.* **2017**, *56*, 8052; *Angew. Chem.* **2017**, *129*, 8164.
[14] H. Liu, Y. C. Du, Y. X. Deng, P. D. Ye, *Chem. Soc. Rev.* **2015**, *44*, 2732 – 2743; D. Y. Zhang, L. Gan, Y. Cao, Q. Wang, L. M. Qi, X. F. Guo, *Adv. Mater.* **2012**, *24*, 2715 – 2720.
[15] a) Y. T. Yew, Z. Sofer, C. C. Mayorga-Martinez, M. Pumer, *Mater. Chem. Front.* **2017**, *1*, 1130 – 1136; b) M. Qiu, Z. T. Sun, D. K. Sang, X. G. Han, H. Zhang, C. M. Niu, *Nanoscale* **2017**, *9*, 13384 – 13403; c) M. B. Erande, M. S. Pawar, D. J. Late, *ACS Appl. Mater. Interfaces* **2016**, *8*, 11548 – 11556; d) A. N. Cao, Z. Liu, S. S. Chu, M. H. Wu, Z. M. Ye, Z. W. Cai, Y. L. Chang, S. F. Wang, Q. H. Gong, Y. F. Liu, *Adv. Mater.* **2010**, *22*, 103; e) A. Ambrosi, Z. Sofer, M. Pumera, *Angew. Chem. Int. Ed.* **2017**, *56*, 10443; *Angew. Chem.* **2017**, *129*, 10579 f) D. Li, A. E. D. R. Castillo, H. Jussila, G. Ye, Z. Ren, J. Bai, X. Chen, H. Lipsanen, Z. Sun, F. Bonaccorso, *Appl. Mater. Today* **2016**, *4*, 17; g) Z. Sofer, D. Sedmidubsky, S. Huber, J. Luxa, D. Bousa, C. Boothroyd, M. Pumera, *Angew. Chem. Int. Ed.* **2016**, *55*, 3382; *Angew. Chem.* **2016**, *128*, 3443; h) C. C. Mayorga-Martinez, Z. Sofer, M. Pumera, *Angew. Chem. Int. Ed.* **2015**, *54*, 14317; *Angew. Chem.* **2015**, *127*, 14525.
[16] a) Y. C. Du, H. Liu, Y. X. Deng, P. D. Ye, *ACS Nano* **2014**, *8*, 10035 – 10042; b) J. Plutnar, Z. Sofer, M. Pumera, *ACS Nano* **2018**, *12*, 8390; c) N. M. Latiff, W. Z. Teo, Z. Sofer, A. C. Fisher, M. Pumera, *Chem. Eur. J.* **2015**, *21*, 13991 ; d) N. M. Latiff, C. C. Mayorga-Martinez, Z. Sofer, A. C. Fisher, M. Pumera, *Appl. Mater. Today* **2018**, *13*, 310.
[17] X. L. Han, R. Gelein, N. Corson, P. Wade-Mercer, J. K. Jiang, P. Biswas, J. N. Finkelstein, A. Elder, G. Oberdorster, *Toxicology* **2011**, *287*, 99 – 104; L. Belyanskaya, P. Manser, P. Spohn, A. Bruinink, P. Wick, *Carbon* **2007**, *45*, 2643 – 2648; J. M. Wörle-Knirsch, K. Pulskamp, H. F. Krug, *Nano Lett.* **2006**, *6*, 1261 – 1268; A. Casey, E. Herzog, M. Davoren, F. M. Lyng, H. J. Byrne, G. Chambers, *Carbon* **2007**, *45*, 1425 – 1432.
[18] R. Parboosing, G. Mzobe, L. Chonco, I. Moodley, *Med. Chem.* **2017**, *13*, 13 – 21.
[19] N. Latiff, W. Z. Teo, Z. Sofer, S. Huber, A. C. Fisher, M. Pumera, *RSC Adv.* **2015**, *5*, 67485 – 67492; A. Kroll, M. H. Pillukat, D. Hahn, J. Schnekenburger, *Eur. J. Pharm. Biopharm.* **2009**, *72*, 370 – 377.
[20] G. Diaz, M. Melis, A. Musinu, M. Piludu, M. Piras, A. M. Falchi, *Eur. J. Histochem.* **2007**, *51*, 213 – 218; Y. B. Liu, D. A. Peterson, H. Kimura, D. Schubert, *J. Neurochem.* **1997**, *69*, 581 – 593.
[21] M. V. Berridge, A. S. Tan, *Arch. Biochem. Biophys.* **1993**, *303*, 474 – 482.
[22] A. A. Stepanenko, V. V. Dmitrenko, *Gene* **2015**, *574*, 193 – 203.
[23] J. O'Brien, I. Wilson, T. Orton, F. Pognan, *Eur. J. Biochem.* **2000**, *267*, 5421 – 5426.
[24] G. Fotakis, J. A. Timbrell, *Toxicol. Lett.* **2006**, *160*, 171 – 177.
[25] T. L. Riss, R. A. Moravec, A. L. Niles in *Mammalian Cell Viability: Methods and Protocols, Vol. 740* (Ed.: M. J. Stoddart), Humana, Totowa, **2011**, pp. 103 – 114.
[26] Z. Sofer, D. Bousa, J. Luxa, V. Mazanek, M. Pumera, *Chem. Commun.* **2016**, *52*, 1563 – 1566.
[27] P. Scherrer in *Bestimmung der inneren Struktur und der Größe von Kolloidteilchen mittels Röntgenstrahlen, Vol. 2,* Springer, Berlin, Heidelberg, **1918**, pp. 98.
[28] S. Das, S. Singh, V. Singh, D. Joung, J. M. Dowding, D. Reid, J. Anderson, L. Zhai, S. I. Khondaker, W. T. Self, S. Seal, *Part. Part. Syst. Charact.* **2013**, *30*, 148 – 157; Y. L. Chang, S. T. Yang, J. H. Liu, E. Dong, Y. W. Wang, A. N. Cao, Y. F. Liu, H. F. Wang, *Toxicol. Lett.* **2011**, *200*, 201 – 210.
[29] H. J. Heipieper, F. J. Weber, J. Sikkema, H. Keweloh, J. A. M. Debont, *Trends Biotechnol.* **1994**, *12*, 409 – 415.
[30] S. J. Song, Y. C. Shin, H. U. Lee, B. Kim, D. W. Han, D. Lim, *Nanomaterials* **2018**, *8*, 10.
[31] M. Rayamajhi, Y. Zhang, E. Miao in *The Inflammasome: Methods and Protocols, Vol. 1040*, Humana, Totowa, **2013**, pp. 85 – 90.
[32] U. T. Shankavaram, S. Varma, D. Kane, M. Sunshine, K. K. Chary, W. C. Reinhold, Y. Pommier, J. N. Weinstein, *BMC Genomics* **2009**, *10*, 277; W. C. Reinhold, M. Sunshine, H. F. Liu, S. Varma, K. W. Kohn, J. Morris, J. Doroshow, Y. Pommier, *Cancer Res.* **2012**, *72*, 3499 – 3511.
[33] M. Maes, T. Vanhaecke, B. Cogliati, S. C. Yanguas, J. Willebrords, V. Rogiers, M. Vinken in *Protocols in In vitro Hepatocyte Research, Vol. 1250* Eds.: M. Vinken, V. Rogiers), Humana, Totowa, **2015**, pp. 349 – 361.
[34] T. A. Zangle, M. A. Teitell, *Nat. Methods* **2014**, *11*, 1221 – 1228.
[35] J. A. Prescher, C. R. Bertozzi, *Nat. Chem. Biol.* **2005**, *1*, 13 – 21; R. Wayne, *Light and Video Microscopy*, Academic Press, Burlington, **2008**.
[36] B. Gál, M. Vesely, J. Collakova, M. Nekulova, V. Juzova, R. Chmelik, P. Vesely, *PLoS One* **2017**, *12*(8): e0183399.

Manuscript received: August 30, 2018
Version of record online: December 13, 2018

© 2019 Wiley-VCH Verlag GmbH & Co. KGaA, Weinheim

15213765, 2019, 1, Downloaded from https://chemistry-europe.onlinelibrary.wiley.com/doi/10.1002/chem.201804434 by Masaryk University, Wiley Online Library on [17/02/2025]. See the Terms and Conditions (https://onlinelibrary.wiley.com/terms-and-conditions) on Wiley Online Library for rules of use; OA articles are governed by the applicable Creative Commons License

AMERICAN SOCIETY FOR MICROBIOLOGY | Antimicrobial Agents and Chemotherapy®

ANTIVIRAL AGENTS

Broad-Spectrum Antiviral Activity of 3′-Deoxy-3′-Fluoroadenosine against Emerging Flaviviruses

Luděk Eyer,[a,b] Pavel Svoboda,[a,c] Jan Balvan,[d,e] Tomáš Vičar,[d,f] Matina Raudenská,[e,g] Michal Štefánik,[a,e] Jan Haviernik,[a,i] Ivana Huvarová,[a] Petra Straková,[a] Ivo Rudolf,[h,i] Zdeněk Hubálek,[h] Katherine Seley-Radtke,[j] Erik de Clercq,[k] Daniel Růžek[a,b]

[a]Department of Virology, Veterinary Research Institute, Brno, Czech Republic
[b]Institute of Parasitology, Biology Centre of the Czech Academy of Sciences, Ceske Budejovice, Czech Republic
[c]Department of Pharmacology and Pharmacy, Faculty of Veterinary Medicine, University of Verterinary and Pharmaceutical Sciences Brno, Brno, Czech Republic
[d]Department of Pathological Physiology, Faculty of Medicine, Masaryk University, Brno, Czech Republic
[e]Department of Chemistry and Biochemistry, Mendel University in Brno, Brno, Czech Republic
[f]Department of Biomedical Engineering, Faculty of Electrical Engineering and Communication, Brno University of Technology, Brno, Czech Republic
[g]Department of Physiology, Faculty of Medicine, Masaryk University, Brno, Czech Republic
[h]Institute of Vertebrate Biology, Czech Academy of Sciences, Brno, Czech Republic
[i]Department of Experimental Biology, Masaryk University, Brno, Czech Republic
[j]Department of Chemistry and Biochemistry, University of Maryland, Baltimore County, Baltimore, Maryland, USA
[k]Rega Institute for Medical Research, KU Leuven, Leuven, Belgium

Luděk Eyer and Pavel Svoboda contributed equally to this work. Author order was determined both alphabetically and in order of decreasing seniority.

ABSTRACT Emerging flaviviruses are causative agents of severe and life-threatening diseases, against which no approved therapies are available. Among the nucleoside analogues, which represent a promising group of potentially therapeutic compounds, fluorine-substituted nucleosides are characterized by unique structural and functional properties. Despite having first been synthesized almost 5 decades ago, they still offer new therapeutic opportunities as inhibitors of essential viral or cellular enzymes active in nucleic acid replication/transcription or nucleoside/nucleotide metabolism. Here, we report evaluation of the antiflaviviral activity of 28 nucleoside analogues, each modified with a fluoro substituent at different positions of the ribose ring and/or heterocyclic nucleobase. Our antiviral screening revealed that 3′-deoxy-3′-fluoroadenosine exerted a low-micromolar antiviral effect against tick-borne encephalitis virus (TBEV), Zika virus, and West Nile virus (WNV) (EC_{50} values from $1.1 \pm 0.1\ \mu$M to $4.7 \pm 1.5\ \mu$M), which was manifested in host cell lines of neural and extraneural origin. The compound did not display any measurable cytotoxicity up to concentrations of $25\ \mu$M but had an observable cytostatic effect, resulting in suppression of cell proliferation at concentrations of $>12.5\ \mu$M. Novel approaches based on quantitative phase imaging using holographic microscopy were developed for advanced characterization of antiviral and cytotoxic profiles of 3′-deoxy-3′-fluoroadenosine *in vitro*. In addition to its antiviral activity in cell cultures, 3′-deoxy-3′-fluoroadenosine was active *in vivo* in mouse models of TBEV and WNV infection. Our results demonstrate that fluoro-modified nucleosides represent a group of bioactive molecules with excellent potential to serve as prospective broad-spectrum antivirals in antiviral research and drug development.

KEYWORDS nucleoside analogue, 3′-deoxy-3′-fluoroadenosine, flavivirus, tick-borne encephalitis virus, antiviral activity, cytotoxicity, mouse model

Emerging flaviviruses (genus *Flavivirus*, family *Flaviviridae*) are transmitted by blood-sucking arthropods, such as ticks or mosquitoes, and are causative agents of serious

Citation Eyer L, Svoboda P, Balvan J, Vičar T, Raudenská M, Štefánik M, Haviernik J, Huvarová I, Straková P, Rudolf I, Hubálek Z, Seley-Radtke K, de Clercq E, Růžek D. 2021. Broad-spectrum antiviral activity of 3′-deoxy-3′-fluoroadenosine against emerging flaviviruses. Antimicrob Agents Chemother 65:e01522-20. https://doi.org/10.1128/AAC.01522-20.

Copyright © 2021 American Society for Microbiology. All Rights Reserved.

Address correspondence to Luděk Eyer, eyer@vri.cz.

Received 17 July 2020
Returned for modification 10 August 2020
Accepted 14 November 2020
Accepted manuscript posted online 23 November 2020
Published 20 January 2021

Downloaded from https://journals.asm.org/journal/aac on 17 February 2025 by 147.251.135.113.

human diseases such as dengue fever, yellow fever, West Nile fever, Japanese encephalitis, and tick-borne encephalitis (1). More than 400 million clinical cases of flavivirus-induced infections are reported annually worldwide, which are in many cases fatal (2). No approved therapy is currently available against infections caused by medically important flaviviruses. Development of new and effective antiviral drugs and therapeutic strategies for infections caused by emerging flaviviruses and other viruses responsible for life-threatening diseases is extremely important. It is particularly crucial in the current era of increased global travel, as well as emerging issues with increasing numbers of zoonotic infections due to the loss of animal habitats, and the growing spread of viral vectors as a result of climate change.

Nucleoside/nucleotide analogues can alter essential biochemical processes by sufficiently mimicking the structure of natural nucleosides/nucleotides for cellular or viral enzyme recognition. This capability makes these compounds attractive candidates for treating various diseases, including those resulting from viral (3, 4), bacterial (5), fungal (6), or parasitic infections (7, 8), or various types of cancers (9, 10). As antivirals, nucleoside analogues operate via numerous modes of action, among which suppression of viral nucleic acid synthesis is considered particularly important due to their highly specific interactions with viral polymerases that subsequently result in premature DNA/RNA chain termination (11). Other modes of action for antiviral nucleosides include: (i) blocking the viral methyltransferases responsible for viral RNA methylation and capping (12, 13); (ii) suppression of *de novo* nucleotide biosynthesis and depletion of the cellular nucleotide pool (14); (iii) accumulation of mutations in viral genomes, leading to error catastrophe (15, 16); and (iv) immunomodulation that promotes the Th1 lymphocyte–based antiviral response (17).

Nucleoside analogues modified with a fluoro substituent at different positions of a sugar ring and/or heterocyclic (purine/pyrimidine) nucleobase were initially synthesized in the 1970s. Soon after, researchers noted unique properties that the fluorine imparts to the nucleoside scaffold (18, 19). In drug design, fluorine is often used as an isosteric replacement because of its similar size to hydrogen, as well as its similar electronegativity to the hydroxyl moiety in ribo/deoxyribonucleosides (20). Because of the exquisite electronegativity of fluorine, this substituent significantly influences the conformational properties of the nucleoside sugar ring by "locking" it into a specific conformation, e.g., in *C2′*-endo/*C3′*-exo, *C2′*-exo/*C3′*-endo or other variations of the envelope/half-chair pentose conformations. This effect can substantially influence the recognition of a nucleoside analogue by DNA/RNA polymerases, reverse transcriptases, and nucleoside/nucleotide kinases. These differences occur because each enzyme prefers a different nucleoside/nucleotide conformation, with the ultimate result being efficient enzyme inhibition and cessation of viral replication (21–23). Furthermore, fluorine increases the stability of neighboring bonds (e.g., *N*-glycosidic or phosphoester bonds), which renders fluoro-modified nucleosides resistant to unwanted catabolic degradation by nucleoside phosphorylases, esterases, and other intracellular hydrolases (21, 24). Finally, fluorine, when incorporated into a pyrimidine or purine base, considerably alters the steric and electronic properties of the base, as well as the hydrogen bonding interactions between the enzyme active site and nucleoside analogue (25–27). Based on these unique properties, use of fluorine substituents is widely agreed to be an advantageous drug modification, and numerous fluorine-substituted nucleoside-based drugs have been developed. Many of these candidates have shown potent anticancer activity (e.g., gemcitabine [2′-dideoxy-2′,2′-difluorocytidine] [28] or floxuridine [2′-deoxy-5-fluorouridine] [29]), while others have been approved to treat serious and life-threatening viral infections, e.g., sofosbuvir, a McGuigan ProTide of 2′-fluoro-2′-methyluridine for treatment of chronic hepatitis C (HCV) infections (30).

Here, we have evaluated the antiflaviviral activity of a series of 28 nucleoside analogues modified with a fluoro substituent at different positions of the ribose ring (predominantly at *C2′* and *C3′*) and/or at the *C2* or *C5* position of the heterocyclic nucleobase. We also tested several fluoro-modified arabino nucleosides. Our antiviral

Downloaded from https://journals.asm.org/journal/aac on 17 February 2025 by 147.251.135.113.

screening revealed that the vast majority of the investigated compounds showed no antiflaviviral effect or were substantially cytotoxic at the tested concentrations. Among the compounds we tested, however, 3′-deoxy-3′-fluoroadenosine exerted a high antiflaviviral potency *in vitro*, showing low-micromolar antiviral effects against tick-borne encephalitis virus (TBEV), Zika virus (ZIKV), and West Nile virus (WNV). 3′-Deoxy-3′-fluoroadenosine displayed observable cytostatic effects at high concentrations, but was well tolerated in the tested cell lines at compound levels of $<12.5\ \mu$M. In addition, a quantitative phase imaging (QPI) approach based on high-resolution holographic microscopy was developed and optimized for advanced characterization/description of antiviral efficacy and cytotoxicity of 3′-deoxy-3′-fluoroadenosine in cell culture. Finally, we also demonstrated an antiviral effect of 3′-deoxy-3′-fluoroadenosine in mouse models of TBEV and WNV infection. To the best of our knowledge, this study is one of the few to describe an antiviral effect of a fluoro-substituted nucleoside against emerging flaviviruses. It also is the first to demonstrate antiviral activity of fluorinated nucleosides against TBEV, a virus responsible for serious neuroinfections in Europe and Northeast Asia. Moreover, our work demonstrates that fluoro-modified nucleoside scaffolds represent an interesting group of bioactive molecules characterized by unique structural properties with potential for use in antiviral research, drug development, and structure optimization as prospective broad-spectrum antivirals.

RESULTS

Initial antiviral screening of fluoro-substituted nucleosides. A series of 28 fluoro-modified nucleoside analogues was initially evaluated for potency in inhibiting TBEV-induced cytopathic effect (CPE) in porcine kidney stable (PS) cells. PS cells are an immortalized cell line widely used for isolation and multiplication of TBEV and other flaviviruses (31). Our attention was predominantly focused on nucleosides with a fluoro-substituent located at the *C2′*, *C3′*, *C2*, or *C5* positions. For some nucleosides, we evaluated both of the ribo- and arabino-stereoisomers. For several of the compounds, a *C2′*-fluoro-substituent was combined with other halogen or alkyl moieties at the *C2*, *C5*, or *N2* positions, resulting in di-substituted compounds (Fig. 1).

In this initial screening, all compounds were tested against TBEV (strain Hypr) at a single concentration of $25\ \mu$M using a 24-h pretreatment assay. We observed that TBEV-infected PS cell monolayers treated with 3′-deoxy-3′-fluoroadenosine, 3′-deoxy-3′-fluoroguanosine, or 3′-deoxy-3′-flurouridine had higher cell viability (70.0, 36.1, and 35.8%, respectively) compared to virus-infected cells treated with other compounds tested ($<30\%$), as well as to virus-infected mock-treated cells (14.6%) (Fig. 2A).

To analyze the anti-TBEV activity of the 3′-deoxy-3′-fluoro-substituted nucleosides in more detail, we tested the antiviral potency of these compounds at concentrations of 0, 6.25, 12.5, and $25\ \mu$M. Viral titers were determined from the collected media using the plaque assay after 72 h of cultivation. Although 3′-deoxy-3′-fluoroguanosine and 3′-deoxy-3′-flurouridine did not reduce viral titers in TBEV-infected cells, 3′-deoxy-3′-fluoroadenosine showed remarkable inhibitory activity (Fig. 2B to D). For this nucleoside, compound concentrations of $6.25\ \mu$M reduced the virus titer by more than 2 orders of magnitude, whereas concentrations of 12.5 and $25\ \mu$M resulted in total abrogation of viral replication *in vitro* (Fig. 2B). Based on the observed antiviral activity of 3′-deoxy-3′-fluoroadenosine, we selected this nucleoside for further antiviral/cytotoxicity studies.

Dose-dependent antiflavivirus activity of 3′-deoxy-3′-fluoroadenosine. We next evaluated the antiviral activity of 3′-deoxy-3′-fluoroadenosine using three representative flaviviruses, i.e., TBEV (strains Hypr and Neudoerfl), ZIKV (strains MR-766 and Paraiba_01), and WNV (strains Eg-101 and 13–104). For antiviral assays, two cell lines were preferentially used: PS cells and human brain cortical astrocytes (HBCA) cells, the latter of which are primary cells of neural origin that are considered to be a clinically relevant model for *in vitro* antiflaviviral studies.

To assess the antiviral effect of 3′-deoxy-3′-fluoroadenosine against TBEV, we initially tested three treatment regimens differing by the time of drug addition to virus-

Downloaded from https://journals.asm.org/journal/aac on 17 February 2025 by 147.251.135.113.

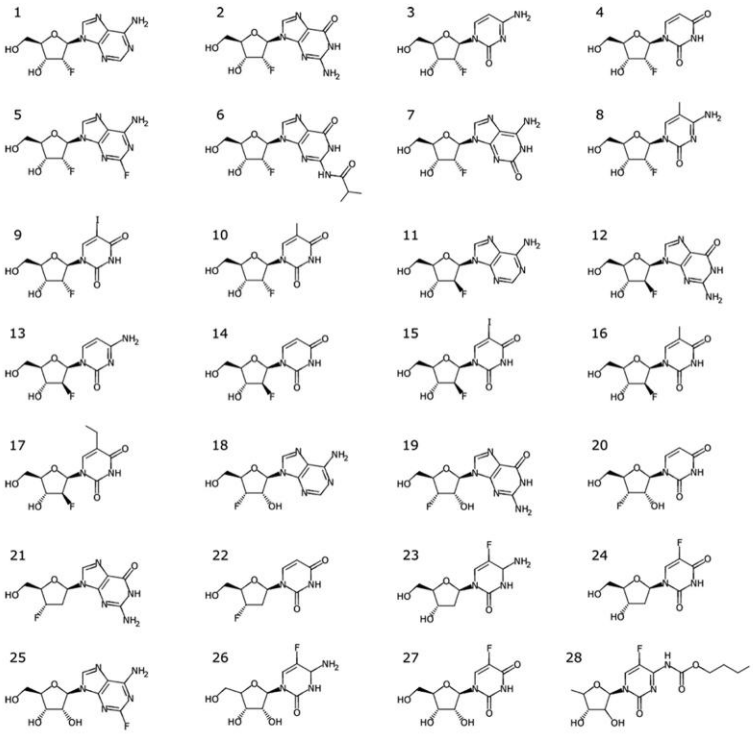

FIG 1 Structures of fluorinated nucleosides used in this study. (1) 2′-Deoxy-2′-fluoroadenosine; (2) 2′-deoxy-2′-fluoroguanosine; (3) 2′-deoxy-2′-fluorocytidine; (4) 2′-deoxy-2′-fluorouridine; (5) 2′-deoxy-2′-fluoro-2-fluoroadenosine; (6) 2′-deoxy-2′-fluoro-*N2*-isobutyrylguanosine; (7) 2′-deoxy-2′-fluoroisoguanosine; (8) 2′-deoxy-2′-fluoro-5-methylcytidine; (9) 2′-deoxy-2′-fluoro-5-iodouridine; (10) 2′-deoxy-2′-fluoro-5-methyluridine; (11) 2′-deoxy-2′-fluoroarabinoadenosine; (12) 2′-deoxy-2′-fluoroarabinoguanosine; (13) 2′-deoxy-2′-fluoroarabinocytidine; (14) 2′-deoxy-2′-fluoro-arabinouridine; (15) 2′-deoxy-2′-fluoro-5-iodoarabinouridine; (16) 2′-deoxy-2′-fluoro-5-methylarabinouridine; (17) 2′-deoxy-2′-fluoro-5-ethylarabinouridine; (18) 3′-deoxy-3′-fluoroadenosine; (19) 3′-deoxy-3′-fluoroguanosine; (20) 3′-deoxy-3′-fluorouridine; (21) 2′,3′-dideoxy-3′-fluoroguanosine; (22) 2′,3′-dideoxy-3′-fluorouridine; (23) 2′-deoxy-5-fluorocytidine; (24) 2′-deoxy-5-fluorouridine (floxuridine); (25) 2-fluoroadenosine; (26) 5-fluorocytidine; (27) 5-fluorouridine; and (28) capecitabine.

infected cells (see Materials and Methods) as follows: (i) a 24-h pretreatment; (ii) a simultaneous treatment; and (iii) a 2-h posttreatment. Notably, 3′-deoxy-3′-fluoroadenosine showed a strong anti-TBEV effect in all tested treatment regimens. Although all of the dose-response curves were similar in shape and slope, the compound-induced inhibitory activity was most pronounced using the pretreatment assay, as was obvious from the 100% inhibition of viral replication at compound concentrations higher than 10 μM (Fig. 2E and F). Based on these results, we decided to use a 24-h pretreatment for all other analyses of the nucleoside's antiviral activity.

Anti-TBEV potency in PS cells reached low-micromolar concentrations, with 50% effective concentration (EC_{50}) values of $2.2 \pm 0.6\,\mu$M and $1.6 \pm 0.3\,\mu$M for Hypr and Neudoerfl strains, respectively. The antiviral activity of 3′-deoxy-3′-fluoroadenosine was slightly lower in HBCA cells, providing EC_{50} values of $3.1 \pm 1.1\,\mu$M for Hypr and $4.5 \pm 1.5\,\mu$M for Neudoerfl (Fig. 3E and F; Table 1). For both cell lines, the anti-TBEV effect of 3′-deoxy-3′-fluoroadenosine was stable over time, and the inhibition of virus replication was clearly apparent at 48 and 72 h postinfection (p.i.). (Fig. 3A to D).

Downloaded from https://journals.asm.org/journal/aac on 17 February 2025 by 147.251.135.113.

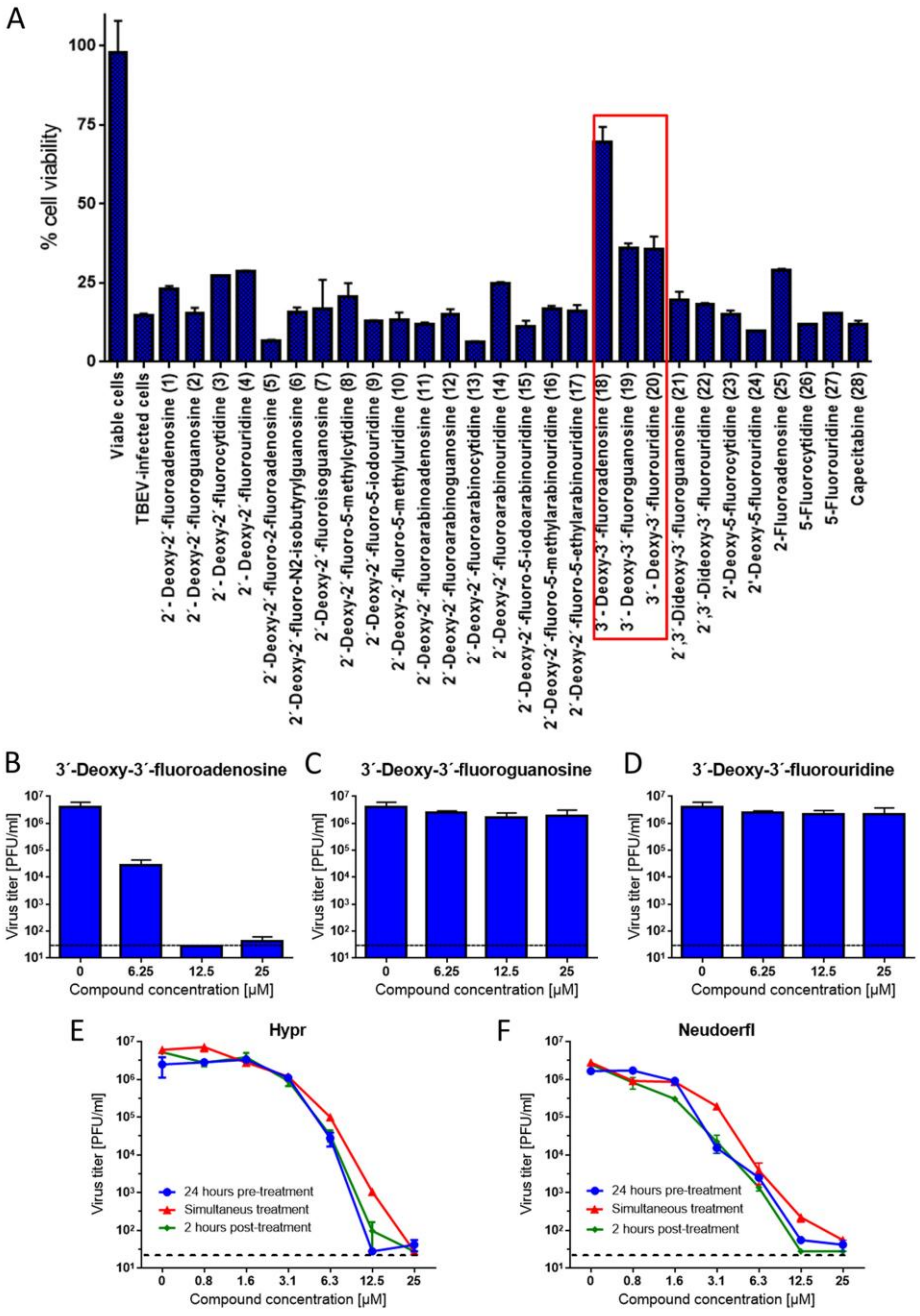

FIG 2 Inhibition of TBEV-induced CPE formation by the indicated fluoro-substituted nucleosides. (A) PS cells were pretreated with the compounds (25 μM) for 24 h and subsequently infected with TBEV (strain Hypr) at an MOI of 0.1. The infected cells were then

(Continued on next page)

Downloaded from https://journals.asm.org/journal/aac on 17 February 2025 by 147.251.135.113.

TABLE 1 Antiviral and cytotoxicity characteristics of 3′-deoxy-3-adenosine

		EC_{50} (μM)[a,b]		CC_{50} (μM)[a]		SI[c]	
Virus	Strain	PS	HBCA	PS	HBCA	PS	HBCA
TBEV	Hypr	2.2 ± 0.6	3.1 ± 1.1			> 11.4	> 8.1
	Neudoerfl	1.6 ± 0.3	4.5 ± 1.5			> 15.6	> 5.6
ZIKV	MR-766	1.1 ± 0.1	4.7 ± 1.3	> 25	> 25	> 22.7	> 5.3
	Paraiba_01	1.6 ± 0.2	4.5 ± 1.4			> 15.6	> 5.6
WNV	Eg-101	3.7 ± 1.2	4.3 ± 0.3			> 6.8	> 5.8
	13-104	4.7 ± 1.5	4.3 ± 0.6			> 5.3	> 5.8

[a]Determined from three independent experiments. EC_{50}, 50% effective concentration; CC_{50}, 50% cytotoxic concentration.
[b]Expressed as a 50% reduction in viral titers and calculated as inflection points of sigmoidal inhibitory curves, which were obtained by a nonlinear fit of transformed inhibitor concentrations versus normalized response using GraphPad Prism 7.04 (GraphPad Software, Inc., USA).
[c]SI (selectivity index) = CC_{50}/EC_{50}.

Sensitivity of both ZIKV strains to 3′-deoxy-3′-fluoroadenosine appeared to be comparable to that for TBEV. In PS cells, the anti-ZIKV effect was characterized by EC_{50} values of 1.1 ± 0.1 μM and 1.6 ± 0.2 μM for MR-766 and Paraiba_01, respectively (Fig. 3E; Table 1). After 72 h p.i., complete inhibition of virus replication was achieved at concentrations of 25 μM (for MR-766) and 12.5 μM and 25 μM (for Paraiba_01) (Fig. 3B). The efficacy of 3′-deoxy-3′-fluoroadenosine in suppressing ZIKV replication in HBCA was 3- to 4-fold lower than in PS cells, but it still reached low-micromolar values for both ZIKV strains (EC_{50} values of 4.7 ± 1.3 μM and 4.5 ± 1.4 μM) (Fig. 3D and F; Table 1). In addition to ZIKV, 3′-deoxy-3′-fluoroadenosine significantly inhibited *in vitro* replication of both tested WNV strains. Compared with TBEV and ZIKV, the anti-WNV effect was characterized by slightly higher EC_{50} values: 3.7 ± 1.2 μM (for Eg-101) and 4.7 ± 1.5 μM (for 13–104) in PS cells, and 4.3 ± 0.3 μM (for Eg-101) and 4.3 ± 0.6 μM (for 13–104) for HBCA cells (Fig. 3C, D, and F; Table 1).

Dose-dependent antiflaviviral effects of 3′-deoxy-3′-fluoroadenosine identified in viral titer inhibition assays were confirmed by immunofluorescent staining, which was used to assess the expression of flaviviral surface E antigen in PS cells as a parameter of viral infectivity and replication *in vitro*. Although the surface E protein was highly expressed in virus-infected mock-treated cells (Fig. 4A), we observed a gradually decreasing fluorescence signal in cell monolayers treated with ascending compound concentrations monitored at 72 h p.i. A nucleoside concentration of 25 μM was strong enough to completely inhibit protein E expression of all tested flaviviruses in PS cell culture (Fig. 4A).

We then proceeded to study the antiviral activity of 3′-deoxy-3′-fluoroadenosine using a monitoring system based on QPI with high-resolution holographic microscopy to measure multiple parameters describing the physiological state of the monitored cells. These parameters included the following: (i) covered area (μm^2) and (ii) cell dry mass (pg) (both used to characterize cell growth and proliferation activity); (iii) cell speed (μm/min) (describing cell movement intensity); (iv) circularity (characterizing

FIG 2 Legend (Continued)
incubated with the compounds for 72 h. Following incubation, PS monolayers were stained by naphthalene black and absorbance was measured at 540 nm. 3′-Deoxy-3′-fluoro-modified nucleosides that were further analyzed for their antiviral activity/toxicity are framed in red. Compound numbers correspond to those in Fig. 1. (B to D) TBEV titer reduction with 3′-deoxy-3′-fluoroadenosine (B), 3′-deoxy-3′-fluoroguanosine (C), and 3′-deoxy-3′-fluorouridine (D) at the indicated concentrations. The treatment regimen for B to D was the same as that for A; after 72 h of incubation, virus titers were determined using a plaque assay. (E) Antiviral activity of 3′-deoxy-3′-fluoroadenosine against TBEV strain Hypr when the compound was added to PS cells at 24 h prior to infection (blue), simultaneously with infection (red), or 2 h after infection (green). The growth media were collected after 72 h of cultivation and analyzed using the plaque assay. (F) Antiviral activity of 3′-deoxy-3′-fluoroadenosine against TBEV strain Neudoerfl in PS cells at a 24 h pretreatment (blue), simultaneous treatment (red) or 2 h posttreatment (green). The growth media were analyzed using the plaque assay after 72 h of incubation. The mean titers or % cell viabilities from three biological replicates are shown, and error bars indicate standard errors of the mean ($n = 3$). The horizontal dashed line indicates the minimum detectable threshold of 1.44 $\log_{10}$ PFU/ml.

Downloaded from https://journals.asm.org/journal/aac on 17 February 2025 by 147.251.135.113.

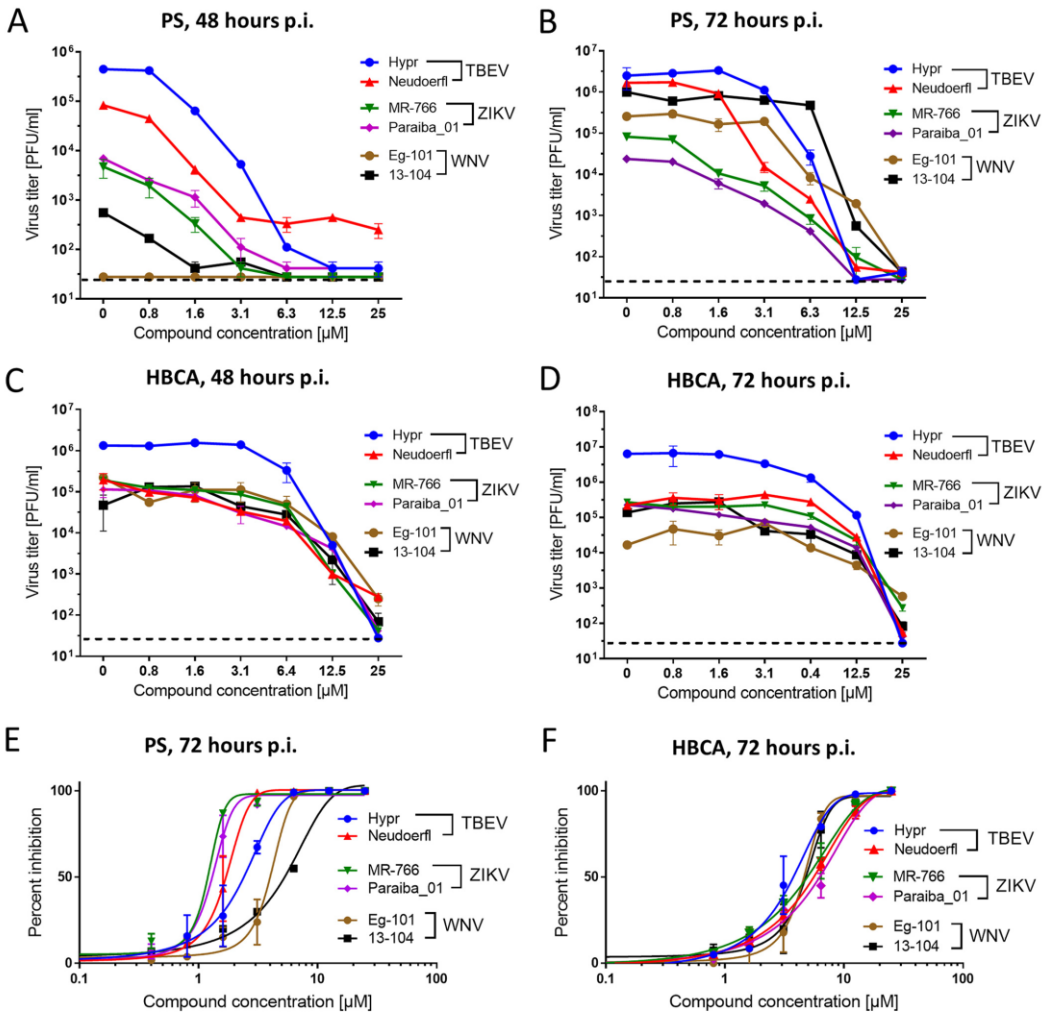

FIG 3 Dose-dependent anti-flaviviral activity of 3′-deoxy-3′-fluoroadenosine and cytotoxicity studies. (A and B) Growth curves for TBEV, ZIKV, and WNV in PS cells treated with 3′-deoxy-3′-fluoroadenosine at the indicated concentrations. PS cells were pretreated with the compounds at the indicated concentrations for 24 h and subsequently infected with the indicated flaviviruses at an MOI of 0.1. The infected cells were then incubated with the compound for 48 h p.i. or 72 h p.i. and viral titers were determined using the plaque assay. Data used for construction of dose-response curves for Hypr and Neudoerfl TBEV at 72 h p.i. (B) were reused from Fig. 2E and F, as those were two identical experiments. (C and D) Growth curves for TBEV, ZIKV, and WNV in HBCA cells treated with 3′-deoxy-3′-fluoroadenosine at the indicated concentrations. The treatment regimen was the same as in A and B, with the viral titers determined after 48 or 72 h p.i. (E and F) Inhibition curves of 3′-deoxy-3′-fluoroadenosine for the indicated flaviviruses cultivated with the compound in PS cells (E) or HBCA cells (F) for 72 h p.i. The mean titers from three biological replicates are shown, and error bars indicate standard errors of the mean ($n = 3$). The horizontal dashed line indicates the minimum detectable threshold of 1.44 $\log_{10}$ PFU/ml.

morphological changes of the cells and the rate of round cells); (v) density (pg/μm^2); and (vi) cell dynamic score (to determine cell death).

QPI revealed that control cells displayed typical signs of normal physiological growth, proliferation, and movement, a low degree of morphological circularity (normal-shaped cells prevailed), and low mass density related to a low degree of apoptosis. In contrast, heat-killed cells exhibited sharp and fast alterations in cellular parameters

Downloaded from https://journals.asm.org/journal/aac on 17 February 2025 by 147.251.135.113.

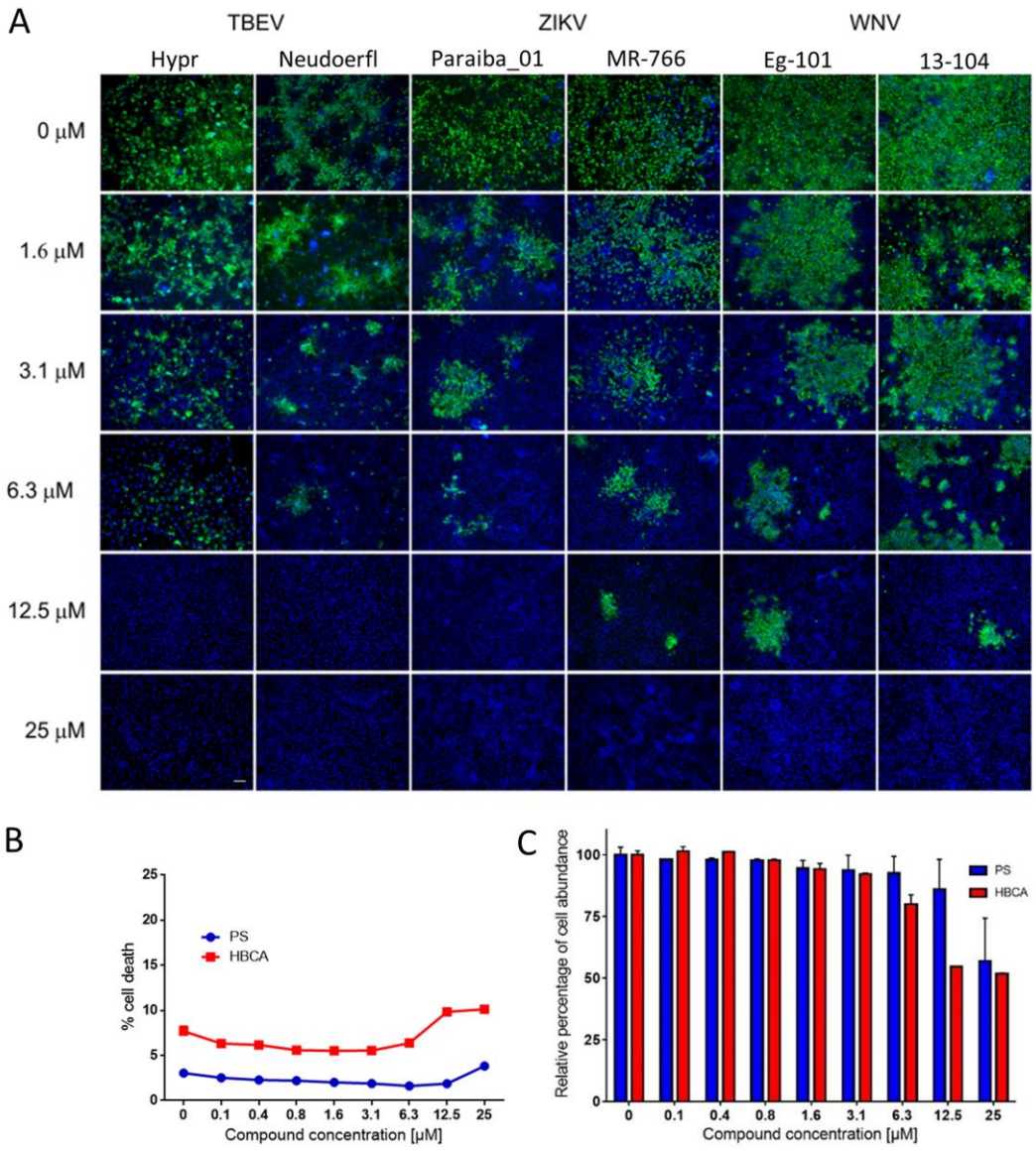

FIG 4 Inhibition of flavivirus surface E antigen expression by 3′-deoxy+3′-fluoroadenosine and cytotoxicity studies. (A) PS cells were pretreated with the compound for 24 h and subsequently infected with the indicated flaviviruses at an MOI of 0.1. PS cells were fixed on slides at 72 h postinfection, stained with flavivirus-specific antibody labeled with FITC (green), and counterstained with DAPI (blue). Scale bar, 50 μm. (B and C) Cytotoxicity of 3′-deoxy-3′-fluoroadenosine expressed as a percentage of cell death (B) and relative percentage of cell abundance (C). The mean percentage of cell death or mean relative percentage of cell abundance from three biological replicates is shown, and error bars indicate standard errors of the mean ($n = 3$).

and low cell dynamic scores typical of lytic cell death (Fig. 5 and 6; Fig. S1 in the supplemental material). TBEV-infected cell monolayers were characterized by low values for the covered area, gradually decreasing cell dry mass, and slowing cell speed. Moreover, TBEV-infected cells exhibited an increased cell circularity and higher mass

Downloaded from https://journals.asm.org/journal/aac on 17 February 2025 by 147.251.135.113.

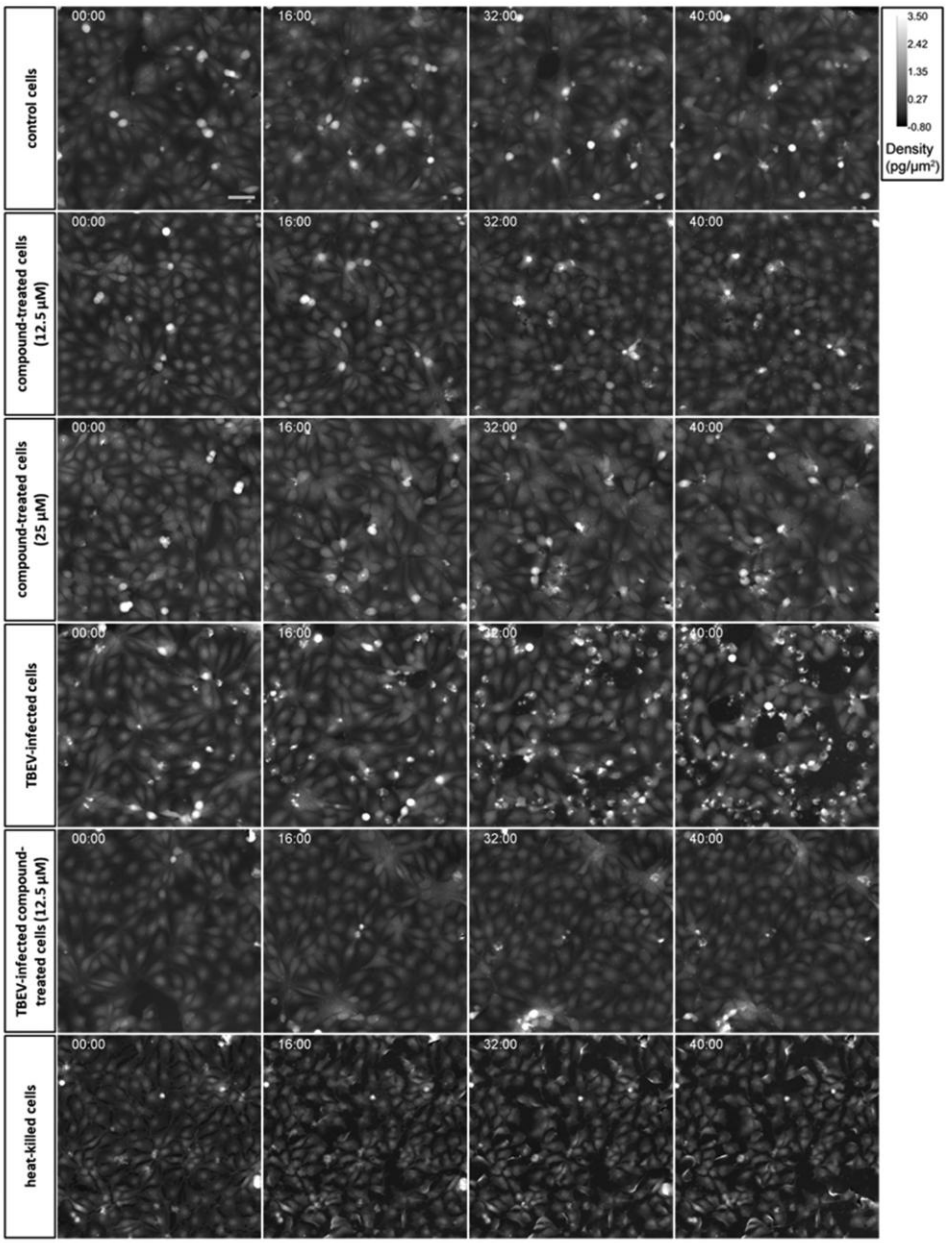

FIG 5 Real-time QPI signals for PS cells at different time points. PS cells in flow chambers were treated with the compound and inoculated with TBEV (strain Hypr) as described in the Materials and Methods. Control cells, compound-treated cells (12.5 μM, and 25 μM), and TBEV-infected compound-treated cells (12.5 μM) maintained normal growth in a confluent monolayer with no morphological signs of ongoing cell death. TBEV-infected cells underwent apoptotic cell death with the presence of blebbing and apoptotic bodies (at 16 h, 32 h, and 40 h). Heat-killed cells underwent a lytic form of cell death without the presence of blebbing cells and apoptotic bodies. Scale bar = 30 μm.

Downloaded from https://journals.asm.org/journal/aac on 17 February 2025 by 147.251.135.113.

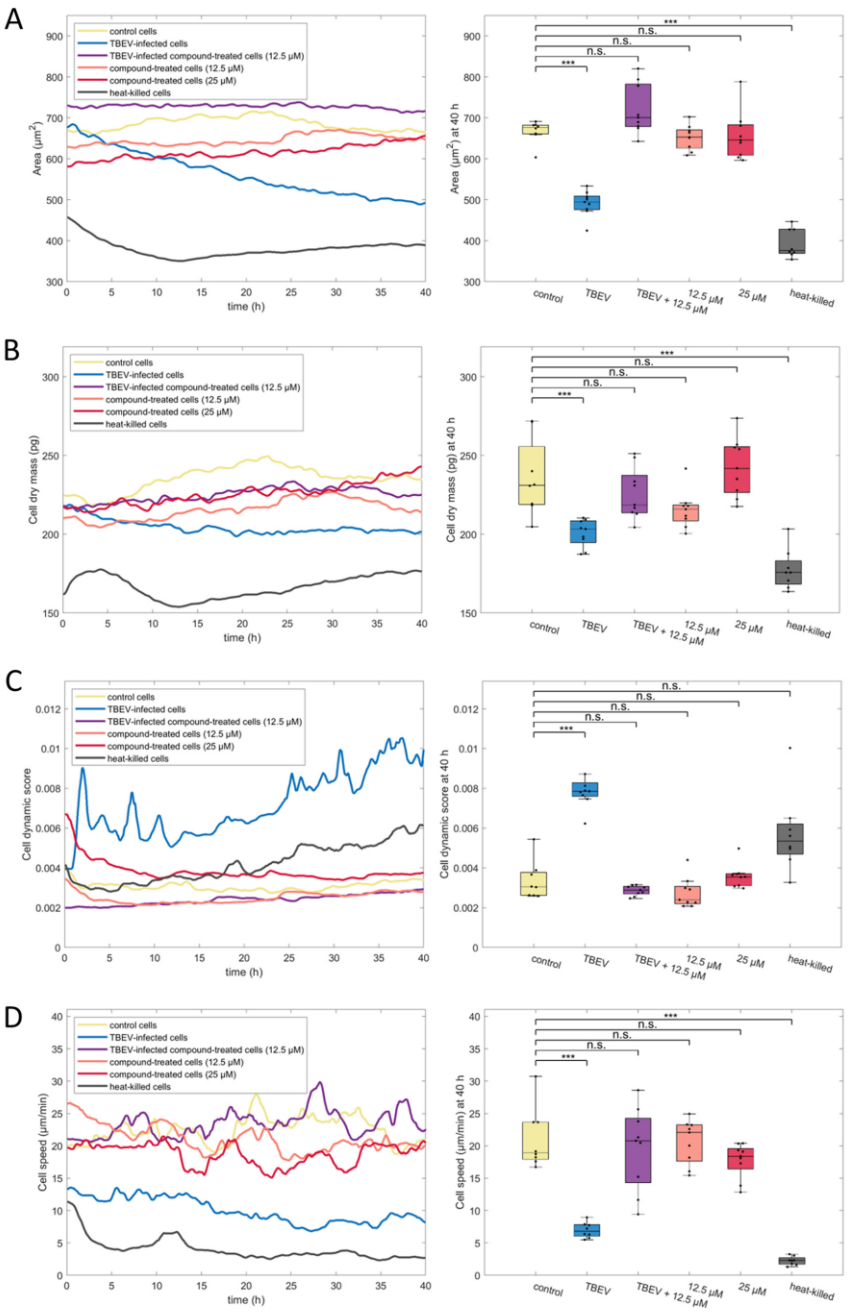

FIG 6 Real-time QPI parameters for PS cells for advanced characterization/description of antiviral efficacy and cytotoxicity of 3′-deoxy-3′-fluoroadenosine in cell culture. (A) Real-time QPI-measured area of the cell population (left) and the endpoint area values of the cell population after 40 h of treatment (right).

(Continued on next page)

Downloaded from https://journals.asm.org/journal/aac on 17 February 2025 by 147.251.135.113.

density, related to a virus-induced CPE formation/apoptosis, as also demonstrated by the cell dynamic score, an average intensity change in cell pixels typical for membrane blebbing, and intensive changes in CPE-associated cell mass distribution. Finally, TBEV-infected cells treated with 3′-deoxy-3′-fluoroadenosine (12.5 μM) showed parameter values similar to those of control cells, highlighting the ability of 3′-deoxy-3′-fluoroadenosine to inhibit viral replication and suppress CPE formation and apoptosis (Fig. 5 and 6; Fig. S1).

Cytotoxicity of 3′-deoxy-3′-fluoroadenosine. We investigated the potential cytotoxicity of 3′-deoxy-3′-fluoroadenosine for PS and HBCA cells in terms of (i) cell death and (ii) relative percentage of cell abundance (a parameter corresponding with the total abundance of lactate dehydrogenase in the cell population, which can be used as an index of total cell count), using the CytoTox 96 non-radioactive cytotoxicity assay (Promega, WI, USA). Measurement of the released amount of lactate dehydrogenase in compound-treated cells revealed no substantial toxicity of 3′-deoxy-3′-fluoroadenosine for PS cells up to 25 μM (cell death values were 3.8 $\pm$ 0.1% for compound-treated cells [25 μM] and 3.0 $\pm$ 0.3% for mock-treated cells) (Fig. 4B). For HBCA, the compound was only slightly cytotoxic at a concentration of 25 μM (cell death value of 10.1 $\pm$ 0.2%) compared with mock-treated cells (cell death value of 7.7 $\pm$ 0.8%) (Fig. 4B).

Treatment with 3′-deoxy-3′-fluoroadenosine resulted in substantial differences in relative percentage of cell abundance, however, in compound-treated PS/HBCA cells compared to mock-treated monolayers, where a relative percentage of cell abundance in PS monolayers treated with the compound at 25 μM was only 56.9 $\pm$ 17.3% compared to control cells. Of note, this parameter was not substantially affected when the cell monolayers were treated with compound concentrations of 12.5 μM or less (Fig. 4C). This effect was even higher in HBCA cells and reached 80.0 $\pm$ 3.8%, 54.7 $\pm$ 0.1%, and 51.8 $\pm$ 0.3% for concentrations of 6.3, 12.5, and 25 μM, respectively (Fig. 4C). The observed differences in relative percentage of cell abundance indicated that the compound concentrations of 25 μM (for PS) and 12.5 μM and 25 μM (for HBCA) considerably suppressed cell proliferation (Fig. 4C) but did not result in extensive cell death or cell monolayer damage (Fig. 4B). Based on these results, it can be concluded that 3′-deoxy-3′-fluoroadenosine exerted an observable cytostatic effect at the above-mentioned concentrations for both cell lines tested.

QPI of cells treated with 12.5 μM or 25 μM 3′-deoxy-3′-fluoroadenosine yielded dose-response curves that were similar in shape and slope to those for control cells. They were, however, somewhat flatter, indicating slower progress in area coverage and growth of cell dry mass and almost the same degree of mass density within the whole monitoring period. This result can be explained as a consequence of the compound's cytostatic effect, which confirmed the findings obtained previously in colorimetric cell-based assays. We found no signs of apoptosis or other types of cell death in compound-treated PS cells (Fig. 5 and 6; Fig. S1).

Antiviral efficacy of 3′-deoxy-3′-fluoroadenosine in a mouse model of lethal flavivirus infection. Based on the observation that 3′-deoxy-3′-fluoroadenosine strongly inhibited replication of emerging flaviviruses *in vitro*, we then proceeded to investigate its anti-WNV and anti-TBEV effects in mouse infection models (Fig. 7A). BALB/c mice injected subcutaneously with a lethal dose of WNV strain Eg-101 (10^3 PFU/mouse) exhibited characteristic clinical signs of infection, such as ruffled fur,

FIG 6 Legend (Continued)
A significant drop in cell-covered area was noticeable after TBEV and heat treatment. This effect of TBEV was reversed after 3′-deoxy-3′-fluoroadenosine treatment. (B) Real-time QPI-measured cell dry mass (left) and the endpoint cell dry mass values after 40 h of treatment (right). A significant drop in cell dry mass was noticeable after TBEV and heat treatment. This effect of TBEV was reversed after 3′-deoxy-3′-fluoroadenosine treatment. (C) Real-time QPI-measured cell dynamic score (left) and the endpoint cell dynamic score values after 40 h of treatment (right). High cell dynamic score indicating apoptosis was observable after TBEV treatment. This effect of TBEV was reversed after 3′-deoxy-3′-fluoroadenosine treatment. (D) Real-time QPI-measured cell speed (left) and the endpoint cell-speed values of cells after 40 h of treatment (right). n.s., not significant, $P > 0.05$; *, $P < 0.05$; ***, $P < 0.001$. Boxes: main box edges are 25th and 75th percentiles, central line indicates the median, and whiskers indicate the lowest and highest values of the 1.5 interquartile range. Each dot in the boxplot represents the average value for one field of view.

Downloaded from https://journals.asm.org/journal/aac on 17 February 2025 by 147.251.135.113.

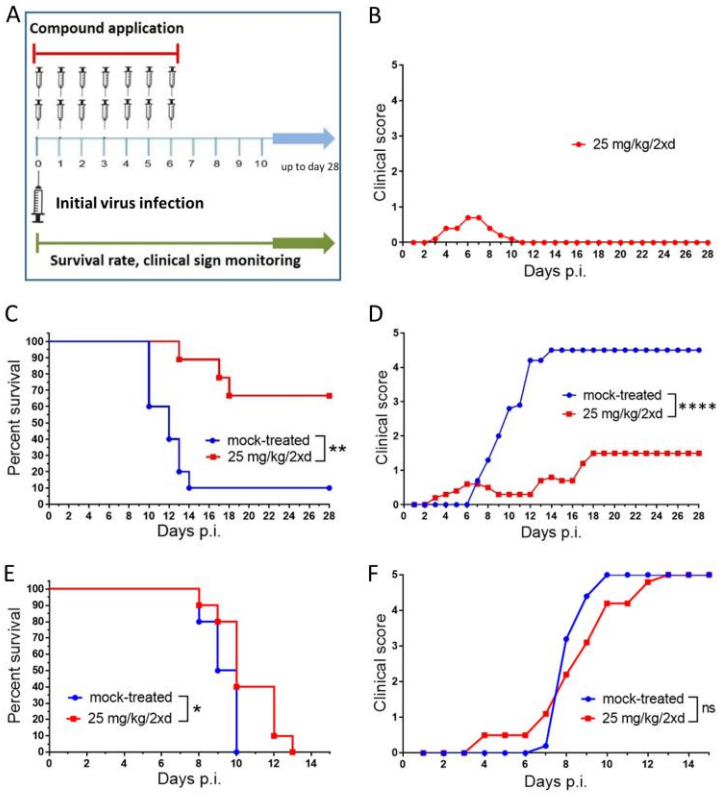

FIG 7 Antiviral efficacy of 3′-deoxy-3′-fluoroadenosine in mouse models of WNV and TBEV infection. (A) The design of the *in vivo* antiviral experiment. (B) Toxicity evaluation of 3′-deoxy-3′-fluoroadenosine in mice. The compound (25 mg/kg) was administered twice daily to adult BALB/c mice for 6 days. (C) Groups of adult BALB/c mice were infected with a lethal dose of WNV (strain Eg-101) and treated twice daily with intraperitoneal 25 mg/kg 3′-deoxy-3′-fluoroadenosine or phosphate-buffered saline (mock treatment) at the indicated times after WNV infection. Survival rates were monitored daily. (D) Clinical signs of WNV infection were scored daily as follows: 0, no signs; 1, ruffled fur; 2, slowing of activity or hunched posture; 3, asthenia or mild paralysis; 4, lethargy, tremor, or complete paralysis of the limbs; and 5, death. (E) Groups of adult BALB/c mice were infected with a lethal dose of TBEV (strain Hypr) and treated twice daily with intraperitoneal 25 mg/kg 3′-deoxy-3′-fluoroadenosine or phosphate-buffered saline (mock treatment) at the indicated times after TBEV infection. Survival rates were monitored daily. (F) Clinical signs of TBEV infection were scored daily as described in D. ns, not significant, $P > 0.05$; *, $P < 0.05$; **, $P < 0.01$; ****, $P < 0.0001$.

hunched posture, tremor, and paralysis of the limbs, within 7 to 13 days p.i., with most mice requiring euthanasia. The mortality rate was 90%, with a mean survival time of 12 ± 1.6 days p.i. Similarly, mice injected with TBEV strain Hypr (10^3 PFU/mouse, a subcutaneous route) showed typical signs of infection within days 8 to 10 days p.i. The mortality rate was ultimately 100%, with a mean survival time of 9.0 ± 1.0 days (Fig. 7C and D).

In order to evaluate toxicity of the compound *in vivo*, 3′-deoxy-3′-fluoroadenosine (a dose of 25 mg/kg/2×day) was administered to BALB/c mice intraperitoneally for 6 days and clinical scores of the treated animals were monitored daily. In seven mice, the treatment was associated with moderate side effects starting at day 3 after treatment initiation (manifested by slightly ruffled hair or hunched posture), which led to a gradual increase in the average clinical score up to 0.7 within days 6 to 7. After we

Downloaded from https://journals.asm.org/journal/aac on 17 February 2025 by 147.251.135.113.

stopped the compound administration (at day 6), the observed side effects gradually disappeared (Fig. 7B). As expected, moderate side effects were observed in both WNV- or TBEV-infected compound-treated mice starting on day 3 or 4 p.i. (Fig. 7D and F). The increase of clinical score was probably related with the cytostatic activity of the compound, as demonstrated by *in vitro* (cell-based) assays.

In WNV-infected BALB/c mice, 3′-deoxy-3′-fluoroadenosine (25 mg/kg/2×day) administered intraperitoneally (the administration was initiated from the time of virus inoculation and ceased at day 6 p.i.) significantly protected the animals from disease development and mortality (70% survival rate, $P < 0.01$). In 70% of WNV-infected compound-treated mice, no signs of clinical infection were observed up to the end of the experiment (day 28 p.i.). In 30% of mice, the compound substantially prolonged the time of mouse survival (14.5 ± 2.4 days) compared with controls (Fig. 7C and D).

Treatment with 25 mg/kg/2×day of 3′-deoxy-3′-fluoroadenosine initiated at the time of TBEV inoculation and ceasing at day 6 p.i. resulted in a slight but statistically significant survival prolongation among TBEV-infected compound-treated mice ($P < 0.05$). Although all treated mice eventually died, they showed slightly slowed development of clinical signs of neuroinfection within days 8 to 13 p.i. and had an increased mean survival time of 10.5 ± 1.9 days compared with control animals (Fig. 7E and F).

DISCUSSION

Fluoro-substituted nucleosides show unique chemical, biochemical, and biological properties and are widely used as treatment for numerous viral, bacterial, fungal, and protozoal infections, in addition to many cancers (18, 19). So far, however, only a few of these compounds have been tested against flaviviruses to assess their antiviral *in vitro* and *in vivo* effects (32–34). In this study, we evaluated the antiviral activity of a series of 28 fluoro-modified nucleosides against TBEV in the PS cell line. To our surprise, we found little to no inhibition of virus-induced CPE formation by almost all of the tested compounds, and some of them proved to be highly cytotoxic. No antiviral activity or high toxicity was observed in particular with nucleosides modified with a fluoro-substituent at *C2′*, *C2*, or *C5*. Inactivity of 2′-fluoro-modified nucleosides against TBEV could be explained by elimination of the 2′-hydroxy hydrogen bond donor, which results in a dramatic decrease in hydrogen-bonding capacity with the polymerase or the incoming nucleoside triphosphate and the inability of such nucleosides to trigger inhibition of viral RNA synthesis (35).

Changes in stereochemistry at the *C2′* position from the ribo-configuration to the arabino-orientation also can lead to compound inactivity, as illustrated with a series of 2′-deoxy-2′-fluoroarabinonucleosides tested in this study. Similarly, the addition of a fluoro-substituent to the *C2/C5* positions of a purine/pyrimidine yielded compounds with no anti-TBEV efficacy, likely due to electronic or steric hindrance with the viral NS5 RdRp active site (35). Alternatively, inactivity of these nucleoside analogues may be the result of inefficient compound uptake mediated by specific nucleoside transporters, low conversion efficacy into active (phosphorylated) forms by cellular kinases, or a high degradation rate caused by nucleoside/nucleotide catabolic enzymes (4). As a result, those mechanisms could be interesting targets for further investigation.

As might be expected, nucleosides lacking the 3′-hydroxyl group could be potent inhibitors of flaviviral NS5 RdRp-mediated RNA synthesis, acting as obligate RNA chain terminators (11). Indeed, 3′-deoxy-3′-fluoroguanosine 5′-triphosphate was previously described as interacting directly with NS5B RdRp of HCV, resulting in suppression of viral RNA synthesis by disruption of further extension of the replicating viral RNA (35). The potency to inhibit HCV NS5B polymerase activity was also observed in 3′-deoxy-3′-fluoroadenosine 5′-triphosphate; however, the inhibitory activity was considerably lower than its guanosine counterpart (35). Our *in vitro* antiviral assays revealed that two 3′-deoxy-3′-fluoro–substituted nucleosides, 3′-deoxy-3′-fluoroguanosine and 3′-deoxy-3′-fluorouridine, did not suppress multiplication of TBEV in PS cells. In contrast,

Downloaded from https://journals.asm.org/journal/aac on 17 February 2025 by 147.251.135.113.

3′-deoxy-3′-fluoroadenosine, a nucleoside first synthesized in the late 1980s at the Rega Institute for Medical Research in Belgium (36, 37), showed potent, low-micromolar antiviral inhibition of *in vitro* TBEV replication. Moreover, this compound suppressed replication of two other medically important flaviviruses, WNV and ZIKV, in PS cells, as well as in primary HBCA cells. The antiviral effect was stable over time, with inhibition of viral replication observed at 48 and 72 h p.i., and the compound was highly active even if added to PS cells at 2 h after infection. The ability of 3′-deoxy-3′-fluoroadenosine to inhibit multiple arthropod-borne flaviviruses demonstrates potent, broad-spectrum antiviral activity across the genus *Flavivirus*. Broad-spectrum inhibitory effects for 3′-deoxy-3′-fluoroadenosine have also been described in earlier papers for numerous RNA viruses of the *Picornaviridae*, *Togaviridae*, *Reoviridae*, and *Arenaviridae* families (36, 38).

Notably, we did not observe any measurable *in vitro* cytotoxicity of 3′-deoxy-3′-fluoroadenosine in PS and HBCA cells within compound concentrations used for antiviral activity evaluation (0 to 25 μM). This result is in agreement with earlier studies showing a minimum cytotoxic concentration of 40 μM for primary rabbit kidney cells, Vero cells, and HeLa cells (36, 37). However, 3′-deoxy-3′-fluoroadenosine did have observable cytostatic effects at 25 μM in PS cells and at 12.5 μM and 25 μM in HBCA cells. Cytostatic properties of 3′-deoxy-3′-fluoroadenosine were previously described for murine leukemia cells (L1210), human B-lymphoblast (Raji) cells, human T-lymphocyte (H9) cells, and human T4-lymphocytes (MT-4), acting at concentrations ranging from 1.6 to 23 μM (37, 39).

It could be speculated that the cytostatic activity is related to low selectivity of 3′-deoxy-3′-fluoroadenosine 5′-triphosphate for viral RdRps over other types of polymerases. The extremely broad range of viruses sensitive to this nucleoside, including vaccinia virus among DNA viruses, supports this hypothesis (36). In accordance with this claim, 3′-deoxy-3′-fluoroadenosine has also been described as terminating RNA synthesis catalyzed by DNA-dependent RNA polymerase from *E. coli* (40). In addition, 3′-deoxy-3′-fluoroadenosine inhibited incorporation of ^{3}H-labeled uridine into cellular RNA, resulted in abrogation of cellular RNA synthesis in actively growing Vero cells (38). Alternatively, the broad range of antiviral activity of 3′-deoxy-3′-fluoroadenosine and the reported suppression of cellular RNA synthesis could also be explained as a result of compound-mediated inhibition of purine/pyrimidine biosynthesis and nucleotide depletion, as was recently described for a broad-spectrum antiviral and anticancer drug gemcitabine (2′-dideoxy-2′,2′-difluorocytidine) (41). In order to explain a broad spectrum antiviral efficacy of 3′-deoxy-3′-fluoroadenosine, this compound was also tested for its potential inhibition of S-adenosylhomocysteine (SAH) hydrolase. However, no inhibitory activity to SAH hydrolase was demonstrated, unless it was used at a rather high concentration (36).

Based on our observation that 3′-deoxy-3′-fluoroadenosine showed a strong antiviral potency in cell culture (*in vitro*), we evaluated its activity *in vivo* using mouse models of WNV and TBEV infection. Treatment of WNV-infected mice with 25 mg/kg of 3′-deoxy-3′-fluoroadenosine twice a day resulted in a significant decrease of mortality and in a substantial elimination of clinical signs of neuroinfection. In TBEV-infected mice, the antiviral effect of 3′-deoxy-3′-fluoroadenosine (25 mg/kg/2×day) was not as strong; however, the compound administration resulted in significantly longer survival time and slower progress of development of clinical signs compared with control animals. A lower efficacy of 3′-deoxy-3′-fluoroadenosine against TBEV (strain Hypr) *in vivo* could be explained by a rapid/aggressive course of TBEV infection in mice, where the average survival time of TBEV-infected mice was shorter than that of WNV-infected mice (9.0 ± 1.0 days versus 12 ± 1.6 days, respectively). 3′-Deoxy-3′-fluoroadenosine was previously demonstrated to show high efficacy in suppressing the formation of tail lesions in vaccinia virus–infected rodents. The compound, administered intravenously for 5 days at concentrations of 50 and 100 mg/kg/day, reduced the number of pox tail

Downloaded from https://journals.asm.org/journal/aac on 17 February 2025 by 147.251.135.113.

lesions by 25% and 80%, respectively. A dose of 200 mg/kg/day was reported to be lethal for mice (36).

Previous studies have shown that nucleosides with antiviral activity against arthropod-borne flaviviruses contain one of the following sugar ring modifications: (i) a methyl substitution at *C2′* (42), (ii) an ethynyl substitution at *C2′* (43, 44), or (iii) an azido substitution at *C4′* (45). An observable (but weaker) antiflaviviral effect also has been reported for nucleosides with (iv) a cyano substitution at *C1′* (46). These chemical modifications are used in combination with appropriate heterocyclic bases or their modified counterparts (e.g., with 7-deazaadenine) and/or with modifications of *N*-glycosidic bond (e.g., switching to a *C*-glycosidic bond) (4). Herein we have described the first results showing that a fluoro-substitution at the *C3′* position of adenosine represents another useful nucleoside modification that exhibited low-micromolar inhibitory activity against emerging flavivirus replication. While the increased cytostatic activity of 3′-deoxy-3′-fluoroadenosine *in vitro* limits its potential use for further clinical applications; however, additional chemical modifications could improve this compound's cytotoxic/cytostatic profile. This is exemplified by 2′-deoxy-2′-fluorinated nucleosides, in which the addition of *C2′* methyl and *C5′* phosphoramidate groups led to increased nucleoside selectivity toward viral RdRp, manifested as high inhibitory potency and low toxicity. These characteristics have been demonstrated for the anti-HCV drug sofosbuvir (47, 48), illustrating the considerable potential of fluoro-substituted nucleoside analogues as prospective starting points in developing effective antivirals for treating flavivirus-associated diseases.

MATERIALS AND METHODS

Ethics statement. This study was carried out in strict accordance with Czech law and guidelines for the use of experimental animals and protection of animals against cruelty (Animal Welfare Act 246/1992 Coll.). All procedures were reviewed by the local ethics committee and approved by the Ministry of Agriculture of the Czech Republic (permit no. 13522/2019-MZE-18134).

Cell cultures, virus strains, and antiviral compounds. PS cells (31) were cultured at 37°C in Leibovitz (L-15) medium. HBCA (ScienCell, Carlsbad, CA) cells were cultivated in Astrocyte medium (Thermo Fisher Scientific). The media were supplemented with 3% (L-15) and 6% (Astrocyte medium) newborn calf serum and 100 U/ml penicillin, 100 μg/ml streptomycin, and 1% glutamine (Sigma-Aldrich, Prague, Czech Republic).

The following emerging flaviviruses were tested: TBEV (strains Hypr and Neudoerfl, both members of the West European TBEV subtype, provided by the Collection of Arboviruses, Institute of Parasitology, Biology Center of the Czech Academy of Sciences, Ceske Budejovice, Czech Republic http://www.arboviruscollection.cz/index.php?lang=en), ZIKV (African strain MR-766 and Brazilian strain Paraiba_01, kindly provided by Carla Torres Braconi and Paolo M. de A. Zanotto, University of Sao Paolo), and WNV (Eg-101, a member of genomic lineage 1, originally isolated from human serum in Egypt, and 13–104, a representative of genomic lineage 2, isolated from the *Culex modestus* mosquito in the Czech Republic).

Nucleoside analogues were purchased from Carbosynth (Compton, UK) (2′-deoxy-2′-fluoroadenosine, 2′-deoxy-2′-fluoroguanosine, 2′-deoxy-2′-fluorocytidine, 2′-deoxy-2′-fluorouridine, 2′-deoxy-2′-fluoro-2-fluoroadenosine, 2′-deoxy-2′-fluoro-*N2*-isobutyrylguanosine, 2′-deoxy-2′-fluoroisoguanosine, 2′-deoxy-2′-fluoro-5-methylcytidine, 2′-deoxy-2′-fluoro-5-iodouridine, 2′-deoxy-2′-fluoro-5-methyluridine, 2′-deoxy-2′-fluoroarabinoadenosine, 2′-deoxy-2′-fluoroarabinoguanosine, 2′-deoxy-2′-fluoroarabinocytidine, 2′-deoxy-2′-fluoroarabinouridine, 2′-deoxy-2′-fluoro-5-iodoarabinouridine, 2′-deoxy-2′-fluoro-5-methylarabinouridine, 2′-deoxy-2′-fluoro-5-ethylarabinouridine, 3′-deoxy-3′-fluoroadenosine, 3′-deoxy-3′-fluoroguanosine, 3′-deoxy-3′-fluorouridine, 2′,3′-dideoxy-3′-fluoroguanosine, and 2′,3′-dideoxy-3′-fluorouridine) and from Sigma-Aldrich (Prague, Czech Republic) (2-fluoroadenosine, 5-fluorocytidine, 2′-deoxy-5-fluorocytidine, capecitabine, 5-fluorouridine, and 2′-deoxy-5-fluorouridine [floxuridine]). Test compounds were solubilized in 100% dimethyl sulfoxide (DMSO) to yield 10 mM stock solutions.

Initial antiviral screening with CPE reduction assay. The 28 fluoro-substituted nucleosides were first screened at a single concentration of 25 μM for their ability to inhibit cytopathic effects (CPE) mediated by TBEV infection (strain Hypr) in PS cells. The cells were seeded in 96-well plates (approximately 2×10^4 cells per well) and incubated for 24 h to form a confluent monolayer. Following incubation, the medium was aspirated from the wells and replaced with 200 μl of fresh medium containing 25 μM of the test compound (three wells per compound) and incubated for an additional 24 h (i.e., 24-h pretreatment). DMSO was added to virus-infected cells as a negative control at a final concentration of 0.5% (vol/vol). After 24 h, the medium was aspirated again and replaced with 200 μl of compound-containing medium (25 μM) inoculated with TBEV at a multiplicity of infection (MOI) of 0.1. The CPE was monitored visually using the Olympus BX-5 microscope equipped with an Olympus DP-70 CCD camera. At 72 h p.i.,

Downloaded from https://journals.asm.org/journal/aac on 17 February 2025 by 147.251.135.113.

cell monolayers were stained by naphthalene black. The rate of CPE was expressed in terms of cell viability as the absorbance at 540 nm by compound-treated cells relative to the absorbance by DMSO-treated cells, as described previously (49). To analyze the anti-TBEV activity of 3′-deoxy-3′-fluoroadenosine, 3′-deoxy-3′-fluoroguanosine, and 3′-deoxy-3′-fluorouridine in more detail, we treated PS cell monolayers with these compounds at concentrations of 0, 6.25, 12.5, and 25 μM and incubated for 24 h. Then, the growth medium was aspirated and replaced with fresh medium containing the same concentrations of the tested compounds and TBEV inoculum (strain Hypr, MOI of 0.1). Viral titers were estimated from the collected media using the plaque assay after a 72-h cultivation.

Optimization of the compound treatment regimen. PS cells were seeded in 96-well plates (approximately 2×10^4 cells per well) and incubated for 24 h to form a confluent monolayer. For testing the optimal compound treatment regimen, we performed three independent experiments, differing in the time of drug addition to infected PS cells. (i) For a pretreatment assay, 200 μl of medium with 3′-deoxy-3′-fluoroadenosine at a concentration range of 0 to 25 μM (2-fold dilutions, three wells per concentration) was added to PS cell monolayers at 24 h prior to infection. After a 24-h incubation, medium was aspirated and replaced with 200 μl of fresh compound-containing medium in the same concentration range and inoculated with TBEV (Hypr or Neudoerfl) at an MOI of 0.1. Cells were then incubated for an additional 72 h. (ii) For a simultaneous treatment, medium containing 3′-deoxy-3′-fluoroadenosine at a concentration range of 0 to 25 μM inoculated with TBEV (MOI of 0.1) was added to cells and incubated for 72 h. (iii) For the posttreatment assay, PS cells were first infected with TBEV (MOI of 0.1), and after 2 h (the time needed for virus adsorption and internalization), medium containing 3′-deoxy-3′-fluoroadenosine at a concentration range of 0 to 25 μM was added to the infected cells and incubated for 72 h. Following incubation, the viral titers were determined from the collected supernatant media by a plaque assay and used to construct dose-response curves.

Dose-response studies using the viral titer reduction assay. To study the dose-response effect of 3′-deoxy-3′-fluoroadenosine, we used a viral titer reduction assay. PS or HBCA cell monolayers were pretreated with medium containing 3′-deoxy-3′-fluoroadenosine at a concentration range of 0 to 25 μM (2-fold dilutions, three wells per compound) for 24 h. The medium was aspirated, replaced with 200 μl of fresh medium containing the compound at the same concentration range, inoculated with TBEV (strains Hypr and Neudoerfl), ZIKV (strains MR-766 and Paraiba_1), or WNV (strains Eg-101 and 13–104) at an MOI of 0.1, and incubated for an additional 48 or 72 h. Viral titers were determined from the collected supernatant media by a plaque assay and used to construct dose-response and inhibition curves. The data used for TBEV strains Hypr and Neudoerfl (24 h pretreatment) in Fig. 2E and F were reused in Fig. 3B, as those were two identical experiments. The viral titers obtained at 72 h p.i. were used for calculation of the 50% effective concentrations (EC_{50}; the concentration of compound required to inhibit the viral titer by 50% compared to the control value). The individual points of the inhibition curves were calculated by transformation of virus titer values to percent inhibition according to equation 1,

$$\text{Percent inhibition} = 100 - (A/B \times 100) \quad (1)$$

where A is the virus titer for the individual compound concentrations tested (0.8 to 25 μM) (PFU/ml) and B is the virus titer for a compound concentration of 0 μM (PFU/ml).

Plaque assays. Plaque assays were performed in PS cells (to determine TBEV titers) or Vero cells (for ZIKV and WNV titers) as described previously (42, 50). Briefly, 10-fold dilutions of TBEV, WNV, or ZIKV were prepared in 24-well tissue culture plates, and PS (for TBEV) or Vero (for WNV and ZIKV) cells were added to each well (0.6 to 1.5×10^5 cells per well). After a 4-h incubation, the suspension was overlaid with 1.5% (wt/vol) carboxymethylcellulose in L-15 (for PS) or Dulbecco's modified Eagle's medium (DMEM) (for Vero). Following a 5-day incubation at 37°C, the infected plates were washed with phosphate-buffered saline, and the cell monolayers were stained with naphthalene black. The virus titer was expressed as PFU/ml.

Immunofluorescence staining. To measure the compound-induced inhibition of viral surface antigen expression, a cell-based flavivirus immunostaining assay was performed as previously described (42). Briefly, PS cells were seeded onto 96-well microtitration plates and treated with the test compound at a concentration range of 0 to 25 μM (2-fold dilutions, three wells per concentration) for 24 h. After a 24-h pretreatment, the cell monolayers were infected with the appropriate flaviviruses at an MOI of 0.1 and cultured for 3 days at 37°C. After cold acetone-methanol (1:1) fixation and blocking with 10% fetal bovine serum, we incubated the cells with a mouse monoclonal antibody targeting the flavivirus group surface antigen (protein E) (1:250; antibody clone D1-4G2-4-15; Sigma-Aldrich, Prague, Czech Republic) and subsequently labeled it with an anti-mouse goat secondary antibody conjugated with fluorescein isothiocyanate (FITC; 1:500) by incubation for 1 h at 37°C. The cells were counterstained with 4′,6-diamidino-2-phenylindole (DAPI; 1 μg/ml) for visualization of the cell nuclei and the fluorescence signal was recorded with an Olympus IX71 epifluorescence microscope.

Cytotoxicity assays. PS or HBCA cell monolayers in 96-well plates were treated with 3′-deoxy-3′-fluoroadenosine at a concentration range of 0 to 25 μM (2-fold dilutions, three wells per concentration) and cultured for 96 h (a 24-h pretreatment followed by a 72-h incubation, i.e., the same time duration as for antiviral assays). The cytotoxic/cytostatic activity of 3′-deoxy-3′-fluoroadenosine was determined in terms of (i) cell death or (ii) relative percentage of cell abundance using the CytoTox 96 non-radioactive cytotoxicity assay (Promega, Fitchburg, WI, USA) following the manufacturer's instructions. This assay is based on quantitative measurement of lactate dehydrogenase, a stable cytosolic enzyme that is released upon cell lysis. Cell death was estimated as the percentage of colorimetric absorbance at 490 nm by the compound-treated cells relative to the absorbance by totally lysed

Downloaded from https://journals.asm.org/journal/aac on 17 February 2025 by 147.251.135.113.

(chemically killed) cells. We assessed relative percentage of cell abundance as the percentage of colorimetric absorbance at 490 nm by lysed compound-treated cells relative to the absorbance by lysed mock-treated cells.

Quantitative phase imaging. Quantitative phase imaging (QPI) was performed using a multimodal holographic microscope, Q-PHASE (TESCAN GROUP a.s., Brno, Czech Republic). PS cells were seeded in flow chambers μ-Slide I Luer Family (Ibidi, Martinsried, Germany) (approximately 2×10^4 cells per chamber) and cultivated for 24 h to form a confluent monolayer. We performed the following independent experiments based on: (i) mock-infected and mock-treated cells as a negative control (growth medium was aspirated from the chamber and replaced with fresh medium); (ii) TBEV-infected and mock-treated cells (growth medium was aspirated from the chamber and replaced with fresh medium containing TBEV [Hypr] of MOI = 0.1); (iii) TBEV-infected cells treated with 3′-deoxy-3′-fluoroadenosine at a concentration of 12.5 μM (growth medium was aspirated from the chamber and replaced with fresh medium containing TBEV [Hypr, MOI = 0.1] and 12.5 μM of the compound; virus and compound were added to the cells in the same time); (iv) mock-infected and compound-treated cells (12.5 μM) (growth medium was aspirated and replaced with fresh medium containing 12.5 μM of the compound); (v) mock-infected and compound-treated cells (25 μM) (growth medium was aspirated and replaced with fresh medium with 25 μM of the compound); and (vi) heat-killed cells used as a model of lytic cell death (a positive control). Cells were cultivated in the chambers for 40 h postinfection and the QPI parameters, such as covered area, cell dry mass, cell speed, circularity, density, and cell dynamic score were continuously monitored. To maintain ideal cultivation conditions (37°C, 60% humidified air) during time-lapse experiments, cells were placed in a gas chamber (H201-Mad City Labs [MCL]-Z100/500 piezo Z-stages; Okolab, Ottaviano NA, Italy). To image enough cells in one field of view, we chose the Nikon Plan 10×/0.30. For each treatment, nine fields of view were observed with a frame rate of 3 min/frame for 40 h.

Holograms were captured using a CCD camera (XIMEA MR4021 MC-VELETA). Complete QPI reconstruction and image processing were performed with Q-PHASE control software. Cell dry mass values were derived according to references 51 and 52 from the phase (equation 2), where m is cell dry mass density (in pg/μm^2), φ is detected phase (in rad), λ is wavelength in μm (0.65 μm in Q-PHASE), and α is specific refraction increment (~0.18 μm^3/pg). All values in the formula except the φ are constant. The value of φ (phase) is measured directly by the microscope.

$$m = \frac{\varphi\lambda}{2\pi\alpha} \tag{2}$$

Integrated phase shift through a cell is proportional to its dry mass, which enables studying changes in cell mass distribution (52).

Image analysis was performed with customized MATLAB software developed by our laboratory. The analysis process consists of segmentation, the interconnection of matching cells in adjacent time frames, and extraction of the analyzed dynamical and morphological cell features. The details of the cell segmentation algorithm that we used are described in reference 53. Cell death detection and the distinction between apoptotic and lytic cell death using QPI have been described in detail (54).

Mouse infections. We evaluated the anti-TBEV effect of 3′-deoxy-3′-fluoroadenosine using five groups of 6-week-old female BALB/c mice (purchased from AnLab, Prague, Czech Republic) as follows: group 1 ($n = 10$) intraperitoneally injected with 3′-deoxy-3′-fluoroadenosine at 25 mg/kg/2×day to evaluate the compound toxicity; group 2 ($n = 10$) was subcutaneously injected with TBEV strain Hypr (10^3 PFU/mouse) and treated intraperitoneally with 200 μl of 3′-deoxy-3′-fluoroadenosine at 25 mg/kg/2×day (treatment started simultaneously with infection); group 3 ($n = 10$) was subcutaneously injected with TBEV strain Hypr (10^3 PFU/mouse) and treated with vehicle (control animals); group 4 ($n = 10$) was subcutaneously injected with WNV strain Eg-101 (10^3 PFU/mouse) and treated intraperitoneally with 200 μl of 3′-deoxy-3′-fluoroadenosine at 25 mg/kg/2×day (treatment started simultaneously with infection); and group 5 ($n = 10$) was subcutaneously injected with WNV strain Eg-101 (10^3 PFU/mouse) and treated with vehicle (control animals). 3′-Deoxy-3′-fluoroadenosine was freshly solubilized in sterile saline buffer before each injection and administered to the animals twice daily for 6 days. The clinical scores and survival rates of virus-infected mice were monitored daily throughout the experiment for 28 days. Illness signs were evaluated as follows: 0 for no symptoms; 1 for ruffled fur; 2 for slowing of activity or hunched posture; 3 for asthenia or mild paralysis; 4 for lethargy, tremor, or complete paralysis of the limbs; and 5 for death. All mice exhibiting disease consistent with a clinical score of 4 were terminated humanely (cervical dislocation) immediately upon detection.

Statistical analysis. Data are expressed as mean ± standard deviation (SD) and the significance of differences between groups was evaluated using the one sample Wilcoxon test (to compare clinical scores of treated mice with control animals) or ANOVA followed by Tukey-Kramer posttest (to compare multiple QPI parameters in compound-treated/TBEV-infected cells with controls). Survival rates were analyzed using the logrank Mantel-Cox test. All tests were performed with GraphPad Prism 7.04 (GraphPad Software, Inc., San Diego, CA, USA). $P < 0.05$ was considered significant.

SUPPLEMENTAL MATERIAL

Supplemental material is available online only.

SUPPLEMENTAL FILE 1, PDF file, 0.4 MB.

Downloaded from https://journals.asm.org/journal/aac on 17 February 2025 by 147.251.135.113.

ACKNOWLEDGMENTS

This study was supported by a grant from the Ministry of Education, Youth, and Sports of the Czech Republic (grant LTAUSA18016) (to L.E.).

REFERENCES

1. Baier A. 2011. Flaviviral infections and potential targets for antiviral therapy, p 89–104. *In* Ruzek D (ed), Flavivirus encephalitis. InTech, Rijeka, Croatia.
2. Pierson TC, Diamond MS. 2020. The continued threat of emerging flaviviruses. Nat Microbiol 5:796–812. https://doi.org/10.1038/s41564-020-0714-0.
3. De Clercq E. 2011. A 40-year journey in search of selective antiviral chemotherapy. Annu Rev Pharmacol Toxicol 51:1–24. https://doi.org/10.1146/annurev-pharmtox-010510-100228.
4. Eyer L, Nencka R, de Clercq E, Seley-Radtke K, Růžek D. 2018. Nucleoside analogs as a rich source of antiviral agents active against arthropod-borne flaviviruses. Antivir Chem Chemother 26:2040206618761299. https://doi.org/10.1177/2040206618761299.
5. Niu G, Tan H. 2015. Nucleoside antibiotics: biosynthesis, regulation, and biotechnology. Trends Microbiol 23:110–119. https://doi.org/10.1016/j.tim.2014.10.007.
6. Andriole VT. 1999. Current and future antifungal therapy: new targets for antifungal agents. J Antimicrob Chemother 44:151–162. https://doi.org/10.1093/jac/44.2.151.
7. Wataya Y, Hiraoka O, Sonobe Y, Yoshioka A, Matsuda A, Miyasaka T, Saneyoshi M, Ueda T. 1984. Anti-parasite activity of nucleoside analogues in Leishmania tropica promastigotes. Nucleic Acids Symp Ser (Oxf) 15:69–71.
8. Wataya Y, Satake H, Hiraoka O, Aji T, Morishige K, Kimura JY, Ishii A, Matsuda A, Ueda T, Fukukawa K. 1986. Anti-parasite activity of nucleoside analogues: the metabolism of carbocyclic inosine in promastigotes of Leishmania tropica and Leishmania donovani and its activity against amastigotes of Leishmania donovani in vitro. Nucleic Acids Symp Ser (Oxf) 17:149–151.
9. Guinan M, Benckendorff C, Smith M, Miller GJ. 2020. Recent advances in the chemical synthesis and evaluation of anticancer nucleoside analogues. Molecules 25:2050. https://doi.org/10.3390/molecules25092050.
10. Miura S, Izuta S. 2004. DNA polymerases as targets of anticancer nucleosides. Curr Drug Targets 5:191–195. https://doi.org/10.2174/1389450043490578.
11. De Clercq E, Neyts J. 2009. Antiviral agents acting as DNA or RNA chain terminators. Handb Exp Pharmacol 189:53–84. https://doi.org/10.1007/978-3-540-79086-0_3.
12. Chen H, Liu L, Jones SA, Banavali N, Kass J, Li Z, Zhang J, Kramer LD, Ghosh AK, Li H. 2013. Selective inhibition of the West Nile virus methyltransferase by nucleoside analogs. Antiviral Res 97:232–239. https://doi.org/10.1016/j.antiviral.2012.12.012.
13. Vernekar SK, Qiu L, Zhang J, Kankanala J, Li H, Geraghty RJ, Wang Z. 2015. 5 '-Silylated 3 '-1,2,3-triazolyl thymidine analogues as inhibitors of West Nile virus and Dengue virus. J Med Chem 58:4016–4028. https://doi.org/10.1021/acs.jmedchem.5b00327.
14. Leyssen P, Balzarini J, De Clercq E, Neyts J. 2005. The predominant mechanism by which ribavirin exerts its antiviral activity in vitro against flaviviruses and paramyxoviruses is mediated by inhibition of inosine monophosphate dehydrogenase. J Virol 79:1943–1947. https://doi.org/10.1128/JVI.79.3.1943-1947.2005.
15. Crotty S, Cameron CE, Andino R. 2001. RNA virus error catastrophe: direct molecular test by using ribavirin. Proc Natl Acad Sci U S A 98:6895–6900. https://doi.org/10.1073/pnas.111085598.
16. Graci JD, Cameron CE. 2002. Quasispecies, error catastrophe, and the antiviral activity of ribavirin. Virology 298:175–180. https://doi.org/10.1006/viro.2002.1487.
17. Weiland O, Milich DR, S√§LIberg M, Hultgren C. 1998. The antiviral compound ribavirin modulates the T helper (Th)1/Th2 subset balance in hepatitis B and C virus-specific immune responses. J Gen Virol 79:2381–2391. https://doi.org/10.1099/0022-1317-79-10-2381.
18. Seley-Radtke KL, Yates MK. 2018. The evolution of nucleoside analogue antivirals: a review for chemists and non-chemists. 2018. Part 1: early structural modifications to the nucleoside scaffold. Antiviral Res 154:66–86. https://doi.org/10.1016/j.antiviral.2018.04.004.
19. Yates MK, Seley-Radtke KL. 2019. The evolution of antiviral nucleoside analogues: a review for chemists and non-chemists. Part II: complex modifications to the nucleoside scaffold. Antiviral Res 162:5–21. https://doi.org/10.1016/j.antiviral.2018.11.016.
20. Liu P, Sharon A, Chu CK. 2008. Fluorinated nucleosides: synthesis and biological implication. J Fluor Chem 129:743–766. https://doi.org/10.1016/j.jfluchem.2008.06.007.
21. Wojtowicz-Rajchel H. 2012. Synthesis and applications of fluorinated nucleoside analogues. J Fluor Chem 143:11–48. https://doi.org/10.1016/j.jfluchem.2012.06.026.
22. Saenger W. 1984. Defining terms for the nucleic acids, p 9–28. *In* Cantor CR (ed), Principles of nucleic acid structure, Springer-Verlag Inc., New York.
23. Ikeda H, Fernandez R, Wilk A, Barchi JJ, Jr, Huang X, Marquez VE. 1998. The effect of two antipodal fluorine-induced sugar puckers on the conformation and stability of the Dickerson-Drew dodecamer duplex [d(CGCGAATTCGCG)]2. Nucleic Acids Res 26:2237–2244. https://doi.org/10.1093/nar/26.9.2237.
24. Park BK, Kitteringham NR, O'Neill PM. 2001. Metabolism of fluorine-containing drugs. Annu Rev Pharmacol Toxicol 41:443–470. https://doi.org/10.1146/annurev.pharmtox.41.1.443.
25. De Clercq E. 2010. Historical perspectives in the development of antiviral agents against poxviruses. Viruses 2:1322–1339. https://doi.org/10.3390/v2061322.
26. Whitley RJ. 1996. The past as prelude to the future: history, status, and future of antiviral drugs. Ann Pharmacother 30:967–971. https://doi.org/10.1177/106002809603000911.
27. Kaufman HE, Heidelberger C. 1964. Therapeutic antiviral action of 5-trifluoromethyl-2′-deoxyuridine in herpes simplex keratitis. Science 145:585–586. https://doi.org/10.1126/science.145.3632.585.
28. Hertel LW, Boder GB, Kroin JS, Rinzel SM, Poore GA, Todd GC, Grindey GB. 1990. Evaluation of the antitumor activity of gemcitabine (2',2'-difluoro-2'-deoxycytidine). Cancer Res 50:4417–4422.
29. Jin C, Zhang H, Zou J, Liu Y, Zhang L, Li F, Wang R, Xuan W, Ye M, Tan W. 2018. Floxuridine homomeric oligonucleotides "hitchhike" with albumin in situ for cancer chemotherapy. Angew Chem Int Ed Engl 57:8994–8997. https://doi.org/10.1002/anie.201804156.
30. Sofia MJ, Bao D, Chang W, Du J, Nagarathnam D, Rachakonda S, Reddy PG, Ross BS, Wang P, Zhang HR, Bansal S, Espiritu C, Keilman M, Lam AM, Steuer HM, Niu C, Otto MJ, Furman PA. 2010. Discovery of a β-D-2'-deoxy-2'-α-fluoro-2'-β-C-methyluridine nucleotide prodrug (PSI-7977) for the treatment of hepatitis C virus. J Med Chem 53:7202–7218. https://doi.org/10.1021/jm100863x.
31. Kozuch O, Mayer V. 1975. Pig kidney epithelial (PS) cells: a perfect tool for study of flaviviruses and some other arboviruses. Acta Virologica 19:498.
32. Mumtaz N, Jimmerson LC, Bushman LR, Kiser JJ, Aron G, Reusken CBEM, Koopmans MPG, van Kampen JJA. 2017. Cell-line dependent antiviral activity of sofosbuvir against Zika virus. Antiviral Res 146:161–163. https://doi.org/10.1016/j.antiviral.2017.09.004.
33. Bullard-Feibelman KM, Govero J, Zhu Z, Salazar V, Veselinovic M, Diamond MS, Geiss BJ. 2017. The FDA-approved drug sofosbuvir inhibits Zika virus infection. Antiviral Res 137:134–140. https://doi.org/10.1016/j.antiviral.2016.11.023.
34. Ferreira AC, Zaverucha-do-Valle C, Reis PA, Barbosa-Lima G, Vieira YR, Mattos M, Silva PP, Sacramento C, de Castro Faria Neto HC, Campanati L, Tanuri A, Brüning K, Bozza FA, Bozza PT, Souza TML. 2017. Sofosbuvir protects Zika virus-infected mice from mortality, preventing short- and long-term sequelae. Sci Rep 7:9409. https://doi.org/10.1038/s41598-017-09797-8.
35. Eldrup AB, Allerson CR, Bennett CF, Bera S, Bhat B, Bhat N, Bosserman MR, Brooks J, Burlein C, Carroll SS, Cook PD, Getty KL, MacCoss M, McMasters DR, Olsen DB, Prakash TP, Prhavc M, Song QL, Tomassini JE, Xia J. 2004. Structure-activity relationship of purine ribonucleosides for inhibition of hepatitis C virus RNA-dependent RNA polymerase. J Med Chem 47:2283–2295. https://doi.org/10.1021/jm030424e.
36. Van Aerschot A, Herdewijn P, Janssen G, Cools M, De Clercq E. 1989. Synthesis and antiviral activity evaluation of 3'-fluoro-3'-deoxyribonucleosides:

Downloaded from https://journals.asm.org/journal/aac on 17 February 2025 by 147.251.135.113.

broad-spectrum antiviral activity of 3'-fluoro-3'-deoxyadenosine. Antiviral Res 12:133–150. https://doi.org/10.1016/0166-3542(89)90047-8.
37. Van Aerschot A, Balzarini J, De Clercq E, Herdewijn P. 1989. Synthesis of 3'-fluoro-3'-deoxyribonucleosides: anti-HIV-1 and cytostatic properties. Nucleosides, Nucleotides & Nucleic Acids 8:1123–1124. https://doi.org/10.1080/07328318908054305.
38. Smee DF, Morris JL, Barnard DL, Van Aerschot A. 1992. Selective inhibition of arthropod-borne and arenaviruses in vitro by 3'-fluoro-3'-deoxyadenosine. Antiviral Res 18:151–162. https://doi.org/10.1016/0166-3542(92)90035-4.
39. Mikhailopulo IA, Poopeiko NE, Prikota TI, Sivets GG, Kvasyuk EI, Balzarini J, De Clercq E. 1991. Synthesis and antiviral and cytostatic properties of 3'-deoxy-3'-fluoro- and 2'-azido-3'-fluoro-2',3'-dideoxy-D-ribofuranosides of natural heterocyclic bases. J Med Chem 34:2195–2202. https://doi.org/10.1021/jm00111a040.
40. Mikhailopulo IA, Pricota TI, Poopeiko NE, Sivets GG, Kvasyuk EI, Sviryaeva TV, Savochkina LP, Beabealashvilli RS. 1989. 3'-Fluoro-3'-deoxyribonucleoside 5'-triphosphates: synthesis and use as terminators of RNA biosynthesis. FEBS Lett 250:139–141. https://doi.org/10.1016/0014-5793(89)80706-9.
41. Lee K, Kim D-E, Jang K-S, Kim S-J, Cho S, Kim C. 2017. Gemcitabine, a broad-spectrum antiviral drug, suppresses enterovirus infections through innate immunity induced by the inhibition of pyrimidine biosynthesis and nucleotide depletion. Oncotarget 8:115315–115325. https://doi.org/10.18632/oncotarget.23258.
42. Eyer L, Valdés JJ, Gil VA, Nencka R, Hřebabecký H, Šála M, Salát J, Černý J, Palus M, De Clercq E, Růžek D. 2015. Nucleoside inhibitors of tick-borne encephalitis virus. Antimicrob Agents Chemother 59:5483–5493. https://doi.org/10.1128/AAC.00807-15.
43. Chen YL, Yin Z, Duraiswamy J, Schul W, Lim CC, Liu B, Xu HY, Qing M, Yip A, Wang G, Chan WL, Tan HP, Lo M, Liung S, Kondreddi RR, Rao R, Gu H, He H, Keller TH, Shi PY. 2010. Inhibition of dengue virus RNA synthesis by an adenosine nucleoside. Antimicrob Agents Chemother 54:2932–2939. https://doi.org/10.1128/AAC.00140-10.
44. Lo MK, Shi PY, Chen YL, Flint M, Spiropoulou CF. 2016. In vitro antiviral activity of adenosine analog NITD008 against tick borne flaviviruses. Antiviral Res 130:46–49. https://doi.org/10.1016/j.antiviral.2016.03.013.
45. Eyer L, Šmídková M, Nencka R, Neča J, Kastl T, Palus M, De Clercq E, Růžek D. 2016. Structure-activity relationships of nucleoside analogues for inhibition of tick-borne encephalitis virus. Antiviral Res 133:119–129. https://doi.org/10.1016/j.antiviral.2016.07.018.
46. Lo MK, Jordan R, Arvey A, Sudhamsu J, Shrivastava-Ranjan P, Hotard AL, Flint M, McMullan LK, Siegel D, Clarke MO, Mackman RL, Hui HC, Perron M, Ray AS, Cihlar T, Nichol ST, Spiropoulou CF. 2017. GS-5734 and its parent nucleoside analog inhibit Filo-, Pneumo-, and Paramyxoviruses. Sci Rep 7:43395. https://doi.org/10.1038/srep43395.
47. Lam AM, Murakami E, Espiritu C, Steuer HM, Niu C, Keilman M, Bao H, Zennou V, Bourne N, Julander JG, Morrey JD, Smee DF, Frick DN, Heck JA, Wang P, Nagarathnam D, Ross BS, Sofia MJ, Otto MJ, Furman PA. 2010. PSI-7851, a pronucleotide of beta-D-2'-deoxy-2'-fluoro-2'-C-methyluridine monophosphate, is a potent and pan-genotype inhibitor of hepatitis C virus replication. Antimicrob Agents Chemother 54:3187–3196. https://doi.org/10.1128/AAC.00399-10.
48. Clark JL, Hollecker L, Mason JC, Stuyver LJ, Tharnish PM, Lostia S, McBrayer TR, Schinazi RF, Watanabe KA, Otto MJ, Furman PA, Stec WJ, Patterson SE, Pankiewicz KW. 2005. Design, synthesis, and antiviral activity of 2'-deoxy-2'-fluoro-2'-C-methylcytidine, a potent inhibitor of hepatitis C virus replication. J Med Chem 48:5504–5508. https://doi.org/10.1021/jm0502788.
49. Eyer L, Fojtíková M, Nencka R, Rudolf I, Hubálek Z, Ruzek D. 2019. Viral RNA-dependent RNA polymerase inhibitor 7-deaza-2'-C-methyladenosine prevents death in a mouse model of West Nile virus infection. Antimicrob Agents Chemother 63:e02093-18. https://doi.org/10.1128/AAC.02093-18.
50. De Madrid AT, Porterfield JS. 1969. A simple micro-culture method for study of group B arboviruses. Bull World Health Organ 40:113–121.
51. Prescher JA, Bertozzi CR. 2005. Chemistry in living systems. Nat Chem Biol 1:13–21. https://doi.org/10.1038/nchembio0605-13.
52. Park Y, Depeursinge C, Popescu G. 2018. Quantitative phase imaging in biomedicine. Nature Photon 12:578–589. https://doi.org/10.1038/s41566-018-0253-x.
53. Feith M, Vičar T, Gumulec J, Raudenská M, Gjörloff Wingren A, Masařík M, Balvan J. 2020. Quantitative phase dynamics of cancer cell populations affected by blue light. Appl Sci 10:2597. https://doi.org/10.3390/app10072597.
54. Vicar T, Raudenska M, Gumulec J, Balvan J. 2020. The quantitative-phase dynamics of apoptosis and lytic cell death. Sci Rep 10:1566. https://doi.org/10.1038/s41598-020-58474-w.

Downloaded from https://journals.asm.org/journal/aac on 17 February 2025 by 147.251.135.113.

4.4 Mechanisms of cell death resistance in metastatic cancer cells

Cancer metastasis and treatment resistance are the main causes of treatment failure and cancer-related deaths. The detailed mechanisms behind these phenomena are not yet completely understood and are thought to be linked to the existence of cancer stem cells (CSCs). These CSCs represent a minor group of extremely tumorigenic cells that possess the ability to differentiate into various cell types and can self-replicate, placing them at the top of the cellular hierarchy.

4.4.1 Autophagy as a mechanism of resistance

Autophagy is an essential pathway for maintaining cellular balance through the breakdown and recycling of cellular components. There has been growing interest in the positive effects of promoting autophagy in various diseases, such as aiding in the elimination of protein aggregates linked to neurodegenerative disorders [11, 12]. Conversely, in the context of cancer, the function of autophagy is more nuanced and varies according to the stage of the tumor, its biological characteristics, and the microenvironment it resides in. Autophagy could facilitate the degradation of proteins critical for maintaining differentiation status, thereby hindering the reprogramming process, while simultaneously eliminating proteins that should not be present in pluripotent cells. Based on insights from principal component analysis, we suggest that the expression of BIRC plays a crucial role in mitigating metabolic stress in naive PC-3 cells, but it may also inhibit reprogramming mechanisms. The protein product of the BIRC gene, survivin, not only prevents apoptotic cell death but also inhibits autophagy. Autophagy may enhance the efficiency of generating pluripotent stem cells. Additionally, PC-3 cells exhibit relatively low levels of another autophagy inhibitor, CCL2, which further contributes to the complexity of these regulatory mechanisms. Prostate cancers frequently exhibit substantial heterogeneity within tumors across various measurable traits, such as metabolism, gene expression, cell structure, and potential for metastasis [11]. Certain cell populations within the tumor appear to have a greater ability to withstand high levels of metabolic stress. One mechanism of resistance involves the efficient management and elimination of damaged mitochondria that produce reactive oxygen species (ROS) through a process known as mitophagy. As a result, autophagy is activated as a protective strategy, contributing to the resistance observed in some cancer cells during ROS-inducing treatments in our study involving apoptosis-resistant, androgen-independent, metastatic prostate cancer (PC-3 cell line). Recent insights have suggested that autophagy might induce cell

death in apoptosis-defective cancer cells; however, this does not apply to the PC-3 line. Additionally, we propose that autophagy may facilitate the formation of cell-in-cell structures, thereby playing a crucial role in polyploidization and the dedifferentiation of cells into a pluripotent state and the possible formation of CSCs.

Author's publications relevant to this chapter

1. Balvan, J. et al. Oxidative stress resistance in metastatic prostate cancer: Renewal by self-eating. *PLoS One* **10**, e0145016 (2015).
   IF (2015) 3.752; 23 citations (WOS)
2. Gumulec, J., Balvan, J., *et al*. Cisplatin-resistant prostate cancer model: Differences in antioxidant system, apoptosis and cell cycle. *International Journal of Oncology.* **44**, 923–933 (2014).
   IF (2014) 4.5; 65 citations (WOS)

PLOS ONE

RESEARCH ARTICLE

Oxidative Stress Resistance in Metastatic Prostate Cancer: Renewal by Self-Eating

Jan Balvan[1,2], Jaromir Gumulec[1,2], Martina Raudenska[1,2], Aneta Krizova[2,3], Petr Stepka[4], Petr Babula[4], Rene Kizek[2,5], Vojtech Adam[2,5], Michal Masarik[1]*

1 Department of Pathological Physiology, Faculty of Medicine, Masaryk University / Kamenice 5, CZ-625 00, Brno, Czech Republic, **2** Central European Institute of Technology, Brno University of Technology, Technicka 3058/10, CZ-616 00, Brno, Czech Republic, **3** TESCAN Brno, s.r.o., Brno, Czech Republic, **4** Department of Physiology, Faculty of Medicine, Masaryk University / Kamenice 5, CZ-625 00, Brno, Czech Republic, **5** Department of Chemistry and Biochemistry, Mendel University in Brno / Zemedelska 1, CZ-613 00, Brno, Czech Republic

* masarik@med.muni.cz

CrossMark
click for updates

OPEN ACCESS

Citation: Balvan J, Gumulec J, Raudenska M, Krizova A, Stepka P, Babula P, et al. (2015) Oxidative Stress Resistance in Metastatic Prostate Cancer: Renewal by Self-Eating. PLoS ONE 10(12): e0145016. doi:10.1371/journal.pone.0145016

Editor: Natasha Kyprianou, University of Kentucky College of Medicine, UNITED STATES

Received: September 15, 2015

Accepted: November 25, 2015

Published: December 15, 2015

Copyright: © 2015 Balvan et al. This is an open access article distributed under the terms of the Creative Commons Attribution License, which permits unrestricted use, distribution, and reproduction in any medium, provided the original author and source are credited.

Data Availability Statement: All relevant data are within the paper and its Supporting Information files.

Funding: This work was supported by funds from the Faculty of Medicine, Masaryk University to junior researcher (Michal Masarik) and by the project MUNI/A/1549/2014 and MUNI/A/1326/2014 with the support of the Specific University Research Grant, as provided by the Ministry of Education, Youth and Sports of the Czech Republic in the year 2015. The funders had no role in study design, data collection and analysis, decision to publish, or preparation of the manuscript. The commercial company (TESCAN) provided support in the form of salary for author

Abstract

Resistant cancer phenotype is a key obstacle in the successful therapy of prostate cancer. The primary aim of our study was to explore resistance mechanisms in the advanced type of prostate cancer cells (PC-3) and to clarify the role of autophagy in these processes. We performed time-lapse experiment (48 hours) with ROS generating plumbagin by using multimodal holographic microscope. Furthermore, we also performed the flow-cytometric analysis and the qRT-PCR gene expression analysis at 12 selected time points. TEM and confocal microscopy were used to verify the results. We found out that autophagy (namely mitophagy) is an important resistance mechanism. The major ROS producing mitochondria were coated by an autophagic membrane derived from endoplasmic reticulum and degraded. According to our results, increasing ROS resistance may be also accompanied by increased average cell size and polyploidization, which seems to be key resistance mechanism when connected with an escape from senescence. Many different types of cell-cell interactions were recorded including entosis, vesicular transfer, eating of dead or dying cells, and engulfment and cannibalism of living cells. Entosis was disclosed as a possible mechanism of polyploidization and enabled the long-term survival of cancer cells. Significantly reduced cell motility was found after the plumbagin treatment. We also found an extensive induction of pluripotency genes expression (*NANOG*, *SOX2*, and *POU5F1*) at the time-point of 20 hours. We suppose, that overexpression of pluripotency genes in the portion of prostate tumour cell population exposed to ROS leads to higher developmental plasticity and capability to faster respond to changes in the extracellular environment that could ultimately lead to an alteration of cell fate.

Aneta Krizova, but did not have any additional role in the study design, data collection and analysis, decision to publish, or preparation of the manuscript. The specific role of this author is articulated in the 'author contributions' section.

Competing Interests: The cooperation with a commercial company (TESCAN) does not alter the authors' adherence to PLOS ONE policies on sharing data and materials.

Introduction

Prostate cancer (PC) is one of the most frequently diagnosed cancer types in men. Most of prostate cancers are initially responsive to androgen deprivation therapy, but later would emerge an aggressive, androgen-independent phenotype resistant to conventional therapies. This advanced type of prostate cancer easily metastasizes. Hematogeneous metastases are usually present in 35% of prostate cancer patients with the most frequent localisation in bones (90%). The widely studied model for androgen-independent, advanced, metastases-producing prostate cancer is the PC-3 cell line established from the lumbar metastasis of a 62 year old Caucasian male with grade 4 of prostatic adenocarcinoma. PC-3 cells are hemizygous for 17p chromosome, and their sole copy of the *p53* gene has a stop codon at position 169 [1]. As a result, PC-3 cells do not express the functional p53 protein, which makes it rather resistant to p53-mediated apoptosis [2]. Furthermore, we chose PC-3 cell line and not DU145, because DU145 prostate cancer cells express PTEN, which is not expressed by PC-3 cells [3, 4]. Multiple functional studies support the role of PTEN as a critical tumour suppressor in prostate cancer [5–7].

In our previous study we demonstrated that the PC-3 cell line showed higher resistance to cisplatin-induced apoptosis and no decreasing proportion of G2/M fraction (4N DNA content) evident in 22Rv1 cells [8]. Cisplatin is primarily considered as a DNA-damaging agent, forming different types of hard-reparable adducts with cellular DNA [9]. Apart from DNA damage, cisplatin also induces reactive oxygen species (ROS) [10]. Due to the fact, we have focused on another ROS-producing reagent, plumbagin [11], which does not form DNA adducts, to assess importance of cell death modulation and dealing with ROS for PC-3 resistance. Plumbagin (5-hydroxy-2-methyl-1,4-naphthoquinone) occurs naturally in the medicinal herb *Plumbago zeylanica L.* and belongs to naphthoquinones. Naphthoquinones display their cytotoxic actions through two ways: as pro-oxidants, reducing oxygen to reactive oxygen species; and as electrophiles, which form covalent bonds with tissue nucleophiles [12]. Furthermore, plumbagin was also shown to suppress the activation of nuclear factor-κB (NF-κB) [13].

In recent studies, ROS generation was associated with the mitochondria as a consequence of impaired mitochondrial protein synthesis [10]. Furthermore, it was pointed out, that cells with a deficit of functional mitochondria are more resilient to cell damage by cisplatin [14]. However, Panov *et al.* found out, that the prostate cancer cell lines LNCaP, PC-3, and DU145 contained 2 to 4 times more mitochondria per gram of cells than normal prostate epithelial cells. Respiratory activities of mitochondria isolated from normal prostate epithelial cells were also 5-20-fold lower than those of mitochondria isolated from prostate cancer cells [15]. Therefore, we presume the existence of some protective mechanisms against ROS in PC-3 cells. Many cell injuries caused by ROS could be sublethal (especially if the studied cells have disrupted apoptosis-triggering mechanisms) and result in an altered steady state in which the damaged cells are able to survive. Even if a damaged cell is driven to oncosis (oncosis is a pre-lethal phase that follows a serious cell injury) or senescence, there are probably some mechanisms to reverse this process [16–18], particularly if the cell is able to get rid of damaging factors and restore ATP production. A possible way to gain enough energy for the survival could be autophagy [19], cannibalism or entosis [20, 21]. Autophagy was at first considered a mechanism that suppresses malignant transformation. However, strong evidences for a dual role of autophagy were discovered [22]. In early tumours, autophagy could be truly a potent tumour suppressor because it can assure organelle and protein quality control and prevent genomic instability and aneuploidy organelle [23]. However, there are significant evidences that autophagy has a cancer-promoting role in established tumours [24].

One of the significant histopathological features of human solid tumours is the occurrence of large atypical cancer cells with multiplicated nuclear DNA that are known as polyploid giant cancer cells (PGCCs). Increased PGCCs numbers usually appear in late disease stages and grades or as a consequence of chemotherapy [25]. An important goal of our study was to explore possible mechanisms of defence against ROS in the advanced type of prostate cancer cells. We tried to assess the role of autophagy and the formation of polyploid giant cancer cells (PGCCs) in the advanced type of prostate cancer. We also attempted to verify a hypothesis that autophagy could be the mechanism of resistance against ROS rather than the mechanism of cell death. This hypothesis is supported by recent findings indicating that well-characterized autophagy activators and mTOR inhibitors (such as rapamycin, PP242, or resveratrol) markedly improve the speed and efficiency of puripotent stem cells generation [26].

Materials and Methods

Chemical and biochemical reagents

Ham's F12 medium, fetal bovine serum (FBS), (mycoplasma free), penicillin/streptomycin and trypsin were purchased from PAA Laboratories GmbH (Pasching, Austria). Phosphate-buffered saline (PBS) was purchased from Invitrogen Corp. (Carlsbad, CA, USA). Ethylenediaminetetraacetic acid (EDTA), plumbagin and other chemicals of ACS purity were purchased from Sigma-Aldrich Co. (St. Louis, MO, USA), unless noted otherwise.

Cell cultures and cultured cell conditions

Human PC-3 prostate cancer cells were used in this study (passage 18–24). The PC-3 cell line was established from grade 4 prostatic adenocarcinoma from 62 years old Caucasian male and derived from the metastatic site in bones. The PC-3 cell line was purchased from HPA Culture Collections (Salisbury, UK).

PC-3 cells were cultured in Ham's F12 medium with 7% FBS. The medium was supplemented with penicilin (100 U/ml) and the cells were maintained at 37°C in humidified incubator with 5% CO_2. Hypoxy/starvation-resistant PC-3 were selected by cultivation without the access of oxygen and with no medium replacement for one month.

Plumbagin treatment

The stock solution of plumbagin was prepared in dimethylsulfoxide (DMSO) and diluted with the medium. An equal volume of DMSO (final concentration $\leq$ 0.1%) was added to the controls. The plumbagin treatment was initialized after the cells reached confluence of ~50%. For cytotoxicity assessment, a range of concentrations 0, 0.5, 1, 1.5, 2, 2.5, 3, 4, 5, and 6 μmol/l of plumbagin was used. Time points for cell harvesting and thus for subsequent analyses were 0 h, 40 min., 1,5, 4, 6, 8, 10, 16, 20, 24, 36, and 48 h.

Cell content quantification

Total cell content was measured using Casy model TT system (Roche Applied Science, USA) and the following protocol: first, calibration was performed from the samples of viable and necrotic cells. For the necrotic cells, 100 μl cell suspension and 800 μl Casy Blue solution were mixed and left for 5 minutes at room temperature. Subsequently, 9 ml CasyTone was added. To prepare a viable cell standard, 100 μl of cell suspension was mixed with 10 ml CasyTone. All subsequent measurements were performed on 100x diluted 100 μl cell suspension. Prior to each measurement, the background was subtracted. All samples were measured in duplicates.

Measurement of cell viability—MTT test

The suspension of 5000 cells was added to each well of standard microtiter plates. Volume of 200 μl was transferred to wells 2–11. The medium (200 μl) was added to the first and to the last column (1 and 12, control). The plates were incubated for 2 days at 37°C to ensure cell growth. The medium was removed from columns 2 to 11. Columns 3–10 were filled with 200 μl of medium containing an increased concentration of plumbagin (0–6 μmol/l). As a control, columns 2 and 11 were filled with the medium without plumbagin. The plates were incubated for 12 and 24 h, then the medium was removed and the cells were washed in PBS. Columns 1–11 were filled with 200 μl of medium containing 50 μl of MTT (5mg/ml in PBS), incubated in humidified atmosphere for 4 h at 37°C, and wrapped in aluminium foil. After the incubation, the MTT-containing medium was replaced with 200 μl of 99.9% dimethylsulfoxide (DMSO) to dissolve MTT-formazan crystals. Subsequently, 25 μl of glycine buffer was added to all wells and absorbance was determined immediately at 570 nm (VersaMax microplate reader, Molecular Devices, Sunnyvale, CA, USA).

Cell growth and proliferation assay using impedance measurement

Cell growth was analyzed using the real-time cell analysis (RTCA) system (xCELLigence; Roche Applied Science and ACEA Biosciences). Firstly, the optimal seeding concentration for proliferation and cytotoxic assay was determined. PC-3 cells were seeded at a density of 7000 cells per well in E-Plates 16. After seeding the total number of cells in 200 μl medium to each well, in E-Plate 16, the attachment, proliferation and spreading of the cells was monitored every 15 min. After 24 hours, plumbagin was added and the cell index (CI), which reflects cell viability, was monitored. All experiments were carried out for 250h. The results are expressed as a cell index using the manufacturer's software (Roche Applied Science and ACEA Biosciences). The experiments were made in duplicates.

Flow cytometric analysis of cell death

Double-staining with fluorescein isothiocyanate (FITC)/propidium iodide (PI) was undertaken using the Annexin V-FLUOS-staining kit (Roche Applied Science) according to the manufacturer's protocol in order to determine percentages of viable, apoptotic and necrotic cells following the exposure to plumbagin. Briefly, the cells were harvested by repetitive pipetting and washed two times with PBS (centrifuged at 2000 rpm for 5 min), resuspended in 100 μl of Annexin-V-FLUOS labelling solution and incubated for 15 min. in the dark at 15–25°C. Annexin V-FITC binding was detected by flow cytometry (Partec GmbH, Münster, Germany) (Ex = 488 nm, Em = 533 nm, FL1 filter for Annexin-V-FLUOS and FL3 filter for PI).

Flow cytometric detection of autophagosomes

Autophagosome formation in PC-3 cells was detected using the CYTO-ID Autophagy Detection Kit (Enzo, PA, USA) following the manufacturer's instruction. The CYTO-ID green fluorescent reagents specifically detect acid autophagic vacuoles formed during autophagy. Briefly, the cells were harvested by gentle repetitive pipetting, spun down and washed twice in RPMI 1640 with 5% fetal bovine serum (FBS). The cells were resuspended in 500 μl of freshly diluted CYTO-ID staining reagent and incubated in the dark at 37°C for 30 min. CYTO-ID fluorescence of cells was immediately analyzed by flow cytometry using the flow cytometr (Partec GmbH, Münster, Germany) (Ex = 480 nm, Em = 530 nm, FL1 filter for CYTO-ID, SSC for cellular granularity). The percentage of cells with CYTO-ID staining was used to represent the formation of autophagosomes.

Flow cytometric analysis of intact healthy cells

The cell pellet was prepared as mentioned above. The cells were resuspended in 500 μl of freshly diluted 1 μM SYTO 16 (Thermo Fisher Scientific, Waltham, MA, USA) staining solution and incubated in the dark at 37°C for 45 min. SYTO 16 fluorescence of cells was immediately analyzed on the same instrument as mentioned above (Ex = 488 nm, Em = 518 nm, FL1 filter for SYTO 16, FSC for cell size). The percentage of SYTO 16-positive cells was analyzed. The data were analyzed using the FloMax software (Partec GmbH, Münster, Germany).

Fluorescence microscopy and cell staining

For fluorescence microscopy, the cells were cultivated directly on microscope glass slides (75x25 mm, thickness 1mm, Menzel Glässer, Braunschweig, Germany) in Petri dishes in the above-described cultivation media (see Cultured cell conditions). The cells were transferred directly onto the slides, which were submerged in the cultivation media. After the treatment, the microscope glass slides with a monolayer of cells were removed from the Petri dishes, rinsed in the cultivation medium without plumbagin supplementation and PBS buffer and directly used for staining and fluorescence microscopy.

The cells were incubated with the following highly specific fluorescent probes: reactive oxygen species were visualized using CellROX Deep Red reagent (Life Technologies, USA, 5 μM, cell-permeant, life-cell stain with absorption/emission maxima of 644/665 nm), mitochondria were visualized using MitoTracker Green FM (Life Technologies, USA, 300 nM, cell-permeant life-cell stain with absorption/emission maxima of 490/516 nm), and endoplasmic reticulum was visualized using ER-Tracker Red (Life Technologies, USA, 1 μM, cell-permeant, life-cell stain with absorption/emission maxima of 587/615 nm). After incubation (45 min, 37°C, dark), the cells were washed three times with PBS buffer (0.05 M, pH 7.0) and observed under the confocal microscope (Leica TCS SP8 X, Germany) using appropriate excitation and emission wavelengths.

TEM visualization of PC-3 ultrastructure

The PC-3 cells were gently harvested by repetitive pipetting and spun down (2000 rpm, 5 min.). Briefly, the cells were fixed with 3% glutaraldehyde in cacodylate buffer for 2 hours and washed three times for 30 minutes in 0.1 M cacodylate buffer. Following this, they were fixed with 0.02 M OsO_4 dissolved in 0.1 M cacodylate buffer, dehydrated in alcohol, and infiltrated with acetone and No. 1 Durcuptan mixture overnight. On the following day, the cells were infiltrated with No. 2 Durcuptan mixture, embedded and polymerized. Ultrathin sections (90 nm, Ultramicrotome LKB, Bromma, Stockholm, Sweden) were transferred onto grids covered with the Formvar membrane (Marivac Ltd., Halifax, Canada). 2% uranyl acetate and Reynold's solution were used for contrast staining. The sections were viewed in the transmission electron microscope (Morgagni 268, FEI Europe B.V., Eindhoven Netherlands). Software AnalySIS (Soft Imaging System, GmbH, Münster, Germany) was used for image analysis of cell ultrastructure.

Quantitative phase imaging

Quantitative phase imaging is a non-invasive technique with high intrinsic contrast even for naturally transparent objects such as live cells. Therefore this method is suitable for long term observations of cell reactions to treatment without any additional staining. In these experiments quantitative phase imaging was performed by Tescan multimodal holographic

microscope Q-PHASE. Q-PHASE is based on the original concept of coherence-controlled holographic microscope [27, 28].

Quantitative phase imaging was initiated immediately after plumbagin treatment. Cells were cultivated in Flow chambers μ-Slide I Lauer Family (Ibidi, Martinsried, Germany) In order to image enough number of cells in one field of view, objectives Nikon Plan 10/0.30 were chosen. Holograms were captured by CCD camera (XIMEA MR4021 MC-VELETA). The entire image reconstruction and image processing were performed in Q-PHASE control software. Quantitative phase images are shown in grayscale with units of pg/μm^2 that were recalculated from original radians according to Barer and Davies [29, 30]. Movies with identification arrows were prepared in ImageJ software.

RNA Isolation and Reverse Transcription

TriPure Isolation Reagent (Roche, Basel, Switzerland) was used for RNA isolation. RNA samples without reverse transcription were used as negative control for qRT-PCR to exclude DNA contamination. The isolated RNA was used for the cDNA synthesis. RNA (1000 ng) was transcribed using the transcriptor first strand cDNA synthesis kit (Roche, Switzerland), which was applied according to manufacturer's instructions. The cDNA (20 μl) prepared from the total-RNA was diluted with RNase-free water to 100 μl and the amount of 5 μl was directly analyzed by using the LightCycler®480 II System (Roche, Basel, Switzerland).

Quantitative real-time polymerase chain reaction

qRT-PCR was performed using TaqMan gene expression assays and the LightCycler®480 II System (Roche, Basel, Switzerland). The amplified DNA was analyzed by the comparative Ct method using β-actin as a reference gene. The primer and probe sets for ACTB (assay ID: Hs99999903_m1), BECN1 (Hs00186838_m1), BIRC5 (Hs00153353_m1), CCL2 (Hs00234140_m1), MAP1LC3 (Hs00797944_s1), SOX2 (Hs01053049_s1), NANOG (Hs04260366_g1), POU5F1 (Hs04260367_gH), and HIF1A (Hs00153153_m1) were selected from the TaqMan gene expression assays (Life Technologies, USA). The qRT-PCR was performed under the following amplification conditions: total volume of 20 μl, initial incubation at 50°C/2 min followed by denaturation at 95°C/10 min, then 45 cycles at 95°C/ 15 sec and at 60°C/1 min.

Statistics

Pearson correlation, principal component analysis and cluster analysis were performed to reveal associations between cases and variables. These analyses were performed on standardized data; the cluster analysis was performed using Ward's method. All charts are depicted with means and standard deviations. Software Statistica (StatSoft, Tulsa, OK, USA) was used for analysis.

Results

Determination of IC50 for plumbagin

To assess the cytotoxic effect of plumbagin on the PC-3 cell line, and to select concentrations for further analyses, MTT test and real time cell analysis (RTCA) impedance based test were performed with concentrations 0 (no drug added), 0.5, 1, 1.5, 2, 2.5, 3, 4, 5, and 6 μmol/l. Using the logistic regression, IC50 concentrations were determined at time-points 6 and 24h (see Fig 1A, 1B, 1C and 1D). The output of RTCA method is a cell index value (CI), see Fig 1A, that reflects the number of cells, as well as morphological parameters, such as the size, shape, and

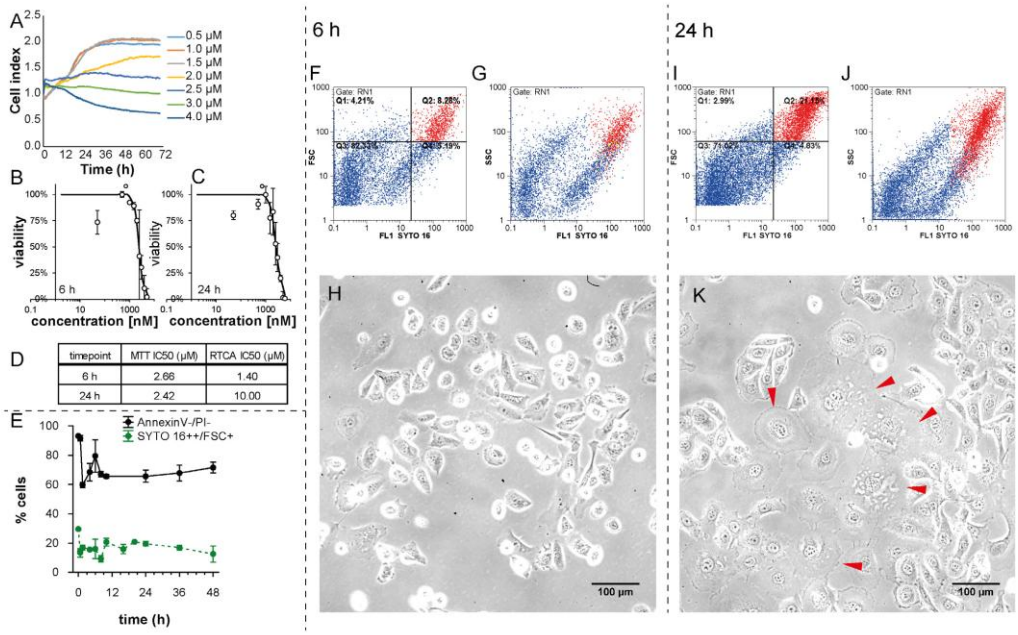

Fig 1. Effect of plumbagin treatment on viability and size of cells. (A) Real-time monitoring of relative cell impedance (showed as a cell index) using the RTCA system. **(B)** MTT-assessed response to 6h plumbagin treatment. **(C)** MTT-assessed response to 24h plumbagin treatment. **(D)** IC50 values according to RTCA and MTT and length of treatment. **(E)** Time-dependent changes in the quantity of large cells with intact nuclei (SYTO 16++/FSC+) and intact cells (AnnexinV-/PI-) assessed by flow-cytometry. **(F)** Numbers of large healthy cells depicted as SYTO 16++ /FSC+ (red) cluster at flow-cytometric dot plot at 6h time-point; Forward-scattered light (FSC) is proportional to cell-surface area or size. **(G)** Granularity of large healthy cells depicted as SYTO 16++ /SSC+ (red) cluster at flow-cytometric dot plot at 6h time-point; Side-scattered light (SSC) is proportional to cell granularity or internal complexity. **(H)** Morphology of PC-3 cells after 6h plumbagin treatment, 20x magnification, phase contrast microscopy. **(I)** Numbers of large healthy cells depicted as SYTO 16++/FSC+ (red) cluster at flow-cytometric dot plot at 24h time-point; Forward-scattered light (FSC) is proportional to cell-surface area or size. **(J)** Granularity of large healthy cells depicted as SYTO 16++/SSC+ (red) cluster at flow-cytometric dot plot at 24h time-point; Side-scattered light (SSC) is proportional to cell granularity or internal complexity. **(K)** Morphology of PC-3 cells after 24h plumbagin treatment; giant PC-3 cells with polyploid giant cancer cell (PGCCs)-like morphology are highlighted by arrows. 20x magnification, phase contrast microscopy.

doi:10.1371/journal.pone.0145016.g001

degree of cell attachment to the substrate. This means that an increase in the average size of surviving cells could affect the CI value and could correlate with higher IC50 values (1.4 µM and 10 µM IC50 after 6h and 24h treatment, respectively). We performed the flow-cytometric analysis by using SYTO 16 double-positivity as a marker of viable cells and forward scatter (FSC) to detect the size of surviving cells after the 2 µM plumbagin treatment. Numbers of large healthy cells depicted as a SYTO 16++ /FSC+ (red) cluster at the flow-cytometric dot plot were elevated at 24h time-point in comparison with 6h time-point; see Fig 1F, 1G, 1I and 1J. This experiment was done in triplicates. The average rate of large SYTO 16++ was 15.92% after 6h of plumbagin treatment and 19.58% after 24h of plumbagin treatment (Fig 1E). As we observed no dividing cells during the treatment (compare treated and untreated time-lapse, S1 and S5 Videos; cell division was apparent only in untreated cells), emergence of larger cancer cells could be assumed namely because no increase in the percentage of annexin V-/propidium iodide (PI)- cells (healthy cells that would result from dividing) was observed between 5h time-

point and 24h time-point of the treatment (Fig 1E). According to these results, the shift in IC50 values identified by the RTCA method may reflect the increased cell size between 6h and 24h time-points, as corroborated by the microscopic analysis; see Fig 1H and 1K.

PC3 cell line is predisposed to mitophagy

To assess the relative intensity of mitophagy related genes expression (*PINK1*, *FUNDC1*, *SMURF1*, and *PARL*) in the PC-3 cell line, we used the CellMiner Database (http://discover.nci.nih.gov/cellminer/). It allows to precisely determine selected genes expression patterns from 5 microarray platforms in 60 cell lines (NCI60 panel) (S1 Appendix). Pro-mitophagic genes *PINK1*, *FUNDC1*, and *SMURF1* were relatively overexpressed in PC-3 as compared with other cell lines; on the other hand, *PARL* (responsible for PINK1 cleavage) was underexpressed. These data suggest that PC-3 cells have possibly a high level of mitochondrial quality control and are able to effectively identify and then degrade damaged mitochondria.

Endoplasmic reticulum-affected mitophagy

In order to establish whether the majority of reactive oxygen species (ROS) in the cell is produced by the mitochondria, we applied fluorescent staining after the plumbagin treatment. General accumulation of ROS was monitored using CellROX Deep Red Reagent. Clear colocalisation of ROS and mitochondria staining was found (see Fig 2B and 2C). Major ROS producing mitochondria (see arrows) were coated by isolation membrane derived from ER (see Fig 2D). This observation was corroborated by transmission electron microscopy (TEM) (see Fig 2F). Swollen and damaged mitochondria were wrapped by engulfing membrane and gradually degraded (see Fig 2G). No coating membrane was found around the healthy mitochondria (see Fig 2E).

Time-lapse imaging

A time-lapse Video was captured by holographic microscope to observe the intensity of cell migration and also to quantify the kinetics of PC-3 cells death in 48 hour period. Many different types of cell-cell interactions were monitored and identified during this period including vesicular transfer (Fig 3F and 3G), eating of dead or dying cells (frequency of observation 2.5%; Fig 3C, S3 Video) and engulfment and cannibalism of living cells (frequency of observation 0.8%; Fig 3B). During the cannibalism of living cell, a cannibalic cell came into contact with a target cell. The next step was a gradual engulfment of target cell. The nucleus of the target cell appeared initially unaltered whereas the engulfing cell's nucleus began to change into a more semilunar shape. Bird eye structure typical for cannibalism was observed (Fig 3B, S2 Video). Finally, the target cell died off. The 2 μM plumbagin treatment had a particular impact on cell motility and on changes in cell-to-cell communication. A significant reduction of cell motility and communication was found after the plumbagin treatment (see Fig 3H and 3I, S1 and S5 Videos).

In oncosis, early changes included marked alterations in the cell shape and volume (Fig 3D, S1 Video). Oncotic cells formed cytoplasmic blebs and showed chromatin clumping followed by necrotic features such as cells membrane rupture and detachment from the surface. Nevertheless, some oncotic cells escaped this fate and were able to reverse processes leading to necrosis. Triggering of oncosis is not an irreversible process; oncosis can be reverted (see Fig 3E, S4 Video).

Moreover, we observed entosis triggering 20 h after the plumbagin treatment in the tumour cell population exposed to plumbagin. During entosis, cells invaded neighbouring cells, which led to the formation of cell-in-cell structure (see Fig 3A, S1 Video), no bird eye structure was

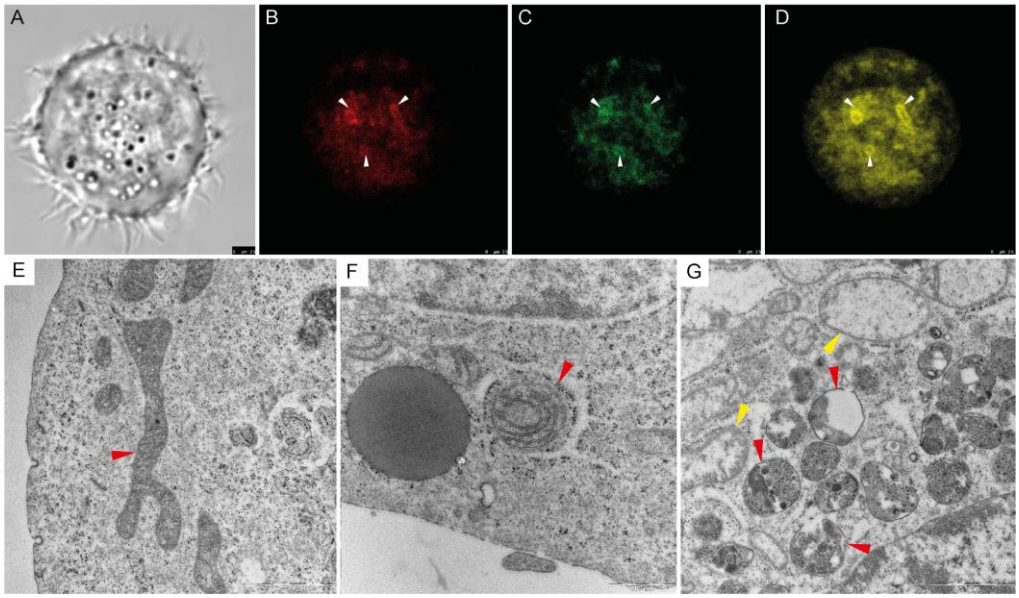

Fig 2. Reactive oxygen species (ROS)-induced mitophagy. (A) Phase contrast microscopy of PC-3 cell after plumbagin treatment. **(B)** General accumulation of ROS after plumbagin treatment monitored by confocal microscopy by using CellROX Deep Red Reagent. Areas with ROS accumulation are highlighted by arrows. **(C)** Mitochondria staining monitored by confocal microscopy using MitoTracker Green; area associated with ROS in Fig 2B are highlighted by arrows. **(D)** Endoplasmic reticulum (ER) staining monitored by confocal microscopy using ERTracker Red; areas associated with ROS in Fig 2B are highlighted by arrows. **(E)** Untreated PC-3 cell, cross-section of undamaged mitochondria (highlighted by red arrow); Transmission Electron Microscope (TEM) visualization. **(F)** plumbagin-treated PC-3 cell, mitochondria coated by ER membrane with ribosomes (highlighted by red arrow); TEM visualization. **(G)** Plumbagin-treated PC-3 cell, gradual degradation of mitochondria in autophagosomes visualised by TEM (red arrows); Swollen mitochondria as a marker of damage (yellow arrow).

doi:10.1371/journal.pone.0145016.g002

observed. Internalized cells played an active role in their engulfment (see Fig 4), which resulted in complete internalization. Cells which have undergone entosis (both engulfing and even engulfed cells) lived about five hours longer than the other observed tumour cells (frequency of this phenomenon was 2.5%). After 48 h of treatment, all PC-3 cells observed by holographic-microscopy were dead.

Time-lapse flow-cytometry

To evaluate the amount of cells positive or negative for typical markers, such as phosphatidyl serine exposure, presence of autophagosomes, or intact cellular membrane and nuclear DNA content, we used flow-cytometry at 12 time points (0h, 40min, 1.5h, 4h, 6h, 8h, 10h, 16h, 20h, 24h, 36h, and 48h). Phosphatidyl serine exposure was detected by Annexin V staining, cell viability by propidium iodide (PI) and SYTO 16 staining, and CYTO-ID Green was used as a marker of autophagosome formation. To determine the proportion of large cells with intact DNA, we used SYTO 16 and FSC. At the beginning of the experiment, about 30% of all cells were large with an intensive SYTO 16++ signal (Fig 1E). A decrease in the amount of SYTO 16 ++ large cells was shown during the first 8 hours of plumbagin treatment (ca. 15% SYTO 16+ + large cells) and an increase in the amount of SYTO 16++ large cells were shown after 10h of

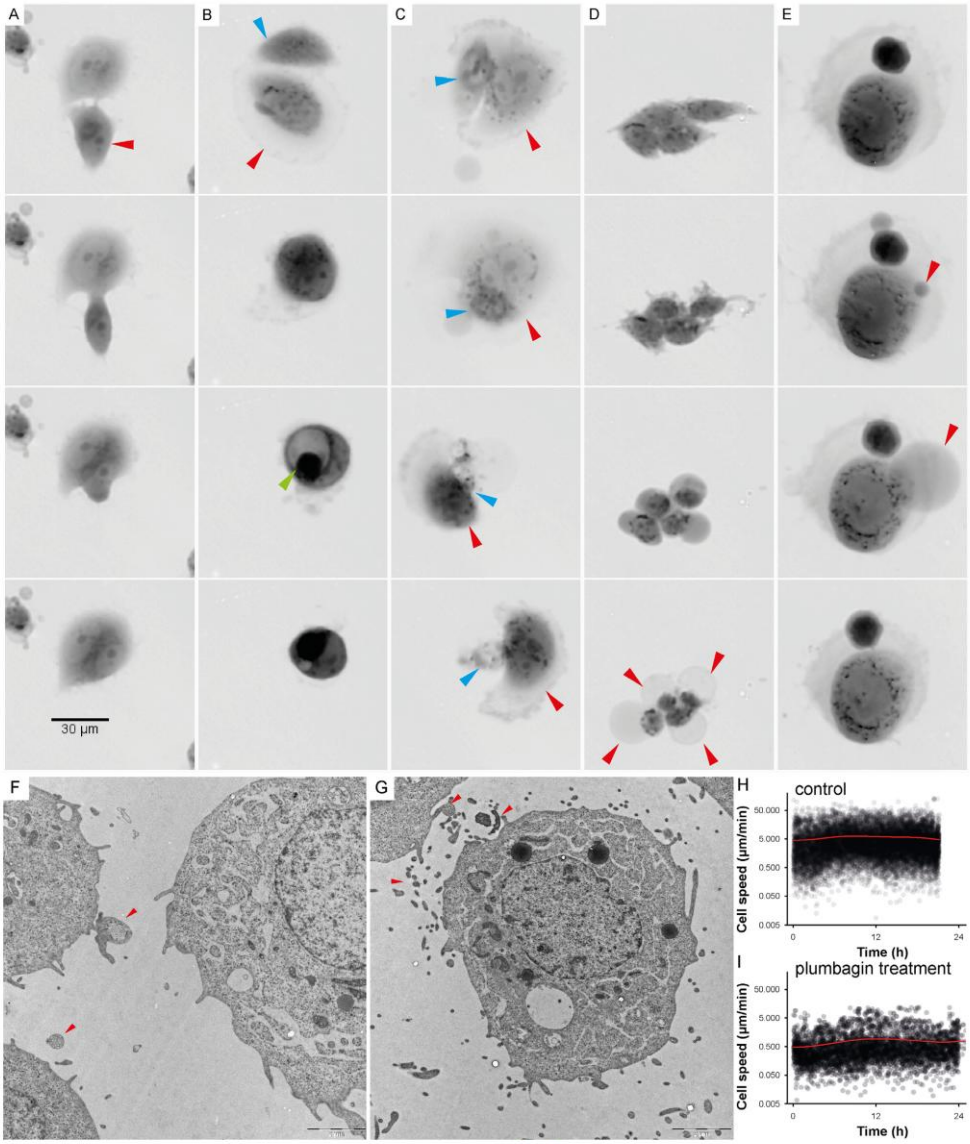

Fig 3. Time-lapse of cell interactions. For detailed time-lapse Videos see S1–S4 Videos. **(A)** Time-lapse imaging of entosis; internalized cell (red arrow) played an active role in its engulfment, which resulted in complete internalization. Both types of cells (engulfing and engulfed) were viable for a long time and lived by about five hours longer than the other observed plumbagin-treated tumour cells. **(B)** Time-lapse imaging of cell fusion with cannibalism (digestion of engulfed cell); during fusion-cannibalism of living cells, the cannibalic cell (red arrow) came in contact with the target cell (blue arrow). The next step was gradual engulfment of the target cell. The nucleus of the target cell appeared initially unaltered whereas the engulfing cell's nucleus began to change into a

semilunar shape. Bird eye structure was observed as a consequence of target cell vacualisation (see green arrow). **(C)** Time-lapse imaging of cannibalism without fusion; the dying cell (blue arrow) was attacked and exploited by the cannibalic cell (red arrow). The target cell was dead after the attack. **(D)** Time-lapse imaging of oncosis; oncotic cells formed typical cytoplasmic blebs that usually lead to necrosis (see red arrow). **(E)** Time-lapse imaging of reverse oncosis; initial forming of oncotic blebs (see red arrow) did not lead to necrosis; the bleb was absorbed and the cell remained viable. (**A-E**) Multimodal holographic microscopy, 10x magnification. **(F)** Communication between PC-3 cells; visualised by TEM (see red arrows). **(G)** Vesicular transfer between PC-3 cells; visualised by TEM (see red arrows). **(H)** Speed of the migration of untreated PC-3 cell population; assessed from holographic microscopy data by CellProfiller software by measurement of "distance travelled"parameter. **(I)** Speed of the migration of PC-3 cell population after 2 μM plumbagin treatment.

doi:10.1371/journal.pone.0145016.g003

treatment (about 20%). As we observed no dividing cells during the treatment (see S1 Video), emergence of giant cancer cells (PGCCs) larger than the average population could be assumed namely because no increase in the percentage of annexin V-/PI- cells (healthy cells that would result from dividing) was observed around the 10h time-point of treatment (Fig 1E).

Furthermore, we used the CYTO-ID Green autophagy dye for autophagy detection. Previously, CYTO-ID was validated by observing co-localization of the dye and RFP-LC3 in HeLa cells using fluorescence microscopy. An increase in CYTO-ID signal indicates the accumulation of autophagosomes [31]. Nevertheless, we detected two cell populations according to the intensity of CYTO-ID signal (CYTO-ID+, CYTO-ID++) (Fig 5A and 5E). The CYTO-ID + population correlated with the LC3-I form assessed by western-blotting (Fig 5F and 5G) ($r = 0.66$; $p = 0.001$) and the CYTO-ID++ population correlated with the LC3-II/LC3-I ratio ($r = 0.49$; $p = 0.016$). A correlation between total CYTO-ID staining and the LC3-II/LC3-I ratio was found, too ($r = 0.70$; $p = 0.0001$). According to our observation, plumbagin functions as an inductor of autophagy in the context of PC-3 cells. We also performed the flow-cytometric CYTO-ID analysis of non-treated PC-3 (Fig 5D), and plumbagin (Fig 5E) and bafilomycin (Fig 5C) (inhibitor of autophagy) treatments. During the plumbagin treatment, a high positive peak of CYTO-ID++ was shown at the time point of 8h. After the 8h peak, signal diminution was observed (probably LC3-II deconjugation and partial degradation of acid autophagic vacuoles);

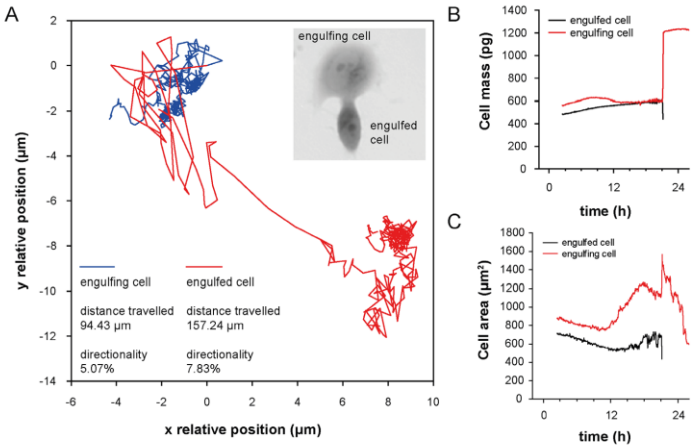

Fig 4. Mechanistic characterization of engulfed and engulfing cells in entosis. (A) Trajectory travelled of both engulfing and engulfed cell until cell fusion. See differences in the travelled distance and in directionality of individual cells. Directionality describes "purposefulness" of the movement where 0% indicate random movement and 100% indicate straight line trajectory between starting and ending position. Position (0.0, 0.0) indicate place of cell fusion. **(B)** Changes in cell mass and **(C)** cell area of engulfed and engulfing cell.

doi:10.1371/journal.pone.0145016.g004

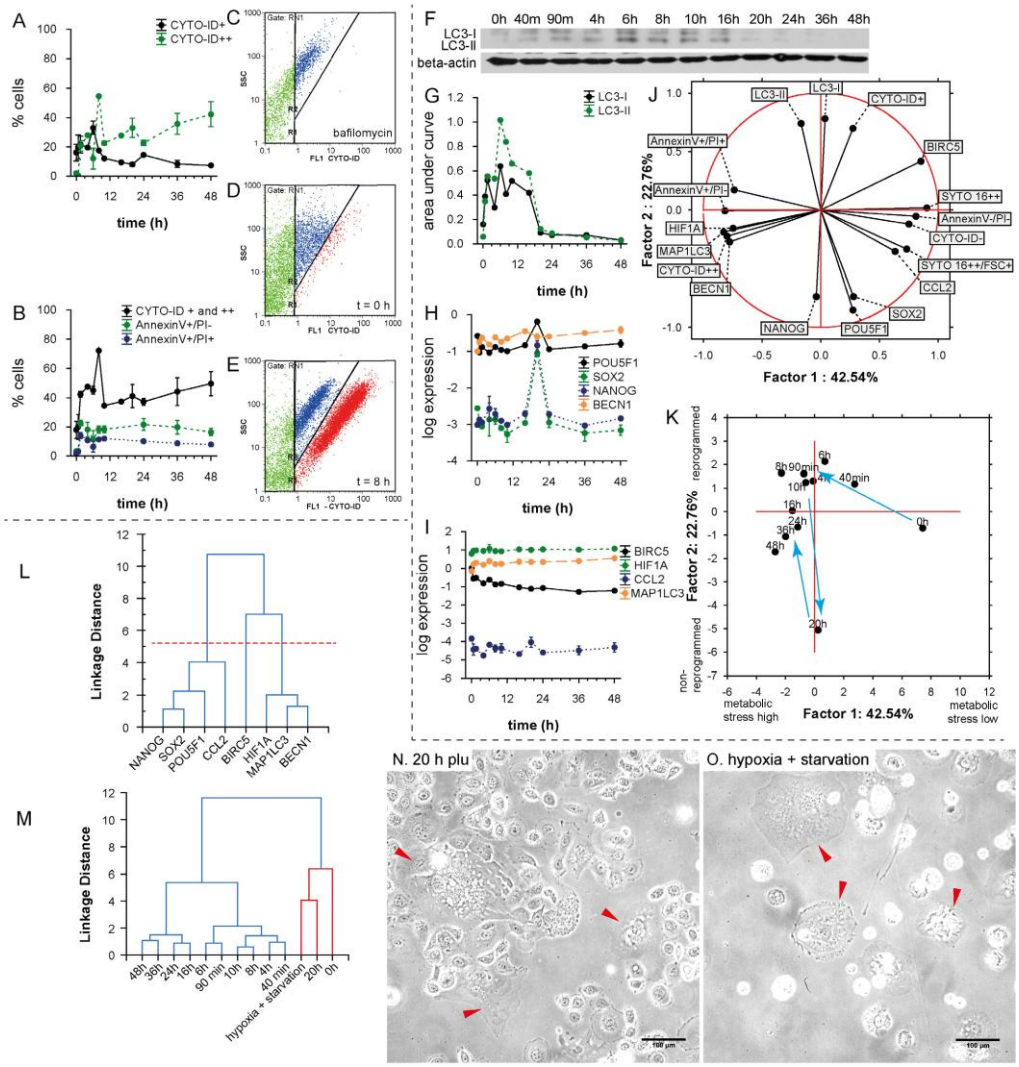

Fig 5. Autophagy and self-renewal after plumbagin treatment. (A) Time dependent dynamics of CYTO-ID Green (CYTO-ID+, CYTO-ID++) after 2 μM plumbagin treatment. See autophagy peak at 8h-time point. **(B)** Time dependent dynamics of cell deaths after 2 μM plumbagin treatment; total CytoID staining (CYTO-ID+ and CYTO-ID++) depicts autophagy, AnnexinV+/PI- depicts apoptosis or early oncosis, and AnnexinV+/PI+ depicts necrosis (raw data and gating strategy in S2 Appendix). **(C)** Amount of autophagic cells after bafilomycin treatment; red cluster depicts CYTO-ID++ population, blue cluster Cyto-ID+ population. **(D)** Amount of autophagic cells in control (not-treated population); red cluster depicts CYTO-ID++ population, blue cluster CYTO-ID + population. **(E)** Amount of autophagic cells after plumbagin treatment; red cluster depicts CYTO-ID++ population, blue cluster CYTO-ID+ population. **(F)** Western blot for LC3-I and LC3-II isoforms at 12 time-points after 2 μM plumbagin treatment (raw data in S3 Appendix). **(G)** Graphic representation of western blot results for LC3-I and LC3-II isoforms at 12 time-points after 2 μM plumbagin treatment. **(H)** Time dependent dynamics of *POU5F*, *SOX2*, *NANOG*, and *BECN1* gene expression after 2 μM plumbagin treatment. **(I)** Time dependent dynamics of *BIRC5*, *HIF1A*, *CCL2*, and *MAP1LC3* gene expression after 2 μM

plumbagin treatments. **(J)** Principal component analysis—projection of variables on the two-factor plane. See distinct clustering of genes with flow-cytometric measurements based on metabolic stress and reprogramming (for details see results). **(K)** Principal component analysis—projection of time-points on the two-factor plane. The first and the second factor are designated as "metabolic stress high-low" and "non-reprogrammed-reprogrammed", respectively (for details see results). **(L)** Cluster analysis of gene expression. The "reprogramming cluster"involved *POU5F*, *SOX2*, *NANOG*, and *CCL2*; the "autophagic and hypoxia cluster"involved *HIF1A*, *MAP1LC3*, and *BECN1*; the third cluster involved *BIRC5* gene. **(M)** Cluster analysis of gene expression of 12 time-points after 2 μM plumbagin treatment and PGCCs selected by hypoxia and starvation; based on correlations of gene expression patterns, similarity between PGCCs and PC-3 cells after 20h plumbagin treatment was found. **(N)** Morphology of cells after 20h plumbagin treatment; cells with polyploid giant cancer cell (PGCCs)-like morphology are highlighted by arrows. **(O)** Morphology of PC-3 cells after 1 month of hypoxia and starvation; cells with PGCCs-like morphology are highlighted by arrows.

doi:10.1371/journal.pone.0145016.g005

see Fig 5A. A decrease in the CYTO-ID++ signal after the time-point of 8h indicates that there is not only the simple accumulation of autophagosomes, but also the degradation of their content. During the whole experiment (48 h), the level of CYTO-ID++ signal was higher than at the zero time-point.

The highest percentage of autophagic cells (according to the accumulation of autophagosomes) was observed 8 hours after the treatment; see Fig 5B. Due to the triggering of autophagic mechanisms, almost no increase of necrotic (AnnexinV+/PI+) and early oncotic or apoptotic (AnnexinV+/PI-) cells was induced (Fig 5B). Almost 40% of cells were autophagic during the 48 h experiment. The quantity of AnnexinV+/PI+ and AnnexinV+/PI- did not exceed 20% at any observed time-point.

Time-lapse gene expression profiling

We isolated RNA (in duplicates) from the PC-3 cells at 12 time-points (0h, 40min, 1.5h, 4h, 6h, 8h, 10h, 16h, 20h, 24h, 36h, and 48h) of plumbagin treatment and performed qRT-PCR. Expression was assessed of *BECN1*, *MAP1LC3A*, *HIF1A*, *BIRC*, *CCL2*, *POU5F1*, *SOX2*, and *NANOG*. During the experiment, we observed a gradual increase in the expression of autophagy-related genes *MAP1LC3A* and *BECN1* and a gradual decrease of *BIRC*. The expression of autophagy-related genes was in a good correlation ($r = 0.92$, $p<0.001$) and correlated also with *HIF1A* ($r = 0.87$, $p<0.001$ and $r = 0.79$, $p<0.001$); see Fig 5L. We also found an extensive induction of pluripotency-associated genes expression (*NANOG*, *SOX2*, and *POU5F1*) at the time-point of 20 h; see Fig 5H. No dramatic changes in *HIF1A* expression were observed during the 12 time-points measurements (Fig 5I). Among the analyzed genes, three different expression clusters were found (see Fig 5L). The most expressed gene cluster was autophagic promoting cluster of genes (*BECN1*, *MAP1LC3A*, and *HIF1A)*. Of all the observed genes, the least expressed one was *CCL2* (Fig 5I).

Principal component analysis

In addition to the correlation analysis, the component analysis made it possible for us to detect the structure of relationships between the observed time-points, thus helping us to assess main variables in the particular time-points. Moreover, this analysis allowed us to classify variables based on the flow-cytometric and expression profiles. To illustrate the model of metabolic stress and self-renewal, two-factor analysis was chosen with a total cumulative variance of 65.3% and eigenvalues 42.54% and 22.76% for factor 1 and factor 2, respectively (Fig 5J). This two-axis model represents both metabolic stress (factor 1) and "self-renewal and reprogramming capacity" (factor 2). These conclusions are based on the following findings: (a) *NANOG*, *SOX2*, and *POU5F1* are genes, which strongly correlate with the pluripotency and self-renewal, (b) annexinV+/PI+ status refers to cell death; (c) PI positivity, Annexin V positivity, CYTO-ID positivity, *BECN1*, *MAP1LC3A*, and *HIF1A* expression are directed to the negative values of factor 1 (high metabolic stress). Taken together, positive values of factor 1 are associated with

the healthy cells rather than with the cell damage, and negative values of factor 2 are associated with cell reprogramming processes, rather than with the naive PC-3 cells. When we accept this model, large cells with the intensive SYTO 16++ signal seem to be further in reprogramming processes than the average SYTO 16++ population of PC-3 cells and naive PC-3 harvested at the zero time-point, and *BIRC* expression is very important for preventing metabolic stress in the naive PC-3, but could also prevent reprogramming mechanisms.

When these factors are used to project cases (time-points), another apparent trend is evident: At the time-point of 20h, PC-3 cells seem to break free from the bondage of metabolic stress by triggering the reprogramming processes. This "reprogrammed" PC-3, are associated with the lower metabolic stress (as represented by positive values of factor 1). However, when the stress continues, the cells are being pushed to higher metabolic stress again, staying partially reprogrammed though; see Fig 5K time-point 48 h. We could assume some cyclic characteristic of stress resistance processes and reprogramming. During these cycles of adaptation, the cells are pushed to a state that is increasingly dedifferentiated.

Polyploid giant cancer cells (PGCCs) expression profiling

When the PC-3 cancer cell line was cultured under normal conditions, some large cells with enlarged nuclei (PGCCs) were sporadically observed. However, the exposure of PC-3 cancer cells to long-term starvation and hypoxia (for at least one month) induced the formation of cells with larger cell and nuclear size, while cells of normal morphology were almost eliminated. PGCCs were highly resistant to oxygen deprivation and could generate regular-sized cancer cells through budding or bursting. The PGCCs induced by starvation and hypoxia were 2–10 times larger than normal cells, and had a distinctive morphology (see Fig 5O).

Next, qRT-PCR gene expression profiling was performed to analyze the specific molecular pattern expressed in PGCCs. Expression profiles of eight genes (*BECN1*, *MAP1LC3A*, *HIF1A*, *BIRC*, *CCL2*, *POU5F1*, *SOX2*, and *NANOG*) were assessed and compared with the normal PC-3 cell expression patterns obtained at the particular time points during the plumbagin treatment by cluster analysis (see Fig 5M). After 20h of plumbagin treatment, the expression pattern of PC-3 cells matched with the PGCCs characteristics as well as the cell morphology (see Fig 5N and 5O).

Discussion

Panov *et al.* found out, that the PC-3 prostate cancer cell line contained 2 to 4 times more mitochondria with enhanced respiratory activity [15], which may cause high sensitivity of PC-3 cells to ROS—produced massively during the plumbagin treatment. However, in cytotoxicity tests we have noticed differences in sensitivity to plumbagin measured by metabolic-based MTT and impedance-based RTCA. The output of RTCA method is a cell index value (CI; see Fig 1A) that reflects the number of cells as well as morphological parameters such as size, shape, and degree of cell attachment to the substrate. This means that an increase in the average size of surviving cells affects CI and could correlate with higher IC50 values (1.4 μM resp. 10 μM IC50 after 6h resp. 24h treatment) As we observed no dividing cells during the 2 μM plumbagin treatment (S1 Video), we assumed that the cells increased their volume between the time-points of 6h and 24h. Accordingly, an increase in the amount of SYTO 16++ large cells was shown at the 20h time-point as compared with the 6h time-point (see Fig 1F and 1I). This might indicate the emergence of giant polyploid cancer cells. SYTO 16 is effective at staining the DNA of cells, because it binds preferentially to DNA over RNA at a ratio of approximately 20:1 [32] and shows specific information about the cell nuclei, such as size and distribution. Furthermore, Manusco *et al.* used SYTO16 staining to enumerate circulating

endothelial cells with a high DNA content [33] and Ibrahim *et al.* identified multinucleate cells during the growth cycle of *Mycobacterium avium* by SYTO 16 staining [34]. Importantly, Wlodkowic *et al.* have recently showed that SYTO dyes do not adversely affect normal cellular physiology. The cytometric detection of SYTO 16 fluorescence loss is even a sensitive marker of early apoptotic events [35].

Unlike the RTCA IC50 values, these values measured by MTT were relatively stable (2.66 μM resp. 2.42 μM IC50 after 6h resp. 24h treatment). The main mechanism of MTT assay is a reduction of tetrazolium salts to formazan by mitochondrial succinate dehydrogenase (SDH). SDH loses its activity by damage of the respiratory chain [36]. According to our results, main reduction of SDH activity takes place during the first 6 hours. As mitochondria are the main producer of ROS, they are an easy target of ROS-mediated damage, too. Thus, the ROS-mediated damage plays a key role in the induction of cellular senescence [37]. In this study we disclosed that the major ROS producing mitochondria in the PC-3 cells are coated by ER membranes. Since the ER mitochondria encounter structure (ERMES) plays a key role in mitophagy in yeast and Boeckler *et al.* showed that successful mitophagy depends on mitochondrial ER tethering, [38], we assume that the major ROS producers in PC-3 are destined for degradation by mitophagy. Mitophagy helps to eliminate damaged mitochondria and maintains their healthy pool [39]. Mitophagy also presents a possible way to gain enough energy for survival [19] and simultaneously removes the ROS producing mitochondria [40]. Accordingly, PC-3 cells express a high amount of pro-mitophagic genes *PINK1*, *FUNDC1*, and *SMURF1* in comparison with the other cell lines of NCI60 panel. On the other hand, *PARL* (responsible for PINK1 cleavage) was underexpressed. The PINK1 protein is connected with the mitochondrial quality control by targeting damaged mitochondria for degradation [41]. The loss of PINK1 also impairs stress-induced autophagy and cell survival [42]. Furthermore, the mitochondrial outer-membrane protein FUNDC1 could mediate hypoxia-induced mitophagy [43]. According to these data, it seems possible that PC-3 cells have a high level of mitochondrial quality control and are able to identify and then degrade the damaged mitochondria. It could seem that getting rid of mitochondria is not much favourable for the tumour cell in the long run, because tumour cells without mitochondrial DNA (mtDNA) show retarded tumour growth [44]. Nevertheless, the tumour formation could be associated with the acquisition of mtDNA from host cells [44] and this temporary handicap could be thus compensated.

Severely damaged cells often exhibit accumulation of autophagosomes and hence seem to be subject to autophagic cell death. Nevertheless, in many cases, this "autophagic cell death" is the cell death during autophagy rather than the cell death by autophagy [45]. In our study, the highest percentage of autophagic cells was observed 8 hours after the treatment (see Fig 5B). Due to the triggering of autophagic mechanisms, almost no increase of necrotic (AnnexinV +/PI+) and early oncotic or apoptotic (AnnexinV+/PI-) cells was induced. It follows that induction of autophagy does not seem to be directly related to cell death. Conversely, our results suggest that autophagy can promote the survival of cells under oxidative stress, which is in accordance with the results of other studies [24, 46]. According to our results, autophagy precedes several mechanisms such as self-renewal and entosis. Sun *et al.* found out that tumour cells with high deformability preferentially engulf neighbouring cells with low deformability in heterogeneous populations. They also found out that downregulation of contractile myosin allows the internalization of neighbouring cells and that a mechanical differential between the engulfing and engulfed cells is required for entosis to progress [47]. Therefore, we would like to present a hypothesis, that reduction in membrane and cell stiffness due to protein catabolism by autophagy could reflect increased entotic activity. Moreover, the entotic vacuole membrane encircling the internalized cells recruits the autophagy protein LC-3 [48]. The initiation of entosis, instead of apoptosis or necrosis, might give the cell additional time to survive the

transient deleterious conditions. The cell in cell structure results in the decreased surface-to-volume ratio, thereby minimizing cell membrane requirements (one membrane for two nuclei) (Fig 4). Furthermore, a live cell internalized by entosis could disrupt host cell division. Subsequently, cytokinesis often fails, which causes the formation of binucleate cells that are able to generate aneuploid cell lineages [49]. It was also shown that the frequency of entotic structures correlates well with the tumour grade [49]. According to this observation, we speculate, that entosis and competition between cells by cannibalism is rather late-stage process in cancer cells and requires activation of mechanisms leading to higher developmental plasticity, changes in cytoskeletal proteins [47] and some kind of de-differentiation of cells accompanied with changes in transcription regulators. All of these could be supported by ROS. For example, transcription factor C/EBPbeta (LIP), is elevated by endoplasmic reticulum stress and oncogenic signalling [50, 51]. Recently, expression of LIP was connected with enhanced autophagy and engulfment of neighbouring cells in the human breast cancer cell line (MDA-MB-468 cell line with mutant p53 [52]) [53]. In our experiment, entotic cells lived by about five hours longer than the other observed tumour cells. Although the all observed PC-3 cells were dead after 48h treatment, it could probably be only the consequence of relatively low numbers of cells (ca. 50 cells) which can be seen in the holographic-microscope field of view. Nevertheless, according to the flow-cytometry results, more than 60% of cells were annexinV-/PI- after 48 h of 2 μM plumbagin treatment. About 18% of these cells were large and SYTO 16++.

Similar to mitophagy, digestion of the cytoplasm of neighbouring cells can provide a source of amino acids, indicating that cannibalism could be a survival mechanism for tumour cells during starvation and other adverse conditions [54]. Significant reduction of cell motility and cannibalism were found after the plumbagin treatment. Furthermore, plumbagin is able to suppress activation of nuclear factor-κB (NF-κB) [13], and therefore could repress anoikis resistance [55], which may be an explanation why plumbagin is probably more toxic for the PC-3 cell line than cisplatin (2.42 μM vs. 75 μM IC50 value after 24h treatment) [8].

We have also found out that specific processes leading to induction of reprogramming to pluripotency (depicted by significant overexpression of *NANOG*, *SOX2*, and *POU5F1* [17, 26, 56]) were triggered 20h after the treatment in the tumour cell population exposed to ROS. These three pluripotency-related transcription factors, Oct 3/4, Nanog, and Sox-2, form a core regulatory network that coordinates the self-renewal and differentiation of stem cells. Transfection of NANOG, SOX2, OCT4, and LIN28 in human fibroblasts induced pluripotency, indicating a key position of these factors in the reprogramming of somatic cells [57]. These self-renewal molecules highly contribute to tumourigenesis [17, 58]. Takahashi *et al.* also showed that the introduction of transcription factors Oct3/4, Sox2, c-Myc, and Klf4 into mouse adult fibroblasts was able to reprogramme differentiated cells to an embryonic-like, pluripotent state [59, 60]. Nanog overexpression was found to be one of the distinctive features of the population of fibroblasts that escaped from Ras-induced senescence [61]. Furthermore, Nanog was found to be promoting the transfer of pluripotency after the cell fusion of reprogrammed and non-reprogrammed cell [62]. Nanog seems to be required during the final stages of somatic cell reprogramming. Once the pluripotent state is established, Nanog is no longer needed [63], which is in accordance with the peak-character of *NANOG* expression observed by us (see Fig 5H). Bambrik *et al.* postulated that the activation of endogenous Oct4 or Nanog may be a marker for fully reprogrammed induced pluripotent stem cells (iPSCs) [64]. We rather suppose, that overexpression of *NANOG*, *SOX2*, and *POU5F* in the prostate tumour cell population (especially in PGCCs; [65]) exposed to ROS leads to higher developmental plasticity and capability to faster respond to changes in the extracellular environment that could ultimately lead to alteration of cell fate (epithelial features vs. mesenchymal character etc.). Similar process was observed in Mitchell et al. study [66]. Expression of pluripotency genes results in

functional reprogramming that could provide to tumour cells higher developmental potency [67] as well as higher stemness [25]. For example, it was observed that differentiated cancer cells and tumor stroma can be originated directly from polyploid giant cancer cells induced by paclitaxel [67].

Here, we hypothesize that autophagy and cell-in-cell structures accompanied with polyploidization could also play an important role in the survival, remodelling and dedifferentiation of cells to a pluripotent state (for summary see Fig 6). Autophagy could cause the degradation of proteins important for the status of differentiation, which could restrain the process of reprogramming, and simultaneously could eliminate proteins that should not be expressed in the pluripotent cells. According to our model arisen from the principal component analysis, *BIRC* expression is very important for preventing metabolic stress in naive PC-3, but could prevent reprogramming mechanisms, too. Protein product of *BIRC* gene (survivin) is able to prevent apoptotic cell death, but also inhibits autophagy [68, 69], which could contribute to the efficiency of puripotent stem cells generation [26]. Furthermore, relatively little expressed in PC-3 cells is another autophagy inhibitor *CCL2* [69].

In our experiment, the expression pattern of PC-3 cells as well as their morphology after 20h of plumbagin treatment matched with the PGCCs characteristics. This observation is in accordance with the idea that entering polyploidy is part of a strictly regulated process that could provide a survival advantage to cells with DNA damage [17]. Notably, the polyploid state can affect the resistance of cancer cells and could also contribute to the generation of cancer stem cells in response to stress [17, 25]. According to our model, large cells with an intensive SYTO 16++ signal (probably PGCCs) seem to be further in reprogramming to pluripotency processes than naive PC-3 cells. Erenpreisa *et al.* discussed, that senescence, polyploidy and self-renewal are three steps to immortality of cancer cells [17]. We predict that autophagy could play an important role in all these three processes, particularly because PC-3 are p53 deficient and hence could be resistant to senescence, which is a natural barrier for reprogramming [26]. PC-3 seem to be predisposed to reprogramming [70–72].

We have already tested other prostate cell lines such as PNT1A and 22Rv1, but they both have partially active p53 and therefore they are not resistant to cell cycle arrest, senescence and cell death [8] triggered due to polyploidization. It is in accordance with other studies where initiation and maintenance of senescence seems to be p53 dependent [37, 73] as well as cell death triggering after polyploidization [74]. According to these results, we supposed, that polyploidization and PGCCs forming as mechanism of resistance is rather typical for cell lines that have p53-deficiency and metastatic potential and is not unique for prostate cancer cell lines. Recent work by Zhang et al. has confirmed the importance of PGCCs in therapy resistance and ovarian cancer progression [25, 75]. In contrast with polyploidization, we supposed that mitophagy is more general principle of coping with cell stress in immortalized cells, which is in accordance with other studies [76–78].

Prostate cancers often show large intra-tumour heterogeneity in almost all measurable characteristics including metabolism, gene expression, cellular morphology, and metastatic potential. Some cell populations inside the tumour seem to be predisposed to resist high levels of metabolic stress. One of the ways how to resist is proper control and degradation of damaged ROS producing mitochondria by mitophagy. Accordingly, autophagy was activated as a protective mechanism and mediated the resistance phenotype of some cancer cells during the ROS-producing treatment in our model of apoptosis-resistant, androgen-independent, metastasis producing prostate cancer (PC-3 cell line). In recent years, it seemed possible that autophagy can execute cell death in cancer cells which are apoptosis defective, but this is not true for the PC-3 cell line. We also assume that autophagy could promote arousal of cell-in-cell structures and thus play a significant role in polyploidization and dedifferentiation of cells to a

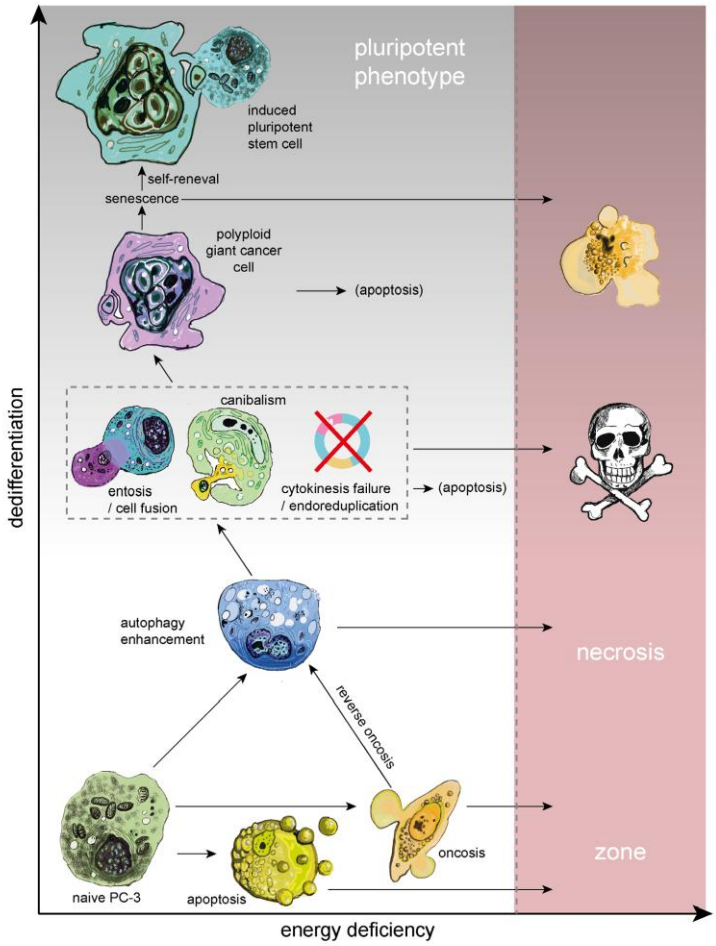

Fig 6. Possible cell fate under oxidative stress. Prolonged oxidative stress (ROS) leads to severe cell damage and depletion of cell energy reserves. Nevertheless, many cell injuries caused by ROS could be sublethal, especially because PC-3 cells have non-functional p53 and therefore disrupt the triggering of apoptosis. Even if a damaged cell is driven to oncosis, reversion of this process is possible, particularly if the cell is able to restore ATP production. A way to gain enough energy for survival could be autophagy. Similar to autophagy, digestion of the cytoplasm of neighbouring cells can provide a source of amino acids. Retention of a foreign nucleic acid by cannibalistic engulfment could result in aneuploid or polyploid state. Furthermore, reduction in membrane and cell stiffness due to protein catabolism by autophagy could reflect increased entotic activity. Cell in cell structure results in the decreased surface-to-volume ratio, thereby minimizing cell membrane requirements. Furthermore, a live cell internalized by entosis could disrupt host cell division. Subsequently, cytokinesis often fails, which can lead to the formation of polyploid giant cancer cells (PGCCs). PGCCs often dye by apoptosis or senescence, but a small fraction of these cells is able to survive and even produce aneuploid progeny. Senescence, polyploidy and self-renewal seem to be three steps to immortality of cancer cells. Autophagy could play an important role in all of them.

doi:10.1371/journal.pone.0145016.g006

pluripotent state. Inasmuch as androgen-independent prostate cancer cells with non-functional p53 are able to quite easy cope with damages caused by ROS producing agents and ROS can even participate in positive selection of resistant PGCCs with some pluripotent characteristics, prostate cancer therapies based on ROS producing agents could be a misleading concept.

Supporting Information

S1 Appendix. Expression of mitophagy-related genes by NCI60 platform. For the assessment of the relative intensity of mitophagy related genes expression (*PINK1*, *FUNDC1*, *SMURF1*, and *PARL*) in the PC3 cell line we used CellMiner Database (http://discover.nci.nih.gov/cellminer/). It allows the determination of selected genes expression patterns from 5 microarray platforms in 60 cell lines (NCI60 panel). The tool output includes relative transcript intensity presented as z-scores and visualized as a bar graph. The bars for each cell line are colour-coded by the tissue of origin.
(TIF)

S2 Appendix. Flow-cytometric analyses. Gating strategy of time-lapse analysis of plumbagin-treated cells using AnnexinV/Propidium iodide, SYTO 16 and CYTO-ID staining and raw data.
(PDF)

S3 Appendix. Western blotting of LC-3. The cropped part of the blot identical to Fig 4 and whole membrane with LC-3 and beta-actin antibodies.
(TIF)

S1 Video. Time-lapse imaging of entosis and oncosis. 2μM plumbagin treatment. **No cell division** appears during 48 hour of plumbagin treatment; red square areas highlight main points of interest; A) during entosis, internalized cell plays an active role in process of internalization. Both, engulfing and engulfed cell live about five hours longer than the other PC-3 cells. B) Oncotic cells formed cytoplasmic blebs and showed chromatin clumping followed by necrotic features such as cell membrane rupture and detaching from the surface.
(MP4)

S2 Video. Time-lapse imaging of cannibalism with the cell fusion (digestion of engulfed cell, detail). Target-cell is gradually engulfed by active cannibalic polynuclear cell. Bird eye structure typical for cannibalism appears. Then the target cell dies off.
(MP4)

S3 Video. Time-lapse imaging of cannibalism without the cell fusion (detail). Weakened target- cell is contacted by cannibalic cell, exploited and left to die.
(MP4)

S4 Video. Time-lapse imaging of reverse oncosis (detail). Recuperation of oncotic cell forming cytoplasmic blebs.
(MP4)

S5 Video. Time-lapse imaging of untreated PC-3 cell line. Unaffected PC-3 cells. Red arrows depict cell division.
(MP4)

Acknowledgments

We thank Dr. Lucia Knopfova for assistance in western blot analysis and Dr. Miroslava Sedlackova for assistance in transmission electron microscopy.

Author Contributions

Conceived and designed the experiments: JB JG MR MM. Performed the experiments: JB JG MR AK PS PB MM. Analyzed the data: JG AK RK VA. Contributed reagents/materials/analysis tools: PB VA RK MM. Wrote the paper: JB JG MR RK VA MM.

References

1. Carroll AG, Voeller HJ, Sugars L, Gelmann EP. P53 oncogene mutations in 3 human prostate-cancer cell-lines. Prostate 1993; 23: 123–34. PMID: 8104329
2. Rubin SJ, Hallahan DE, Ashman CR, Brachman DG, Beckett MA, Virudachalam S, et al. 2 prostate carcinoma cell-lines demonstrate abnormalities in tumor suppressor genes. Journal of Surgical Oncology 1991; 46: 31–6. PMID: 1986144
3. Gustin JA, Maehama T, Dixon JE, Donner DB. The PTEN tumor suppressor protein inhibits tumor necrosis factor-induced nuclear factor kappa B activity. Journal of Biological Chemistry 2001; 276: 27740–4. PMID: 11356844
4. Barbieri CE, Bangma CH, Bjartell A, Catto JW, Culig Z, Gronberg H, et al. The mutational landscape of prostate cancer. Eur Urol 2013; 64: 567–76. doi: 10.1016/j.eururo.2013.05.029 PMID: 23759327
5. Bertram J, Peacock JW, Fazli L, Mui AL, Chung SW, Cox ME, et al. Loss of PTEN is associated with progression to androgen independence. Prostate 2006; 66: 895–902. PMID: 16496415
6. Wu Z, Conaway M, Gioeli D, Weber MJ, Theodorescu D. Conditional expression of PTEN alters the androgen responsiveness of prostate cancer cells. Prostate 2006; 66: 1114–23. PMID: 16637073
7. Choucair K, Ejdelman J, Brimo F, Aprikian A, Chevalier S, Lapointe J. PTEN genomic deletion predicts prostate cancer recurrence and is associated with low AR expression and transcriptional activity. Bmc Cancer 2012; 12.
8. Gumulec J, Balvan J, Sztalmachova M, Raudenska M, Dvorakova V, Knopfova L, et al. Cisplatin-resistant prostate cancer model: Differences in antioxidant system, apoptosis and cell cycle. International Journal of Oncology 2014; 44: 923–33. doi: 10.3892/ijo.2013.2223 PMID: 24366574
9. Sedletska Y, Giraud-Panis MJ, Malinge JM. Cisplatin is a DNA-damaging antitumour compound triggering multifactorial biochemical responses in cancer cells: importance of apoptotic pathways. Curr Med Chem Anticancer Agents 2005; 5: 251–65. PMID: 15992353
10. Marullo R, Werner E, Degtyareva N, Moore B, Altavilla G, Ramalingam SS, et al. Cisplatin Induces a Mitochondrial-ROS Response That Contributes to Cytotoxicity Depending on Mitochondrial Redox Status and Bioenergetic Functions. Plos One 2013; 8.
11. Powolny AA, Singh SV. Plumbagin-induced Apoptosis in Human Prostate Cancer Cells is Associated with Modulation of Cellular Redox Status and Generation of Reactive Oxygen Species. Pharmaceutical Research 2008; 25: 2171–80. doi: 10.1007/s11095-008-9533-3 PMID: 18213451
12. Castro FAV, Mariani D, Panek AD, Eleutherio ECA, Pereira MD. Cytotoxicity Mechanism of Two Naphthoquinones (Menadione and Plumbagin) in Saccharomyces cerevisiae. Plos One 2008; 3.
13. Sandur SK, Ichikawa H, Sethi G, Ahn KS, Aggarwal BB. Plumbagin (5-hydroxy-2-methyl-1,4-naphthoquinone) suppresses NF-kappaB activation and NF-kappaB-regulated gene products through modulation of p65 and IkappaBalpha kinase activation, leading to potentiation of apoptosis induced by cytokine and chemotherapeutic agents. J Biol Chem 2006; 281: 17023–33. PMID: 16624823
14. Qian W, Nishikawa M, Haque AM, Hirose M, Mashimo M, Sato E, et al. Mitochondrial density determines the cellular sensitivity to cisplatin-induced cell death. American Journal of Physiology-Cell Physiology 2005; 289: C1466–C75. PMID: 16107504
15. Panov A, Orynbayeva Z. Bioenergetic and Antiapoptotic Properties of Mitochondria from Cultured Human Prostate Cancer Cell Lines PC-3, DU145 and LNCaP. Plos One 2013; 8.
16. Balvan J, Krizova A, Gumulec J, Raudenska M, Zbysek S, Sedlackova M, et al. Multimodal holographic microscopy: distinction between apoptosis and oncosis. Plos One 2015; 10: e0121674. doi: 10.1371/journal.pone.0121674 PMID: 25803711
17. Erenpreisa J, Cragg MS. Three steps to the immortality of cancer cells: senescence, polyploidy and self-renewal. Cancer Cell International 2013; 13.

18. Trump BF, Berezesky IK, Chang SH, Phelps PC. The pathways of cell death: Oncosis, apoptosis, and necrosis. Toxicologic Pathology 1997; 25: 82–8. PMID: 9061857
19. Singh R, Kaushik S, Wang Y, Xiang Y, Novak I, Komatsu M, et al. Autophagy regulates lipid metabolism. Nature 2009; 458: 1131–5. doi: 10.1038/nature07976 PMID: 19339967
20. Kroemer G, Perfettini J-L. Entosis, a key player in cancer cell competition. Cell Research 2014; 24: 1280–1. doi: 10.1038/cr.2014.133 PMID: 25342563
21. Krajcovic M, Krishna S, Akkari L, Joyce JA, Overholtzer M. mTOR regulates phagosome and entotic vacuole fission. Molecular Biology of the Cell 2013; 24: 3736–45. doi: 10.1091/mbc.E13-07-0408 PMID: 24088573
22. Degenhardt K, Mathew R, Beaudoin B, Bray K, Anderson D, Chen GH, et al. Autophagy promotes tumor cell survival and restricts necrosis, inflammation, and tumorigenesis. Cancer Cell 2006; 10: 51–64. PMID: 16843265
23. Mathew R, Kongara S, Beaudoin B, Karp CM, Bray K, Degenhardt K, et al. Autophagy suppresses tumor progression by limiting chromosomal instability. Genes & Development 2007; 21: 1367–81.
24. Kimmelman AC. The dynamic nature of autophagy in cancer. Genes & Development 2011; 25: 1999–2010.
25. Zhang S, Mercado-Uribe I, Xing Z, Sun B, Kuang J, Liu J. Generation of cancer stem-like cells through the formation of polyploid giant cancer cells. Oncogene 2014; 33: 116–28. doi: 10.1038/onc.2013.96 PMID: 23524583
26. Menendez JA, Vellon L, Oliveras-Ferraros C, Cufi S, Vazquez-Martin A. mTOR-regulated senescence and autophagy during reprogramming of somatic cells to pluripotency: a roadmap from energy metabolism to stem cell renewal and aging. Cell Cycle 2011; 10: 3658–77. doi: 10.4161/cc.10.21.18128 PMID: 22052357
27. Kolman P, Chmelik R. Coherence-controlled holographic microscope. Optics Express 2010; 18: 21990–2003. doi: 10.1364/OE.18.021990 PMID: 20941100
28. Slaby T, Kolman P, Dostal Z, Antos M, Lost'ak M, Chmelik R. Off-axis setup taking full advantage of incoherent illumination in coherence-controlled holographic microscope. Optics Express 2013; 21: 14747–62. doi: 10.1364/OE.21.014747 PMID: 23787662
29. Davies HG, Wilkins MHF. Interference microscopy and mass determination. Nature 1952; 169: 541-. PMID: 14929230
30. Barer R. Refractometry and interferometry of living cells. Journal of the Optical Society of America 1957; 47: 545–56. PMID: 13429433
31. Chan LL-Y, Shen D, Wilkinson AR, Patton W, Lai N, Chan E, et al. A novel image-based cytometry method for autophagy detection in living cells. Autophagy 2012; 8: 1371–82. doi: 10.4161/auto.21028 PMID: 22895056
32. Udovich JA, Besselsen DG, Gmitro AF. Assessment of acridine orange and SYTO 16 for in vivo imaging of the peritoneal tissues in mice. Journal of Microscopy-Oxford 2009; 234: 124–9.
33. Mancuso P, Calleri A, Bertolini F, Tacchetti C, Heymach JV, Shalinsky DR. Quantification of Circulating Endothelial Cells by Flow Cytometry Response. Clinical Cancer Research 2009; 15: 3640–1. doi: 10.1158/1078-0432.CCR-09-0160 PMID: 19451598
34. Ibrahim P, Whiteley AS, Barer MR. SYTO16 labelling and flow cytometry of Mycobacterium avium. Letters in Applied Microbiology 1997; 25: 437–41. PMID: 9449859
35. Wlodkowic D, Skommer J, Darzynkiewicz Z. Rapid quantification of cell viability and apoptosis in B-cell lymphoma cultures using cyanine SYTO probes. Methods Mol Biol 2011; 740: 81–9. doi: 10.1007/978-1-61779-108-6_10 PMID: 21468970
36. Aitken RJ, Whiting S, De Iuliis GN, McClymont S, Mitchell LA, Baker MA. Electrophilic Aldehydes Generated by Sperm Metabolism Activate Mitochondrial Reactive Oxygen Species Generation and Apoptosis by Targeting Succinate Dehydrogenase. Journal of Biological Chemistry 2012; 287: 33048–60. PMID: 22851170
37. Rufini A, Tucci P, Celardo I, Melino G. Senescence and aging: the critical roles of p53. Oncogene 2013; 32: 5129–43. doi: 10.1038/onc.2012.640 PMID: 23416979
38. Boeckler S, Westermann B. Mitochondrial ER Contacts Are Crucial for Mitophagy in Yeast. Developmental Cell 2014; 28: 450–8. doi: 10.1016/j.devcel.2014.01.012 PMID: 24530295
39. Ashrafi G, Schwarz TL. The pathways of mitophagy for quality control and clearance of mitochondria. Cell Death and Differentiation 2013; 20: 31–42. doi: 10.1038/cdd.2012.81 PMID: 22743996
40. Ding W-X, Yin X-M. Mitophagy: mechanisms, pathophysiological roles, and analysis. Biological Chemistry 2012; 393: 547–64. doi: 10.1515/hsz-2012-0119 PMID: 22944659

41. Youle RJ, van der Bliek AM. Mitochondrial Fission, Fusion, and Stress. Science 2012; 337: 1062–5. doi: 10.1126/science.1219855 PMID: 22936770

42. Parganlija D, Klinkenberg M, Dominguez-Bautista J, Hetzel M, Gispert S, Chimi MA, et al. Loss of PINK1 Impairs Stress-Induced Autophagy and Cell Survival. Plos One 2014; 9.

43. Liu L, Feng D, Chen G, Chen M, Zheng Q, Song P, et al. Mitochondrial outer-membrane protein FUNDC1 mediates hypoxia-induced mitophagy in mammalian cells. Nature Cell Biology 2012; 14: 177–85. doi: 10.1038/ncb2422 PMID: 22267086

44. Tan AS, Baty JW, Dong L-F, Bezawork-Geleta A, Endaya B, Goodwin J, et al. Mitochondrial Genome Acquisition Restores Respiratory Function and Tumorigenic Potential of Cancer Cells without Mitochondrial DNA. Cell Metabolism 2015; 21: 81–94. doi: 10.1016/j.cmet.2014.12.003 PMID: 25565207

45. Kroemer G, Levine B. Autophagic cell death: the story of a misnomer. Nature Reviews Molecular Cell Biology 2008; 9: 1004–10. doi: 10.1038/nrm2529 PMID: 18971948

46. Karantza-Wadsworth V, Patel S, Kravchuk O, Chen G, Mathew R, Jin S, et al. Autophagy mitigates metabolic stress and genome damage in mammary tumorigenesis. Genes & Development 2007; 21: 1621–35.

47. Sun Q, Luo T, Ren Y, Florey O, Shirasawa S, Sasazuki T, et al. Competition between human cells by entosis. Cell Research 2014; 24: 1299–310. doi: 10.1038/cr.2014.138 PMID: 25342560

48. Florey O, Kim SE, Sandoval CP, Haynes CM, Overholtzer M. Autophagy machinery mediates macroendocytic processing and entotic cell death by targeting single membranes. Nature Cell Biology 2011; 13: 1335–U118. doi: 10.1038/ncb2363 PMID: 22002674

49. Krajcovic M, Johnson NB, Sun Q, Normand G, Hoover N, Yao E, et al. A non-genetic route to aneuploidy in human cancers. Nature Cell Biology 2011; 13: 324–U07. doi: 10.1038/ncb2174 PMID: 21336303

50. Nakajima S, Kato H, Takahashi S, Johno H, Kitamura M. Inhibition of NF-kappa B by MG132 through ER stress-mediated induction of LAP and LIP. Febs Letters 2011; 585: 2249–54. doi: 10.1016/j.febslet.2011.05.047 PMID: 21627972

51. Li Y, Bevilacqua E, Chiribau CB, Majumder M, Wang CP, Croniger CM, et al. Differential control of the CCAAT/enhancer-binding protein beta (C/EBP beta) products liver-enriched transcriptional activating protein (LAP) and liver- enriched transcriptional inhibitory protein (LIP) and the regulation of gene expression during the response to endoplasmic reticulum stress. Journal of Biological Chemistry 2008; 283: 22443–56. doi: 10.1074/jbc.M801046200 PMID: 18550528

52. Lim LY, Vidnovic N, Ellisen LW, Leong CO. Mutant p53 mediates survival of breast cancer cells. British Journal of Cancer 2009; 101: 1606–12. doi: 10.1038/sj.bjc.6605335 PMID: 19773755

53. Abreu M, Sealy L. Cells Expressing the C/EBPbeta Isoform, LIP, Engulf Their Neighbors. Plos One 2012; 7.

54. Buchheit CL, Weigel KJ, Schafer ZT. Cancer cell survival during detachment from the ECM: multiple barriers to tumour progression. Nat Rev Cancer 2014; 14: 632–41. doi: 10.1038/nrc3789 PMID: 25098270

55. Howe EN, Cochrane DR, Cittelly DM, Richer JK. miR-200c Targets a NF-kappa B Up-Regulated TrkB/NTF3 Autocrine Signaling Loop to Enhance Anoikis Sensitivity in Triple Negative Breast Cancer. Plos One 2012; 7.

56. Loh YH, Wu Q, Chew JL, Vega VB, Zhang WW, Chen X, et al. The Oct4 and Nanog transcription network regulates pluripotency in mouse embryonic stem cells. Nature Genetics 2006; 38: 431–40. PMID: 16518401

57. Yu J, Vodyanik MA, Smuga-Otto K, Antosiewicz-Bourget J, Frane JL, Tian S, et al. Induced pluripotent stem cell lines derived from human somatic cells. Science 2007; 318: 1917–20. PMID: 18029452

58. Ling G-Q, Chen D-B, Wang B-Q, Zhang L-S. Expression of the pluripotency markers Oct3/4, Nanog and Sox2 in human breast cancer cell lines. Oncology Letters 2012; 4: 1264–8. PMID: 23197999

59. Takahashi K, Yamanaka S. Induction of pluripotent stem cells from mouse embryonic and adult fibroblast cultures by defined factors. Cell 2006; 126: 663–76. PMID: 16904174

60. Park IH, Zhao R, West JA, Yabuuchi A, Huo HG, Ince TA, et al. Reprogramming of human somatic cells to pluripotency with defined factors. Nature 2008; 451: 141–U1. PMID: 18157115

61. Kohsaka S, Sasai K, Takahashi K, Akagi T, Tanino M, Kimura T, et al. A population of BJ fibroblasts escaped from Ras-induced senescence susceptible to transformation. Biochemical and Biophysical Research Communications 2011; 410: 878–84. doi: 10.1016/j.bbrc.2011.06.082 PMID: 21703241

62. Silva J, Chambers I, Pollard S, Smith A. Nanog promotes transfer of pluripotency after cell fusion. Nature 2006; 441: 997–1001. PMID: 16791199

63. Saunders A, Faiola F, Wang JL. Concise Review: Pursuing Self-Renewal and Pluripotency with the Stem Cell Factor Nanog. Stem Cells 2013; 31: 1227–36. doi: 10.1002/stem.1384 PMID: 23653415

64. Brambrink T, Foreman R, Welstead GG, Lengner CJ, Wernig M, Suh H, et al. Sequential expression of pluripotency markers during direct reprogramming of mouse somatic cells. Cell Stem Cell 2008; 2: 151–9. doi: 10.1016/j.stem.2008.01.004 PMID: 18371436

65. Salmina K, Jankevics E, Huna A, Perminov D, Radovica I, Klymenko T, et al. Up-regulation of the embryonic self-renewal network through reversible polyploidy in irradiated p53-mutant tumour cells. Experimental Cell Research 2010; 316: 2099–112. doi: 10.1016/j.yexcr.2010.04.030 PMID: 20457152

66. Mitchell R, Szabo E, Shapovalova Z, Aslostovar L, Makondo K, Bhatia M. Molecular Evidence for OCT4-Induced Plasticity in Adult Human Fibroblasts Required for Direct Cell Fate Conversion to Lineage Specific Progenitors. Stem Cells 2014; 32: 2178–87. doi: 10.1002/stem.1721 PMID: 24740884

67. Zhang S, Mercado-Uribe I, Liu J. Tumor stroma and differentiated cancer cells can be originated directly from polyploid giant cancer cells induced by paclitaxel. International Journal of Cancer 2014; 134: 508–18.

68. Roca H, Varsos Z, Pienta KJ. CCL2 Protects Prostate Cancer PC3 Cells from Autophagic Death via Phosphatidylinositol 3-Kinase/AKT-dependent Survivin Up-regulation. Journal of Biological Chemistry 2008; 283: 25057–73. doi: 10.1074/jbc.M801073200 PMID: 18611860

69. Roca H, Varsos ZS, Mizutani K, Pienta KJ. CCL2, survivin and autophagy—New links with implications in human cancer. Autophagy 2008; 4: 969–71. PMID: 18758234

70. Stadtfeld M, Hochedlinger K. Induced pluripotency: history, mechanisms, and applications. Genes & Development 2010; 24: 2239–63.

71. Mali P, Ye ZH, Hommond HH, Yu XB, Lin J, Chen GB, et al. Improved efficiency and pace of generating induced pluripotent stem cells from human adult and fetal fibroblasts. Stem Cells 2008; 26: 1998–2005. doi: 10.1634/stemcells.2008-0346 PMID: 18511599

72. Zhang H, Chi Y, Gao K, Zhang X, Yao J. p53 Protein-mediated Up-regulation of MAP Kinase Phosphatase 3 (MKP-3) Contributes to the Establishment of the Cellular Senescent Phenotype through Dephosphorylation of Extracellular Signal-regulated Kinase 1/2 (ERK1/2). Journal of Biological Chemistry 2015; 290: 1129–40. doi: 10.1074/jbc.M114.590943 PMID: 25414256

73. Beausejour CM, Krtolica A, Galimi F, Narita M, Lowe SW, Yaswen P, et al. Reversal of human cellular senescence: roles of the p53 and p16 pathways. Embo Journal 2003; 22: 4212–22. PMID: 12912919

74. Zemskova M, Lilly MB, Lin Y-W, Song JH, Kraft AS. p53-Dependent Induction of Prostate Cancer Cell Senescence by the PIM1 Protein Kinase. Molecular Cancer Research 2010; 8: 1126–41. doi: 10.1158/1541-7786.MCR-10-0174 PMID: 20647331

75. Zhang L, Ding P, Lv H, Zhang D, Liu G, Yang Z, et al. Number of Polyploid Giant Cancer Cells and Expression of EZH2 Are Associated with VM Formation and Tumor Grade in Human Ovarian Tumor. Biomed Research International 2014.

76. Liu Y-q, Ji Y, Li X-z, Tian K-l, Young CYF, Lou H-x, et al. Retigeric acid B-induced mitophagy by oxidative stress attenuates cell death against prostate cancer cells in vitro. Acta Pharmacologica Sinica 2013; 34: 1183–91. doi: 10.1038/aps.2013.68 PMID: 23892275

77. Basu HS, Schrieber CL, Sperger JM, Naundorf M, Weichman AM, Mehraein-Ghomi F, et al. Abstract 2899: Mitophagy imparts enzalutamide resistance in prostate cancer. Cancer Research 2015; 75: 2899.

78. Zhang HF, Bosch-Marce M, Shimoda LA, Tan YS, Baek JH, Wesley JB, et al. Mitochondrial autophagy is an HIF-1-dependent adaptive metabolic response to hypoxia. Journal of Biological Chemistry 2008; 283: 10892–903. doi: 10.1074/jbc.M800102200 PMID: 18281291

INTERNATIONAL JOURNAL OF ONCOLOGY 44: 923-933, 2014

Cisplatin-resistant prostate cancer model: Differences in antioxidant system, apoptosis and cell cycle

JAROMIR GUMULEC[1,4], JAN BALVAN[1], MARKETA SZTALMACHOVA[1,2], MARTINA RAUDENSKA[1,4], VERONIKA DVORAKOVA[1], LUCIA KNOPFOVA[3], HANA POLANSKA[1], KRISTYNA HUDCOVA[1], BRANISLAV RUTTKAY-NEDECKY[2,4], PETR BABULA[5], VOJTECH ADAM[2,4], RENE KIZEK[2,4], MARIE STIBOROVA[6] and MICHAL MASARIK[1,4]

[1]Department of Pathological Physiology, Faculty of Medicine, Masaryk University, CZ-625 00 Brno; [2]Department of Chemistry and Biochemistry, Mendel University in Brno, CZ-613 00 Brno; [3]Department of Experimental Biology, Faculty of Science, Masaryk University, CZ-625 00 Brno; [4]Central European Institute of Technology, Brno University of Technology, CZ-616 00 Brno; [5]Department of Natural Drugs, Faculty of Pharmacy, University of Veterinary and Pharmaceutical Sciences, CZ-612 42 Brno; [6]Department of Biochemistry, Faculty of Science, Charles University, CZ-128 40 Prague 2, Czech Republic

Received September 24, 2013; Accepted November 11, 2013

DOI: 10.3892/ijo.2013.2223

Abstract. Differences in the antioxidant system, apoptotic mechanism and in cell cycle between prostatic cell lines could partially elucidate the development of cisplatin resistance. The aim of this study was to identify the most characteristic parameter for a particular cell line and/or a particular cisplatin treatment using a general regression model and to assess whether it is possible to use measured parameters as markers of cisplatin resistance. This study integrates the results of viability, antioxidant, flow cytometric and quantitative PCR assays in order to characterize the resistance of prostate cancer to cisplatin. Cell growth using metabolic- (MTT) and impedance-based assays, the expression of key cell death signaling proteins (p53, Bax and Bcl-2), cell cycle, activity of antioxidant system-related proteins (superoxide dismutase, glutathione peroxidase, glutathione reductase and metallothionein) and free radical scavenging capacity assays [free radicals (FR), ferric reducing antioxidant power (FRAP), ABTS] were analyzed in the cell lines 22Rv1, PC-3 and PNT1A with respect to rising concentrations (0-150 μM) and different length of cisplatin treatment (12-72 h). The non-functional-p53 PC-3 cell line showed decreased BAX ($p<0.05$) and, in contrast to PNT1A and 22Rv1, no cisplatin-induced effects on cell cycle. All cell lines showed increasing levels of free radical scavenging activity by ABTS, FRAP and FR assays in a time- and dose-dependent manner ($r>0.76$ at $p<0.001$ for ABTS, FRAP and FR at $p<0.001$). PC-3 showed increased ($p<0.05$) levels of free radical scavenging activity by ABTS and FR methods. These findings, together with significantly elevated MT, decreased p53 and Bax indicate PC-3 to be cisplatin-resistant. The differences in the antioxidant system and apoptotic mechanisms in PC-3 cells may elucidate the development of cisplatin resistance and indicate that this cell line may be further studied as a model of cytostatic resistance.

Correspondence to: Dr Michal Masarik, Department of Pathological Physiology, Faculty of Medicine, Masaryk University, Kamenice 5, CZ-625 00 Brno, Czech Republic
E-mail: masarik@med.muni.cz

Key words: prostate cancer, cell cycle, resistance, cisplatin, oxidative stress

Introduction

Cis-diamminedichloroplatinum or cisplatin is an inorganic compound that is widely used as a therapy of cancers. The biochemical mechanisms of cisplatin cytotoxicity involve the binding of the drug to DNA and non-DNA targets and the subsequent induction of cell death through apoptosis, necrosis, or both (1). It follows that altered expression of regulatory proteins involved in signal transduction pathways that control the apoptosis, necrosis or cell defense mechanisms (Fig. 1) can additionally make certain types of cancer rather insensitive to cytotoxic effects of cisplatin (2,3), which is, among others, case of later stages of prostate cancer. Cellular mechanisms of resistance to cisplatin are multifactorial and result in severe limitations in clinical use (4-6). Therefore, cisplatin resistance model was formed from prostatic cell lines PNT1A, PC-3, and 22Rv1 in this study. The PC-3 cell line was derived from a metastasis of a high grade androgen irresponsive prostate cancer. Cisplatin resistance is presumed in these cells due non-functional p53 (7). Tumor suppressor protein p53 plays a critical role in regulating cell cycle arrest, DNA repair and apoptosis (8). Accordingly, tumor cells lacking functional p53 were found more resistant to cisplatin than cells that contained functional p53 and the resistant cell lines were sensitized to cisplatin upon reconstitution with wild-type p53 (9).

Among other alterations in cellular response to the cisplatin, oxidative stress might be triggered (10,11). In previous studies, the central role of mitochondria damage in the cisplatin-induced toxicity was demonstrated and it is suggested that it probably

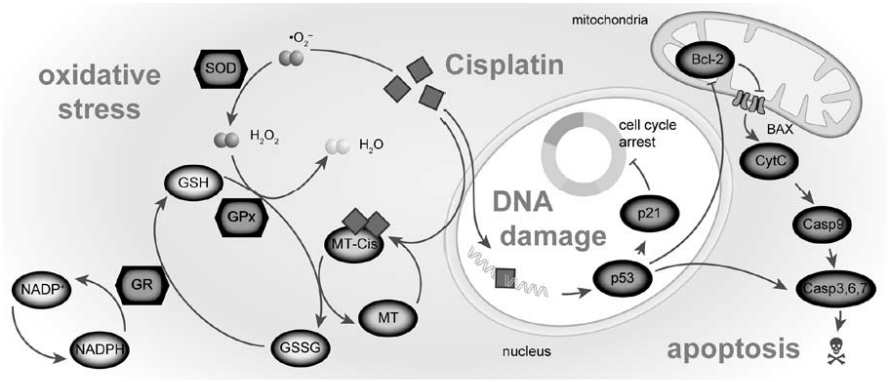

Figure 1. Cisplatin-induced DNA damage, oxidative stress and apoptosis. Cisplatin-cell interaction results in DNA damage, leading to p53 activation. DNA-repair mechanism is allowed due to p21-modulated cell cycle arrest. When damage is irreparable, p53 promotes apoptosis by inhibition of antiapoptic Bcl-2 and consequent caspase activation. Cisplatin binds to metallothionein (MT) and glutathione and thus oxidizes these compounds (GSH, reduced form of glutathione; GSSG, oxidized form of glutathione). Cisplatin generates superoxide radical ($\cdot O_2^-$), transformed by superoxiddismutase (SOD) to hydrogen peroxide, subsequently reduced by GSH in cooperation with glutathione peroxidase (GPx). GSSG is reduced by glutathione reductase (GR) in cooperation with reduced (NADPH).

occurs due to augmented ROS (reactive oxygen species) generation, with consequent impairment of mitochondrial function and structure, depletion of the key components of the mitochondrial antioxidant defense system (GSH and NADPH) and cellular death by apoptosis (12,13). Therefore, understanding the expression of anti- and pro-apoptotic proteins and their relationship to redox system in the cells upon cisplatin treatment will provide valuable insight into the development of cisplatin resistance (11). Therefore, the expression of key apoptosis signaling genes (Bax and Bcl-2) and cell defensive thiol-containing molecule metallothionein (MT) were investigated in this study in different cisplatin concentrations and length of treatment. Additionally, main antioxidant enzymes superoxide dismutase (SOD), glutathione peroxidase (GPx) and glutathione reductase (GR) and antioxidant capacity with respect to the cisplatin treatment were analyzed in this study. MT binds rapidly to platinum and thus sequester cisplatin and remove it from the cells. This binding has primarily been associated with the development of resistance (9). However, there is still a level of inconsistence between studies. In some cases, the levels of MT are higher in cisplatin-resistant cells, but in other cases, the MT levels are unaffected (2).

In summary, differences in antioxidant system, apoptotic mechanism and in cell cycle between prostatic cell lines could partially elucidate the development of cisplatin resistance. Thus, the aim of this study was: i) to identify the most characteristic parameter for particular cell line and/or particular cisplatin treatment using general regression model and ii) to assess, whether it is possible to use measured parameters as markers of cisplatin resistance.

Materials and methods

Chemical and biochemical reagents. RPMI-1640 medium, Ham's F12 medium, fetal bovine serum (FBS) (mycoplasma-free), penicillin/streptomycin and trypsin were purchased from PAA Laboratories GmbH (Pasching, Austria). Phosphate-buffered saline (PBS) was purchased from Invitrogen Corp. (Carlsbad, CA, USA). Ethylenediaminetetraacetic acid (EDTA), cisplatin 0.5 mg/ml solution (Medac, Germany), RIPA buffer and all other chemicals of ACS purity were purchased from Sigma-Aldrich Co. (St. Louis, MO, USA), unless noted otherwise.

Cell cultures. Three human prostatic cell lines were used in this study: i) PNT1A human cell line established by immortalization of normal adult prostatic epithelial cells by transfection with a plasmid containing SV40 genome with a defective replication origin. The primary culture was obtained from the prostate of a 35-year-old male post mortem; ii) 22Rv1 is a human prostate carcinoma epithelial cell line derived from a xenograft that was serially propagated in mice after castration-induced regression and relapse of the parental, androgen-dependent CWR22 xenograft. iii) PC-3 human cell line established from a grade 4 androgen independent and unresponsive prostatic adenocarcinoma from 62-year-old Caucasian male and derived from metastatic site in bone. All cell lines used in this study were purchased from Health Protection Agency Culture Collections (Salisbury, UK).

Culture conditions. PNT1A and 22Rv1 cells were cultured in RPMI-1640 medium with 10% FBS. PC-3 cells were cultured in Ham's F12 medium with 7% FBS. All media were supplemented with penicillin (100 U/ml) and streptomycin (0.1 mg/ml), and the cells were maintained at 37˚C in a humidified incubator (Sanyo, Japan) with 5% CO_2.

Cisplatin treatment. The cisplatin treatment was initiated after cells reached ~50% confluence. The concentration range 0, 10, 25, 50, 100, 150 μmol/l was used for all cell lines. Time points for cell harvest and thus for all subsequent analyses were set subsequently: 12, 24, 48 and 72 h. Thus, 6 (concentrations) x 4 (time points) lyzates were created. Cells were then harvested and washed four times with 1X PBS, pH 7.4.

Cell content quantification. Total cell content was analyzed using Casy model TT system (Roche Applied Science, USA) using following protocol: first, calibration was performed from

samples of viable and necrotic cells. For necrotic cells, 100 µl cell suspension and 800 µl Casy Blue solution was mixed and left for 5 min in room temperature. Subsequently, 9 ml Casy Tone was added. To prepare viable cell standard, 100 µl cell suspension was mixed with 10 ml Casy Tone. All subsequent measurements were performed on 100x diluted 100 µl cell suspension. Prior each measurement, background was subtracted. All samples were measured in duplicates.

Measurements of cell viability - MTT test. The suspension of 5,000 cells was added to each well of standard microtiter plates. Volume of 200 µl was transferred to 2-11 wells. Medium (200 µl) was added to the first and to the last column (1 and 12, control). Plates were incubated for 2 days at 37˚C to ensure cell growth. Medium was removed from columns 2 to 11. Columns 3-10 were filled with 200 µl of medium containing increasing concentration of cisplatin (0-150 µmol/l). As control, columns 2 and 11 were filled with medium without cisplatin. Plates were incubated for 12, 24, 48 and 72 h; then, media were removed and replaced by a fresh medium, three times a day. Columns 1-11 were filled with 200 µl of medium containing 50 µl of MTT (5 mg/ml in PBS) and incubated in a humidified atmosphere for 4 h at 37˚C, wrapped in aluminium foil. After the incubation, MTT-containing medium was replaced by 200 µl of 99.9% dimethyl sulphoxide (DMSO) to dissolve MTT-formazan crystals. Then, 25 µl of glycine buffer was added to all wells and absorbance was immediately determined at 570 nm (VersaMax microplate reader, Molecular Devices, Sunnyvale, CA, USA).

Cell growth and proliferation assay using impedance measurement with xCELLigence system. The xCELLigence system (Roche Applied Science and ACEA Biosciences, San Diego, CA, USA) consists of four main components: the RTCA analyzer, the RTCA station, the RTCA computer with integrated software and disposable E-plate 16. Firstly, the optimal seeding concentration for proliferation and cytotoxic assay was determined. After seeding the total number of cells in 200 µl medium to each well in E-plate 16, the attachment, proliferation and spreading of the cells was monitored every 15 min. All experiments were carried out for 250 h. The results are expressed as relative impedance using the manufacturer's software (Roche Applied Science and ACEA Biosciences).

Flow cytometric analysis of cell cycle. The cells were harvested and fixed with ice-cold 70% ethanol for 30 min. After washing with 1X PBS, the cells were incubated with DNA staining solution consisting of propidium iodide (PI; 50 µg/ml) and RNase (100 µg/ml) for 30 min at 37˚C in the dark. Samples were analyzed with FACSVerse flow cytometer (BD Biosciences, USA) and the data obtained were analyzed using FACSuite software (BD Biosciences).

RNA isolation and reverse transcription. High pure total-RNA isolation kit (Roche, Basel, Switzerland) was used for isolation. The medium was removed and samples were twice washed with 5 ml of ice-cold PBS. Cells were scraped off, transferred to clean tubes and centrifuged at 20,800 x g for 5 min at 4˚C. After this step, lysis buffer was added and RNA isolation was carried out according to manufacturer's instructions. Isolated RNA was used for cDNA synthesis. RNA (600 ng) was transcribed using transcriptor first strand cDNA synthesis kit (Roche, Switzerland) was used according to manufacturer's instructions. Prepared cDNA (20 µl) from total-RNA was diluted with RNase-free water to 100 µl and 5 µl was directly analyzed by 7500 RT-PCR system (Applied Biosystems).

Quantitative polymerase chain reaction (q-PCR). q-PCR was performed in triplicate using the TaqMan gene expression assay system with the 7500 RT-PCR system (Applied Biosystems) and the amplified DNA was analyzed by the comparative Ct method using β-actin as an endogenous control for metallothionein MT2A, Bax, Bcl-2 and p53 gene expression quantification. The primer and probe sets for β-actin (assay ID: Hs99999903_m1), MT2A (Hs02379661_g1) Bcl-2 (Hs99999018_m1), p53 (Hs01034649_m1), and Bax (Hs00180269_m1) were selected from TaqMan gene expression assays (Life Technologies, USA). q-PCR was performed under the following amplification conditions: total volume of 20 µl, initial incubation 50˚C/2 min followed by denaturation 95˚C/10 min, then 45 cycles 95˚C/15 sec, 60˚C/1 min.

Electrochemical detection of metallothionein. Electrochemical detection was used for quantification of metallothionein. Detection was carried out using AUTOLAB Analyser (EcoChemie, The Netherlands) with classical three-electrode arrangement using of differential pulse voltammetry Brdicka reaction. Analysed sample was accumulated on the surface of a working electrode which is represented by hanging mercury drop electrode. After accumulation, detection proceeded in a supporting electrolyte containing cobaltic (cobalt^{3+}) salt in ammonia buffer of pH 9.6 (14).

Spectrophotometric measurement. Spectrophotometric measurements were carried out using an automated chemical analyser BS-400 (Mindray, P.R. China). It is composed of cuvette space tempered to 37±1˚C, reagent space with a carousel for reagents (tempered to 4±1˚C), sample space with a carousel for preparation of samples, and an optical detector. Transfer of samples and reagents is provided by robotic arm equipped with a dosing needle (error of dosage up to 5% of volume). Cuvette contents are mixed by an automatic mixer including a stirrer immediately after addition of reagents or samples. Contamination is reduced due to its rinsing system, including rinsing of the dosing needle as well as the stirrer by MilliQ water. For detection itself, the following range of wavelengths can be used - 340, 380, 412, 450, 505, 546, 570, 605, 660, 700, 740, and 800 nm.

Determination of SOD. Kit 19160 SOD (Sigma Aldrich, USA) was used for assay of SOD, EC 1.15.1.1. First, 200 µl volume of reagent R1 (WTS solution 20 times diluted with buffer) was pipetted into a plastic cuvette and agent was incubated at 37˚C for 108 sec. Afterwards, 20 µl volume of sample was pipetted and in 378 sec, the reaction was started by adding 20 µl volume of reagent R2 (enzyme solution 167 times diluted with buffer). It was incubated for 72 sec and then absorbance was measured at λ=450 nm. Kinetic reaction was measured for 108 sec and absorbance was read every 9 sec.

Determination of glutathione reductase and peroxidase. A glutathione reductase and peroxidase cellular activity assay kits

(Sigma Aldrich) were used for GR and GPx activity determination. Reagents R1 and R2 were prepared by dissolving in an assay buffer (100 mmol/l potassium phosphate buffer, pH 7.5, with 1 mmol/l EDTA). The reagent R1 of 260 μl volume (1.15 mmol/l oxidized glutathione in the assay buffer) was poured with 10 μl of sample and 30 μl volume of reagent R2 (1 mmol/l NADPH in GR assay buffer) into a plastic cuvette. The decrease in absorbance was measured at 340 nm using kinetic program for 126 sec.

Determination of antioxidant activity by the FRAP method. The FRAP method (ferric reducing antioxidant power) is based on the reduction of complexes of 2,4,6-tripyridyl-s-triazine with ferric chloride hexahydrate ($FeCl_3 \cdot 6H_2O$); these substances are almost colorless, and eventually slightly brownish. After the reduction, blue ferrous complexes are formed. Procedure for the determination was used as in Sochor *et al* (15). After 150 μl volume of reagent is injected into a plastic cuvette with subsequent addition of a 3-μl sample, absorbance is measured at 605 nm for 12 min. Difference between absorbance at the last (the 12th) min and the 2nd min of the assay procedure was used for calculating of the antioxidant activity.

Determination of antioxidant activity by the free radicals method. This method is based on ability of chlorophyllin (the sodium-copper salt of chlorophyl) to accept and donate electrons with a stable change of maximum absorption. This effect is conditioned by an alkaline environment and the addition of catalyst.

Procedure for the determination was used as in Sochor *et al* (15). Reagent of 150 μl volume is injected into a plastic cuvette with subsequent addition of a 6-μl sample. Absorbance is measured at 450 nm in the second min of assay and the last (the 12th) min. Difference of the two absorbances is considered as an outputting value.

Statistical analysis. First, data were tested for normality using χ^2-test and log-normal fitted data were recalculated to log scale. General regression model method was used to reveal relationships between multiple continuous and categorical variables.

Prior to regression analysis, Pearson's correlation was performed to verify concordant trends among cell lines. Subsequently, partial correlations were used to analyze residuals of time/concentration after adjustment of all other variables. To reveal differences between cell lines, Tukey's post-hoc test within homogeneous groups was employed after adjustment of all other variables. Prior to these analyses, residuals were tested for outliers (no-normally distributed data with outliers was excluded from subsequent analyses). Hierarchical clustering on standardized data was used to determine similar trends within determined parameters. Unless noted otherwise, $p<0.05$ was considered statistically significant. Software Statistica 10 (StatSoft, Inc., USA) was used for analysis.

Results

Effect of treatment on cell viability - comparison of MTT and impedance-based data. To assess the cytotoxic effect of cisplatin on prostate cell lines, and to select concentrations for further analyses, MTT test was performed with concentrations 0 (no drug added), 10, 25, 50, 100, 150, 200 and 250 μmol/l on all cell lines (Fig. 2A). Using logistic regression, IC_{50} concentrations were determined at time points 12, 24, 48 and 72 h. As expected, cisplatin cytotoxicity increases in time-dependent manner (Table I). To understand these temporal changes, real-time cell growth monitoring was employed with the same cisplatin concentrations. Using this method, transient increase in impedance resulting in peaks on growth curves was determined in the first 24 h of treatment (Fig. 2B). This method also showed a similar time-dependent cytotoxicity increase as seen by MTT. However, IC_{50} values calculated by this method were on average 1.3-fold higher compared to MTT and no significant correlation was observed between MTT- and impedance-based IC_{50} values ($r=0.13$ at $p=0.70$).

Flow cytometric analysis of the cell cycle. To reveal the impact of cisplatin on the cell cycle, flow cytometric analysis was performed after the confluence of cells was ~50%. This confluence was reached within 24 to 48 h of treatment. Cisplatin-induced effects on cell cycle is evident in PNT1A and 22Rv1 cell lines (Fig. 2C and D). In these cells, 100 μM cisplatin dose increases the proportion of sub-G1 stage cells; up to 26.7% and 73.2% in PNT1A and 22Rv1, respectively. Flow cytometric analysis of 22Rv1 cells exposed 150 μmol/l cisplatin was below the detection limits due to the low cell counts in the sample. In contrast, PC-3 cell line does not show cell cycle arrest, maintaining <1.3% of cells in sub-G1 in all concentrations without significant increase or decrease.

Effect of treatment on gene expression. Subsequently, dose- and time-dependent response of apoptosis- and oxidative stress-related genes was analyzed. First, the level of metallothionein isoform 2A (RNA and protein), cellular tumor antigen p53 (RNA and protein), apoptosis regulators Bcl-2 and Bcl-2-associated X protein (Bax, RNA only) were analyzed (Fig. 3).

All detected RNAs and proteins were affected in treatment time-, dose- or cell line-dependent manner to some extent. For a more comprehensive understanding, residual analysis of treatment time and cisplatin dose after adjustment of other variables is desirable. Conditions for such residual analysis are met, because all lines showed consistently significant increasing/decreasing trends for all substances, the difference was seen only in the extent of increase/decrease. Partial correlations of time-, cell line-, and dose-adjusted residuals were determined to elucidate the unique contribution of the treatment time and dose individually (Table II). To analyze redundant trends, hierarchical cluster analysis of oxidative markers and RNA and protein was performed. As seen in Fig. 3A and B, Bcl-2, Bax and p53 show similar time- and dose-dependent response are thus clustered together.

First, the unique contribution of cisplatin dose after adjustment of all other variables (treatment time and cell line) is presented here. Significant elevation (i.e., significant partial correlation $r>0$) was determined in Bax (partial $r=0.34$ at $p<0.01$) and metallothionein (partial $r=0.73$ at $p<0.001$ and $r=0.45$ at $p<0.001$ for RNA and protein, respectively). Second, unique contribution of treatment duration was analyzed. p53 and Bcl-2 showed time-dependent increasing trends, $r=0.34$ at $p<0.01$ and $r=0.63$ at $p<0.001$, respectively. The remaining

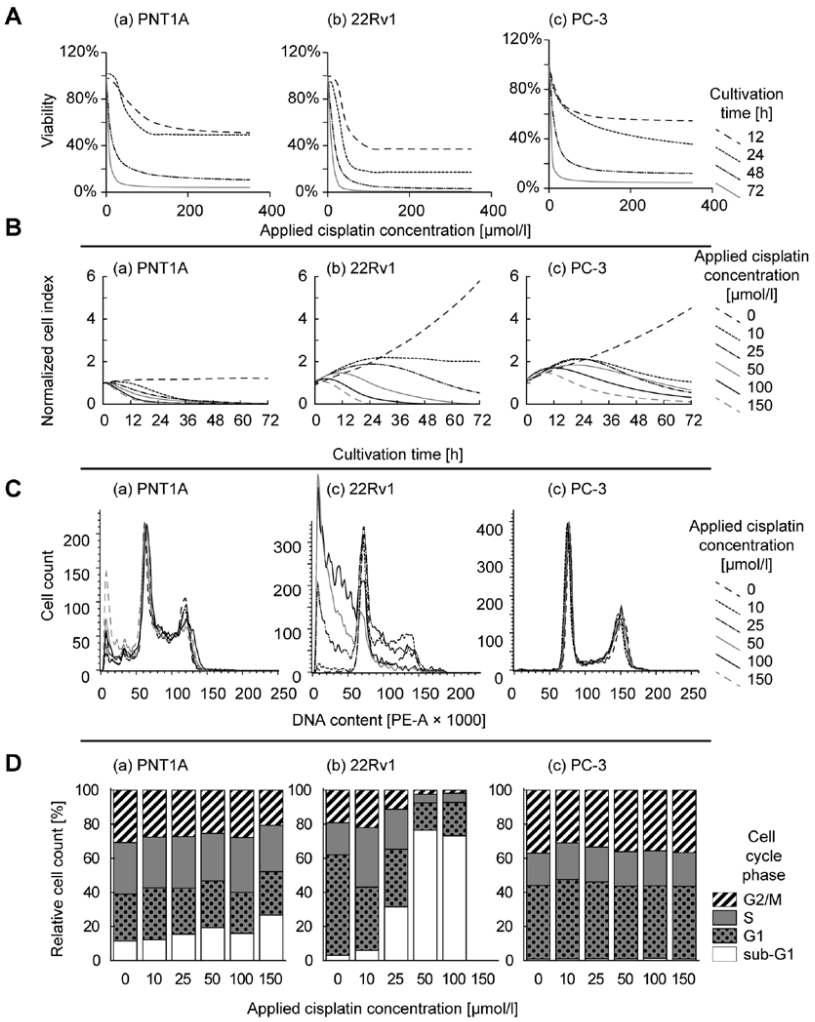

Figure 2. Cisplatin, cell growth and cell cycle. Each column shows one cell line (a-c). A, MTT test: dose-response curves measured in 12, 24, 48 and 72 h. Evident metabolic activity decrease in later measurements. B, Real-time cell growth analysis. The impedance-based signal is represented as a cell index normalized to value 1.0 at the beginning of the treatment. Transient increase in cell index in the first 24 h as a result of cell size and/or adhesivity change following cisplatin treatment. C, Flow cytometric analysis of the cell cycle. Increasing proportion of sub-G1 (increasing peaks) evident in PNT1A and 22Rv1 cells and not in p53-defective PC-3 cells (a, b vs. c). D, Dose-dependent proportion of cells in various stages of the cell cycle. Note cisplatin treatments >150 μM are not shown for better clarity of charts.

Table I. Half-maximal concentrations.[a]

	MTT IC_{50} (μmol/l)				xCELLigence IC_{50} (μmol/l)			
Cell line/time	12 h	24 h	48 h	72 h	12 h	24 h	48 h	72 h
PC-3	18.3	74.9	10.6	1.0	339.6	77.4	25.6	7.0
22Rv1	40.4	30.8	12.7	7.9	Undet.	2413.8	10.5	2.6
PNT1A	61.5	44.0	7.9	3.7	185.7	97.1	12.1	2.7

[a]Time-dependent comparison of IC_{50} determined by MTT and xCELLigence. See evident time-dependent increase of cytotoxicity using both methods. Undet., undeterminable, out of range.

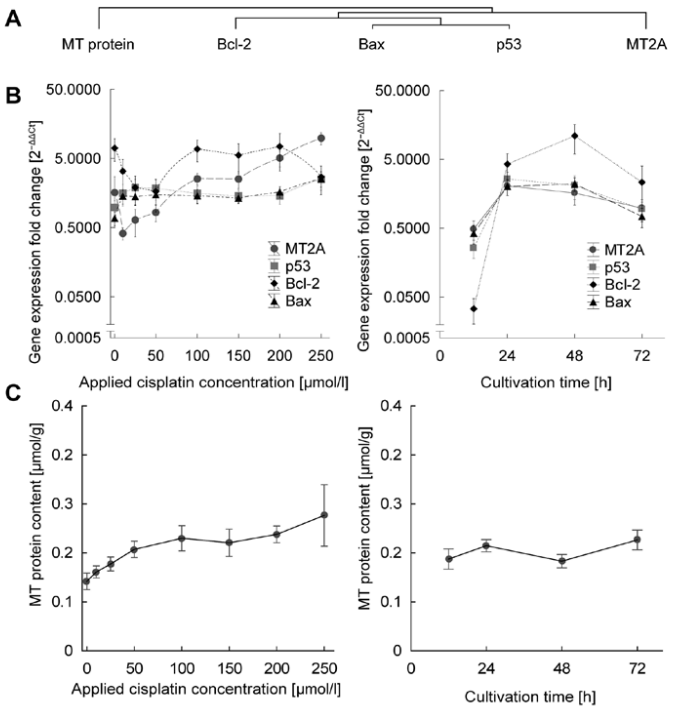

Figure 3. Gene expression and metallothionein protein level following cisplatin treatment. The effect of dosage after adjustment of all other variables shown in the left column, the effect of cultivation time on the right. A, Cluster analysis. See close relation of p53 and Bax in dendrogram resulting in similar trend of these genes in panel B. B, RNA level. There was distinct elevation of gene expression during first 24 h. Note y-axis in log-scale, gene expression fold change relative to PNT1A cell line. MT2A, metallothionein 2A. C, Metallothionein protein level. Distinct cisplatin concentration-related MT increased. For subsequent correlation coefficients see Table II. Data displayed as mean ± SE.

Table II. Dependence of parameters on time, cisplatin concentration and cell lines.[a]

Correlation coefficients (r)	MT protein	MT RNA	p53 RNA	Bcl-2 RNA	Bax RNA	SOD	GR	GPx	FR	FRAP	ABTS
Simple correlation											
Time (h)	0.03	0.09	0.12	0.36[c]	0.05	-0.14	-0.26[b]	0.23[b]	0.22[b]	0.18	0.09
Cisplatin (μmol/l)	0.43[d]	0.71[d]	0.03	0.02	0.24[b]	-0.18	-0.59[d]	0.25[b]	0.82[d]	0.64[d]	0.79[d]
Multiple regression											
Overall	0.59[d]	0.73[d]	0.84[d]	0.69[d]	0.61[d]	0.53[d]	0.82[d]	0.64[d]	0.89[d]	0.76[d]	0.85[d]
Time	0.07	0.22	0.24[b]	0.49[d]	0.13	-0.20	-0.43[d]	0.36[c]	0.52[d]	0.36[c]	0.26[b]
Cisplatin (μmol/l)	0.45[d]	0.73[d]	0.17	0.12	0.34[c]	-0.21	-0.72[d]	0.34[c]	0.88[d]	0.71[d]	0.82[d]
22Rv1 cells	-0.14	0.10	0.34[c]	0.63[d]	0.46[d]	-0.22	0.59[d]	0.48[d]	-0.36[c]	0.40[d]	-0.39[d]
PC-3 cells	0.43[d]	-0.13	-0.82[d]	-0.46[d]	-0.56[d]	-0.29[b]	-0.03	0.06	0.36[c]	-0.01	0.40[d]

[a]Pearson correlation coefficients (R) showing ambiguous results. Second, general regression model is used to show multiple R (see 'Overall' row) and partial correlation coefficients (other parameters). Significant at [b]$p<0.05$, [c]$p<0.01$, [d]$p<0.001$. MT, metallothionein.

RNAs are not dose- or cultivation time-dependent. Despite this fact, time-dependent analysis of all genes exhibit biphasic relation (Fig. 3B). Cisplatin dramatically increases the expression, in particular in first 24 h; up to 60-fold in Bcl-2, 10-fold in p53 and 5-fold in Bax and MT2A genes. However, after 24 h a plateau in expression is observed. As a result, the relation of MT RNA and

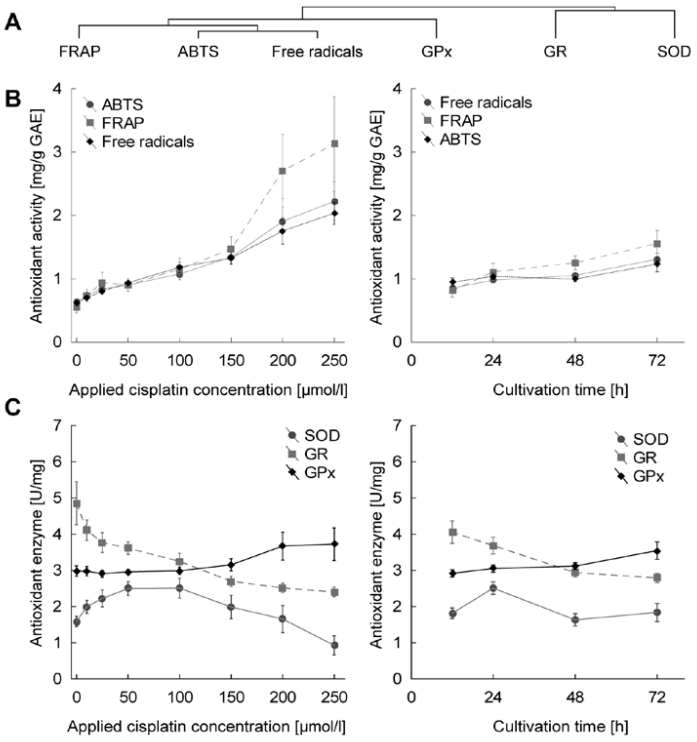

Figure 4. Oxidative stress after cisplatin treatment. The effect of dosage after adjustment of all other variables shown in the left column, the effect of cultivation time on the right. A, Cluster analysis. B, Markers of antioxidant capacity. Note the concordant trend of all three markers. C, Glutathione-related enzymes. Note the dose- and time-dependent GR decrease. Contrary to GR, no distinct cisplatin-related trends were determined in SOD. For subsequent correlation coefficients see Table II. Data displayed as mean ± SE.

protein shows weak, but significant positive correlation (r=0.24 at p=0.016).

Apart from gene expression analysis, protein level of MT was studied (Fig. 3C). Significant positive correlation was observed between MT protein and applied cisplatin dose (r=0.59 at p<0.001) and no correlation was observed in relation to cultivation time.

Effect of treatment on antioxidant capacity. All markers of antioxidant capacity correlate with each other significantly (data not shown). This is well evident in Fig. 4B and corresponds to cluster analysis, where these markers are closely clustered (Fig. 4A). In terms of statistical significance, all markers of antioxidant capacity increased significantly in dose-dependent manner, r=0.88, 0.71 and 0.82 for free radicals, FRAP and ABTS, respectively, at p<0.001. The duration of treatment affects parameters at lower levels of significance with r=0.52, 0.36 and 0.26 for free radicals, FRAP and ABTS (Fig. 4B).

With regard to glutathione-related enzymes, increasing dose- and time-dependent trend is shown only by glutathione peroxidase (r=0.34 and 0.36 for concentration and time at p<0.01), in contrast, glutathione reductase decrease in both time- and dose-dependent manner (at r=-0.72 for concentration and r=-0.43 for time at p<0.001). Superoxide dismutase showed no time- or concentration-dependent trends (Fig. 4C).

Effect of cell lines. Subsequently, the effect of cell lines was analyzed after adjustment of all other variables. Using Tukey's test for homogeneous groups, no significant difference, except in metallothionein RNA, between cell lines was identified. All other parameters showed significantly higher/lower trends between cell lines to some extent.

To identify similar patterns between cell lines, cluster analysis was employed, creating two characteristic branches. The first branch comprises markers of antioxidant capacity, glutathione-related enzymes and metallothionein, in contrast, the second branch includes apoptosis-related genes and SOD (Fig. 5A).

Close similarity is observed between ABTS and FR, showing significant difference between tumorous cell lines only (higher in PC-3). MT, similarly to ABTS and FR, shows significant difference between tumorous lines only. Glutathione peroxidase shows significant difference between all cell lines, while lowest level was observed in healthy cell line, thus, showing similarity to glutathione reductase. Similar trend is observed also in FRAP, where only PNT1A and 22Rv1 differ significantly.

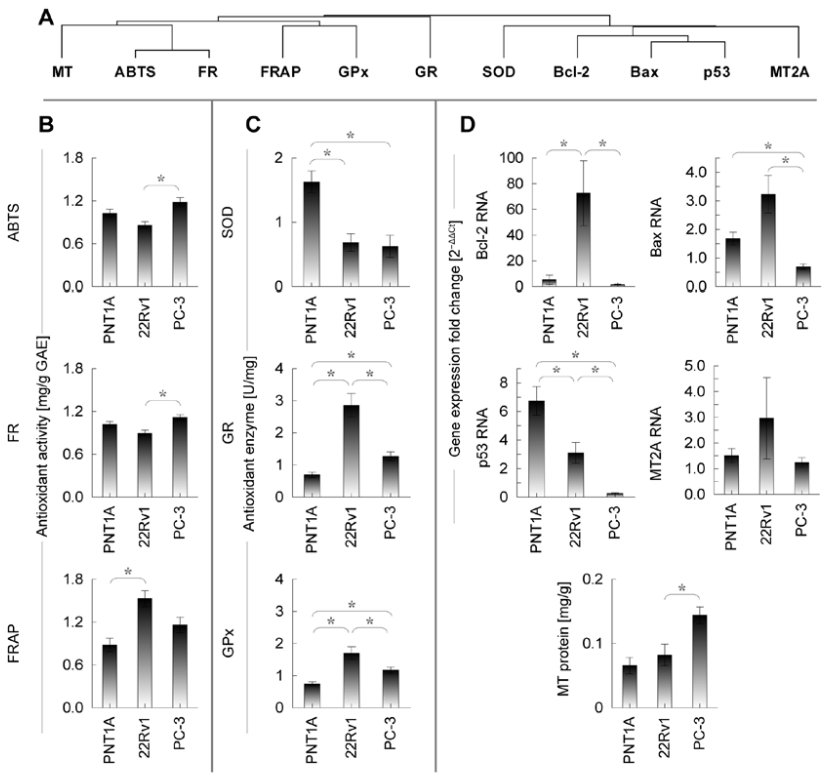

Figure 5. Cell lines and selected markers. The effect of each cell line after adjustment of treatment time and cisplatin dose. A, Cluster analysis. B, Markers of antioxidant capacity. Values displayed in mg/g of galic acid equivalent. FRAP, ABTS - C, Glutathione-related enzymes. D, RNA and protein level of selected genes. RNA level in relative gene expression fold change relative to PNT1A. *Significant at $p<0.05$ using Tukey's post-hoc test. Data displayed as mean ± SE.

With regard to apoptosis-related genes and superoxide dismutase, no difference can be seen in MT mRNA, significantly increased Bax in PC-3 cell line, significantly increased SOD in healthy PNT1A, significant difference between all cell lines in case of p53 (lowest in PC-3, highest in PNT1A) and significantly increased Bcl-2 in tumorous 22Rv1.

Discussion

This study provides time- and dose-dependent description of cisplatin-induced changes in antioxidant properties, apoptosis and cell cycle regulation on prostate cancer cell lines. These approaches clearly illustrate the development of resistance in advanced forms of prostate cancer, represented by the PC-3 cell line.

Cell growth, cell cycle. The results of viability assays distinctly show that the cytostatic effect of cisplatin is unpredictable in first hours of treatment, showing low cytotoxic potential, in particular, when detected using impedance-based method (Fig. 2A). This method provides transient increase in growth curves in particular in the first 24 h of treatment. Inasmuch as this detection method is influenced not only by the number of cells, but also by their size and adhesivity (16,17) and while these transient changes cannot be caused by cell count increase in such a short interval, here we provide evidence of cisplatin-influenced change of cell morphology and/or adhesivity. The steady state stabilization occurs between 24-48 h.

Even after stabilization, high level of disagreement was observed between metabolic-based MTT and impedance-based viability assays. While MTT test demonstrates the most toxic effect on 'aggressive metastatic' PC-3 cells, impedance-based (cell amount-, size- and adhesivity-dependent) technique demonstrates, in contrast, least toxic effects on this cell line (compare MTT- and impedance-based IC_{50} values in Table I, Fig. 2). To find an answer for this seemingly conflicting finding it is appropriate to relate it to the changes in cell cycle and apoptosis in these cell lines.

PC-3 cells are hemizygous for chromosome 17p, and their single copy of the *p53* gene has a deletion at codon 138 that has caused a frameshift and a new in-frame stop codon at position 169 (18). As a result, PC-3 cells do not express p53 protein (19). Our results are in agreement with these findings (20): level of p53 RNA was almost under the detection limits in PC-3 cell line (Fig. 4). P53 acts as a tumor suppressor through the induction of growth arrest and apoptosis (8). PNT1A cell line, which was

used in this experiment as a non-tumor model, was transfected using simian virus 40 (SV40) vector. However, SV40 induces T-antigen expression, which, on the other hand, inhibits the activity of p53 (21). Therefore, cell lines transfected using this vector have limited predictive value in terms of p53-dependent effects. Nevertheless, T-antigen p53 inhibition can be disrupted using oxidants (22), including cisplatin. The objective of the p53 detection in this study was neither to describe subtle concentration-dependent trends in p53 levels nor to describe p53-dependent cascades in detail, but rather to demonstrate a detectable induciblity of p53 expression when exposed to oxidative stress. The fact that detectable p53 content was determined in PNT1A under cisplatin load indicates p53-dependent pathways can be triggered in this cell line. Therefore, PNT1A might be used as model to study p53-dependent pathways, however, only if exposed to oxidative stress. The differences between p53-positive and negative cells are evident in our flow cytometric results: whereas both p53-expressing cells PNT1A and 22Rv1 show cisplatin-induced cell cycle changes accompanied by an increased proportion of sub-G1 phase cells, PC-3 cell does not show similar phenomenon (Fig. 2C and D). Similar phenomenon was demonstrated and linked with cisplatin resistance in non-small cell lung cancer cell line, for instance (23). It has been repeatedly demonstrated that apoptosis is the major mechanism for eliminating damaged cells in cisplatin-induced cells injury (24-26). Thus, PC-3 cells without functional p53 signaling cascade may divide and grow when treated with cisplatin or other p53-targeting cytostatic drug. Because PC-3 is derived from an aggressive metastatic form of prostate cancer, using the description of the monitored genes and parameters, this study provides a good model of cisplatin resistance. In addition, similarly to cisplatin, more pronounced apoptosis in 22Rv1 compared to PC-3 was observed by Gravina *et al* when exposed to 5-azacitine or bicalutamide (27). Taken together, contradictory results of MTT assay and an impedance-based method can be caused by false reduced viability of PC-3, which could be caused by low metabolic activity of cells in autophagy status. The main principle of MTT assay is the tetrazolium salt reduction to formazan, which is quantified photometrically, by mitochondrial succinate dehydrogenase (SDH). SDH is only active in cells with an intact metabolism and respiratory chain. Fasting and oxidative stress, which is present by cisplatin treatment, was associated with a significant decrease of SDH activity, and the reduction was proportional with the decrease in the amount of SDH total protein (28,29). Blocking apoptosis was found to promote autophagy in PC-3 and DU145 cells (30).

In accordance with this finding, we propose an impedance-based method as more reliable for growth monitoring of cytostatic-induced cells. Similar changes between these assays were reported also in our previous study (31).

Cisplatin effects - model of cisplatin resistance? To obtain initial insight into how all the markers and substances mentioned herein change after the exposure to cisplatin, 3-axis dependency graphs were visualized and calculated the simple correlations for each cell line. However, such analysis provides weak correlations and has limited power to emphasize complex multi-dimensional relations (Table II). Based on these graphs it is possible to draw the following conclusions: first, cisplatin concentration or treatment time clearly results in either increase or decrease in the levels of detected substances in all cell lines. Thus, none of the parameters increase in one cell line and decrease in the other in time- or dose-dependent manner. Second, both time and concentration cause more or less distinct changes in the levels of almost all monitored markers and substances. Third, some markers or substances rather increase, while others decrease, depending on the time or concentration.

Inasmuch as representation of graphs with their correlation coefficients would be confusing, statistically insufficiently powerful and, most importantly, such analysis would not refer to the obvious connection between the parameters, general regression model was used to show the effect of cell lines, concentrations of cisplatin and time of measurement simultaneously. This method provides benefits of both multiple linear regression and ANOVA and thus provide a more comprehensive view of all detected substances together. In this context, we focused on the identification of the most characteristic parameter for particular cell line and/or particular cisplatin treatment. Additionally, a hypothesis was verified, whether all measured markers may be used to describe cisplatin resistance.

To evaluate the effect of cisplatin concentration, duration of this cytotoxic effect or combination of these, partial correlations were calculated after the adjustment of all other variables. Partial correlations obtained by general regression model were subsequently compared to initially performed Pearson correlation results. Because significant trends were found mainly after adjusting using general regression model and no parameter correlated only before adjusting (i.e., in Pearson correlations), it is evident, that just variables 'concentration', 'time' and 'cell line' contribute to elucidate the variability (i.e., affect the level of detected substances). This manner explained up to 80% of the variability in data attributing it to the change in detection time, cisplatin concentration or cell line (R^2=0.80 in 'free radicals' method, for instance).

In this context, a hypothesis was formulated, whether all the measured parameters are rather influenced by the duration of the stress conditions (treatment time), or by the stress intensity (drug concentration). Whereas the markers of antioxidant capacity FRAP, ABTS and FR and GPx increase in dose- and time-dependent manner, p53 and Bcl-2 are time-dependent and BAX and MT are dose-dependent only. Interestingly, GR shows a decreasing time- and concentration-dependence. These findings are in agreement with what is inherently predictable: the increased p53 level contributes to apoptosis through Bax-cytochrome C mitochondrial apoptotic pathway by inhibition of Bcl-2 (8,32) (Fig. 1). As a result of such balance, Bax level follows analogous trends in dose-, time- and cell line-dependent manner (Figs. 3 and 5). An agreement with these findings was observed by Kharaziha *et al* (33). Agreement with our data was also provided by Li *et al* demonstrating a simultaneous increase in ROS, p53 and caspases in response to another platinum-based cytostatic drug dicycloplatin (34).

Metallothionein protein level increases with increasing cisplatin concentration due to its (cisplatin-induced) reactive-oxygen-species buffering properties. In contrast, metallothionein is not affected by the duration of cisplatin treatment due to the fact that the concentration of this drug (and thus cisplatin-generated oxidative stress) remain relatively stable after steady state stabilization (Fig. 3). The highest MT levels are determined in an

aggressive, metastasis-derived PC-3 cells. Similar finding was observed by several research teams (35-37). These data suggest MT is an important protective mechanism in cisplatin-induced stress and thus an important mechanism in the development and progression of cytostatic resistance. Such finding was already reported (35). No observed metallothionein RNA-protein match may appear to be a surprising result. However, it cannot be assumed, that significant RNA-protein correlation must be present. A pool of metallothionein capable to buffer limited amounts of oxidative stress is present more or less in all cells and thus RNA-response may not be apparent (38,39).

With regard to the activity of enzymes included in oxidative stress buffering (SOD, GR and GPx), a specific pattern is observed. Whereas non-tumor cell line shows higher activity of SOD and lower activity of GR and GPx, tumorous cells show an inverse trend. When exposed to cisplatin, GPx increases, GR decreases and SOD does not show any significant trend. The decreasing dose- and time-dependent trends in glutathione reductase may seem surprising at first glance. Generally, one would assume that the increase in oxidative stress will also increase oxidized glutathione and thus the activity of glutathione reductase. However, cisplatin causes a depletion of the key components of the mitochondrial antioxidant defense system, including NADPH (13). Because of NADPH oxidation, GR activity is expected to decrease. Similar finding with GR and GPx when treated with cisplatin is reported by Pratibha *et al* in a rat model (40). The authors propose a cisplatin-induced alteration in enzymatic antioxidant status with an increase in lipid peroxidation indicating that these enzymes play an important role in combating oxidative stress induced by free radicals (40).

With regard to markers of antioxidant capacity, it is worth mentioning that all radical scavenging activity detection methods correlate, showing an increase after cisplatin treatment. More pronounced increase is observed in tumorous cell lines particularly in the PC-3. These data suggest an increased ability of tumorous cells to cope with such conditions. There is no evidence on using these methods to describe antioxidant capacity on prostate cancer cell lines. This finding, together with elevated MT, decreased p53 and Bax suggest that the PC-3 cell line has unique features to cope with stress conditions and thus to be resistant to natural regulatory mechanisms such as apoptosis and cell cycle arrest and to stress cytostatics. Thus, this cell line may further be utilized as a model of cytostatic resistance, and markers and substances detected herein illustrate resistance development as well.

In this study, the cell-growth, cell cycle, apoptosis and oxidative stress-related methods were analyzed to describe the development of cisplatin resistance in prostate cancer. In p53-defective PC-3 cells no cisplatin-induced cell cycle arrest and reduced apoptosis was observed. In addition, higher free radical scavenging activity and higher metallothionein was observed in these cells. In contrast to impedance-based real-time cell growth analysis, reduced MTT-based viability suggests reduced metabolic activity and thus cells are expected to turn to autophagy. Thus, we propose an impedance-based method as more reliable for growth monitoring of cytostatic-treated cells.

Taken together, results of this study clearly illustrate, that the prostate cancer cell line PC-3 shows signs of resistance to cytostatics accompanied by an increase in antioxidant capacity, by increased metallothionein expression, by inhibition of cell cycle arrest, and by decreased expression of proapoptic genes. Therefore, PC-3 cell line may be used for further analyses as a model for cytostatic resistance as well as protocols used in this study. However, precise mechanisms affecting the orientation of cells toward autophagy or apoptosis are open topics for further research.

Acknowledgements

The authors gratefully acknowledge financial support from the following projects: the Grant Agency of the Czech Republic (CYTORES GA CR P301/10/0356), Center of Experimental Biomedicine (CZ.1.07/2.3.00/20.0183) and the Central European Institute of Technology (CEITEC CZ.1.05/1.1.00/02.0068).

References

1. Gonzalez VM, Fuertes MA, Alonso C and Perez JM: Is cisplatin-induced cell death always produced by apoptosis? Mol Pharmacol 59: 657-663, 2001.
2. Kartalou M and Essigmann JM: Mechanisms of resistance to cisplatin. Mutat Res 478: 23-43, 2001.
3. Niedner H, Christen R, Lin X, Kondo A and Howell SB: Identification of genes that mediate sensitivity to cisplatin. Mol Pharmacol 60: 1153-1160, 2001.
4. Herraez E, Gonzalez-Sanchez E, Vaquero J, *et al*: Cisplatin-induced chemoresistance in colon cancer cells involves FXR-dependent and FXR-independent up-regulation of ABC proteins. Mol Pharm 9: 2565-2576, 2012.
5. Liu YB, Bernauer AM, Yingling CM and Belinsky SA: HIF1 alpha regulated expression of XPA contributes to cisplatin resistance in lung cancer. Carcinogenesis 33: 1187-1192, 2012.
6. Wu YC, Ling TY, Lu SH, *et al*: Chemotherapeutic sensitivity of testicular germ cell tumors under hypoxic conditions is negatively regulated by SENP1-controlled sumoylation of OCT4. Cancer Res 72: 4963-4973, 2012.
7. Skjoth IHE and Issinger OG: Profiling of signaling molecules in four different human prostate carcinoma cell lines before and after induction of apoptosis. Int J Oncol 28: 217-229, 2006.
8. Faria MHG, Neves EHC, Alves MKS, Burbano RMR, De Moraes MO and Rabenhorst SHB: TP53 mutations in astrocytic gliomas: an association with histological grade, TP53 codon 72 polymorphism and p53 expression. APMIS 120: 882-889, 2012.
9. Fuertes MA, Alonso C and Perez JM: Biochemical modulation of cisplatin mechanisms of action: enhancement of antitumor activity and circumvention of drug resistance. Chem Rev 103: 645-662, 2003.
10. Righetti SC, Perego P, Carenini N, *et al*: Molecular alterations of cells resistant to platinum drugs: role of PKC alpha. Biochim Biophys Acta 1763: 93-100, 2006.
11. Brozovic A, Ambriovic-Ristov A and Osmak M: The relationship between cisplatin-induced reactive oxygen species, glutathione, and BCL-2 and resistance to cisplatin. Crit Rev Toxicol 40: 347-359, 2010.
12. Santos NAG, Catao CS, Martins NM, Curti C, Bianchi MLP and Santos AC: Cisplatin-induced nephrotoxicity is associated with oxidative stress, redox state unbalance, impairment of energetic metabolism and apoptosis in rat kidney mitochondria. Arch Toxicol 81: 495-504, 2007.
13. Martins NM, Santos NAG, Curti C, Bianchi MLP and Santos AC: Cisplatin induces mitochondrial oxidative stress with resultant energetic metabolism impairment, membrane rigidification and apoptosis in rat liver. J Appl Toxicol 28: 337-344, 2008.
14. Kizek R, Trnkova L and Palecek E: Determination of metallothionein at the femtomole level by constant current stripping chronopotentiometry. Anal Chem 73: 4801-4807, 2001.
15. Sochor J, Ryvolova M, Krystofova O, *et al*: Fully automated spectrometric protocols for determination of antioxidant activity: advantages and disadvantages. Molecules 15: 8618-8640, 2010.
16. Quereda JJ, Martinez-Alarcon L, Mendoca L, *et al*: Validation of xCELLigence real-time cell analyzer to assess compatibility in xenotransplantation with pig-to-baboon model. Transplant Proc 42: 3239-3243, 2010.

4.5 Crosstalk between cell metabolism, cell death, and extracellular vesicle secretion

4.5.1 Crosstalk between autophagy and extracellular vesicle secretion

Autophagy traditionally serves to preserve cellular health under stress by targeting cytosolic elements for degradation and recycling through lysosomal pathways. However, emerging evidence suggests that autophagy-related genes (ATGs) also play roles in non-degradative functions, such as cellular secretion [13]. While autophagy generally provides protective benefits to cells, disruptions in its mechanisms or excessive autophagic activity can lead to cell death. Beyond supporting intracellular energy and metabolic balance, autophagy can also mediate cell death under specific circumstances [14]. For instance, autophagy-dependent cell death (ADCD) is crucial for the degradation of the larval midgut during *Drosophila* development, with disruption of relevant ATG-encoding genes significantly delaying this process [8].

Recent findings indicate that autophagy, a well-conserved mechanism of cellular self-digestion vital for maintaining homeostasis and adapting to stress, may also facilitate cargo secretion through specific populations of extracellular vesicles (EVs). These EVs comprise a diverse group of nano-sized, double-membrane-bound structures released by cells into the extracellular space. Initially understood as a means for cells to selectively eliminate proteins, nucleic acids, and lipids, EVs are now recognized as important mediators of intercellular communication that can influence a wide range of physiological and pathological phenomena [15].

The initiation and progression of cancer are promoted by the interactions between emerging pre-neoplastic or malignant cells and other cellular components within the tumor, as well as host cells in the surrounding tissue and throughout the body. This intercellular communication can lead to alterations in the microenvironment, affecting tumor growth and the spread of cancerous cells. Such interactions may occur through the release of soluble factors or the exchange of extracellular vesicles (EVs) [16]. Bidirectional signaling through EVs has been observed among various cell types within both primary and metastatic tumor microenvironments. EVs possess diverse functions that are essential for cancer progression, likely due to their varied origins and compositions [7].

Author's publications relevant to this chapter

1. Raudenska M, Balvan J, Masarik MJMC. Crosstalk between autophagy inhibitors and endosome-related secretory pathways: a challenge for autophagy-based treatment of solid cancers. *Molecular Cancer*, 20(1):1–27 (2021)
   IF (2021) 41.44; 63 citations (WOS)
2. Hanelova K, Raudenska M, Masarik M, Balvan J. Protein cargo in extracellular vesicles as the key mediator in the progression of cancer. *Cell Communication and Signalling*, 22 (2024)
   IF (2023) 8.2; 28 citations (WOS)
3. Bugajova M, Raudenska M, Masarik M, Kalfert D, Betka J, Balvan J. RNAs in tumour-derived extracellular vesicles and their significance in the tumour microenvironment. *International Journal of Cancer*; 155(7): 1147-1161. 155(7): 1147-1161 (2024)
   IF (2023) 5.7; 1 citation (WOS)

Raudenska *et al. Mol Cancer* (2021) 20:140
https://doi.org/10.1186/s12943-021-01423-6

Molecular Cancer

REVIEW Open Access

Crosstalk between autophagy inhibitors and endosome-related secretory pathways: a challenge for autophagy-based treatment of solid cancers

Martina Raudenska[1,2,3†], Jan Balvan[1,2,3†] and Michal Masarik[1,2,3,4,5*]

Abstract

Autophagy is best known for its role in organelle and protein turnover, cell quality control, and metabolism. The autophagic machinery has, however, also adapted to enable protein trafficking and unconventional secretory pathways so that organelles (such as autophagosomes and multivesicular bodies) delivering cargo to lysosomes for degradation can change their mission from fusion with lysosomes to fusion with the plasma membrane, followed by secretion of the cargo from the cell. Some factors with key signalling functions do not enter the conventional secretory pathway but can be secreted in an autophagy-mediated manner.

Positive clinical results of some autophagy inhibitors are encouraging. Nevertheless, it is becoming clear that autophagy inhibition, even within the same cancer type, can affect cancer progression differently. Even next-generation inhibitors of autophagy can have significant non-specific effects, such as impacts on endosome-related secretory pathways and secretion of extracellular vesicles (EVs). Many studies suggest that cancer cells release higher amounts of EVs compared to non-malignant cells, which makes the effect of autophagy inhibitors on EVs secretion highly important and attractive for anticancer therapy. In this review article, we discuss how different inhibitors of autophagy may influence the secretion of EVs and summarize the non-specific effects of autophagy inhibitors with a focus on endosome-related secretory pathways. Modulation of autophagy significantly impacts not only the quantity of EVs but also their content, which can have a deep impact on the resulting pro-tumourigenic or anticancer effect of autophagy inhibitors used in the antineoplastic treatment of solid cancers.

Keywords: Autophagy, Autophagy inhibitors, Cancer, Endosomes, Multivesicular bodies, Extracellular vesicles, Exosomes, Amphisomes, Non-conventional secretory pathways

Introduction

Autophagy is a highly evolutionarily conserved mechanism best known for its role in organelle and protein turnover, cell quality control, and metabolism. Lysosome-mediated degradative autophagy provides a source of nutrients and energy by digestion of cytoplasmic elements and serves for the clearance of toxic protein aggregates and defective organelles [1]. This recycling pathway can also profoundly affect cellular specialization and differentiation [2], protein trafficking, and unconventional secretion [3, 4]. Three types of autophagy have been observed in mammalian cells: macroautophagy, microautophagy, and chaperone-mediated autophagy. During microautophagy the lysosomal membrane

*Correspondence: masarik@med.muni.cz
†Martina Raudenska and Jan Balvan contributed equally to this work.
[3] Department of Pathological Physiology, Faculty of Medicine, Masaryk University, Kamenice 5, CZ-625 00 Brno, Czech Republic
Full list of author information is available at the end of the article

© The Author(s) 2021. **Open Access** This article is licensed under a Creative Commons Attribution 4.0 International License, which permits use, sharing, adaptation, distribution and reproduction in any medium or format, as long as you give appropriate credit to the original author(s) and the source, provide a link to the Creative Commons licence, and indicate if changes were made. The images or other third party material in this article are included in the article's Creative Commons licence, unless indicated otherwise in a credit line to the material. If material is not included in the article's Creative Commons licence and your intended use is not permitted by statutory regulation or exceeds the permitted use, you will need to obtain permission directly from the copyright holder. To view a copy of this licence, visit http://creativecommons.org/licenses/by/4.0/. The Creative Commons Public Domain Dedication waiver (http://creativecommons.org/publicdomain/zero/1.0/) applies to the data made available in this article, unless otherwise stated in a credit line to the data.

insulates the autophagic cargo directly, whereas, during macroautophagy, double-membrane structures called autophagosomes are formed to deliver autophagic cargo to endosomes or lysosomes. Macroautophagy also participates in the specific degradation of organelles during mitophagy, ribophagy, or pexophagy. Chaperone-mediated autophagy involves the selective degradation of KFERQ-like motif-bearing proteins supplied to the lysosomes via chaperone HSC70 and other cochaperones (e.g. CHIP, HOP, and heat shock protein 40). Internalization of cargo into lysosomes is managed via the receptor lysosome-associated membrane protein type 2A (LAMP2A) [5]. In this review article, we will focus on macroautophagy (hereafter referred to as autophagy).

Endocytosis is the process by which cells can sequester substances from the external environment by engulfing them in vesicles. Endocytosis includes the clathrin-dependent pathway as well as clathrin-independent pathways such as phagocytosis, pinocytosis, raft-mediated endocytosis, and ARF6-dependent internalization. As well as autophagy, endocytosis can culminate into lysosomal degradation, but here the cargo is internalized from the plasma membrane, not from the cytoplasm [6]. After internalization, the cargo is sorted by highly dynamic compartments, called early endosomes (EEs), marked by unique adaptor proteins, effector proteins, and small Rab GTPases such as RAB4, RAB5, early endosomal antigen-1 (EEA1), VPS34, and SNAREs. EEs are the major cellular sorting platform as they can mature into endosomes destined for various cellular fates. EE cargo can be recycled to the plasma membrane via recycling endosomes, transported to or from the Golgi apparatus via the retromer complex, or routed to lysosomes via multivesicular bodies (MVBs)/late endosomes [7]; see Fig. 1. Autophagy and endocytic pathways cooperate at some stages and share many components of the molecular machinery.

Recent studies also show that there are many interconnections between autophagy, exosome/amphisome biogenesis, and exocytosis of extracellular vesicles (EVs) [3, 4]. To release exosomes and/or amphisomes, several steps need to be performed such as the biogenesis of intraluminal vesicles (ILVs) in MVBs, transport of MVBs to autophagosomes or the plasma membrane and fusion of MVBs and/or amphisomes with the plasma membrane [8]. These steps are deeply affected by molecules of autophagy machinery [9, 10] including many Rab GTPases such as RAB7, RAB11, RAB35, RAB27A, RAB27B and the vesicle-associated membrane protein 7 (VAMP7) [11]. RAB7 and RAB11 also participate in autophagosome formation and RAB7 has a key role in autophagosome maturation (for further details see the chapter Autophagy and MVBs) [12]. Consequently, autophagy can have both stimulatory or inhibitory effects on the secretion of extracellular vesicles (EVs) and these effects will probably be deeply context-dependent. This can partially explain the double-edged sword character of autophagy in cancer progression. In this review article, we discuss how different inhibitors of autophagy may influence the secretion of EVs and summarize the non-specific effects of autophagy inhibitors with a focus on endosome-related secretory pathways. Modulation of autophagy significantly impacts not only the quantity of EVs but also their content which can have a deep impact on the resulting pro-tumourigenic or anticancer effect of autophagy inhibitors used in antineoplastic treatment of solid cancers.

Basic molecular mechanism of degradative macroautophagy

Macroautophagy (hereafter referred to as autophagy) is a process in which double-membrane vesicles (autophagosomes) are formed around a segment of the cytoplasm. Once autophagosomes are formed, they can either fuse with lysosomes and form autolysosomes, or they can bring together organelles of endosomal origin to form amphisomes with a single limiting membrane [13–15].

Autophagosome formation goes through five main stages — initiation, nucleation, elongation, fusion, and cargo degradation. The detailed molecular mechanism of autophagy has been extensively reviewed in Klionsky et al. [16], therefore, we present here only the basic molecular mechanisms important for the understanding of the effects of autophagy inhibitors on macroautophagy.

The initiation phase of autophagy is preceded by the inhibition of mTORC1. mTORC1 is inhibited by cellular and environmental stresses that are incompatible with continued growth, such as glucose or amino acid deprivation, DNA damage, or hypoxia. mTORC1 consists of three core components: mTOR (highly conserved serine/threonine-protein kinase belonging to the PI3K-related kinase family), RAPTOR (regulatory protein associated with mTOR responsible for mTORC1 localization and substrate recruitment), and mLST8. In addition to these three core components, mTORC1 also contains two inhibitory subunits DEPTOR (DEP domain-containing mTOR interacting protein) and PRAS40 (proline-rich Akt substrate of 40 kDa) [17]. A decrease in cellular energy activates the stress-responsive metabolic regulator AMPK (AMP-activated protein kinase), which inhibits mTORC1 indirectly through activation of Tuberous Sclerosis Complex (TSC), or directly through the phosphorylation of RAPTOR by protein kinase A (PKA) [18, 19]. TSC suppresses mTORC1 by converting Rheb GTPase from an active GTP-bound form to an inactive GDP-bound state. The TSC complex requires G3BPs (Ras

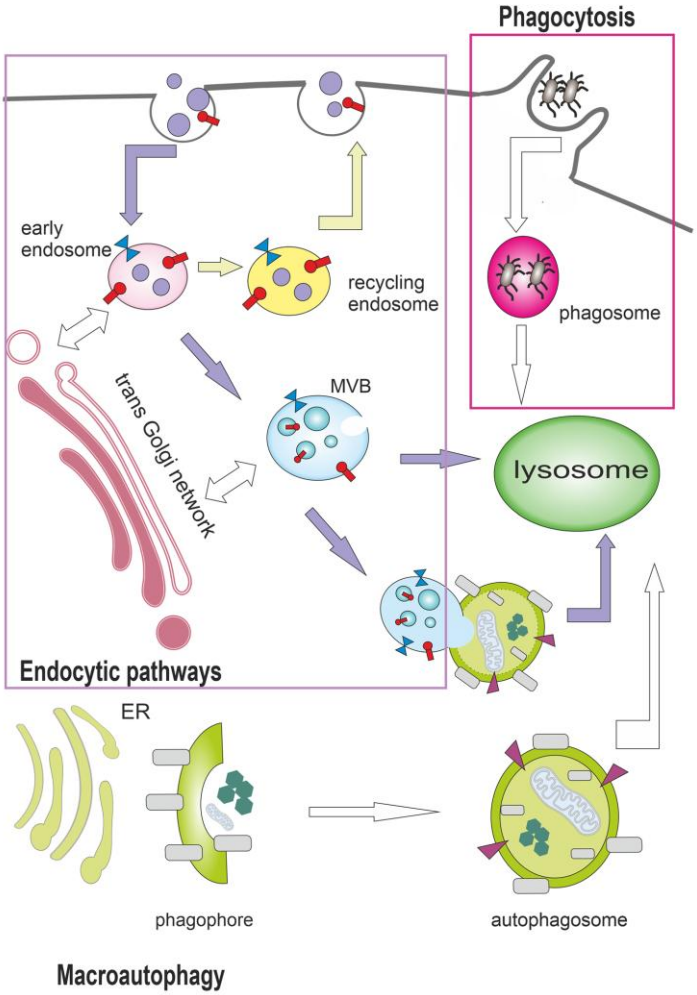

Fig. 1 Autophagy and endocytic pathways can culminate in lysosomes. Endocytosis enables the transport of substances from the external environment and includes the clathrin-dependent pathway as well as clathrin-independent pathways such as phagocytosis. Phagocytosis is the endocytosis of large molecules or intact microorganisms. Protrusions of plasma membrane surround and internalize the extracellular cargo into single-membrane structures called phagosomes, which are then transported to the lysosome for degradation. Endocytosis (clathrin-mediated endocytosis is shown here) involves invagination of the plasma membrane and biogenesis of small intracellular vesicles that contain constituents of the plasma membrane and extracellular components. These small vesicles fuse and establish the compartment called the early endosome (EE). EE cargo can be recycled to the plasma membrane via recycling endosomes, transported to or from the Golgi apparatus via the retromer complex, or routed to lysosomes via multivesicular bodies (MVBs). During macroautophagy, double-membrane structures called autophagosomes are formed to deliver autophagic cargo to lysosomes or to fuse with MVBs. Autophagy and endocytic pathways cooperate at some stages and share many components of the molecular machinery

GTPase-activating protein-binding proteins) as its lysosomal tether [20].

For sensing the levels of nutrients, the presence of mTORC1 on lysosomes is crucial [21]. In response to amino acids, mTORC1 present on lysosomes can be activated by Rag and Rheb guanosine triphosphatases (GTPases) and can trigger anabolic processes [22]. A key player in Rag-mTORC1 activation is the vacuolar H^+ ATPase (V-ATPase) that couples ATP hydrolysis (peripheral V1 domain) to proton translocation through the lysosomal membrane (integral V0 domain) to acidify the lysosomes and enable their degradative functions. When the level of amino acids in the lumen of lysosomes is low, the V-ATPase turns off the activity of Rag GTPases. In contrast, when amino acids are abundant, the V-ATPase undergoes conformational changes leading to the activation of Rag heterodimers and the recruitment of mTORC1 to lysosomes [23] (see Fig. 2). Lysosomes are usually localized closer to the plasma membrane when amino acids and growth factors are abundant. On the contrary, when they are limited, the Rap1-GTPases imprison lysosomes in the perinuclear region and reduce lysosome abundance, therefore reducing the lysosomal surface available for mTORC1 activation, which suppresses mTORC1 signalling [24]. The inactivation of mTORC1 leads to rapid translocation of transcription factors TFEB and TFE3 to the nucleus. Active TFEB upregulates the expression of lysosomal genes and critical regulators of autophagy, including several proteins implicated in the formation of autophagosomes and autolysosomes. Therefore, TFEB contributes to the synchronization of autophagy and lysosomes [25]. TFEB can also mediate lysosomal exocytosis and secretion of their cargo including the proteolytic enzymes, such as cathepsins, which results in extracellular matrix remodelling and invasion of cancer cells [26].

The early stage of autophagy machinery is the activation of the ULK1 (unc51-like autophagy-activating kinase 1) complex. This complex consists of ULK1, FIP200, ATG13, and ATG101 (see Fig. 3). ULK1 complex forms puncta usually associated with the endoplasmic reticulum (ER). ER membrane provides local support for many (putatively different) membrane sources and initiates the formation of the isolation membrane (commonly referred to as the phagophore) from the omegasome (a phosphatidylinositide-3-phosphate (PI3P)-enriched subdomain of the ER membrane) [27, 28]. The omegasome serves as a cornerstone for the formation of the phagophore. To the omegasomes, ATG9 vesicles and coat protein complex II (COPII) vesicles are recruited to elongate the autophagosome. The origin of the rest of the lipid bilayers is currently unknown [29]. ATG9 migrates through the trans-Golgi network and the endosomal system under nutrient-rich conditions and transiently binds to the autophagosome in case of autophagy induction. The trafficking of ATG9 through the recycling endosomes may be a fundamental step for autophagosome genesis [30] as ATG9 meets and fuses with ATG16L1 in a VAMP3-dependent manner in recycling endosomes [31].

Once activated, ULK1 phosphorylates the class III phosphoinositide 3-kinase (PI3K) complex I (consisting of VPS34, VPS15, Beclin1, ATG14L, and NRBF2 [16]; see Fig. 3). VPS34 generates PI3P enabling the recruitment of autophagy-related PI3P-binding proteins such as WIPI and DFCP1 [32]. In some circumstances, such as shear stress, PI3KC2α-dependent and VPS34-independent generation of PI3P can take place [33]. Expansion of the phagophore requires the ATG2A-WIPI4 complex mediating ER–phagophore association and establishing the transfer of lipid membranes from the ER and the vesicles to the phagophore [34, 35]. One of the key molecular events of autophagosome formation is the lipidation of ATG8-family proteins with phosphatidylethanolamine (PE). Mammals express 2 subfamilies of ATG8 proteins: the LC3 subfamily consisting of LC3A, LC3B, LC3B2, and LC3C (referred to here as LC3; microtubule-associated protein light chain 3) and the GABARAP subfamily consisting of GABARAP, GABARAPL1, and GABARAPL2 (referred to here as GABARAP). Lipidation of LC3 and GABARAP is a membrane-curvature dependent process [36] catalysed by E1-like activating enzyme ATG7, E2-like conjugating enzyme ATG3 and enhanced by the ATG12–ATG5–ATG16L1 system formed in the previous step [37, 38]. The cysteine protease ATG4B executes two LC3/GABARAP processing events: priming of newly synthesized pro-LC3/GABARAP to enable lipidation (newly translated LC3B, called pro-LC3, is cleaved by the cysteine protease ATG4B at the C-terminal section to give LC3-I) and deconjugation of lipidated LC3/GABARAP after cargo degradation in autolysosome [39] (see Fig. 4). ATG4B is considered to be the main isoform of ATG4 as it possessed the broadest spectrum against all substrates, followed by ATG4A, whereas ATG4C and ATG4D had minimal activity [40]. The final conjugation of LC3-I to PE molecules results in the formation of membrane-bound LC3-II. LC3-II is specifically targeted to the elongating phagophore and remains on autophagosomes until their fusion with lysosomes [37]. The proper closure of the autophagosomal membrane requires the ESCRT-III component CHMP2A and the activity of VPS34 [41]. While the LC3 subfamily mediates the elongation of the phagophore, GABARAP proteins probably function in the final sealing of the autophagosome [42]. GABARAP subfamily positively regulates ULK1 activity and phagophore formation in response to starvation. On

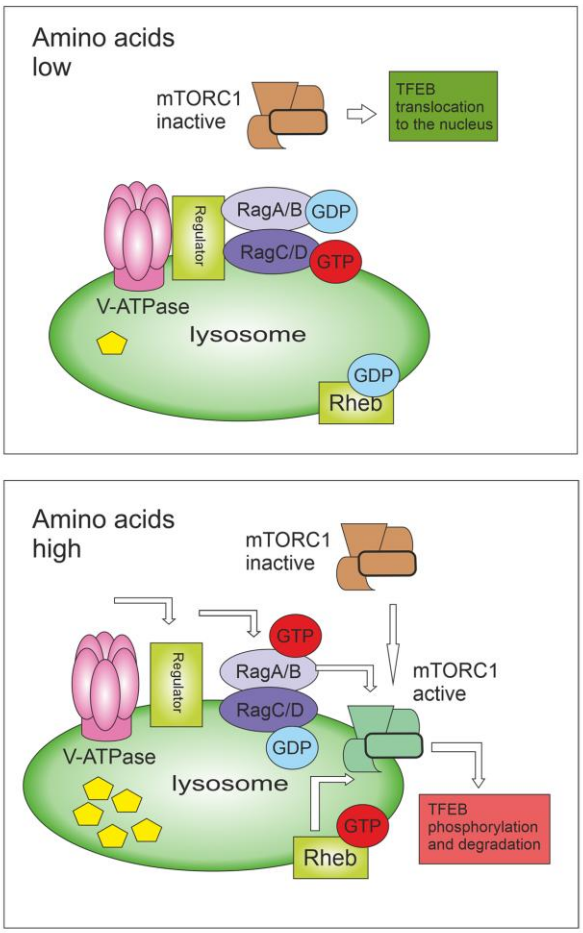

Fig. 2 Amino acid-based mTORC1 activation. By amino acid starvation, the inactive V-ATPase-Ragulator complex is unable to activate Rag GTPases on the lysosomal surface, thus mTORC1 is not recruited to the lysosome. The inactivation of mTORC1 leads to rapid translocation of transcription factors TFEB and TFE3 to the nucleus. Active TFEB upregulates the expression of lysosomal genes and critical regulators of autophagy. By amino acid abundancy, the V-ATPase undergoes conformational changes leading to the activation of Regulator, which in turn promotes the Rag heterodimer activation. Active Rag heterodimer (RagA/B(GTP)-RagC/D(GDP)) then recruits mTORC1 to the lysosomal surface where Rheb is present. Rheb can directly bind and activate mTORC1. TFEB is recruited on the lysosomal membrane, phosphorylated by active mTORC1, and then degraded by the proteasome

the other hand, the LC3 subfamily regulates them negatively [43].

Autophagosomes are transported along microtubules, which require the function of dynein. Consequently, inhibition of dynein-dependent transport or depolymerization of microtubules results in the inhibition of autophagy [44]. The degradative autophagy culminates in a fusion of closed autophagosomes with lysosomes where the cargo is eventually degraded. The autophagosome-lysosome fusion is managed by Syntaxin-17 (STX17) on autophagosomes (see Fig. 4), which binds the VAMP8 (vesicle-associated membrane protein 8) on

the lysosomal membrane via the Qbc-SNARE SNAP29 (synaptosome-associated protein 29). Accessory proteins such as ATG14 and homotypic fusion, protein sorting (HOPS) tethering complex, ESCRT, RAB7, and the class C VPS proteins are also needed [45, 46]. Some studies indicate that the kinase ULK1 regulates STX17 engagement during autophagosome maturation. Unphosphorylated ULK1 recruits STX17 and increases its affinity towards SNAP29. Protein kinase C alpha (PKCα) mediated phosphorylation of ULK1 does not change its kinase activity but decreases autophagosome-lysosome fusion [47, 48]. Inactivation of mTORC1 might also be required to facilitate the fusion between autophagosomes and lysosomes [49]. In addition to managing autophagy induction in complex I, complex VPS34-Beclin1 has a role in the fusion of autophagosomes with lysosomes as complex II (see Fig. 3). UVRAG competes with ATG14L for binding to Beclin1 [50]. When bound to Beclin1, UVRAG stimulates RAB7 GTPase activity and autophagosome fusion with lysosomes or multivesicular bodies (late endosomes; MVBs) [51]. VPS34–Beclin1-UVRAG complex may also contribute to autophagy induction via Bif-1/Endophilin B1-mediated activation of VPS34 [52].

Autophagy in the progression and therapy of solid cancers

Autophagy is undoubtedly an important tumour suppressive mechanism maintaining cellular homeostasis by executing lysosomal degradation of toxic material in the cell, as well as mediating intercellular communication via proteins and hormones with signalling function that can be secreted in an autophagy-mediated manner [53]. During the early phases of cancerogenesis, autophagy has significant cytoprotective and tumour-suppressive potential. Dysfunction of this process is associated with an increased risk of cancer development. Haploinsufficiency of the *BECN1* gene was observed in 40–75% of sporadic human breast and ovarian cancers [54, 55] and more than 25% of gastric and colorectal tumours are haploinsufficient in one of the *ATG2B*, *ATG5*, *ATG9B*, or *ATG12* genes [56]. In multiple cancer types, *ATG5* mutations and alternative mRNA splicing disrupt the ATG16L1-binding to ATG5 and impair the ATG12-ATG5 conjugation. Furthermore, ATG16L2 is overexpressed in several cancers and competes with ATG16L1 for binding to ATG5 resulting in proteasomal degradation of ATG16L1 and disruption of autophagy [57]. The tumour-suppressive effect of autophagy is also supported by the fact that autophagy is stimulated by some tumour suppressors, including PTEN, TSC, or DEPTOR [58–61] (Role of autophagy-related proteins in solid cancers is summarized in Table 1). Nevertheless, if tumourigenesis has been started up, autophagy can further support tumour progression. Many aggressive tumours need autophagy for important tumour-promoting processes (e.g. autophagy enables ERBB2 (Erb-B2 Receptor Tyrosine Kinase 2) trafficking and supports tumourigenesis in ERBB2-driven breast cancer [111]). Increased autophagic activity mediates an escape of premalignant cells from genotoxic stress or anoikis, suppresses immune surveillance and can result in intrinsic resistance against anticancer therapy [112–114]. Autophagy also increases the metabolic plasticity of tumour cells, allowing them to survive in adverse conditions and supports forming of cancer stem cells [115].

Because the induction of autophagy has been observed as a side effect of many cytotoxic anticancer therapies causing therapy resistance, a large number of strategies using autophagy inhibition have been proposed to increase the efficacy of these therapies [116]. Inhibition of autophagy in the tumour microenvironment can disrupt metabolic communication between tumour and stromal cells [117] and decrease

(See figure on next page.)

Fig. 3 Macroautophagy pathways. The autophagic process is divided into five stages including initiation, phagophore nucleation, phagophore formation, autophagosome-lysosome fusion, and cargo degradation in autolysosomes. Signals activating macroautophagy usually originate from starvation, hypoxia, oxidative stress, and stress of the endoplasmic reticulum (ER). These signals trigger the activity of Unc-51-like kinase 1 (ULK1) complex (consisting of ULK1, FIP200, ATG13, and ATG101), which then starts phosphorylation of components of the class III PI3K (PI3KC3) complex I (consisting of VPS34, VPS15, Beclin1, ATG14L, and NRBF2) enabling nucleation of the phagophore. VPS34 produces phosphatidylinositol-3-phosphate (PI3P) allowing the recruitment of autophagy-associated PI3P-binding proteins such as DFCP1 and WIPI mediating the initial stages of autophagosome formation by associating ATG2A stably to PI3P-containing areas. Expansion of the phagophore requires the ATG2A-WIPI complex mediating ER–phagophore association and establishing the transfer of lipid membranes from the ER and the vesicles to the phagophore. WIPI was also shown to bind ATG16L1, thus recruiting the ATG12–ATG5–ATG16L1 complex. Elongation of autophagosomes requires the ubiquitin-like conjugation system managing the orchestrated activity of ATG proteins and LC3 (microtubule-associated protein light chain 3) and/or GABARAP. The ATG12–ATG5–ATG16L1 complex enhances the final connection of phosphatidylethanolamine (PE) molecules resulting in the formation of membrane-bound LC3-II and/or GABARAP-PE. Cellular membranes, including the mitochondrial membrane, the plasma membrane, recycling endosomes, and the Golgi complex, contribute to the elongation of the phagophore by providing membrane material. Elongation of the phagophore gives rise to double-layered vesicles called autophagosomes. In addition to managing autophagy induction in complex I, complex VPS34-Beclin1 has also a role in the fusion of autophagosomes with lysosomes as complex II. UVRAG competes with ATG14L for binding to Beclin1. When bound to Beclin1, UVRAG stimulates RAB7 GTPase activity and autophagosome fusion with lysosomes. Autophagosome-lysosome fusion is managed by Syntaxin-17 (STX17) on autophagosomes, VAMP8 on lysosomes, and by accessory proteins such as ATG14 and homotypic fusion, and protein sorting (HOPS) tethering complex

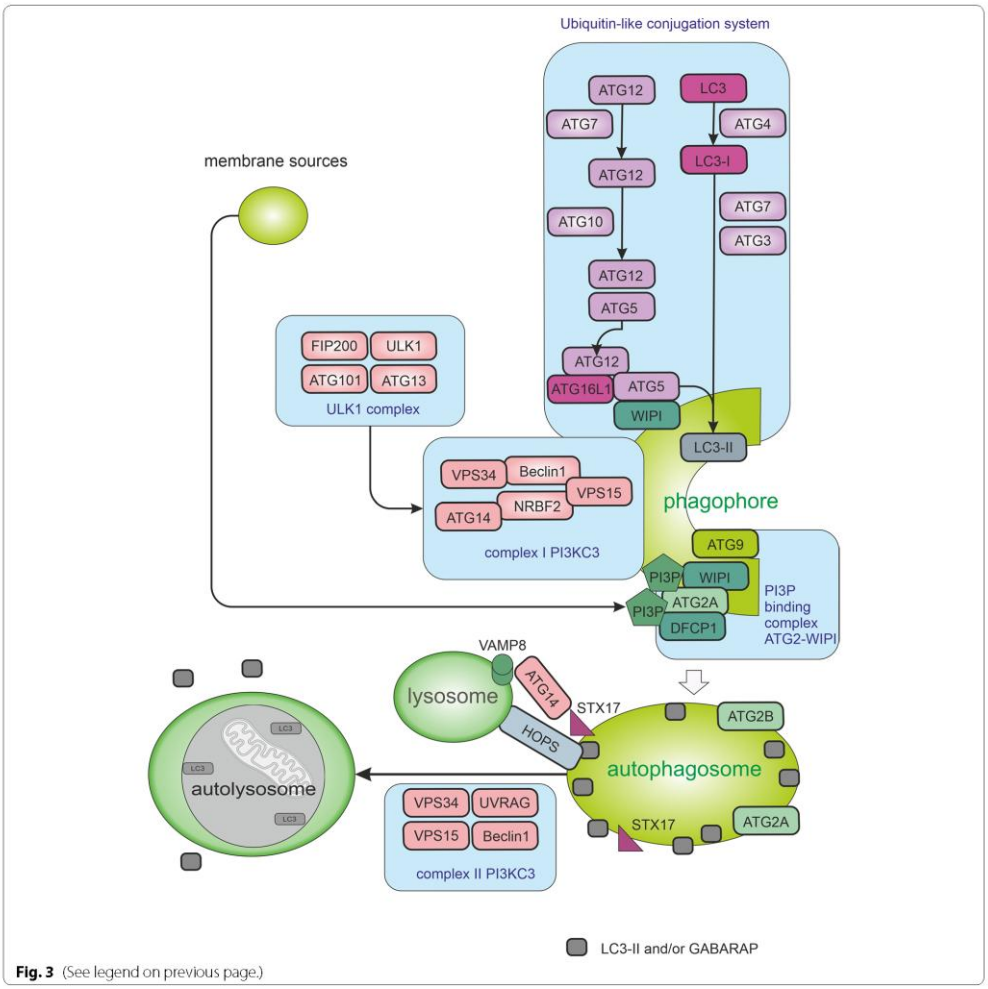

Fig. 3 (See legend on previous page.)

cell motility of metastatic tumour cells as inhibition of autophagy reduces disassembly of focal adhesions at the leading edge of the cell [118]. Systemic acute deletion of ATG7 in adult mice with preexisting non-small cell lung cancer reversed lung adenocarcinomas initiated by the KRASG12D oncogenic mutation and p53 deficiency to a benign form of tumour (oncocytomas) and blocked cell proliferation and cancer cell survival [119]. Furthermore, loss of tuberous sclerosis complex 2 (TSC2) sensitizes cancer cells to nelfinavir−bortezomib therapy due to intensifying endoplasmic reticulum stress-induced cell death [61]. On the other hand, autophagy induction causes a decrease in the levels of transcription factors triggering EMT [120], reduces 6-phosphofructo-2-kinase/fructose-2,6-biphosphatase 3 (Pfkfb3) expression and elicits metastatic dormancy in breast cancer stem cells [121]. Consequently, many studies are demonstrating the benefit of autophagy during cancer therapies, especially in inducing immunogenic cell death. Tumour cells dying of autophagic

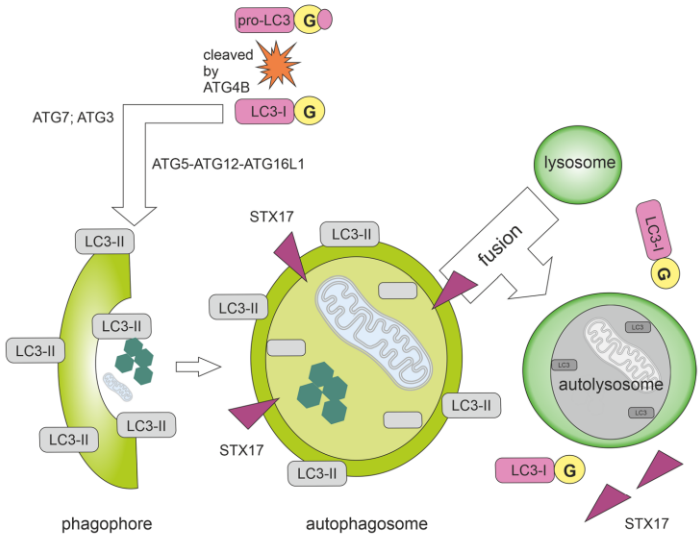

Fig. 4 Autophagy with emphasis on the state of MAP1LC3B (LC3B). Newly translated LC3B, called pro-LC3, is cleaved by the cysteine protease ATG4B at the C-terminal end with subsequent exposure of glycine residues (G). A cleaved form of a protein (LC3-I; soluble LC3) is further processed by ATG7 and ATG3, which conjugates LC3-I to phosphatidylethanolamine (PE) molecules. The ATG12–ATG5–ATG16L1 complex enhances the final conjugation of LC3-I to PE molecules resulting in the formation of membrane-bound LC3-II specifically targeted to the elongating autophagosomal membrane. The two ends of the insulating membrane are subsequently joined together to form an autophagosome with a double membrane. STX17, which is located on the outer autophagosomal membrane (not on the isolation or lysosomal membrane), is required for the fusion of an autophagosome with a lysosome. In the resulting autolysosome, the material is cleaved by acid hydrolases. During internal degradation, STX17 proteins are released from the outer membrane of the autophagosome. LC3-II molecules conjugated to the inner autophagosomal membrane are degraded by acids hydrolases, while the LC3-II molecules on the outer membrane of the autophagosome are cleaved by ATG4B and recycled as LC3-I

cell death leads to the recruitment of immune cells to the tumour site and the activation of a tumour-specific immune response. Accordingly, caloric restriction (which promotes autophagy by inactivating mTORC1) has resulted in increased control of the immune system over the tumour, but only in tumours capable of autophagy [122].

Autophagy may be one of the key modulators of the tumour microenvironment (TME). The autophagy-dependent secreted soluble factors or factors contained in EVs may enable metabolic manipulation of non-cancer cells in the tumour microenvironment, stimulate cellular proliferation, invasive phenotype, and promote immunosuppression [53]. This TME-modulating theory is supported by the fact that autophagy facilitates the selection of material for unconventional secretion of certain cytoplasmic proteins [123]. Intact autophagy machinery is required for the secretion of multiple factors favouring invasion, including interleukin-6 (IL-6), MMP2, and WNT5a [124]. Autophagy is also closely related to the biogenesis and secretion of exosomes and amphisomes.

Autophagy and MVBs

Autophagy and endocytic pathways are important in managing many aspects of homeostasis as both endosomes and autophagosomes are known to deliver cellular material to lysosomes for degradation. Autophagy and exocytosis seem to be largely interconnected as autophagy cargo can be released by amphisomes derived from multivesicular bodies (MVBs) and phosphoinositide-3-phosphate (PI3P) is essential for the genesis of both endosomes and autophagosomes, and their positioning as PI3P promotes the microtubule-dependent translocation of late endosomes and lysosomes to the cell periphery. This PI3P-dependent lysosome translocation to the cell periphery promotes mTORC1 activation [125]. The most of cellular PI3P is generated by class III PI3K VPS34 in complex II with a small contribution of class II PI3Ks [126]. Binding and activation of VPS34

Table 1 Autophagy-related proteins in cancer

Autophagy-related protein	Type of aberration	Effect on	Type of solid cancer	Reference
AMPK	genetic and transcriptional aberrations	energy homeostasis; tissue-dependent pro- or anticancer impact	many cancer types	[62]
ATG101	overexpression	immunotherapy response	many cancer types	[63]
ATG16L2	overexpression	proteasomal degradation of ATG16L1	many cancer types	[57]
ATG2B, ATG5, ATG9B, ATG12	genetic aberrations, haploinsufficiency	cytoprotection	gastric and colorectal tumours	[56]
ATG9A	overexpression	proliferation	breast cancer	[64]
DEPTOR	reduced expression/overexpression	epithelial to mesenchymal transition (EMT)	low DEPTOR levels in cancer of pancreas, prostate, lungs; triple-negative and breast cancer; high DEPTOR levels in osteosarcoma and differentiated thyroid carcinoma	[60, 65–69]
FIP200	aberrant activation	immune checkpoint therapy response	breast cancer; glioblastoma	[70, 71]
mLST8	overexpression	cancer progression	hepatocellular carcinoma	[72]
mTORC1	overactivation	survival of stem cells; reprogramming of metabolism; tumour invasion and metastasis	many cancer types	[73–75]
PRAS40	overexpression	proliferation; enhanced NF-κB activity	hepatocellular carcinoma; lung adenocarcinoma; cutaneous melanoma	[76, 77]
RAP1	changes in the RAP1 activation	formation of cell adhesions and junctions; migration and polarization; may suppress oncogenic Ras phenotype	Rap1 inhibits invasion and metastasis in the bladder, lung, and brain cancer; it has the opposite effect in melanoma and breast cancer or oesophageal squamous cell, head and neck squamous cell pancreatic, and non-small cell lung carcinomas	[78, 79]
RAPTOR	overexpression	proliferation and migration; the resistance to PI3K-mTOR inhibition	colorectal cancer; renal cancer; oropharyngeal squamous cell carcinoma	[80–82]
TFE3	gene fusions	insulin-dependent metabolism; retinoblastoma-dependent cell cycle arrest	renal cell carcinoma	[83]
TFEB	gene fusions, transcriptional aberrations	biology of lysosomes; lysosomal exocytosis; proliferation; glutamine metabolism; regulator of tumour-associated macrophages; role in the TME, WNT and TGFβ signalling	Pancreatic, breast , and renal cancer; melanoma; colorectal cancer; gastric carcinoma; non-small cell lung cancer	[84–87]
TSC1/2	genetic aberrations	anticancer impact	many cancer types	[88]
ULK1	aberrant activation, genetic and transcriptional aberrations	antitumour immunity; NADPH production; innate immune response; cell cycle progression	LKB1-mutant lung cancer and many other types of cancer	[89–92]
V-ATPase	deregulation of some subunits, overexpression	biogenesis of endosomes and lysosomes; treatment resistance	breast cancer, lung and oesophagal tumours	[93–95]

Table 1 (continued)

Autophagy-related protein	Type of aberration	Effect on	Type of solid cancer	Reference
VPS34	aberrant activation	antitumour immunity; survival of cancer stem cells; activation of p62; antigen cross-presenting CD8α+ dendritic cells	melanoma; colorectal cancer; hepatocellular carcinoma	[96–99]
WIPI3	genetic and transcriptional aberrations	cell cycle and spliceosome	hepatocellular carcinoma	[100]
VAMP3	deletion of WDFY2 (negative regulator of VAMP3 recycling)	increase in extracellular matrix degradation	metastatic ovarian and prostate cancers	[101, 102]
GABARAP	transcriptional aberrations	tumour differentiation; EMT	colorectal cancer; breast cancer	[103, 104]
MAP1LC3A or B	transcriptional aberrations	cancer progression	breast cancer; renal cell carcinoma	[105, 106]
p62/SQSTM1	accumulation	cancer progression	many cancer types	[107]
RAB7	reduced expression	biogenesis of endosomes; autophagosomes; and lysosomes	highly invasive breast cancer	[93]
ESCRT	polymorphism in ESCRT-III (rs35094336, CHMP4C)	endosomal-sorting; cytokinetic abscission; genome instability	many cancer types	[108]
UVRAG	inhibition	cytokine production; oncogenic signalling; progression of age-related malignancies	many cancer types	[109]
Beclin1	genetic and transcriptional aberrations	cytoprotection; proliferation under hypoxia and nutrient starvation	haploinsufficiency in breast and ovarian cancer; overexpression in colorectal and gastric carcinomas	[54, 55, 110]

on endosomes are initiated through the recruitment of RAB5 to endosomes by the guanine nucleotide exchange factor Rabex5 (RAB Guanine Nucleotide Exchange Factor 1) [127]. VPS34 then produces PI3P increasing the binding of RAB5 and other downstream effectors, including early endosome autoantigen 1 (EEA1), the hepatocyte growth factor-regulated tyrosine kinase substrate (HRS; ESCRT-0 subunit) regulating MVBs formation via ESCRT recruitment to endosomes [128]), and endosomal sorting nexin protein family (SNX) [129]. Overexpression of SNX3 may alter the morphology of endosomes and delay their transport to the lysosome [130]. SNX18 was identified as a positive regulator of autophagosome formation [131]. Consequently, VPS34 plays a crucial role in endosome biogenesis through EAA1 and other RAB5 effectors, vesicle invagination and cargo selection within MVBs, and the fusion of autophagosomes with lysosomes. Inhibition of VPS34 resulted in dysfunction in autophagy, vesicular trafficking, and endocytic recycling and sorting [132, 133]. Furthermore, proteins such as Beclin1 and ATG14L that regulate PI3P levels are positive modulators of autophagy [134]. Some data suggest that surface delivery of endosomal cargo requires hydrolysis of PI3P mediated by MTM1 as the endosomal accumulation of PI3P inhibits exocytosis. Defects caused by mutations in MTM1 can be partially reversed by pharmacological inhibition of VPS34 [135].

Endosomal maturation is accompanied by conversion from early endosomal RAB5 to late endosomal RAB7 and active cargo sorting into intraluminal vesicles (ILVs) by the ESCRT complex. The transition from early to late endosomes is complicated by a positive feedback loop between Rabex5 and RAB5. It was demonstrated that SAND1/MON1A is needed to interrupt this positive feedback loop by displacing Rabex5 from endosomal membranes. SAND1/MON1A also manages the recruitment of RAB7 (see Fig. 5) [127]. Then VPS34 recruits TBC1D2 protein to endosomes in a RAB7-dependent manner to further inactivate RAB5 and to facilitate early to late endosome maturation. VPS34 inhibition causes hyperactivation of RAB7, autolysosomal dysfunction, a phenotype with large late endosomes and an enhanced release of atypical exosomes harbouring poly-ubiquitinated proteins [136–138]. Interestingly, RAB7 can participate in both MVBs degradation and/or MVBs-related secretion as it regulates autolysosome maturation and simultaneously the secretion of syntenin and syndecan-containing exosomes [139]. RAB7-associated endosomal processes depend not only on RAB7 GTP-based state but also on modifications with ubiquitin [140]. Endosomal maturation during the late endosome/lysosome pathway is accompanied by conversion of PI3P to PI(3,5)P_2 at the limiting membrane of late endosomes. This process depends on PIKfyve (phosphoinositide kinase, FYVE-type zinc finger containing). Consequently, the activity of PIKfyve is vital for the sorting of cargo into MVBs [141].

In addition to the role in the degradation and recycling of cellular waste, autophagic and endo-lysosomal systems can play a key role in secretory pathways (see Fig. 6) as autophagy cargo can be released by amphisomes derived from multivesicular bodies (MVBs). MVBs are late endosomes containing many intraluminal vesicles (ILVs) formed by the invagination of the endosomal membrane. ILVs start to be generated in early endosomes and accumulate until the late endosomal stage. *In vitro* budding of ILVs into MVBs is regulated by syntenin-syndecan interactions requiring Alix which is known to interact with several ESCRT proteins including TSG101 and CHMP4 [142, 143]. MVBs can fuse with the plasma membrane to release intraluminal vesicles (ILVs) to the extracellular space as exosomes. During exosome biogenesis, Alix forms a complex with the scaffold protein syntenin, mediating the loading of cargo into exosomes and promoting exosome release. These Alix-dependent processes are controlled by ATG12–ATG3 and cells lacking ATG12–ATG3 showed reduced exosome biogenesis. Both ATG12–ATG3 and Alix promote basal, but not starvation-induced, autophagic flux [9]. Some results indicate that activated c-Src in the endosomal membrane promotes the secretion of exosomes. Alix was identified as a c-Src–interacting protein in exosomes, resulting in the upregulation of exosome secretion in c-Src–transformed cells [143]. The small GTPase ADP ribosylation factor 6 (Arf6) and its effector phospholipase D2 (PLD2) also regulate the syntenin pathway [144]. MVBs morphology and their docking to the plasma membrane is significantly disrupted by the loss of RAB27a and/or RAB27b activity [145]. Critical plasma membrane docking and secretion sites for MVBs are invasive actin structures called invadopodia. Invadopodia degrade the extracellular matrix through the local deposition of matrix metalloproteinases (MMPs) and manage cancer cell invasion [146]. Protein WDFY2 (WD Repeat and FYVE Domain Containing 2) is frequently lost in metastatic cancers (e.g. ovarian and prostate cancers). Through its interaction with VAMP3, WDFY2 restricts the budding of MMP14-containing VAMP3 vesicles from actin-stabilized endosomal tubules. Upon deletion of WDFY2, this negative control is disrupted and faster recycling of MMP14 to the plasma membrane leads to increased matrix degradation and cell invasion [102]. Furthermore, long non-coding RNA HOTAIR promotes the colocalization of VAMP3 with SNAP23 leading to MVBs fusion with the plasma membrane and exosome secretion in hepatocellular carcinoma [147].

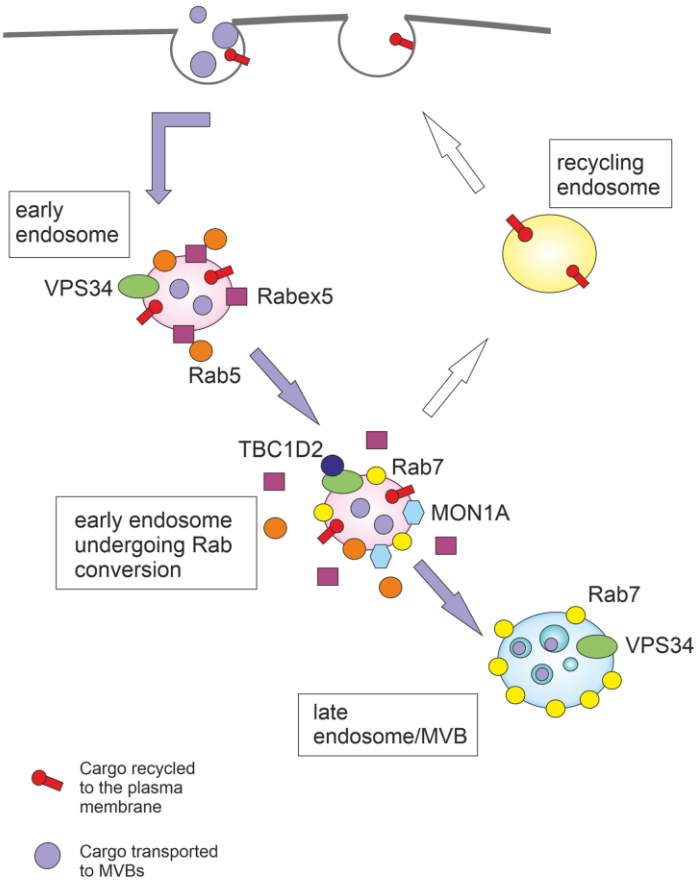

Fig. 5 The transition from early to late endosomes. Binding and activation of VPS34 on endosomes are initiated through the recruitment of RAB5 to endosomes by the guanine nucleotide exchange factor Rabex5. VPS34 then produces PI3P increasing the binding of RAB5 and other downstream effectors. The transition from early to late endosomes is complicated by a positive feedback loop between Rabex5 and RAB5. MON1A is needed to interrupt this positive feedback loop by displacing Rabex5 from endosomal membranes. MON1A also manages the recruitment of RAB7. VPS34 recruits TBC1D2 protein to endosomes in a RAB7-dependent manner to further inactivate RAB5 and to facilitate early to late endosome maturation

The HOTAIR also activates autophagy by upregulating ATG3 and ATG7 [148]. Long intergenic noncoding RNA 00511 (LINC00511) promotes exosome secretion by regulation of the expression of RAB27B and the colocalization of VAMP7 and SNAP23, which are involved in MVBs trafficking and their fusion with the plasma membrane [149]. LINC00511 is highly expressed in diverse cancers and correlates with poor clinical outcomes [150]. LINC00511 knockdown suppressed proliferation, invasion and autophagy in trophoblast cells [151]. Exosome secretion was also promoted by cortactin through stabilizing cortical actin-rich MVBs docking sites [152].

Nevertheless, in healthy cells, the majority of MVBs fuse with the lysosomes, resulting in degradation of their content. ISGylation of the MVB protein TSG101 by ISG15 (interferon-α/β-induced ubiquitin-like protein) induces its aggregation and degradation, being sufficient to impair exosome secretion. The secretion of exosomes is recovered when the fusion of MVBs

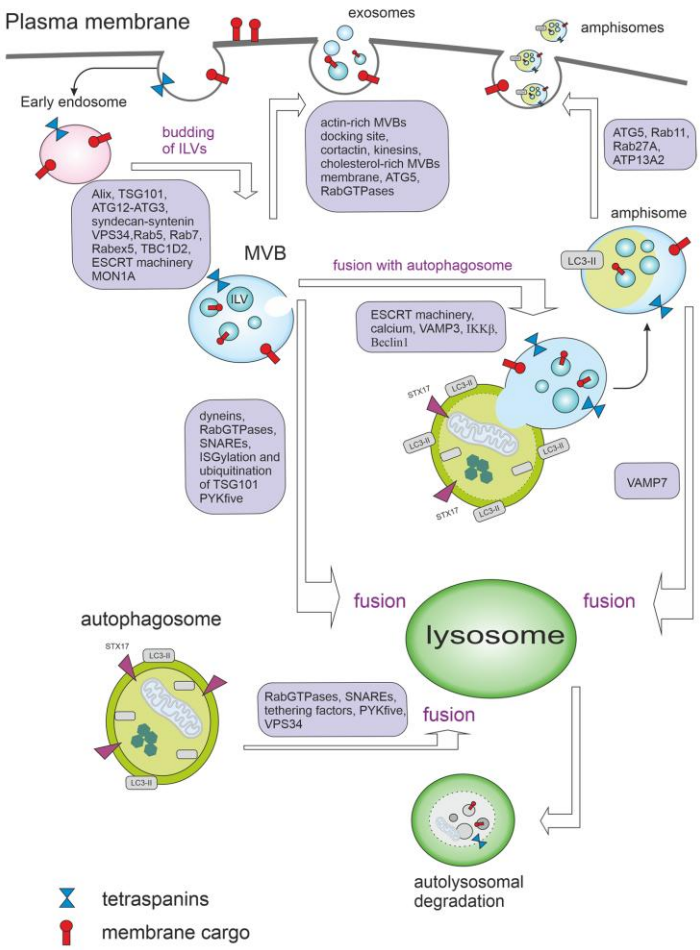

Fig. 6 Multivesicular bodies and autophagy. After maturation of early endosomes to multivesicular bodies (MVBs), MVBs can fuse with the plasma membrane to release intraluminal vesicles (ILVs) to the extracellular space as exosomes. With the help of specific proteins, MVBs are trafficked towards the plasma membrane and/or lysosome. Under certain conditions, MVBs can fuse with autophagosomes to generate hybrid organelles called amphisomes. Amphisomes contain typical autophagosomal markers such as lipidated LC3, and due to their origin from endosomes, they also contain endosomal markers such as CD63, RAB5, RAB7, and RAB11. The fusion of MVBs with the lysosome (direct or via autophagosome) results in autophagic degradation. The MVBs-related secretion and autophagy pathways are connected via many proteins, including RAB GTPases, ESCRTs, SNAREs, Beclin1, ATG proteins, and LC3

with lysosomes or autophagosomes is inhibited, indicating that the inhibition of exosome secretion is mainly mediated by the induction of MVBs degradation by the lysosomes. ISGylation reduces the number of MVBs but does not inhibit the formation of ILVs. It also promotes selective autophagy and degradation of MVBs without inducing a global autophagy response [153]. The fusion of MVBs with lysosomes can be also triggered via the ubiquitination of TSG101 by MGRN1 [154].

Interestingly, ubiquitination of the cargo proteins can also profoundly influence the fate of MVBs. While MVBs containing ubiquitinated major histocompatibility complex (MHC-II) underwent lysosomal degradation in immature dendritic cells, non-ubiquitinated MHC-II placed into CD9-bearing MVBs was targeted for plasma membrane fusion and secretion in activated dendritic cells. Sorting of MHC II into exosomes correlated with its incorporation into CD9 containing detergent-resistant membranes [155]. Exosomes are probably preferentially secreted from cholesterol-rich detergent-resistant MVBs whereas the cholesterol-poor MVBs are subjected to degradation [156, 157]. The alternative fate of MVBs can be also governed by their connection to dynein or kinesin. Connection to dynein motor protein (minus end-directed transport) leads to perinuclear accumulation of MVBs and lysosomal degradation of cargo by recruitment of HOPS complex. By contrast, connection to kinesin (plus end-directed transport) causes accumulation of MVBs at cell periphery [158, 159].

Different autophagic effectors were shown to influence the biogenesis of extracellular vesicles and their secretion. Exosome production is strongly reduced in cells lacking ATG5 and ATG16L1 as these proteins protect MVBs from lysosomal degradation and direct them into the secretory pathway. ATG5 detaches V1V0-ATPase (vacuolar proton pump) from the MVBs via LC3 which specifically decreases acidification of MVBs lumen [160]. Emerging exosomes were strongly enriched in LC3-II (versus LC3-I) compared with the ratio of LC3-II to LC3-I in the corresponding cell lysates. This suggests that ATG5 and LC3 are sorted into these exosomes [160]. On the other hand, overexpression of LC3 or autophagy inducers such as starvation or rapamycin caused an enlargement of the vacuoles decorated with RAB11 and their colocalization with LC3. This situation led to the inhibition of exosome release. Even though RAB11 activity stimulates MVBs genesis and exosome release [161], the stimulatory effect of RAB11 in exosome secretion was nullified by overexpression of the autophagic protein LC3 [10].

Under certain conditions (such as shear stress [162]), autophagosomes fuse with MVBs to generate hybrid organelles called amphisomes [13]. Amphisomes contain typical autophagosomal markers such as lipidated LC3, and due to their origin from endosomes, they also contain endosomal markers such as CD63, RAB5, RAB7, and RAB11 [163]. Maturation of MVBs by ESCRT machinery is required for their fusion with autophagosomes [164] and the fusion of MVBs with the autophagosome compartment seems to be calcium- and VAMP3-dependent event [10, 163]. The resulting amphisomes are either degraded by fusion with lysosomes or released from the cell [162, 165]. ATG9 is required to form intraluminal vesicles in amphisomes and/or autolysosomes and is also needed for local acidification within amphisomes/autolysosomes [166]. The fusion between amphisomes and lysosomes requires VAMP7 but not VAMP3 [163]. VAMP7 is also needed for the homotypic fusion of ATG16L1 precursors, which is a key event in the early phases of autophagy enabling membrane acquisition and autophagosome biogenesis [167]. VAMP7-labelled vesicles can be loaded with ATP and starvation triggers the delivery of the ATP-containing amphisomes toward the plasma membrane, their release, and the import of ATP to the extracellular space [168].

Amphisomes, but not exosomes, were shown to be vehicles for the active release of DNA from the cell [169]. The formation of an amphisome may negatively regulate the coordination between exosome secretion and autophagy. For example, rapamycin or starvation promoted MVBs-autophagosome fusion and reduced exosome secretion in the K562 cell line [10]. On the other hand, the exosome release of toxic/damaged material may provide a cellular mechanism bypassing the autophagic defects caused by ageing or different pathological states [170].

Amphisomes can participate in immune response as they can function as anti-viral machinery by sequestering and exporting viral proteins from the cell [171]. IFNγ is a cytokine critical for innate and adaptive immunity against viral infections. Upon IFNγ-induced autophagy in lung epithelial cells, amphisomes containing annexin 2 (ANXA2) were released. This process was dependent on ATG5, RAB11, and RAB27A [165].

Interleukins IL-1β and IL-18 are potent pro-inflammatory cytokines crucial for responses to infection and injury. Secretion levels of these cytokines increased when low-autophagy cells were treated with the autophagy-inducing tat-Beclin1 peptide and decreased when ATG7 was silenced in high-autophagy cells [172]. An unobstructed autophagy pathway and functional MVBs are necessary for inflammasome-dependent IL-1β and IL-18 secretion [173, 174]. Nevertheless, it is not completely clear if IL-1β is secreted by amphisomes or by modified autophagosomes. Similarly to the degradative autophagosomes, modified secretory autophagosomes have a double membrane decorated with LC3-II. In degradative autophagosomes, STX17 manages the fusion with the lysosome. However, in secretory autophagosomes, SEC22B in combination with plasma membrane syntaxin 3 and syntaxin 4 as well as SNAP23 and SNAP29 facilitate fusion with the plasma membrane and cargo secretion [175, 176]. Autophagy-dependent secretion of IL-1β, IL-6, CSF3/G-CSF, CXCL1, TREM1, CCL2, CCL3/MIP-1α, and CXCL2 in response to UVB radiation was

also described. Secretion of these cytokines was blocked by conditional ATG7 depletion [177].

Another factor interconnecting cell stress and immune response with autophagy and amphisome genesis is IκB kinase (IKKβ). IKKβ is the predominant catalytic subunit of the IKK complex and is required for the activation of the canonical NF-κB signalling pathways. IKKβ activation also induces the fusion of MVBs with autophagosomes to form amphisomes and promotes their secretion in tumour cells. This secretion was absent or strongly reduced when autophagosome formation was impaired by 3-methyladenine or ATG7 inactivation [178]. In breast cancer cells independent of autophagy, ATG7 inhibition by shRNAs increased IL-6 secretion. On the other hand, in autophagy-dependent cells, ATG7 inhibition decreased IL-6 secretion, cell survival and mammosphere formation [179]. Besides RNA interference-mediated ATG7 depletion, pyrazolopyrimidine sulfamate compounds were found to be potent selective inhibitors of ATG7 [180].

In cancer cells, selective and non-selective autophagy and EVs secretion are often amplified because of harsh conditions in TME, such as hypoxia or ER stress [181–183]. Some regulators such as GAIP interacting protein C terminus (GIPC) control both EVs and autophagy pathways [184]. GIPC knockdown led to significant inhibition of pancreatic carcinoma growth in an orthotopic mouse model [185]. The crosstalk between endosome-related secretory pathways and autophagy orchestrates the intratumoural communication as autophagy significantly impacts not only the quantity of EVs but also their content. On the other hand, EVs can significantly influence the dynamic of autophagy in TME [186, 187]. Exosomes derived from breast cancer cells stimulate beige/brown differentiation and reprogram metabolism in stromal adipocytes to promote cancer progression [187]. It was also shown that hypoxic glioma-derived exosomes promote M2-like macrophage polarization by enhancing autophagy induction [188] and MCF-7 breast cancer cells with undetectable MMP2 protein acquired expression of MMP2 and corresponding gelatinase activity after stimulation with exosomes derived from mesenchymal stromal stem cells [189].

Autophagy modulators and their effect on EVs secretion

Autophagy is a multi-step process. Each step can potentially be inhibited. Progress within the field has led to the development of agents targeting almost all phases of this process (see Fig. 7). Targeting the specific stage of autophagy may profoundly influence resulting secretory pathways as the early-stage autophagy inhibition does not seem to be equivalent to the late-stage inhibition. Furthermore, one compound (such as tacrine-melatonin heterodimer C10) can induce the early stages of autophagy and inhibit it at the late stages. Transitory treatment by C10 induced secretion of proinflammatory cytokine IL-6, proving interconnection between autophagy and secretory pathway [190]. Some amount of IL-6 produced was found to be secreted by exosomes [191, 192]. On the other hand, IL-6 inhibits starvation-induced autophagy and activates stress-induced autophagy via the STAT3 signalling pathway [193, 194].

ULK1 inhibitors

ULK1 is a serine/threonine-protein kinase. In most cell lines, loss of ULK1 is sufficient to disrupt autophagy [196]. However, ULK2 acts with a degree of redundancy with ULK1 [197]. MRT68921 potently inhibits both ULK1 and ULK2. ULK1 inhibition results in the accumulation of immature early autophagosomal structures, indicating a role for ULK1 in the initiation and maturation of autophagosomes [198]. ULK1 activity also manages the trafficking of ATG9 [199] which is required for intraluminal vesicle formation within amphisomes and autolysosomes [166]. Consequently, inhibition of ATG9 causes a reduced capacity to degrade endosomal cargo, which may result in enhanced EVs secretion. Amino acid starvation or rapamycin causes a redistribution of ATG9 from the trans-Golgi network to peripheral, endosomal membranes. The redistribution of ATG9 requires PI3K activity and is reversed after the restoration of amino acids [199]. On the other hand, AMPK-ULK1-mediated but mTOR-independent signalling plays an important role in the induction of autophagy-mediated PARK7 secretion. 6-hydroxydopamine-induced oxidative stress triggered PARK7 secretion which was suppressed by co-treatment with MRT68921 [200]. Nevertheless, PARK7 seems not to be secreted by classical exosomes [169]. MRT68921 can also disrupt the signals between lysosomes and autophagic machinery. The lysosomal calcium channel TRPML1 connects lysosomal calcium to autophagosome biogenesis through the triggering of the CaMKKβ/VPS34 pathway. TRPML1-mediated generation of PI3P requires functional VPS34 and ULK1 [201]. RNAi-mediated knockdown of ULK1 and/or ULK2 resulted in impaired endocytosis of nerve growth factor (NGF) [202]. MRT68921 was also shown to be a potent inhibitor of NUAK1 (NUAK family SNF1-like kinase 1) which is a critical component of the antioxidant defence necessary for the survival of tumour cells during cytotoxic therapy and EMT. As cytotoxic therapy induces elevated ROS levels and triggers the ULK1 pathway to activate protective autophagy and mitophagy, dual targeting of NUAK1 and ULK1 by MRT68921 can be beneficial in tumour management [203]. ULK1 inhibition also

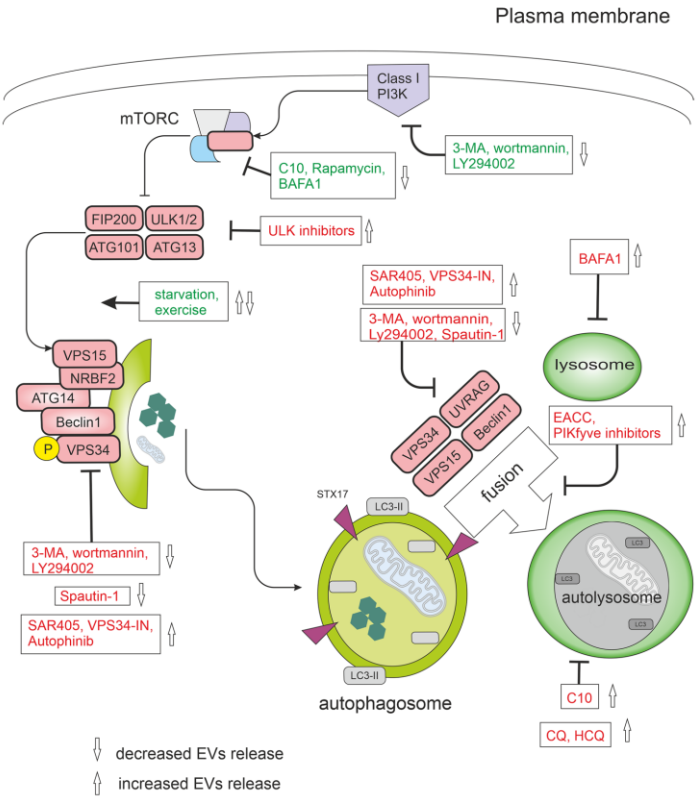

Fig. 7 Modulators of autophagy and their effect on EVs release. In nutrient-rich conditions, mTORC1 constitutively blocks the ULK complex and autophagy. mTORC1 signals can be inhibited directly by C10, rapamycin, exercise, or starvation and indirectly by bafilomycin A1 (BAFA1) through lysosomal inhibition. Physical exercise was shown to induce the release of small extracellular vesicles (EVs) into the circulation [195]. The ULK complex activates the VPS34 complex. VPS34 is a class III phosphatidylinositol 3-phosphate-kinase (PI3KC3). A group of PI3K inhibitors, including 3-methyladenine (3-MA), wortmannin, and synthetic inhibitor LY294002, inhibits both class I as well as class III PI3Ks. VPS34 inhibitors include Spautin-1, autophinib, SAR405, and VPS34-IN1. Spautin-1 initiates the degradation of Beclin1 due to the inhibition of two of its deubiquitinases. SAR405 and VPS34-IN1 are highly potent inhibitors of VPS34 selective for the VPS34 and not affecting the closely related class I and class II PI3Ks. Autophinib is an ATP-competitive inhibitor of VPS34 decreasing the accumulation of the lipidated protein LC3 on the autophagosomal membrane. The late stages of the autophagic machinery include fusion and degradation. During fusion, the mature autophagosome fuses with lysosomes creating an autolysosome. PIKfyve (phosphoinositide kinase, FYVE-type zinc finger containing) inhibitors and EACC block autophagosome-lysosome fusion. BAFA1 inhibits the acidification of the autolysosome by blocking the V-ATPase while chloroquine (CQ) and 3-hydroxychloroquine (HCQ) impair the maturation of autolysosomes. All drugs are depicted within the rectangles. Effects of modulators activating autophagy are green, inhibitory effects are red

overcomes compromised antigen presentation in LKB1 (liver kinase B1)-mutant lung cancer [89].

Pan-PI3K inhibitors

Phosphoinositide 3-kinases (PI3Ks) are divided into three classes: class I, class II, and class III. Class I PI3Ks predominantly produce PI(3,4,5)P3 (and indirectly, PI(3,4)P2), class III PI3Ks synthesise PI3P, and to a lesser extent, class II PI3Ks synthesise PI3P and PI(3,4)P2). PI(3,4)P2 was described as a key mediator of the late stages of clathrin-mediated endocytosis [126]. PI(3,4,5)P3 at the plasma membrane recruits effectors

such as the protein kinase B/Akt. Active Akt controls many downstream pathways such as the mTORC1 pathway. Activated mTORC1 destabilizes the ULK1 complex and inhibits autophagy [204]. The role of PI3P has been discussed above.

A group of PI3K inhibitors includes 3-methyladenine (3-MA), wortmannin, and synthetic inhibitor LY294002. These compounds inhibit class I PI3Ks as well as class III PI3Ks. Wortmannin and 3-MA have been routinely used as autophagy inhibitors due to their suppressive effect on class III PI3Ks. Nevertheless, 3-MA with a prolonged period of treatment (up to 9 hours) was also found to promote autophagy even under nutrient-rich conditions. 3-MA also does not inhibit Beclin1-independent autophagy [205], however, it can still suppress starvation-induced autophagy [206]. In contrast, wortmannin suppresses autophagy regardless of the nutrient status [206]. The effect of 3-MA (but not wortmannin) is further complicated by differential temporal effects on class I and class III PI3Ks. 3-MA persistently blocks class I PI3Ks, whereas its impact on class III PI3Ks is only transient [206]. Furthermore, activation of autophagy was shown in gastric cancer cell line SGC7901 due to LY294002 treatment [207]. Another problem is that LY294002, and to a lesser extent wortmannin (but not 3-MA [208]), can inhibit proteosynthesis [209] and 3-MA can induce a decrease in cell viability not driven by the inhibition of the Akt/mTOR axis. The cytotoxicity induced by 3-MA correlated with massive DNA damage monitored by γ-H2AX and was observed using the 10 mM concentration, the usual concentration used to inhibit autophagy [210].

Off-target activities of PI3K inhibitors influence proteasome degradation, PI3K/Akt signalling pathways, endocytosis, lysosomal acidification, mitochondrial permeability transition, and glycogen metabolism [211, 212]. Moreover, it is known that PI3Ks also participate in the biogenesis of MVBs and their activity is required for the correct maturation of the ILVs [10, 129]. As would be expected, factors having some effect on the formation of MVBs also affect the secretion of exosomes. Consequently, conventional exosome production can be decreased by PI3K inhibitors [213–215]. Accordingly, wortmannin reduced the secretion of prostasomes from PC-3 cells [216]. On the other hand, inhibition of autophagy by wortmannin or CRISPR/Cas9-mediated knockout of ATG5 greatly increased the release of exosome-associated prions [217]. In fibroblasts, wortmannin caused swollen endosome phenotype coupled with the failure of membrane recycling but not the inhibition of MVBs biogenesis [218]. Nevertheless, wortmannin can change the inner content of ILVs [129]. The efficacy of wortmannin may be diminished by its covalent binding to free amino acids [219].

Inhibition of autophagy with 3-MA or wortmannin can have profound effects on cytokine secretion. In macrophages, toll-like receptor ligands initiate sequestration of pro-IL-1β into autophagosomes and activation of autophagy with rapamycin triggered the degradation of this sequestrated pro-IL-1β and blocked secretion of the mature cytokine. When treated with 3-MA or wortmannin, LPS-stimulated bone marrow-derived macrophages (iBMM) and dendritic cells (BMDC) secreted increased levels of IL-1β. At the 10 mM concentration, 3-MA induced IL-1β but inhibited IL-6 secretion from BMDC and iBMM. In contrast, 3-MA and wortmannin markedly reduced IL-1β secretion induced by LPS + ATP in human neutrophils [220]. 3-MA, in combination with LPS, increased IL-1α secretion by BMDC and IL-18 secretion by iBMM. 3-MA also activates the inflammasome through inhibition of type III PI3Ks [221]. Wortmannin was found to enhance IL-12 production in dendritic cells [222]. In contrast, LY294002 prevented IL-12 secretion in dendritic cells [209].

VPS34 inhibitors

VPS34 is involved not only in autophagy but also in the endosomal trafficking of receptors such as the epidermal growth factor receptor (EGFR) [129]. In addition to managing autophagy induction in complex I, VPS34 also has a role in the fusion of autophagosomes with lysosomes. Disruption of neuronal VPS34 function impairs autophagy, lysosomal degradation, as well as lipid metabolism, causing endolysosomal membrane damage. PI3P deficiency caused by a malfunction of VPS34 also promotes the secretion of unique exosomes enriched for undigested lysosomal substrates [223]. Considering the key role of VPS34 in autophagy, many compounds aim to target this kinase. The following section will present the characterization of VPS34 inhibitors Spautin-1, autophinib, SAR405, VPS34-IN1, and Cpd18.

Spautin-1 does not directly affect the catalytic activity of VPS34 but promotes the degradation of VPS34 complexes by inhibiting ubiquitin-specific peptidases USP10 and USP13. Under glucose-free conditions, Spautin-1 supports the ubiquitination of Beclin1 and triggers its degradation leading to destabilization and degradation of VPS34 complexes and inhibition of autophagy. VPS34 complexes also provide a molecular mechanism for class III PI3K to control the levels of p53. Therefore, levels of p53 are reduced in the tissues of BECN1+/− mice [224]. Exosome production was found to be regulated by the p53 response as up-regulation of TSAP6 transcription by activated p53 can increase exosome release [225]. The destabilization of the PI3K complex

that occurs upon suppressing Beclin1 (either via siRNA-mediated knockdown or Spautin-1 treatment) reduced both exosome release and autophagy flux in chronic myeloid leukaemia cells [226]. Alternatively, Beclin1 may regulate autophagosome formation [227] and fusion of endosomes and autophagosomes leading to amphisome formation [228, 229]. In addition, it was also found that Beclin1 is needed for autophagosome fusion with lysosomes [230].

Autophinib is an ATP-competitive inhibitor of VPS34 decreasing the accumulation of the lipidated protein LC3 on the autophagosomal membrane. It inhibits autophagy induced by rapamycin or by amino acid starvation. The *in vitro* IC50 value for VPS34 is 19 nM [231]. Since VPS34 has also a role in the fusion of autophagosomes with lysosomes, VPS34 inhibition causes autolysosomal dysfunction, a phenotype with large late endosomes and an enhanced release of atypical exosomes harbouring polyubiquitinated proteins [136–138].

SAR405 and VPS34-IN1 are highly potent and selective inhibitors of VPS34 not affecting the closely related class I and class II PI3Ks. SAR405 and VPS34-IN1 cause defects in autophagosome formation and endosomal trafficking [232]. SAR405 can inhibit autophagy induced by starvation and/or mTOR inhibition [233]. SAR405 prevents the catalytic activity of ATG14L and UVRAG-containing VPS34 complexes, induces late endosome swelling, and affects late endosome-lysosome compartments [233]. Using SAR405 decreased the tumour growth and improved mouse survival in multiple tumour models by inducing tumour infiltration of NK, CD8+, and CD4+ T effector cells [96] and repressed viability of liver cancer stem cells [97]. Nevertheless, VPS34 function is critical in dendritic cells where it controls antigen cross-presenting. Consequently, VPS34 inhibition may lead to impaired T-cell–mediated immunity that may limit the use of SAR405 in anticancer therapy [99].

VPS34-IN1 selectively decreased PI3P levels, increased Beclin1 levels, but did not downregulate its other interacting partners from complex I, namely ATG14L, and VPS15 (in contrast to knockout of VPS34), ruling out indirect effects of destabilization of these proteins [223]. PI3P deficiency was shown to promote the secretion of unique exosomes enriched in undigested lysosomal substrates, including amyloid precursor protein C-terminal fragments, specific sphingolipids, and the phospholipid bis(monoacylglycero)phosphate. Secretion of these exosomes needs neutral sphingomyelinase 2 and sphingolipid synthesis. It was noted that proteins typically associated with exosomes such as Alix and CD63, or with ESCRT-dependent ILV sorting (TSG101 and Hrs) were minimally affected, suggesting that VPS34-IN1 likely affects composition rather than quantity of extracellular vesicles [223]. Neurons treated with VPS34-IN1 showed delayed degradation of EGFR following EGF stimulation. The remaining degradation was blocked by V-ATPase inhibitor bafilomycin A1, suggesting that VPS34 inhibition only partially impairs lysosomal function [223].

Cpd18 and 3-MA are structurally related compounds that differ only in a methyl piperidine group at the C6 of the adenine, but unlike 3-MA, Cpd18 does not inhibit class I PI3Ks. Cpd18 inhibits omegasome formation [234]. Nevertheless, the concentrations of Cpd18 that presented a greater attenuation of the autophagic flux are associated with cytotoxicity [210] and decreased ubiquitin/proteasome-dependent proteolysis in living cells [234].

Late autophagy inhibitors

Another way to inhibit autophagy is to target the later stages of the autophagy machinery, such as the fusion of autophagosomes with lysosomes and the degradation of autolysosome content by the lysosomal enzymes. Autophagosome–lysosome fusion involves the action of SNAREs. Autophagosome-lysosome fusion is orchestrated by the autophagosomal SNAREs STX17 and SNAP29, lysosomal R-SNARE VAMP8, HOPS tethering complex, small GTPase RAB7, and accessory proteins such as ATG14. Interestingly, the translocation of STX17 occurs only on complete autophagosomes and not on partially formed autophagosomes. EACC blocks autophagosome-lysosome fusion by preventing STX17 and SNAP29 loading onto autophagosomes without impeding the completion of autophagosomes. It also causes an accumulation of LC3-II and reduces the interaction of STX17 with the HOPS subunit VPS33A and the lysosomal VAMP8. On the other hand, autophagy induction, the number of autophagosome biogenesis sites, expansion of the phagophore, lysosomal pH, localization of lysosomal SNAREs or RABs, and cargo recognition remain unaltered in the presence of EACC [235] although STX17 was also shown to be involved in autophagy initiation [46]. Interestingly, STX17 depletion increased the production of exosomes in A549 cells [236] and effectively blocks the formation of axonal amphisomes after 3 hours starvation in dorsal root ganglion neurons [237].

Chloroquine (CQ) and its derivatives (such as 3-hydroxychloroquine HCQ or Lys05) inhibit the maturation of autolysosomes and block late steps of autophagy. In contradiction with previous studies [238], some more recent studies indicate that CQ does not substantially decrease lysosomal acidity, and the lysosomes retain their capacity to degrade delivered material [239]. Although CQ may induce a temporal elevation of lysosomal pH, this elevation may be only transient and can be followed by reacidification of the lysosomes [240].

The kinetics of this transient phase may differ between cell types [239]. The greater part of the confusion about CQ effects on lysosomal pH might be attributed to how it was measured because LysoTracker Red dye, often used to estimate lysosomal pH, is not a pH sensor and the intensity of its fluorescence signal does not correlate with the lysosomal pH [239]. Nevertheless, CQ behaves as a weak base and accumulates in the lysosomes causing lysosomal stress. Lysosomal stress may cause the release of EVs to eliminate cellular waste [223]. Accordingly, the production of exosomes was increased due to CQ treatment [236]. CQ treatment led to marked lysosomal swelling and recruitment of Galectin-3 to sites of membrane damage [241]. In response to lysosomal damage, IL-1β can be recognized by secretory autophagy cargo receptor TRIM16 [176]. Strikingly, glucose starvation or hexokinase inhibition by 2-deoxyglucose prevented CQ from inducing lysosomal damage and subsequent cell death [241]. Accordingly, IL-1β release correlates with the degree of lysosome damage [242] and glucose is required for LPS-induced IL-1β production by monocytes [243]. Furthermore, autophagy inhibition with CQ also induced the secretion of pro-inflammatory cytokines MIF (Macrophage migration inhibitory factor) and IL-6 in triple-negative breast cancer cells [244].

Although CQ and HCQ are indisputably impairing the autophagic flux, their use entails multiple side effects including the disorganization of the Golgi and endo-lysosomal networks, dysregulation of STX17 and SNAP29 targeting, and even a temporary induction of autophagic sequestration activity (probably by inhibiting mTORC1 in a Rag-dependent manner [245]) and a drop in ATP content [227, 239]. Furthermore, during starvation or CQ-induced lysosomal stress, TFEB and TFE3 rapidly translocate to the nucleus to initiate lysosomal biogenesis [240]. CQ was also shown to increase amphisome and IFN-α production in human plasmacytoid dendritic cells stimulated by the Herpes simplex virus. On the other hand, when Beclin1 was knocked down, virus-induced IFN-α production was significantly suppressed [246].

Bafilomycin A1 (BAFA1) is a V-ATPase inhibitor that blocks the autophagic flux by inhibiting autophagosome-lysosome fusion (possibly by inhibiting the ATP2A/SERCA pump [247]) and autolysosomal and/or lysosomal acidification. It also reduces the delivery of internalized molecules from MVBs to lysosomes [248]. On the other hand, trafficking through early and late endosomes continues upon BAFA1 treatment [249]. BAFA1-treated cells display phenotypes associated with an inhibition of the degradation capacity of lysosomes such as the presence of intact cytoplasm in the lysosomal lumen and a loss of acidity [239]. BAFA1 inhibits lysosomal degradation and thereby negatively affects the amino acid efflux from the lysosomes, possibly impairing mTOR signalling which is dependent on this organelle (mTOR localizes to lysosomes and its activation depends on amino acids inside the lysosomal lumen) [245]. mTOR inhibition strongly decreased exosomal prion release [217]. In contrast, starvation stimulated exosome release through a RAB27a-dependent mechanism but did not significantly alter exosomal cargo content [250]. BAFA1 also triggers BAX- and/or BAK-dependent cytotoxicity and caspase activation [210] and has indirect effects on Golgi trafficking [251]. According to some indications, BAFA1 can also inhibit signals from the lysosomal P5-type ATPase ATP13A2 (also known as PARK9) [252]. ATP13A2 has been found to regulate both autophagic degradation and exosomal release [253]. Elevated levels of ATP13A2 enhance the externalization of α-synuclein through amphisomal structures, which is proposed to be accomplished through ATP13A2-mediated modulation of intraluminal zinc ion levels in MVBs [254, 255]. On the other hand, the exosomal release was enhanced due to BAFA1 treatment [153, 236]. Inhibition of autophagy with BAFA1 markedly reduced IL-1β secretion induced by LPS+ATP in human neutrophils [220].

The principal enzymatic activity of PIKfyve (phosphoinositide kinase, FYVE-type zinc finger containing) is to phosphorylate PI3P to PI(3,5)P2. PIKfyve inhibitors, such as YM201636, vacuolin-1, and apilimod mesylate, disrupt lysosome turnover, the heterotypic fusion of lysosomes with autophagosomes and/or MVBs, and the formation of autolysosomes resulting in autophagy inhibition [256]. Acute inhibition of PIKfyve also blocks protein sorting and their turnover in late endosomes. Both PI(3,5)P2-deficient cells and cells that lack TRPML1 exhibited enlarged endolysosomes and trafficking defects in the late endocytic pathway [257]. Furthermore, PI(3,5)P2 is required for lysosomal acidification by the V-ATPase [258]. Consequently, PIKfyve inhibition enhances exosome release and triggers secretory autophagy in PC-3 cells (probably to relieve stress caused by disruption of recycling pathways). These exosomes bear the typical exosomal markers (TSG101, Alix) and a subset of ATGs [259].

Conclusion

Autophagy and MVBs-related secretory pathways are interconnected at many levels. These pathways, collectively with the ubiquitin-proteasome system, orchestrate the dynamics of intracellular waste removal, where each pathway may complement the deficiencies of the other. In other words, exosome secretion can reduce stress when degradative and recycling pathways are disrupted. On the other hand, unwanted MVBs with damaged material may be directed to lysosomes. Furthermore, some parts

Table 2 Inhibitors of autophagy

Drug	Systematic name	Known targets	Status	Limitations	References
MRT68921	N-[3-[[5-Cyclopropyl-2-[(1,2,3,4-tetrahydro-2-methyl-6-isoquinolinyl)amino]-4-pyrimidinyl]amino]propyl]-cyclobutanecarboxamide dihydrochloride	ULK1, ULK2, NUAK1	Preclinical	Mitotic dysregulation; crosstalk with endocytic pathways	[166, 202, 203, 260]
3-MA	3-Methyladenine	PI3Ks	preclinical	non-selectivity; activation of autophagy in a longer period of treatment; cytotoxicity; crosstalk with endocytic pathways	[206, 210–212]
Wortmannin	(1alpha,11alpha)-11-(Acetyloxy)-1-(methoxymethyl)-2-oxaandrosta-5,8-dieno(6,5,4-bc)furan-3,7,17-trione	PI3Ks, DNA-PK	preclinical	failed clinical translation due to drug-delivery challenges; proteosynthesis inhibition; crosstalk with endocytic pathways	[209, 211, 261]
LY294002	2-(4-Morpholinyl)-8-phenyl-4H-1-benzopyran-4-one	PI3Ks	preclinical	activation of autophagy; proteosynthesis inhibition; crosstalk with endocytic pathways	[207, 209, 211, 212]
Spautin-1	C43, 6-Fluoro-N-[(4-fluorophenyl)methyl]-4-quinazolinamine	USP10, USP13	preclinical	ROS-mediated DNA damag; Beclin1 degradation; crosstalk with endocytic pathways	[224, 228, 229, 262]
Autophinib	6-Chloro-N-(5-methyl-1H-pyrazol-3-yl)-2-(4-nitrophenoxy)-pyrimidinamine	VPS34	preclinical	pleiotropic impact of VPS34 inhibition; impaired T-cell–mediated immunity	[99, 231]
SAR405	(8S)-9-[(5-chloro-3-pyridinyl)methyl]-6,7,8,9-tetrahydro-2-[(3R)-3-methyl-4-morpholinyl]-8-(trifluoromethyl)-4H-pyrimido[1,2-a]pyrimidin-4-one	VPS34	preclinical	pleiotropic impact of VPS34 inhibition; defects in endosomal trafficking; impaired T-cell–mediated immunity	[99, 232, 233]
VPS34-IN1	1-((2-((2-chloropyridin-4-yl)amino)-4'-(cyclopropylmethyl)-[4,5'-bipyrimidin]-2'-yl)amino)-2-methylpropan-2-ol	VPS34	preclinical	pleiotropic impact of VPS34 inhibition; defects in endosomal trafficking; impaired T-cell–mediated immunity	[99, 232]
Cpd18	3-methyl-6-(3-methylpiperidin-1-yl)-3H-purine	omegasomes	preclinical	toxicity; decreased ubiquitin/proteasome-dependent proteolysis	[210, 234]
Chloroquine	4-N-(7-chloroquinolin-4-yl)-1-N,1-N-diethylpentane-1,4-diamine	autolysosomes; lysosomes; endosomes	21 clinical trials phase 1 or 2; only one phase 3 study (NCT00224978)	lysosomal stress; crosstalk with endocytic pathways; uptake may differ based on pH	[223, 236, 241, 244, 246, 263]
HCQ	2-[4-[(7-chloroquinolin-4-yl)amino]pentyl-ethylamino]ethanol	autolysosomes; lysosomes; endosomes	94 clinical trials; only one phase 2/3 study (NCT03008148)	uptake may differ based on pH	[227, 239, 264]

Table 2 (continued)

Drug	Systematic name	Known targets	Status	Limitations	References
Bafilomycin A1	(3Z,5E,7R,8S,9S,11E,13E,15S,16R)-16-[(2S,3R,4S)-4-[(2R,4R,5S,6R)-2,4-dihydroxy-5-methyl-6-propan-2-yloxan-2-yl]-3-hydroxypentan-2-yl]-8-hydroxy-3,15-dimethoxy-5,7,9,11-tetramethyl-1-oxacyclohexadeca-3,5,11,13-tetraen-2-one	V-ATPase	preclinical	cytotoxicity and caspase activation; effects on Golgi trafficking; crosstalk with endocytic pathways	[210, 251, 265]
YM201636	6-amino-N-[3-(6-morpholin-4-yl-8-oxa-3,5,10-triazatricyclo[7.4.0.02,7]trideca-1(9),2(7),3,5,10,12-hexaen-4-yl)phenyl]pyridine-3-carboxamide	PIKfyve	preclinical	block of protein sorting; crosstalk with endocytic pathways and exocytosis	[257, 259]
Vacuolin-1	2-N-[(E)-(3-iodophenyl) methylideneamino]-6-morpholin-4-yl-4-N,4-N-diphenyl-1,3,5-triazine-2,4-diamine	PIKfyve	preclinical	block of protein sorting; crosstalk with endocytic pathways and exocytosis	[257, 259]
Apilimod mesylate	methanesulfonic acid;N-[(E)-(3-methylphenyl) methylideneamino]-6-morpholin-4-yl-2-(2-pyridin-2-ylethoxy) pyrimidin-4-amine	PIKfyve	preclinical	block of protein sorting; crosstalk with endocytic pathways and exocytosis	[257, 259]
EACC	ethyl (2-(5-nitrothiophene-2-carboxamido) thiophene-3-carbonyl) carbamate.	STX17	preclinical	crosstalk with endocytic pathways and exocytosis	[236, 237]

of functional autophagy machinery are important for the genesis of endosomes and amphisomes. Consequently, autophagy inhibition can both promote and/or decrease EVs release. The resulting effect is largely context-dependent and could be significantly affected by different kinds of autophagy modulators. Moreover, modulation of autophagy significantly impacts not only EVs quantity but probably also their content. Late and early autophagy inhibitors can have a profoundly different effect on secretion. For example, Spautin-1 and CQ are both autophagy inhibitors but have nearly opposite effects on EVs release. Many studies suggest that cancer cells release higher amounts of EVs compared to non-malignant cells, which makes the effect of autophagy inhibitors on EVs secretion highly important and attractive for anticancer therapy. In future studies, it should be carefully assessed how exactly autophagy could be targeted (late versus early autophagy inhibitors) to maximize patient benefit and improve cancer therapy. For safe and successful clinical use of autophagy inhibitors, we need to carefully explore the molecular mechanisms underlying the effects of autophagy on tumour progression and possibly discover all pathways affected by particular autophagy inhibitors (see Table 2).

Abbreviations

3-MA: 3-methyladenine; AKT: Rac-alpha serine/threonine-protein kinase; Alix: Apoptosis-linked gene 2-interacting protein X; AMBRA1: Autophagy and Beclin 1 regulator 1; AMPK: AMP-activated protein kinase; ANXA2: Annexin 2; Arf6: ADP ribosylation factor 6; ATG: Autophagy-related genes; ATP: Adenosine triphosphate; ATP13A2: ATPase cation transporting 13A2; Beclin1: Coiled-coil, moesin-like BCL2 interacting protein; Bif-1: Bax-interacting factor 1; BMDC: Bone marrow-derived dendritic cells; CaMKKβ: Calcium/calmodulin-dependent protein kinase kinase β; CCL: C-C motif chemokine ligand; COPII: Coat protein complex II; CQ: Chloroquine; CSF3/G-CSF: Granulocyte colony-stimulating factor; c-Src: Proto-Oncogene Tyrosine-Protein Kinase Src; CXCL: C-X-C motif chemokine ligand,; DEPTOR: DEP domain-containing mTOR interacting protein; DFCP1: Double FYVE-containing protein 1; EGFR: Epidermal growth factor receptor; EMT: Epithelial to mesenchymal transition; ER: Endoplasmic reticulum; ESCRT: Endosomal sorting complexes required for transport; EVs: Extracellular vesicles; FIP200: FAK family-interacting protein of 200 kDa; G3BP: Ras GTPase-activating protein SH3-domain-binding protein; GDP: Guanosine diphosphate; GTP: Guanosine triphosphate; GTPase: Guanosine triphosphatase; HCQ: Hydroxychloroquine; HOPS: Homotypic fusion, and protein sorting complex; CHMP: Charged multivesicular body protein; iBMM: Bone marrow-derived macrophages; IFN-α: Interferon alpha; IKKβ: IκB kinase; IL: Interleukin; ILVs: Intraluminal vesicles; ISG15: Interferon (IFN)-α/β-induced ubiquitin-like protein; LAMP2: Lysosome-associated membrane protein 2; LC3: Microtubule-associated protein 1A/1B-light chain 3; LKB1: Liver kinase B1; LPS: Bacterial lipopolysaccharides; MGRN1: Mahogunin ring finger 1; MHC: Major histocompatibility complex (MHC-II); MIF: Macrophage migration inhibitory factor; mLST8: Mammalian lethal with Sec13 protein 8, alias GβL; MMP: Matrix metalloproteinase; mTOR: Mammalian target of rapamycin; mTORC: Mammalian target of rapamycin complex; MVBs: Multivesicular bodies; NF-κB: Nuclear factor-kappa B; NUAK1: NUAK family SNF1-like kinase 1; p115: Vesicular transport factor p115; PARK7: Parkinsonism-associated deglycase 7; PI(3,4,5)P3: Phosphatidylinositol (3,4,5)-trisphosphate; PI3K: Phosphoinositide 3-kinase; PI3P: Phosphatidylinositide-3-phosphate; PIKfyve: Phosphoinositide kinase, FYVE-type zinc finger containing; PKA: Protein kinase A; PLD2: Phospholipase D2; PRAS40: Proline-rich Akt substrate of 40 kDa; Rab: Ras-associated GTP-binding protein; Rag: Ras-related GTP-binding protein; RAPTOR: Regulatory-associated protein of mTOR also known as KIAA1303; Rheb: Ras homolog enriched in brain; SEC22b: SEC22 vesicle-trafficking protein homolog B; shRNA: Small hairpin RNA; siRNA: Small interfering RNA; SNAP29: Synaptosome-associated protein 29; SNARE: Soluble N-ethylmaleimide-sensitive fusion attachment protein receptors; STAT3: Signal transducer and activator of transcription 3; STX17: Syntaxin-17; TBC-2: TBC domain-containing protein 2; TFE3: Transcription factor binding to IGHM Enhancer 3; TFEB: Transcription factor EB; TME: Tumour microenvironment; TREM1: Triggering receptor expressed on myeloid cells 1; TRPML1: Transient receptor potential channel mucolipin 1; TSC: Tuberous sclerosis complex; TSG101: Tumuor susceptibility 101; ULK: Unc51-like autophagy-activating kinase; UVB: Ultraviolet light B; UVRAG: UV resistance-associated gene; VAMP: Vesicle-associated membrane protein; V-ATPase: V1V0-vacuolar-type ATPase; VPS: Vacuolar protein sorting; WIPI: WD repeat domain phosphoinositide-interacting protein; γ-H2AX: Phosphorylation of the Ser-139 of the histone variant H2AX.

Acknowledgements

Not applicable

Authors' contributions

MR wrote the manuscript, JB conceived the structure and revised the manuscript, MM revised the manuscript. All authors read and approved the final manuscript.

Funding

This work was supported by the Ministry of Health of the Czech Republic (NU20J-08-00018), by Grant Agency of the Czech Republic (GACR - 21-06873S), by funds from Specific University Research Grant, as provided by the Ministry of Education, Youth and Sports of the Czech Republic in the year 2021 (MUNI/A/1698/2020 and MUNI/A/1246/2020), by the "Center for Tumor Ecology – Research of the Cancer Microenvironment Supporting Cancer Growth and Spread" (reg. no. CZ.02.1.01/0.0/0.0/16_019/0000785) supported by the Operational Program Research, Development and Education and by the Ministry of Education, Youth and Sports of the Czech Republic, project Advanced Functional Nanorobots reg. No. CZ.02.1.01/0.0/0.0/15_003/0000444.

Availability of data and materials

Not applicable

Declarations

Ethics approval and consent to participate

Not applicable

Consent for publication

Not applicable

Competing interests

The authors declare that they have no competing interests.

Author details

[1]Department of Physiology, Faculty of Medicine, Masaryk University, Kamenice 5, CZ-625 00 Brno, Czech Republic. [2]Department of Chemistry and Biochemistry, Mendel University in Brno, Zemedelska 1, CZ-613 00 Brno, Czech Republic. [3]Department of Pathological Physiology, Faculty of Medicine, Masaryk University, Kamenice 5, CZ-625 00 Brno, Czech Republic. [4]BIOCEV, First Faculty of Medicine, Charles University, Prumyslova 595, CZ-252 50 Vestec, Czech Republic. [5]Center for Advanced Functional Nanorobots, Department of Inorganic Chemistry, Faculty of Chemical Technology, University of Chemistry and Technology in Prague, Technická 5, CZ-166 28 Prague, Czech Republic.

Received: 1 June 2021 Accepted: 11 September 2021
Published online: 27 October 2021

References

1. Mizushima N. Physiological functions of autophagy. Curr Top Microbiol Immunol. 2009;335:71–84.

2. Clarke AJ, Simon AK. Autophagy in the renewal, differentiation and homeostasis of immune cells. Nat Rev Immunol. 2019;19(3):170–83.
3. Deretic V, Jiang S, Dupont N. Autophagy intersections with conventional and unconventional secretion in tissue development, remodeling and inflammation. Trends Cell Biol. 2012;22(8):397–406.
4. Salimi L, et al. Synergies in exosomes and autophagy pathways for cellular homeostasis and metastasis of tumor cells. Cell Biosci. 2020;10(1):64.
5. Kaushik S, Cuervo AM. The coming of age of chaperone-mediated autophagy. Nat Rev Mol Cell Biol. 2018;19(6):365–81.
6. Jovic M, et al. The early endosome: a busy sorting station for proteins at the crossroads. Histol Histopathol. 2010;25(1):99–112.
7. Barysch SV, et al. Sorting in early endosomes reveals connections to docking- and fusion-associated factors. Proc Natl Acad Sci. 2009;106(24):9697–702.
8. Hessvik NP, Llorente A. Current knowledge on exosome biogenesis and release. Cell Mol Life Sci. 2018;75(2):193–208.
9. Murrow L, Malhotra R, Debnath J. ATG12–ATG3 interacts with Alix to promote basal autophagic flux and late endosome function. Nat Cell Biol. 2015;17(3):300–10.
10. Fader CM, et al. Induction of autophagy promotes fusion of multivesicular bodies with autophagic vacuoles in K562 cells. Traffic. 2008;9(2):230–50.
11. Abels ER, Breakefield XO. Introduction to extracellular vesicles: biogenesis, RNA cargo selection, content, release, and uptake. Cell Mol Neurobiol. 2016;36(3):301–12.
12. Ao X, Zou L, Wu Y. Regulation of autophagy by the Rab GTPase network. Cell Death Differ. 2014;21(3):348–58.
13. Fengsrud M, et al. Ultrastructural characterization of the delimiting membranes of isolated autophagosomes and amphisomes by freeze-fracture electron microscopy. Eur J Cell Biol. 2000;79(12):871–82.
14. Lucocq J, Walker D. Evidence for fusion between multilamellar endosomes and autophagosomes in HeLa cells. Eur J Cell Biol. 1997;72(4):307–13.
15. Klionsky DJ, Eskelinen E-L, Deretic V. Autophagosomes, phagosomes, autolysosomes, phagolysosomes, autophagolysosomes... wait, I'm confused. Autophagy. 2014;10(4):549–51.
16. Klionsky DJ, et al. Guidelines for the use and interpretation of assays for monitoring autophagy (4th edition)(1). Autophagy. 2021;17(1):1–382.
17. Saxton RA, Sabatini DM. mTOR signaling in growth, metabolism, and disease. Cell. 2017;168(6):960–76.
18. Jewell JL, et al. GPCR signaling inhibits mTORC1 via PKA phosphorylation of Raptor. Elife. 2019;8.
19. Gwinn DM, et al. AMPK phosphorylation of raptor mediates a metabolic checkpoint. Mol Cell. 2008;30(2):214–26.
20. Prentzell MT, et al. G3BPs tether the TSC complex to lysosomes and suppress mTORC1 signaling. Cell. 2021.
21. González A, Hall MN. Nutrient sensing and TOR signaling in yeast and mammals. EMBO J. 2017;36(4):397–408.
22. Sancak Y, et al. Ragulator-Rag complex targets mTORC1 to the lysosomal surface and is necessary for its activation by amino acids. Cell. 2010;141(2):290–303.
23. Zoncu R, et al. mTORC1 senses lysosomal amino acids through an inside-out mechanism that requires the vacuolar H+-ATPase. Science. 2011;334:678–83.
24. Mutvei AP, et al. Rap1-GTPases control mTORC1 activity by coordinating lysosome organization with amino acid availability. Nat Commun. 2020;11(1):1416.
25. Settembre C, et al. TFEB links autophagy to lysosomal biogenesis. Science. 2011;332(6036):1429–33.
26. Kundu ST, et al. TMEM106B drives lung cancer metastasis by inducing TFEB-dependent lysosome synthesis and secretion of cathepsins. Nat Commun. 2018;9(1):2731.
27. Karanasios E, et al. Autophagy initiation by ULK complex assembly on ER tubulovesicular regions marked by ATG9 vesicles. Nat Commun. 2016;7:12420.
28. Karanasios E, et al. Dynamic association of the ULK1 complex with omegasomes during autophagy induction. J Cell Sci. 2013;126(22):5224–38.
29. Shima T, Kirisako H, Nakatogawa H. COPII vesicles contribute to autophagosomal membranes. J Cell Biol. 2019;218(5):1503–10.
30. Imai K, et al. Atg9A trafficking through the recycling endosomes is required for autophagosome formation. J Cell Sci. 2016;129(20):3781–91.
31. Puri C, et al. ATG16L1 meets ATG9 in recycling endosomes: additional roles for the plasma membrane and endocytosis in autophagosome biogenesis. Autophagy. 2014;10(1):182–4.
32. Lamb CA, Yoshimori T, Tooze SA. The autophagosome: origins unknown, biogenesis complex. Nat Rev Mol Cell Biol. 2013;14(12):759–74.
33. Boukhalfa A, et al. PI3KC2α-dependent and VPS34-independent generation of PI3P controls primary cilium-mediated autophagy in response to shear stress. Nat Commun. 2020;11(1):294.
34. Chowdhury S, et al. Insights into autophagosome biogenesis from structural and biochemical analyses of the ATG2A-WIPI4 complex. Proc Natl Acad Sci. 2018;115(42):E9792.
35. Maeda S, Otomo C, Otomo T. The autophagic membrane tether ATG2A transfers lipids between membranes. Elife. 2019;8.
36. Dancourt J, Melia TJ. Lipidation of the autophagy proteins LC3 and GABARAP is a membrane-curvature dependent process. Autophagy. 2014;10(8):1470–1.
37. Tanida I, Ueno T, Kominami E. LC3 conjugation system in mammalian autophagy. Int J Biochem Cell Biol. 2004;36(12):2503–18.
38. Kharaziha P, Panaretakis T. Dynamics of Atg5-Atg12-Atg16L1 Aggregation and Deaggregation. Methods Enzymol. 2017;587:247–55.
39. Agrotis A, et al. Redundancy of human ATG4 protease isoforms in autophagy and LC3/GABARAP processing revealed in cells. Autophagy. 2019;15(6):976–97.
40. Li M, et al. Kinetics comparisons of mammalian Atg4 homologues indicate selective preferences toward diverse Atg8 substrates. J Biol Chem. 2011;286(9):7327–38.
41. Takahashi Y, et al. An autophagy assay reveals the ESCRT-III component CHMP2A as a regulator of phagophore closure. Nat Commun. 2018;9(1):2855.
42. Weidberg H, et al. LC3 and GATE-16/GABARAP subfamilies are both essential yet act differently in autophagosome biogenesis. EMBO J. 2010;29(11):1792–802.
43. Grunwald DS, et al. GABARAPs and LC3s have opposite roles in regulating ULK1 for autophagy induction. Autophagy. 2020;16(4):600–14.
44. Yamamoto M, Suzuki SO, Himeno M. The effects of dynein inhibition on the autophagic pathway in glioma cells. Neuropathology. 2010;30(1):1–6.
45. Tong J, Yan X, Yu L. The late stage of autophagy: cellular events and molecular regulation. Protein Cell. 2010;1(10):907–15.
46. Kumar S, et al. Phosphorylation of Syntaxin 17 by TBK1 controls autophagy initiation. Dev Cell. 2019;49(1):130–44 e6.
47. Wang C, et al. Phosphorylation of ULK1 affects autophagosome fusion and links chaperone-mediated autophagy to macroautophagy. Nat Commun. 2018;9(1):3492.
48. Viret C, Faure M. Regulation of syntaxin 17 during autophagosome maturation. Trends Cell Biol. 2019;29(1):1–3.
49. Choi YJ, et al. Inhibitory effect of mTOR activator MHY1485 on autophagy: suppression of lysosomal fusion. PLoS One. 2012;7(8):e43418.
50. Itakura E, et al. Beclin 1 forms two distinct phosphatidylinositol 3-kinase complexes with mammalian Atg14 and UVRAG. Mol Biol Cell. 2008;19(12):5360–72.
51. Liang C, et al. Beclin1-binding UVRAG targets the class C Vps complex to coordinate autophagosome maturation and endocytic trafficking. Nat Cell Biol. 2008;10(7):776–87.
52. Takahashi Y, et al. Bif-1 interacts with Beclin 1 through UVRAG and regulates autophagy and tumorigenesis. Nat Cell Biol. 2007;9(10):1142–51.
53. Keulers TG, Schaaf MBE, Rouschop KMA. Autophagy-dependent secretion: contribution to tumor progression. Front Oncol. 2016;6(251).
54. Liang XH, et al. Induction of autophagy and inhibition of tumorigenesis by beclin 1. Nature. 1999;402(6762):672–6.
55. Yue Z, et al. Beclin 1, an autophagy gene essential for early embryonic development, is a haploinsufficient tumor suppressor. Proc Natl Acad Sci U S A. 2003;100(25):15077–82.

56. Kang MR, et al. Frameshift mutations of autophagy-related genes ATG2B, ATG5, ATG9B and ATG12 in gastric and colorectal cancers with microsatellite instability. J Pathol. 2009;217(5):702–6.
57. Wible DJ, et al. ATG5 cancer mutations and alternative mRNA splicing reveal a conjugation switch that regulates ATG12-ATG5-ATG16L1 complex assembly and autophagy. Cell Discov. 2019;5:42.
58. Ueno T, et al. Loss of Pten, a tumor suppressor, causes the strong inhibition of autophagy without affecting LC3 lipidation. Autophagy. 2008;4(5):692–700.
59. Hou W, et al. Mutation analysis of key genes in RAS/RAF and PI3K/PTEN pathways in Chinese patients with hepatocellular carcinoma. Oncol Lett. 2014;8(3):1249–54.
60. Chen X, et al. DEPTOR is an in vivo tumor suppressor that inhibits prostate tumorigenesis via the inactivation of mTORC1/2 signals. Oncogene. 2020;39(7):1557–71.
61. Johnson CE, et al. Loss of tuberous sclerosis complex 2 sensitizes tumors to nelfinavir-bortezomib therapy to intensify endoplasmic reticulum stress-induced cell death. Oncogene. 2018;37(45):5913–25.
62. Chang WH, Lai AG. An integrative pan-cancer investigation reveals common genetic and transcriptional alterations of AMPK pathway genes as important predictors of clinical outcomes across major cancer types. BMC Cancer. 2020;20(1):773.
63. Zijian, Z., et al., Research square, 2021.
64. Claude-Taupin A, et al. ATG9A is overexpressed in triple negative breast cancer and its in vitro extinction leads to the inhibition of pro-cancer phenotypes. Cells. 2018;7(12):248.
65. Caron A, et al. DEPTOR at the nexus of cancer, metabolism, and immunity. Physiol Rev. 2018;98(3):1765–803.
66. Hu B, et al. Downregulation of DEPTOR inhibits the proliferation, migration, and survival of osteosarcoma through PI3K/Akt/mTOR pathway. Onco Targets Ther. 2017;10:4379–91.
67. Chen R, Yang Q, Lee J-D. BMK1 kinase suppresses epithelial–mesenchymal transition through the Akt/GSK3β signaling pathway. Cancer Res. 2012;72(6):1579–87.
68. Parvani JG, et al. Deptor enhances triple-negative breast cancer metastasis and chemoresistance through coupling to survivin expression. Neoplasia. 2015;17(3):317–28.
69. Pei L, et al. Overexpression of DEP domain containing mTOR-interacting protein correlates with poor prognosis in differentiated thyroid carcinoma. Mol Med Rep. 2011;4(5):817–23.
70. Okamoto T, et al. FIP200 suppresses immune checkpoint therapy responses in breast cancers by limiting AZI2/TBK1/IRF signaling independent of its canonical autophagy function. Cancer Res. 2020;80(17):3580–92.
71. Wang D, et al. Downregulation of FIP200 induces apoptosis of glioblastoma cells and microvascular endothelial cells by enhancing Pyk2 activity. PLoS One. 2011;6(5):e19629.
72. Yu X-N, et al. Enhanced mLST8 expression correlates with tumor progression in hepatocellular carcinoma. Ann Surg Oncol. 2020;27(5):1546–57.
73. Chen S, et al. Inhibition of PI3K/Akt/mTOR signaling in PI3KR2-overexpressing colon cancer stem cells reduces tumor growth due to apoptosis. Oncotarget. 2017;8(31):50476–88.
74. Mossmann D, Park S, Hall MN. mTOR signalling and cellular metabolism are mutual determinants in cancer. Nat Rev Cancer. 2018;18(12):744–57.
75. Zou Z, et al. mTOR signaling pathway and mTOR inhibitors in cancer: progress and challenges. Cell Biosci. 2020;10(1):31.
76. Qi Z, et al. PRAS40 hyperexpression promotes hepatocarcinogenesis. EBioMedicine. 2020;51.
77. Zhu G, et al. PRAS40 promotes NF-κB transcriptional activity through association with p65. Oncogenesis. 2017;6(9):e381.
78. Nussinov R, et al. The mystery of Rap1 suppression of oncogenic ras. Trends Cancer. 2020;6(5):369–79.
79. Zhang Y-L, et al. Roles of Rap1 signaling in tumor cell migration and invasion. Cancer Biol Med. 2017;14(1):90–9.
80. Earwaker P, et al. RAPTOR up-regulation contributes to resistance of renal cancer cells to PI3K-mTOR inhibition. PLoS One. 2018;13(2):e0191890.
81. Wang T, et al. RAPTOR promotes colorectal cancer proliferation by inducing mTORC1 and upregulating ribosome assembly factor URB1. Cancer Med. 2020;9(4):1529–43.
82. Kondo S, et al. Raptor and rictor expression in patients with human papillomavirus-related oropharyngeal squamous cell carcinoma. BMC Cancer. 2021;21(1):87.
83. Kauffman EC, et al. Molecular genetics and cellular features of TFE3 and TFEB fusion kidney cancers. Nat Rev Urol. 2014;11(8):465–75.
84. Kim JH, et al. TFEB supports pancreatic cancer growth through the transcriptional regulation of glutaminase. Cancers. 2021;13(3):483.
85. Li Y, et al. TFEB is a master regulator of tumor-associated macrophages in breast cancer. J ImmunoTher Cancer. 2020;8(1):e000543.
86. Medina DL, et al. Transcriptional activation of lysosomal exocytosis promotes cellular clearance. Dev Cell. 2011;21(3):421–30.
87. Astanina E, Bussolino F, Doronzo G. Multifaceted activities of transcription factor EB in cancer onset and progression. Mol Oncol. 2021;15(2):327–46.
88. Astrinidis A, et al. Tuberin, the tuberous sclerosis complex 2 tumor suppressor gene product, regulates Rho activation, cell adhesion and migration. Oncogene. 2002;21(55):8470–6.
89. Deng J, et al. ULK1 inhibition overcomes compromised antigen presentation and restores antitumor immunity in LKB1-mutant lung cancer. Nat Can. 2021;2(5):503–14.
90. Kumar M, Papaleo E. A pan-cancer assessment of alterations of the kinase domain of ULK1, an upstream regulator of autophagy. Sci Rep. 2020;10(1):14874.
91. TAN L, TAN Y, LIU D. Functions of ULK1 in autophagy and non-autophagy pathways and its implications in human physiology and disease. Biocell. 2020;44(4):535–43.
92. Li Z, et al. ULK1-ATG13 and their mitotic phospho-regulation by CDK1 connect autophagy to cell cycle. PLoS Biol. 2020;18(6):e3000288.
93. De Luca M, Romano R, Bucci C. Role of the V1G1 subunit of V-ATPase in breast cancer cell migration. Sci Rep. 2021;11(1):4615.
94. Huang L, et al. ABCG2/V-ATPase was associated with the drug resistance and tumor metastasis of esophageal squamous cancer cells. Diagn Pathol. 2012;7:180.
95. Lu Q, et al. The expression of V-ATPase is associated with drug resistance and pathology of non-small-cell lung cancer. Diagn Pathol. 2013;8:145.
96. Noman MZ, et al. Inhibition of Vps34 reprograms cold into hot inflamed tumors and improves anti–PD-1/PD-L1 immunotherapy. Sci Adv. 2020;6(18):eaax7881.
97. Liu F, et al. PIK3C3 regulates the expansion of liver CSCs and PIK3C3 inhibition counteracts liver cancer stem cell activity induced by PI3K inhibitor. Cell Death Dis. 2020;11(6):427.
98. Jiang X, et al. VPS34 stimulation of p62 phosphorylation for cancer progression. Oncogene. 2017;36.
99. Parekh VV, et al. Autophagy-related protein Vps34 controls the homeostasis and function of antigen cross-presenting CD8α⁺ dendritic cells. Proc Natl Acad Sci. 2017;114(31):E6371–80.
100. Liang T-T, et al. Systemic expression analysis reveals prognostic significance of WIPI3 in hepatocellular carcinoma. Front Genet. 2020;11(847).
101. Kean MJ, et al. VAMP3, syntaxin-13 and SNAP23 are involved in secretion of matrix metalloproteinases, degradation of the extracellular matrix and cell invasion. J Cell Sci. 2009;122(Pt 22):4089–98.
102. Sneeggen M, Schink KO, Stenmark H. Tumor suppression by control of matrix metalloproteinase recycling. Mol Cell Oncol. 2019;6(6):e1646606.
103. Miao Y, et al. GABARAP is overexpressed in colorectal carcinoma and correlates with shortened patient survival. Hepatogastroenterology. 2010;57(98):257–61.
104. Liu Y, et al. GABARAP suppresses EMT and breast cancer progression via the AKT/mTOR signaling pathway. Aging. 2021;13(4):5858–74.
105. Othman EQ, et al. Immunohistochemical expression of MAP1LC3A and MAP1LC3B protein in breast carcinoma tissues. J Clin Lab Anal. 2009;23(4):249–58.
106. Kang HM, et al. Ubiquitination of MAP1LC3B by pVHL is associated with autophagy and cell death in renal cell carcinoma. Cell Death Dis. 2019;10(4):279.
107. Li X, He S, Ma B. Autophagy and autophagy-related proteins in cancer. Mol Cancer. 2020;19(1):12.
108. Sadler JBA, et al. A cancer-associated polymorphism in ESCRT-III disrupts the abscission checkpoint and promotes genome instability. Proc Natl Acad Sci U S A. 2018;115(38):E8900–8.
109. Song Y, Quach C, Liang C. UVRAG in autophagy, inflammation, and cancer. Autophagy. 2020;16(2):387–8.

110. Ahn CH, et al. Expression of beclin-1, an autophagy-related protein, in gastric and colorectal cancers. APMIS. 2007;115(12):1344–9.
111. Hao M, Yeo SK, Guan J-L. Autophagy inhibition perturbs ERBB2 trafficking and abolishes tumorigenesis in ERBB2-driven breast cancer. Autophagy. 2021;17(4):1059–60.
112. Cararo-Lopes E, et al. Autophagy buffers Ras-induced genotoxic stress enabling malignant transformation in keratinocytes primed by human papillomavirus. Cell Death Dis. 2021;12(2):194.
113. Jiang G-M, et al. The relationship between autophagy and the immune system and its applications for tumor immunotherapy. Mol Cancer. 2019;18(1):17.
114. Fung C, et al. Induction of autophagy during extracellular matrix detachment promotes cell survival. Mol Biol Cell. 2008;19(3):797–806.
115. Nazio F, et al. Autophagy and cancer stem cells: molecular mechanisms and therapeutic applications. Cell Death Differ. 2019;26(4):690–702.
116. Pérez-Hernández M, et al. Targeting autophagy for cancer treatment and tumor chemosensitization. Cancers. 2019;11(10):1599.
117. Maes H, et al. Autophagy: shaping the tumor microenvironment and therapeutic response. Trends Mol Med. 2013;19(7):428–46.
118. Sharifi MN, et al. Autophagy promotes focal adhesion disassembly and cell motility of metastatic tumor cells through the direct interaction of paxillin with LC3. Cell Rep. 2016;15(8):1660–72.
119. Karsli-Uzunbas G, et al. Autophagy is required for glucose homeostasis and lung tumor maintenance. Cancer Discov. 2014;4(8):914–27.
120. Catalano M, et al. Autophagy induction impairs migration and invasion by reversing EMT in glioblastoma cells. Mol Oncol. 2015;9(8):1612–25.
121. La Belle Flynn A, et al. Autophagy inhibition elicits emergence from metastatic dormancy by inducing and stabilizing Pfkfb3 expression. Nat Commun. 2019;10(1):3668.
122. Pietrocola F, et al. Caloric restriction mimetics enhance anticancer immunosurveillance. Cancer Cell. 2016;30(1):147–60.
123. Kimura T, et al. Cellular and molecular mechanism for secretory autophagy. Autophagy. 2017;13(6):1084–5.
124. Lock R, et al. Autophagy-dependent production of secreted factors facilitates oncogenic RAS-driven invasion. Cancer Discov. 2014;4(4):466–79.
125. Hong Z, et al. PtdIns3P controls mTORC1 signaling through lysosomal positioning. J Cell Biol. 2017;216(12):4217–33.
126. Marat AL, Haucke V. Phosphatidylinositol 3-phosphates—at the interface between cell signalling and membrane traffic. EMBO J. 2016;35(6):561–79.
127. Poteryaev D, et al. Identification of the Switch in early-to-late endosome transition. Cell. 2010;141(3):497–508.
128. Bache KG, et al. Hrs regulates multivesicular body formation via ESCRT recruitment to endosomes. J Cell Biol. 2003;162(3):435–42.
129. Futter CE, et al. Human VPS34 is required for internal vesicle formation within multivesicular endosomes. J Cell Biol. 2001;155(7):1251–64.
130. Xu Y, et al. SNX3 regulates endosomal function through its PX-domain-mediated interaction with PtdIns(3)P. Nat Cell Biol. 2001;3(7):658–66.
131. Knævelsrud H, et al. Membrane remodeling by the PX-BAR protein SNX18 promotes autophagosome formation. J Cell Biol. 2013;202(2):331–49.
132. Bechtel W, et al. Vps34 deficiency reveals the importance of endocytosis for podocyte homeostasis. J Am Soc Nephrol. 2013;24(5):727–43.
133. Siddhanta U, et al. Distinct roles for the p110alpha and hVPS34 phosphatidylinositol 3'-kinases in vesicular trafficking, regulation of the actin cytoskeleton, and mitogenesis. J Cell Biol. 1998;143(6):1647–59.
134. Nascimbeni AC, Codogno P, Morel E. Phosphatidylinositol-3-phosphate in the regulation of autophagy membrane dynamics. FEBS J. 2017;284(9):1267–78.
135. Ketel K, et al. A phosphoinositide conversion mechanism for exit from endosomes. Nature. 2016;529(7586):408–12.
136. Miranda AM, Di Paolo G. Endolysosomal dysfunction and exosome secretion: implications for neurodegenerative disorders. Cell Stress. 2018;2(5):115–8.
137. Law F, et al. The VPS34 PI3K negatively regulates RAB-5 during endosome maturation. J Cell Sci. 2017;130(12):2007–17.
138. Jaber N, et al. Vps34 regulates Rab7 and late endocytic trafficking through recruitment of the GTPase-activating protein Armus. J Cell Sci. 2016;129(23):4424–35.
139. Baietti MF, et al. Syndecan–syntenin–ALIX regulates the biogenesis of exosomes. Nat Cell Biol. 2012;14(7):677–85.
140. Sapmaz A, et al. USP32 regulates late endosomal transport and recycling through deubiquitylation of Rab7. Nat Commun. 2019;10(1):1454.
141. Odorizzi G, Babst M, Emr SD. Fab1p PtdIns(3)P 5-kinase function essential for protein sorting in the multivesicular body. Cell. 1998;95(6):847–58.
142. Falguières T, et al. In vitro budding of intralumenal vesicles into late endosomes is regulated by Alix and Tsg101. Mol Biol Cell. 2008;19(11):4942–55.
143. Hikita T, et al. Src in endosomal membranes promotes exosome secretion and tumor progression. Sci Rep. 2019;9(1):3265.
144. Ghossoub R, et al. Syntenin-ALIX exosome biogenesis and budding into multivesicular bodies are controlled by ARF6 and PLD2. Nat Commun. 2014;5:3477.
145. Ostrowski M, et al. Rab27a and Rab27b control different steps of the exosome secretion pathway. Nat Cell Biol. 2010;12(1):19–30 sup pp 1-13.
146. Hoshino D, et al. Exosome secretion is enhanced by invadopodia and drives invasive behavior. Cell Rep. 2013;5(5):1159–68.
147. Yang L, et al. Long non-coding RNA HOTAIR promotes exosome secretion by regulating RAB35 and SNAP23 in hepatocellular carcinoma. Mol Cancer. 2019;18(1):78.
148. Yang L, et al. The long noncoding RNA HOTAIR activates autophagy by upregulating ATG3 and ATG7 in hepatocellular carcinoma. Mol BioSyst. 2016;12(8):2605–12.
149. Peng X, et al. LINC00511 drives invasive behavior in hepatocellular carcinoma by regulating exosome secretion and invadopodia formation. J Exp Clin Cancer Res. 2021;40(1):183.
150. Agbana YL, et al. LINC00511 as a prognostic biomarker for human cancers: a systematic review and meta-analysis. BMC Cancer. 2020;20(1):682.
151. Dong X, et al. Long noncoding RNA LINC00511 regulates the proliferation, apoptosis, invasion and autophagy of trophoblast cells to mediate pre-eclampsia progression through modulating the miR-31-5p/homeobox protein A7 axis. J Obstet Gynaecol Res. 2020;46(8):1298–309.
152. Sinha S, et al. Cortactin promotes exosome secretion by controlling branched actin dynamics. J Cell Biol. 2016;214(2):197–213.
153. Villarroya-Beltri C, et al. ISGylation controls exosome secretion by promoting lysosomal degradation of MVB proteins. Nat Commun. 2016;7:13588.
154. Majumder P, Chakrabarti O. Mahogunin regulates fusion between amphisomes/MVBs and lysosomes via ubiquitination of TSG101. Cell Death Dis. 2015;6(11):e1970.
155. Buschow SI, et al. MHC II in dendritic cells is targeted to lysosomes or T cell-induced exosomes via distinct multivesicular body pathways. Traffic. 2009;10(10):1528–42.
156. Möbius W, et al. Immunoelectron microscopic localization of cholesterol using biotinylated and non-cytolytic perfringolysin O. J Histochem Cytochem. 2002;50(1):43–55.
157. Möbius W, et al. Recycling compartments and the internal vesicles of multivesicular bodies harbor most of the cholesterol found in the endocytic pathway. Traffic. 2003;4:222–31.
158. Jordens I, et al. The Rab7 effector protein RILP controls lysosomal transport by inducing the recruitment of dynein-dynactin motors. Curr Biol. 2001;11(21):1680–5.
159. Jongsma ML, et al. SKIP-HOPS recruits TBC1D15 for a Rab7-to-Arl8b identity switch to control late endosome transport. EMBO J. 2020;39(6):e102301.
160. Guo H, et al. Atg5 disassociates the V1V0-ATPase to promote exosome production and tumor metastasis independent of canonical macroautophagy. Dev Cell. 2017;43(6):716–730.e7.
161. Savina A, et al. Rab11 promotes docking and fusion of multivesicular bodies in a calcium-dependent manner. Traffic. 2005;6(2):131–43.
162. Wang K, et al. Mechanical stress-dependent autophagy component release via extracellular nanovesicles in tumor cells. ACS Nano. 2019;13(4):4589–602.
163. Fader CM, et al. TI-VAMP/VAMP7 and VAMP3/cellubrevin: two v-SNARE proteins involved in specific steps of the autophagy/multivesicular body pathways. Biochim Biophys Acta. 2009;1793(12):1901–16.

164. Lefebvre C, Legouis R, Culetto E. ESCRT and autophagies: Endosomal functions and beyond. Semin Cell Dev Biol. 2018;74:21–8.
165. Chen Y-D, et al. Exophagy of annexin A2 via RAB11, RAB8A and RAB27A in IFN-γ-stimulated lung epithelial cells. Sci Rep. 2017;7(1):5676.
166. Bader CA, et al. Atg9 is required for intraluminal vesicles in amphisomes and autolysosomes. Biol Open. 2015;4(11):1345–55.
167. Moreau K, et al. Autophagosome precursor maturation requires homotypic fusion. Cell. 2011;146(2):303–17.
168. Fader CM, Aguilera MO, Colombo MI. ATP is released from autophagic vesicles to the extracellular space in a VAMP7-dependent manner. Autophagy. 2012;8(12):1741–56.
169. Jeppesen DK, et al. Reassessment of exosome composition. Cell. 2019;177(2):428–445.e18.
170. Baixauli F, López-Otín C, Mittelbrunn M. Exosomes and autophagy: coordinated mechanisms for the maintenance of cellular fitness. Front Immunol. 2014;5:403.
171. Omi J, et al. The inducible amphisome isolates viral hemagglutinin and defends against influenza A virus infection. Nat Commun. 2020;11(1):162.
172. Kraya AA, et al. Identification of secreted proteins that reflect autophagy dynamics within tumor cells. Autophagy. 2015;11(1):60–74.
173. Dupont N, et al. Autophagy-based unconventional secretory pathway for extracellular delivery of IL-1β. EMBO J. 2011;30(23):4701–11.
174. Zhang M, et al. Translocation of interleukin-1β into a vesicle intermediate in autophagy-mediated secretion. Elife. 2015;4.
175. New J, Thomas SM. Autophagy-dependent secretion: mechanism, factors secreted, and disease implications. Autophagy. 2019;15(10):1682–93.
176. Kimura T, et al. Dedicated SNAREs and specialized TRIM cargo receptors mediate secretory autophagy. EMBO J. 2017;36(1):42–60.
177. Qiang L, et al. Autophagy gene ATG7 regulates ultraviolet radiation-induced inflammation and skin tumorigenesis. Autophagy. 2017;13(12):2086–103.
178. Peng X, et al. IKKβ activation promotes amphisome formation and extracellular vesicle secretion in tumor cells. Biochim Biophys Acta Mol Cell Res. 1868;2021(1):118857.
179. Maycotte P, et al. Autophagy supports breast cancer stem cell maintenance by regulating IL6 secretion. Mol Cancer Res. 2015;13(4):651–8.
180. Huang S-C, et al. Discovery and optimization of pyrazolopyrimidine sulfamates as ATG7 inhibitors. Bioorg Med Chem. 2020;28(19):115681.
181. King HW, Michael MZ, Gleadle JM. Hypoxic enhancement of exosome release by breast cancer cells. BMC Cancer. 2012;12:421.
182. Daskalaki I, Gkikas I, Tavernarakis N. Hypoxia and selective autophagy in cancer development and therapy. Front Cell Dev Biol. 2018;6(104).
183. Kanemoto S, et al. Multivesicular body formation enhancement and exosome release during endoplasmic reticulum stress. Biochem Biophys Res Commun. 2016;480(2):166–72.
184. Bhattacharya S, et al. GAIP interacting protein C-terminus regulates autophagy and exosome biogenesis of pancreatic cancer through metabolic pathways. PLoS One. 2014;9(12):e114409.
185. Muders MH, et al. Targeting GIPC/synectin in pancreatic cancer inhibits tumor growth. Clin Cancer Res. 2009;15(12):4095–103.
186. Dutta S, et al. Interactions between exosomes from breast cancer cells and primary mammary epithelial cells leads to generation of reactive oxygen species which induce DNA damage response, stabilization of p53 and autophagy in epithelial cells. PLoS One. 2014;9(5):e97580.
187. Wu Q, et al. Exosomes from the tumour-adipocyte interplay stimulate beige/brown differentiation and reprogram metabolism in stromal adipocytes to promote tumour progression. J Exp Clin Cancer Res. 2019;38(1):223.
188. Xu J, et al. Hypoxic glioma-derived exosomes promote M2-like macrophage polarization by enhancing autophagy induction. Cell Death Dis. 2021;12(4):373.
189. Yang Y, et al. Acquisition of new tumor cell properties by MSC-derived exosomes. Int J Oncol. 2015;47(1):244–52.
190. Kucharewicz K, et al. Simultaneous induction and blockade of autophagy by a single agent. Cell Death Dis. 2018;9(3):353.
191. Chen Y, et al. Increased interleukin-6 levels in the astrocyte-derived exosomes of sporadic amyotrophic lateral sclerosis patients. Front Neurosci. 2019;13(574).
192. Im K, et al. The comparison of exosome and exosomal cytokines between young and old individuals with or without gastric cancer. Int J Gerontol. 2018;12(3):233–8.
193. Qin B, et al. IL-6 Inhibits Starvation-induced Autophagy via the STAT3/Bcl-2 Signaling Pathway. Sci Rep. 2015;5:15701.
194. Linnemann A, et al. Interleukin 6 protects pancreatic β cells from apoptosis by stimulation of autophagy. FASEB J. 2017;31.
195. Frühbeis C, et al. Physical exercise induces rapid release of small extracellular vesicles into the circulation. J Extracell Vesicles. 2015;4(1):28239.
196. Follo C, et al. Inhibition of autophagy initiation potentiates chemosensitivity in mesothelioma. Mol Carcinog. 2018;57(3):319–32.
197. Zachari M, Ganley IG. The mammalian ULK1 complex and autophagy initiation. Essays Biochem. 2017;61(6):585–96.
198. Petherick KJ, et al. Pharmacological inhibition of ULK1 kinase blocks mammalian target of rapamycin (mTOR)-dependent autophagy. J Biol Chem. 2015;290(18):11376–83.
199. Young ARJ, et al. Starvation and ULK1-dependent cycling of mammalian Atg9 between the TGN and endosomes. J Cell Sci. 2006;119(18):3888–900.
200. Urano Y, et al. 6-Hydroxydopamine induces secretion of PARK7/DJ-1 via autophagy-based unconventional secretory pathway. Autophagy. 2018;14(11):1943–58.
201. Scotto Rosato A, et al. TRPML1 links lysosomal calcium to autophagosome biogenesis through the activation of the CaMKKβ/VPS34 pathway. Nat Commun. 2019;10(1):5630.
202. Zhou X, et al. Unc-51-like kinase 1/2-mediated endocytic processes regulate filopodia extension and branching of sensory axons. Proc Natl Acad Sci. 2007;104(14):5842–7.
203. Chen Y, et al. Dual targeting of NUAK1 and ULK1 using the multitargeted inhibitor MRT68921 exerts potent antitumor activities. Cell Death Dis. 2020;11(8):712.
204. Palamiuc L, Ravi A, Emerling BM. Phosphoinositides in autophagy: current roles and future insights. FEBS J. 2020;287(2):222–38.
205. Zhou C, et al. The heme oxygenase-1 inhibitor ZnPPIX induces non-canonical, Beclin 1-independent, autophagy through p38 MAPK pathway. Acta Biochim Biophys Sin. 2012;44:815–22.
206. Wu YT, et al. Dual role of 3-methyladenine in modulation of autophagy via different temporal patterns of inhibition on class I and III phosphoinositide 3-kinase. J Biol Chem. 2010;285(14):10850–61.
207. Xing C, et al. Class I phosphatidylinositol 3-kinase inhibitor LY294002 activates autophagy and induces apoptosis through p53 pathway in gastric cancer cell line SGC7901. Acta Biochim Biophys Sin Shanghai. 2008;40(3):194–201.
208. Seglen PO, Gordon PB. 3-Methyladenine: specific inhibitor of autophagic/lysosomal protein degradation in isolated rat hepatocytes. Proc Natl Acad Sci U S A. 1982;79(6):1889–92.
209. Lelouard H, et al. Regulation of translation is required for dendritic cell function and survival during activation. J Cell Biol. 2007;179(7):1427–39.
210. Chicote J, et al. Cell death triggered by the autophagy inhibitory drug 3-methyladenine in growing conditions proceeds with DNA damage. Front Pharmacol. 2020;11:580343. https://doi.org/10.3389/fphar.2020.580343.
211. Caro LH, et al. 3-Methyladenine, an inhibitor of autophagy, has multiple effects on metabolism. Eur J Biochem. 1988;175(2):325–9.
212. Korolchuk VI, et al. Autophagy inhibition compromises degradation of ubiquitin-proteasome pathway substrates. Mol Cell. 2009;33(4):517–27.
213. Zhang H-G, Grizzle WE. Exosomes: a novel pathway of local and distant intercellular communication that facilitates the growth and metastasis of neoplastic lesions. Am J Pathol. 2014;184(1):28–41.
214. Zhang J, et al. Exosomes/tricalcium phosphate combination scaffolds can enhance bone regeneration by activating the PI3K/Akt signaling pathway. Stem Cell Res Ther. 2016;7:136.
215. Clayton A, et al. Analysis of antigen presenting cell derived exosomes, based on immuno-magnetic isolation and flow cytometry. J Immunol Methods. 2001;247(1-2):163–74.
216. Llorente A, de Marco MAC, Alonso MA. Caveolin-1 and MAL are located on prostasomes secreted by the prostate cancer PC-3 cell line. J Cell Sci. 2004;117(22):5343–51.

217. Abdulrahman BA, Abdelaziz DH, Schatzl HM. Autophagy regulates exosomal release of prions in neuronal cells. J Biol Chem. 2018;293(23):8956–68.
218. Bright NA, et al. The relationship between lumenal and limiting membranes in swollen late endocytic compartments formed after wortmannin treatment or sucrose accumulation. Traffic. 2001;2(9):631–42.
219. Isosaki M. Inhibition of wortmannin activities by amino compounds. Biochem Biophys Res Commun. 2004;324(4):1406–12.
220. Iula L, et al. Autophagy mediates interleukin-1β secretion in human neutrophils. Front Immunol. 2018;9:269.
221. Harris J, et al. Autophagy controls IL-1beta secretion by targeting pro-IL-1beta for degradation. J Biol Chem. 2011;286(11):9587–97.
222. Fukao T, et al. PI3K-mediated negative feedback regulation of IL-12 production in DCs. Nat Immunol. 2002;3(9):875–81.
223. Miranda AM, et al. Neuronal lysosomal dysfunction releases exosomes harboring APP C-terminal fragments and unique lipid signatures. Nat Commun. 2018;9(1):291.
224. Liu J, et al. Beclin1 controls the levels of p53 by regulating the deubiquitination activity of USP10 and USP13. Cell. 2011;147(1):223–34.
225. Yu X, Harris SL, Levine AJ. The regulation of exosome secretion: a novel function of the p53 protein. Cancer Res. 2006;66(9):4795–801.
226. Liu J, et al. Distinct dasatinib-induced mechanisms of apoptotic response and exosome release in imatinib-resistant human chronic myeloid leukemia cells. Int J Mol Sci. 2016;17(4):531.
227. Wang C, et al. Autophagic lipid metabolism sustains mTORC1 activity in TSC-deficient neural stem cells. Nat Metab. 2019;1(11):1127–40.
228. McKnight NC, et al. Beclin 1 is required for neuron viability and regulates endosome pathways via the UVRAG-VPS34 complex. PLoS Genet. 2014;10(10):e1004626.
229. McKnight NC, Yue Z. Beclin 1, an essential component and master regulator of PI3K-III in health and disease. Curr Pathobiol Rep. 2013;1(4):231–8.
230. Gladue DP, et al. Foot-and-mouth disease virus nonstructural protein 2C interacts with Beclin1, modulating virus replication. J Virol. 2012;86(22):12080–90.
231. Robke L, et al. Phenotypic identification of a novel autophagy inhibitor chemotype targeting lipid kinase VPS34. Angew Chem Int Ed. 2017;56(28):8153–7.
232. Marsh T, Debnath J. Ironing out VPS34 inhibition. Nat Cell Biol. 2014;17:1–3.
233. Ronan B, et al. A highly potent and selective Vps34 inhibitor alters vesicle trafficking and autophagy. Nat Chem Biol. 2014;10(12):1013–9.
234. Wu Y, et al. Synthesis and screening of 3-MA derivatives for autophagy inhibitors. Autophagy. 2013;9(4):595–603.
235. Vats S, Manjithaya R. A reversible autophagy inhibitor blocks autophagosome–lysosome fusion by preventing Stx17 loading onto autophagosomes. Mol Biol Cell. 2019;30(17):2283–95.
236. Keller MD, et al. Decoy exosomes provide protection against bacterial toxins. Nature. 2020;579(7798):260–4.
237. Cheng X-T, et al. Axonal autophagosomes recruit dynein for retrograde transport through fusion with late endosomes. J Cell Biol. 2015;209(3):377–86.
238. Al-Bari A. Chloroquine analogues in drug discovery: New directions of uses, mechanisms of actions and toxic manifestations from malaria to multifarious diseases. J Antimicrob Chemother. 2015;70.
239. Mauthe M, et al. Chloroquine inhibits autophagic flux by decreasing autophagosome-lysosome fusion. Autophagy. 2018;14(8):1435–55.
240. Lu S, et al. Lysosomal adaptation: how cells respond to lysosomotropic compounds. PLoS One. 2017;12(3):e0173771.
241. Gallagher LE, et al. Lysosomotropism depends on glucose: a chloroquine resistance mechanism. Cell Death Dis. 2017;8(8):e3014.
242. Davis MJ, Swanson JA. Technical advance: Caspase-1 activation and IL-1β release correlate with the degree of lysosome damage, as illustrated by a novel imaging method to quantify phagolysosome damage. J Leukoc Biol. 2010;88(4):813–22.
243. Orlinska U, Newton RC. Role of glucose in interleukin-1 beta production by lipopolysaccharide-activated human monocytes. J Cell Physiol. 1993;157(1):201–8.
244. Cotzomi-Ortega I, et al. Autophagy inhibition induces the secretion of macrophage migration inhibitory factor (MIF) with autocrine and paracrine effects on the promotion of malignancy in breast cancer. Biology. 2020;9(1):20.
245. Li M, et al. Suppression of lysosome function induces autophagy via a feedback down-regulation of MTOR complex 1 (MTORC1) activity. J Biol Chem. 2013;288(50):35769–80.
246. Deng J, et al. The role of autophagy and amphisomes in virus recognition, TLR 9 recruitment and virus-stimulated IFN-α production by human plasmacytoid dendritic cells (pDC) (45.19). J Immunol. 2012;188(1 Supplement):45.19.
247. Mauvezin C, et al. Autophagosome-lysosome fusion is independent of V-ATPase-mediated acidification. Nat Commun. 2015;6:7007.
248. van Deurs B, Holm PK, Sandvig K. Inhibition of the vacuolar H(+)-ATPase with bafilomycin reduces delivery of internalized molecules from mature multivesicular endosomes to lysosomes in HEp-2 cells. Eur J Cell Biol. 1996;69(4):343–50.
249. van Weert AW, et al. Transport from late endosomes to lysosomes, but not sorting of integral membrane proteins in endosomes, depends on the vacuolar proton pump. J Cell Biol. 1995;130(4):821–34.
250. Zou W, et al. Exosome release is regulated by mTORC1. Adv Sci. 2019;6(3):1801313.
251. Palokangas H, et al. Retrograde transport from the pre-Golgi intermediate compartment and the Golgi complex is affected by the vacuolar H+-ATPase inhibitor bafilomycin A1. Mol Biol Cell. 1998;9(12):3561–78.
252. Chen Q, et al. Knockdown of Parkinson's disease-related gene ATP13A2 reduces tumorigenesis via blocking autophagic flux in colon cancer. Cell Biosci. 2020;10(1):144.
253. Bento CF, et al. The Parkinson's disease-associated genes ATP13A2 and SYT11 regulate autophagy via a common pathway. Nat Commun. 2016;7(1):11803.
254. Kong SM, et al. Parkinson's disease-linked human PARK9/ATP13A2 maintains zinc homeostasis and promotes α-Synuclein externalization via exosomes. Hum Mol Genet. 2014;23(11):2816–33.
255. Minakaki G, et al. Autophagy inhibition promotes SNCA/alpha-synuclein release and transfer via extracellular vesicles with a hybrid autophagosome-exosome-like phenotype. Autophagy. 2018;14(1):98–119.
256. Sharma G, et al. A family of PIKFYVE inhibitors with therapeutic potential against autophagy-dependent cancer cells disrupt multiple events in lysosome homeostasis. Autophagy. 2019;15(10):1694–718.
257. Dong XP, et al. PI(3,5)P(2) controls membrane trafficking by direct activation of mucolipin Ca(2+) release channels in the endolysosome. Nat Commun. 2010;1(4):38.
258. Li SC, et al. The signaling lipid PI(3,5)P_2 stabilizes V_1-$V_{(o)}$ sector interactions and activates the V-ATPase. Mol Biol Cell. 2014;25(8):1251–62.
259. Hessvik NP, et al. PIKfyve inhibition increases exosome release and induces secretory autophagy. Cell Mol Life Sci. 2016;73(24):4717–37.
260. Ji X, Zhang X, Li Z. ULK1 inhibitor induces spindle microtubule disorganization and inhibits phosphorylation of Ser10 of histone H3. FEBS Open Biol. 2020;10(11):2452–63.
261. Karve S, et al. Revival of the abandoned therapeutic wortmannin by nanoparticle drug delivery. Proc Natl Acad Sci U S A. 2012;109(21):8230–5.
262. Guo J, et al. Potent USP10/13 antagonist spautin-1 suppresses melanoma growth via ROS-mediated DNA damage and exhibits synergy with cisplatin. J Cell Mol Med. 2020;24(7):4324–40.
263. Pellegrini P, et al. Acidic extracellular pH neutralizes the autophagy-inhibiting activity of chloroquine: implications for cancer therapies. Autophagy. 2014;10(4):562–71.
264. Collins KP, Jackson KM, Gustafson DL. Hydroxychloroquine: A Physiologically-Based Pharmacokinetic Model in the Context of Cancer-Related Autophagy Modulation. J Pharmacol Exp Ther. 2018;365(3):447–59.
265. Bayer N, et al. Effect of bafilomycin A1 and nocodazole on endocytic transport in HeLa cells: implications for viral uncoating and infection. J Virol. 1998;72(12):9645–55.

Publisher's Note

Springer Nature remains neutral with regard to jurisdictional claims in published maps and institutional affiliations.

Hánělová *et al.*
Cell Communication and Signaling (2024) 22:25
https://doi.org/10.1186/s12964-023-01408-6

Cell Communication and Signaling

REVIEW Open Access

Protein cargo in extracellular vesicles as the key mediator in the progression of cancer

Klára Hánělová[1], Martina Raudenská[1,2], Michal Masařík[1,2,3] and Jan Balvan[1*]

Abstract

Exosomes are small vesicles of endosomal origin that are released by almost all cell types, even those that are pathologically altered. Exosomes widely participate in cell-to-cell communication via transferring cargo, including nucleic acids, proteins, and other metabolites, into recipient cells. Tumour-derived exosomes (TDEs) participate in many important molecular pathways and affect various hallmarks of cancer, including fibroblasts activation, modification of the tumour microenvironment (TME), modulation of immune responses, angiogenesis promotion, setting the pre-metastatic niche, enhancing metastatic potential, and affecting therapy sensitivity and resistance. The unique exosome biogenesis, composition, nontoxicity, and ability to target specific tumour cells bring up their use as promising drug carriers and cancer biomarkers. In this review, we focus on the role of exosomes, with an emphasis on their protein cargo, in the key mechanisms promoting cancer progression. We also briefly summarise the mechanism of exosome biogenesis, its structure, protein composition, and potential as a signalling hub in both normal and pathological conditions.

Keywords Extracellular vesicles, Exosomes, Exosomal proteins, Cancer, Tumour microenvironment, Cancer-associated fibroblasts, Angiogenesis, Cell death, Immune evasion, Metastasis, Therapy resistance, Biomarkers

Introduction

Extracellular vesicles (EVs) belong to the group of heterogeneous membranous structures derived from all cell types, even those pathologically altered [1]. Depending on the cell type they originated from, EVs can contain various sets of specific proteins. Based on their size and biogenesis, EVs can be divided into three main groups: apoptotic bodies, ectosomes, and exosomes. Apoptotic bodies are released by cells that have undergone apoptosis and are 1,000–5,000 nm in diameter. Ectosomes, formed from plasma membrane outward budding (ectocytosis), are 150–1,000 nm in diameter and include vesicles such as oncosomes and microvesicles [2, 3]. Exosomes are generated by the endolysosomal system by exocytosis of intraluminal vesicles (ILVs) formed within the multivesicular bodies (MVBs) and are, typically, 30–150 nm in diameter [4].

EVs are nanosized particles formed by phospholipid membrane, that carry various sets of proteins, lipids, nucleic acids, glycans, and others that reflect the content of their cell of origin [5]. EVs are essential mediators of intercellular communication and delivery vehicles of molecular signals through the extracellular space. They play crucial roles in the homeostasis of healthy tissues and the progression of pathological states, including cancer, by stimulating cell proliferation, angiogenesis, metastasis, and other tumour-promoting processes. Via their content, EVs can regulate various signalling pathways [6, 7]. Cells in pathological conditions secrete large quantities of various EVs into body fluids, reflecting the

*Correspondence:
Jan Balvan
jan.balvan@med.muni.cz
[1] Department of Pathological Physiology, Faculty of Medicine, Masaryk University, Kamenice 5, Brno CZ-625 00, Czech Republic
[2] Department of Physiology, Faculty of Medicine, Masaryk University, Kamenice 5, Brno CZ-625 00, Czech Republic
[3] BIOCEV, First Faculty of Medicine, Charles University, Prumyslova 595, Vestec CZ-252 50, Czech Republic

© The Author(s) 2024. **Open Access** This article is licensed under a Creative Commons Attribution 4.0 International License, which permits use, sharing, adaptation, distribution and reproduction in any medium or format, as long as you give appropriate credit to the original author(s) and the source, provide a link to the Creative Commons licence, and indicate if changes were made. The images or other third party material in this article are included in the article's Creative Commons licence, unless indicated otherwise in a credit line to the material. If material is not included in the article's Creative Commons licence and your intended use is not permitted by statutory regulation or exceeds the permitted use, you will need to obtain permission directly from the copyright holder. To view a copy of this licence, visit http://creativecommons.org/licenses/by/4.0/. The Creative Commons Public Domain Dedication waiver (http://creativecommons.org/publicdomain/zero/1.0/) applies to the data made available in this article, unless otherwise stated in a credit line to the data.

organism's disease state. Therefore, these disease-specific EV surfaces and contents could be used as sensitive biomarkers and have great potential as liquid biopsy agents for various diseases [8–10].

To understand how different types of EVs affect cancer development, accurate nomenclature is essential. The International Society for Extracellular Vesicles (ISEV) proposed the Minimal Information for Studies of Extracellular Vesicles ("MISEV") guidelines in 2014, which were updated four years later [11, 12]. The recommendation is to use the term "extracellular vesicle" as a "generic term for particles naturally released from the cell that are delimited by a lipid bilayer and cannot replicate" [11, 13]. The term exosome was initially used to refer to a membrane vesicle released by reticulocytes during their maturation [4, 14]; now it is used to describe MVB-origin EVs [13]. In this review, we are mainly focused on cancer-associated exosomes and their protein content, and discuss other EVs in comparison if relevant.

The structure and content of exosomes

The secretion of exosomes was originally proposed as a mechanism that serves to eliminate unnecessary proteins from the cell [15]. However, in the 1990s, it was suggested that exosomes could play a role in intracellular communication, especially if connected to immune responses and cancer [16, 17]. This concept was supported later in 2007, when mRNAs and miRNAs were shown to be present in exosomes in their functional form and thus able to alter cell behaviour. This RNA was called "exosomal shuttle RNA" (esRNA) [18]. Besides esRNAs, exosome content includes several molecules, such as proteins, lipids, other nucleic acids, and metabolites, highly reflecting the identity and molecular state of their cell of origin [19]. Approximately 4400 proteins, 194 lipids, 1639 mRNAs and 764 miRNAs were identified in exosomes from different cell types, which points to their potential functional diversity and complexity [20, 21].

Exosomal cargo is protected from enzymatic degradation as it is encapsulated within the lipid bilayer of exosomes. Exosomal proteins can maintain the native conformation and functionality (for example, exosomal phosphoproteins were stable over a storage period of 5 years [22]). This makes them useful for the transfer of intact and functional proteins between cells. The protein content of the exosomes can directly influence the behaviour of the targeted cells, their microenvironment, and cell-to-cell communication [23, 24] (mRNA must be translated to have some influence). Therefore, exosomal proteins can provide better interpretable and more accurate information about the nature of communication in the tumour microenvironment (TME), disease progression and the degree of TME transformation. The selection of exosome cargo is not a random process. It requires the involvement of complex sorting mechanisms [19]. The state of the cell that produced these EVs can influence the content and biogenesis of these vesicles by various molecular signals. For example, tumour cells in a state of hypoxia secrete EVs that help to enhance angiogenic and metastatic potential [25]. Exosomes are potentially highly attractive objects for proteomic research as they are highly enriched in membrane and other proteins, which are poorly represented in most purely proteomic studies for their low concentrations or biophysical properties in isolated samples. Additionally, the presence of a specific set of proteins enables the recognition of specific cell types in the investigated sample and even sheds light on changes in cellular behaviour [19].

As mentioned above, exosomes are membrane vesicles composed of a hydrophilic core surrounded by a lipid bilayer which express, on the surface, various ligands, receptors and other bioactive molecules derived from the source cells [26]. The key components of the lipid membrane are phosphatidylcholines (PC), phosphatidylethanolamines (PE), phosphatidylinositols (PS-PI), sphingomyelins (SM), gangliosides, ceramides, cholesterol, or diacylglycerols (DAG) [27–30]. The ratio of lipids in the exosomal membrane differs slightly from the composition of these lipids in the plasma membrane. In addition, exosome membrane "flip-flop" transitions are more common than in the plasma membrane due to the lack of flippases [31]. Consequently, some EVs, such as apoptotic exosome-like vesicles [32] but also exosomes secreted by cancer cells, can expose phosphatidylserine (PS) on the surface [24, 33, 34]. Besides the structural role of lipids in the exosomal membrane, they are essential for exosome formation and release [35]. The lipid content of the exosomal core is mainly represented by phospholipids, glycolipids and free fatty acids, in contrast to microvesicles, which are enriched in ceramides and sphingomyelins [36]. Exosomes also carry surface receptors, adhesion molecules (ICAMs), integrins, tetraspanins (CD9, CD63, CD81, CD82, CD53, and CD37) and other transmembrane or surface proteins. The protein content of exosomes is represented by the cytosolic and cytoskeletal proteins (β-actin), enzymes (GTPases, proteases), heat shock proteins (HSP60, HSP70, HSP90), cytokines, endosome-associated proteins (Alix, Tsg101, Rab proteins), or oncoproteins [37]. Some of these molecules, such as tetraspanins CD9, CD63, and CD81, or Tumour susceptibility gene 101 (Tsg101) and ALG-2-interacting protein X (Alix), are considered exosomal markers [38–40].

Exosome biogenesis and trafficking

The biogenesis of exosomes consists of many complex steps and is regulated by various intra- and extracellular signals. Firstly, the biogenesis mechanism involves the formation of an early endosome, which is derived from the plasma membrane by endocytosis. Secondly, the inward budding of the early endosome creates small intraluminal vesicles (ILVs), giving rise to multivesicular endosomes (MVEs), also called multivesicular bodies (MVBs) or late endosomes [41]. Finally, these MVBs fuse with the plasma membrane and release ILVs into the extracellular space as exosomes [42] (see Fig. 1). This unique process differentiates exosomes from other EVs, such as apoptotic bodies, oncosomes, or necrotic blebs. Exosome biogenesis usually requires the endosomal sorting complex required for transport (ESCRT), although an ESCRT–independent pathway has also been identified [43]. Exosome biogenesis allows the regulation of protein quality, as it enables cells to retrieve proteins from the plasma membrane selectively. Released exosomes play a role in a wide range of processes, such as signal and molecular transmission to other cells, or extracellular matrix (ECM) remodelling [44].

The ESCRT machinery comprises around 30 proteins assembled into 5 functional subcomplexes. The ESCRT-0 sequesters ubiquitinated cargo, ESCRT-I/II/III are implicated in ILVs budding, and the VPS4 complex is responsible for membrane scission. The ESCRT machinery enables both the selection of endocytic cargo incorporated into ILVs and the formation of ILVs themselves by membrane remodelling and scission. The cargo selection is mediated by the accessory Alix/Syntenin/Syndecan complex, which also directs the biogenesis of ILVs [45, 46]. The formation of MVBs driven by ESCRT is critical not only for exosome biogenesis but also for lysosomal degradation via targeting ubiquitylated proteins [47].

On the other hand, the ESCRT–independent pathway is driven by lipids and associated proteins like tetraspanin CD63 in a lipid-mediated process dependent on the self-organising of lipid and cargo domains. The presence of ceramide, lysophospholipid and glycosphingolipid molecules on the limiting membrane induces spontaneous budding within the MVBs to produce ILVs and tetraspanin sorting into ILVs [48–50]. Rab GTPase Rab31 drives and controls exosome biogenesis independent of ESCRT differently than ceramides and tetraspanins. Rab31, which enables ILV formation, inactivates Rab7 and suppresses the fusion of MVBs with lysosomes, thereby promoting the secretion of exosomes. Therefore, Rab31 represents the key checkpoint for exosome biogenesis and determines its fate by balancing with Rab7 [51, 52].

Exosome secretion, uptake and cargo delivery

The microtubule network is responsible for the transport of MVBs towards the plasma membrane. It requires altered actin polymerisation near the plasma membrane, followed by actomyosin cytoskeleton contraction [53]. The fusion of MVBs with the plasma membrane was found to be mediated by SNARE (SNAP receptor) complex formed by vesicular v-SNARE and target membrane t-SNARE [54]. After the contact of these two membranes, the SNARE complex overcomes the fusion energy barrier due to its association with the V-ATPase subunit V0. Exosomes are also rich in various Rab GTPases, which are believed to regulate membrane trafficking and secretion, Rab4, Rab5, Rab11 and Rab27 in particular [55].

The mechanism of exosome release is classified as constitutive or inducible, depending on the cell of origin. The constitutive secretion pathway is provided by Rab GTPases, heterotrimeric G-protein, and protein kinase D [56]. The inducible secretion is mediated by various types of physical, biological, and chemical stimuli, such as low pH, DNA damage, change in extracellular ATP levels, hypoxia, and increased intracellular Ca^{2+}. For example, under the influence of hypoxia, cardiomyocytes release an increased number of exosomes [57]. Exosome secretion also depends on lipid mediators, like diacylglycerol, and is regulated by p53 via TSAP6 (Tumour suppressor activated pathway-6) [47, 58]. However, fusion with the plasma membrane is not the only fate MVBs can undergo. MVBs can also be directed to lysosomes, where their content is degraded and not secreted from the cell. By fusion with autophagosomes, MVBs can give rise to amphisomes, which may fuse with the plasma membrane and release their content extracellularly or can be degraded in lysosomes [45, 59].

The specific targeting towards recipient cells depends on the composition of the exosome surface. For instance, complex lipids influence exosome targeting in cancer cells. Sphingomyelin-enriched melanoma-derived exosomes exhibit enhancement in targeting within the TME [28]. Similarly, exosomes derived from glioblastoma cells enriched with phosphatidylethanolamine mainly target glioblastoma cells [60]. Exosomes mediate cell-to-cell communication, both locally and systemically, and may pass multiple uptake and release cycles allowing them to access several layers of tissues of multiple organs, including the liver, kidney, lung, pancreas, spleen, colon, ovaries and last, but not least brain [61, 62]. In contrast, large EVs (> 200μm) are predominantly accumulated in bones, liver and lymph nodes, which points to the fact that the transport of exosomes is also influenced by their size [63].

The internalisation of exosomes into the recipient cell can be provided through a non-specific process, such as

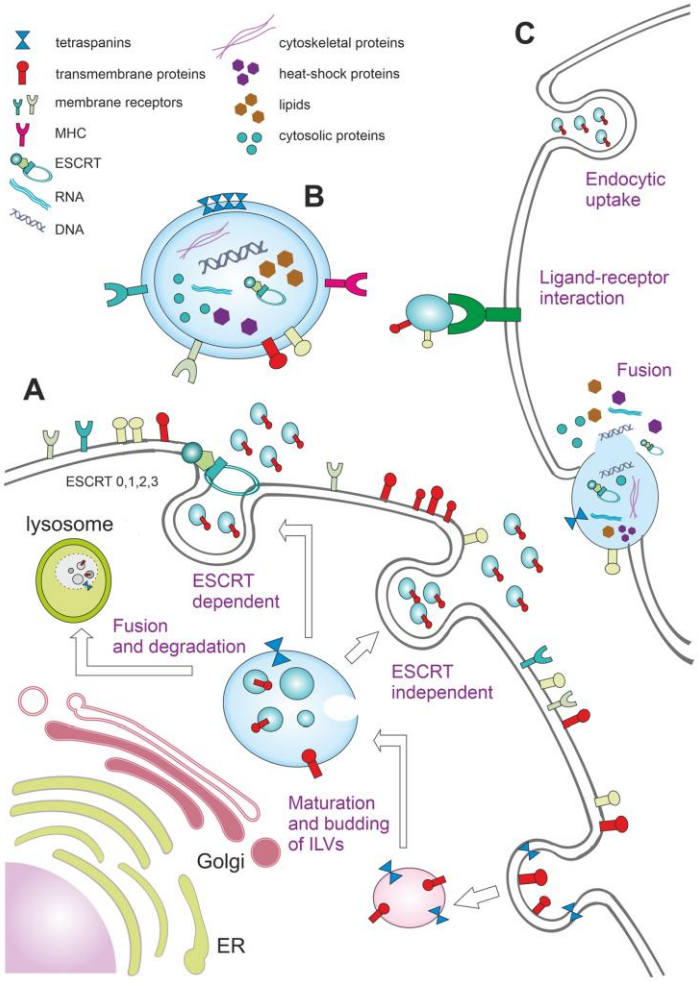

Fig. 1 Exosome biogenesis, release, structure, content, and uptake by recipient cells. **A** Exosomes originate from the invagination of the plasma membrane, forming an early endosome. The inward budding of the endosome creates ILVs within the MVB (late endosome), which can be either degraded in lysosome, or secreted into the extracellular space as exosomes via ESCRT-dependent, or ESCRT-independent pathway, in which case lipid domains are involved. **B** Exosomes are formed by the lipid bilayer with integrated bioactive molecules at its surface, such as cell adhesion molecules, tetraspanins, cytokine or MHC receptors, and integrins. The exosome content comprises cytosolic and cytoskeletal proteins, enzymes, ESCRT components, various types of nucleic acids, and lipids. **C** The exosome uptake can be provided non-specifically by endocytosis and simple fusion with the plasma membrane or specifically by the ligand-receptor interaction

endocytosis, including caveolae-dependent and clathrin-dependent endocytosis, pinocytosis and phagocytosis [64], or specifically by receptor-dependent pathway [53]. The specific targeting is proposed to be mediated by many proteins localised on the cell surface, including integrins, lectins, and T-cell immunoglobulin, or mucin domain-containing protein 4 (Tim4) [65, 66]. Tim4 is a transmembrane protein expressed on macrophages,

which specifically binds the phosphatidylserine displayed on the EV surface [67]. Nevertheless, the uptake route may be more dependent on the recipient cell type than on the exosomes themselves [53]. However, exosomes can transmit information not only by integrating into the recipient cells but also by acting at the cell surface, for example, during an immune response. In this case, exosomes harbouring major histocompatibility complex (MHC) can activate related T-cell receptors on T-lymphocytes [68].

Interestingly, exosome release and uptake by cancer cells can be highly influenced by a low pH in the TME. On the metastatic melanoma cells was shown, that compared to buffered conditions, low pH conditions increased both, exosome release and uptake [69, 70]. The study by Parolini et al. also showed a change in exosome membrane rigidity in a low pH in association with the increased amount of N-acetylneuraminyl-galactosylglucosylceramide (GM3) and sphingomyelin (SM), which are known to be parts of membrane microdomains, also known as lipid rafts. This elucidates the increased fusion capacity of exosomes in a low pH, as sphingomyelin modulates the efficiency of membrane fusion [69, 71]. In addition, the amount of EVs and their content can be influenced by the autophagy machinery [34, 72]. The secretion of pro-angiogenic EVs during hypoxia is dependent on the autophagy-related protein GABARAPL1 [73]. The starvation of cancer cells significantly altered the composition of the protein content of phosphatidylserine-positive EVs (PS-EVs) produced by these cells. Starvation increased the exosomal abundance of matrix metalloproteinase 13 (MMP13), which can promote angiogenesis, and decreased the abundance of periostin and regucalcin (RGN) in PS-EVs [34]. Secreted POSTN can promote cancer stemness in head and neck cancer, and RGN promotes dormancy in cancer cells [74, 75].

Exosomal proteins as signal molecules

Recently, a growing body of evidence has emerged to support the involvement of exosomes in the regulation of a variety of signalling pathways, including WNT and KRAS signalling [76] or PI3K/AKT or MAPK/ERK pathways [77]. These pathways can influence stem cell maintenance, cell differentiation, tissue repair and regeneration processes. Consequently, exosomes have important signalling roles in affecting their surroundings, the recipient cells or even distant environment [78]. Exosomal proteins can contain growth factors and cytokines that trigger signalling pathways promoting cell growth, proliferation, or angiogenesis. For example, exosomes containing EGFR influence the liver microenvironment, facilitating the metastasis of gastric cancer to the liver [79]. Proteins involved in drug efflux transport, like P-glycoprotein, can be packaged within exosomes, protecting cells from chemotherapy agents [80]. Some types of exosomes can carry hormonal signals, such as steroid hormones, which have been detected in urinary exosomes [81]. Exosomal proteins can also deliver activation signals to recipient cells. Immune cells can be stimulated by exosomes from antigen-presenting cells (APCs) like macrophages and dendritic cells (DCs). These exosomes carry MHC molecules with antigens on their surface. Their uptake by the T-cell receptor (TCR) of specific T-cells subsequently leads to T-cell activation [82]. Exosomes can contribute to inflammatory signalling by transporting pro-inflammatory or anti-inflammatory cytokines [83] and may also carry immunomodulatory proteins, such as programmed death-ligand 1 (PD-L1), which can suppress the activity of cytotoxic T-cells, leading to immune evasion by tumour cells [84].

Many proteins identified in exosomes including lactate dehydrogenase A (LDHA), annexin A1/2 (ANXA1/2), or HSP90, are known to be mutated in multiple cancer types [21]. Specifically, exosomal extracellular matrix protein 1 (ECM1) was found to promote progression and even metastatic invasion in most cancers. Thus, ECM1 is thought to be an indicator of increased metastatic potential of tumour cells and was linked to poor prognosis [85, 86]. Another protein identified in exosomes, alpha-2-HS-glycoprotein (AHSG), was found to promote breast cancer progression and was associated with the risk of colorectal carcinoma and non-small cell lung cancer (NSCLC) [87–89].

Some membrane proteins were found to possess therapeutic properties, but those are achievable only if these proteins remain in their native, or close to native conformation. Fortunately, exosomes can act as scaffolds for membrane proteins, thus they can be maintained in their native state [90]. For example, TNF-related apoptosis-inducing ligand (TRAIL) located on the exosomal surface could deliver apoptosis signals to tumour cells and promote apoptosis [91].

EVs are, among other processes, involved in unconventional protein secretion (UPS) [92]. This mechanism includes proteins lacking a signal sequence in their gene, which enables them to enter the ER—Golgi apparatus (GA) conventional pathway, such as interleukin-1β, fibroblast growth factor 2 (FGF-2), or bacterial enzymes [93, 94]. These proteins are essential molecules that function in cell signalling, immune modulation and many other extracellular pathways [95, 96]. The fact that EVs are present in several body fluids enables them to trigger biological responses in distant locations, such as metastatic sites, and supports their potential as biomarkers and therapeutic vehicles [25, 97, 98].

Exosomal proteins in cancer progression

Both tumour and stromal cell-derived exosomes are implicated in processes important for all stages of cancer progression, including tumour growth and cell proliferation, cell death avoidance, angiogenesis, immune evasion, invasion and metastasis, or even therapy resistance (see Fig. 2). Cancer cells secrete higher amounts of exosomes than normal cells, these exosomes are of altered composition. Several oncogenes and tumour suppressors have been found that are implicated in the regulation of exosomal biogenesis and production [99]. In addition, tumour cells can reprogram their metabolism in favour of glycolysis by enhancing the activity of glucose transporters. Increased glucose uptake leads to the elevation in lactate production through aerobic glycolysis and, thus, to intracellular accumulation of protons. This process is called the Warburg effect [100]. Accumulated protons are actively transported into the extracellular microenvironment via vacuolar ATPase (V-ATPase), Na^+/H^+ exchanger (NHE), monocarboxylate transporters (MCTs), and carbonic anhydrase (CAs) [101]. Elevated extracellular levels of acidic metabolites then lead to a lowering in extracellular pH. Low pH condition is considered one of the hallmarks of cancer, which can potentially influence exosome secretion and uptake [70, 102]. Moreover, exosomes released in acidic conditions (pH 6.0) were found to contain higher amounts of certain protein categories engaged in focal adhesion, actin cytoskeleton regulation, leukocyte migration through endothelia, or cell morphology modification. These molecules include H-Ras (Harvey rat sarcoma virus), N-Ras (Neuroblastoma RAS viral oncogene homolog), GANAB (glucosidase II alpha

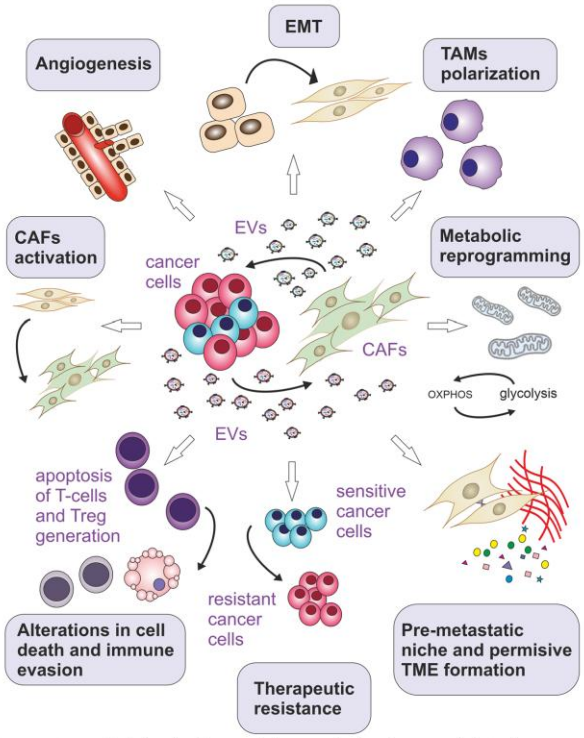

Fig. 2 The role of exosomal proteins in specific hallmarks of cancer. Both stromal cell and cancer cell-derived exosomes are implicated in processes promoting cancer progression. These include epithelial-mesenchymal transition (EMT), angiogenesis, activation of cancer-associated fibroblasts (CAFs), immune evasion, polarisation of tumour-associated macrophages, insensitivity to cell death signals, pre-metastatic niche formation and metastasis, and even therapy resistance. Treg represents an immunosuppressive type of CD4 + T-cells. Treg can suppress anticancer immunity and cause immune evasion

subunit), HSP90B1 (heat shock protein 90 beta family member 1), TIMP3 (tissue inhibitor of metalloproteinase-3) and other proteins, which are also linked to metastatic melanoma patient's poor prognosis [70, 103].

As mediators of cell-to-cell communication, exosomes play a pivotal role in the tumour microenvironment (TME). Various bioactive molecules loaded to exosomes are necessary signals for reprogramming of TME in favour of cancerogenesis [104]. For example, delta-like 4 protein (DLL4) increases vessel branching and promotes cancer-associated modifications of the TME [105]. DLL4 was associated with tumour aggressiveness and an unfavourable clinical outcome in colorectal cancer patients [106]. Integrins are a family of proteins that direct exosomes to specific tissues, thus being partly responsible for premetastatic niche formation and metastatic tropism during breast cancer development [107]. Exosomal transforming growth factor-beta (TGFβ) triggers fibroblast and mesenchymal stem cell differentiation into myofibroblasts, promoting cancer proliferation and invasiveness, for example, in prostate cancer [108, 109]. Exosomal tetraspanin 8 (Tspan8) promotes angiogenesis in adenocarcinoma through increasing endothelial cell proliferation, migration and sprouting [110].

The TME is comprised of diverse cell types, such as endothelial cells, fibroblasts, and immune cells, with various functions, including impact on cancer development and progression [111]. Because of its heterogeneity and adaptability, the TME is partly responsible for therapy resistance [112]. The recruitment of immune cells into the TME is governed by dynamic signalling, part of which are exosomes [113]. Tumour-derived exosomes (TDEs) can directly influence the differentiation and activity of NK (natural killer) cells, macrophages, T-cells and B-cells [114]. Fibroblasts are an integral part of the TME. They play a critical role in maintaining homeostasis in connective tissues by producing extracellular matrix (ECM) components and various cytokines. Fibroblasts are usually in a quiescent state, as their levels of proliferation and metabolic activity are low [115]. In response to cancer cell presence, stromal fibroblasts can be activated into cancer-associated fibroblasts (CAFs) that can promote invasive growth and metastasis [116]. CAFs are characterised by morphological features, such as spindle shape and lack of expression of non-mesenchymal cell markers typical for epithelial, endothelial, immune, or neuronal cells [117, 118]. CAFs express specific protein markers, such as fibroblast activation protein α (FAP), α-smooth muscle actin (α-SMA), fibroblast-specific protein 1 (FSP1), podoplanin (PDPN), and platelet-derived growth factor receptor (PDGFR) [115, 119]. CAFs also produce a variety of proinflammatory and inflammation-activating factors, like nuclear factor kappa B (NF-κB), IL-6, FGF-2 (also known as bFGF), or TGFβ [120]. The mechanism of fibroblast activation is still not well understood. However, TDEs are believed to be important factors promoting CAF activation and proliferation, as they contain TGFβ and activate SMAD-dependent signalling [121, 122]. Following the interaction with TDEs, mesenchymal stem cells (MSCs) might also give rise to CAFs. Exosomes secreted from breast cancer cells (MCF-7, or MDA-MB-231 cells) induced the differentiation of adipose-derived mesenchymal stem cells into the myofibroblastic type of CAFs. This process is accompanied by the increased secretion of CAF-produced factors, such as vascular endothelial growth factor (VEGF), stromal cell-derived factor 1 (SDF-1), and TGFβ, which are engaged in tumour progression and metastasis regulation [123] as CAFs can contribute to the establishment of a pre-metastatic niche [124, 125].

Exosomal CD151 and Tspan8 are essential for cancer cells and CAFs communication with a contribution to ECM remodelling. TDEs derived from lung-tropic tumours express high levels of specific integrins, α6β1 or α6β4, which enable TDEs to bind to lung fibroblasts, leading to the formation of pre-metastatic niche in lung [107, 126]. Exosomes are key players not only in CAF activation but also in the crosstalk between CAFs and tumour cells because CAF-secreted exosomes can affect the tumour phenotype via their specific cargo [120]. These exosomes can fuel cancer cell metabolism by transporting various metabolites, like amino acids, lipids, Krebs cycle metabolites, or even mitochondria [127, 128].

Angiogenesis

Angiogenesis is the process of forming new blood vessels, and it has a pivotal role in tumour progression to advanced stages of cancer (neovascularisation is necessary when the tumour volume exceeds 1 mm^3) [129], including metastatic site formation. The formation of new vessels from pre-existing ones is induced by an imbalance between pro- and anti-angiogenic factors, VEGF overproduction, in particular. Cancer cells can obtain angiogenic phenotype in the process called angiogenic transition, which leads to uncontrolled production of proangiogenic factors and excessive angiogenesis. Manipulation of angiogenesis has become one of the approaches for cancer therapy, although its current efficacy is limited [130]. Specifically, bevacizumab is a widely used angiogenesis inhibitor for metastatic colorectal carcinoma therapy [131]. According to numerous studies, exosomes can accelerate angiogenesis via their cargo.

An important factor significantly involved in angiogenesis is TGFβ-I. The study on head and neck squamous cell carcinoma (HNSCC) cell lines reveals that TGFβ-enriched TDEs are major factors driving angiogenesis

in the TME [132]. Surprisingly, TDEs promote TGFβ-signalling not only in endothelial cells but also in other cell types within the TME, such as macrophages. TDEs enriched in TGFβ promote the differentiation of non-activated macrophages into a tumour-associated macrophage-like (M2-like) phenotype, which is proangiogenic [133]. These TGFβ-enriched exosomes might be promising targets in anti-angiogenic therapy via blocking TGFβ interactions using mRER-mediated silencing. TGFβ signalling is blocked by neutralising extracellular TGFβ by mRER [134]. mRER is a newly developed TGFβ inhibitor that acts as a ligand trap for TGFβ and significantly inhibits angiogenesis [133]. Due to its high efficiency even in picomolar concentrations and small size, mRER enables better penetration of dense tissues, for example, the extracellular matrix [135].

The protein content of TDEs, including various pro-angiogenic factors, widely differs in distinct types of cancer. Specifically, glioblastoma-derived exosomes carry angiogenin, VEGF, TGFβ, IL-6, IL-8, and tissue inhibitor of metalloproteinase-1/2 (TIMP-1/2), which regulate MMP activity [136, 137]. In nasopharyngeal carcinoma, exosomes are highly enriched in intercellular adhesion molecule-1 (ICAM-1), CD44 variant isoform 5 (CD44v5) and matrix metalloproteinase 13 (MMP-13), in contrast, angio-suppressive protein TSP-1 is downregulated in these exosomes [138, 139]. Exosomes derived from multiple myeloma contain VEGF, bFGF, MMP-9, hepatocyte growth factor (HGF), and serpin E1 [140]. In lung adenocarcinoma, exosomes enriched in sortilin (also known as neurotensin receptor 3, NTSR3) might upregulate the level of expression of some pro-angiogenic proteins, namely endothelin-1, IL-8, thrombospondin-2 (TSP-2), uPA, and VEGF. Sortilin also promotes the release of TDEs themselves and may be useful as a diagnostic and prediction marker of cancer progression [141, 142]. Exosomal annexin II promotes angiogenesis in breast cancer by acting as a co-receptor for tissue plasminogen activator (tPA) [143]. In bladder cancer exosomes, EGF-like repeats and discoidin I-like domain-3 (EDIL-3), which is essential in angiogenesis and vascular development, is overexpressed [144].

As tumour grows, the demand for oxygen and nutrients increases. Existing blood vessels may not be sufficient to meet this demand and the formation of new blood vessels through neoangiogenesis may not always keep pace with the rapid growth of the tumour mass, leading to the persistence of hypoxic regions within the tumour. Hypoxia is one of the critical conditions responsible for the influence on exosome biogenesis, their release and content, hence on cancer progression. The adaptation of cells to reduced oxygen supplies is provided by hypoxia-inducible factors (HIFs) [145]. High expression of HIF-1α contributes to the heterogeneity of tumours and more aggressive phenotype [146]. The HIF-1 pathway acts as a key regulator of angiogenesis in both physiological (e.g., embryonic development, wound healing) and pathological (e.g., cancer, chronic inflammation) processes. HIF-1 works synergistically with other pro-angiogenic factors, namely VEGF, placental growth factor (PlGF), and angiopoietin 1/2 and upregulates their expression [147]. HIF-1 can be activated not only by hypoxia but also by genetic alterations in malignant cells that block HIF-1α ubiquitination, and therefore its proteasomal degradation [148]. Specifically, the deletion of tumour suppressor genes like *p53*, *p21*, *pRb*, or *PTEN* leads to HIF-dependent stimulation of VEGF and, thus, to angiogenesis stimulation [149]. Knowing that, HIF-1 seems to be a promising therapeutic target for many diseases linked to angiogenesis, including cancer [147]. Furthermore, HIF-1α induces exosome release via transactivating the small GTPase Rab22A in breast cancer [150]. Hypoxia-regulated exosome secretion in different tumours can be induced by an actin dynamics regulator RHO-associated protein kinase (ROCK), or calpain, which is responsible for membrane phospholipids asymmetry and membrane bending [151]. The hypoxic state causes a higher secretion of TDEs of altered content [152]. Alterations in exosome cargo under hypoxic conditions mediate tumour microenvironment remodelling and promote tumour progression, including immune evasion, angiogenesis, metastasis, and therapy resistance. The key proteins loaded to hypoxic exosomes include, for example, HIF-1α (nasopharyngeal carcinoma) [153], lysyl oxidases, PDGFs, thrombospondin-1 (TSP-1), plasminogen activator inhibitor 1 (PAI1), caveolin-1 (all in glioblastoma) [154–156], annexin II (prostate cancer) [157], or signal transducer and activator of transcription 3 (STAT3) (ovarian cancer) [152].

Cell death and proliferation

The replicative immortality of cancer cells is often accompanied by an altered sensitivity to regulated cell death (RCD), which includes apoptosis, necroptosis, ferroptosis, and pyroptosis [158]. RCD encompasses the organised demise of cells under the control of specific genes and molecular pathways, aiming to uphold homeostasis. Cancer is, among others, characterised by dysregulated cell death and increased proliferation of cancer cells. Typically, cancer cells sustain proliferative activity through the activation of the PI3K/AKT (phosphatidylinositol 3-kinase/protein kinase B, also PKB) or MAPK/ERK (mitogen-activated protein kinase/extracellular signal-regulated kinase) pathways. These pathways can be directly activated by TDEs. For example, in NSCLC, bladder and prostate cancer, PI3K/AKT is activated, while in gastric cancer, both the PI3K/AKT and the MAPK/ERK

signalling pathways are activated by TDEs [159]. TDEs are also able to support evasion from growth suppression. However, the role of TDEs in this process is less defined. For example, TDEs could downregulate growth suppression via delivering exosomal oncogenic H-Ras and N-Ras transcripts or Rab proteins [160]. The replicative immortality can be obtained by the upregulation of telomerase, which is stimulated by various transcription factors and coregulators. Factors that significantly modulate telomerase activity, such as c-Myc, p53 and β-catenin, are known to be TDE cargo, but a direct role of exosomes in telomerase activation is not known [159].

With ongoing research, it is becoming increasingly apparent that EVs possess the ability to modulate cell death responses in recipient cells. These EVs can be either derived from living cells or from apoptotic cells themself. For example, exosomes with membrane-bound TNF-α produced by fibroblasts can inhibit activation-induced cell death (AICD) in $CD4^+$ T-cells [161]. Similarly, AICD of T-cells can be triggered by Fas ligand-bearing exosomes [162]. Exosomes derived from N-myc amplified neuroblastoma cells enhance the survival of non-N-myc amplified cells by inducing chemoresistance to doxorubicin [163]. On the other hand, colorectal cancer cells can induce apoptosis of T-cells through the release of proapoptotic microvesicles [164]. Additionally, TDEs can contain inhibitors of apoptosis (IAP) such as survivin, XIAP, cIAP1 or cIAP2 [165], which can inhibit apoptosis in cancer cells. Bladder cancer TDEs were shown to inhibit apoptosis through the upregulation of Bcl-2 and cyclin D1, and Bax and caspase-3 downregulation in target cells [166].

A newly discovered group of EVs released during apoptosis, called apoptotic exosomes (ApoExos), may represent a significant player in communication and signalling in the TME. ApoExos are implicated in diverse pathophysiological processes, including vascular homeostasis, sterile inflammation, as well as proliferation and survival of cancer cells [167], and are released as a consequence of pre-apoptotic stress or post-apoptotic necrosis [168]. Autolysosomes were also identified as a site of ApoExos biogenesis, and caspase-3 as a key regulator of the secretion of various types of EVs, including ApoExos [169]. In glioblastoma, a highly aggressive brain cancer, it has been discovered that specific components of the spliceosomes present in ApoExos facilitate tumour cell proliferation and confer resistance to therapy [170]. ApoExos widely express exosomal marker CD63, lysosomal marker LAMP1 (lysosomal associated membrane protein 1), and HSP70, which is commonly expressed under apoptotic conditions [167]. A crucial role in regulated cell death, apoptosis and pyroptosis in particular, is played by a group of cysteine aspartic proteases known as caspases (casp), classified as apoptotic (casp-3/6/7/8/9) and inflammatory (casp-1/4/5/12) [171]. Caspases play a part in EV biogenesis, cargo loading and processing and can also be loaded into exosomes. For example, casp-3 dependent intra-vesicular cleavage of Bcl-xL (B-cell lymphoma-extra-large) is required for the uptake of EVs by malignant blood cells. Casp-3 inhibition then results in reduced cell proliferation of recipient tumour cells [172]. Targeting caspases as novel anticancer therapy is being currently developed with a focus on small drugs or gene editing [173].

Necroptosis is defined as a regulated form of cell death accompanied by inflammation. The activation of necroptosis could also mediate the immune escape of cancer cells and the rise of metastasis through the attraction of tumour-associated macrophages, for instance, in pancreatic cancer cells by releasing CXCL5 (C-X-C motif chemokine 5) [174, 175]. Surprisingly, necroptotic cells are also able to release EVs loaded with various cargo, including proteome unique for necroptotic EVs. Specifically, casp-8, mixed lineage kinase domain-like kinase (MLKL), charged multivesicular body protein 4B (CHMP4B), ESCRT-III components, several Rab proteins (Rab5A/B/C), SNAREs, flotillin-1/2, and lipid-raft-associated proteins are detected in higher levels in necroptotic EVs. In addition, necroptotic EVs induce the secretion of pro-inflammatory molecules, such as IL-6, TNF-α, and CCL2 (C–C motif chemokine ligand 2) [176, 177]. Since many cancers are associated with a decrease or absence of necroptotic factors, which leads to necroptosis resistance, necroptosis appears to be a promising target for cancer therapy [177]. TDEs preferentially target malignant cells, as will be discussed later, and can also be engineered to start the necroptosis pathway. A novel therapeutic strategy proposed a method for CRISPR/Cas9 delivery via exosomes. In principle, two CRISPR/Cas9 vectors might target and inactivate IAP1/2 (inhibitor of apoptosis protein 1/2) and casp-8, resulting in necroptosis activation [178].

Another form of RCD, ferroptosis, is characterised by an iron-dependent accumulation of lipid hydroxyperoxides and is regulated by glutathione peroxidase 4 (GPX-4). The intracellular iron homeostasis contributes to ferroptosis sensitivity in diverse cells. Since free iron levels vary between various stages of cancer (metastatic vs. non-metastatic cells), differences in ferroptosis sensitivity are expected. To set an example, breast cancer cells can resist ferroptotic cell death by upregulating iron export out of the cell, for instance, via exosomes. This resistance can be suppressed by a blockage of prominin 2, a pentaspanin protein that promotes MVBs formation, and thus iron secretion via exosomes [179]. In the TME, ferroptosis drives macrophage polarisation and thus promotes

tumour growth. Specifically, extracellular protein K-ras was found to be packed into TDEs that are uptaken into macrophages. K-ras uptake leads to a switch from M1 to M2 macrophage phenotype and cancer progression. Similarly to necroptosis, ferroptosis-inducing components, such as erastin, can be loaded into exosomes to target cancer cells [180]. For instance, imidazole ketone erastin (IKE) reduced tumour growth by inducing ferroptosis in a diffuse large B cell lymphoma (DLBCL) mouse xenograft model [181].

Immune system, inflammation, and immune evasion

Immune evasion in cancer refers to the ability of cancer cells to evade or escape recognition and attack by the immune system. Inflammation and immune evasion are interconnected processes that play crucial roles in cancer development and progression. For example, chronic inflammation can suppress cytotoxic T-cell activity and was associated with tumour progression [182, 183]. TDEs are known to be strongly involved in these immunomodulatory processes. Cytokines, small proteins, which are key mediators of immunity and inflammation, are extensively associated with exosomes. These cytokines include IL-1α, IL-1β, IL-6, IL-8, IL-18, TNF-α, COX-2 (cyclooxygenase 2), VEGF, CCL2, CCL3, CCL4, CCL5, CCL20 [184, 185]. The proinflammatory response may also be stimulated by HSP70, which is elevated in cancer exosomes. HSP70 enriched exosomes can trigger NF-κB activation and TNF-α release or increased IFN-γ and IL-13 production [185, 186]. The group of aminoacyl-tRNA synthetases (ARSs) is also involved in immune and inflammatory modulation, angiogenesis, or apoptosis if it occurs extracellularly. Specifically, lysyl-tRNA synthetase (KRS) is secreted via colorectal cancer cell-derived exosomes, which induces proinflammatory cytokines production [187].

Tumour cells are capable of escaping the immune system reaction with the help of tumour-infiltrating regulatory T-cells (Tregs) by releasing immunosuppressive cytokines, namely IL-10 and TGFβ1 [188]. TDEs enable Treg generation and expansion, thus promoting cancer progression. Moreover, Th17-cells ($CD4^+$ T-lymphocytes secreting essential amounts of IL-17A [189]) might also induce immunosuppression and angiogenesis to facilitate tumour progression, or they can recruit immune cells to promote antitumour immune response [190]. The role of Th17 in the context of tumour growth depends on the ratio of Treg/Th17 [191]. TDEs also highly express tumour antigens on their surface. This characteristic has led to the suggestion that they could serve as tumour vaccines. However, they can also suppress T-cell signalling molecules and induce apoptosis in T-lymphocytes. For instance, ovarian cancer cell-derived exosomes exhibit FasL to suppress the immune response by inhibiting T-cells and inducing their apoptosis [192].

TNF-α is a pro-inflammatory cytokine mainly produced by macrophages, NK cells, and T-cells, but also by non-immune cells like fibroblasts, endothelial cells, and neurons. TNF-α exhibits a dual role in relation to cancer. On the one hand, the anticancer property of TNF-α is to induce cancer cell death, but on the other hand, TNF-α also stimulates cell proliferation, migration and angiogenesis and is highly overexpressed in many cancers [193, 194]. Since TNF-α is often present in TDEs, for example, in colorectal carcinoma, there may be a beneficial effect of decreasing TNF-α in anti-cancer therapy [195]. Natural killers (NK) are a group of cells involved in antitumour immune response via the natural killer group 2 member D (NKG2D) activating receptor [196]. Loss of the NKG2D receptor or its function leads to immune evasion. TDEs can contribute to NK-cells activity suppression by the expression of NKG2D ligands, which depress NKG2D receptors on NK-cells and inhibit their cytotoxicity [197].

In addition, tumour-derived exosomes are known to inhibit the maturation and differentiation of monocytes (monocytes give rise to macrophages and dendritic cells), and consequently induce immunosuppression. The mechanism of immunosuppression might be dependent on the protein composition of exosomes, namely TGFβ, IL-6, or prostaglandin E2 (PGE2) [198]. To set an example, the secretion of IL-6, which functions in the PI3K/AKT/mTOR pathway [199], by TDEs inhibits the differentiation of bone marrow myeloid precursors into DCs. DC maturation can also be affected by the intake of exosomal TGF-β1 by immature DCs [200]. Furthermore, TDEs can influence macrophages to switch into polarised M2 phenotype. For example, TDEs derived from triple-negative breast cancer (TNBC) play role in M2 macrophages polarisation, which benefits tumour growth and lymph-node metastasis formation [201]. M2 macrophages then secrete high amounts of cytokines, growth factors and enzymes, including already mentioned VEGF, PDGF, TGFβ, and some MMPs, that facilitate immunosuppression, angiogenesis, metastasis, or treatment resistance [202, 203]. Monocytes that fused with TDEs possess an immunosuppressive effect, which leads to a high CD14 expression. $CD14^+$ monocytes (but without HLA-DA expression) were proven to be increased in the serum of many cancer patients as tumour-induced immunosuppressors [200]. To promote their growth and proliferation, tumours also respond to endoplasmic reticulum stress (ER stress), which helps them evade the immune system recognition and response. ER stress also increases the production of pro-inflammatory factors in macrophages and modifies immune cell function

[204]. A study on oral squamous cell carcinoma (OSCC) revealed that macrophage polarisation toward the M2 subtype is promoted by programmed death ligand 1 (PD-L1) enriched exosomes derived from ER-stressed cancer cells. PD-L1 overexpression was linked to the poor overall survival of OSCC patients [205, 206]. PD-L1 expression can also be enhanced in acidic TME [207]. Macrophages can also be switched to the M2 phenotype by high lactic acid and the hypoxic environment through the expression of arginase 1 (ARG1) [208].

Furthermore, myeloid-derived suppressor cell (MDSC) accumulation negatively affects antigen processing and presentation and produces immunosuppressive factors. This function of MDSCs is potentiated by TDEs [200]. In renal cancer, exosomal HSP70 enhances MDSC activation via activating TLR2 signalling [209]. Next, TGFβ and PGE2 in exosomes isolated from breast cancer help to accumulate MDSCs, thus enhancing tumour growth [210]. Exosomes derived from OSCC cells under hypoxic conditions enhanced the immunosuppressive function of MDSCs to interfere with the group of $\gamma\delta$ T-cells via miR-21/PTEN/PD-L1 signalling [211].

Pre-metastatic niche formation, invasion, and metastasis

The formation of pre-metastatic niches, invasion, and metastasis are critical steps of cancer progression and are responsible for the widespread dissemination of cancer cells throughout the body. Exosomal proteins participate in various pro-metastatic mechanisms, including invasive behaviour promotion, induction of tumour neovascularisation, disrupting vascular barrier, mediating specific organ colonisation, and setting pre-metastatic niches. Tumour-derived exosomes participate in permissive niche formation, supporting the "seed and soil" hypothesis. This concept was introduced by Stephen Paget [212], who proposed that tumour cell (seed) growth requires the appropriate local microenvironment (soil). Although circulating tumour cells (CTCs) can be found in the vasculature of multiple organs, they do not necessarily give rise to metastasis. However, in advance of tumour cell dissemination, primary tumours can appropriate secondary sites, creating a pre-metastatic niche, which facilitates subsequent colonisation of this location by tumour cells [213, 214]. This is provided by the systemic signalling of tumour cells, including exosome secretion [215].

The essential TDEs-carried molecules for ECM remodelling and epithelial-mesenchymal transition (EMT) are TGF-β, HIF1α, β-catenin, IL-6, caveolin-1, or vimentin [216]. Tumour-derived EGFR (epidermal growth factor receptor)-containing exosomes are capable of remodelling the liver microenvironment presenting a novel mechanism concerning liver-tropism of gastric cancer metastasis [79]. Hepatocellular carcinoma (HCC) and breast cancer are known to metastasise in bone, which causes fractures due to osteolytic bone destruction. To survive, metastasised cells interfere with normal bone remodelling through the suppression of bone formation and activation of bone resorption. This is enabled by osteoclast differentiation, which leads to the release of bone-derived factors that support tumour growth [217]. HCC-derived exosomes were highly enriched in Tumour necrosis factor-α (TNF-α), which promotes osteoclast differentiation. TNF-α also regulates hepatocyte proliferation in liver cancer under uncontrolled inflammation [218]. To conclude, primary TDEs contribute to tumour metastasis by educating the primary and distant soil [219]. Moreover, exosomes also play a crucial role in the metastatic process by recruiting mesenchymal stem cells (MSCs) or regulating nutrient availability in the TME. MSCs associated with the tumour-like phenotype undergo morphological and structural changes due to TDE induction. The tumour-like phenotype includes atypical microvilli, pseudopods, higher vesicle secretion, and other changes, such as higher proliferation, invasive potential, and migration. Furthermore, proteins loaded in exosomes directly identify organs that are suitable for metastatic site formation [124]. Exosomal proteins not only promote tumour growth and metastasis but also serve as early markers of disease, as they are easily accessible for clinical detection and highly secreted in cancer patients [37]. HSP70 was found to be expressed in the membranes of TDEs, in contrast to normal cells. Levels of HSP70-enriched exosomes are also increased in metastatic patients compared to non-metastatic patients or healthy individuals, thus, HSP70 may be used as a biomarker of cancer progression [220].

In breast cancer exosomes, fibronectin is involved in promoting metastasis via EMT and production of pro-inflammatory cytokines and MMP-9 [221], metastasis-associated protein 1 (MTA1) is linked to enhanced metastatic potential and unfavourable prognosis in breast cancer patients [222]. Exosomal TSP1 mediates the disruption of endothelial cell integrity and the reduction of junction proteins VE-cadherin and ZO-1 expression, thus, facilitating trans-endothelial migration of breast cancer cells [221, 223]. A study on mice with breast cancer revealed that exosomal nephronectin (NPNT) regulates the ability of breast cancer cells to colonise lung [224]. Cell migration-inducing and hyaluronan-binding protein (CEMIP) from brain metastatic cell-derived exosomes contributes to brain tumour invasion and association with brain vasculature, leading to enhanced tumour growth. In addition, CEMIP induces pro-inflammatory cytokines secretion, such as chemokines coded by *CCL/CXCL* genes or the *TNF* superfamily, thus promoting metastasis [225]. S100

calcium-binding protein A4 (S100A4) plays a pivotal role in tumour metastasis by regulating ECM remodelling, cellular adhesion, and motility. S100A4 identified in highly metastatic HCC exosomes promotes metastasis via the phosphorylation of STAT3 and upregulation of osteopontin, a typical HCC promoter [226]. In pancreatic cancer cell-derived exosomes, proteins CXCR4 (C-X-C motif chemokine receptor 4) and MMP-9 were found to enhance the metastatic capabilities of pancreatic cancer cells [227]. Similarly, enhanced secretion of exosomal MMP-1 promotes tumour cell invasion in gastrointestinal stromal tumours (GIST). The oncogenic protein tyrosine kinase (KIT)-containing exosomes trigger the conversion of progenitor smooth muscle cells to tumour-like phenotype and mediate the release of MMP-1 [228].

We have mentioned so far that cancer cells are able to take advantage of exosomal protein cargo by its uptake, however, they can also decrease intracellular levels of unwanted proteins or tumour-suppressors via exosome secretion. For example, metastatic duodenal carcinoma cells (AZ-P7a) do not tolerate intracellular accumulation of polyadenylate-binding protein 1 (PABP1). Consequently, PABP1 was found to be highly enriched in metastatic duodenal carcinoma (AZ-P7a) derived exosomes compared to normal cells (AZ-521) [229]. Furthermore, ST6Gal 1(beta-galactoside alpha-2,6-sialyltransferase)-depleted colorectal cancer cells remove tumour-metastasis suppressor kangai 1 (KAI1, also known as CD82) via exosomes as a mechanism to enhance metastatic formation [124, 230]. Stimulator of interferon genes (STING), which serves as an adaptor protein in the innate immune response to DNA damage or virus infection, can also be translocated into EVs through interaction with signal transducing adapter molecule (STAM). The translocation of STING into EVs served for STING degradation. EV-secreted STING downregulated the innate immune response [231].

Cancer treatment and therapy resistance

The effectiveness of cancer screening, as well as successful early diagnosis and accurate risk assessment for cancer, are highly dependent on the specificity and quality of the biomarkers used. Many studies suggest that TDEs may be very promising cancer biomarkers. In recent years, exosomes were widely investigated in clinical trials (listed on ClinicalTrials.gov (https://clinicaltrials.gov/) with applications as biomarkers, drug-delivery systems, cancer vaccines, or exosome-based therapies. ClinicalTrials.gov includes 116 studies, of which 58 (50%) have been involved in studies of exosome biomarkers and 74.13% of those 58 trials were in relation to cancer. Another 33 studies (28.44%) have been registered for exosome-based therapy, most of them were focused on exosomes derived from MSCs. Overall, 6 studies (5.17%) have been registered for drug-delivery systems, and 2 clinical trials (1.72%) for exosome-based vaccines. The remaining 17 trials (14.66%) have been focused on basic analysis [232]. Here we present clinical trials from ClinicalTrials.gov focussed on exosomal protein content as a potential biomarker in relation to cancer (Table 1).

Alterations in protein or nucleic acid content of exosomes in plasma strongly correlate with pathological states of many diseases, including cancer even in early stages. Each millilitre of human blood contains over 10^9 exosomes; thus in vivo detection of exosomes is highly sensitive [37, 234, 235]. The summary of exosomal proteins with potential for clinical diagnostic applications of various types of cancer is listed in Table 2.

Another great potential of exosomes lies in their use as drug carriers. As mentioned before, exosomes protect their content with the lipid bilayer, and they can easily enter recipient cells. In addition, as exosomes are native to the organism, they do not cause any major side effects [265]. The ability of exosomes to serve as drug carriers was proven in many studies, for example, cisplatin-loaded exosomes extended the survival time

Table 1 Clinical trials focused on exosomal proteins as cancer biomarkers

Number	Status	Cancer type	Exosomal content
NCT01840306	Completed	HER2 + Breast Cancer	Not specified
NCT05463107	Not yet recruiting	Follicular Thyroid Cancer	thyroglobulin, Gal-3, calprotectin A8/A9, keratin 8/19, afamin, angiopoietin-1
NCT02862470	Completed	Anaplastic Thyroid Cancer	thyroglobulin, Gal-3 [233]
NCT04529915	Active	NSCLC	Not specified
NCT05735704	Recruiting	Haematological malignancies	Not specified
NCT03581435	Unknown	Gallbladder Carcinoma	Protein profile
NCT03985696	Recruiting	Non-Hodgkin B-cell Lymphomas	CD-20, PD-L1

Gal-3 galectin-3, *NCT* National Clinical Trials, *PD-L1* Programmed death-ligand 1, *CD* cluster of differentiation

Table 2 Exosomal proteins with potential for cancer diagnostics

Protein marker	Cancer type	Fluid	Diagnostic efficiency	Reference
Panel of 17 exosomal proteins[a], TMEM256	Prostate cancer	Urine	Sensitivity 100%, specificity 60–100% (highest TMEM256)	[236–238]
Del-1	Breast cancer	Plasma	Sensitivity 94.70%, specificity 86.36%	[239, 240]
CA125	Ovarian cancer	Plasma	Sensitivity 71%, specificity 98%	[241–244]
GPC-1	Pancreatic cancer	Peripheral blood, Serum	Sensitivity 100%, specificity 100%	[244–247]
c-Met	Pancreatic cancer	Serum	Sensitivity 70%, specificity 85%	[238, 248]
GKN-1	Gastric cancer	Serum	Sensitivity 91.2%, specificity 96.0%	[249, 250]
L1CAM	Gastric cancer	Serum	Sensitivity 83.1%, specificity 62.2%	[251]
Panel of 6 exosomal proteins[b]	Colorectal cancer	Tissue	Sensitivity 70–100%, specificity 70–100%	[252]
CAE	Colorectal cancer	Serum	Sensitivity 89.47%, specificity 95.88%	[253, 254]
LG3BP	Hepatocellular carcinoma	Serum	Sensitivity 96.6%, specificity 71.8%	[238, 255, 256]
PIGR	Hepatocellular carcinoma	Serum	Sensitivity 82.8%, specificity 71.8%	[238, 255, 256]
TACSTD2	Bladder cancer	Urine	Sensitivity 73.6%, specificity 76.5%	[238, 257]
CD151	Lung cancer	Plasma	Sensitivity 60%, specificity 75%	[37, 258]
CD91	Lung cancer	Serum	Sensitivity 60%, specificity 89%	[238, 259]
AHSG	NSCLC	Serum	Sensitivity 54.9%, specificity 84.8%	[89]
CXCL7	OSCC	Serum	Sensitivity 60%, specificity 80%	[260]
BATF2	Nasopharyngeal carcinoma	Serum	Sensitivity 81%, specificity 82%	[261, 262]
PD-L1	Melanoma	Plasma	Sensitivity 80%, specificity 89.47%	[84]
Caveolin-1	Melanoma	Plasma	Sensitivity 69.0%, specificity 96.3%	[263]
EGFR VIII	Glioblastoma	Plasma	Sensitivity 68%, specificity 100%	[137, 238, 264]

Del-1 developmental endothelial locus-1, *GPC-1* glypican-1, *c-Met* proto-oncogene mesenchymal-epithelial transition factor, *GKN-1* gastrokine 1, *L1CAM* L1 cell adhesion molecule, also CD171, *CAE* carcinoembryonic antigen, *LG3BP* galectin-3-binding protein, *PIGR* polymeric immunoglobulin receptor, *TACSTD2* tumor-associated calcium signal transducer 2, *AHSG* alpha-2-HS-glycoprotein, *CXCL7* C-X-C motif ligand 7, *BATF2* Basic Leucine Zipper ATF-Like Transcription Factor 2

[a] Including: TMEM256 (transmembrane protein 256), ADIRF (adipogenesis regulatory factor), LAMTOR1 (late endosomal/lysosomal adaptor and mitogen-activated protein kinase 1), plastin-2, several Rab-class members (e.g. Rab-2A, Rab-3B, Rab-3D, Rab-7A, Rab-6A), VALT (V-type proton ATPase 16 kDa proteolipid subunit), STEAP4 (Six-transmembrane epithelial antigen of prostate 4), DJ-1 (protein deglycase/ Parkinson disease protein 7), S100-P, synaptotagmin-like protein 4, ADP-ribosylation factor-like protein 8B, proton myo-inositol cotransporter, tetraspanin-6

[b] Including: NHP2 (H/ACA ribonucleoprotein complex subunit 2), OLFM4 (olfactomedin-4), TOP1 (DNA topoisomerase 1), SAMP (serum amyloid P-component), TAGL (transgelin), TRIM28 (tripartite motif-containing protein 28)

of mice with ovarian cancer [266], macrophage-derived exosomes with paclitaxel inhibited Lewis lung cancer cells proliferation, and even possess better stability of loaded paclitaxel than other loading approaches [267]. Adding more, since tumour cells frequently communicate via exosomes, TDEs may also deliver therapeutic drugs to other tumour cells. For instance, prostate cancer-derived exosomes loaded with paclitaxel can be uptaken by prostate cancer cells [268], similarly, exosomes from pancreatic cancer cells can deliver curcumin and induce cell apoptosis in pancreatic cancer cells [269]. Many preclinical studies on the role of exosomes as therapeutic drug carriers for cancer therapy have already been assessed, but more must be investigated [90]. Another promising therapeutic approach might be targeting cancer exosome release itself. Exosome secretion is mediated by an intracellular increase of calcium (Ca^{2+}), which is regulated by the H^+/Na^+ and Na^+/Ca^{2+} channels [270]. Blocking these channels with dimethyl amiloride (DMA), for example, reduced the amount of secreted exosomes in mice with colon carcinoma (CT26) [271].

Monoclonal antibodies (mAbs) are used in cancer immunotherapy to stimulate the function of the immune system and enhance the targeting of conventional anticancer drugs. Upon binding to tumour-associated antigens (TAAs), mAbs can disrupt crucial pathways that play a significant role in cancer cell activity. Nevertheless, TDEs carry several TAAs, therefore, they can decrease the efficacy of mAbs [272] as TAAs can bind antibodies used against cancer cells, which results in insufficient amounts of antibodies that can reach cancer tissue. For example, exosomes secreted from cancer cells reduce the therapeutic activity of trastuzumab (HER2 blocker, normally activates Ab-dependent cell-mediated cytotoxicity) in breast cancer therapy [273]. On the other hand, TDEs can represent an attractive alternative source of TAAs for cell-free cancer vaccines for personalised tumour immunotherapy [274]. TDEs can transfer TAAs to antigen-presenting dendritic cells (DCs). Some studies [275]

showed that TDEs promote DC maturation and enhance antigen cross-presentation more potently than tumour cell lysates, which directly contributed to a more robust tumour-specific response of cytotoxic T-lymphocytes. Consequently, DCs treated by TDEs have the potential to effectively reverse immunosuppression in the TME. There have also been developed cell-free tumour vaccines containing α-fetoprotein-enriched DC-derived exosomes, which stimulate immune cells to produce IFN-γ and IL-2 and reduce the expression of TGFβ and IL-10 at the site of the tumour, thus, inducing antigen-specific response to cancer cells. This led to tumour growth inhibition and metastatic ability limitation [276].

Moreover, exosomal PD-L1 might represent a promising therapeutic target. It has been shown that metastatic cancer cells produce a high level of exosomes, that carry PD-L1 on their surface. PD-L1 then binds the PD-1 receptor on T-cells leading to the suppression of T-cell activity [84]. Blockade of PD-L1 can possibly bypass the current resistance to antibody therapies [277]. PD-L1 and CTL-associated antigen 4 (CTLA-4) serve as checkpoint receptors that are targeted for relieving exhaustion of CD8 T-cells caused by immunosuppression within the TME [278]. In addition, more possible targets may be relevant in this treatment strategy, namely T-cell immunoglobulin- and mucin-domain-containing molecule 3 (Tim-3), and its ligand galectin-9 [279]. Additionally, immune cell-derived exosomes can also participate in adoptive cell therapy (ACT), immunotherapy based on redelivering tumour-infiltrating lymphocytes (TILs) [280].

Concluding remarks

As we discussed, exosomes are involved in many critical steps of cancer progression, including ECM remodelling, angiogenesis, immune regulation, invasion, metastasis, and therapy resistance, and their content plays a pivotal role as a signalling hub in the tumour microenvironment. Exosomal cargo is protected from enzymatic degradation because it is encapsulated within the lipid bilayer of exosomes, allowing exosomal proteins to retain their native conformation and functionality. Specific proteins loaded to exosomes not only reflect the proteome of the cell of origin but also serve as markers of the pathological state of the cell. As the exosomal content varies depending on the cell of origin, exosomes may be used as specific biomarkers that can provide information about the genetic and molecular heterogeneity of tumours. Exosomes play a significant role in intercellular communication, and their content can provide valuable information for cancer diagnosis, prognosis, and treatment (clinical studies dealing with exosomal proteins are listed in Table 1). Moreover, exosomal uptake by certain cells in the TME can be applied to cancer therapy, as exosomes can be loaded with various treatment drugs. The quantity of exosomes in the bloodstream or other body fluids may also indicate the stage and aggressiveness of cancer, as higher levels of exosomes may be associated with advanced disease. Alterations in tumour cell metabolism and decreased pH conditions within the TME promote TDE secretion.

Exosomes can serve as a source of "liquid biopsy" material, which can replace or complement traditional tissue biopsies. This non-invasive approach is suitable for regular testing and monitoring and is particularly useful for patients for whom invasive procedures are not possible. Exosomes find primary clinical utility as biomarkers, cell-free therapeutic agents, vehicles for drug delivery, and as a component in cancer vaccines. Ongoing research continues to uncover their specific roles and applications in different cancer types, bringing us closer to more effective and personalized approaches to managing cancer. While exosomes hold great promise, challenges include standardizing isolation and analysis techniques, as well as distinguishing between exosomes from cancer cells and those from non-malignant cells.

Authors' contributions
KH conceived the structure and wrote the manuscript, MR wrote the manuscript and created images, JB and MM revised the manuscript. All authors read and approved the final manuscript.

Funding
This work was supported by the Ministry of Health of the Czech Republic (NU22-03-00202), by the Grant Agency of the Czech Republic (GACR-21-06873 S), and by funds from Specific University Research Grant, as provided by the Ministry of Education, Youth and Sports of the Czech Republic in the year 2023 (MUNI/A/1370/2022 and MUNI/A/1343/2022). We also thank the project National Institute for Cancer Research (Programme EXCELES, ID project no. LX22NPO5102), funded by the European Union-Next Generation EU. This work was also supported by the National Institute for Neurological Research (Programme EXCELES, ID Project No. LX22NPO5107), funded by the European Union-Next Generation EU.

Availability of data and materials
Not applicable.

Declarations

Competing interests
The authors declare no competing interests.

Received: 27 September 2023 Accepted: 24 November 2023
Published online: 10 January 2024

References
1. Iraci N, Leonardi T, Gessler F, Vega B, Pluchino S. Focus on extracellular vesicles: physiological role and signalling properties of extracellular membrane vesicles. Int J Mol Sci. 2016;17:171.
2. van Niel G, et al. Challenges and directions in studying cell-cell communication by extracellular vesicles. Nat Rev Mol Cell Biol. 2022;23:369–82.
3. Lischnig A, Bergqvist M, Ochiya T, Lässer C. Quantitative proteomics identifies proteins enriched in large and small extracellular vesicles. Mol Cell Proteomics MCP. 2022;21:100273.

4. van Niel G, D'Angelo G, Raposo G. Shedding light on the cell biology of extracellular vesicles. Nat Rev Mol Cell Biol. 2018;19:213–28.
5. Yáñez-Mó M, et al. Biological properties of extracellular vesicles and their physiological functions. J Extracell Vesicles. 2015;4:27066.
6. Hallal S, Tűzesi Á, Grau GE, Buckland ME, Alexander KL. Understanding the extracellular vesicle surface for clinical molecular biology. J Extracell Vesicles. 2022;11:e12260.
7. Pathan M, et al. Vesiclepedia 2019: a compendium of RNA, proteins, lipids and metabolites in extracellular vesicles. Nucleic Acids Res. 2019;47:D516–9.
8. Reátegui E, et al. Engineered nanointerfaces for microfluidic isolation and molecular profiling of tumor-specific extracellular vesicles. Nat Commun. 2018;9:175.
9. Freeman DW, et al. Altered extracellular vesicle concentration, cargo, and function in diabetes. Diabetes. 2018;67:2377–88.
10. Tian J, Casella G, Zhang Y, Rostami A, Li X. Potential roles of extracellular vesicles in the pathophysiology, diagnosis, and treatment of autoimmune diseases. Int J Biol Sci. 2020;16:620.
11. Théry C, et al. Minimal information for studies of extracellular vesicles 2018 (MISEV2018): a position statement of the International society for extracellular vesicles and update of the MISEV2014 guidelines. J Extracell Vesicles. 2018;7:1535750.
12. Lötvall J, et al. Minimal experimental requirements for definition of extracellular vesicles and their functions: a position statement from the international society for extracellular vesicles. J Extracell Vesicles. 2014;3:26913.
13. Witwer KW, Théry C. Extracellular vesicles or exosomes? On primacy, precision, and popularity influencing a choice of nomenclature. J Extracell Vesicles. 2019;8:1648167.
14. Johnstone RM, Adam M, Hammond JR, Orr L, Turbide C. Vesicle formation during reticulocyte maturation. Association of plasma membrane activities with released vesicles (exosomes). J Biol Chem. 1987;262:9412–20.
15. Pan BT, Teng K, Wu C, Adam M, Johnstone RM. Electron microscopic evidence for externalization of the transferrin receptor in vesicular form in sheep reticulocytes. J Cell Biol. 1985;101:942–8.
16. Raposo G, et al. B lymphocytes secrete antigen-presenting vesicles. J Exp Med. 1996;183:1161–72.
17. Wolfers J, et al. Tumor-derived exosomes are a source of shared tumor rejection antigens for CTL cross-priming. Nat Med. 2001;7:297–303.
18. Valadi H, et al. Exosome-mediated transfer of mRNAs and microRNAs is a novel mechanism of genetic exchange between cells. Nat Cell Biol. 2007;9:654–9.
19. de la Torre Gomez C, Goreham RV, Bech Serra JJ, Nann T, Kussmann M. "Exosomics"—a review of biophysics, biology and biochemistry of exosomes with a focus on human breast milk. Front Genet. 2018;9:92.
20. Kim DK, Kang B, Kim OY, Choi D, Lee J, Kim SR, et al. EVpedia: an integrated database of high-throughput data for systemic analyses of extracellular vesicles. J Extracell Vesicles. 2013;2:20384. https://doi.org/10.3402/jev.v2i0.20384.
21. Keerthikumar S, et al. ExoCarta: a web-based compendium of exosomal cargo. J Mol Biol. 2016;428:688–92.
22. Chen I-H, et al. Phosphoproteins in extracellular vesicles as candidate markers for breast cancer. Proc Natl Acad Sci U S A. 2017;114:3175–80.
23. Doyle LM, Wang MZ. Overview of extracellular vesicles, their origin, composition, purpose, and methods for exosome isolation and analysis. Cells. 2019;8:727.
24. Sharma R, Huang X, Brekken RA, Schroit AJ. Detection of phosphatidylserine-positive exosomes for the diagnosis of early-stage malignancies. Br J Cancer. 2017;117:545–52.
25. D'Souza-Schorey C, Schorey JS. Regulation and mechanisms of extracellular vesicle biogenesis and secretion. Essays Biochem. 2018;62:125–33.
26. Luan X, et al. Engineering exosomes as refined biological nanoplatforms for drug delivery. Acta Pharmacol Sin. 2017;38:754–63.
27. Laulagnier K, et al. Mast cell- and dendritic cell-derived exosomes display a specific lipid composition and an unusual membrane organization. Biochem J. 2004;380:161–71.
28. Gurung S, Perocheau D, Touramanidou L, Baruteau J. The exosome journey: from biogenesis to uptake and intracellular signalling. Cell Commun Signal. 2021;19:47.
29. Zhang Y, Liu Y, Liu H, Tang WH. Exosomes: biogenesis, biologic function and clinical potential. Cell Biosci. 2019;9:19.
30. Sakai-Kato K, Yoshida K, Takechi-Haraya Y, Izutsu K. Physicochemical characterization of liposomes that mimic the lipid composition of exosomes for effective intracellular trafficking. Langmuir. 2020;36:12735–44.
31. Tamkovich SN, Tutanov OS, Laktionov PP. Exosomes: generation, structure, transport, biological activity, and diagnostic application. Biochem Mosc Suppl Ser Membr Cell Biol. 2016;10:163–73.
32. Brodeur A, et al. Apoptotic exosome-like vesicles transfer specific and functional mRNAs to endothelial cells by phosphatidylserine-dependent macropinocytosis. Cell Death Dis. 2023;14:1–15.
33. Rausch L, et al. Phosphatidylserine-positive extracellular vesicles boost effector CD8+ T cell responses during viral infection. Proc Natl Acad Sci. 2023;120:e2210047120.
34. Hanelova K, et al. Autophagy modulators influence the content of important signalling molecules in PS-positive extracellular vesicles. Cell Commun Signal. 2023;21:120.
35. Skotland T, Hessvik NP, Sandvig K, Llorente A. Exosomal lipid composition and the role of ether lipids and phosphoinositides in exosome biology. J Lipid Res. 2019;60:9–18.
36. Haraszti RA, et al. High-resolution proteomic and lipidomic analysis of exosomes and microvesicles from different cell sources. J Extracell Vesicles. 2016;5:32570.
37. Li W, et al. Role of exosomal proteins in cancer diagnosis. Mol Cancer. 2017;16:145.
38. Skryabin GO, Komelkov AV, Savelyeva EE, Tchevkina EM. Lipid rafts in exosome biogenesis. Biochem Mosc. 2020;85:177–91.
39. Kugeratski FG, et al. Quantitative proteomics identifies the core proteome of exosomes with syntenin-1 as the highest abundant protein and a putative universal biomarker. Nat Cell Biol. 2021;23:631–41.
40. Yang Y, Hong Y, Cho E, Kim GB, Kim I-S. Extracellular vesicles as a platform for membrane-associated therapeutic protein delivery. J Extracell Vesicles. 2018;7:1440131.
41. Cruz De los Santos M, Dragomir MP, Calin GA. The role of exosomal long non-coding RNAs in cancer drug resistance. Cancer Drug Resist. 2019;2:1178–92.
42. Miyado M, Kang W, Kawano N, Miyado K. Microexosomes versus exosomes: shared components but distinct structures. Regen Ther. 2019;11:31–3.
43. Al-shubaily FA, Al-Zahrani MH. Characterization and fine structure of exosomes. In: Alzahrani FA, Saadeldin IM, editors. Role of exosomes in biological communication systems. Springer; 2021. p. 27–75. https://doi.org/10.1007/978-981-15-6599-1_2.
44. Pegtel DM, Gould SJ. Exosomes. Annu Rev Biochem. 2019;88:487–514.
45. Juan T, Fürthauer M. Biogenesis and function of ESCRT-dependent extracellular vesicles. Semin Cell Dev Biol. 2018;74:66–77.
46. Alonso Y Adell M, Migliano SM, Teis D. ESCRT-III and Vps4: a dynamic multipurpose tool for membrane budding and scission. FEBS J. 2016;283:3288–302.
47. Jadli AS, Ballasy N, Edalat P, Patel VB. Inside(sight) of tiny communicator: exosome biogenesis, secretion, and uptake. Mol Cell Biochem. 2020;467:77–94.
48. Yue B, et al. Exosome biogenesis, secretion and function of exosomal miRNAs in skeletal muscle myogenesis. Cell Prolif. 2020;53:e12857.
49. Colombo M, et al. Analysis of ESCRT functions in exosome biogenesis, composition and secretion highlights the heterogeneity of extracellular vesicles. J Cell Sci. 2013;126:5553–65.
50. Li S, Lin Z, Jiang X, Yu X. Exosomal cargo-loading and synthetic exosome-mimics as potential therapeutic tools. Acta Pharmacol Sin. 2018;39:542–51.
51. Wei D, et al. RAB31 marks and controls an ESCRT-independent exosome pathway. Cell Res. 2021;31:157–77.
52. Kenific CM, Zhang H, Lyden D. An exosome pathway without an ESCRT. Cell Res. 2021;31:105–6.
53. Mathieu M, Martin-Jaular L, Lavieu G, Théry C. Specificities of secretion and uptake of exosomes and other extracellular vesicles for cell-to-cell communication. Nat Cell Biol. 2019;21:9–17.
54. Flaumenhaft R. Chapter 18 - platelet secretion. In: Michelson AD, editors. Platelets. 3rd ed. Academic Press; 2013. p. 343–366. https://doi.org/10.1016/B978-0-12-387837-3.00018-3.

55. Jan AT, et al. Expedition into exosome biology: a perspective of progress from discovery to therapeutic development. Cancers. 2021;13:1157.
56. Ostrowski M, et al. Rab27a and Rab27b control different steps of the exosome secretion pathway. Nat Cell Biol. 2010;12:19–30.
57. Gupta S, Knowlton AA. HSP60 trafficking in adult cardiac myocytes: role of the exosomal pathway. Am J Physiol Heart Circ Physiol. 2007;292:H3052-3056.
58. Wan C, et al. Exosome-related multi-pass transmembrane protein TSAP6 is a target of rhomboid protease RHBDD1-induced proteolysis. PLoS One. 2012;7:e37452.
59. Simonsen A, Tooze SA. Coordination of membrane events during autophagy by multiple class III PI3-kinase complexes. J Cell Biol. 2009;186:773–82.
60. Toda Y, et al. Effective internalization of U251-MG-secreted exosomes into cancer cells and characterization of their lipid components. Biochem Biophys Res Commun. 2015;456:768–73.
61. Morishita M, Takahashi Y, Nishikawa M, Takakura Y. Pharmacokinetics of exosomes-an important factor for elucidating the biological roles of exosomes and for the development of exosome-based therapeutics. J Pharm Sci. 2017;106:2265–9.
62. Murphy DE, et al. Extracellular vesicle-based therapeutics: natural versus engineered targeting and trafficking. Exp Mol Med. 2019;51:1–12.
63. Zhang H, et al. Identification of distinct nanoparticles and subsets of extracellular vesicles by asymmetric flow field-flow fractionation. Nat Cell Biol. 2018;20:332–43.
64. Horibe S, Tanahashi T, Kawauchi S, Murakami Y, Rikitake Y. Mechanism of recipient cell-dependent differences in exosome uptake. BMC Cancer. 2018;18:47.
65. Mulcahy LA, Pink RC, Carter DRF. Routes and mechanisms of extracellular vesicle uptake. J Extracell Vesicles. 2014;3:24641.
66. Raposo G, Stahl PD. Extracellular vesicles: a new communication paradigm? Nat Rev Mol Cell Biol. 2019;20:509–10.
67. Nakai W, et al. A novel affinity-based method for the isolation of highly purified extracellular vesicles. Sci Rep. 2016;6:33935.
68. Tkach M, et al. Qualitative differences in T-cell activation by dendritic cell-derived extracellular vesicle subtypes. EMBO J. 2017;36:3012–28.
69. Parolini I, et al. Microenvironmental pH is a key factor for exosome traffic in tumor cells. J Biol Chem. 2009;284:34211–22.
70. Boussadia Z, et al. Acidic microenvironment plays a key role in human melanoma progression through a sustained exosome mediated transfer of clinically relevant metastatic molecules. J Exp Clin Cancer Res CR. 2018;37:245.
71. Federici C, et al. Exosome release and low pH belong to a framework of resistance of human melanoma cells to cisplatin. PLoS One. 2014;9:e88193.
72. Hu S-Q, et al. Autophagy regulates exosome secretion in rat nucleus pulposus cells via the RhoC/ROCK2 pathway. Exp Cell Res. 2020;395:112239.
73. Keulers TG, et al. Secretion of pro-angiogenic extracellular vesicles during hypoxia is dependent on the autophagy-related protein GABARAPL1. J Extracell Vesicles. 2021;10:e12166.
74. Yu B, et al. Periostin secreted by cancer-associated fibroblasts promotes cancer stemness in head and neck cancer by activating protein tyrosine kinase 7. Cell Death Dis. 2018;9:1–18.
75. Sharma S, et al. Regucalcin promotes dormancy of prostate cancer. Oncogene. 2021;40:1012–26.
76. Bahrami A, Binabaj MM, Ferns GA. Exosomes: emerging modulators of signal transduction in colorectal cancer from molecular understanding to clinical application. Biomed Pharmacother. 2021;141:111882.
77. Qu J-L, et al. Gastric cancer exosomes promote tumour cell proliferation through PI3K/Akt and MAPK/ERK activation. Dig Liver Dis Off J Ital Soc Gastroenterol Ital Assoc Study Liver. 2009;41:875–80.
78. Hsu M-T, Wang Y-K, Tseng YJ. Exosomal proteins and lipids as potential biomarkers for lung cancer diagnosis, prognosis, and treatment. Cancers. 2022;14:732.
79. Zhang H, et al. Exosome-delivered EGFR regulates liver microenvironment to promote gastric cancer liver metastasis. Nat Commun. 2017;8:15016.
80. Xavier CPR, et al. The role of extracellular vesicles in the transfer of drug resistance competences to cancer cells. Drug Resist Updat. 2022;62:100833.
81. Chu L, et al. Sex steroid hormones in urinary exosomes as biomarkers for the prediction of prostate cancer. Clin Chim Acta Int J Clin Chem. 2022;531:389–98.
82. Vincent-Schneider H, et al. Exosomes bearing HLA-DR1 molecules need dendritic cells to efficiently stimulate specific T cells. Int Immunol. 2002;14:713–22.
83. Walsh SA, Davis TA. Key early proinflammatory signaling molecules encapsulated within circulating exosomes following traumatic injury. J Inflamm. 2022;19:6.
84. Chen G, et al. Exosomal PD-L1 contributes to immunosuppression and is associated with anti-PD-1 response. Nature. 2018;560:382–6.
85. Gómez-Contreras P, et al. Extracellular matrix 1 (ECM1) regulates the actin cytoskeletal architecture of aggressive breast cancer cells in part via S100A4 and Rho-family GTPases. Clin Exp Metastasis. 2017;34:37–49.
86. Gan L, et al. Extracellular matrix protein 1 promotes cell metastasis and glucose metabolism by inducing integrin β4/FAK/SOX2/HIF-1α signaling pathway in gastric cancer. Oncogene. 2018;37:744–55.
87. Guillory B, et al. Lack of Fetuin-A (α2-HS-Glycoprotein) reduces mammary tumor incidence and prolongs tumor latency via the transforming growth factor-β signaling pathway in a mouse model of breast cancer. Am J Pathol. 2010;177:2635–44.
88. Nimptsch K, et al. Plasma fetuin-A concentration, genetic variation in the AHSG gene and risk of colorectal cancer. Int J Cancer. 2015;137:911–20.
89. Niu L, et al. Tumor-derived exosomal proteins as diagnostic biomarkers in non-small cell lung cancer. Cancer Sci. 2019;110:433–42.
90. Zhao X, et al. Exosomes as drug carriers for cancer therapy and challenges regarding exosome uptake. Biomed Pharmacother. 2020;128:110237.
91. Rivoltini L, et al. TNF-Related Apoptosis-Inducing Ligand (TRAIL)-armed exosomes deliver proapoptotic signals to tumor site. Clin Cancer Res Off J Am Assoc Cancer Res. 2016;22:3499–512.
92. Meldolesi J. Unconventional protein secretion dependent on two extracellular vesicles: exosomes and ectosomes. Front Cell Dev Biol. 2022;10:877344.
93. Rabouille C. Pathways of unconventional protein secretion. Trends Cell Biol. 2017;27:230–40.
94. Zhao L, et al. OutCyte: a novel tool for predicting unconventional protein secretion. Sci Rep. 2019;9:19448.
95. Cohen MJ, Chirico WJ, Lipke PN. Through the back door: Unconventional protein secretion. Cell Surf. 2020;6:100045.
96. Keller M, Rüegg A, Werner S, Beer H-D. Active caspase-1 is a regulator of unconventional protein secretion. Cell. 2008;132:818–31.
97. Agrahari V, Agrahari V, Burnouf P-A, Chew CH, Burnouf T. Extracellular microvesicles as new industrial therapeutic frontiers. Trends Biotechnol. 2019;37:707–29.
98. Record M, Silvente-Poirot S, Poirot M, Wakelam MO. Extracellular vesicles: lipids as key components of their biogenesis and functions. J Lipid Res. 2018;59:1316–24.
99. Bebelman MP, Janssen E, Pegtel DM, Crudden C. The forces driving cancer extracellular vesicle secretion. Neoplasia. 2021;23:149–57.
100. Warburg O. On the origin of cancer cells. Science. 1956;123:309–14.
101. Spugnini EP, et al. Proton channels and exchangers in cancer. Biochim Biophys Acta. 2015;1848:2715–26.
102. Boussadia Z, Zanetti C, Parolini I. Role of microenvironmental acidity and tumor exosomes in cancer immunomodulation. Transl Cancer Res. 2020;9:5775–86.
103. Lazar I, et al. Proteome characterization of melanoma exosomes reveals a specific signature for metastatic cell lines. Pigment Cell Melanoma Res. 2015;28:464–75.
104. Tai Y, Chen K, Hsieh J, Shen T. Exosomes in cancer development and clinical applications. Cancer Sci. 2018;109:2364–74.
105. Sheldon H, et al. New mechanism for Notch signaling to endothelium at a distance by Delta-like 4 incorporation into exosomes. Blood. 2010;116:2385–94.
106. Zhang Z, et al. Delta-like ligand 4 level in colorectal cancer is associated with tumor aggressiveness and clinical outcome. Cancer Biomark Sect Dis Markers. 2022;33:415–22.

107. Hoshino A, et al. Tumour exosome integrins determine organotropic metastasis. Nature. 2015;527:329–35.
108. Webber J, Steadman R, Mason MD, Tabi Z, Clayton A. Cancer exosomes trigger fibroblast to myofibroblast differentiation. Cancer Res. 2010;70:9621–30.
109. Chowdhury R, et al. Cancer exosomes trigger mesenchymal stem cell differentiation into pro-angiogenic and pro-invasive myofibroblasts. Oncotarget. 2015;6:715–31.
110. Nazarenko I, et al. Cell surface tetraspanin Tspan8 contributes to molecular pathways of exosome-induced endothelial cell activation. Cancer Res. 2010;70:1668–78.
111. Li I, Nabet BY. Exosomes in the tumor microenvironment as mediators of cancer therapy resistance. Mol Cancer. 2019;18:32.
112. Junttila MR, De Sauvage FJ. Influence of tumour micro-environment heterogeneity on therapeutic response. Nature. 2013;501:346–54.
113. Fridman WH, Pagès F, Sautès-Fridman C, Galon J. The immune contexture in human tumours: impact on clinical outcome. Nat Rev Cancer. 2012;12:298–306.
114. Théry C, Ostrowski M, Segura E. Membrane vesicles as conveyors of immune responses. Nat Rev Immunol. 2009;9:581–93.
115. Li C, Teixeira AF, Zhu H-J, ten Dijke P. Cancer associated-fibroblast-derived exosomes in cancer progression. Mol Cancer. 2021;20:154.
116. LeBleu VS, Kalluri R. A peek into cancer-associated fibroblasts: origins, functions and translational impact. Dis Model Mech. 2018;11:dmm029447.
117. Nurmik M, Ullmann P, Rodriguez F, Haan S, Letellier E. In search of definitions: cancer-associated fibroblasts and their markers. Int J Cancer. 2020;146:895–905.
118. Kobayashi H, et al. Cancer-associated fibroblasts in gastrointestinal cancer. Nat Rev Gastroenterol Hepatol. 2019;16:282–95.
119. Park D, Sahai E, Rullan A. SnapShot: cancer-associated fibroblasts. Cell. 2020;181:486-486.e1.
120. Yang X, Li Y, Zou L, Zhu Z. Role of exosomes in crosstalk between cancer-associated fibroblasts and cancer cells. Front Oncol. 2019;9:356.
121. Ringuette Goulet C, et al. Exosomes induce fibroblast differentiation into cancer-associated fibroblasts through TGFβ signaling. Mol Cancer Res. 2018;16:1196–204.
122. Zou M-L, et al. The smad dependent TGF-β and BMP signaling pathway in bone remodeling and therapies. Front Mol Biosci. 2021;8:593310.
123. Cho JA, Park H, Lim EH, Lee KW. Exosomes from breast cancer cells can convert adipose tissue-derived mesenchymal stem cells into myofibroblast-like cells. Int J Oncol. 2012;40:130–8.
124. Zhao H, et al. The key role of extracellular vesicles in the metastatic process. Biochim Biophys Acta. 2018;1869:64–77.
125. Lugini L, et al. Exosomes from human colorectal cancer induce a tumor-like behavior in colonic mesenchymal stromal cells. Oncotarget. 2016;7:50086–98.
126. Maia J, Caja S, Strano Moraes MC, Couto N, Costa-Silva B. Exosome-based cell-cell communication in the tumor microenvironment. Front Cell Dev Biol. 2018;6:18.
127. Zhao H, et al. Tumor microenvironment derived exosomes pleiotropically modulate cancer cell metabolism. eLife. 2016;5:250.
128. Dong L-F, et al. Mitochondria on the move: Horizontal mitochondrial transfer in disease and health. J Cell Biol. 2023;222:e202211044.
129. Katayama Y, et al. Tumor neovascularization and developments in therapeutics. Cancers. 2019;11:316.
130. Olejarz W, Kubiak-Tomaszewska G, Chrzanowska A, Lorenc T. Exosomes in angiogenesis and anti-angiogenic therapy in cancers. Int J Mol Sci. 2020;21:5840.
131. Javan MR, Khosrojerdi A, Moazzeni SM. New insights into implementation of mesenchymal stem cells in cancer therapy: prospects for anti-angiogenesis treatment. Front Oncol. 2019;9:840.
132. Ludwig N, Yerneni SS, Razzo BM, Whiteside TL. Exosomes from HNSCC promote angiogenesis through reprogramming of endothelial cells. Mol Cancer Res. 2018;16:1798–808.
133. Ludwig N, et al. TGFβ+ small extracellular vesicles from head and neck squamous cell carcinoma cells reprogram macrophages towards a pro-angiogenic phenotype. J Extracell Vesicles. 2022;11:12294.
134. Zhu H, et al. A novel TGF-β trap blocks chemotherapeutics-induced TGF-β1 signaling and enhances their anticancer activity in gynecological cancers. Clin Cancer Res Off J Am Assoc Cancer Res. 2018;24:2780–93.
135. Ludwig N, et al. Novel TGF-β inhibitors ameliorate oral squamous cell carcinoma progression and improve the anti-tumor immune response of anti-PD-L1 immunotherapy. Mol Cancer Ther. 2021;20:1102–11.
136. Giusti I, et al. From glioblastoma to endothelial cells through extracellular vesicles: messages for angiogenesis. Tumor Biol. 2016;37:12743–53.
137. Skog J, et al. Glioblastoma microvesicles transport RNA and protein that promote tumor growth and provide diagnostic biomarkers. Nat Cell Biol. 2008;10:1470–6.
138. Chan Y-K, et al. Proteomic analysis of exosomes from nasopharyngeal carcinoma cell identifies intercellular transfer of angiogenic proteins. Int J Cancer. 2015;137:1830–41.
139. You Y, et al. Matrix metalloproteinase 13-containing exosomes promote nasopharyngeal carcinoma metastasis. Cancer Sci. 2015;106:1669–77.
140. Wang J, et al. Multiple myeloma exosomes establish a favourable bone marrow microenvironment with enhanced angiogenesis and immunosuppression. J Pathol. 2016;239:162–73.
141. Wilson CM, et al. Sortilin mediates the release and transfer of exosomes in concert with two tyrosine kinase receptors. J Cell Sci. 2014;127:3983–97.
142. Ghaemimanesh F, Mehravar M, Milani S, Poursani EM, Saliminejad K. The multifaceted role of sortilin/neurotensin receptor 3 in human cancer development. J Cell Physiol. 2021;236:6271–81.
143. Maji S, et al. Exosomal annexin II promotes angiogenesis and breast cancer metastasis. Mol Cancer Res. 2017;15:93–105.
144. Beckham CJ, et al. Bladder cancer exosomes contain EDIL-3/Del1 and facilitate cancer progression. J Urol. 2014;192:583–92.
145. Kumar A, Deep G. Exosomes in hypoxia-induced remodeling of the tumor microenvironment. Cancer Lett. 2020;488:1–8.
146. Jing X, et al. Role of hypoxia in cancer therapy by regulating the tumor microenvironment. Mol Cancer. 2019;18:157.
147. Zimna A, Kurpisz M. Hypoxia-inducible factor-1 in physiological and pathophysiological angiogenesis: applications and therapies. BioMed Res Int. 2015;2015:549412.
148. Pugh CW, Ratcliffe PJ. Regulation of angiogenesis by hypoxia: role of the HIF system. Nat Med. 2003;9:677–84.
149. Ravi R, et al. Regulation of tumor angiogenesis by p53-induced degradation of hypoxia-inducible factor 1alpha. Genes Dev. 2000;14:34–44.
150. Wang T, et al. Hypoxia-inducible factors and RAB22A mediate formation of microvesicles that stimulate breast cancer invasion and metastasis. Proc Natl Acad Sci U S A. 2014;111:E3234.
151. Meng W, Hao Y, He C, Li L, Zhu G. Exosome-orchestrated hypoxic tumor microenvironment. Mol Cancer. 2019;18:57.
152. Dorayappan KDP, et al. Hypoxia-induced exosomes contribute to a more aggressive and chemoresistant ovarian cancer phenotype: a novel mechanism linking STAT3/Rab proteins. Oncogene. 2018;37:3806–21.
153. Aga M, et al. Exosomal HIF1α supports invasive potential of nasopharyngeal carcinoma-associated LMP1-positive exosomes. Oncogene. 2014;33:4613–22.
154. de Jong OG, van Balkom BWM, Gremmels H, Verhaar MC. Exosomes from hypoxic endothelial cells have increased collagen crosslinking activity through up-regulation of lysyl oxidase-like 2. J Cell Mol Med. 2016;20:342–50.
155. Kucharzewska P, et al. Exosomes reflect the hypoxic status of glioma cells and mediate hypoxia-dependent activation of vascular cells during tumor development. Proc Natl Acad Sci. 2013;110:7312–7.
156. Kore RA, et al. Hypoxia-derived exosomes induce putative altered pathways in biosynthesis and ion regulatory channels in glioblastoma cells. Biochem Biophys Rep. 2018;14:104–13.
157. Ramteke A, et al. Exosomes secreted under hypoxia enhance invasiveness and stemness of prostate cancer cells by targeting adherens junction molecules. Mol Carcinog. 2015;54:554–65.
158. Gong L, Huang D, Shi Y, Liang Z, Bu H. Regulated cell death in cancer: from pathogenesis to treatment. Chin Med J (Engl). 2023;136:653–65.
159. Meehan K, Vella LJ. The contribution of tumour-derived exosomes to the hallmarks of cancer. Crit Rev Clin Lab Sci. 2016;53:121–31.
160. Abd Elmageed ZY, et al. Neoplastic reprogramming of patient-derived adipose stem cells by prostate cancer cell-associated exosomes. Stem Cells Dayt Ohio. 2014;32:983–97.

161. Zhang H-G, et al. A membrane form of TNF-α presented by exosomes delays T cell activation-induced cell death1. J Immunol. 2006;176:7385–93.
162. Alonso R, Mazzeo C, Mérida I, Izquierdo M. A new role of diacylglycerol kinase α on the secretion of lethal exosomes bearing Fas ligand during activation-induced cell death ofT lymphocytes. Biochimie. 2007;89:213–21.
163. Sanwlani R, Gangoda L. Role of extracellular vesicles in cell death and inflammation. Cells. 2021;10:2663.
164. Huber V, et al. Human colorectal cancer cells induce T-cell death through release of proapoptotic microvesicles: role in immune escape. Gastroenterology. 2005;128:1796–804.
165. Valenzuela MMA, et al. Exosomes secreted from human cancer cell lines contain Inhibitors of Apoptosis (IAP). Cancer Microenviron Off J Int Cancer Microenviron Soc. 2015;8:65–73.
166. Yang L, Wu X-H, Wang D, Luo C-L, Chen L-X. Bladder cancer cell-derived exosomes inhibit tumor cell apoptosis and induce cell proliferation in vitro. Mol Med Rep. 2013;8:1272–8.
167. Kakarla R, Hur J, Kim YJ, Kim J, Chwae Y-J. Apoptotic cell-derived exosomes: messages from dying cells. Exp Mol Med. 2020;52:1–6.
168. Lynch C, Panagopoulou M, Gregory CD. Extracellular vesicles arising from apoptotic cells in tumors: roles in cancer pathogenesis and potential clinical applications. Front Immunol. 2017;8:1174.
169. Beillevaire D, et al. Autolysosomes and caspase-3 control the biogenesis and release of immunogenic apoptotic exosomes. Cell Death Dis. 2022;13:1–13.
170. Pavlyukov MS, et al. Apoptotic cell-derived extracellular vesicles promote malignancy of glioblastoma via intercellular transfer of splicing factors. Cancer Cell. 2018;34:119-135.e10.
171. McIlwain DR, Berger T, Mak TW. Caspase functions in cell death and disease. Cold Spring Harb Perspect Biol. 2013;5:a008656.
172. Hill C, Dellar ER, Baena-Lopez LA. Caspases help to spread the message via extracellular vesicles. FEBS J. 2023;290:1954–72.
173. Boice A, Bouchier-Hayes L. Targeting apoptotic caspases in cancer. Biochim Biophys Acta Mol Cell Res. 2020;1867:118688.
174. Ando Y, et al. Necroptosis in pancreatic cancer promotes cancer cell migration and invasion by release of CXCL5. PLoS One. 2020;15:e0228015.
175. Luo Z, et al. A panel of necroptosis-related genes predicts the prognosis of pancreatic adenocarcinoma. Transl Oncol. 2022;22:101462.
176. Shlomovitz I, et al. Proteomic analysis of necroptotic extracellular vesicles. Cell Death Dis. 2021;12:1059.
177. Raden Y, Shlomovitz I, Gerlic M. Necroptotic extracellular vesicles – present and future. Semin Cell Dev Biol. 2021;109:106–13.
178. Gulei D, Berindan-Neagoe I. Activation of necroptosis by engineered self tumor-derived exosomes loaded with CRISPR/Cas9. Mol Ther Nucleic Acids. 2019;17:448–51.
179. Brown CW, et al. Prominin2 drives ferroptosis resistance by stimulating iron export. Dev Cell. 2019;51:575-586.e4.
180. Wu S, Li T, Liu W, Huang Y. Ferroptosis and cancer: complex relationship and potential application of exosomes. Front Cell Dev Biol. 2021;9:733751.
181. Zhang Y, et al. Imidazole ketone erastin induces ferroptosis and slows tumor growth in a mouse lymphoma model. Cell Chem Biol. 2019;26:623-633.e9.
182. Lim S-O, et al. Deubiquitination and stabilization of PD-L1 by CSN5. Cancer Cell. 2016;30:925–39.
183. Grinberg-Bleyer Y, Ghosh S. A novel link between inflammation and cancer. Cancer Cell. 2016;30:829–30.
184. van Hezel ME, Nieuwland R, van Bruggen R, Juffermans NP. The ability of extracellular vesicles to induce a pro-inflammatory host response. Int J Mol Sci. 2017;18:1285.
185. Chan BD, et al. Exosomes in Inflammation and Inflammatory Disease. Proteomics. 2019;19:1800149.
186. Zhang G, et al. Tumor induces muscle wasting in mice through releasing extracellular Hsp70 and Hsp90. Nat Commun. 2017;8:589.
187. Kim SB, et al. Caspase-8 controls the secretion of inflammatory lysyl-tRNA synthetase in exosomes from cancer cells. J Cell Biol. 2017;216:2201–16.
188. Wada J, et al. Surface-bound TGF-β1 on effusion-derived exosomes participates in maintenance of number and suppressive function of regulatory T-cells in malignant effusions. Anticancer Res. 2010;30:3747–57.
189. Alizadeh D, Katsanis E, Larmonier N. The multifaceted role of Th17 lymphocytes and their associated cytokines in cancer. Clin Dev Immunol. 2013;2013:957878.
190. Guéry L, Hugues S. Th17 cell plasticity and functions in cancer immunity. BioMed Res Int. 2015;2015:e314620.
191. Zhou J, et al. Exosomes released from tumor-associated macrophages transfer miRNAs that induce a Treg/Th17 cell imbalance in epithelial ovarian cancer. Cancer Immunol Res. 2018;6:1578–92.
192. Taylor DD, Gerçel-Taylor C. Tumour-derived exosomes and their role in cancer-associated T-cell signalling defects. Br J Cancer. 2005;92:305–11.
193. Mercogliano MF, Bruni S, Elizalde PV, Schillaci R. Tumor necrosis factor α blockade: an opportunity to tackle breast cancer. Front Oncol. 2020;10:584.
194. Wang X, Lin Y. Tumor necrosis factor and cancer, buddies or foes? Acta Pharmacol Sin. 2008;29:1275–88.
195. Kong H, Kim SB. Exosomal communication between the tumor microenvironment and innate immunity and its therapeutic application. Immune Netw. 2022;22:e38.
196. Lam PY, Nissen MD, Mattarollo SR. Invariant natural killer T cells in immune regulation of blood cancers: harnessing their potential in immunotherapies. Front Immunol. 2017;8:1355.
197. Mincheva-Nilsson L, Baranov V. Cancer exosomes and NKG2D receptor–ligand interactions: impairing NKG2D-mediated cytotoxicity and anti-tumour immune surveillance. Semin Cancer Biol. 2014;28:24–30.
198. Yu S, et al. Tumor exosomes inhibit differentiation of bone marrow dendritic cells1. J Immunol. 2007;178:6867–75.
199. Bent EH, Gilbert LA, Hemann MT. A senescence secretory switch mediated by PI3K/AKT/mTOR activation controls chemoprotective endothelial secretory responses. Genes Dev. 2016;30:1811–21.
200. Wang M, Zhang B. The immunomodulation potential of exosomes in tumor microenvironment. J Immunol Res. 2021;2021:e3710372.
201. Piao YJ, et al. Breast cancer cell-derived exosomes and macrophage polarization are associated with lymph node metastasis. Oncotarget. 2017;9:7398–410.
202. Yunna C, Mengru H, Lei W, Weidong C. Macrophage M1/M2 polarization. Eur J Pharmacol. 2020;877:173090.
203. Mantovani A, Sozzani S, Locati M, Allavena P, Sica A. Macrophage polarization: tumor-associated macrophages as a paradigm for polarized M2 mononuclear phagocytes. Trends Immunol. 2002;23:549–55.
204. Chen X, Cubillos-Ruiz JR. Endoplasmic reticulum stress signals in the tumour and its microenvironment. Nat Rev Cancer. 2021;21:71–88.
205. Yuan Y, et al. Endoplasmic reticulum stress promotes the release of exosomal PD-L1 from head and neck cancer cells and facilitates M2 macrophage polarization. Cell Commun Signal. 2022;20:12.
206. Shao B, et al. Effects of tumor-derived exosome programmed death ligand 1 on tumor immunity and clinical applications. Front Cell Dev Biol. 2021;9:760211.
207. Wang JX, et al. Lactic acid and an acidic tumor microenvironment suppress anticancer immunity. Int J Mol Sci. 2020;21:8363.
208. El-Kenawi A, et al. Acidity promotes tumour progression by altering macrophage phenotype in prostate cancer. Br J Cancer. 2019;121:556–66.
209. Gao Y, et al. Renal cancer-derived exosomes induce tumor immune tolerance by MDSCs-mediated antigen-specific immunosuppression. Cell Commun Signal. 2020;18:106.
210. Xiang X, et al. Induction of myeloid-derived suppressor cells by tumor exosomes. Int J Cancer. 2009;124:2621–33.
211. Li L, et al. Microenvironmental oxygen pressure orchestrates an anti- and pro-tumoral γδ T cell equilibrium via tumor-derived exosomes. Oncogene. 2019;38:2830–43.
212. Paget S. The distribution of secondary growths in cancer of the breast. 1889. Cancer Metastasis Rev. 1989;8:98–101.
213. Hiratsuka S, et al. MMP9 induction by vascular endothelial growth factor receptor-1 is involved in lung-specific metastasis. Cancer Cell. 2002;2:289–300.
214. Kaplan RN, et al. VEGFR1-positive haematopoietic bone marrow progenitors initiate the pre-metastatic niche. Nature. 2005;438:820–7.
215. Cox TR, Gartland A, Erler JT. The pre-metastatic niche: is metastasis random? BoneKEy Rep. 2012;1:80.

216. Mashouri L, et al. Exosomes: composition, biogenesis, and mechanisms in cancer metastasis and drug resistance. Mol Cancer. 2019;18:75.
217. Le Pape F, Vargas G, Clézardin P. The role of osteoclasts in breast cancer bone metastasis. J Bone Oncol. 2016;5:93–5.
218. Li C-H, et al. Exosomal tumor necrosis factor-α from hepatocellular cancer cells (Huh-7) promote osteoclast differentiation. J Cell Biochem. 2021;122:1749–60.
219. Liu Q, et al. Factors involved in cancer metastasis: a better understanding to "seed and soil" hypothesis. Mol Cancer. 2017;16:176.
220. Chanteloup G, et al. Monitoring HSP70 exosomes in cancer patients' follow up: a clinical prospective pilot study. J Extracell Vesicles. 2020;9:1766192.
221. Tan Y, et al. Tumor-derived exosomal components: the multifaceted roles and mechanisms in breast cancer metastasis. Cell Death Dis. 2021;12:1–18.
222. Hannafon BN, et al. Metastasis-associated protein 1 (MTA1) is transferred by exosomes and contributes to the regulation of hypoxia and estrogen signaling in breast cancer cells. Cell Commun Signal. 2019;17:13.
223. Cen J, et al. Exosomal thrombospondin-1 disrupts the integrity of endothelial intercellular junctions to facilitate breast cancer cell metastasis. Cancers. 2019;11:1946.
224. Steigedal TS, et al. Nephronectin is correlated with poor prognosis in breast cancer and promotes metastasis via its integrin-binding motifs. Neoplasia N Y N. 2018;20:387–400.
225. Rodrigues G, et al. Tumour exosomal CEMIP protein promotes cancer cell colonization in brain metastasis. Nat Cell Biol. 2019;21:1403–12.
226. Sun H, et al. Exosomal S100A4 derived from highly metastatic hepatocellular carcinoma cells promotes metastasis by activating STAT3. Signal Transduct Target Ther. 2021;6:1–12.
227. Yu Z, et al. Pancreatic cancer-derived exosomes promote tumor metastasis and liver pre-metastatic niche formation. Oncotarget. 2017;8:63461–83.
228. Atay S, et al. Oncogenic KIT-containing exosomes increase gastrointestinal stromal tumor cell invasion. Proc Natl Acad Sci. 2014;111:711–6.
229. Ohshima K, et al. Exosome-mediated extracellular release of polyadenylate-binding protein 1 in human metastatic duodenal cancer cells. Proteomics. 2014;14:2297–306.
230. Jung YR, et al. Silencing of ST6Gal I enhances colorectal cancer metastasis by down-regulating KAI1 via exosome-mediated exportation and thereby rescues integrin signaling. Carcinogenesis. 2016;37:1089–97.
231. Liang J, Yin H. STAM transports STING oligomers into extracellular vesicles, down-regulating the innate immune response. J Extracell Vesicles. 2023;12:12316.
232. Rezaie J, Feghhi M, Etemadi T. A review on exosomes application in clinical trials: perspective, questions, and challenges. Cell Commun Signal. 2022;20:145.
233. Huang T-Y, Wang C-Y, Chen K-Y, Huang L-T. Urinary exosomal thyroglobulin in thyroid cancer patients with post-ablative therapy: a new biomarker in thyroid cancer. Front Endocrinol. 2020;11:382.
234. Lin J, et al. Exosomes: novel biomarkers for clinical diagnosis. Sci World J. 2015;2015:e657086.
235. Huang D, Rao D, Xi X, Zhang Z, Zhong T. Application of extracellular vesicles proteins in cancer diagnosis. Front Cell Dev Biol. 2022;10:1007360.
236. Øverbye A, et al. Identification of prostate cancer biomarkers in urinary exosomes. Oncotarget. 2015;6:30357–76.
237. Erozenci LA, Böttger F, Bijnsdorp IV, Jimenez CR. Urinary exosomal proteins as (pan-)cancer biomarkers: insights from the proteome. FEBS Lett. 2019;593:1580–97.
238. Hu C, et al. Potentiality of exosomal proteins as novel cancer biomarkers for liquid biopsy. Front Immunol. 2022;13:792046.
239. Moon P-G, et al. Identification of developmental endothelial locus-1 on circulating extracellular vesicles as a novel biomarker for early breast cancer detection. Clin Cancer Res. 2016;22:1757–66.
240. Piombino C, et al. The role of exosomes in breast cancer diagnosis. Biomedicines. 2021;9:312.
241. Li J, et al. Claudin-containing exosomes in the peripheral circulation of women with ovarian cancer. BMC Cancer. 2009;9:244.
242. Norouzi-Barough L, et al. Early diagnosis of breast and ovarian cancers by body fluids circulating tumor-derived exosomes. Cancer Cell Int. 2020;20:187.
243. Zhao Z, Yang Y, Zeng Y, He M. A microfluidic ExoSearch chip for multiplexed exosome detection towards blood-based ovarian cancer diagnosis. Lab Chip. 2016;16:489–96.
244. Soung YH, Ford S, Zhang V, Chung J. Exosomes in cancer diagnostics. Cancers. 2017;9:8.
245. Buscail E, et al. High clinical value of liquid biopsy to detect circulating tumor cells and tumor exosomes in pancreatic ductal adenocarcinoma patients eligible for up-front surgery. Cancers. 2019;11:1656.
246. Melo SA, et al. Glypican1 identifies cancer exosomes and facilitates early detection of cancer. Nature. 2015;523:177–82.
247. Herreros-Villanueva M, Bujanda L. Glypican-1 in exosomes as biomarker for early detection of pancreatic cancer. Ann Transl Med. 2016;4:64.
248. Lux A, Kahlert C, Grützmann R, Pilarsky C. c-Met and PD-L1 on circulating exosomes as diagnostic and prognostic markers for pancreatic cancer. Int J Mol Sci. 2019;20:3305.
249. Yoon JH, Park YG, Nam SW, Park WS. The diagnostic value of serum gastrokine 1 (GKN1) protein in gastric cancer. Cancer Med. 2019;8:5507–14.
250. Yoon JH, et al. Gastrokine 1 protein is a potential theragnostic target for gastric cancer. Gastric Cancer. 2018;21:956–67.
251. Chu L-Y, et al. Circulating levels of L1-cell adhesion molecule as a serum biomarker for early detection of gastric cancer and esophagogastric junction adenocarcinoma. J Cancer. 2020;11:5395–402.
252. Zhou G-Y-J, et al. Proteomics-based identification of proteins in tumor-derived exosomes as candidate biomarkers for colorectal cancer. World J Gastrointest Oncol. 2023;15:1227–40.
253. Li A, Zhang T, Zheng M, Liu Y, Chen Z. Exosomal proteins as potential markers of tumor diagnosis. J Hematol Oncol J Hematol Oncol. 2017;10:1754.
254. Yokoyama S, et al. Clinical implications of carcinoembryonic antigen distribution in serum exosomal fraction—measurement by ELISA. PLoS One. 2017;12:e0183337.
255. Arbelaiz A, et al. Serum extracellular vesicles contain protein biomarkers for primary sclerosing cholangitis and cholangiocarcinoma. Hepatol Baltim Md. 2017;66:1125–43.
256. Meng X, Pan J, Sun S, Gong Z. Circulating exosomes and their cargos in blood as novel biomarkers for cancer. Transl Cancer Res. 2018;7:S226-42.
257. Chen C-L, et al. Comparative and targeted proteomic analyses of urinary microparticles from bladder cancer and hernia patients. J Proteome Res. 2012;11:5611–29.
258. Sandfeld-Paulsen B, et al. Exosomal proteins as diagnostic biomarkers in lung cancer. J Thorac Oncol Off Publ Int Assoc Study Lung Cancer. 2016;11:1701–10.
259. Ueda K, et al. Antibody-coupled monolithic silica microtips for highthroughput molecular profiling of circulating exosomes. Sci Rep. 2014;4:6232.
260. Li C, et al. Potential markers from serum-purified exosomes for detecting oral squamous cell carcinoma metastasis. Cancer Epidemiol Biomarkers Prev. 2019;28:1668–81.
261. Wu T, Liu Y, Ali NM, Zhang B, Cui X. Effects of exosomes on tumor bioregulation and diagnosis. ACS Omega. 2023;8:5157–68.
262. Cui Z, et al. Diagnostic and prognostic potential of circulating and tissue BATF2 in nasopharyngeal carcinoma. Front Mol Biosci. 2021;8:724373.
263. Logozzi M, et al. High levels of exosomes expressing CD63 and Caveolin-1 in plasma of melanoma patients. PLoS One. 2009;4:e5219.
264. Shao H, et al. Protein typing of circulating microvesicles allows real-time monitoring of glioblastoma therapy. Nat Med. 2012;18:1835–40.
265. Kim MS, et al. Engineering macrophage-derived exosomes for targeted paclitaxel delivery to pulmonary metastases: in vitro and in vivo evaluations. Nanomed Nanotechnol Biol Med. 2018;14:195–204.
266. Tang K, et al. Delivery of chemotherapeutic drugs in tumour cell-derived microparticles. Nat Commun. 2012;3:1282.
267. Kim MS, et al. Development of exosome-encapsulated paclitaxel to overcome MDR in cancer cells. Nanomed Nanotechnol Biol Med. 2016;12:655–64.
268. Saari H, et al. Microvesicle- and exosome-mediated drug delivery enhances the cytotoxicity of Paclitaxel in autologous prostate cancer cells. J Controlled Release. 2015;220:727–37.
269. Osterman CJD, et al. Curcumin modulates pancreatic adenocarcinoma cell-derived exosomal function. PLoS One. 2015;10:e0132845.

270. Taylor J, Azimi I, Monteith G, Bebawy M. Ca2+ mediates extracellular vesicle biogenesis through alternate pathways in malignancy. J Extracell Vesicles. 2020;9:1734326.
271. Chalmin F, et al. Membrane-associated Hsp72 from tumor-derived exosomes mediates STAT3-dependent immunosuppressive function of mouse and human myeloid-derived suppressor cells. J Clin Invest. 2010;120:457–71.
272. Whiteside TL. Chapter four - tumor-derived exosomes and their role in cancer progression. In: Makowski GS, editor. Advances in clinical chemistry. Cambridge: Elsevier; 2016;74:103–141.
273. Ciravolo V, et al. Potential role of HER2-overexpressing exosomes in countering trastuzumab-based therapy. J Cell Physiol. 2012;227:658–67.
274. André F, et al. Tumor-derived exosomes: a new source of tumor rejection antigens. Vaccine. 2002;20:A28–31.
275. Wang C, et al. Tumor cell-associated exosomes robustly elicit anti-tumor immune responses through modulating dendritic cell vaccines in lung tumor. Int J Biol Sci. 2020;16:633–43.
276. Lu Z, et al. Dendritic cell-derived exosomes elicit tumor regression in autochthonous hepatocellular carcinoma mouse models. J Hepatol. 2017;67:739–48.
277. Poggio M, et al. Suppression of exosomal PD-L1 induces systemic anti-tumor immunity and memory. Cell. 2019;177:414-427.e13.
278. Farhood B, Najafi M, Mortezaee K. CD8+ cytotoxic T lymphocytes in cancer immunotherapy: a review. J Cell Physiol. 2019;234:8509–21.
279. Gao J, et al. Expression profiles and clinical value of plasma exosomal Tim-3 and Galectin-9 in non-small cell lung cancer. Biochem Biophys Res Commun. 2018;498:409–15.
280. Li J, et al. Exosomes derived from rAAV/AFP-transfected dendritic cells elicit specific T cell-mediated immune responses against hepatocellular carcinoma. Cancer Manag Res. 2018;10:4945–57.

Publisher's Note

Springer Nature remains neutral with regard to jurisdictional claims in published maps and institutional affiliations.

Ready to submit your research? Choose BMC and benefit from:

- fast, convenient online submission
- thorough peer review by experienced researchers in your field
- rapid publication on acceptance
- support for research data, including large and complex data types
- gold Open Access which fosters wider collaboration and increased citations
- maximum visibility for your research: over 100M website views per year

At BMC, research is always in progress.

Learn more biomedcentral.com/submissions

BMC

4.6 Phosphatidylserine-positive extracellular vesicles in intercellular communication in the tumor microenvironment

Phosphatidylserine (PS) is a negatively charged phospholipid typically located on the inner layer of the cell membrane under normal physiological conditions. During the onset of apoptosis, enzymes like scramblases can alter the asymmetric distribution of PS, leading to its exposure on the outer membrane. This externalized PS serves as an "eat-me" signal for receptors on macrophages, facilitating the removal of apoptotic cell debris. Notably, recent research indicates that viable cells can also display externalized PS as a strategy for evading immune detection. There is increasing evidence that, in contrast to normal non-tumorigenic cells, many tumor cells expose PS on their surface by a mechanism that is unrelated to PS externalisation commonly seen in dying apoptotic cells [17]. Phosphatidylserine-positive extracellular vesicles (PS+ EVs) are often associated with cell death processes, particularly their release during apoptosis. Our results suggest that phosphatidylserine positivity is not only characteristic of EVs formed during cell death processes, but that the presence of PS is common to the membranes of almost all EVs released by cancer cells.

In this research, we explored how autophagy modulators influence the protein composition of phosphatidylserine-positive extracellular vesicles (PS+ EVs) released by head and neck squamous cell carcinoma (HNSCC) cells, as well as the interaction between cancer cells and fibroblasts. We examined how media conditioned by HNSCC cells, which contained PS+ EVs from both autophagy-modulated and non-modulated cancer cells, affected the metabolism and senescence-related proteins in healthy fibroblasts. We have provided evidence that the metabolic state of cancer cells, such as autophagy induction/inhibition or glutamine and serum starvation, plays a pivotal role in shaping the behaviour of surrounding stromal fibroblasts. We have shown that these effects can be mediated through signalling by (PS+ EVs). Under metabolic stress, cancer cells release (PS+ EVs) with distinct cargo profiles, including mitochondrial RNAs, autophagy-related proteins and specific EV-associated cytokines. For example, lysosome-affecting compounds BAFA1 and HCQ induced the inclusion of p62 into PS-EVs. Cancer cells can also manipulate the lysosomal and autolysosomal genesis in fibroblasts. This effect was partially mitigated by pretreating cancer cells with the autophagy inhibitor CPD18 (Hanelova, 2023). Glutamine and serum starvation caused mitochondrial fragmentation and increased TSG101 on mitochondria, promoting mitochondrial cargo sorting into EVs and elevating mtRNA levels in cancer cell-derived EVs (Bugajova 2024). Many studies suggest that cancer cells release higher amounts of EVs compared to non-malignant cells, making the effect

of autophagy modulators on EV secretion critical and attractive for anticancer therapy. Autophagy influences both EV quantity and content, shaping their downstream effects. Internalised by fibroblasts, PS-EVs modulate autophagic flux, mitochondrial metabolism, and the expression of factors like MMP-3 and p21 (Hanelova 2023). Thus, the metabolic status of tumour cells not only reflects their adaptive response to the microenvironment but also actively reprograms the function and metabolism of fibroblasts, reinforcing a metabolic feedback loop that sustains the tumour microenvironment.

In the field of extracellular vesicles, I have also been active in the establishment of a network of scientific groups dealing with this topic. In 2024, the Czech Society for Extracellular Vesicles (CzeSEV, https://www.sci.muni.cz/czesev) was founded, of which I am one of the founding members. CzeSEV brings together experienced researchers, early-career scientists, students, and industry experts from across the Czech Republic. Our mission is to promote networking, encourage collaboration, and strengthen relationships within the extracellular vesicle (EV) research community. As members of ISEV (International Society for Extracellular Vesicles), we are contributing to the ISEV mission of advancing EV research for a better understanding of EV biology and their use in clinics. We advocate for EVs by endorsing the EV topic during our lectures as well as by promoting the ISEV standards for EV research.

Author's publications relevant to this chapter

1. Hanelova, K., Raudenska, M., Kratochvilova, M. *et al.* Autophagy modulators influence the content of important signalling molecules in PS-positive extracellular vesicles. *Cell Communication and Signalling* **21**, 120 (2023)
   IF (2023) 8.2; 8 citations (WOS)
2. Bugajova, M., Raudenska, M., Hanelova, K. *et al.* Glutamine and serum starvation alters the ATP production, oxidative stress, and abundance of mitochondrial RNAs in extracellular vesicles produced by cancer cells. *Scientific Reports* **14**, 25815 (2024)
   IF (2023) 3.8; 2 citations (WOS)

Hanelova *et al.*
Cell Communication and Signaling (2023) 21:120
https://doi.org/10.1186/s12964-023-01126-z

Cell Communication and Signaling

RESEARCH Open Access

Autophagy modulators influence the content of important signalling molecules in PS-positive extracellular vesicles

Klara Hanelova[1†], Martina Raudenska[1,2†], Monika Kratochvilova[2], Jiri Navratil[1], Tomas Vicar[1,3], Maria Bugajova[1], Jaromir Gumulec[1], Michal Masarik[1,2,4] and Jan Balvan[1*]

Abstract

Extracellular vesicles (EVs) are important mediators of intercellular communication in the tumour microenvironment. Many studies suggest that cancer cells release higher amounts of EVs exposing phosphatidylserine (PS) at the surface. There are lots of interconnections between EVs biogenesis and autophagy machinery. Modulation of autophagy can probably affect not only the quantity of EVs but also their content, which can deeply influence the resulting pro-tumourigenic or anticancer effect of autophagy modulators. In this study, we found that autophagy modulators autophinib, CPD18, EACC, bafilomycin A1 (BAFA1), 3-hydroxychloroquine (HCQ), rapamycin, NVP-BEZ235, Torin1, and starvation significantly alter the composition of the protein content of phosphatidylserine-positive EVs (PS-EVs) produced by cancer cells. The greatest impact had HCQ, BAFA1, CPD18, and starvation. The most abundant proteins in PS-EVs were proteins typical for extracellular exosomes, cytosol, cytoplasm, and cell surface involved in cell adhesion and angiogenesis. PS-EVs protein content involved mitochondrial proteins and signalling molecules such as SQSTM1 and TGFβ1 pro-protein. Interestingly, PS-EVs contained no commonly determined cytokines, such as IL-6, IL-8, GRO-α, MCP-1, RANTES, and GM-CSF, which indicates that secretion of these cytokines is not predominantly mediated through PS-EVs. Nevertheless, the altered protein content of PS-EVs can still participate in the modulation of the fibroblast metabolism and phenotype as p21 was accumulated in fibroblasts influenced by EVs derived from CPD18-treated FaDu cells. The altered protein content of PS-EVs (data are available via ProteomeXchange with identifier PXD037164) also provides information about the cellular compartments and processes that are affected by the applied autophagy modulators.

Keywords Extracellular vesicles, Phosphatidylserine-positive extracellular vesicles, Autophagy, Autophagy modulation, Head and neck cancer, Proteomics, SQSTM1, Senescence, p21, Autophinib, CPD18, EACC, Bafilomycin A1, 3-hydroxychloroquine, Rapamycin, NVP-BEZ235, Torin1, Starvation

†Klara Hanelova and Martina Raudenska contributed equally to this work.

*Correspondence:
Jan Balvan
jan.balvan@med.muni.cz
Full list of author information is available at the end of the article

© The Author(s) 2023. **Open Access** This article is licensed under a Creative Commons Attribution 4.0 International License, which permits use, sharing, adaptation, distribution and reproduction in any medium or format, as long as you give appropriate credit to the original author(s) and the source, provide a link to the Creative Commons licence, and indicate if changes were made. The images or other third party material in this article are included in the article's Creative Commons licence, unless indicated otherwise in a credit line to the material. If material is not included in the article's Creative Commons licence and your intended use is not permitted by statutory regulation or exceeds the permitted use, you will need to obtain permission directly from the copyright holder. To view a copy of this licence, visit http://creativecommons.org/licenses/by/4.0/. The Creative Commons Public Domain Dedication waiver (http://creativecommons.org/publicdomain/zero/1.0/) applies to the data made available in this article, unless otherwise stated in a credit line to the data.

Introduction

The evolutionary success of tumour cells largely depends on the manipulation of their tumour microenvironment (TME), especially cancer-associated fibroblasts (CAFs) [1, 2]. Fibroblasts reflect the stress within the TME in a variety of ways that allow them to adapt to stressful conditions. Nevertheless, such adaptation can enhance the malignant behaviour of tumour cells as stress responses in fibroblasts include their activation to CAFs or senescence [3]. Key mediators of intercellular communication are extracellular vesicles (EVs). While originally thought to function mainly in the elimination of cellular waste, it is now understood that the purpose of EVs is much more complex [4]. EVs involve a heterogeneous population of membrane vesicles that are created through various mechanisms. The three main EV subpopulations include bodies released by apoptotic cells (1,000–5,000 nm), ectosomes (150–1,000 nm), and exosomes (30–150 nm). Apoptotic bodies are released from dying cells and are usually pelleted at 2000 to 10,000 g. Ectosomes comprise diverse types of EVs such as oncosomes and microvesicles that are generated at the plasma membrane from its outward budding and are isolated at 10,000 to 20,000 g [5, 6].

Exosomes are a subtype of EVs generated by an endosomal system, pelleted at > 100,000 g centrifugation [6, 7]. The release of exosomes involves the formation of multivesicular endosomes (MVEs) that, upon transport towards and fusion with the plasma membrane, release their intraluminal vesicles (ILVs) as exosomes [4]. Exosome biogenesis is complex, varies depending on the cargo and the cell type they are derived from, and can be influenced by other signals and pathological stimuli. EVs mirror the composition of their parent cells and contain various biomolecules, including proteins, lipids, and nucleic acids, which can influence the behaviour of specific target cells. Some studies suggest that cancer cells release higher amounts of extracellular vesicles and that EVs produced by tumour cells often expose phosphatidylserine (PS) at the surface [8–10].

Autophagic machinery collectively with the ubiquitin–proteasome system and exosomal secretion orchestrate the dynamics of intracellular waste removal, where each pathway may complement the deficit of the other. Consequently, the secretion of EVs with waste material (proteins, RNA, parts of organelles) can reduce stress when degradative and recycling pathways are disrupted [11, 12]. Recent studies confirm that there are many interconnections between exosome biogenesis and autophagy and that autophagy machinery can have both stimulatory and inhibitory impacts on the secretion of EVs. These impacts will be probably deeply context-dependent and could be significantly affected by different kinds of autophagy modulators (the significant effect can be expected especially for autophagy modulators impairing lysosome homeostasis [13]). Modulation of autophagy can significantly affect not only the quantity of EVs but also their content, which can deeply influence the resulting protumourigenic or anticancer effect of autophagy modulators [14–17].

In this study, we investigated the impact of autophagy modulators on the protein content of PS-positive EVs (PS-EVs) produced by head and neck cancer cells (HNSCC) and following communication between cancer cells and fibroblasts. The effect of HNSCC cells-conditioned media containing PS-EVs (derived from cancer cells with and without autophagy modulation) on the metabolism and senescence-associated proteins of healthy fibroblasts was studied. Nine modulators were chosen for modulation of the autophagy machinery (autophinib (APB), CPD18, EACC, bafilomycin A1 (BAFA1), 3-hydroxychloroquine (HCQ), rapamycin (RAPA), NVP-BEZ235 (BEZ), Torin1, and starvation). Autophinib is an ATP-competitive inhibitor of VPS34 decreasing the accumulation of the lipidated protein LC3 on the autophagosomal membrane. CPD18 inhibits omegasome formation via the inhibition of class III PI3K. CPD18 is structurally related to 3-methyladenine (3-MA), but unlike 3-MA, CPD18 does not inhibit class I PI3Ks [18]. EACC is a reversible autophagy inhibitor, which selectively inhibits the translocation of autophagosome-specific SNARE Stx17, thereby blocking autophagosome-lysosome fusion. EACC blocks autophagosome-lysosome fusion but does not affect endo-lysosomal function [19]. BAFA1 is a V-ATPase inhibitor that blocks the autophagic flux by inhibiting autophagosome-lysosome fusion and autolysosomal and/or lysosomal acidification [20]. HCQ inhibits the maturation of autolysosomes and blocks late steps of autophagy. HCQ behaves as a weak base and accumulates in the lysosomes causing lysosomal stress [21]. Rapamycin is a potent allosteric mTORC1 inhibitor. NVP-BEZ235 binds to the ATP-binding clefts of PI3K and mTOR kinase, thereby inhibiting their activities [22]. Torin1 is a highly potent and selective ATP-competitive mTOR inhibitor that directly inhibits both complexes (mTORC1 and mTORC2) [23].

We found that autophagy modulators significantly altered the composition of the protein content of PS-positive EVs (PS-EVs) produced by cancer cells. This protein content involves important cytokines, mitochondrial proteins, and signalling molecules such as SQSTM1 and TGFβ1 pro-protein. The altered protein content of PS-EVs may contribute to the modulation of the fibroblast metabolism and phenotype (p21 was accumulated in fibroblasts influenced by EVs derived from CPD18-treated FaDu cells). EVs also provide information about

the cellular compartments and processes that are affected by the applied compounds.

Material and methods

Model cell lines

The cell line FaDu (HTB-43TM), derived from a squamous cell carcinoma (SCC) of the hypopharynx, and the human gingival fibroblast cell line HGF (derived from the histologically normal gingival biopsy; Cell Lines Service product number: 300703) were used in this study. The authenticated cell lines were purchased from the American Type Culture Collection (ATCC; Manassas, Virginia, USA) and CLS within the last five years. Homozygous deletion of SMAD4 was observed in FaDu cells [24, 25]. SMAD4 gene depletion can induce autophagy. The protein level of SMAD4 was inversely correlated with autophagy in orthotopic tumour tissue samples [26].

The cell lines were grown in a Dulbecco's Modified Eagle's medium/Nutrient Mixture F-12 Ham (DMEM/F12, Biosera) supplemented with antibiotics (penstrep) and 10% fetal bovine serum in a humidified atmosphere of 5% CO_2 and 95% air at 37 °C. Two passages before the experiment, cell harvest, or EVs isolation, the cell lines were washed with PBS and grown in a medium supplemented with Exosome-depleted FBS (GibcoTM, A2720801); hereafter referred to as exofree medium. The passages of all cell lines performed in our lab ranged from 5 to 15. All experiments were performed with mycoplasma-free cells. Mycoplasma was detected by PCR (primers MYCO_A: GGCGAATGGGTGAGT AACACG and MYCO_B: CGGATAACGCTTGCGACC TATG).

Autophagy modulation

For autophagy modulation, FaDu cells were treated for 24 h with 5 nM bafilomycin A1 (Sigma-Aldrich, B1793), 50 μM of hydroxychloroquine sulphate (Sigma-Aldrich, H0915), 100 μM of CPD18 (Calbiochem), 50 nM of autophinib (Sigma, SML2632), 10 μM of EACC (MedChemExpress), 200 nM of rapamycin (Sigma-Aldrich, R0395), 3 nM of Torin-1 (MedChemExpress), or 30 nM of NVP-BEZ235 (MedChemExpress). To induce starvation, cells were cultured in DMEM F12 without glutamine and without FBS (Biosera). Modulation of autophagy did not reduce the viability of FaDu cells (the viability ranged 98.1 to 99.9% across treatments).

Conditioned media preparation

15 ml of conditioned medium (CM) was collected from 90–95% confluent FaDu cells grown in 75cm^2 cell culture flasks after 24 h of the selected treatment. The collected media were first subjected to a centrifugation step of 400 g for 10 min at room temperature (RT) to pellet and remove cells. All following centrifugation steps were performed at 4 °C. Next, the supernatant was centrifuged at 2,000 g for 20 min to remove debris and apoptotic bodies [6]. Then, to remove large EVs, the supernatant was centrifuged at 10,000 g for 40 min. To remove any remaining large EVs, the supernatant from the first 10,000 g step was passed through a 0.22 μm pore PES filter (MF-Millipore TM Membrane Filter, GSWP01300). The conditioned medium resulting from this process is hereinafter referred to as CM1.

To remove the remaining exogenous treatments from the CM1, we concentrated the 15 ml volume to a 1 ml volume using Amicon® Ultra-15 Centrifugal Filter Unit (Merc, UCF9100, 100 kDa MWCO) at 2000 g for 3 min. Then we added 2 ml of pure DMEM F12 medium supplemented with exosome-depleted FBS to this volume. The conditioned medium resulting from this process is hereinafter referred to as CM2. This conditioned medium was subsequently used for the treatment of HGF cells.

Cytokine array

Human Cytokine Antibody Arrays (ab 133,996 and ab133997, Abcam) were used for the simultaneous detection of 23 resp. 42 cytokines in each CM sample according to the manufacturer's instructions. The array membranes were incubated for 30 min at room temperature in a blocking buffer. CM samples were then incubated on the membranes overnight at 4 °C. Following one large volume wash in Wash buffer I for an extended time of 30 min, three washes in Wash buffer I and two washes in Wash buffer II, membranes were incubated in Biotin-Conjugated Anti-Cytokines overnight at 4 °C. After washing as described above, membranes were incubated in HRP-Conjugated Streptavidin overnight at 4 °C. Washed arrays were finally incubated with Chemiluminescence Detection reagents and images were captured using the Azure c400 Imager (Azure Biosystems). Pixel density (signal density) of each spot on the membrane was quantified using ImageJ—Array Analysis plugin [27].

Extracellular vesicle isolation and characterization

For all EVs-isolation methods, CM2 was used. During processing, the conditioned medium was kept on ice. EVs were isolated from the pre-cleared concentrated medium (CM2) according to the manufacturer's instructions. The following kits were used for EVs isolation by immunoaffinity methods: (Exosome-Human EpCAM Isolation Reagent, Invitrogen; Exosome Isolation Kit CD63, Miltenyi Biotec; MagCapture™ Exosome Isolation Kit PS, FUJIFILM Wako Pure Chemical Corporation, Japan). For ultracentrifugation, the CM2 was transferred to a fresh 38 ml thin-wall polyallomer SW 28 UC tube and centrifuged for 120,000 g for 4 h in an SW 28 Ti Swinging

Bucket rotor (k-factor of 246) using Optima XPN 90 K Ultracentrifuge (Beckman Coulter). The crude EVs pellet was resuspended in a large volume of PBS followed by ultracentrifugation at 120,000 g for 4 h to wash the sample. The pellet was placed in filtered ice-cold PBS. All isolated EVs were then placed in 1,5 ml Protein LoBind Tubes (Sigma, EP0030108116) and stored in the manufacturers' elution buffers (filtered PBS in the case of ultracentrifugation) at -80 °C.

According to the MISEV2018 recommendations [28], five categories of proteins should be evaluated when characterizing EVs. The first category includes transmembrane proteins or glycosylphosphatidylinositol (GPI)-anchored proteins localized in the plasma membrane or endosomes, the presence of which demonstrates a lipid bilayer specific for EVs. The second category includes cytosolic proteins enclosed in EVs. The third category includes proteins often isolated together with EVs (e.g., proteins contained in the cytoplasm outside EVs, culture medium, serum, or urine). Evaluation of their presence helps to assess the degree of purity of isolated EVs. The fourth category includes transmembrane, lipid-bound, and soluble proteins associated with intracellular compartments other than the plasma membrane/endosomes (i.e., the membrane donor may be mitochondria, endoplasmic reticulum, Golgi apparatus, autophagosomes). The fifth category includes secreted or luminal proteins that may associate with EVs through binding to receptors on the surface of EVs; often cytokines, interleukins, and growth factors, which may represent a functional component of EVs in intercellular communication. The fifth category of proteins also reflects the native state of isolated exosomes (ligand-receptor binding is preserved). After evaluating all protein categories by LC–MS, the phosphatidylserine (PS)-based MagCapture™ method was judged to be the best method for isolating native EVs; see Additional file 1 Fig. S1. Due to the high viability of the observed cell populations after exposure to individual compounds and due to the size of the observed EVs, contamination of PS-EVs with apoptotic bodies is not expected. Moreover, apoptotic bodies are usually pelleted at low centrifugation, such as 2000 to 10,000 g [6]. Ribosomal proteins (RPS27A, RPS8) were found to be the largest contaminants of isolated EVs.

Dynamic Light Scattering (DLS)

Prior to the DLS measurements, each EVs sample (PS-positive EVs) was gently shaken at 4 °C for 20 min to dissolve possible EVs aggregates. About 50µL of each sample was added to a low-volume quartz batch cuvette (ZEN2112, Malvern Panalytical). DLS measurements were conducted at 25 °C using a Zetasizer Ultra (Malvern Instruments Ltd., UK) operating at 633 nm and recording the back scattered light at an angle of 173°. The sample temperature was allowed to equilibrate for 10 min before each measurement. The light scattering was recorded for 2 s with 35 replicate measurements (35 runs). The data were processed using the ZS Xplorer software (Malvern Panalytical).

Negative stain transmission electron microscopy and cryo-electron microscopy

EVs fractions (protein concentrations ranging from 243 to 417 µg/ml) were prepared for transmission electron microscopy (TEM) by absorption at activated Formvar/Carbon coated grids (HF35Cu, Pyser-SGI Limited, Kent, UK) for 5 min at RT. This was accomplished by pipetting 10 µl of the EVs containing elution buffer on the grid. Following sample adsorption, grids were quickly and gently blotted on filter paper and immediately floated for 5 min on 1 mL of 2% uranyl acetate and dried on filter paper at RT. EVs were examined at 70 kV with a Morgagni 268D transmission electron microscope (ThermoScientific) equipped with a MegaViewIII digital camera (Soft Imaging System). In all cases, TEM was performed on a fresh sample of EVs that had not been subjected to freezing temperatures at any step of purification or processing.

For cryo-electron microscopy, 3.5 µl of the EVs sample was applied to freshly plasma-cleaned TEM grids (Quantifoil, Cu, 200mesh, R2/1) and vitrified into liquid ethane using ThermoScientific Vitrobot Mark IV (18 °C, 100% rel. humidity, 30 s waiting time, 4 s blotting time). The grids were subsequently mounted into the Autogrid cartridges and loaded to Talos Arctica (ThermoScientific) transmission electron microscope for imaging. The microscope was operated at 200 kV. The EVs cryo-TEM micrographs were collected on Falcon3 direct electron detection camera at the 73,000× and 120,000× nominal magnification with the under focus in the range 3–10 µm and the overall dose of < 20 e/Å2.

Fluorescence microscopy

The autophagosomal/autolysosomal/lysosomal dynamics of affected cells were observed using the combination of PremoTM Autophagy Tandem Sensor (P36239, Invitrogen) with the far-red emitting LysoTracker® Deep Red (L12492, Invitrogen) (Ex 647 nm/Em 668 nm). By combining acid-sensitive Emerald GFP (eGFP) (Ex 488 nm/Em 509 nm) with acid-insensitive TagRFP (Ex 555 nm/Em 584 nm) in the PremoTM kit, autophagosomes and autolysosomes labelling (yellow and red, respectively) is possible.

Immediately after transduction with 12 µl PremoTM Autophagy Tandem Sensor/2 ml cell suspension, cells were seeded at 5×10^5 into 35-mm glass-bottomed

gelatin-coated dishes (Ibidi, µ-Dish 35 mm, high Glass Bottom) and cultured for 48 h to equilibrate expression levels. Subsequently, cells were exposed to the selected agents for 6, 12, 24 and 48 h before imaging. LysoTracker® Deep Red staining was performed 1 h before imaging.

To monitor the uptake of isolated PS-EVs by fibroblasts, we stained EVs with PKH67 (Sigma, PKH67GL) and then removed the remaining dye using Exosome Spin Columns (MW 3000) (Thermo Scientific, #4484449). The stained EVs were then suspended in 400 µl of cultivation medium and added to HGF cells growing for 24 h in Ibidi µ-Slide I Luer (Ibidi, 80176). Image acquisition was performed 24 h after EVs addition. 1 µl of 1 µg/ml of Hoechst 33342 (Enzo) (Ex 350 nm/ Em 461 nm) nuclear stain was added 1 h before imaging.

To determine the viability of the cell population prior to isolation of EVs, cells were left in a culture dish with 1 ml of culture medium to which propidium iodide (Sigma-Aldrich) and Hoechst 33342 were added 45 min before capturing. Cells positive for propidium iodide signal were considered dead. Images were automatically processed using custom MATLAB software, where live and dead cells were automatically detected and counted for individual fluorescence channels, which resulted in viability for individual fields of view. Automatic cell detection was based on Laplacian of Gaussian filter (sigma = 6), which was post-processed with maxima detector with required minimal distance between cells (10 px) and intensity threshold.

To maximize the possibility of comparison between samples, all samples (from a single cell line) were captured on the same day in a single run using the same microscope settings. For each time and each treatment, 10–12 fields of view were captured from randomized sites of the culture dish. Confocal microscopy images were acquired using Laser scanning confocal microscope Zeiss LSM 880 with AiryscanFast module (Carl Zeiss Inc.) using a C-Apochromat 40x/1.20W and C-Apochromat 63x /1.20W. LysoTracker® Deep Red was excited with 633 nm solid-state laser and emitted light was detected at 638–759 nm. Emerald GFP was excited with 488 nm using Argon laser, and emitted light was detected at 493–576 nm. TagRFP and PI were excited using DPSS 561 nm laser, and emitted light was detected at 570–650 nm. Hoechst 33342 was excited with a 405 nm solid-state laser, and emitted light was detected at 410–508 nm. Fluorescence images were acquired by the PMT/GaAsP PMT detectors.

Images were analyzed using custom MATLAB software developed in our laboratory. The analysis process consists of the segmentation of cells from the background and extraction of the intensity of fluorescence channels (TagRFP, eGFP, LysoTracker) inside cells. First, single cells were segmented. For segmentation, a thresholding-based method was used, where a manually selected threshold was applied. Segmentation was applied to the image created as the sum of all fluorescence channels to achieve segmentation independent of the intensity of individual channels. To achieve better segmentation without noisy pixels, fluorescence images were preprocessed with median filter (7×7) and Gaussian filter (standard deviation 1); additionally, binary segmentation was post-processed with morphological closing and removal of small binary connected components (< 5000px). For intensity measurements, the mean value of regions corresponding to cells was extracted from each field of view. Besides individual fluorescence channels, the mean colocalization of TagRFP and GFP was calculated with a pixel-wise multiplication of TagRFP and eGFP channels. Confocal images (autophagy dual labelling) used for the analyses are available online in the Zenodo repository (https://doi.org/10.5281/zenodo.7116549, https://doi.org/10.5281/zenodo.7116549).

Cell lysis and immunoblot analyses

For protein extraction from cells, these were washed twice with ice-cold 1xPBS and lysed for 20 min on ice in RIPA (Sigma, R0278) or Tris–EDTA SDS lysis buffer (pH 8, 1 M Tris–HCl, 0,5 M EDTA, 10%SDS), supplemented with protease (Roche, 04693132001) and phosphatase inhibitors (MedChemExpress, HY-K0021). Protein concentration was determined using the Pierce BCA protein assay (Thermo Scientific, 23225). Equal amounts of total protein (15 µg) were separated by SDS–PAGE, transferred to a PVDF (GE, GE10600023) or nitrocellulose (Bio-Rad, 1620112) membrane and analysed by using the following antibodies (in a dilution range of 1:500 – 1:5000): phospho 4-EBP1 (Thr 37/46) (#9459); phospho S6K (Thr 389) (#9206), LAMP2 (D5C2P) (#49067) (Cell Signaling), ULK1 (D8H5) (#8054), Atg13 (D4P1K) (#13273), FIP200 (D10D11) (#12436), Atg101 (E1Z4W) (#13492), Phospho-ULK1 (Ser757) (D7O6U) (#14202), Phospho-ULK1 (Ser556) (D1H4) (#5869) from Cell Signaling; CD63 (ab59479), CD9 (ab236630), CD81 (ab109201), Atg7 (ab133528), Atg5 (ab108327), SQSTM1/p62 (ab56416), LC3I/II (ab192890), GABARAP/GABARPL1/GABARAPL2 (ab109364), ACTB (ab16039), Tubulin (ab7219), EpCAM (ab71916) from Abcam; PI3K p100 (sc-365404), BECN1 (E8) (sc-48341), p-mTOR (Ser2448) (sc-293133) LAMP2 (sc-18822), Atg7 (sc-376212), Atg5 (sc-133158), mTOR (sc-517464) from Santa Cruz. Secondary antibodies (diluted 1:1000): HRP-linked Anti-rabbit IgG (#7074) from Cell Signaling, HRP-linked Anti-Rabbit and Anti-Mouse IgG (H + L) from Promega (W4011 and W402B). For detection, the Clarity Western-ECL substrate (Bio-Rad) was used. Blot luminiscence was

measured using Azure c400 Imager (Azure Biosystems) and subsequent densitometry was performed in ImageJ gel analyser tools.

For protein extraction from isolated extracellular vesicles, the total yields from all methods used for EVs isolation (including magnetic beads) were lysed in RIPA buffer on ice for 20 min. Concentrations were measured using the Micro BCA™ Protein Assay Kit (Thermo Scientific, 23,235). Proteins were separated by PAGE under nonreducing conditions and transferred to a PVDF membrane (GE, GE10600023) and processed as described above.

LC–MS

The EVs samples were diluted using SDT buffer (4% SDS, 0.1 M DTT, 0.1 M Tris/HCl, pH 7.6; SDT buffer:EVs ratio 1:1) and incubated in a thermomixer (Eppendorf ThermoMixer® C, 20 min, 95 °C, 1000 rpm). After that, samples were centrifuged (15 min, 20,000 × g) and the supernatant was further processed using filter-aided sample preparation (FASP, 30 kDa cut-off cartridges) as described elsewhere [29] using 0.5 µg of trypsin (sequencing grade; Promega). The resulting peptides were cleared from any residual SDS using liquid–liquid extraction step using ethyl acetate [30] and transferred into the LC–MS vial. The resulting peptides were analysed by nanoElute system (Bruker) connected to timsTOF Pro spectrometer (Bruker) using 68 min long non-linear gradient and diaPASEF acquisition mode. DiaPASEF data were processed in DIA-NN (version 1.8 [31]) in library-free mode against the modified cRAP database (based on http://www.thegpm.org/crap/) and UniProtKB protein database for *Homo sapiens* (https://ftp.uniprot.org/pub/databases/uniprot/current_release/knowledgebase/reference_proteomes/Eukaryota/UP000005640/UP000005640_9606.fasta.gz; version 2021/06, number of protein sequences: 20,600). Protein MaxLFQ intensities reported in the DIA-NN main report file were statistically evaluated. The mass spectrometry proteomics data have been deposited to the ProteomeXchange Consortium via the PRIDE [32] partner repository with the dataset identifier PXD037164. Detailed version of the LC–MS methodology is in Additional file 1.

EV-TRACK

We have submitted all relevant data of our experiments to the EV-TRACK knowledgebase (EV-TRACK ID: EV220362) [33].

Real time cell metabolic analysis

To examine the effect of the autophagy modulators or EVs on the cellular metabolism, cells were seeded at the density of 1×10^4 cells per well in a Seahorse 24-well plate (Agilent Technologies, Santa Clara, USA) and incubated for 24 h at 37 °C in the CAF-derived conditioned media. A day before the analysis, Seahorse cartridge (Agilent Technologies) was hydrated and incubated at 37 °C without CO_2. On the day of the experiment, the Seahorse XFe24 analyzer (Agilent Technologies, Santa Clara, CA, USA) was calibrated using hydrated cartridge. The culture medium was changed to Seahorse XF RPMI medium, pH 7.4 (Agilent Technologies). After incubating cells for 1 h at 37 °C without CO_2, the Seahorse ATP rate assay was performed by measuring the extracellular acidification rates (ECAR) as a proxy for glycolytic readouts and the oxygen consumption rates (OCR) as a proxy for oxidative phosphorylation readouts. The data were acquired and analysed using Wave 2.6.3 software (Agilent Technologies).

Statistical analysis

The raw data from proteomic analysis were normalized (log2 normalization) and the quality of each sample was determined. Of all 5405 identified proteins only 2538 had enough proteotypic peptides determined. Outlying replicates were removed and missing values in individual cases were imputed by random distribution around the minimal value of the whole dataset. Moderated t-test was performed in R using LIMMA package, and p values were adjusted on multiple hypothesis testing using Benjamini & Hochberg method [34]. All samples were compared to the control (CTR). The results were visualised using "volcano plots" (EnhancedVolcano package; https://github.com/kevinblighe/EnhancedVolcano). Over-representation analysis (ORA) using Gene Ontology (GO) database was performed using the clusterProfiler 4.0 package from Bioconductor [35]. The individual samples were compared with compareCluster. In the dotplot visualisation are showed enhanced terms from the cellular compartment and biological process ontologies. Samples were also characterised using Venn diagrams (nVennR package) [36], treemaps (treemap package) [37], and heatmaps (heatmap package) [38]. For data analysis, common packages like tidyverse, ggplot2, or data.table were used [39, 40].

Results and discussion

Effect of studied modulators on mTOR and autophagy machinery in FaDu cells

For modulation of the autophagy machinery, nine modulators were chosen (autophinib (APB), CPD18, EACC, bafilomycin A1 (BAFA1), 3-hydroxychloroquine (HCQ), rapamycin (RAPA), NVP-BEZ235 (BEZ), Torin1, and starvation).

As a first step, we evaluated the effect of these autophagy modulators on proteins in the mTOR/4EBP1 and mTOR/S6K signalling pathways (see Fig. 1a, b, c,

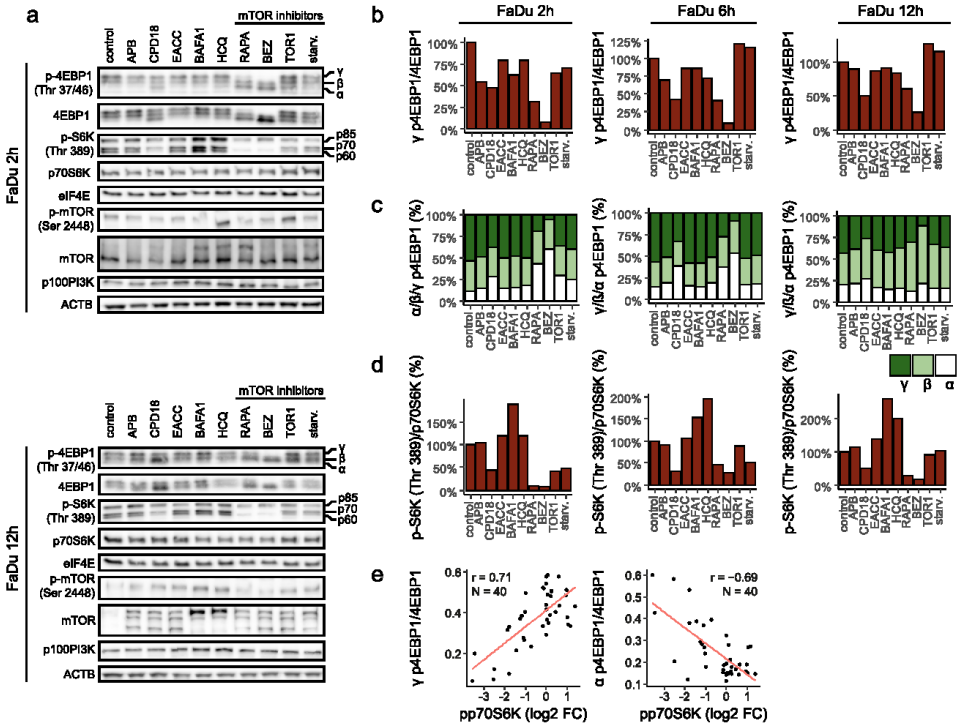

Fig. 1 Expression level of proteins in the mTOR/4EBP1 and mTOR/P70S6K signalling pathways. (**a**) Protein expression of p-4EBP1(Thr 37/46), 4EBP1, p-S6K (Thr 389), P70S6K, eIF4E, p-mTOR (Ser 2448), mTOR, p100PI3K; p- indicates phosphorylation. Uncropped western blots for this figure are shown in Additional file 3. (**b**) Densitometric analysis. The ratio of γ 4EBP1 phosphorylation isoform (hyperphosphorylated form) to levels of 4EBP1 protein. (**c**) Densitometric analysis. The levels of α-β-γ 4EBP1 phosphorylation isoforms. (**d**) Densitometric analysis. The ratio of S6K protein phosphorylation on Thr 389 to levels of p70S6K protein. (**e**) Pearson correlation. The level of p-p70S6K was in negative correlation with the presence of α-4EBP1 isoform (hypophosphorylated) ($p \leq 0.0001$) and in positive correlation with γ-4EBP1 isoform (hyperphosphorylated) ($p \leq 0.0001$)

d, and S2). Treatment of FaDu cells with rapamycin or BEZ prevented the hyperphosphorylation of 4EBP1 (the α-β-γ 4EBP1 isoforms represent the phosphorylation status with α being hypophosphorylated and γ being hyperphosphorylated). While BEZ potently inhibited 4EBP1 hyperphosphorylation throughout the whole duration of treatment (2 h, 6 h, 12 h, 24 h), after rapamycin treatment, 4EBP1 partially recovered in phosphorylation within 12 h despite initial inhibition (2 h). Therefore, cap-dependent translation can be partially maintained in the presence of rapamycin, but probably not in the presence of BEZ. This reemerged 4EBP1 phosphorylation after rapamycin was also shown in Choo et al. study [41]. Interestingly, other mTOR inhibitors Torin1 and starvation showed no such significant effect. The expression of the α isoform was enhanced by CPD18, RAPA, and BEZ.

Rapamycin and BEZ potently inhibited the phosphorylation of p70S6K throughout the duration of treatment (24 h). Phosphorylation of p70S6K was also inhibited by Torin1 and starvation but this inhibition was not so pronounced and long-lasting. The inhibitory effect on p70S6K phosphorylation was observable also after CPD18 treatment. On the other hand, BAFA1 and HCQ enhanced the phosphorylation of all three S6K isoforms (p85S6K, p70S6K, p60S6K). This could be partially explained by higher levels of mTOR after BAFA1 and HCQ treatment compared to control (see Fig. 1a). Consequently, BAFA1 and HCQ can support protein and DNA synthesis [42, 43]. Accordingly, it was shown that

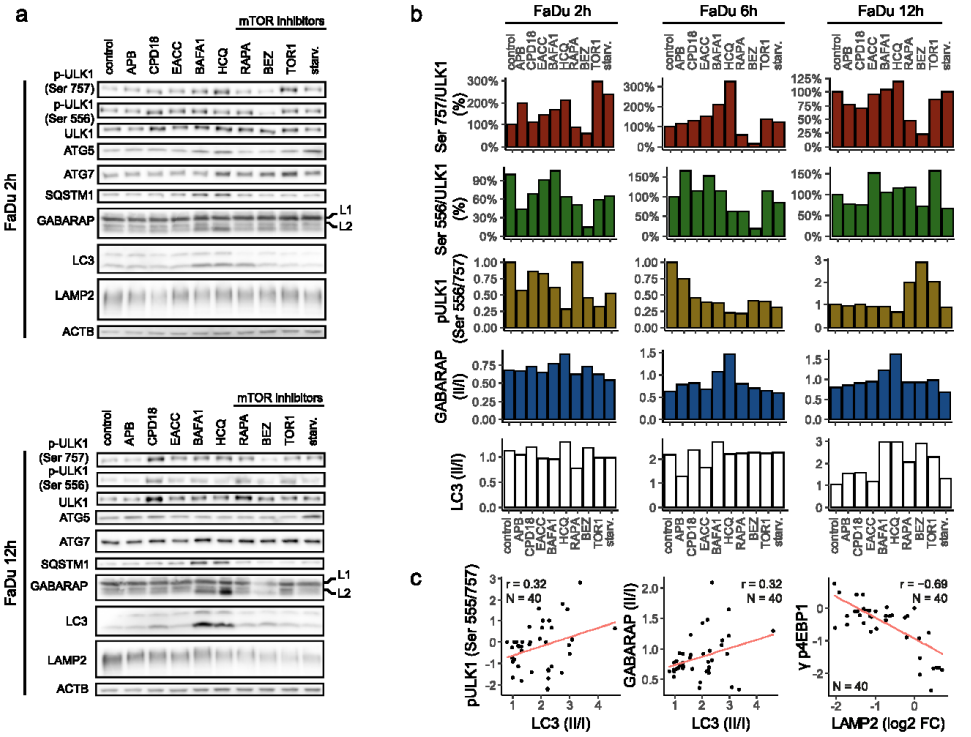

Fig. 2 Expression of proteins involved in the autophagy machinery. (**a**) Protein expression of p-ULK1 (Ser 757), p-ULK1 (Ser 556), ULK1, ATG5, ATG7, SQSTM1, GABARAP, LC3, and LAMP2; p- indicates phosphorylation. Uncropped western blots for this figure are shown in Additional file 3. (**b**) Densitometric analyses: the ratio of ULK1 phosphorylation on Ser 757 to ULK1 expression; the ratio of ULK1 phosphorylation on Ser 556 to ULK1 expression; the ratio of ULK1 phosphorylation on Ser 556/ Ser 757; the ratio of GABARAP II/I; the ratio of LC3 II/I. (**c**) Pearson correlation. The ratio of ULK1 phosphorylation on Ser-556 to Ser-757 was in positive correlation with LC3II/I ratio ($p = 0.046$). GABARAPII/I ratio and LC3II/I ratio were in positive correlation ($p = 0.044$). LAMP2 expression was in negative correlation with γ-4EBP1 ($p \leq 0.0001$)

lysosomotropic agents can activate the mTORC1 signalling pathway [44] and can induce eIF2α phosphorylation which triggers the integrated stress response [45].

The level of phosphorylation of p70S6K (p-p70S6K) was in negative correlation with the presence of α-4EBP1 isoform (hypophosphorylated) and in positive correlation with γ-4EBP1 isoform (hyperphosphorylated) (see Fig. 1e). This finding is in accordance with the fact that both p-p70S6K and γ-4EBP1 need mTOR to be active.

As a second step, we evaluated the effect of modulators on proteins involved in the autophagy machinery (see Fig. 2a, b, and Additional file 1 Fig. S3). Phosphorylation of ULK1 at Ser-556 stimulates autophagy, whereas phosphorylation at Ser-757 is inhibitory. Treatment with CPD18, EACC, BAFA1, HCQ, RAPA, BEZ, and Torin1 increased ULK1 expression in the time frame 2 h-12 h. The effect of CPD18 was the strongest and long-lasting (2 h, 6 h, 12 h, 24 h). Increased ratio Ser-556/Ser-757 indicating ULK1 activation was clearly observable due to mTOR inhibitors after 12 h (RAPA, BEZ, Torin1). Starvation showed this effect only after 24 h (see Additional file 1 Fig. S3). On the other hand, autophagy inhibitors decreased this ratio after 6 h treatment. No significant changes in Ser-556/Ser-757 ratio between autophagy inhibitors and control were observable at the time point of 12 h. Ratio Ser-556/Ser-757 indicating ULK1 activation was in positive correlation with LC3II/I ratio. GABARAPII/I ratio and LC3II/I ratio were also in positive correlation. LAMP2 expression was in negative correlation with γ-4EBP1 (expressing mTOR activity) (see

Fig. 2c). Accordingly, it was shown that activation of mTORC1 by free fatty acids suppresses LAMP2 expression [46]. Starvation led to the accumulation of ATG5. Overexpression of ATG5 in mice was shown to activate autophagy and extend lifespan [47]. P62 (SQSTM1), GABARAP-II, and LC-3II were accumulated after BAFA1 and HCQ treatment during all time points. LC3II/I ratio was decreased after EACC and APB treatment (at 6 h). EACC may increase LC3II degradation by the proteasome [48].

Autophagic flux was also morphologically traced with the mRFP-GFP-LC3 tandem construct (see Fig. 3a, b, Additional file 1 Fig. S4 and S5), where autophagosomes and autolysosomes were labelled in yellow and red, respectively. GFP fluorescence can be quenched by the low pH inside the lysosomes, whereas mRFP fluorescence is stable. Mean yellow (autophagosomes) and red (autolysosomes) signals per cell were detected at the time point of 12 h and 24 h (for a wider field of view see Additional file 1 Fig. S4 and S5). The intensity of the yellow signal (situations where autophagosome is positive for both red and green signal; calculated as a multiple of signals of the green and red channels; further designated as "yellow signal") was significantly diminished after APB, CPD18, EACC, and BAFA1 treatment.Some increase in the yellow signal was observed after RAPA, Torin1, and starvation (see Fig. 3a, b), however, this increase was statistically insignificant. The meanRFP signal was largely diminished after APB, CPD18, EACC, and BAFA1. The simultaneous decrease of both yellow and red signals indicates decreased autophagic flux [49]. The meanRFP signal was enhanced after HCQ indicating swelling of autolysosomes or their increased numbers. Although LC-3II was accumulated after BAFA1 treatment during all time points on WB, the yellow and red signal of the mRFP-GFP-LC3 tandem construct was diminished after BAFA1 treatment. It was found recently that whereas BAFA1 treatment increases the cellular levels of LC3-II, it results in a reduced recruitment of LC3 to autophagosomes. In contrast, HCQ, which increases the content of LC3-II in a similar fashion to BAFA1, did not affect the autophagosomal recruitment of LC3 [48].

LysoTracker-based fluorescent staining specific for lysosomal structures and other acidic organelles (autolysosomes) was applied to analyze the effect of autophagy modulators on lysosomes. Increased LysoTracker fluorescence intensity was observed within cells treated with HCQ (see Fig. 3a, b) indicating an increase in lysosomal size (probably lysosomal swelling) and in the number of lysosomes. HCQ can diffuse across the membranes of cells and organelles to acidic cytoplasmic vesicles (late endosomes, autolysosomes, and lysosomes). Once protonated, HCQ is trapped in the acidic organelles and can no longer freely diffuse out. This effect can cause lysosomal swelling. Lysosomotropic agents have also been shown to activate master lysosomal biogenesis transcription factor EB (TFEB) and ultimately lysosomal biogenesis [50]. An increase in lysosomal biogenesis and LysoTracker fluorescence intensity can be also expected after treatment with TFEB-activating agent Torin1 [50] and Akt-inhibiting rapamycin. Rapamycin inhibits Akt and ERK phosphorylation mainly via the mTORC2 signalling pathway because of the silencing of Rictor [51]. Consequently, TFEB activation via Akt inhibition promotes lysosomal biogenesis [52]. An increase in LysoTracker fluorescence intensity after Torin1 and rapamycin was observable after 12 h-treatment but disappeared after 24 h (see Additional file 1 Fig. S5). On the other hand, BAFA1 caused the vanishing of the fluorescent signal of acidic organelles from the cytoplasm due to the blockage of V-ATPase-based acidification. LC3II/I ratio assessed by WB was in positive correlation with the LC3-mRFP signal (red = autolysosomes) and with the yellow signal; see Fig. 3c.

Our results confirmed that the effect of all used autophagy modulators is realized within the first 24 h after the treatment. Therefore, we decided to isolate exosomes after 24 h-lasting treatment.

Real-time cell metabolic analysis revealed that total ATP production is enhanced after APB, BAFA1, and HCQ treatment. On the other hand, BEZ and starvation decreased total ATP production. BAFA1 and HCQ caused an increase of proton efflux rate following oligomycin treatment, indicating an increase of glycolysis; see Fig. 3d and e. Increased glycolysis rates after HCQ was also observed in metastatic renal cancer cells [53]. Lysosomotropic agents can activate the mTORC1 signalling pathway [44] which can upregulate glucose uptake and glycolysis [54]. RAPA, BEZ, and starvation decreased glycolytic production of ATP. As mTORC1 upregulates glucose uptake and glycolysis, inhibition of glycolysis after RAPA, BEZ, and starvation (all can inhibit mTORC1 signalling) could be expected [54]. Inhibition of glycolysis after Torin1 was visible but not statistically significant. Oxidative phosphorylation (OXPHOS) was significantly enhanced by starvation, as evidenced by a decrease in oxygen consumption rate (OCR) by oligomycin treatment.

Characterization of isolated EVs

We have isolated small PS-positive EVs (about 118.5 nm; assessed by DLS) using the MagCapture™ Exosome Isolation Kit PS, which proved to be the most suitable of all tested methods; see Fig. 4 and Additional file 1 Fig. S1. Exosomes are typically 30-150 nm in size, which corresponds to the size of EVs isolated using the MagCapture™ method. PS-EVs content shares

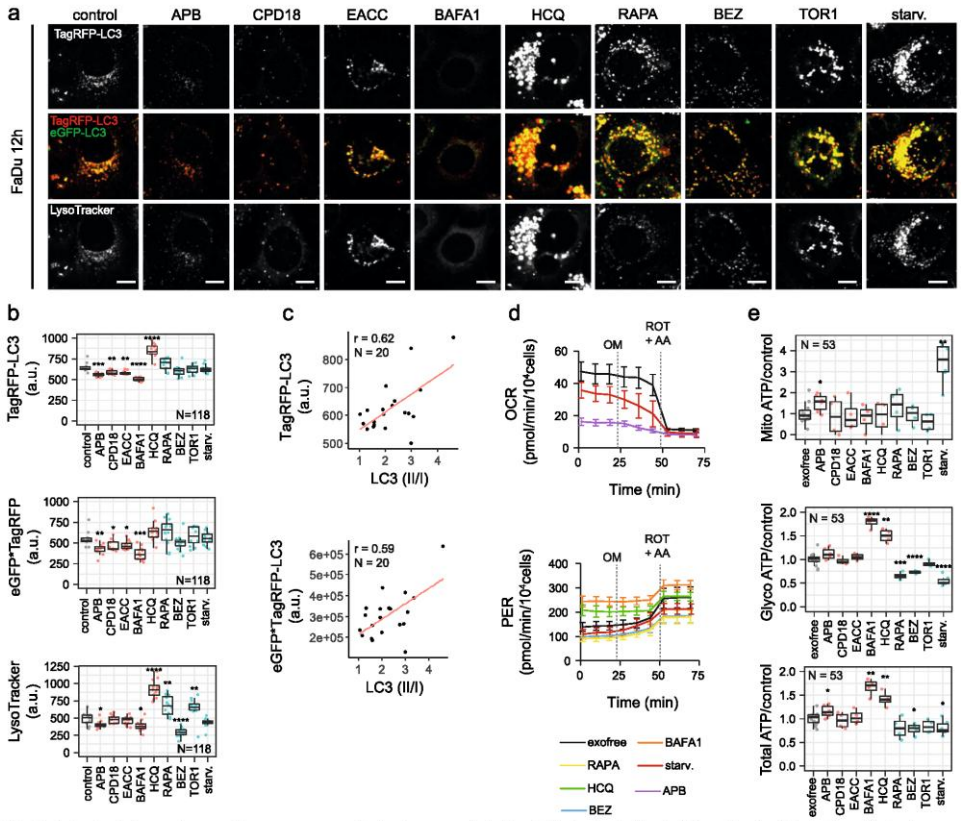

Fig. 3 Autophagic flux and energetic consequences of autophagy manipulation. (**a**) Autophagic flux in FaDu cells after 12 h-lasting effect of treatment traced with an mRFP-GFP-LC3 tandem construct; scale bar equals 10 µm. Autophagosomes and autolysosomes are labelled in yellow and TaqRFP, respectively. (**b**) The mean RFP signal (signal of autolysosomes) was significantly diminished after APB, CPD18, EACC, and BAFA1 and enhanced after HCQ treatment. The intensity of the yellow signal (situation where the autophagosome is positive for both red and green signal) was significantly diminished after APB, CPD18, EACC, and BAFA1 treatment indicating decreased autophagic flux. Significantly increased LysoTracker fluorescence intensity was observed for cells treated with HCQ, Torin1, and rapamycin. On the other hand, BAFA1 caused the vanishing of the fluorescent signal of acidic organelles from the cytoplasm. P-values from group comparisons based on the t-test are shown. Asterisks represent statistical significance (* $p < 0.05$; ** $p < 0.01$; *** $p < 0.001$). One dot represents single cell. (**c**) Pearson correlation. LC3II/I ratio assessed by WB was in positive correlation with LC3-mRFP signal (red = autolysosomes) ($p = 0.0003$) and with yellow signal (meanRFP-times-GFP) ($p = 0.006$). (**d**) and (**e**) ATP production from glycolysis and OXPHOS based on Seahorse parameters OCR (oxygen consumption rate) and ECAR (extracellular acidification rate) obtained from XF Real-Time ATP Rate Assay before and after autophagy inhibitors treatment; PER = Proton efflux rate, rate of protons extruded into the extracellular medium during glycolysis. OM = oligomycin; ROT = rotenone; AA = antimycin A. P-values from group comparisons based on the t-test are shown. Asterisks represent statistical significance (* $p < 0.05$; ** $p < 0.01$; *** $p < 0.001$). One dot represents a replicate in a single well

similarities with exosome content databases. A total of 2538 proteins were identified in the extracted PS-EVs. This number refers to the total number of proteins with enough proteotypic peptides identified in at least one replicate in all analyzed samples (after all autophagy-modulating treatments). When comparing this EVs content with the human exosome proteome databases (ExoCarta and Vesiclepedia), out of 2538 proteins found in PS-EVs, 2028 were present in the ExoCarta database, which constitutes 79.9% of the total protein content of the extracted EVs. In addition, the extracted

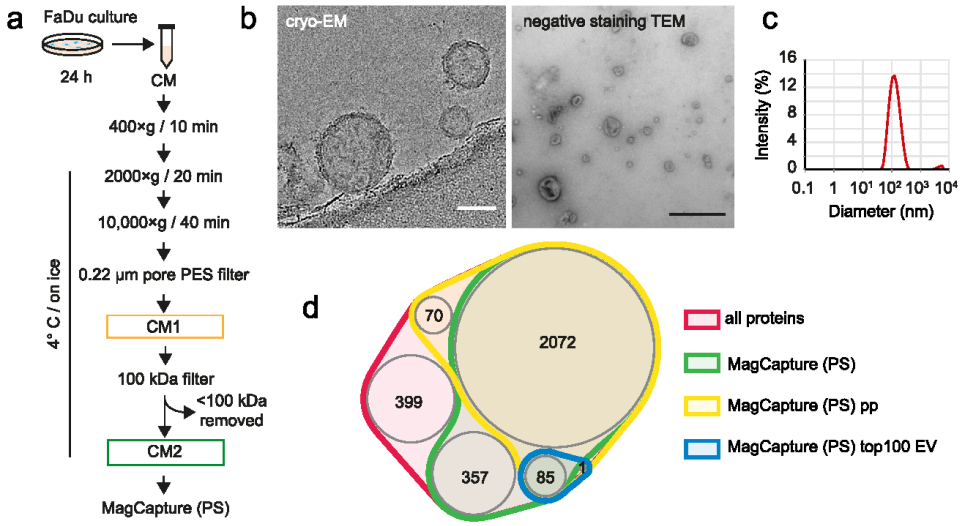

Fig. 4 Isolation and characterization of PS-positive EVs. (**a**) Flowchart of the PS-EVs isolation process. (**b**) Cryo-electron microscopy of non-collapsed extracellular vesicles (left), demonstrating the native character of isolated vesicles, with an apparently intact double membrane. The EVs cryo-TEM micrographs were collected on Falcon3 direct electron detection camera at the 120,000× nominal magnification with the under focus in the range 3–10 µm and the overall dose of < 20 e/Å2; scale bar equals 50 nm. Negative staining transmission electron micrograph of cup-shaped extracellular vesicles (right). Shown is a heterogeneous population of vesicles consisting of a range of sizes (30–200 nm) with low densities typical for exosomes. The extracellular vesicles were isolated by MagCapture isolation kit and embedded in a mixture of 2% uranyl-acetate. EVs were examined at 70 kV with a Morgagni 268D transmission electron microscope. Both Cryo-electron and TEM microscopy were performed on a fresh sample of EVs not subjected to freezing temperatures; scale bar equals 500 nm. (**c**) Size of isolated extracellular vesicles determined by DLS (Dynamic Light Scattering). (**d**) MagCapture (PS) pp = PS-EVs proteins characterized with a sufficient number of proteotypic peptides; MagCapture (PS) topEV = PS-EVs proteins identified in this study and present in the Top 100 proteins list of often identified in EVs according to EV databases ExoCarta and Vesiclepedia

PS-EVs shared 2349 common proteins with the Vesiclepedia database (92.5% of PS-EVs total protein content). These results confirm the validity of our PS-EVs isolation approach and make our data comparable with established vesicle proteome research. Furthermore, possible changes in representation of MISEV2018-recommended EV proteins [28] due to treatment with autophagy modulators were verified. No significant changes in these proteins caused by used treatments were observed (see Additional file 1 Fig. S1f). This suggests that modulators of autophagy do not significantly affect the predominant type of isolated PS-EVs. The third group of MISEV2018 proteins which includes contaminating proteins, often isolated together with EVs, was represented the least. The most abundant contaminant was the APOB protein. Accordingly, it was shown that lipoproteins (predominantly low-density lipoproteins) can be co-purified with EVs [55].

Autophagy modulators significantly change the production of important cytokines by FaDu cells but only a small portion of them is secreted through PS-EVs

In the first part of the experiment, we determined the presence of cytokines in a medium conditioned by FaDu cells that had undergone treatment with different autophagy modulators. The collected conditioned media (CM) were subjected to centrifugation steps to remove cells, debris, and apoptotic bodies. To remove large EVs, the supernatant was centrifuged at 10,000 g for 40 min. To remove any remaining large EVs, a 0.22 µm pore PES filter was used. In the resulting CM1, everything except large EVs (up to 220 nm) and apoptotic bodies can be presented (free cytokines + cytokines in small EVs) (see Fig. 5a).

Modulation of autophagy significantly affected the spectrum of cytokines released by FaDu cells into CM1 (see Fig. 5b). Obviously, the mechanism of action of a given inhibitor is very important as well as its function as an early or late autophagy inhibitor. This finding has implications for the use of autophagy inhibitors as

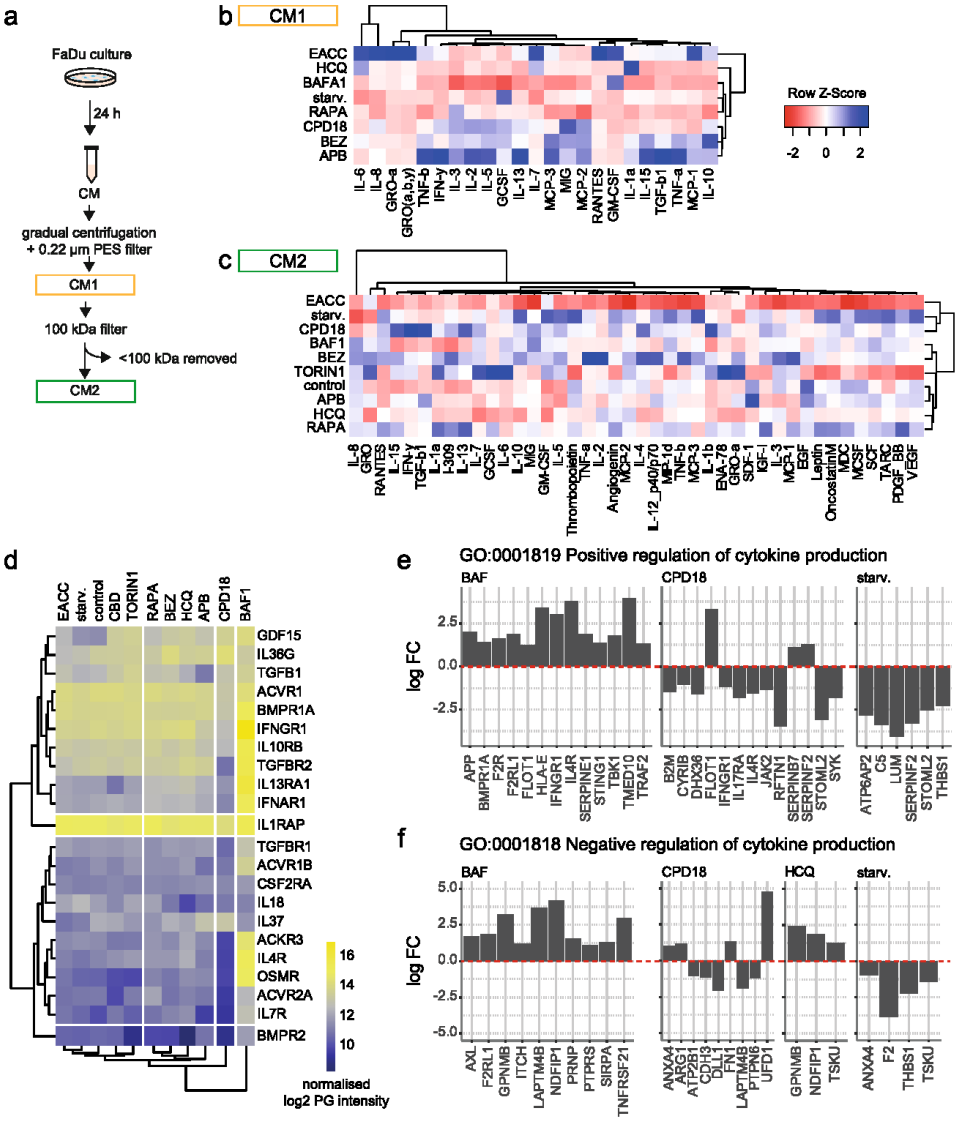

Fig. 5 Effect of autophagy modulators on cytokine production by FaDu cells. (**a**) Conditioned media (CM1 and CM2) preparation scheme. In CM1, everything except large EVs (up to 220 nm) and apoptotic bodies can be presented. CM1 involves free cytokines + cytokines in small EVs. CM2 was prepared from CM1. CM1 was concentrated and all molecules smaller than 100 kDa were removed (to remove free cytokines). (**b**) Heatmap of normalized cytokine levels in CM1. IL-6 and IL-8 respond similarly to autophagy modulation. Their expression is most promoted due to autophagy inhibition by EACC and, conversely, starvation suppresses their expression. (**c**) Heatmap of normalized cytokine levels in CM2. The biggest changes were seen in the levels of IL-8. (**d**) Cytokines detected in PS-EVs during proteomic analysis. PG = protein group (**e**) and (**f**) proteins involved in cytokine production were significantly changed in PS-EVs after treatment with autophagy modulators. BAFA1 = bafilomycin, HCQ = 3-hydroxychloroquine, RAPA = rapamycin, BEZ = NVP-BEZ235, starv = starvation, APB = autophinib

supportive drugs in antineoplastic therapy. For example, the late autophagy inhibitor EACC, which blocks autophagosome-lysosome fusion, significantly increases the production of interleukins) IL-6 and IL-8, which play a critical role in HNSCC carcinogenesis [56]. IL-6 is vitally important for malignant cells. Besides that, it is a critical molecule significantly shaping the tumour microenvironment [57]. The action of EACC also increases the levels of GRO-α, MCP-1, RANTES, and GM-CSF. Both GRO-α and IL-8 can activate TAK1/NFκB signalling via the CXCR2 receptor and are associated with increased cancer aggressiveness [58]. Furthermore, these cytokines can recruit monocytes and macrophages to sites of inflammation, and levels of cytokines were correlated with cancer progression [59–61]. The levels of these factors in CM1 were lower after autophagy induction by starvation or rapamycin and also after FaDu treatment with some early autophagy inhibitors (e.g. CPD18). Cytokine profiles of cancer cells were significantly affected by modulators of autophagy. It can be assumed that this is due, among other things, to changes in the spectrum and composition of small extracellular vesicles produced by FaDu cells. To assess cytokine content in small EVs, CM2 was prepared from CM1. CM1 was concentrated and all molecules smaller than 100 kDa were removed (to remove free cytokines). The changes in cytokine profiles were smaller in this setting. The biggest changes were seen in the levels of IL-8 (see Fig. 5c). Unlike in CM1, changes in IL-6 were insignificant and IL-8 levels were higher after BAFA1 and BEZ treatment due to CM2. EACC did not significantly change the production of IL-6, IL-8, GRO-α, MCP-1, RANTES, or GM-CSF. Thus, we can assume that these cytokines are not released predominantly through small EVs after EACC treatment.

Only one cytokine from the 42 measured cytokines in the cytokine assay was detected in PS-EVs during proteomic analysis, which indicates that secretion of commonly determined cytokines is not predominantly mediated through PS-EVs. This cytokine was transforming growth factor beta-1 proprotein, which is the precursor of the Latency-associated peptide (LAP) and Transforming growth factor beta-1 (TGF-beta-1) chains, which constitute the regulatory and active subunit of TGF-beta-1 (see Fig. 5d).

Nevertheless, other proteins involved in cytokine signalling were present in PS-EVs such as Bone morphogenetic protein receptor type-2, Interleukin-7 receptor subunit alpha, Activin receptor type-2A (ACVR2A), Oncostatin-M-specific receptor subunit beta, Interleukin-4 receptor subunit alpha, Atypical chemokine receptor 3, IL-37, IL-18, Activin receptor type-1B (ACVR1B), TGF-beta receptor type-1 and 2 (TGFBR1, TGFBR2), Interferon alpha/beta receptor 1 (IFNAR1), Interleukin-13 receptor subunit alpha-1 (IL13RA1), Interleukin-10 receptor subunit beta, Interferon-gamma receptor 1, Bone morphogenetic protein receptor type-1A, Activin receptor type-1, IL-36 gamma, and Growth/differentiation factor 15.

Moreover, proteins involved in cytokine production (GO:0001819, 0001818) were significantly changed in PS-EVs after treatment with autophagy modulators (see Fig. 5e and f). For example, levels of Flotillin 1 (FLOT1) were increased in PS-EVs after BAFA1 or CPD18. High expression of FLOT1 correlates with tumour progression [62]. Levels of Lysosome-associated transmembrane protein 4B (LAPTM4B) were increased in PS-EVs after BAFA1 and decreased after starvation. Elevated LAPTM4B levels contribute to chemotherapy resistance in cancer [63]. Levels of Tsukushi (TSKU), that enable TGF-β binding activity, were increased in PS-EVs after HCQ treatment and decreased after starvation. Levels of SERPIN proteins in PS-EVs were also changed due to treatment with autophagy modulators. Serpins can promote cancer cell survival and vascular cooption in metastasis [64].

Autophagy modulators significantly change the protein content of PS-EVs. Many of these proteins are important signalling molecules

The most abundant proteins in PS-EVs were proteins typical for extracellular exosomes, cytosol, cytoplasm, and cell surface involved in cell adhesion, angiogenesis, and apoptotic processes; see Fig. 6a and b. The protein content of PS-EVs was the most significantly influenced by HCQ, BAFA1, CPD18, and starvation (see Additional file 2 and Additional file 1 Fig. S6). The numbers of proteins identified after each treatment and in each replicate are shown in Additional file 2.

(See figure on next page.)

Fig. 6 Protein content of PS-EVs. (**a**) Representation of proteins contained in PS-EVs in biological processes and cellular components. The most abundant proteins in PS-EVs were proteins typical for extracellular exosomes, cytosol, cytoplasm, and cell surface involved in cell adhesion, angiogenesis, and apoptotic processes. PG = protein group (**b**) Categories from the GO database. Changes in biological processes and the representation of PS-EVs proteins in particular cellular compartments caused by autophagy modulators. (**c**) Autophagy modulators change the levels of p62/SQSTM1 in PS-EVs. Bafilomycin and HCQ treatment induces the inclusion of p62/SQSTM1 into PS-EVs. PG = protein group (**d**) Autophagy modulators significantly change the representation of mitochondrial proteins in PS-EVs. PG = protein group (**e**) Autophagy modulators significantly change the representation of some Rab proteins in PS-EVs

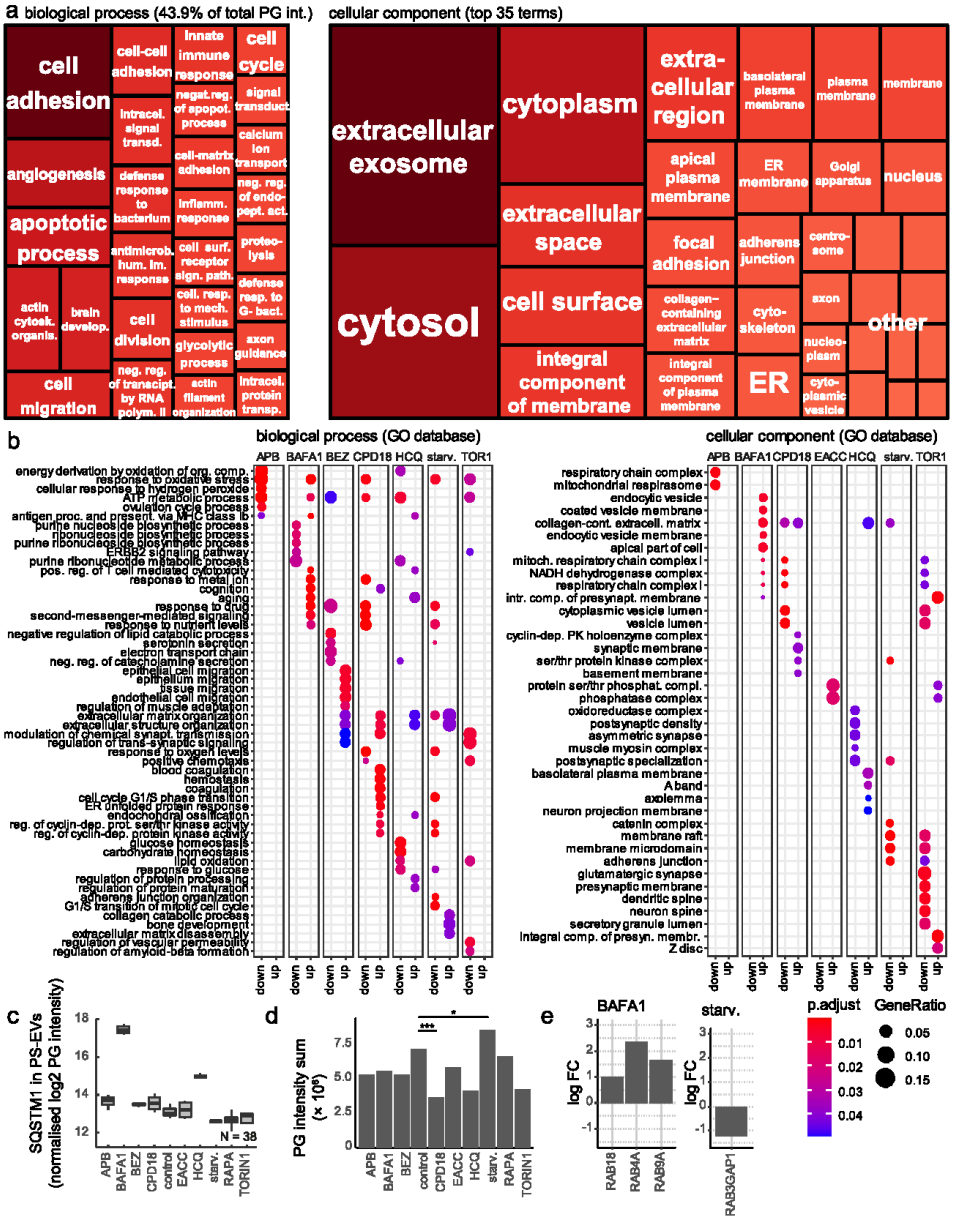

Fig. 6 (See legend on previous page.)

39 proteins were significantly enriched in PS-EVs after HCQ treatment and 8 were significantly less represented compared to control PS-EVs. 292 proteins were significantly enriched in PS-EVs after BAFA1 treatment and 11 were significantly less represented compared to control PS-EVs. 116 proteins were significantly enriched in PS-EVs after CPD18 treatment and 179 were significantly less represented compared to control PS-EVs. 10 proteins were significantly enriched in PS-EVs after starvation and 118 were significantly less represented compared to control PS-EVs. Both lysosome-affecting compounds BAFA1 and HCQ induced the inclusion of p62/SQSTM1 into PS-EVs (Fig. 6c). Similar enrichment of SQSTM1 in exosomes after BAFA1 was also seen in Minakaki et al. study [65] and after lysosomal impairment [66]. The extracellular SQSTM1 can bind to membrane insulin receptors to activate glycolysis and the production of pro-inflammatory cytokines [67]. Both lysosome-affecting treatments identically increased the abundance of the same 35 proteins in PS-EVs (for example BRI3 = Brain protein I3, GLG1 = Golgi glycoprotein 1, GRN = Granulin, or TMEM59 = Transmembrane protein 59). These proteins are involved in biological processes such as vacuolar transport (GO:0007034) or lysosomal transport (GO:0007041). BRI3 plays an important role in TNF-induced cell death, can be localized to lysosomes, and may function through lysosomes. The antisense RNA against BRI3 promoted resistance to TNF-induced cell death [68]. GLG1 (alias Cysteine-rich fibroblast growth factor receptor) was shown to be a potentially useful auxiliary marker for immunohistochemical diagnosis of Ewing sarcoma and decoy receptor for FGF [69, 70]. As FGFR1 (Fibroblast growth factor receptor 1) activation can suppress autophagy [71], GLG1 presence can support the induction of autophagy. Granulin (GRN) is a potent mitogen and growth factor implicated in many human cancers [72]. TMEM59 acts as a regulator of autophagy by promoting the lipidation of LC3 (MAP1LC3A, MAP1LC3B or MAP1LC3C) and subsequent activation of autophagy [73].

BAFA1 also enhanced the inclusion of autophagy regulators GABARAPL2 (enhanced also by HCQ) and LAMP2, and transporter SLC38A2 into PS-EVs. Increased expression of glutamine transporter SLC38A2 promotes glutamine dependence and oxidative stress resistance and is associated with a worse prognosis in triple-negative breast cancer [74]. According to the GO analysis (see Fig. 6b), proteins, whose exosomal abundance is affected by BAFA1 or HCQ, are predominantly part of the ATP metabolic processes = GO:0046034 (BAFA1-upregulated, HCQ-downregulated), purine nucleoside biosynthetic process = GO:0042451 (BAFA1-downregulated, HCQ-downregulated), and aging = GO:0007568 ((BAFA1-upregulated, HCQ-upregulated). The predominant cellular compartments in which the detected proteins occur inside the cell are shown in Fig. 6b. Components of the mitochondrial respiratory chain complex 1 are enriched in the PS-EVs after BAFA1 treatment.

CPD18 increased the abundance of MYCBP (MYC binding protein), OIT3 (Oncoprotein-induced transcript 3 protein), AFP (α-fetoprotein), GCHFR (GTP cyclohydrolase 1 feedback regulatory protein), or CLEC3B (C-type lectin domain family 3 member B) in PS-EVs. Overexpression of MYCBP can promote invasion and migration in gastric cancer [75]. This protein was also more abundant in PS-EVs after HCQ and BAFA1 treatment. OIT3 mediates macrophage polarization and facilitates hepatocellular carcinoma progression [76]. AFP can promote cancer progression by suppressing the HuR-mediated Fas/FADD apoptotic pathway [77]. Overexpression of GCHFR attenuates LPS and cytokine-stimulated nitric oxide production [78]. Fibroblast collagen synthesis is enhanced by nitric oxide (NO). Fibroblasts can be stimulated by cytokines to synthesize NO, while wound-derived fibroblasts synthesize NO spontaneously [79]. Downregulation of exosomal CLEC3B in hepatocellular carcinoma promoted metastasis and angiogenesis via AMP-activated protein kinase (AMPK) and Vascular endothelial growth factor (VEGF) signals [80]. On the other hand, the abundance of Myosin X (MYO10), Bcl-2-like protein 12 (BCL2L12), or the amount of many important proteins regulating mTOR, Wnt, or cytokine and growth factor signalling was decreased after CPD18 treatment in PS-EVs (e.g.: TNFAIP = TNF-alpha-induced protein 3, TNFAIP8L1 = TNF-alpha-induced protein 8-like 1, MEAK7 = mTOR-associated protein, Eak-7 homolog, TGFBR2 = TGF-β receptor type 2, TNIK = TRAF2 And NCK Interacting Kinase, CCNY = Cyclin-Y, PLK1 = Polo-like kinase 1, IL4R = Interleukin-4 receptor, COPZ1 (Coatomer protein complex subunit zeta 1), IL17RA = Interleukin 17 receptor A, JAK2 = Janus Kinase 2). MYO10 regulates genome stability, through which it mediates inflammation in cancer. Depletion of MYO10 ameliorated genomic instability and reduced inflammation signalling [81]. BCL2L12 inhibits the p53 tumour suppressor and contributes to intense therapeutic resistance of gliomas [82]. According to the GO analysis (see Fig. 6b), proteins whose exosomal abundance is affected by CPD18 are part of the cell cycle G1/S transition = GO:0044843 (upregulated), ATP metabolic processes = GO:0046034 (downregulated), response to oxidative stress = GO:0006979 (downregulated), response to drugs = GO:0042493 (downregulated), and response to oxygen levels = GO:0070482 (downregulated). The predominant cellular compartment in which the detected

proteins occur inside the cell is shown in Fig. 6b. Components of the mitochondrial respiratory chain complex 1 are less presented in the PS-EVs after CPD18 treatment.

Starvation increased the abundance of MMP13 (Matrix metalloproteinase 13), which can promote angiogenesis, and decreased the abundance of ALDH1A1 = Aldehyde dehydrogenase 1A1, POSTN = Periostin, RGN = Regucalcin, or GLG1 in PS-EVs [83]. These proteins play an important role in carcinogenesis. Aldehyde dehydrogenase 1 (ALDH1) has been suggested as a putative cancer stem cell marker in several cancer types [84]. Secreted POSTN promoted cancer stemness in head and neck cancer by activating protein tyrosine kinase 7 [85]. RGN promotes dormancy in cancer cells [86]. The abundance of low-density lipoprotein receptor (LDLR), olfactomedin-like 2A (OLFML2A), Stomatin-like protein 2 (STOML2), and stanniocalcin-1 (STC1) in PS-EVs was decreased after both, starvation or CPD18 treatment. Elevated tumour LDLR expression accelerates LDL cholesterol-mediated breast cancer growth [87]. OLFML2A downregulation inhibited glioma proliferation through suppression of Wnt/β-Catenin signalling pathways [88] STOML2 is up-regulated and acts as an oncogenic protein in multiple cancers [89]. STC1 expression is associated with tumour growth and metastasis in breast cancer [90]. Hypothetically, the reduction of these proteins in EVs could contribute to the positive effects of starvation and/or CPD18 during chemotherapy [91]. According to the GO analysis (see Fig. 6b), proteins whose exosomal abundance is affected by starvation are part of the cell cycle G1/S transition = GO:0000082 (downregulated), response to drugs = GO:0042493 (downregulated), and response to oxygen levels and oxidative stress = GO:0070482 and GO:0006979 (downregulated).

Autophagy modulators also significantly changed the representation of mitochondrial proteins and Rab proteins in PS-EVs (see Fig. 6d and e). The highest abundance of mitochondrial proteins in PS-EVs was observable after starvation and the lowest after CPD18 treatment. The representation of mitochondrial proteins in PS-EVs probably reflects ATP production in mitochondria, as this production was highest in FaDu cells during starvation (see Fig. 3e). Recent observation suggests that EV-mediated transfer of mitochondrial content can alter inflammatory responses of recipient cells [92, 93]. Rab proteins coordinate cellular transport because of the effect on vesicle formation, motility, and tethering with target membranes [94]. Rab18, Rab4a, and Rab9a proteins were significantly more presented in PS-EVs after BAFA1 treatment. Rab18 can promote the growth and aggressivity of cancer cells, possibly through STAT3 signalling and the regulation of mitochondrial functions [95–97]. Rab18 knockdown increased autophagy flux and regulated proteostasis [98]. *RAB4A* gene was shown to be amplified in invasive breast cancer [99]. Overexpression of Rab5a and Rab4a proteins may promote the endosomal recycling of epidermal growth factor receptors, which can contribute to tumour progression [100]. Rab9A can play a tumour-promoting role in cancer cells by Akt/mTOR signalling pathway [101]. On the other hand, RAB3GAP1 protein was significantly less presented in FaDu-derived PS-EVs after starvation. RAB3GAP1 can influence protein aggregation and affects autophagy under basal and rapamycin-induced conditions [102].

PS-EVs are phagocytosed into recipient fibroblasts and CM2 containing PS-EVs influence the autophagy flux, p21 expression, and metabolic profiles of fibroblasts

To monitor the uptake of isolated PS-EVs by fibroblasts, we stained EVs with PKH67 and then removed the remaining dye using Exosome Spin Columns (MW 3000). The stained EVs were then suspended in 400 µl of medium and added to HGF cell culture growing for 24 h. Image acquisition was performed 24 h after PS-EVs addition. Stained EVs were presented inside fibroblasts (see Additional file 1 Fig. S7a). Autophagic flux in HGF cells after 12 h, 24 h, and 48 h-lasting effects of treatment was traced with an mRFP-GFP-LC3 tandem construct (see Fig. 7a, b, and Additional file 1 Fig. S8). CPD18-CM2 (medium with removed free cytokines; containing small EVs) from FaDu cells pre-treated by CPD18 enhanced autophagy flux in HGF. The intensities of the yellow signal (calculated as meanRFP-times-GFP) and the mean-RFP signal from the mRFP-GFP-LC3 tandem construct were significantly enhanced (see Fig. 7a, b, and Additional file 1 Fig. S8). The increase in autophagic flux in HGF after CPD18-CM2 was also observed on WB (enhanced expression of LC3II and GAPARAP after 48 h; see Fig. 7c and S7b. This effect is not the result of residual treatment in CM2, as CPD18 rather decreased the autophagic flux in FaDu cells. On the other hand, the effect of HCQ on fibroblasts is probably caused by residual HCQ in CM2 (persistent high LysoTracker signal), despite the concentrating and following dilution of the concentrated conditioned media to remove the treatment residue. Since, judging by the effect on autophagy, the other treatment residues were successfully removed (no persistent and consistent effect on autophagy), we can speculate that the HCQ residue may be contained in the exosomes.

LysoTracker-based fluorescent signal specific for lysosomal structures and other acidic organelles (autolysosomes) was decreased and the abundance of SQSTM1 protein was increased because of media conditioned with cancer cells (FaDu conditioned medium compared to HGF without CM) (see Fig. 7a and b). Consequently, cancer cells can probably manipulate the lysosomal and

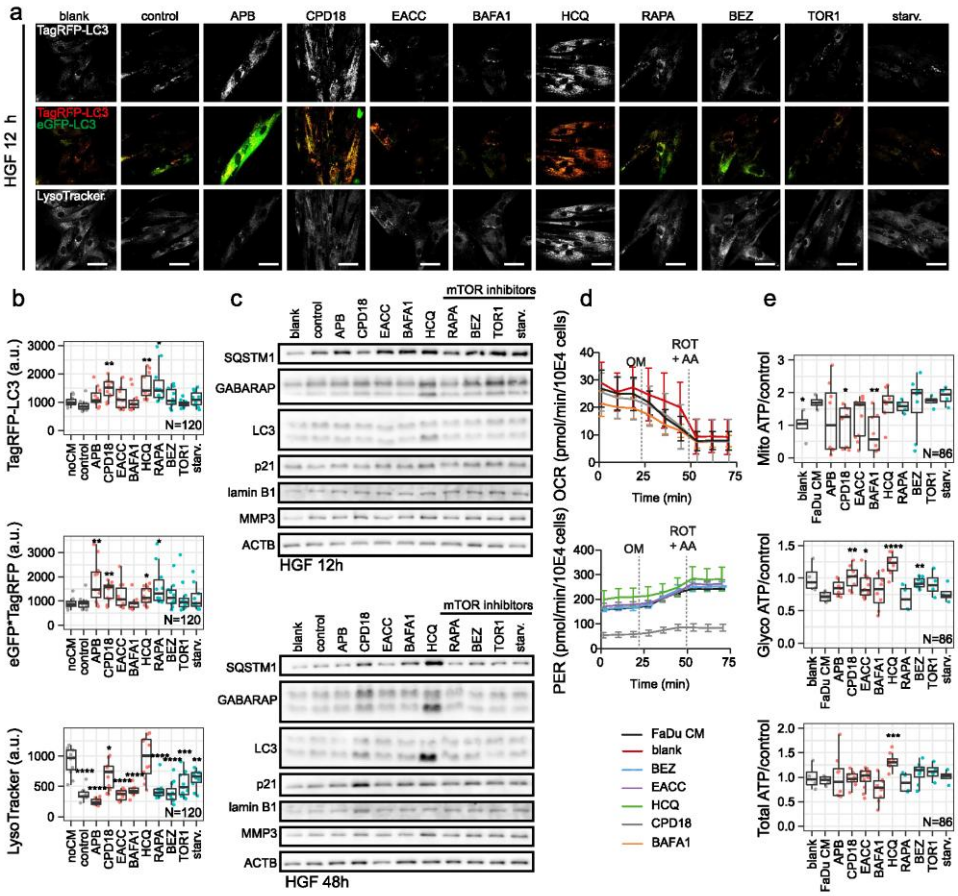

Fig. 7 PS-EVs influence the autophagy flux, expression of senescence-associated proteins, and metabolic profiles of fibroblasts. (**a**) Autophagic flux in HGF cells after 12 h-lasting effect of CM2 treatment traced with an mRFP-GFP-LC3 tandem construct. Autophagosomes and autolysosomes are labelled in yellow and red, respectively. LysoTracker-based fluorescent signal is specific for lysosomal structures and acidic organelles. blank = exofree medium incubated at 37 °C 24 h. control = CM2 medium conditioned by non-treated FaDu cells. Scale bar equals 50 µm. Representative fields of view of minimally 11 per treatment. (**b**) CPD18-CM2 medium from FaDu cells pre-treated by CPD18 enhanced autophagy flux in HGF. The intensities of the yellow signal (calculated as meanRFP-times-GFP) and the meanRFP signal from the mRFP-GFP-LC3 tandem construct were significantly enhanced. noCM = HGF without conditioned medium; control = CM2 medium conditioned by non-treated FaDu cells. N indicates number of cells. (**c**) The expression level of proteins involved in the autophagy machinery or senescence after treatment (12 h; 48 h) with CM2 containing PS-EVs. Uncropped western blots for this figure are shown in Additional file 3. (**d**) and (**e**) ATP production from glycolysis and OXPHOS based on Seahorse parameters OCR (oxygen consumption rate) and ECAR (extracellular acidification rate) obtained from XF Real-Time ATP Rate Assay before and after autophagy inhibitors treatment; PER = Proton efflux rate, rate of protons extruded into the extracellular medium during glycolysis. blank = exofree medium incubated at 37 °C 24 h. FaDu CM = CM2 medium conditioned by non-treated FaDu cells. OM = oligomycin; ROT = rotenone; AA = antimycin A. P-values from group comparisons based on the t-test are shown. Asterisks represent statistical significance (* $p < 0.05$; ** $p < 0.01$; *** $p < 0.001$). Each dot represents a measurement in well. N indicates number of cells

autolysosomal numbers in TME fibroblasts, probably through mitochondrial stress [103, 104]. Pretreatment of FaDu cells with CPD18 somewhat reduced this effect of CM2 on LysoTracker signal in HGF. Pretreatment of FaDu cells with CPD18 also led to the accumulation of p21 protein in HGF influenced by FaDu-derived CPD18-CM2 (after 48 h; see Fig. 7c). p21 acts as an inhibitor of the cell cycle by blocking progression through G1/S and belongs among well-established senescence markers [105]. Cellular senescence involves chromatin remodelling and Ivanov et al. showed that an autophagy-lysosome pathway contributes to this [106]. This may explain the simultaneous upregulation of autophagic flux and p21 expression in fibroblasts after CPD18-CM2.

Lamin B1 loss is a senescence-associated biomarker [107]. Nevertheless, no drop in lamin B1 expression was observed after CPD18-CM2 in fibroblasts. It can be caused by LC3–lamin B1 interaction impairing lamin B1 degradation [108]. Treatment of fibroblasts by different kinds of CM2 also significantly influenced the expression of MMP-3 in fibroblasts. MMP-3 is involved in various cancer-associated processes such as angiogenesis, cell growth and cell invasion. Overexpression of MMP-3 was observed in many cancers [109]. The protein expression level of MMP-3 was also upregulated in irradiated senescent cells [110]. CM2 conditioned by FaDu cells, CPD18-CM2, HCQ-CM2, BEZ-CM2, TORIN1-CM2, and starvation-CM2 enhanced the expression of MMP-3 in HGF. All used CM2 caused the accumulation of SQSTM1 in fibroblasts (see Fig. 7c).

Furthermore, Seahorse analyses revealed that the CM2 medium conditioned by FaDu cancer cells increased relative mitochondrial ATP production in HGF. This effect of CM from tumour cells on fibroblasts was previously observed in Kumar et al. study, where HNSCC-secreted bFGF increased mitochondrial oxidative phosphorylation in CAFs [111]. Pretreatment of FaDu cells with CPD18 has again reduced this effect of CM on OXPHOS in fibroblasts. This is in accordance with the lower presence of PS-EVs proteins representing GO pathways related to ATP metabolic processes after CPD18 treatment. A similar effect was also observed after BAFA1 pretreatment. A statistical nonsignificant but visible drop in glycolysis was observed due to CM2 presence. This effect was reduced by CPD18, EACC, or BEZ pretreatment of FaDu cells (see Fig. 7d and e).

Conclusions

Extracellular vesicles (EVs) are increasingly recognized as key mediators of intercellular communication with prominent roles in many physiological and pathological processes. In this study, we found that autophagy modulators significantly alter the composition of the protein content of phosphatidylserine-positive EVs (PS-EVs) produced by cancer cells. This protein content involves cytokines, mitochondrial proteins, and many important signalling molecules which can actively influence key processes in the tumour microenvironment. Consequently, if autophagy modulators will be used as synergistic agents in cancer therapy, their effect on the protein content of EVs should be considered. The altered protein content of PS-EVs also provides important information about the cellular compartments and processes that are affected by the applied autophagy modulators.

Supplementary Information

The online version contains supplementary material available at https://doi.org/10.1186/s12964-023-01126-z.

Additional file 1: Fig. S1. Isolation and characterization of extracellular vesicles. **Fig. S2.** Expression level of proteins in the mTOR/4EBP1 and mTOR/P70S6K signalling pathways. **Fig. S3.** Expression level of proteins in the autophagy machinery. **Fig. S4.** Autophagic flux in FaDu cells after 12h-lasting effect of treatment traced with an mRFP-GFP-LC3 tandem construct. **Fig. S5.** Autophagic flux in FaDu cells after 24h-lasting effect of treatment traced with the mRFP-GFP-LC3 tandem construct. **Fig. S6.** Volcano plots. Protein content of PS-EVs after treatments which was the most influential (HCQ, BAFA1, CPD18, and starvation). **Fig. S7.** PS-EVs are phagocytosed into recipient fibroblasts and CM2 containing PS-EVs influence the autophagy flux and senescence in HGF. **Fig. S8.** Autophagic flux in HGF cells after 24h and 48h-lasting effect of treatment traced with the mRFP-GFP-LC3 tandem construct.

Additional file 2: Table S1. Changes in the representation of PS-EVs proteins caused by autophagy modulators.

Additional file 3: Full and uncropped western blots.

Acknowledgements

We acknowledge the core facility CELLIM supported by MEYS CR (LM2018129 Czech-BioImaging). We thank the CEITEC MU Proteomics Core Facility of CIISB, Instruct-CZ Centre, supported by the Ministry of Education of the Czech Republic (LM2023042) and the European Regional Development Fund-Project "UP CIISB" (No. CZ.02 1.01/0.0/0.0/18_046/0015974). Computational resources used for proteomic data evaluation were supplied by the project "e-Infrastruktura CZ" (e-INFRA LM2018140) provided within the program Projects of Large Research, Development and Innovations Infrastructures. We acknowledge the support of the Cryo-electron Microscopy and Tomography Core Facility of CEITEC MU CIISB, Instruct-CZ Centre supported by the Ministry of Education of the Czech Republic (LM2023042). We greatly acknowledge Dr. Xia Peng and prof. Martin Pumera for DLS analysis, Dr. Anna Vyhlídalová Kotrbová and Dr. Vendula Hlaváčková Pospíchalová for their help with ultracentrifugation, flow cytometry and for many helpful and supportive hints related to experiments with EVs. We thank Ladislav Ilkovics and Dobromila Klemova for operating the TEM and sample preparation.

Authors' contributions

K.H., J.N., M.B. and J.B. performed the experimental work; J.B., M.R. and M.M. designed the experimental plan; M.K., T.V., J.B. and J.G. evaluated the data, performed statistical analysis and interpreted the results; K.H., M.R., T.V. and J.B. wrote the main text of the paper. The author(s) read and approved the final manuscript.

Funding

This work was supported by the Ministry of Health of the Czech Republic NU22-03–00202 and NU20J-08-00018, by the Grant Agency of the Czech Republic (21-06873S) and by funds from Specific University Research Grant, as provided by the Ministry of Education, Youth and Sports of the Czech Republic in the year 2023 (MUNI/A/1370/2022 and MUNI/A/1343/2022). We were also

supported by CEITEC MU Proteomics Core Facility of CIISB, Instruct-CZ Centre, supported by the Ministry of Education of the Czech Republic (LM2023042) and the European Regional Development Fund-Project "UP CIISB" (No. CZ.02 .1.01/0.0/0.0/18_046/0015974). Computational resources used for proteomic data evaluation were supplied by the project "e-Infrastruktura CZ" (e-INFRA LM2018140 provided within the program Projects of Large Research, Development and Innovations Infrastructures.

Availability of data and materials

Confocal images (autophagy dual labelling) used for the analyses are available online in the Zenodo repository (https://doi.org/10.5281/zenodo.7116549, https://doi.org/10.5281/zenodo.7116549). The mass spectrometry proteomics data have been deposited to the ProteomeXchange Consortium via the PRIDE [32] partner repository with the dataset identifier PXD037164". We have submitted all relevant data of our experiments to the EV-TRACK knowledgebase (EV-TRACK ID: EV220362) [33].

Declarations

Competing interests

The authors declare no competing interests.

Author details

[1]Department of Pathological Physiology, Faculty of Medicine, Masaryk University, Kamenice 5, 625 00 Brno, Czech Republic. [2]Department of Physiology, Faculty of Medicine, Masaryk University, Kamenice 5, 625 00 Brno, Czech Republic. [3]Department of Biomedical Engineering, Faculty of Electrical Engineering and Communication, Brno University of Technology, Technicka 3058/10, Brno, Czech Republic. [4]First Faculty of Medicine, Charles University, Katerinska 32, 12108 Prague, Czech Republic.

Received: 19 January 2023 Accepted: 6 April 2023
Published online: 24 May 2023

References

1. Sonnenschein C, Soto AM. Carcinogenesis explained within the context of a theory of organisms. Prog Biophys Mol Biol. 2016;122:70–6.
2. Peltanova B, Raudenska M, Masarik M. Effect of tumor microenvironment on pathogenesis of the head and neck squamous cell carcinoma: a systematic review. Mol Cancer. 2019;18:63.
3. Prime SS, Cirillo N, Hassona Y, Lambert DW, Paterson IC, Mellone M, et al. Fibroblast activation and senescence in oral cancer. J Oral Pathol Med. 2017;46:82–8.
4. van Niel G, D'Angelo G, Raposo G. Shedding light on the cell biology of extracellular vesicles. Nat Rev Mol Cell Biol. 2018;19:213–28.
5. van Niel G, Carter DRF, Clayton A, Lambert DW, Raposo G, Vader P. Challenges and directions in studying cell–cell communication by extracellular vesicles. Nat Rev Mol Cell Biol. 2022;23:369.
6. Lischnig A, Bergqvist M, Ochiya T, Lässer C. Quantitative proteomics identifies proteins enriched in large and small extracellular vesicles. Mol Cell Proteomics. 2022;21: 100273.
7. Doyle LM, Wang MZ. Overview of extracellular vesicles, their origin, composition, purpose, and methods for exosome isolation and analysis. Cells. 2019;8:727.
8. Sharma R, Huang X, Brekken RA, Schroit AJ. Detection of phosphatidylserine-positive exosomes for the diagnosis of early-stage malignancies. Br J Cancer. 2017;117:545–52.
9. Lea J, Sharma R, Yang F, Zhu H, Ward ES, Schroit AJ. Detection of phosphatidylserine-positive exosomes as a diagnostic marker for ovarian malignancies: a proof of concept study. Oncotarget. 2017;8:14395–407.
10. Matsumura S, Minamisawa T, Suga K, Kishita H, Akagi T, Ichiki T, et al. Subtypes of tumour cell-derived small extracellular vesicles having differently externalized phosphatidylserine. J Extracell Vesicles. 2019;8:1579541.
11 Keulers TG, Schaaf MBE, Rouschop KMA. Autophagy-dependent secretion: contribution to tumor progression. Front Oncol. 2016;6:251.
12. Solvik TA, Nguyen TA, Tony Lin YH, Marsh T, Huang EJ, Wiita AP, et al. Secretory autophagy maintains proteostasis upon lysosome inhibition. J Cell Biol. 2022;221:e202110151.
13. Inpanathan S, Botelho RJ. The lysosome signaling platform: adapting with the times. Front Cell Dev Biol. 2019;7:113-.
14. Leidal AM, Huang HH, Marsh T, Solvik T, Zhang D, Ye J, et al. The LC3-conjugation machinery specifies the loading of RNA-binding proteins into extracellular vesicles. Nat Cell Biol. 2020;22:187–99.
15. Hu SQ, Zhang QC, Meng QB, Hu AN, Zou JP, Li XL. Autophagy regulates exosome secretion in rat nucleus pulposus cells via the RhoC/ROCK2 pathway. Exp Cell Res. 2020;395:112239.
16. Keulers TG, Libregts SF, Beaumont JEJ, Savelkouls KG, Bussink J, Duimel H, et al. Secretion of pro-angiogenic extracellular vesicles during hypoxia is dependent on the autophagy-related protein GABARAPL1. J Extracell Vesicles. 2021;10:e12166.
17. Raudenska M, Balvan J, Masarik M. Crosstalk between autophagy inhibitors and endosome-related secretory pathways: a challenge for autophagy-based treatment of solid cancers. Mol Cancer. 2021;20:140.
18. Wu Y, Wang X, Guo H, Zhang B, Zhang XB, Shi ZJ, et al. Synthesis and screening of 3-MA derivatives for autophagy inhibitors. Autophagy. 2013;9:595–603.
19. Vats S, Manjithaya R. A reversible autophagy inhibitor blocks autophagosome-lysosome fusion by preventing Stx17 loading onto autophagosomes. Mol Biol Cell. 2019;30:2283–95.
20. Mauvezin C, Neufeld TP. Bafilomycin A1 disrupts autophagic flux by inhibiting both V-ATPase-dependent acidification and Ca-P60A/SERCA-dependent autophagosome-lysosome fusion. Autophagy. 2015;11:1437–8.
21. Schrezenmeier E, Dörner T. Mechanisms of action of hydroxychloroquine and chloroquine: implications for rheumatology. Nat Rev Rheumatol. 2020;16:155–66.
22. Ma Y, Jin Z, Yu K, Liu Q. NVP-BEZ235-induced autophagy as a potential therapeutic approach for multiple myeloma. Am J Transl Res. 2019;11:87–105.
23. Thoreen CC, Kang SA, Chang JW, Liu Q, Zhang J, Gao Y, et al. An ATP-competitive mammalian target of rapamycin inhibitor reveals rapamycin-resistant functions of mTORC1. J Biol Chem. 2009;284:8023–32.
24. Qiu W, Schönleben F, Li X, Su GH. Disruption of transforming growth factor beta-Smad signaling pathway in head and neck squamous cell carcinoma as evidenced by mutations of SMAD2 and SMAD4. Cancer Lett. 2007;245:163–70.
25. Lin L-H, Chang K-W, Cheng H-W, Liu C-J. SMAD4 Somatic mutations in head and neck carcinoma are associated with tumor progression. Front Oncol. 2019;9:1379-.
26. Wang F, Xia X, Yang C, Shen J, Mai J, Kim HC, et al. SMAD4 Gene mutation renders pancreatic cancer resistance to radiotherapy through promotion of autophagy. Clin Cancer Res. 2018;24:3176–85.
27. Schindelin J, Arganda-Carreras I, Frise E, Kaynig V, Longair M, Pietzsch T, et al. Fiji: an open-source platform for biological-image analysis. Nat Methods. 2012;9:676–82.
28. Théry C, Witwer KW, Aikawa E, Alcaraz MJ, Anderson JD, Andriantsitohaina R, et al. Minimal information for studies of extracellular vesicles 2018 (MISEV2018): a position statement of the international society for extracellular vesicles and update of the MISEV2014 guidelines. J Extracell Ves. 2018;7:1535750.
29. Wiśniewski JR, Zougman A, Nagaraj N, Mann M. Universal sample preparation method for proteome analysis. Nat Methods. 2009;6:359–62.
30. Yeung YG, Nieves E, Angeletti RH, Stanley ER. Removal of detergents from protein digests for mass spectrometry analysis. Anal Biochem. 2008;382(2):135–7.
31. Demichev V, Messner CB, Vernardis SI, Lilley KS, Ralser M. DIA-NN: neural networks and interference correction enable deep proteome coverage in high throughput. Nat Methods. 2020;17:41–4.
32. Perez-Riverol Y, Bai J, Bandla C, García-Seisdedos D, Hewapathirana S, Kamatchinathan S, et al. The PRIDE database resources in 2022: a hub for mass spectrometry-based proteomics evidences. Nucleic Acids Res. 2022;50:D543–52.
33. Van Deun J, Mestdagh P, Agostinis P, Akay Ö, Anand S, Anckaert J, et al. EV-TRACK: transparent reporting and centralizing knowledge in extracellular vesicle research. Nat Methods. 2017;14:228–32.

34. Ritchie ME, Phipson B, Wu D, Hu Y, Law CW, Shi W, et al. limma powers differential expression analyses for RNA-sequencing and microarray studies. Nucleic Acids Res. 2015;43: e47.
35 Wu T, Hu E, Xu S, Chen M, Guo P, Dai Z, et al. clusterProfiler 4.0: A universal enrichment tool for interpreting omics data. Innov. 2021;2:100141.
36. Pérez-Silva JG, Araujo-Voces M, Quesada V. nVenn: generalized, quasi-proportional Venn and Euler diagrams. Bioinformatics. 2018;34:2322–4.
37. Tennekes M, Ellis P. Treemap: Treemap visualization 2.4-3. In: The Comprehensive R Archive Network. https://cran.r-project.org/web/packages/treemap/. Accessed 18 Apr 2023
38. Kolde R. pheatmap: Pretty Heatmaps 1.0. 12. . In: The Comprehensive R Archive Network. https://cran.r-project.org/web/packages/pheatmap. Accessed 18 Apr 2023.
39. Wickham H, Averick M, Bryan J, Chang W, McGowan L, François R, et al. Welcome to the tidyverse. J Open Source Software. 2019;4:1686.
40. Wickham H. ggplot2: Elegant Graphics for Data Analysis. Incorporated: Springer Publishing Company; 2016.
41. Choo Andrew Y, Yoon S-O, Kim Sang G, Roux Philippe P, Blenis J. Rapamycin differentially inhibits S6Ks and 4E-BP1 to mediate cell-type-specific repression of mRNA translation. Proc Natl Acad Sci. 2008;105:17414–9.
42. Reinhard C, Fernandez A, Lamb NJ, Thomas G. Nuclear localization of p85s6k: functional requirement for entry into S phase. EMBO J. 1994;13:1557–65.
43. Viñals F, Chambard JC, Pouysségur J. p70 S6 Kinase-mediated protein synthesis is a critical step for vascular endothelial cell proliferation *. J Biol Chem. 1999;274:26776–82.
44. Newton P, Vuppalapati K, Bouderlique T, Chagin A. Pharmacological inhibition of lysosomes activates the MTORC1 signaling pathway in chondrocytes in an autophagy-independent manner. Autophagy. 2015;11:1594.
45. Tian A-L, Wu Q, Liu P, Zhao L, Martins I, Kepp O, et al. Lysosomotropic agents including azithromycin, chloroquine and hydroxychloroquine activate the integrated stress response. Cell Death Dis. 2021;12:6.
46 Guo W, Zhong W, Hao L, Sun X, Zhou Z. Activation of mTORC1 by free fatty acids suppresses LAMP2 and autophagy function via ER stress in alcohol-related liver disease. Cells. 2021;10:2730.
47. Pyo J-O, Yoo S-M, Ahn H-H, Nah J, Hong S-H, Kam T-I, et al. Overexpression of Atg5 in mice activates autophagy and extends lifespan. Nat Commun. 2013;4:2300.
48. Stempels FC, Janssens MH, Ter Beest M, Mesman RJ, Revelo NH, Ioannidis M, et al. Novel and conventional inhibitors of canonical autophagy differently affect LC3-associated phagocytosis. FEBS Lett. 2022;596:491–509.
49. Zhou C, Zhong W, Zhou J, Sheng F, Fang Z, Wei Y, et al. Monitoring autophagic flux by an improved tandem fluorescent-tagged LC3 (mTagRFP-mWasabi-LC3) reveals that high-dose rapamycin impairs autophagic flux in cancer cells. Autophagy. 2012;8:1215–26.
50. Collins KP, Witta S, Coy JW, Pang Y, Gustafson DL. Lysosomal biogenesis and implications for hydroxychloroquine disposition. J Pharmacol Exp Ther. 2021;376:294–305.
51. Chen XG, Liu F, Song XF, Wang ZH, Dong ZQ, Hu ZQ, et al. Rapamycin regulates Akt and ERK phosphorylation through mTORC1 and mTORC2 signaling pathways. Mol Carcinog. 2010;49:603–10.
52. Palmieri M, Pal R, Nelvagal HR, Lotfi P, Stinnett GR, Seymour ML, et al. mTORC1-independent TFEB activation via Akt inhibition promotes cellular clearance in neurodegenerative storage diseases. Nat Commun. 2017;8:14338.
53 Lee H-O, Mustafa A, Hudes G, Kruger W. Abstract 5315: Hydroxychloroquine inhibits proliferation and S6 phosphorylation in human renal carcinoma cells. Cancer Res. 2015;75:5315-.
54. Makinoshima H, Takita M, Saruwatari K, Umemura S, Obata Y, Ishii G, et al. Signaling through the Phosphatidylinositol 3-Kinase (PI3K)/Mammalian Target of Rapamycin (mTOR) Axis is responsible for aerobic glycolysis mediated by glucose transporter in Epidermal Growth Factor Receptor (EGFR)-mutated lung adenocarcinoma. J Biol Chem. 2015;290:17495–504.
55. Sódar BW, Kittel Á, Pálóczi K, Vukman KV, Osteikoetxea X, Szabó-Taylor K, et al. Low-density lipoprotein mimics blood plasma-derived exosomes and microvesicles during isolation and detection. Sci Rep. 2016;6:24316.
56. Xu Q, Ma H, Chang H, Feng Z, Zhang C, Yang X. The interaction of interleukin-8 and PTEN inactivation promotes the malignant progression of head and neck squamous cell carcinoma via the STAT3 pathway. Cell Death Dis. 2020;11:405.
57. Španko M, Strnadová K, Pavlíček AJ, Szabo P, Kodet O, Valach J, et al. IL-6 in the ecosystem of head and neck cancer: possible therapeutic perspectives. Int J Mol Sci. 2021;22:11027.
58. Yung MM-H, Tang HW-M, Cai PC-H, Leung TH-Y, Ngu S-F, Chan KK-L, et al. GRO-α and IL-8 enhance ovarian cancer metastatic potential via the CXCR2-mediated TAK1/NFκB signaling cascade. Theranostics. 2018;8:1270–85.
59. Ji WT, Chen HR, Lin CH, Lee JW, Lee CC. Monocyte chemotactic protein 1 (MCP-1) modulates pro-survival signaling to promote progression of head and neck squamous cell carcinoma. PLoS ONE. 2014;9:e88952.
60. Azenshtein E, Luboshits G, Shina S, Neumark E, Shahbazian D, Weil M, et al. The CC chemokine RANTES in breast carcinoma progression: regulation of expression and potential mechanisms of promalignant activity. Cancer Res. 2002;62:1093–102.
61. Gutschalk CM, Herold-Mende CC, Fusenig NE, Mueller MM. Granulocyte colony-stimulating factor and granulocyte-macrophage colony-stimulating factor promote malignant growth of cells from head and neck squamous cell carcinomas in vivo. Cancer Res. 2006;66:8026–36.
62. Li H, Wang R-M, Liu S-G, Zhang J-P, Luo J-Y, Zhang B-J, et al. Abnormal expression of FLOT1 correlates with tumor progression and poor survival in patients with non-small cell lung cancer. Tumor Biol. 2014;35:3311–5.
63. Li Y, Zou L, Li Q, Haibe-Kains B, Tian R, Li Y, et al. Amplification of LAPTM4B and YWHAZ contributes to chemotherapy resistance and recurrence of breast cancer. Nat Med. 2010;16:214–8.
64. Valiente M, Obenauf AC, Jin X, Chen Q, Zhang XHF, Lee DJ, et al. Serpins promote cancer cell survival and vascular co-option in brain metastasis. Cell. 2014;156:1002–16.
65. Minakaki G, Menges S, Kittel A, Emmanouilidou E, Schaeffner I, Barkovits K, et al. Autophagy inhibition promotes SNCA/alpha-synuclein release and transfer via extracellular vesicles with a hybrid autophagosome-exosome-like phenotype. Autophagy. 2018;14:98–119.
66. Sagini K, Buratta S, Delo F, Pellegrino RM, Giovagnoli S, Urbanelli L, et al. Drug-induced lysosomal impairment is associated with the release of extracellular vesicles carrying autophagy markers. Int J Mol Sci. 2021;22:12922.
67. Zou B, Liu J, Klionsky DJ, Tang D, Kang R. Extracellular SQSTM1 as an inflammatory mediator. Autophagy. 2020;16:2313–5.
68. Wu H, Liu G, Li C, Zhao S. bri3, a novel gene, participates in tumor necrosis factor-alpha-induced cell death. Biochem Biophys Res Commun. 2003;311:518–24.
69. Orth MF, Hölting TLB, Dallmayer M, Wehweck FS, Paul T, Musa J, et al. High specificity of BCL11B and GLG1 for EWSR1-FLI1 and EWSR1-ERG Positive Ewing sarcoma. Cancers. 2020;12:644.
70. Yamaguchi F, Hayakawa S, Kawashima S, Asakura T, Oishi Y. Antitumor effect of memantine is related to the formation of the splicing isoform of GLG1, a decoy FGF-binding protein. Int J Oncol. 2022;61:80.
71. Yuan H, Li Z-M, Shao J, Ji W-X, Xia W, Lu S. FGF2/FGFR1 regulates autophagy in FGFR1-amplified non-small cell lung cancer cells. J Exp Clin Cancer Res. 2017;36:72.
72. Wang W-X, Kyprianou N, Wang X, Nelson PT. Dysregulation of the mitogen granulin in human cancer through the miR-15/107 microRNA gene group. Can Res. 2010;70:9137–42.
73. Boada-Romero E, Letek M, Fleischer A, Pallauf K, Ramón-Barros C, Pimentel-Muiños FX. TMEM59 defines a novel ATG16L1-binding motif that promotes local activation of LC3. EMBO J. 2013;32:566–82.
74. Morotti M, Zois CE, El-Ansari R, Craze ML, Rakha EA, Fan S-J, et al. Increased expression of glutamine transporter SNAT2/SLC38A2 promotes glutamine dependence and oxidative stress resistance, and is associated with worse prognosis in triple-negative breast cancer. Br J Cancer. 2021;124:494–505.
75. Gong L, Xia Y, Qian Z, Shi J, Luo J, Song G, et al. Overexpression of MYC binding protein promotes invasion and migration in gastric cancer. Oncol Lett. 2018;15:5243–9.
76. Yang S, Zhang J, Xu Y, Wang J, Zhao H, Lei J, et al. OIT3 mediates macrophage polarization and facilitates hepatocellular carcinoma progression. Cancer Immunol Immunother. 2022;71:2677.

77. Chen T, Dai X, Dai J, Ding C, Zhang Z, Lin Z, et al. AFP promotes HCC progression by suppressing the HuR-mediated Fas/FADD apoptotic pathway. Cell Death Dis. 2020;11:822.
78. Nandi M, Kelly P, Vallance P, Leiper J. Over-expression of GTP-cyclohydrolase 1 feedback regulatory protein attenuates LPS and cytokine-stimulated nitric oxide production. Vasc Med. 2008;13:29–36.
79. Witte MB, Thornton FJ, Efron DT, Barbul A. Enhancement of fibroblast collagen synthesis by nitric oxide. Nitric Oxide. 2000;4:572–82.
80. Dai W, Wang Y, Yang T, Wang J, Wu W, Gu J. Downregulation of exosomal CLEC3B in hepatocellular carcinoma promotes metastasis and angiogenesis via AMPK and VEGF signals. Cell Commun Signal. 2019;17:113.
81. Mayca Pozo F, Geng X, Tamagno I, Jackson MW, Heimsath EG, Hammer JA, et al. MYO10 drives genomic instability and inflammation in cancer. Sci Adv. 2021;7:eabg6908-eabg.
82. Stegh AH, Brennan C, Mahoney JA, Forloney KL, Jenq HT, Luciano JP, et al. Glioma oncoprotein Bcl2L12 inhibits the p53 tumor suppressor. Genes Dev. 2010;24:2194–204.
83. Kudo Y, Iizuka S, Yoshida M, Tsunematsu T, Kondo T, Subarnbhesaj A, et al. Matrix metalloproteinase-13 (MMP-13) directly and indirectly promotes tumor angiogenesis. J Biol Chem. 2012;287:38716–28.
84. Mah V, Elshimali Y, Chu A, Moatamed NA, Uzzell JP, Tsui J, et al. ALDH1 expression predicts progression of premalignant lesions to cancer in Type I endometrial carcinomas. Sci Rep. 2021;11:11949.
85. Yu B, Wu K, Wang X, Zhang J, Wang L, Jiang Y, et al. Periostin secreted by cancer-associated fibroblasts promotes cancer stemness in head and neck cancer by activating protein tyrosine kinase 7. Cell Death Dis. 2018;9:1082-.
86. Sharma S, Pei X, Xing F, Wu SY, Wu K, Tyagi A, et al. Regucalcin promotes dormancy of prostate cancer. Oncogene. 2021;40:1012–26.
87. Gallagher EJ, Zelenko Z, Neel BA, Antoniou IM, Rajan L, Kase N, et al. Elevated tumor LDLR expression accelerates LDL cholesterol-mediated breast cancer growth in mouse models of hyperlipidemia. Oncogene. 2017;36:6462–71.
88. Ma S, Duan L, Dong H, Ma X, Guo X, Liu J, et al. OLFML2A Downregulation inhibits glioma proliferation through suppression of Wnt/β-Catenin Signaling. Front Oncol. 2021;11:717917.
89. Qu H, Jiang W, Wang Y, Chen P. STOML2 as a novel prognostic biomarker modulates cell proliferation, motility and chemo-sensitivity via IL6-Stat3 pathway in head and neck squamous cell carcinoma. Am J Transl Res. 2019;11:683–95.
90. Chang AC, Doherty J, Huschtscha LI, Redvers R, Restall C, Reddel RR, et al. STC1 expression is associated with tumor growth and metastasis in breast cancer. Clin Exp Metastasis. 2015;32:15–27.
91. Raffaghello L, Lee C, Safdie FM, Wei M, Madia F, Bianchi G, et al. Starvation-dependent differential stress resistance protects normal but not cancer cells against high-dose chemotherapy. Proc Natl Acad Sci U S A. 2008;105:8215–20.
92. Todkar K, Chikhi L, Desjardins V, El-Mortada F, Pépin G, Germain M. Selective packaging of mitochondrial proteins into extracellular vesicles prevents the release of mitochondrial DAMPs. Nat Commun. 2021;12:1971.
93. Unuma K, Aki T, Funakoshi T, Hashimoto K, Uemura K. Extrusion of mitochondrial contents from lipopolysaccharide-stimulated cells: Involvement of autophagy. Autophagy. 2015;11:1520–36.
94. Zerial M, McBride H. Rab proteins as membrane organizers. Nat Rev Mol Cell Biol. 2001;2:107–17.
95. Wu B, Qi R, Liu X, Qian L, Wu Z. Rab18 overexpression promotes proliferation and chemoresistance through regulation of mitochondrial function in human gastric cancer. Onco Targets Ther. 2018;11:7805–20.
96. Gong T, Zhou B, Liu M, Chen X, Huang S, Xu Y, et al. RAB18 promotes proliferation and metastasis in hepatocellular carcinoma. Am J Transl Res. 2019;11:1009–19.
97. Ji X, Guo X, Wang Y, Li X, Li H. Rab18 regulates proliferation, invasion and cisplatin sensitivity through STAT3 signaling in head and neck squamous cell carcinoma. Onco Targets Ther. 2020;13:4123–34.
98. BasuRay S. RAB18 modulates autophagy in human stellate cells. J Clin Lipidol. 2019;13:832–8.
99. Frittoli E, Palamidessi A, Marighetti P, Confalonieri S, Bianchi F, Malinverno C, et al. A RAB5/RAB4 recycling circuitry induces a proteolytic invasive program and promotes tumor dissemination. J Cell Biol. 2014;206:307–28.
100. Cao GJ, Wang D, Zeng ZP, Wang GX, Hu CJ, Xing ZF. Direct interaction between Rab5a and Rab4a enhanced epidermal growth factor-stimulated proliferation of gastric cancer cells. World J Gastrointest Oncol. 2021;13:1492–505.
101. Sun P, Li L, Li Z. RAB9A Plays an oncogenic role in human liver cancer cells. Biomed Res Int. 2020;2020:5691671.
102. Spang N, Feldmann A, Huesmann H, Bekbulat F, Schmitt V, Hiebel C, et al. RAB3GAP1 and RAB3GAP2 modulate basal and rapamycin-induced autophagy. Autophagy. 2014;10:2297–309.
103. Fernandez-Mosquera L, Yambire KF, Couto R, Pereyra L, Pabis K, Ponsford AH, et al. Mitochondrial respiratory chain deficiency inhibits lysosomal hydrolysis. Autophagy. 2019;15:1572–91.
104. Fernández-Mosquera L, Diogo CV, Yambire KF, Santos GL, Luna Sánchez M, Bénit P, et al. Acute and chronic mitochondrial respiratory chain deficiency differentially regulate lysosomal biogenesis. Sci Rep. 2017;7:45076.
105. Shtutman M, Chang BD, Schools GP, Broude EV. Cellular model of p21-Induced senescence. Methods Mol Biol. 2017;1534:31–9.
106. Ivanov A, Pawlikowski J, Manoharan I, van Tuyn J, Nelson DM, Rai TS, et al. Lysosome-mediated processing of chromatin in senescence. J Cell Biol. 2013;202:129–43.
107. Freund A, Laberge R-M, Demaria M, Campisi J. Lamin B1 loss is a senescence-associated biomarker. Mol Biol Cell. 2012;23:2066–75.
108. Dou Z, Xu C, Donahue G, Shimi T, Pan J-A, Zhu J, et al. Autophagy mediates degradation of nuclear lamina. Nature. 2015;526:105.
109. Suhaimi SA, Chan SC, Rosli R. Matrix metallopeptidase 3 polymorphisms: emerging genetic markers in human breast cancer metastasis. J Breast Cancer. 2020;23:1–9.
110. Levi N, Papismadov N, Solomonov I, Sagi I, Krizhanovsky V. The ECM path of senescence in aging: components and modifiers. FEBS J. 2020;287:2636–46.
111. Kumar D, New J, Vishwakarma V, Joshi R, Enders J, Lin F, et al. Cancer-associated fibroblasts drive glycolysis in a targetable signaling loop implicated in head and neck squamous cell carcinoma progression. Can Res. 2018;78:3769.

Publisher's Note

Springer Nature remains neutral with regard to jurisdictional claims in published maps and institutional affiliations.

Ready to submit your research? Choose BMC and benefit from:

- fast, convenient online submission
- thorough peer review by experienced researchers in your field
- rapid publication on acceptance
- support for research data, including large and complex data types
- gold Open Access which fosters wider collaboration and increased citations
- maximum visibility for your research: over 100M website views per year

At BMC, research is always in progress.

Learn more biomedcentral.com/submissions



www.nature.com/scientificreports

scientific reports

OPEN

Glutamine and serum starvation alters the ATP production, oxidative stress, and abundance of mitochondrial RNAs in extracellular vesicles produced by cancer cells

Maria Bugajova[1,8], Martina Raudenska[1,2,8], Klara Hanelova[1], Jiri Navratil[1], Jaromir Gumulec[1,2], Frantisek Petrlak[3], Tomas Vicar[1], Sarka Hrachovinova[4], Michal Masarik[1,2,5], David Kalfert[6], Marek Grega[7], Jan Plzak[6], Jan Betka[6] & Jan Balvan[1]✉

Induction of autophagy represents an effective survival strategy for nutrient-deprived or stressed cancer cells. Autophagy contributes to the modulation of communication within the tumor microenvironment. Here, we conducted a study of the metabolic and signaling implications associated with autophagy induced by glutamine (Gln) and serum starvation and PI3K/mTOR inhibitor and autophagy inducer NVP-BEZ235 (BEZ) in the head and neck squamous cell carcinoma (HNSCC) cell line FaDu. We compared the effect of these different types of autophagy induction on ATP production, lipid peroxidation, mitophagy, RNA cargo of extracellular vesicles (EVs), and EVs-associated cytokine secretome of cancer cells. Both BEZ and starvation resulted in a decline in ATP production. Simultaneously, Gln starvation enhanced oxidative damage of cancer cells by lipid peroxidation. In starved cells, there was a discernible fragmentation of the mitochondrial network coupled with an increase in the presence of tumor susceptibility gene 101 (TSG101) on the mitochondrial membrane, indicative of the sorting of mitochondrial cargo into EVs. Consequently, the abundance of mitochondrial RNAs (mtRNAs) in EVs released by FaDu cells was enhanced. Notably, mtRNAs were also detectable in EVs isolated from the serum of both HNSCC patients and healthy controls. Starvation and BEZ reduced the production of EVs by cancer cells, yet the characteristic molecular profile of these EVs remained unchanged. We also found that alterations in the release of inflammatory cytokines constitute a principal response to autophagy induction. Importantly, the specific mechanism driving autophagy induction significantly influenced the composition of the EVs-associated cytokine secretome.

Low amino acid availability can be lethal to cancer cells, so starving cancer cells initiate adaptive responses to nutrient deprivation that go beyond angiogenesis. Starving cells could promote the reorganization of tumor microenvironment (TME) by producing cytokines and extracellular vesicles (EVs) with signaling functions[1,2]. A primary response to amino acid starvation is the inhibition of protein synthesis, induction of autophagy, and protein degradation by the ubiquitin-proteasome system. These processes are connected by the mammalian target of rapamycin complex 1 (mTORC1), which is a central regulator of cell growth and metabolism. mTORC1 inhibition contributes to the downregulation of protein synthesis and the induction of autophagy[3].

[1]Department of Pathological Physiology, Faculty of Medicine, Masaryk University, Kamenice 5, Brno CZ-625 00, Czech Republic. [2]Department of Physiology, Faculty of Medicine, Masaryk University, Kamenice 5, Brno CZ-625 00, Czech Republic. [3]Department of Chemistry and Biochemistry, Mendel University in Brno, Zemedelska 1, Brno CZ-613 00, Czech Republic. [4]Department of Experimental Biology, Faculty of Science, Masaryk University, Kamenice 5, Brno CZ- 625 00, Czech Republic. [5]First Faculty of Medicine, BIOCEV, Charles University, Prumyslova 595, Vestec CZ-252 50, Czech Republic. [6]Department of Otorhinolaryngology and Head and Neck Surgery, First Faculty of Medicine, University Hospital Motol, Charles University, V Uvalu 84, Prague CZ-15006, Czech Republic. [7]Department of Pathology and Molecular Medicine, 2nd Faculty of Medicine, Charles University, University Hospital Motol/ V Uvalu 84, Prague 5 CZ-15006, Czech Republic. [8]These authors contributed equally to this work—Maria Bugajova and Martina Raudenska. ✉email: jan.balvan@med.muni.cz

Glutamine (Gln) alone was shown to be sufficient to restore mTORC1 activity during prolonged amino acid starvation[4]and Gln deprivation could induce autophagy[5]. Nevertheless, the different forms of autophagy induction can strongly influence the resulting adaptive processes in the cell. For example, mTOR-dependent 4E-BP hyperphosphorylation (allowing eIF4E-dependent translation) was strongly inhibited by the PI3K/mTOR inhibitor and autophagy inducer NVP-BEZ235 (BEZ) throughout the 24-hour treatment period, but Gln starvation showed no such significant effect. Therefore, eIF4E-mediated translation can be partially maintained in the presence of Gln starvation, but probably not in the presence of BEZ[6]. Furthermore, NVP-BEZ235 is a dual PI3K/ mTOR inhibitor. On the other hand, mTOR inhibition or Gln starvation can, under some circumstances, induce the PI3K/Akt pathway[7,8].

The composition of EVs has been shown to reflect the metabolic state of the cell[9]and some studies suggest that EVs release is regulated by mTORC1 in response to changes in nutrient and growth factor conditions[10]. Starvation also induces mitochondrial stress, and mitochondrial biogenesis and/or turnover of damaged mitochondria by mitophagy may both be part of the adaptive response[11], as well as changes in the level of oxidative phosphorylation (OXPHOS)[12]. However, the link between cell stress, autophagy, cellular energy metabolism, and content of EVs remains somewhat elusive.

In this study, we focused on the consequences of BEZ- and Gln and FBS starvation-induced autophagy on the RNA cargo of EVs and the EVs-associated cytokine secretome (cytokines can exist internally in EVs and also bound to their membrane[13]). We also compared the effect of these different modes of autophagy induction on ATP production, lipid peroxidation, and mitophagy. We found that Gln and FBS starvation increased the abundance of mitochondrial RNAs in FaDu-derived EVs. This suggests that metabolic reprogramming in head and neck squamous cell carcinoma (HNSCC) cells may be reflected in EVs. As metabolic reprogramming is a key hallmark of malignancy[14], we also tested how these findings could be translated to the whole body level.

Materials and methods

Model cell line and treatments

The cell line FaDu (HTB-43TM, RRID: CVCL_1218) derived from a squamous cell carcinoma (SCC) of the hypopharynx was used in this study. The authenticated cell line was purchased from the American Type Culture Collection (ATCC; Manassas, Virginia, USA) within the last three years. The cell lines were grown in a Dulbecco's Modified Eagle's medium/Nutrient Mixture F-12 Ham (DMEM/F12, Biosera) supplemented with 10% FBS (Biosera) in a humidified atmosphere of 5% CO_2 and 95% air at 37 °C. Two passages before the experiment, cell harvest, or EVs isolation, the cells were washed with PBS and grown in a medium supplemented with Exosome-depleted FBS (Gibco, A2720801); hereafter referred to as exofree medium. The passages of FaDu cells ranged from 5 to 15. All experiments were performed with mycoplasma-free cells. Mycoplasma was detected by PCR (primers MYCO_A: GGCGAATGGGTGAGTAACACG and MYCO_B: CGGATAACGCTTGCGACCTATG). For autophagy modulation, FaDu cells were treated for 24 h with 30 nM of NVP-BEZ235 (MedChemExpress). To induce starvation, cells were cultured in DMEM F12 without glutamine and without FBS. Modulation of autophagy did not reduce the viability of FaDu cells (the viability ranged from 98.1 to 99.9% across treatments).

Conditioned media preparation

15 ml of conditioned medium (CM) was collected from 90 to 95% confluent FaDu cells grown in 75 cm^2 cell culture flasks after 24 h of the selected treatment. The collected media were first subjected to a centrifugation step of 400 g for 10 min at room temperature (RT) to pellet and remove cells. All following centrifugation steps were performed at 4 °C. Next, the supernatant was centrifuged at 2,000 g for 20 min to remove debris and apoptotic bodies. Then, to remove large EVs, the supernatant was centrifuged at 10,000 g for 40 min. To remove any remaining large EVs, the supernatant from the first 10,000 g step was passed through a 0.22 µm pore PES filter (MF-Millipore TM Membrane Filter, GSWP01300). To remove the remaining exogenous treatments, we concentrated the 15 ml volume to a 1 ml volume using Amicon Ultra-15 Centrifugal Filter Unit (Merc, UCF9100, 100 kDa MWCO) at 2000 g for 10 min. Such CM should not contain large EVs (up to 220 nm), apoptotic bodies, or free cytokines.

Extracellular vesicle isolation

During processing, the conditioned media and patient sera were kept on ice. EVs were isolated from the pre-cleared concentrated medium (CM) according to the manufacturer's instructions using the MagCapture Exosome Isolation Kit PS Ver. 2 (FUJIFILM Wako Pure Chemical Corporation, Japan). All isolated EVs were then placed in 1.5 ml Protein LoBind Tubes (Sigma, EP0030108116) and immediately used for further analyzes, or stored in the manufacturers' elution buffer at -80 °C.

Nanoparticle tracking analyzis

Prior to measurement, EVs suspensions were diluted with sterile ice-cold filtered PBS. The concentration of EVs was determined using a Malvern Panalytical NanoSight LM10 nanoparticle tracking system. This instrument was equipped with a 532 nm laser diode, an sCMOS camera and a 20× optical objective. The EVs suspension was dosed into the NanoSight cell for analyzis. Videos of the nanoparticles were recorded at a constant temperature of 25 °C and a frame rate of 30 frames per second using NTA 3.4 software. The software was then used to track the recorded videos under constant parameters, providing data on the size distribution and concentration of EVs per milliliter using Finite Track Length Adjustment (FTLA). These measurements were repeated four times to generate error bars for the data.

Negative stain and Cryo TEM

For negative stain transmission electron microscopy (TEM) EVs samples (concentration 1.48–6.56 × 10^9 EVs/ml) were prepared by absorption at freshly plasma-cleaned Carbon coated copper grids for 30 s at RT. This was accomplished by pipetting 4 µl of the EVs containing elution buffer on the grid. Following sample adsorption, grids were quickly and gently blotted on filter paper and immediately washed with 2% uranyl acetate, which was also immediately and gently blotted on filter paper. Following the washing step, the sample was fixed for 1 min by 2% uranyl acetate which was subsequently blotted on a filter paper. EVs were examined at 200 kV with a Talos F200C transmission electron microscope (ThermoScientific) equipped with a Ceta-D scintillator-based camera (ThermoScientific). In all cases, TEM was performed on a fresh sample of EVs that had not been subjected to freezing temperatures at any step of purification or processing.

For cryo-electron microscopy, 4 µl of the EVs sample was applied to freshly plasma-cleaned TEM grids (Quantifoil, Cu, 300mesh, R2/1) and vitrified into liquid ethane using ThermoScientific Vitrobot Mark IV (4 °C, 100% rel. humidity, 30 s waiting time, 5 s blotting time). The grids were subsequently mounted into the Autogrid cartridges and loaded to Talos Arctica or Glacios (ThermoScientific) transmission electron microscope for imaging. The microscope was operated at 200 kV. The EVs cryo-TEM micrographs were collected on K2 or Falcon4 direct electron detection camera at the 8500× and 92,000× nominal magnification with the under focus in the range 2–4 µm and the overall dose of < 20 e/Å2.

Cytokine array

After 24 h of the selected treatment, Human Cytokine Antibody Array (ab133997, Abcam) was used for the simultaneous detection of 42 cytokines in each CM sample according to the manufacturer's instructions. Experiments were performed in duplicates. The array membranes were incubated for 30 min at room temperature in a blocking buffer. CM samples were then incubated on the membranes overnight at 4 °C. Following one large volume wash in Wash buffer I for an extended time of 30 min, three washes in Wash buffer I and two washes in Wash buffer II, membranes were incubated in Biotin-Conjugated Anti-Cytokines overnight at 4 °C. After washing as described above, membranes were incubated in HRP-Conjugated Streptavidin overnight at 4 °C. Washed arrays were finally incubated with Chemiluminescence Detection reagents and images were captured using the Azure c400 Imager (Azure Biosystems). Pixel density (signal density) of each spot on the membrane was quantified using ImageJ - Array Analyzis plugin[15].

Cell lysis and immunoblot analyzes

For protein extraction from cells, these were washed twice with ice-cold 1× PBS and lysed for 20 min on ice in Tris-EDTA-SDS lysis buffer (pH 8, 1 M Tris-HCl, 0.5 M EDTA, 10% SDS), supplemented with protease (Roche, 04693132001) and phosphatase inhibitors (MedChemExpress, HY-K0021). Protein concentration was determined using the Pierce BCA protein assay (Thermo Scientific, 23225). Equal amounts of total protein (15 µg) were separated by SDS–PAGE, transferred to a PVDF (GE, GE10600023) or nitrocellulose (Bio-Rad, 1620112) membrane and analyzed by using the following antibodies (in a dilution range of 1:500–1:5000): Annexin V (#8555), BNIP3 (D7U1T) (#44060), Caveolin-1 (D46G3) (#3267), CD9 (D8O1A) (#13174), EpCAM (D1B3) (#2626), Flotillin-1 (D2V7Z) (#18634), HSP-70 (D69) (#4876), ULK1 (D8H5) (#8054), Phospho-ULK1 (Ser757) (D7O6U) (#14202), Phospho-ULK1 (Ser556) (D1H4) (#5869), from Cell Signaling; ACTB (ab16039), GPX-4 (ab125066), GABARAP/GABARAPL1/GABARAPL2 (ab109364), SQSTM1/p62 (ab56416) and TSG101 (ab125011) from Abcam; Atg7 (B-9) (sc-376212), Atg5 (C-1) (sc-133158) and MAPLC3B (G-9) (sc-376404) from Santa Cruz.

Secondary antibodies (diluted 1:1000): HRP-linked Anti-Rabbit and Anti-Mouse IgG (H + L) from Promega (W4011 and W402B). For detection, the Clarity Western-ECL substrate (Bio-Rad) was used. Blot luminescence was measured using Azure c400 Imager (Azure Biosystems), and subsequent densitometry was performed using Fiji gel analyzer tools.

For protein extraction from isolated extracellular vesicles, the total yields from all methods used for EVs isolation (including magnetic beads) were lysed in RIPA buffer on ice for 20 min.

Proteins were separated by PAGE under nonreducing conditions, sample loading buffer (5x SDS Sample Buffer) was used without mercaptoethanol addition and transferred to a PVDF membrane (GE, GE10600023) and processed as described above.

Confocal microscopy

Fixed cells

First, the cells were seeded on 18 mm coverslips coated with 0.5% gelatin and cultured under standard conditions. After reaching 70% confluence, the cells were exposed to the desired conditions for 24 h. Prior to fixation, cells were incubated with 150 nM MitoTracker Red CMXRos (Thermo Fisher Scientific, Waltham, Ma, USA) for 45 min and washed three times with a pre-warmed medium. Then, the cells were fixed in a pre-warmed fix solution containing 4% paraformaldehyde, 3% sucrose, PBS, and water for 20 min at 37 °C and washed three times with PBS. Right after, the cells were permeabilized using 0,2% Triton X-100 for 10 min. Permeabilization was followed by the blocking of non-specific Ab-blocking sites in PBS-BSA 0,1% for 60 min. Such prepared cells were incubated with primary antibodies (SQSTM1/p62 1:200, MAPLC3 1:200, BNIP3 1:200, TSG101 1:200) for 90 min at 37 °C. Then, the cells were washed three times with PBS 0.05% Tween 20 (PBS-T) and incubated with compatible secondary antibodies (Alexa Fluor 488, 1:750; Alexa Fluor 647, 1:750) for 60 min in the dark at RT. After secondary antibody incubation, the cells were washed two times with PBS-T and then incubated with 7 µl/50 ml DAPI. Prior to the mounting, cells were washed two times with PBS-T and once with PBS. Coverslips

were mounted on glass slides using ProLong Gold Antifade Mountant (Thermo Fisher Scientific, Waltham, Ma, USA).

Live cells

For live cell imaging, cells were cultured in Ibidi µ-Slide VI 0.4 (ibiTreat, Cat. No. 80606). After reaching 70% confluence, cells were washed twice with PBS and exposed to the treatment for 24 h. For lipid-peroxidation assay Image-iT, a Lipid Peroxidation kit (Thermo Scientific) was used, following the manufacturer's protocol. The Image-iT kit enables the detection of lipid peroxidation in live cells through oxidation of BODIPY 581/591 C11 reagent.

Acquisition

Confocal microscopy images of fixed cells were acquired using Laser scanning confocal microscope Zeiss LSM 880 with AiryscanFast module (Carl Zeiss Inc.) using a Plan-Apochromat 63× / 1.40 OIL objective. DAPI was excited with 405 nm solid state laser, and emitted light was detected at 433 nm. Alexa Fluor™ 488 was excited with 488 nm Argon laser, and emitted light was detected at 516 nm. MitoTracker Red CMXRos was excited with 561 nm solid state laser, and emitted light was detected at 579 nm. Alexa Fluor™ 647 was excited with HeNe 633 nm laser and emitted light was detected at 654 nm. Live cells images were acquired using a Plan-Apochromat C-Apochromat 63× / 1.20 W objective. Oxidized Bodipy was excited with 488 nm Argon laser, and emitted light was detected at 541 nm and reduced Bodipy was excited with 561 nm solid state laser, and emitted light was detected at 640 nm. AiryScan images were acquired using 1.8× magnification and processed using Zen Black software (Carl Zeiss Inc.). Colocalization data were evaluated using Coloc tool using the Zen Blue Software (Carl Zeiss Inc.).

Image analysis of lipid peroxidation was performed using a custom Python script in a semiautomatic manner. For analysis, images were preprocessed using a median filter (7×7) and Gaussian filter (sigma 1). Cells were segmented using thresholding of image created as the sum of both fluorescence channels and morphological operations (closing and filtration of small objects) were applied to resulting masks, with additional manual spiling of individual cells and manual correction of segmentation masks. Then, the median intensity of individual cells was extracted for oxBODIPY/BODIPY fluorescence channels. To assess lipid peroxidation, 12 fields of view were evaluated for all treatments. The numbers of cells evaluated were as follows: 159 for control, 153 for BEZ and 88 for starvation. Five fields of view were evaluated for the colocalization experiments. In total, approximately 30 cells were analyzed.

RNA extraction and characterization

Total EVs RNA was extracted from pre-cleared conditioned cultivation medium (CM) and pre-cleared serum using a commercial column-based exoRNeasy Maxi Kit (Qiagen, 77164). Total amounts and integrity of RNA were assessed using the RNA Nano 6000 Assay Kit of the Bioanalyzer 2100 system (Agilent Technologies, CA, USA). For NGS, RNA samples from each treatment were prepared in tetraplicates.

Next-generation sequencing and data analysis

High-throughput RNA-Seq data were prepared using NEBNext Ultra II Directional RNA Library Prep Kit for Illumina (New England Biolabs, USA) with polyA selection and sequenced on Illumina sequencer (run length 1×75 nt); in cooperation with Core Facility Genomics (CEITEC MU, CZ). Bcl files were converted to Fastq format using bcl2fastq v. 2.20.0.422 Illumina software for basecalling. Quality check of raw single-end fastq reads was carried out by FastQC (http://www.bioinformatics.babraham.ac.uk/projects/fastqc). The adapters and quality trimming of raw fastq reads was performed using Trimmomatic v0.39[16] with settings CROP:250 LEADING:3 TRAILING:3 SLIDINGWINDOW:4:5 MINLEN:35. Trimmed RNA-Seq reads were mapped against the human genome (hs38) and Ensembl GRCh38-p10 annotation using STAR v2.7.3a[17] as splice-aware short read aligner and default parameters except --outFilterMismatchNoverLmax 0.4 and --twopassMode Basic. Quality control after alignment concerning the number and percentage of uniquely- and multi-mapped reads, rRNA contamination, mapped regions, read coverage distribution, strand specificity, gene biotypes and PCR duplication was performed using several tools namely RSeQC v4.0.0[18], Picard toolkit v2.25.6 (https://broadinstitute.github.io/picard/; Broad Institute), Qualimap v.2.2.2[19].

The differential gene expression analysis was calculated based on the gene counts produced using featureCounts from Subread package v2.0[20] and further analyzed by Bioconductor package DESeq2 v1.34.0[21]. Data generated by DESeq2 with independent filtering were selected for the differential gene expression analysis due to its conservative features and to avoid potential false positive results. Genes were considered as differentially expressed based on a cut-off of adjusted p-value < 0.05 and log2(fold-change) ≥ 1 or ≤ -1. Differential expressed genese were visualized by the packages ggplot2, and tidyverse in R[22]. The functional roles of the significantly differentially expressed genes were performed according to the Gene Ontology (GO) enrichment analysis database on gene sets by applying the clusterProfiler package v3.18.1[23]. Clustered heatmaps were generated from selected top differentially regulated genes using R package pheatmap v1.0.12 (https://cran.r-project.org/web/packages/pheatmap/index.html), volcano plots were produced using ggplot2 v3.3.5 package[24] and MA plots were genereted using ggpubr v0.4.0 package (https://cran.r-project.org/web/packages/ggpubr/index.html).

Serum isolation

Human serum was obtained with informed consent from 41 patients with histologically confirmed HNSCC, and 20 healthy non-fasting adult volunteers. All experiments were performed in accordance with relevant guidelines and regulations. The experimental protocols were approved by the ethical committee of Motol University Hospital, Prague, Czech Republic. Patients were completely clinically examined, and serum samples were taken

from patients with verified HNSCC; the inclusion criteria were as follows: histologically confirmed squamous cell carcinoma and no previous oncologic treatment in the last 5 years. Blood was drawn through a S-Monovette needle collection set (Sarstedt AG & Co.) and processed according to manufacturer's instructions. After that, samples were rested upright for 30 min at room temperature (RT) to allow erythrocytes to clot. The clot was subsequently pelleted by centrifugation at 2000 g for 10 min at 4 °C and then upper phase (serum) was retrieved to DNA LowBind tubes (Eppendorf, Cat. No. 0030122208). Serum samples (2–3 ml) were stored at − 80 °C prior to analysis.

RealTime-PCR

Blood sera of HNSCC patients and controls were pre-filtred through a 0.45 µm pore PES filter (MF-Millipore Membrane Filter, HAWP04700) followed by isolation of exosomal RNA using exoRNeasy Maxi Kit (Qiagen, 77164). The exosomal RNA was transcribed using the High-Capacity cDNA Reverse Transcription Kit (Applied Biosystems, Waltham, MA, USA), which was used according to the manufacturer's instructions. qRT-PCR was performed using TaqMan gene expression assays with the LightCycler 480 II System (Roche, Bazel, Switzerland) and the amplified cDNA was analyzed by the comparative Ct method using PSMB2 and ACTB as housekeeping genes. Primer and probe set for PSMB2 (Hs01009704m1), ACTB (Hs99999903m1), MT-RNR1 (Hs02596859g1), MT-RNR2 (Hs02596860g1), MT-CO2 (Hs02596865g1), and MT-CO3 (Hs02596866g1) were selected from the TaqMan gene expression assays (Thermo Fisher Scientific, Waltham, MA, USA). qRT-PCR was performed under the following amplification conditions: total volume 19,7 µl,

initial incubation at 50 °C/2 min followed by denaturation at 95 °C/10 min, then 15 cycles of preamplification (at 95 °C/15 s and 60 °C/1 min) and cooling down to 40 °C/30 s at the end. Subsequently, incubation at 50 °C/2 min followed by denaturation at 95 °C/10 min, 45 cycles of amplification (at 95 °C/15 s and 60 °C/1 min) and cooling down to 40 °C/30 s were done. qRT-PCR experiments were performed in duplicates.

Results

Autophagy induction by glutamine and FBS starvation or NVP-BEZ235 reduces ATP production in cancer cells but only gln starvation enhances oxidative damage

To verify the effect of selected treatments (NVP-BEZ235 and Gln + FBS starvation; further Gln starvation) on autophagy induction, we evaluated the expression of proteins involved in the autophagy machinery such as ULK1 and its phosphorylated forms pULK1Ser-556 and pULK1Ser-757 (phosphorylation of ULK1 at Ser-556 stimulates autophagy, whereas phosphorylation at Ser-757 is inhibitory), p62, GABARAP, and LC3 (see Fig. 1a and Supplementary Fig.S1). Both, NVP-BEZ235 and Gln starvation increased LC3II/I, GABARAPII/I ratio, and decreased Ser-757/ULK1 ratio indicating ULK1 activation and autophagy induction. The predominance of activatory ULK1 phosphorylation over inhibitory ULK1 phosphorylation in the form of an increased Ser-556/Ser-757 ratio was clearly observable in FaDu cells after the 12 h treatment with NVP-BEZ235 (hereafter BEZ). Gln starvation showed the effect on Ser-556/Ser-757 ratio later (after 24 h) (see Fig. 1b). These results suggest that if the content of EVs is to be affected by Gln starvation, their isolation must take place after at least 24 h of Gln starvation.

To assess the metabolic effects of Gln starvation and BEZ, we measured ATP production from glycolysis and OXPHOS based on the Seahorse (Agilent) parameters OCR (oxygen consumption rate) and ECAR (extracellular acidification rate). Both BEZ and Gln starvation decreased total ATP production. This observation supports the requirement of active mTOR for glycolysis and OXPHOS (see Fig. 1c). Furthermore, decreased proton leak was observable under both treatments. Gln starving cells had slightly increased coupling efficiency as compared to control cells (see Fig. 1c). Coupling efficiency is the proportion of the oxygen consumed to drive ATP synthesis compared with that driving proton leak.

We also observed that Gln-starvation leads to an increase in oxidative damage of cancer cells, particularly lipid peroxidation accompanied by depletion of the antioxidant defense protein GPX4 (see Fig. 2a and b). An increase in lipid peroxidation was indicated by a red to green fluorescence shift upon oxidation of BODIPY 581/591 C11 by lipid hydroperoxides. The mitochondrial network underwent significant remodeling during Gln deprivation, such as extensive fragmentation and swelling (see Fig. 2c). Furthermore, the levels of the mitophagy-related protein BNIP3 were increased after BEZ treatment and decreased by Gln starvation (see Fig. 2b), which could be a consequence of its degradation during mitophagy, where it is degraded together with damaged mitochondria. However, lower BNIP3 levels can be also associated with higher resistance to BNIP3-induced cell death. Therefore, we decided to perform confocal microscopy and evaluate the colocalization of mitochondria with BNIP3 and LC3 (a protein involved in autophagy substrate selection and autophagosome biogenesis).

Glutamine starvation fails to elevate mitophagy markers but increases colocalization of TSG101 with mitochondria. Autophagy induction alters the spectrum of EV-associated cytokines

Since the mitochondrial network underwent significant remodeling during Gln deprivation, we further investigated whether mitophagy was involved in this process. Gln starvation or BEZ did not increase the abundance of the mitophagy markers LC3, p62 and BNIP3 on the mitochondrial membrane (see Fig. 3a, b and c, and Supplementary **Fig. S2**). This means that mitochondria damaged by Gln starvation are unlikely to be removed by mitophagy and may contribute to increased oxidative stress in cancer cells. Nevertheless, the colocalization of BNIP3 with mitochondria was high in all tested cells (control, BEZ treatment and Gln starvation). Nevertheless, BNIP3 does not colocalize with LC3 (see Fig. 3c). The colocalization of TSG101 with mitochondria was significantly increased by Gln starvation (see Fig. 3c **and Fig. S3**) indicating sorting of mitochondrial cargo into EVs.

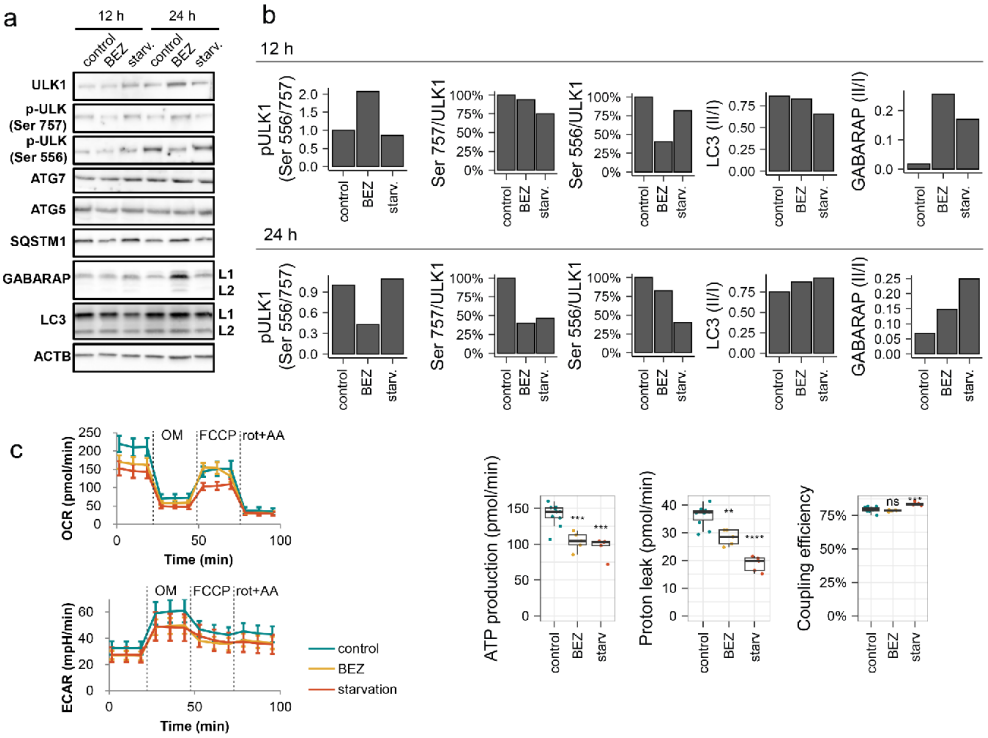

Fig. 1. ATP production in FaDu cells and expression of proteins involved in the autophagy machinery. (a) Expression of autophagy-related proteins ULK1 and its phosphorylated forms p-ULK1 (Ser 757) and p-ULK1 (Ser 556), ATG5, ATG7, SQSTM1, GABARAP, and LC3; p indicates phosphorylation. Uncropped western blots for this figure are shown in supplementary Fig. S1. (b) Densitometric analyzes: the ratio of ULK1 phosphorylation on Ser 757 to ULK1 expression; the ratio of ULK1 phosphorylation on Ser 556 to ULK1 expression; the ratio of ULK1 phosphorylation on Ser 556/ Ser 757; the ratio of GABARAP II/I; the ratio of LC3 II/I. (c) l ATP production based on Seahorse parameters OCR (oxygen consumption rate) and ECAR (extracellular acidification rate). OM = oligomycin; FCCP = carbonyl cyanide-p-trifluoromethoxyphenylhyd razone; rot = rotenone; AA = antimycin A. P-values from group comparisons based on the t-test are shown. Asterisks represent statistical significance (* $p < 0.05$; ** $p < 0.01$; *** $p < 0.001$).

Starving cells could promote TME reorganization by producing cytokines. Some of these cytokines can be associated with EVs (internally in EVs or membrane-bound). To assess small EVs-associated cytokines, conditioned medium (CM) without large EVs (up to 220 nm), apoptotic bodies, or free cytokines was prepared (see Fig. 4a and the Material and Methods section). We identified that the release of EVs-associated inflammatory cytokines is a primary response to autophagy induction and that the mechanism of this induction is important and significantly influences the composition of the EVs-associated cytokine secretome. We observed the up-regulation of IFNγ, IL-13, IL-1α, IL-15, I-309, IL-5, GM-CSF, TARC, RANTES, and IL-6 in response to Gln-starvation and BEZ compared to control cells. On the other hand, EVs-associated EGF and SDF-1 were down-regulated. Opposite effects of Gln-starvation and BEZ was also observed. IL-8, GRO-α, and IL-2 levels were decreased by starvation and increased by BEZ. On the other hand, thrombopoietin, oncostatin M, VEGF, and angiogenin levels were increased by starvation and decreased by BEZ. BEZ also enhanced EVs-associated levels of TNF-α and IL-1β (see Fig. 4b).

Glutamine starvation and NVP-BEZ235 decrease the production of EVs by cancer cells but do not change their characteristic EVs molecules

After NVP-BEZ235 treatment and/or Gln starvation, we have isolated small EVs produced by FaDu cells using the MagCapture Exosome Isolation Kit PS Ver 2. (FUJIFILM). Cryo-electron microscopy of non-collapsed extracellular vesicles and negative staining transmission electron microscopy demonstrated the native character of isolated vesicles, with an intact double membrane and cup-shaped morphology (see Fig. 4c). Their size

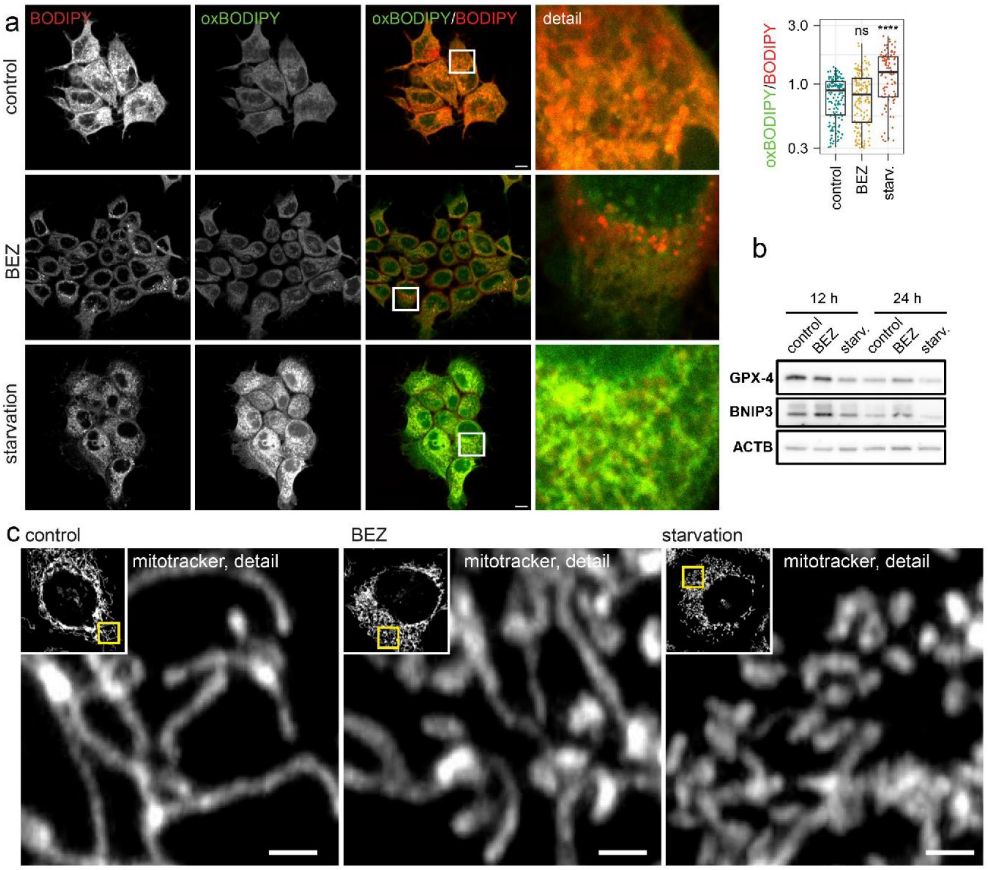

Fig. 2. An increase in lipid peroxidation accompanied by depletion of GPX4 and changes in the mitochondria after Gln-starvation. (a) Lipid peroxidation assessed by the Image-iT Lipid Peroxidation Kit; shift from red to green fluorescence is observable upon oxidation by lipid hydroperoxides. Scale bar: 10 µm, detail 20×20 µm. (b) Protein expression of antioxidant defense protein GPX4 and mitophagy-associated protein BNIP3. Uncropped western blots for this figure are shown in supplementary Fig. S1. (c) Changes in the mitochondrial network structure. MitoTracker Red stained mitochondria undergo significant remodeling during Gln deprivation such as extensive fragmentation and swelling. Scale bar:1 µm.

and concentration were assessed by NanoSight nanoparticle analyzer. The mode size of EVs produced during starvation was 138.7 nm (82.88×10^9 particles/ml). 137.1 nm for control (367.36×10^9 particles/ml), and 149.9 nm (246.96×10^9 particles/ml) for BEZ (see Fig. 4d). The mean size of EVs produced during starvation was 161.9 nm, 149.5 for control, and 156.1 for BEZ. Thus, Gln starvation and NVP-BEZ235 significantly decreased the production of EVs by cancer cells. For deeper characterization of isolated EVs, we performed WB. EVs after all treatments were positive for EpCAM, CD9, Cav-1, flotillin-1, annexin V, and TSG101 (see Fig. 4e). Lower expression of these proteins after Gln starvation is due to a lower concentration of EVs after starvation not because of reduced EpCAM expression in starved FaDu cells (see Fig. 4f). Due to the low protein concentration in the lysates from the isolated EVs, the concentrations of the samples loaded on the gel were not equilibrated. The aim was only to demonstrate sample positivity for selected markers of EVs, not to compare samples with each other.

Glutamine starvation alters the abundance of mitochondrial RNAs in EVs

In further experiments, the content of RNAs in EVs produced by FaDu cells was characterized under Gln starvation and NVP-BEZ-235 treatment. RNAs encoding proteins were the most abundant type of RNAs in EVs

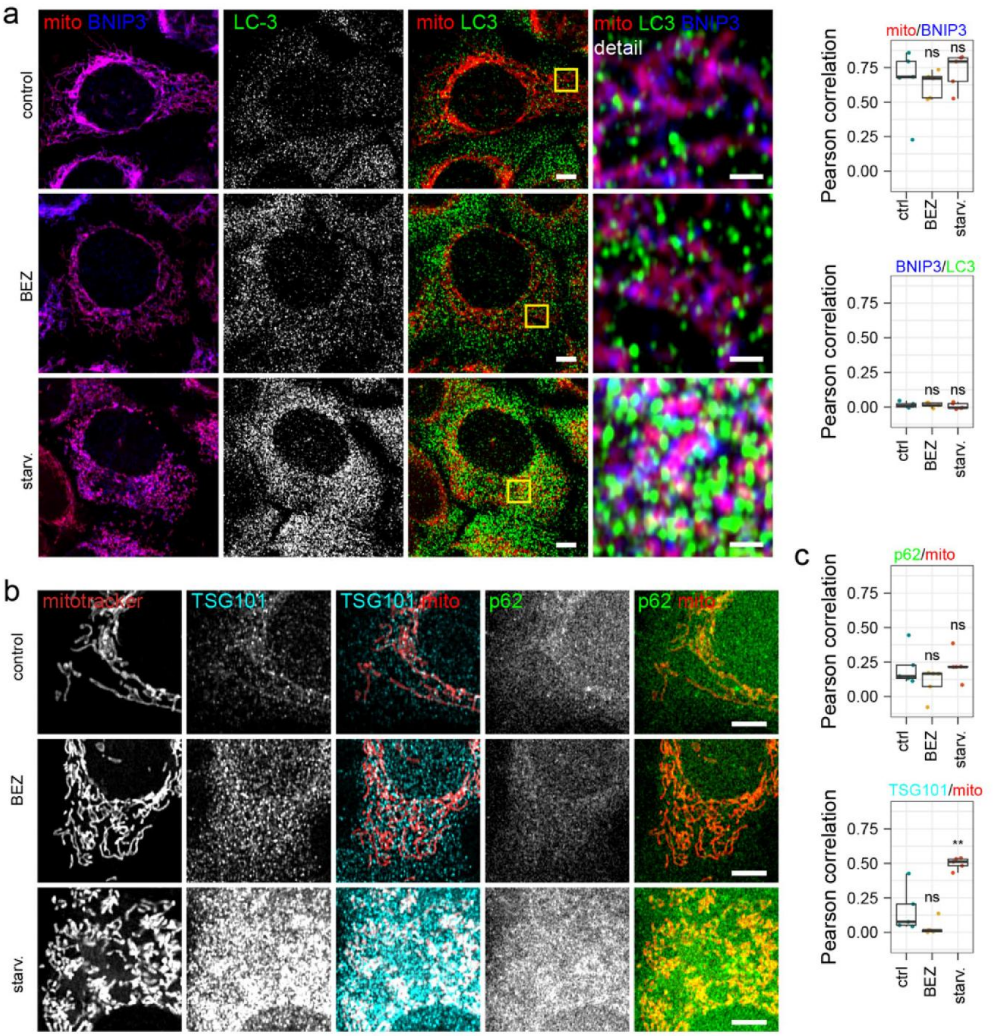

Fig. 3. Immunofluorescence images of FaDu cells under glutamine starvation or treated with NVP-BEZ235. MitoTracker Red, autophagy-related proteins, BNIP3 and TSG101. (a) Confocal immunofluorescence images of MitoTracker Red/BNIP3/LC3 and their mutual colocalization. Scale bar: 5 µm (detail 1 µm) (b) Confocal immunofluorescence images of MitoTracker Red and TSG101 colocalization, and MitoTracker Red and p62 colocalization. Scale bar: 5 µm (c) Pearson correlations depicting the rate of colocalization of BNIP3, LC3 p62, and TSG101 with mitochondria.

produced by FaDu cells. No statistically significant changes in the representation of main RNA biotypes in EVs produced by FaDu cells were found. Weak peaks of ribosomal RNA and miscellaneous RNA were also detected, but this was seen only in EVs produced by cells after Gln starvation (see Fig. 5a). RNA content of EVs was significantly affected by Gln starvation. The effect of PI3K/mTOR inhibitor NVP-BEZ-235 was nonsignificant (see Fig. 5b and supplementary **Fig. S4**). It implies that Gln starvation exerts a higher pressure to alter vesicular communication than induction of autophagy by BEZ. Gln starvation significantly affected the abundance of mitochondrial RNA (e.g., RNAs for NADH-ubiquinone oxidoreductase chains 1 to 6, for cytochrome B, for mitochondrially encoded cytochrome C oxidases I, II, and III, for mitochondrially encoded ATP synthase 6 and

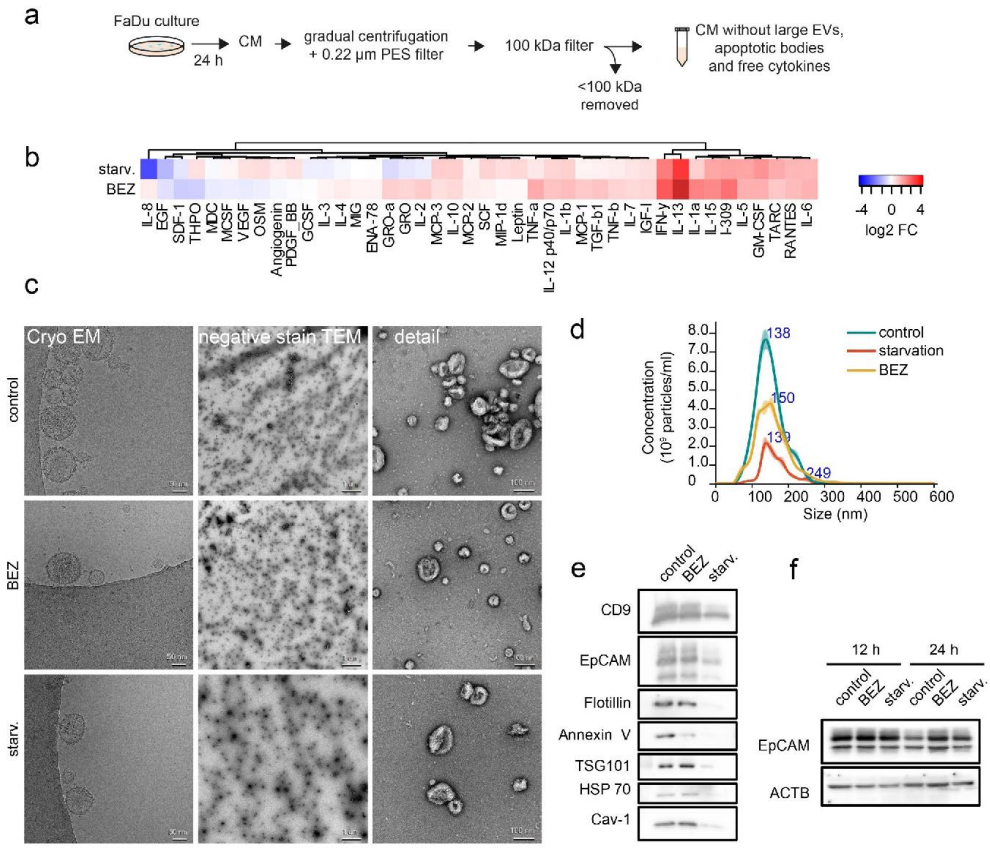

Fig. 4. Characterization of cytokines and extracellular vesicles produced by FaDu cells after NVP-BEZ235 treatment or glutamine starvation. (a) Conditioned media (CMs) preparation scheme. Large EVs (larger than 220 nm), apoptotic bodies, or free cytokines were removed during CM preparation. These CMs were used for the cytokine array.(b) Heatmap of normalized cytokine levels in CM after NVP-BEZ235 treatment or glutamine starvation. This CM should not contain large EVs (larger than 220 nm) apoptotic bodies or free cytokines. (c) (left column) Cryo-electron microscopy of non-collapsed extracellular vesicles demonstrating the native character of isolated vesicles with an apparently intact double membrane. Scale bar equals 50 nm. Negative staining transmission electron micrograph of cup-shaped extracellular vesicles. Shown is a heterogeneous population of vesicles consisting of a range of sizes (30–200 nm) with low densities typical for exosomes. Scale bar equals 1000 nm (the middle column) and 100 nm (the right column). TEM microscopy was performed on a fresh sample of EVs not subjected to freezing temperatures.(d) Size and concentration of EVs assessed by NanoSight nanoparticle analyzer. The sample was diluted 65x before measurement Numbers indicate peak size.(e) Characterization of isolated EVs. Protein expression of EpCAM CD9 Cav-1 flotillin-1 annexin V and TSG101. (f) Protein expression of EpCAM in FaDu cells. Uncropped western blots for this figure are shown in supplementary Fig. S1.

8, or mt-RNR1 and mt-RNR2); see Fig. 5b. According to the Gene Ontology (GO) pathway analyzis, the RNAs changed due to Gln starvation are involved in biological processes such as aerobic respiration, OXPHOS, purine nucleotide biosynthesis, or energy derivation by oxidation of organic compounds (see Fig. 5c).

Mitochondrial RNAs are detectable in EVs isolate from serum of HNSCC patients and healthy controls

A total of 41 patients with head and neck squamous cell cancers (age; median 61; interquartile range 52 to 72) and 20 healthy controls (age; median 55.5; interquartile range 50 to 61) were used in the study. The healthy cohort included men without a cancer diagnosis, diabetes, and/or chronic inflammatory diseases. The HNSCC

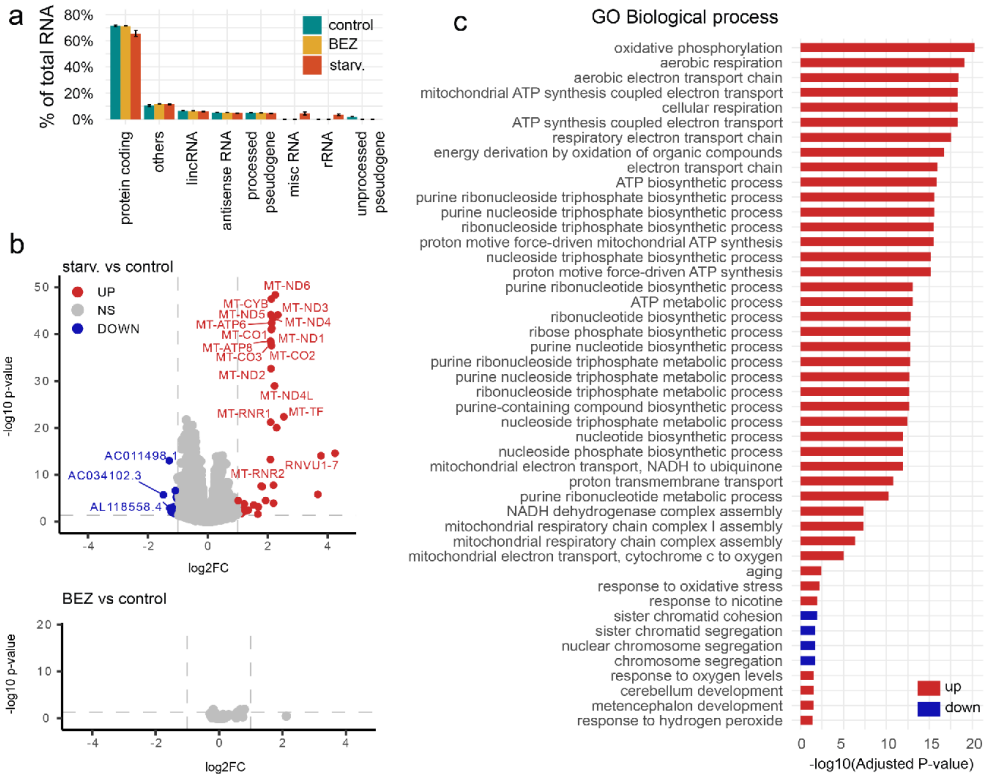

Fig. 5. The RNA content of EVs produced by FaDu cells and its changes after autophagy modulation. (a) Representation of different RNA biotypes in EVs produced by FaDu cells. Sequencing of each treatment variant was performed in tetraplex. (b) Volcano plot of changes in RNA content of FaDu-derived EVs due to Gln starvation and NVP-BEZ-235. Significant changes in expression are marked in red (upregulated; HC_log2FC > 1 and HC_padj <= 0.05) or blue (downregulated; HC_log2FC < 1 and HC_padj <= 0.05). FC = fold change, MT = mitochondrial.(c) Categories of biological processes from the GO database. Changes in biological processes which can be influenced by RNA cargo changes caused by Gln starvation.

patient cohort was defined as follows: squamous cell carcinoma histology, curative therapeutic intention using surgery +/− radio or radio/chemotherapy. Tumors with the following locations were included: oropharynx ($N=29$), larynx ($N=6$), hypopharynx ($N=1$), tongue ($N=4$), and the floor of the mouth ($N=1$). The p16 status was analyzed in all subjects. TNM8 system was used. The description of HNSCC patients is shown in Table 1. Exosomal RNA was isolated from blood serum of HNSCC patients and controls by exoRNeasy Maxi Kit (Qiagen). Expression of mtRNR1, mtRNR2, mt-CO2, and mt-CO3 was detected in both types of EVs, HNSCC patients-derived and healthy controls-derived. There was no statistically significant difference in the expression of the studied mtRNAs between patients and controls. The expression of studied mtRNAs was not associated with age, stage, or grade of HNSCC patients but was higher in patients with oropharyngeal cancer compared to other localizations; (see Fig. 6a **and b**).

Discussion

Induction of autophagy can be a very efficient survival mechanism for starved or stressed cancer cells and other cells in the TME. Induction of autophagy can also alter signaling between cells in the TME[25,26]and can cause TME reorganization[27]. It has been shown that different types of autophagy modulation can have different effects on signaling molecules produced by cancer cells[6]. Here, we studied metabolic and signaling consequences of glutamine (Gln) starvation-induced and NVP-BEZ235-induced autophagy in cancer cells. Both NVP-BEZ235 and Gln starvation decreased ATP production from glycolysis and OXPHOS. This observation supports the requirement of active mTOR for glycolysis[28,29]. It was shown that inhibition of the PI3K/mTOR pathway effectively suppressed glycolysis by preventing membrane localization of glucose transporter 1 (GLUT1)[28].

	Factor/Level	N
Gender		
	F	1
	M	40
Location		
	Floor of the mouth	1
	Larynx	6
	Oropharynx	29
	Tongue	4
	Hypopharynx	1
p16 status		
	p16 neg.	14
	p16 pos.	27
pT		
	1–2	30
	3–4	11
pN		
	< 2	35
	> 2	6
pM		
	0	40
	1	1
Stage		
	I–II	29
	III–IV	11
Smoking status		
	0	21
	1	20

Table 1. Clinico-pathological characterization of HNSCC patients.

mTORC1 also controls mitochondrial activity and biogenesis[30]. Autophagy induction by Gln starvation or NVP-BEZ235 reduces ATP production in cancer cells, but only Gln starvation enhances oxidative damage of cancer cells, particularly lipid peroxidation accompanied by depletion of the antioxidant defense protein GPX4 (GPX4 maintains mitochondrial membrane potential under oxidative stress)[31]and changes in the mitochondrial network structure. Tne mitochondrial network in Gln-starved cells became fragmented, which may be the result of increased oxidative stress[32,33]. Prasad et al. showed that Gln deficiency can promote stemness and chemoresistance in ovarian cancer cells through DRP1-induced mitochondrial fragmentation[34]. On the other hand, Abdullah et al. observed mitochondrial hyper-fusion in 4T1 breast cancer cells facing amino acid starvation[35]. This suggests that the effect of glutamine depletion is cancer type specific. FaDu cells express high levels of the *NFE2L2*mRNA, which encodes the Nrf2 protein[36]. Nrf2 induces the high expression of the cystine/glutamate antiporter SLC7A11 and promotes SLC7A11 membrane transfer[37,38]. Consequently, FaDu cells express high amount of SLC7A11[39]which facilitates the transport of cystine, supporting glutathione biosynthesis and preserving redox balance, thereby shielding cells from ferroptosis. Nonetheless, cancer cells exhibiting high SLC7A11 levels seem to be vulnerable to cell death induced by glucose or glutamine deprivation[40]. It is consistent with our findings that Gln starvation significantly increases oxidative damage in FaDu cells.

One of the strategies to get rid of damaged mitochondria that produce reactive oxidative species is mitophagy[41]. The colocalization of the mitophagy-related protein BNIP3 with mitochondria was high in all tested samples (control, BEZ treatment and Gln starvation). BNIP3 was shown to cause mitochondrial fission[42]and an increase in mitochondrial protease activity promoting degradation of mitochondrial proteins[43]. The protein levels of BNIP3 were increased after BEZ treatment and decreased by Gln starvation, which may be a consequence of its degradation during mitophagy, where it can be degraded together with damaged mitochondria[41] or it can reflect lower susceptibility of Gln starving cells to cell death induced by BNIP3[44]. Nevertheless, colocalization of BNIP3 with LC3 was low and Gln starvation or BEZ did not increase the abundance of the mitophagy markers LC3, p62 or BNIP3 on the mitochondrial membrane. This means that mitochondria damaged by Gln starvation are unlikely to be removed by mitophagy and may contribute to increased oxidative stress in cancer cells. However, the colocalization of TSG101 with mitochondria was significantly increased by Gln starvation (but not by BEZ) indicating the sorting of mitochondrial cargo into EVs[45,46]. Interestingly, we found an increase in mitochondrial RNAs in EVs produced by Gln-starved cells. In our previous study, we found that Gln starvation also increased mitochondrial protein levels in cancer cell-derived EVs[6]. This suggests that if damaged mitochondria and mitochondrial proteins are not sufficiently removed by mitophagy or autophagy, a compensatory mechanism in the form of increased exocytosis of these mitochondrial components (proteins, RNAs) by EVs may be involved[47].

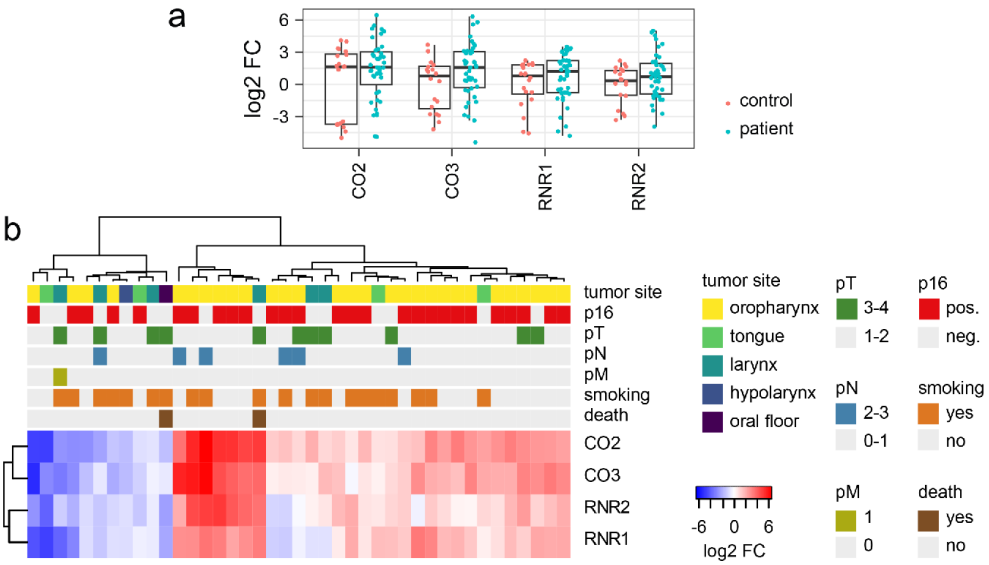

Fig. 6. Expression of mitochondrial RNAs in EVs isolated from sera of HNSCC patients and healthy controls. (a) Differential expression in HNSCC patients ($N=41$) and controls ($N=20$) did not reveal a significant difference in the expression of any of the analyzed genes. (b) Heatmap showing relationship with clinicopathological indicators. Shown as log 2-fold change (FC) relative to the mean of the controls. All selected genes show higher levels in the oropharyngeal location (vs. all other locations). See supplementary Table S1 for details.

TSG101 also binds to PARP1 and is required for PARP1 and NF-κB activation[48]. The level of mitochondrial RNAs in EVs was significantly affected by Gln starvation. The effect of PI3K/mTOR inhibitor NVP-BEZ-235 was nonsignificant. It implies that Gln starvation exerts a higher pressure to alter vesicular communication in the TME than simple PI3K/mTOR inhibition.

In addition to the reorganization of metabolism, we identified the release of EVs-associated inflammatory cytokines as a primary response to autophagy induction by BEZ or Gln starvation. This is consistent with the observation that starvation and antimetabolic therapy promote cytokine release and recruitment of immune cells[49]. For example, higher EVs-associated levels of IL-6, IFNγ, IL-13, IL-1α, TARC, and RANTES (CCL5) were observed in response to Gln-starvation and BEZ treatment. IL-6 plays an important role in angiogenesis in the TME[50]. Moreover, IL-6[51], IL-13[52], or TARC[53]can trigger proliferation of cancer cells. Signaling involving CCL5 and its receptor CCR5 can also promote tumor cell proliferation, induce collagen degradation by activating matrix metalloproteinases in macrophages and fibroblasts and enhance tumor cell migration and invasion by activating integrins and actin polarisation[54]. CCL5-CCR5 interaction can provide anti-apoptotic signals[55]. IL-1α can stimulate proliferation of cancer-associated fibroblasts (CAFs). CAFs then secrete CCL7, CXCL1, and IL-8 cytokines facilitating cancer progression and invasion[56]. Opposite effects of Gln-starvation and BEZ on cytokine production were also observed indicating that the mechanism of the autophagy induction is important and significantly influences the composition of the EVs-associated cytokine secretome. IL-8, GRO-α, and IL-2 levels were decreased by Gln starvation and increased by BEZ. BEZ also enhanced EVs-associated levels of TNF-α and IL-1β. The increased production of these cytokines may be related to the diarrhoea and mucositis reported following treatment with NVP-BEZ235 (dactolisib)[57]as IL-8, TNF-α and IL-1β were associated with post-radiation mucositis in cancer patients[58–60].

Glutamine starvation and NVP-BEZ235 treatment decreased the production of EVs by cancer cells but did not change their characteristic molecules. Fader et al. showed that the initiation of autophagy or the heightened expression of LC3 impeded the release of exosomes. Under circumstances promoting autophagy, the multivesicular bodies (MVBs) were directed toward fusion with autophagic vacuoles, leading to the subsequent inhibition of exosome release[61]. In further experiments, the content of RNAs in EVs produced by FaDu cells was characterized. RNAs encoding proteins were the most abundant type of RNAs in EVs produced by FaDu cells. A weak peak of ribosomal RNA was also detected, but this was only in EVs produced by cells after Gln starvation. RNA profiling performed by Crescitelli et al. showed that ribosomal RNA (rRNA) was primarily detectable in apoptotic bodies. Smaller RNAs without prominent peaks of rRNA were detectable in exosomes. In contrast, microvesicles contained little or no RNA[62]. Based on these facts and the molecules that were detected on the

EVs that we isolated, such as EpCAM, CD9, Cav-1, flotillin, annexin V, and TSG101, we can conclude that they are exosomes.

We found that Gln starvation enhances the abundance of mitochondrial RNAs in FaDu-derived EVs. The study by Dohl et al. showed that Gln depletion can disrupt mitochondrial integrity[63]. Mitochondrial damage may be more pronounced in FaDu cells because they are highly dependent on Gln[64]. Mitochondrial RNA or DNA from stressed mitochondria can be packaged into EVs and serve as an important signaling factor in the TME[65]. For example, packaging and transfer of mitochondrial DNA by EVs regulates the escape from dormancy in breast cancer[66]. Our results suggest that mitochondrial stress and reprogramming of cellular metabolism may be reflected in the molecular content of EVs. Head and neck squamous cell carcinomas (HNSCC) appear to be glutamine-dependent tumor types as HNSCC patients with low expression of glutaminase 1 (GLS1) have better disease-free survival after cancer treatment[64]. Since stress induced by glutamine deficiency is reflected in the abundance of mtRNAs in EVs, it can be concluded that these mtRNAs may be suitable markers of response to HNSCC therapy targeting the metabolic weaknesses of these tumors[67]. Here, we determined the expression of mitochondrial RNAs in EVs isolated from the serum of HNSCC patients and healthy controls. Expression of mtRNR1, mtRNR2, mt-CO2, and mt-CO3 was detected in both types of EVs, HNSCC patients-derived and healthy controls-derived, but there was no statistically significant difference in the expression of studied mt-RNAs between patients and controls. The expression of studied mt-RNAs was not associated with age, stage, or grade of HNSCC patients but was higher in patients with oropharyngeal cancer compared to other localizations.

Data availability

We have submitted all relevant data of our experiments to the EV-TRACK knowledgebase (EV-TRACK ID: EV231021)63. Confocal microscopy data are stored in the Zenodo depository, https://zenodo.org/records/10479096, DOI 10.5281/zenodo.10479096.

Received: 15 April 2024; Accepted: 23 September 2024
Published online: 28 October 2024

References

1. Briukhovetska, D. et al. Interleukins in cancer: from biology to therapy. *Nat. Rev. Cancer.* **21**, 481–499 (2021).
2. Raudenska, M., Balvan, J. & Masarik, M. Crosstalk between autophagy inhibitors and endosome-related secretory pathways: a challenge for autophagy-based treatment of solid cancers. *Mol. Cancer.* **20**, 140 (2021).
3. Zhao, J., Zhai, B., Gygi, S. P. & Goldberg, A. L. mTOR inhibition activates overall protein degradation by the ubiquitin proteasome system as well as by autophagy. *Proceedings of the National Academy of Sciences* 112, 15790–15797 (2015).
4. Tan, H. W. S., Sim, A. Y. L. & Long, Y. C. Glutamine metabolism regulates autophagy-dependent mTORC1 reactivation during amino acid starvation. *Nat. Commun.***8**, 338 (2017).
5. Zhu, Y. et al. L-Glutamine deprivation induces autophagy and alters the mTOR and MAPK signaling pathways in porcine intestinal epithelial cells. *Amino Acids.* **47**, 2185–2197 (2015).
6. Hanelova, K. et al. Autophagy modulators influence the content of important signalling molecules in PS-positive extracellular vesicles. *Cell Communication Signaling: CCS***21**, (2023).
7. Li, N. & Neu, J. Glutamine deprivation alters intestinal tight junctions via a PI3-K/Akt mediated pathway in Caco-2 cells. *J. Nutr.***139**, 710–714 (2009).
8. Shin, S. et al. mTOR inhibition reprograms cellular proteostasis by regulating eIF3D-mediated selective mRNA translation and promotes cell phenotype switching. *Cell. Rep.***42**, 112868 (2023).
9. Kucharzewska, P. et al. Exosomes reflect the hypoxic status of glioma cells and mediate hypoxia-dependent activation of vascular cells during tumor development. *Proc. Natl. Acad. Sci. U S A.* **110**, 7312–7317 (2013).
10. Zou, W. et al. Exosome Release is regulated by mTORC1. *Adv. Sci.***6**, 1801313 (2019).
11. Palikaras, K., Lionaki, E. & Tavernarakis, N. Balancing mitochondrial biogenesis and mitophagy to maintain energy metabolism homeostasis. *Cell. Death Differ.***22**, 1399–1401 (2015).
12. Marini, C. et al. Divergent targets of glycolysis and oxidative phosphorylation result in additive effects of metformin and starvation in colon and breast cancer. *Sci. Rep.***6**, 19569 (2016).
13. Lima, L. G. et al. Tumor microenvironmental cytokines bound to cancer exosomes determine uptake by cytokine receptor-expressing cells and biodistribution. *Nat. Commun.***12**, 3543 (2021).
14. Hõnigova, K. et al. Metabolic tricks of cancer cells. *Biochim. Biophys. Acta Rev. Cancer.* **1877**, 188705 (2022).
15. Schindelin, J. et al. Fiji: an open-source platform for biological-image analysis. *Nat. Methods.* **9**, 676–682 (2012).
16. Bolger, A. M., Lohse, M. & Usadel, B. Trimmomatic: a flexible trimmer for Illumina sequence data. *Bioinformatics.* **30**, 2114–2120 (2014).
17. Dobin, A. et al. STAR: ultrafast universal RNA-seq aligner. *Bioinformatics.* **29**, 15–21 (2013).
18. Wang, L., Wang, S. & Li, W. RSeQC: quality control of RNA-seq experiments. *Bioinformatics.* **28**, 2184–2185 (2012).
19. Okonechnikov, K., Conesa, A. & García-Alcalde, F. Qualimap 2: advanced multi-sample quality control for high-throughput sequencing data. *Bioinformatics.* **32**, 292–294 (2016).
20. Liao, Y., Smyth, G. K. & Shi, W. featureCounts: an efficient general purpose program for assigning sequence reads to genomic features. *Bioinformatics.* **30**, 923–930 (2014).
21. Love, M. I., Huber, W. & Anders, S. Moderated estimation of Fold change and dispersion for RNA-seq data with DESeq2. *Genome Biol.***15**, 550 (2014).
22. Wickham, H. et al. Welcome to the Tidyverse. *J. Open. Source Softw.***4**, 1686 (2019).
23. Wu, T. et al. clusterProfiler 4.0: a universal enrichment tool for interpreting omics data. *Innov. (Camb).* **2**, 100141 (2021).
24. Wickham, H. ggplot2. *WIREs Computational Statistics* 3, 180–185 (2011).
25. O'Donovan, T. R., O'Sullivan, G. C. & McKenna, S. L. Induction of autophagy by drug-resistant esophageal cancer cells promotes their survival and recovery following treatment with chemotherapeutics. *Autophagy.* **7**, 509–524 (2011).
26. Jena, B. C., Rout, L., Dey, A. & Mandal, M. Active autophagy in cancer-associated fibroblasts: recent advances in understanding the novel mechanism of tumor progression and therapeutic response. *J. Cell. Physiol.***236**, 7887–7902 (2021).
27. Bustos, S. O., Antunes, F., Rangel, M. C. & Chammas, R. Emerging autophagy functions shape the Tumor Microenvironment and play a role in Cancer Progression - implications for Cancer Therapy. *Front. Oncol.***10**, 606436 (2020).
28. Makinoshima, H. et al. Signaling through the phosphatidylinositol 3-Kinase (PI3K)/Mammalian target of Rapamycin (mTOR) Axis is responsible for aerobic glycolysis mediated by glucose transporter in Epidermal Growth Factor Receptor (EGFR)-mutated lung adenocarcinoma. *J. Biol. Chem.***290**, 17495–17504 (2015).

29. Yecies, J. L. & Manning, B. D. Transcriptional Control of Cellular Metabolism by mTOR Signaling. *Cancer Res.***71**, 2815–2820 (2011).
30. Morita, M. et al. mTORC1 controls mitochondrial activity and Biogenesis through 4E-BP-Dependent translational regulation. *Cell Metabol.***18**, 698–711 (2013).
31. Liang, H. et al. Gpx4 protects mitochondrial ATP generation against oxidative damage. *Biochem. Biophys. Res. Commun.***356**, 893–898 (2007).
32. Wu, S., Zhou, F., Zhang, Z. & Xing, D. Mitochondrial oxidative stress causes mitochondrial fragmentation via differential modulation of mitochondrial fission–fusion proteins. *FEBS J.***278**, 941–954 (2011).
33. Gwangwa, M. V., Joubert, A. M. & Visagie, M. H. Effects of glutamine deprivation on oxidative stress and cell survival in breast cell lines. *Biol. Res.***52**, 15 (2019).
34. Prasad, P., Ghosh, S. & Roy, S. S. Glutamine deficiency promotes stemness and chemoresistance in tumor cells through DRP1-induced mitochondrial fragmentation. *Cell. Mol. Life Sci.***78**, 4821–4845 (2021).
35. Abdullah, M. O. et al. Mitochondrial hyperfusion via metabolic sensing of regulatory amino acids. *Cell. Rep.***40**, 111198 (2022).
36. Peltanová, B. et al. mRNA subtype of Cancer-Associated fibroblasts significantly affects key characteristics of Head and Neck Cancer cells. *Cancers (Basel).* **14**, 2286 (2022).
37. Feng, L. et al. SLC7A11 regulated by NRF2 modulates esophageal squamous cell carcinoma radiosensitivity by inhibiting ferroptosis. *J. Transl Med.***19**, 367 (2021).
38. Liu, J. et al. Nrf2 and its dependent autophagy activation cooperatively counteract ferroptosis to alleviate acute liver injury. *Pharmacol. Res.***187**, 106563 (2023).
39. Chintala, S. et al. Downregulation of Cystine Transporter xc– by Irinotecan in Human Head and Neck Cancer FaDu xenografts. *Chemotherapy.* **56**, 223–233 (2010).
40. Zhang, C. et al. Crosstalk between ferroptosis and stress—implications in cancer therapeutic responses. *Cancer Innov.***1**, 92–113 (2022).
41. Field, J. T. & Gordon, J. W. BNIP3 and Nix: atypical regulators of cell fate. *Biochimica et Biophys. Acta (BBA) - Molecular Cell. Research.* **1869**, 119325 (2022).
42. Landes, T. et al. The BH3-only Bnip3 binds to the dynamin Opa1 to promote mitochondrial fragmentation and apoptosis by distinct mechanisms. *EMBO Rep.***11**, 459–465 (2010).
43. Rikka, S. et al. Bnip3 impairs mitochondrial bioenergetics and stimulates mitochondrial turnover. *Cell. Death Differ.***18**, 721–731 (2011).
44. Ma, Z. et al. BNIP3 induces apoptosis and protective autophagy under hypoxia in esophageal squamous cell carcinoma cell lines: BNIP3 regulates cell death. *Dis. Esophagus.* **30**, 1–8 (2017).
45. Garrus, J. E. et al. Tsg101 and the Vacuolar protein sorting pathway are essential for HIV-1 budding. *Cell.* **107**, 55–65 (2001).
46. Malerød, L. et al. Cargo-Dependent degradation of ESCRT-I as a feedback mechanism to modulate endosomal sorting. *Traffic.* **12**, 1211–1226 (2011).
47. Liang, W. et al. Mitochondria are secreted in extracellular vesicles when lysosomal function is impaired. *Nat. Commun.***14**, 5031 (2023).
48. Tufan, A. B. et al. TSG101 associates with PARP1 and is essential for PARylation and DNA damage-induced NF-κB activation. *EMBO J.***41**, e110372 (2022).
49. Püschel, F. et al. Starvation and antimetabolic therapy promote cytokine release and recruitment of immune cells. *Proc. Natl. Acad. Sci.***117**, 9932–9941 (2020).
50. Nagasaki, T. et al. Interleukin-6 released by colon cancer-associated fibroblasts is critical for tumour angiogenesis: anti-interleukin-6 receptor antibody suppressed angiogenesis and inhibited tumour–stroma interaction. *Br. J. Cancer.* **110**, 469–478 (2014).
51. Wang, Y., van Boxel-Dezaire, A. H. H., Cheon, H., Yang, J. & Stark, G. R. STAT3 activation in response to IL-6 is prolonged by the binding of IL-6 receptor to EGF receptor. *Proc. Natl. Acad. Sci.***110**, 16975–16980 (2013).
52. Matsui, S. et al. Interleukin-13 and its signaling pathway is associated with obesity-related colorectal tumorigenesis. *Cancer Sci.***110**, 2156–2165 (2019).
53. Goldie, S. J. et al. Loss of GRHL3 leads to TARC/CCL17-mediated keratinocyte proliferation in the epidermis. *Cell. Death Dis.***9**, 1–12 (2018).
54. Aldinucci, D., Borghese, C. & Casagrande, N. The CCL5/CCR5 Axis in Cancer Progression. *Cancers (Basel).* **12**, 1765 (2020).
55. Tyner, J. W. et al. CCL5-CCR5 interaction provides antiapoptotic signals for macrophage survival during viral infection. *Nat. Med.***11**, 1180–1187 (2005).
56. Bae, J. Y. et al. Reciprocal interaction between carcinoma-associated fibroblasts and squamous carcinoma cells through interleukin-1α induces cancer progression. *Neoplasia.* **16**, 928–938 (2014).
57. Pongas, G. & Fojo, T. BEZ235: when Promising Science meets clinical reality. *Oncologist.* **21**, 1033–1034 (2016).
58. Principe, S., Zapater-Latorre, E., Arribas, L., Garcia-Miragall, E. & Bagan, J. Salivary IL-8 as a putative predictive biomarker of radiotherapy response in head and neck cancer patients. *Clin. Oral Investig.* **26**, 437–448 (2022).
59. Sonis, S. T. Oral Mucositis in Head and Neck Cancer: Risk, Biology, and Management. *Am Soc Clin Oncol Educ Book* e236–e240 doi: (2013). https://doi.org/10.14694/EdBook_AM.2013.33.e236
60. Thornton, C. P., Kozachik, S. & Ruble, K. Study protocol to evaluate influences of stress and inflammation on Mucositis in adolescents and Young adults with Cancer. *Nurs. Res.***71**, 404–410 (2022).
61. Fader, C. M., Sánchez, D., Furlán, M. & Colombo, M. I. Induction of autophagy promotes fusion of multivesicular bodies with autophagic vacuoles in k562 cells. *Traffic.* **9**, 230–250 (2008).
62. Crescitelli, R. et al. Distinct RNA profiles in subpopulations of extracellular vesicles: apoptotic bodies, microvesicles and exosomes. *J. Extracell. Vesicles.* **2**, 20677 (2013).
63. Dohl, J. et al. Glutamine depletion disrupts mitochondrial integrity and impairs C2C12 myoblast proliferation, differentiation, and the heat-shock response. *Nutr. Res.***84**, 42–52 (2020).
64. Yang, J. et al. Targeting cellular metabolism to reduce head and neck cancer growth. *Sci. Rep.***9**, 4995 (2019).
65. Puhm, F. et al. Mitochondria are a subset of Extracellular vesicles released by activated monocytes and induce type I IFN and TNF responses in endothelial cells. *Circul. Res.***125**, 43–52 (2019).
66. Sansone, P. et al. Packaging and transfer of mitochondrial DNA via exosomes regulate escape from dormancy in hormonal therapy-resistant breast cancer. *Proceedings of the National Academy of Sciences* 114, E9066–E9075 (2017).
67. Lin, X., Zhou, W., Liu, Z., Cao, W. & Lin, C. Targeting cellular metabolism in head and neck cancer precision medicine era: a promising strategy to overcome therapy resistance. *Oral Dis.***29**, 3101–3120 (2023).
68. Van Deun, J. et al. EV-TRACK: transparent reporting and centralizing knowledge in extracellular vesicle research. *Nat. Methods.* **14**, 228–232 (2017).

Acknowledgements

We acknowledge the core facility CELLIM supported by MEYS CR (LM2018129 Czech-BioImaging). We acknowledge the support of the Cryo-electron Microscopy and Tomography Core Facility of CEITEC MU CII-SB, Instruct-CZ Centre supported by the Ministry of Education of the Czech Republic (LM2018127). We acknowledge the support of the Core Facility Genomics (CEITEC MU, CZ). We acknowledge the support of the

CzechNanoLab project at the CEITEC Nano Research Infrastructure Meys CR (LM2023051).

Author contributions

J.Ba., M.R. and M.M. designed the experimental plan; D.K., M.G., J. Be, J.P. collected serum samples and performed clinical characterization of HNSCC patients; K.H., J.N., M.B., S.H., and J.Ba. performed the biological experiments; J.G., T.V. and F.P. evaluated the NGS data and confocal microscopy data, performed statistical analyzis, and created figures. M.R., K.H., J.Ba. and M.B. evaluated the data and interpreted the results; M.R. and M.B. wrote the main text of the manuscript. J.Ba. supervised the manuscript.

Funding

This work was supported by the Ministry of Health of the Czech Republic (NU20J-08-00018 and NU21-03-00223) and by the Czech Science Foundation (GACR-21–06873 S).

Declarations

Competing interests

The authors declare no competing interests.

Additional information

Supplementary Information The online version contains supplementary material available at https://doi.org/10.1038/s41598-024-73943-2.

Correspondence and requests for materials should be addressed to J.B.

Reprints and permissions information is available at www.nature.com/reprints.

Publisher's note Springer Nature remains neutral with regard to jurisdictional claims in published maps and institutional affiliations.

Open Access This article is licensed under a Creative Commons Attribution-NonCommercial-NoDerivatives 4.0 International License, which permits any non-commercial use, sharing, distribution and reproduction in any medium or format, as long as you give appropriate credit to the original author(s) and the source, provide a link to the Creative Commons licence, and indicate if you modified the licensed material. You do not have permission under this licence to share adapted material derived from this article or parts of it. The images or other third party material in this article are included in the article's Creative Commons licence, unless indicated otherwise in a credit line to the material. If material is not included in the article's Creative Commons licence and your intended use is not permitted by statutory regulation or exceeds the permitted use, you will need to obtain permission directly from the copyright holder. To view a copy of this licence, visit http://creativecommons.org/licenses/by-nc-nd/4.0/.

© The Author(s) 2024

5 Discussion

Cell death processes are integral to maintaining tissue homeostasis, ensuring proper development, and preventing the emergence of malignancies [18]. These mechanisms, primarily apoptosis but also necroptosis, pyroptosis, and autophagic cell death, operate as vital quality control systems to eliminate damaged, infected, or potentially oncogenic cells [5]. Their precise regulation is crucial not only for normal physiology but also for preventing tumorigenesis. Consequently, the failure or evasion of cell death pathways is a hallmark of cancer, contributing to uncontrolled proliferation, metastatic spread, and resistance to therapies [5, 19].

In recent decades, important discoveries have been made in the field of cell death. Lytic cell death processes such as necroptosis, pyroptosis and ferroptosis have been described as regulated and genetically encoded [18]. This challenges the long-held belief that necrosis is an unregulated form of cell death. These processes are of great importance in the pathology and pathophysiology of chronic inflammatory [20], autoimmune [21] and cancer diseases [19], which highlights the need to summarize the results of this research and make them available to scientists, physicians and students. We hope that our review papers and published books have contributed to this important task, helping to refute confusing data, particularly in Czech scientific literature and study materials.

In oncology, understanding the types and dynamics of cell death is indispensable for diagnosis, prognosis, and monitoring treatment efficacy [22]. The ability to accurately detect and distinguish these death modalities in tumor tissues or cell models enables clinicians and researchers to evaluate therapeutic responses and mechanisms of resistance. The development of sophisticated detection methods, ranging from molecular assays to advanced imaging, has significantly enhanced our capacity to observe cell death as it unfolds in real time, providing insights into cellular heterogeneity and the temporal sequence of death-related events. For example, traditional biochemical assays such as flow cytometry with annexin V/PI staining, TUNEL, and caspase activity measurement are broadly used but often limited to endpoint analysis [9, 23]. Their static nature and inability to reliably differentiate overlapping death pathways reduce their applicability in complex tumor environments where multiple dying cell populations coexist. Recent technological advancements have introduced the possibility of live-cell, label-free imaging, such as quantitative phase imaging (QPI), which, when combined with machine

learning algorithms, enables continuous, dynamic assessment of cellular morphology and biophysical properties [10]. This approach provides unprecedented resolution of early morphological alterations such as membrane blebbing, cell shrinkage or swelling, nuclear condensation, before molecular markers become detectable, thus improving diagnostic precision and assay sensitivity.

Such innovative methodologies advance our understanding of how tumors evade cell death, facilitating the development of therapies that can overcome resistance. Furthermore, in the pharmaceutical domain, these imaging techniques are instrumental in preclinical screening, allowing high-throughput, real-time evaluation of drug candidates' capacities to induce desired cell death modalities [22]. Our method, which involves capturing dynamic changes in cell mass distribution within the segmented cell population area mask, is one of the few, if not the only, label-free methods capable of detecting cell death and distinguishing apoptosis from lytic death. Our concept of "Cell Dynamic Score", CDS [24], represents an important parameter describing the behavior of a cell population over time. Its increase during certain processes, such as cell division and apoptosis, can further serve to detect these processes and, overall, to better characterize the dynamics of cell population over time. Our approach demonstrated the ability to differentiate not only between apoptosis and lytic death, but also between the various types of lytic cell death (necroptosis, ferroptosis and apoptosis). Our data confirmed that we have not yet reached the full potential of this method. However, it should be noted that this method is only applicable *in vitro*, which highlights the long-standing issue of detecting cell death *in vivo*, particularly in patients [18].

A significant obstacle in effective cancer treatment remains the tumor’s capacity to develop resistance to cell death. Cancer cells activate an array of adaptive mechanisms that disable or bypass apoptosis, often through genetic changes such as mutations in TP53 [25], amplification of anti-apoptotic genes [26], or alterations that affect death receptor signaling. These alterations enable malignant cells to survive despite exposure to chemotherapy, radiotherapy, and targeted agents, leading to treatment failure and disease progression [3]. Across a wide spectrum of solid tumors, cancer cells develop sophisticated mechanisms to evade cell death, not only by disabling core apoptotic machinery but also by reprogramming stress responses, modifying intracellular degradation pathways, and engaging in active intercellular communication [3, 27, 28]. These adaptations enable tumor cells to survive under therapeutic pressure and to persist in hostile microenvironments, including those shaped by immune attack or metabolic deprivation. Among these survival strategies, autophagy emerges not solely as a form of regulated cell death but as a highly context-dependent process that may promote either survival or demise [14, 29]. In

many tumor types, autophagy is upregulated in response to cytotoxic stress and contributes to resistance by preserving the cellular energy balance and removing damaged organelles. Rather than serving as an executioner of death, it often acts as a buffer that delays or prevents irreversible cellular collapse [30].

Tumor cells use autophagy as a defense mechanism against reactive oxygen species generated by intense metabolism. This is important because many cytostatics cause the production of reactive oxygen species as a side effect of their action. We found that increased autophagy in a metastatic prostate cell line precedes the formation of polyploid cells, cell fusion, the formation of cell-in-cell structures, and an increase in the pluripotency markers NANOG, SOX, and POU5, which may be markers of self-renewal of the cell population leading to a resistant phenotype [31].

Given that endosomal and autophagic mechanisms share certain components, it is easy to see cellular secretion and autophagy as complementary processes, especially with regard to handling cellular waste, such as ROS-damaged mitochondria. Under metabolic stress, cancer cells release phosphatidylserine-positive extracellular vesicles enriched with mitochondrial RNAs, autophagy-related proteins, and specific cytokines. Lysosomal inhibitors such as BAFA1 and HCQ promote the inclusion of p62 into PS+EVs [32], while glutamine and serum starvation induce mitochondrial fragmentation and TSG101 recruitment, enhancing mtRNA loading into EVs [33]. Cancer cells can also alter lysosomal function in fibroblasts, an effect partially reversed by CPD18. Autophagy modulates both EV quantity and content, and these vesicles influence fibroblast metabolism, autophagic flux, and senescence markers [32]. These findings highlight a feedback loop through which tumor metabolic status reprograms the surrounding stroma, sustaining a pro-tumorigenic microenvironment. PS+EVs serve not only as carriers of oncogenic cargo and modulators of the tumor microenvironment but also as dynamic indicators of cellular stress states. Phosphatidylserine (PS), a lipid normally confined to the inner plasma membrane but externalized during apoptosis [17, 34], PS-positivity of EVs provides a compelling mechanistic link between cell death and vesicle-mediated communication.

EVs On one hand, PS serves as a classical “eat-me” signal during apoptosis, marking cells for clearance by phagocytes. On the other, its presence on tumor-derived EVs may enable immune evasion by mimicking apoptotic bodies or modulating recipient cell behavior through PS-sensitive pathways. Moreover, the increased release of PS+EVs under cytotoxic stress suggests that tumor cells use regulated cell death not only to limit their population but also to generate signaling vesicles that promote resistance and adaptation in surviving cells[17].

Our research in the field of extracellular vesicles provide valuable insights into the role of cellular secretion in eliminating damaged organelles or toxic molecules, such as hydroxychloroquine and other lysosomal inhibitors. Although agents that block autophagic flux typically alter the PS+EV proteome significantly, it is surprising that none of the autophagy-stimulating agents we used, such as mTORC1 kinase inhibitors, altered the PS+EV proteome. Consistent with the current literature, these data points to an interconnection between the process of cellular secretion and autophagy-mediated lysosomal degradation in the handling of cellular waste and toxic material.

It should also be noted that my activities in the EV field extend beyond scientific research and work. I am one of the founding members of the Czech Society for Extracellular Vesicles, established in 2023. Our activities in this area, such as organising international conferences and workshops, facilitate the exchange of scientific results on an international level. They also increase the international visibility of our results and enable the exchange of methodological approaches and experience. In particular, they increase the mobility of scientists within European laboratories involved in the MOVE (Mobility for Extracellular Vesicle Research) programme, in which we also actively participate.

6 Conclusion

This thesis mainly describes the results of my scientific activity since completing my PhD. Starting with cell death in cancer cells and methodologies for its detection by innovative microscopic methods, I then moved on to mechanisms of cancer cell resistance, particularly autophagy. Finally, I addressed the issue of extracellular vesicles (EVs), which represent a link between the previous thematic areas. I have optimised and implemented many methodological approaches in the laboratory, including purification, characterisation, and assessment of the biological effect of EVs. Through our close collaboration with clinical partners, particularly Motol University Hospital, we want to align our research with the practical needs of clinicians. Moving forward, we aim to apply our findings, especially in the field of cancer biomarkers, to improve the diagnosis of head and neck squamous cell carcinoma (HNSCC) patients. One planned direction involves analyzing the proteomic composition of extracellular vesicles (EVs) isolated from the serum of patients after radiotherapy. This approach may help evaluate treatment responses and identify the types of cell death triggered by therapy, based on specific death-associated markers present in the EVs. Another key area of our research focuses on identifying urgently needed diagnostic biomarkers for HNSCC in EVs derived from saliva, including the development of a clinically applicable device for their detection (in collaboration with ESSENCE LINE, s.r.o., with whom I collaborated in the TAČR project; FW03010186).

In summary, I would like to emphasise that research on cell death and extracellular vesicles has grown tremendously in recent decades. To make the best use of the large amount of data obtained, it is necessary to make this important information available to a wider professional audience, particularly medical and science students, as persisting dogmas can be harmful in certain circumstances. I took active steps in this direction and wrote a book entitled: Buněčná smrt: její význam ve fyziologii a patologické fyziologii; ISBN: 978-80-271-1260-9.

7 References

1. Balvan J, Raudenská M, Masařík M. *Buněčná smrt a její význam ve fyziologii a patologické fyziologii*. Grada Publishing, a.s.: Praha, 2021.

2. Kerr JF, Wyllie AH, Currie AR. Apoptosis: a basic biological phenomenon with wide-ranging implications in tissue kinetics. *British journal of cancer* 1972, **26**(4)**:** 239-257.

3. Strasser A, Vaux DL. Cell Death in the Origin and Treatment of Cancer. *Molecular Cell* 2020, **78**(6)**:** 1045-1054.

4. Galluzzi L, Vitale I, Aaronson SA, Abrams JM, Adam D, Agostinis P*, et al.* Molecular mechanisms of cell death: recommendations of the Nomenclature Committee on Cell Death 2018. *Cell Death and Differentiation* 2018, **25**(3)**:** 486-541.

5. Zhang M, Lin Y, Chen R, Yu H, Li Y, Chen M*, et al.* Ghost messages: cell death signals spread. *Cell Communication and Signaling* 2023, **21**(1)**:** 6.

6. Théry C, Witwer KW, Aikawa E, Alcaraz MJ, Anderson JD, Andriantsitohaina R*, et al.* Minimal information for studies of extracellular vesicles 2018 (MISEV2018): a position statement of the International Society for Extracellular Vesicles and update of the MISEV2014 guidelines. *Journal of Extracellular Vesicles* 2018, **7**(1)**:** 1535750.

7. Kalluri R, McAndrews KM. The role of extracellular vesicles in cancer. *Cell* 2023, **186**(8)**:** 1610-1626.

8. Kumar MA, Baba SK, Sadida HQ, Marzooqi SA, Jerobin J, Altemani FH*, et al.* Extracellular vesicles as tools and targets in therapy for diseases. *Signal Transduction and Targeted Therapy* 2024, **9**(1)**:** 27.

9. Balvan J, Krizova A, Gumulec J, Raudenska M, Sladek Z, Sedlackova M*, et al.* Multimodal holographic microscopy: Distinction between apoptosis and oncosis. *PLoS ONE* 2015, **10**(3).

10. Vicar T, Raudenska M, Gumulec J, Balvan J. The Quantitative-Phase Dynamics of Apoptosis and Lytic Cell Death. *Scientific Reports* 2020, **10**(1)**:** 1566.

11. Mizushima N, Levine B. Autophagy in Human Diseases. *New England Journal of Medicine* 2020, **383**(16)**:** 1564-1576.

12. Shintani T, Klionsky DJ. Autophagy in health and disease: A double-edged sword. *Science* 2004, **306**(5698)**:** 990-995.

13. Farhan H, Kundu M, Ferro-Novick S. The link between autophagy and secretion: a story of multitasking proteins. *Molecular biology of the cell* 2017, **28**(9)**:** 1161-1164.

14. Denton D, Kumar S. Autophagy-dependent cell death. *Cell Death & Differentiation* 2019, **26**(4)**:** 605-616.

15. Leidal AM, Debnath J. Emerging roles for the autophagy machinery in extracellular vesicle biogenesis and secretion. *FASEB BioAdvances* 2021, **3**(5)**:** 377-386.

16. Clarke AJ, Simon AK. Autophagy in the renewal, differentiation and homeostasis of immune cells. *Nature Reviews Immunology* 2018.

17. Birge RB, Boeltz S, Kumar S, Carlson J, Wanderley J, Calianese D*, et al.* Phosphatidylserine is a global immunosuppressive signal in efferocytosis, infectious disease, and cancer. *Cell Death & Differentiation* 2016, **23**(6)**:** 962-978.

18. Green DR. Cell death: Revisiting the roads to ruin. *Developmental Cell* 2024, **59**(19)**:** 2523-2531.

19. Raudenská M, Balvan J, Masařík M. Cell death in head and neck cancer pathogenesis and treatment. *Cell Death and Disease* 2021, **12**(2).

20. Galluzzi L, Buque A, Kepp O, Zitvogel L, Kroemer G. Immunogenic cell death in cancer and infectious disease. *Nature Reviews Immunology* 2017, **17**(2)**:** 97-111.

21. Singh R, Letai A, Sarosiek K. Regulation of apoptosis in health and disease: the balancing act of BCL-2 family proteins. *Nature Reviews Molecular Cell Biology* 2019, **20**(3)**:** 175-193.

22. Ahmed A, Tait SWG. Targeting immunogenic cell death in cancer. *Molecular Oncology* 2020, **14**(12)**:** 2994-3006.

23. Pavillon N, Kuehn J, Moratal C, Jourdain P, Depeursinge C, Magistretti PJ*, et al.* Early Cell Death Detection with Digital Holographic Microscopy. *Plos One* 2012, **7**(1).

24. Vicar T, Raudenska M, Gumulec J, Balvan J. The Quantitative-Phase Dynamics of Apoptosis and Lytic Cell Death. *Sci Rep* 2020, **10**(1)**:** 1566.

25. Sullivan KD, Palaniappan VV, Espinosa JM. ATM regulates cell fate choice upon p53 activation by modulating mitochondrial turnover and ROS levels. *Cell Cycle* 2015, **14**(1)**:** 56-63.

26. Panov A, Orynbayeva Z. Bioenergetic and Antiapoptotic Properties of Mitochondria from Cultured Human Prostate Cancer Cell Lines PC-3, DU145 and LNCaP. *Plos One* 2013, **8**(8).

27. Cao J, Zhang M, Xie F, Lou J, Zhou X, Zhang L*, et al.* Exosomes in head and neck cancer: Roles, mechanisms and applications. *Cancer Letters* 2020, **494:** 7-16.

28. Noman ASM, Parag RR, Rashid MI, Islam S, Rahman MZ, Chowdhury AA*, et al.* Chemotherapeutic resistance of head and neck squamous cell carcinoma is mediated by EpCAM induction driven by IL-6/p62 associated Nrf2-antioxidant pathway activation. *Cell Death & Disease* 2020, **11**(8)**:** 663.

29. Kimmelman AC, White E. Autophagy and Tumor Metabolism. *Cell Metabolism* 2017, **25**(5)**:** 1037-1043.

30. Sannigrahi MK, Singh V, Sharma R, Panda NK, Khullar M. Role of autophagy in head and neck cancer and therapeutic resistance. *Oral Diseases* 2015, **21**(3)**:** 283-291.

31. Balvan J, Gumulec J, Raudenska M, Krizova A, Stepka P, Babula P*, et al.* Oxidative stress resistance in metastatic prostate cancer: Renewal by self-eating. *PLoS ONE* 2015, **10**(12).

32. Hanelova K, Raudenska M, Kratochvilova M, Navratil J, Vicar T, Bugajova M*, et al.* Autophagy modulators influence the content of important signalling molecules in PS-positive extracellular vesicles. *Cell Communication and Signaling* 2023, **21**(1)**:** 120.

33. Bugajova M, Raudenska M, Hanelova K, Navratil J, Gumulec J, Petrlak F*, et al.* Glutamine and serum starvation alters the ATP production, oxidative stress, and abundance of mitochondrial RNAs in extracellular vesicles produced by cancer cells. *Scientific Reports* 2024, **14**(1)**:** 25815.

34. Suzuki J, Imanishi E, Nagata S. Exposure of phosphatidylserine by Xk-related protein family members during apoptosis. *The Journal of biological chemistry* 2014, **289**(44)**:** 30257-30267.